THE KINEMATICS AND VELOCITY ELLIPSOID OF THE G III STARS
R. L. Branham Jr. 197

SPECKLE INTERFEROMETRY AT THE OBSERVATORIO ASTRONÓMICO NACIONAL. III
V. G. Orlov, V. V. Voitsekhovich, C. A. Guerrero, F. Ángeles, A. Farah Simon, E. Luna, & R. Vázquez Robledo 211

UPPER MAIN SEQUENCE STARS WITH ANOMALOUS ABUNDANCES. THE HGMN STARS HR 3273, HR 8118, HR 8567 AND HR 8937
C. Saffe, N. Núñez, & H. Levato 219

ON THE STELLAR AND BARYONIC MASS FRACTIONS OF CENTRAL BLUE AND RED GALAXIES
A. Rodríguez-Puebla, V. Avila-Reese, C. Firmani, & P. Colín 235

SPECTRAL MORPHOLOGY AND ROTATION IN THE OPEN CLUSTER NGC 6025 *M. Grosso & H. Levato* 255

WIND STRUCTURE OF THE WOLF-RAYET STAR EZ CMA=HD 50896
A. Flores, G. Koenigsberger, O. Cardona, & L. de la Cruz 261

VARIABLE JETS WITH NON-TOP HAT EJECTION CROSS SECTIONS: A MODEL FOR THE KNOTS OF THE HH 34 JET
A. C. Raga, A. Noriega-Crespo, P. Kajdic, F. De Colle, D. López-Cámara, & A. Esquivel 277

AN INTEPRETIVE BALLISTIC MODEL FOR QUASI-SYMMETRIC BIPOLAR JET SYSTEMS
A. C. Raga, A. Noriega-Crespo, J. C. Rodríguez-Ramírez, V. Lora, K. R. Stappelfeldt, & S. J. Carey 289

V1898 CYGNI: AN INTERACTING ECLIPSING BINARY IN THE VICINITY OF NORTH AMERICA NEBULA
A. Dervişoğlu, Ö. Çakırlı, C. İbanoğlu, & E. Sipahi 297

$UVBY-\beta$ PHOTOELECTRIC PHOTOMETRY OF THE OPEN CLUSTERS NGC 6811 AND NGC 6830
J. H. Peña, L. Fox Machado, H. García, A. Rentería, S. Skinner, A. Espinosa, & E. Romero 309

THE COMETARY CAVITY CREATED BY AN ALIGNED STREAMING ENVIRONMENT/COLLIMATED OUTFLOW INTERACTION
D. López-Cámara, A. Esquivel, J. Cantó, A. C. Raga, P. F. Velázquez, & A. Rodríguez-González 323

CONTENTS

THE PROPER MOTION OF THE LARGE MAGELLANIC CLOUD REVISITED *M. H. Pedreros* 333

SPACE REDDENINGS FOR FIFTEEN GALACTIC CEPHEIDS *D. G. Turner, R. F. MacLellan, A. A. Henden, & L. N. Berdnikov* 345

MISSING SEYFERT GALAXIES *H. M. Tovmassian & O. Yam* 357

THE NATURE AND ORIGIN OF NARROW LINE AGN ACTIVITY IN A SAMPLE OF ISOLATED SDSS GALAXIES *R. Coziol, J. P. Torres-Papaqui, I. Plauchu-Frayn, J. M. Islas-Islas, R. A. Ortega-Minakata, D. M. Neri-Larios, & H. Andernach* 361

KINEMATICS FROM SPECTRAL LINES FOR AGN OUTFLOWS BASED ON TIME-INDEPENDENT RADIATION-DRIVEN WIND THEORY *J. M. Ramírez* 385

KINEMATIC AGES OF THE CENTRAL STARS OF PLANETARY NEBULAE *W. J. Maciel, T. S. Rodrigues, & R. D. D. Costa* 401

ATMOSPHERIC AEROSOL VARIABILITY OVER THE REGION OF SAN PEDRO MÁRTIR FROM MODIS DATA *M. R. Araiza Quijano & I. Cruz-González* 409

AN OVERVIEW OF THE OBSERVATIONAL AND THEORETICAL STUDIES OF HH 1 AND 2 *A. C. Raga, B. Reipurth, J. Cantó, M. M. Sierra-Flores, & M. V. Guzmán* 425

OBITUARY – JOHN PETER PHILLIPS *S. Kemp, S. G. Navarro, & L. J. Corral* 439

OBITUARY – ALFONSO SERRANO *A. Carramiñana* 441

AUTHOR INDEX 443

Revista Mexicana de Astronomía y Astrofísica, **47**, 197–209 (2011)

THE KINEMATICS AND VELOCITY ELLIPSOID OF THE G III STARS

Richard L. Branham, Jr.

Instituto Argentino de Nivología, Glaciología y Ciencias Ambientales, Argentina

Received 2010 October 27; accepted 2011 March 10

RESUMEN

Para estudiar la cinemática de las estrellas G gigante (clase de luminosidad III) se usan movimientos propios y paralajes de 3,075 estrellas, de las cuales 658 tienen velocidades radiales. Estas estrellas provienen de la reducción nueva hecha por van Leeuwen del catálogo Hipparcos. La solución da para la velocidad solar 16.72 ± 0.41 km s^{-1}; para las constantes de Oort, en unidades de km s^{-1} kpc^{-1}, $A = 14.05 \pm 3.28$ y $B = -9.30 \pm 2.87$, valores que representan una velocidad local de rotación de 198.48 ± 26.95 km s^{-1} si suponemos una distancia al centro Galáctico de 8.2 ± 1.1 kpc. Para las dispersiones de velocidades obtenemos, en unidades de km s^{-1}: $\sigma_x = 51.78 \pm 0.55$, $\sigma_y = 42.81 \pm 0.32$, $\sigma_z = 28.45 \pm 0.22$ con una desviación del vértice de $3.^\circ88 \pm 6.^\circ62$. Una comparasión de esta dispersión con las obtenidas de otras clases espectrales indica que la discontinuidad de Parengo existe también para las estrellas gigantes.

ABSTRACT

To study the kinematics of the G giant stars (luminosity class III) use is made of proper motions and parallaxes taken from van Leeuwen's new reduction of the Hipparcos catalog. 3,075 stars, of which 658 have radial velocities, were used in the final study. The solution gives: solar velocity of 16.72 ± 0.41 km s^{-1}; Oort's constant's, in units of km s^{-1} kpc^{-1}, $A = 14.05 \pm 3.28$ and $B = -9.30 \pm 2.87$, implying a rotational velocity of 198.48 ± 26.95 km s^{-1} if we take the distance to the Galactic center as 8.2 ± 1.1 kpc; velocity dispersions, in units of km s^{-1}, of: $\sigma_x = 51.78 \pm 0.55$, $\sigma_y = 42.81 \pm 0.32$, $\sigma_z = 28.45 \pm 0.22$ with a vertex deviation of $3.^\circ88 \pm 6.^\circ62$. A comparison of the velocity dispersions with those given by other spectral types shows that Parenago's discontinuity also exists for the giant stars.

Key Words: Galaxy: kinematics and dynamics — methods: numerical

1. INTRODUCTION

This paper continues a series on the kinematics and velocity ellipsoids of the giant stars (luminosity class III). Previously studied were the O-B5 giants (Branham 2006), the M giants (Branham 2008), the B6-9 and A giants (Branham 2009a), the K giants (Branham 2009b), and the F giants (Branham 2010). The G giants fill the remaining lacuna and complete the investigation of all of the giant stars. A search of the ADS data base[1] shows that the G giants as a group have not been studied since the research of Parenago in 1951 (Delhaye 1965), which adds impetus to this current study.

The methodology remains similar to that for the previous studies, so similar that I will eschew presentation of the mathematical development and refer the reader to the relevant previous publications where the necessary equations can be found. As in my investigation of the F giants the velocity ellipsoid calculation uses the singular value decomposition (SVD) to include stars for which only tangential velocities, but no radial velocities, are available. The section on the equations of condition briefly discusses this matter.

[1] `http://adswww.harvard.edu/`.

Little evidence exists to suggest that G stars form part of the Gould belt. There appears to be a clean break between the O-B stars and the later spectral types regarding participation in the Gould belt; O-B stars have definite Gould belt members whereas the others do not. Nevertheless, a plane will be fit to the G giants in a later section, but to examine the randomness of the data, not to infer that some G giants actually belong to the Gould belt.

To summarize briefly the mathematical procedure used, one solves for the kinematics and velocity ellipsoid of the G giants by use of semi-definite programming (SDP), which forces the solar motion calculated from the velocity ellipsoid to be the same as that calculated from the kinematical parameters. Nor is it necessary to use the same adjustment criterion for the two sets of calculations: the kinematical parameters may be reduced by use of a least squares criterion whereas the velocity ellipsoid may be calculated with the robust L_1 criterion (minimize the sum of the absolute values of the residuals), or with the same L_1 criterion for both. For a readable discussion of SDP see Vandenberge & Boyd (1996).

In their classical work *Statistical Astronomy*, Trumpler & Weaver (1962) refer to two incompleteness factors, K_1, which compensates for the deficiency of proper motions in a parallax catalog compared with a proper motion catalog, and K_2, which corrects for the absence of proper motions nearly in the line of sight and thus not detectable in either a proper motion or a parallax catalog. This study, however, shows that the calculation of incompleteness factors for the G giants is unnecessary or counterproductive.

2. THE OBSERVATIONAL DATA

The proper motions and parallaxes used in this study were taken from van Leeuwen's version of the Hipparcos catalog (van Leeuwen 2007), henceforth called simply the Hipparcos catalog, the radial velocities from the Wilson (Nagy 1991) and Strasbourg Data Centre (Barbier-Brossat & Figon 2000) catalogs. van Leeuwen's catalog (2007) omits a few stars contained in the original catalog (ESA 1997). For those few stars the relevant data were taken directly from the original catalog. The equinox of the Hipparcos catalog is J2000 and the catalog epoch is J1991.25. Stars listed as spectral class G, luminosity class III were extracted from the catalog. This resulted in a total of 3,075 G giants, of which 658 have radial velocities. The G giants are skewed towards the later giants; over 94% fall between G5 and G9, and the G8 stars alone account for 64.9% of the total.

The star's HD number determined if either of the two radial velocity catalogs contained an entry for that particular star. Not all of the data could be accepted. Negative parallaxes were excluded as were parallaxes smaller than 1 mas because the Ogorodnikov-Milne (OM) model was used for the equations of condition (Ogorodnikov 1965, pp. 61–63). This model, valid out to about 1 kpc, should be adequate because the minimum parallax used in this study, 1 mas, corresponds to a distance of 1 kpc. For a justification of this distance limit see Smart (1968, p. 285). Parallaxes smaller than 1 mas have such large mean errors that their inclusion seems unwarranted because of the uncertainty in their distances. Known multiple stars, flagged in the catalog, contaminate the proper motion by confusing orbital motion with genuine proper motion and were also excluded. And some of the solutions for the astrometric data in the catalog, also flagged, are substandard and were likewise excluded. Smith & Eichhorn (1996) have derived a procedure to correct the observed parallaxes, and this procedure was used to transform all of the parallaxes used in this study. In my study of the M giants (Branham 2008) I show that the Smith-Eichhorn correction seems to leave little residual parallax error.

What about the quality of the data? I have already commented on the high quality of the Hipparcos proper motions (Branham 2009b). Tangential velocities calculated from proper motions, therefore, should also be high quality. The radial velocities, however, come from disparate sources incorporated into the Wilson and the Strasbourg Data Center catalogs. My study of the F giants showed lower homogeneity in the radial velocities. One could perform a similar analysis with the G giants, but this seems otiose. The data are what they are and must be used as they are. The radial velocities, moreover, are not used alone but multiplied by the parallax in the equations of condition. A runs test shows that the radial velocities are of somewhat lower quality than the tangential velocities, but of acceptable quality. See the § 6. The runs test measures how often a variable, distributed about the mean, changes sign from plus to negative or negative to positive. The changes of sign, the runs, have a mean for n data points of $n/2 + 1$ and a variance of $n(n-2)/4(n-1)$. An advantage of the runs test over other tests for randomness resides in its being nonparametric, making no assumption about the normality of the data, although to actually calculate probabilities for the observed runs one does assume approximate normality. For a detailed description of the runs test see Wonnacott & Wonnacott (1972, pp. 409–411).

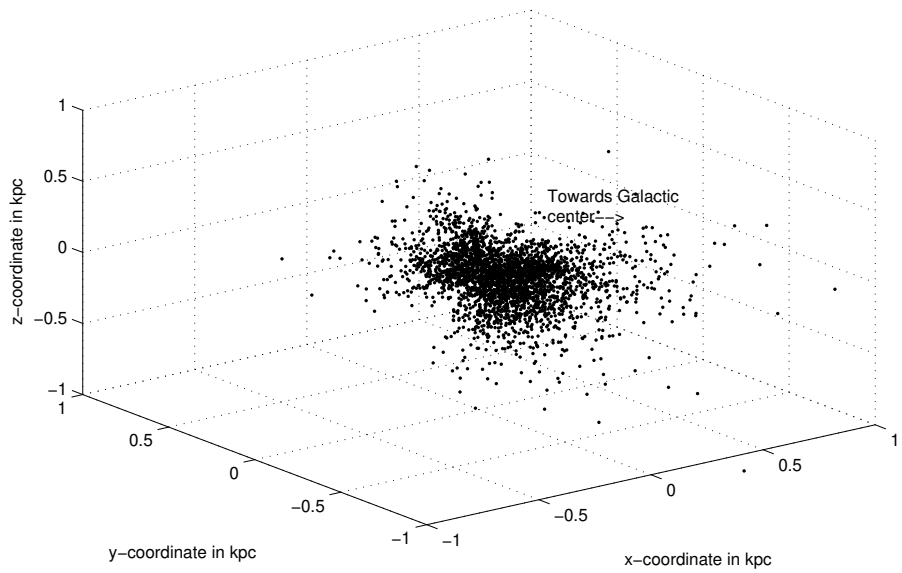

Fig. 1. Space distribution of G giants.

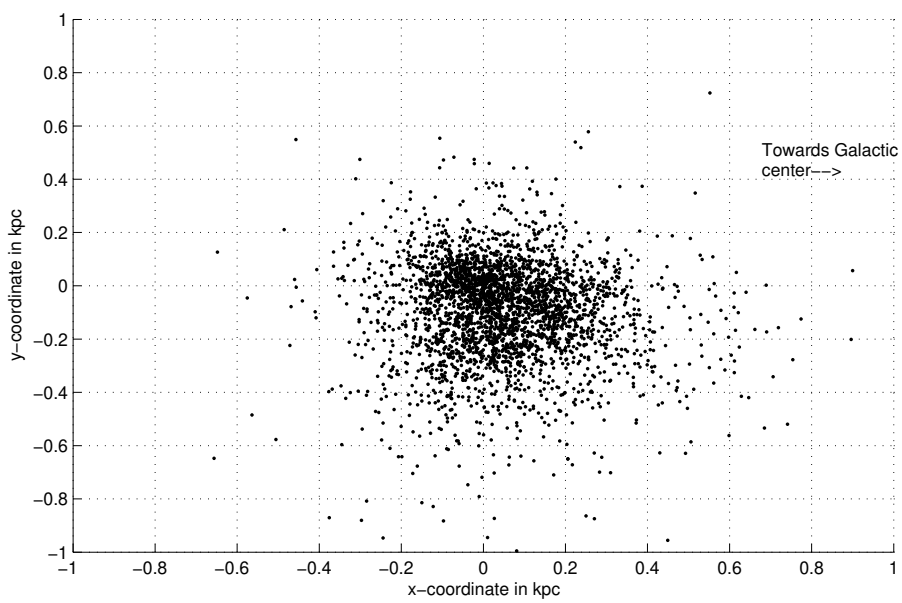

Fig. 2. Distribution in $x - y$ plane.

3. THE SPACE DISTRIBUTIONS

Let x, y, z be rectangular coordinates with origin at the Sun: x points towards the Galactic centre, y is perpendicular to x in the direction if increasing l, and z is positive for positive Galactic latitude. From ϖ, the star's parallax, l, its Galactic longitude, and b, its Galactic latitude, we calculate

$$\begin{pmatrix} x \\ y \\ z \end{pmatrix} = \frac{1}{\varpi} \begin{pmatrix} \cos l \cos b \\ \sin l \cos b \\ \sin b \end{pmatrix}. \tag{1}$$

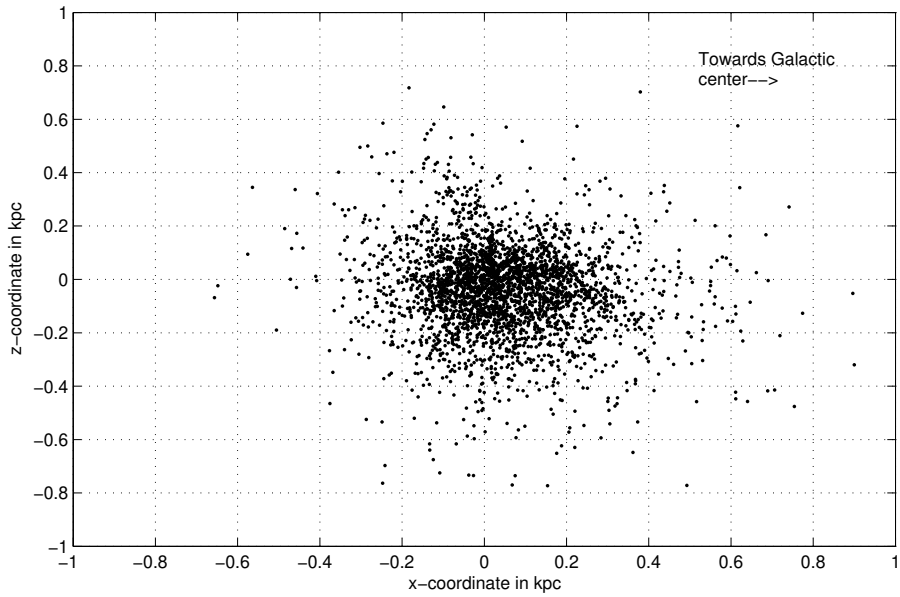

Fig. 3. Distribution in $x - z$ plane.

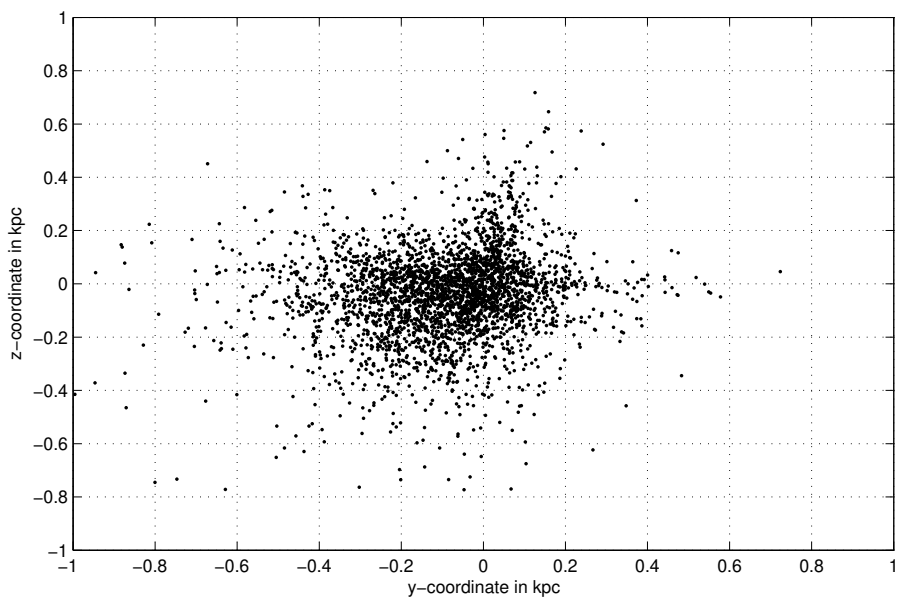

Fig. 4. Distribution in $y - z$ plane.

Figure 1 shows the distribution of the G giants in space, Figures 2, 3, and 4 the distributions in the $x - y$, $x - z$, and $y - z$ planes. Define a moment matrix, referred to the centroid of the distances, $\bar{x}, \bar{y}, \bar{z}$, from the x, y, z:

$$\begin{pmatrix} \sum_i (x_i - \bar{x})^2 & \sum_i (x_i - \bar{x})(y_i - \bar{y}) & \sum_i (x_i - \bar{x})(z_i - \bar{z}) \\ \sum_i (y_i - \bar{y})(x_i - \bar{x}) & \sum_i (y_i - \bar{y})^2 & \sum_i (y_i - \bar{y})(z_i - \bar{z}) \\ \sum_i (z_i - \bar{z})(x_i - \bar{x}) & \sum_i (z_i - \bar{z})(y_i - \bar{y}) & \sum_i (z_i - \bar{z})^2 \end{pmatrix}. \tag{2}$$

Before use of the moment matrix outliers should be eliminated from the distances. The criterion selected for the cutoff was five times the median of the distances to the stars. This cutoff results in only a sparse trim

of the data. Stigler (1977) has shown that modest trimming works better than extreme trimming. Although the eigenvalues of the moment matrix indicate little concentration towards the Galactic plane, 129.7, 94.0, and 80.9 pc^2, the normalized eigenvector associated with the z-axis points towards $b_g = 55.°671$, a significant tilt with respect to the Galactic plane. This tilt, however, seems to be a selection effect associated with the giants rather than a tilt associated with the Gould belt. Look at the G stars as a whole without discrimination as to luminosity class. There are 82 supergiants, 184 bright giants, 3,075 giants, 1,152 subgiants, 4,656 main sequence, and 9,332 unspecified luminosity class G stars. With this heterogeneous group the tilt becomes 79.°494. Further evidence that the tilt seems not associated with the Gould belt arises from an attempt to fit a plane to the G giants. Branham (2003) outlines the procedure for doing this. 1,389 stars are classified as "Gould belt", but the tilt of the plane of the remaining, supposedly "Galactic belt", stars becomes even worse, 35.°58, and with high correlations, up to 40%, among the x, y, z coordinates.. Thus, the procedure that works so well with the O-B5 stars to discriminate between Gould belt and Galactic belt stars fails completely for the G giants.

That the tilt should not unduly bias the solution can be inferred from a look at the randomness of the rectangular coordinates. The correlation between x and y is -10.1%, between x and z -12.9%, and between y and z 11.3%. Regarding the randomness in distance a runs test yields, after elimination of discordant distances, 1,487 runs out of an expected 1531 implying an 11.3% chance that the distances are random. The statistics for the G giants, therefore, indicate *relative* randomness.

4. EQUATION OF CONDITION FOR KINEMATICS AND THE VELOCITY ELLIPSOID

The equations of condition, given in detail in Branham (2009a) and which come from Ogordnikov (1965, pp. 74–75), involve twelve unknowns for the kinematical parameters: the components of the reflex solar motion X, Y, Z and the components of the displacement tensor $u_x, u_y, u_z, v_x, v_y, v_z, w_x, w_y, w_z$. All of these quantities are referred to Galactic latitude and longitude, l and b, rather than right ascension α and declination δ. Proper motions in α and δ are converted to proper motions in l and b expressed in milli-arc-seconds (mas) per year; radial velocity is expressed in km s^{-1}. Parallax ϖ is also expressed in mas. These kinematical parameters are calculated from the least squares criterion because there are fewer discordant observations, handled by a 2.5% trim of the data, than with the velocity ellipsoid calculation, for which the robust L_1 criterion is indicated. As with linear programming, one does this by minimization of an objective function. If r_i is one of m residuals from a solution for the kinematical parameters and r is the m-vector of the residuals, then we impose the condition $r^T \cdot r - \tau = 0$, where τ is an arbitrary parameter, and minimize τ in the objective function.

A sparse trim of the data seems indicated not only by what Stigler (1977) has found, light trimming or even no trimming works better than extreme trimming, but by what a General Colby reported to the Astronomer Royal, Sir George Airy (Airy 1854). In a geodetic adjustment for the determination of the scale of longitudes for England, inclusion of all data rather than just the most concordant data gave results that went from, to use Airy's words, "considerably in error" to "perfectly good."

The equations as derived by Ogorodnikov actually use the distance $1/\varpi$ rather than the parallax ϖ itself, but it is important to recast the equations to remove the parallax error from the denominator and thus ameliorate any possible Lutz-Kelker bias. The equations, therefore, are multiplied by ϖ, which places the parallax in the numerator.

To calculate the velocity ellipsoid use $\dot{x}, \dot{y}, \dot{z}$, the space velocities of a star, found from the proper motions and radial velocity and expressed in km s^{-1} are:

$$\begin{pmatrix} \dot{x} \\ \dot{y} \\ \dot{z} \end{pmatrix} = \begin{pmatrix} -\sin l & -\cos l \sin b & \cos l \cos b \\ \cos l & -\sin l \sin b & \sin l \cos b \\ 0 & \cos b & \sin b \end{pmatrix} \cdot \begin{pmatrix} \kappa \mu_l \cos b/\varpi \\ \kappa \mu_b/\varpi \\ \dot{r} \end{pmatrix}. \tag{3}$$

If radial velocities are unavailable, then we seem unable to calculate the space velocities. This, however, can be done if we use the SVD to employ only the tangential velocities. See Branham (2010) for details. There are other possibilities. Fuchs et al. (2009) use a deprojection formulation for the proper motions that assumes the lines of sight towards the stars are statistically uncorrelated with the velocities of the stars. The Section 7 shows that the SVD approach satisfies the assumption of statistical randomness and seems, therefore, satisfactory.

One fits a quadric surface with ten coefficients, $a, b, c, d, e, f, g, h, k, l$, to these velocities. To assure that the equation indeed corresponds to an ellipsoid one must impose the condition that the matrix of the a, b, c coefficients

$$A = \begin{pmatrix} a & c/2 & d/2 \\ c/2 & b & e/2 \\ d/2 & e/2 & c \end{pmatrix},$$

in fact be positive-definite and symmetric. To avoid the trivial solution $a = b = \cdots = q = 0$ another condition must be imposed. The one I use is that the volume of the ellipsoid must be a maximum. Because the volume is proportional to the determinant of A, the condition becomes $\det(A) = \max$. An eigenvalue-eigenvector decomposition of the matrix A yields the axes of the velocity ellipsoid and their orientation with respect to the Galactic coordinate system. Because of generally greater error in the data, the coefficients $a, \ldots, l$ are calculated by use of the robust L_1 criterion. SDP allows one to combine without difficulty the least squares criterion for the kinematical parameters and the L_1 criterion for the velocity ellipsoid. For the latter if there are n space velocities with n corresponding residuals $r_{sv,i}$, let $\gamma_i, i = 1, \ldots, n$, be n *positive* parameters. Then minimize the γ in the objective function subject to the conditions

$$\mathrm{diag}(\gamma + r_{sv}) > 0; \qquad \mathrm{diag}(\gamma - r_{sv}) > 0; \qquad \mathrm{diag}(\gamma) > 0.$$

The SDP formulation of the velocity ellipsoid calculation along with the L_1 criterion for the minimization of the residuals offers advantages over competing methods. The ellipsoid calculated is unique and represents a global minimum of the reduction criterion when that criterion is the L_1 (Calafiore 2002). Bochanski, Hawley, & West (2011) prefer a geometric simplex minimization with the least squares criterion. Although simplex minimization can be used with the L_1 criterion, thus making the procedure robust-see the algorithm in Branham (1990, pp. 191–197), the method can converge to a local rather than to a global minimum, particularly when many parameters are being fit, unless a good starting approximation is available. Pourbaix (1998) , using the simplex algorithm to calculate orbits of double stars, estimates that when n parameters are being fit there are $\approx \mathrm{O}(e^n)$ local minima. He implements a simulated annealing modification of the simplex algorithm to reject the local minima. With SDP and the L_1 criterion such a strategy becomes unnecessary because the minimum *is* global.

The solar velocity, $S_0 = \sqrt{X^2 + Y^2 + Z^2}$, calculated from both the solution for the kinematical parameters $X, Y, \ldots, w_y, w_z$ and the coefficients of the velocity ellipsoid must be the same. This condition can be imposed when one uses the SDP formulation of the problem.

5. SOME CORRECTIONS TO THE OBSERVATIONS AND COVARIANCE MATRICES

The total space motions needed in the velocity ellipsoid calculation should be corrected for the effects of Galactic rotation by modifying the proper motions and radial velocities used in the calculations to remove the rotation. This was done by the same procedure used in Branham (2009a).

In theory one should also apply a correction for the incompleteness of the sample of the G giant stars taken from the Hipparcos catalogue. Trumpler & Weaver (1962, p. 374) define a factor of incompleteness K_1 as

$$K_1 = \frac{N(m, \mu)}{N_\varpi(m, \mu)}, \tag{4}$$

where $N(m, \mu)$ is the number of stars in the sky for magnitude interval $m \pm \Delta m/2$ and proper motion interval $\mu \pm \Delta\mu/2$ and $N_\varpi(m, \mu)$ is the number of stars in the parallax catalogue for the same intervals. Equation (4) is difficult to apply if there is insufficient overlap between the proper motion catalog and the parallax catalog. For the Hipparcos parallaxes a logical proper motion catalog would be the Tycho II catalog (Høg et al. 2000). But for K_1 the sparse overlap between the two catalogs assures that the factor becomes large with large mean errors. One must question whether such corrections are realistic and should be applied. I feel they should not and that the randomness of the data is more important.

Trumpler & Weaver (1962, p. 375) also define a second incompleteness factor, K_2, to correct for the absence of proper motions in the parallax catalog nearly along the line of sight and hence undetectable. K_2 depends

TABLE 1

SOLUTION FOR KINEMATIC PARAMETERS FOR THE G III STARS

Quantity	Value	Mean Error
$\sigma(1)$ (mean error of unit weight in mas km s^{-1})	112.44	···
u_x (in mas km s^{-1})	−7.63	6.13
u_y (in mas km s^{-1})	23.35	4.06
u_z (in mas km s^{-1})	−3.59	5.23
v_x (in mas km s^{-1})	4.75	4.63
v_y (in mas km s^{-1})	−8.08	6.00
v_z (in mas km s^{-1})	−6.87	5.21
w_x (in mas km s^{-1})	1.57	4.15
w_y (in mas km s^{-1})	−7.68	3.74
w_z (in mas km s^{-1})	−11.39	5.86
S_0 (solar velocity in km s^{-1})	16.72	0.41
A (Oort constant in km s^{-1} kpc^{-1})	14.05	3.28
B (Oort constant in km s^{-1} kpc^{-1})	−9.30	2.87
$V0$ (Circular velocity in km s^{-1})	198.48	26.95
l_1 (longitude displacement)	−26.°45	7.°05
K (K term in km s^{-1})	−7.85	4.99

TABLE 2

VELOCITY DISPERSION AND VERTEX DEVIATION OF THE G III STARS

Quantity	Value	Mean Error
Mean absolute deviation of residuals in km s^{-1}	11.00	···
S_0 (solar velocity in km s^{-1})	16.72	1.05
σ_1 (velocity dispersion in x in km s^{-1})	51.78	0.55
σ_2 (velocity dispersion in y in km s^{-1})	42.81	0.32
σ_3 (velocity dispersion in z in km s^{-1})	28.45	0.22
l_1 (longitude of σ_1)	3.°88	6.°62
b_1 (latitude of σ_1)	0.°28	0.°61
l_2 (longitude of σ_2)	93.°93	1.°90
b_2 (latitude of σ_2)	9.°86	0.°65
l_3 (longitude of σ_3)	−87.°72	1.°62
b_3 (latitude of σ_3)	80.°14	0.°49

on the velocity ellipsoid. Branham (2009b) shows how this incompleteness factor can be evaluated. For the G giants this factor becomes an insignificant $5.6 \cdot 10^{-7}$. Therefore, neither the K_1 nor the K_2 incompleteness factor need be applied.

The covariance matrix to calculate mean errors is given in equation (25) of Branham (2006), and equation (26) of that publication shows how to calculate the errors for quantities, such as the Oort constants, derived from the displacement tensor.

6. RESULTS

After the equations of condition for the kinematical parameters had been formed, I applied two checks for the adequacy of the reduction model. The first check simply calculates the singular values of the matrix of

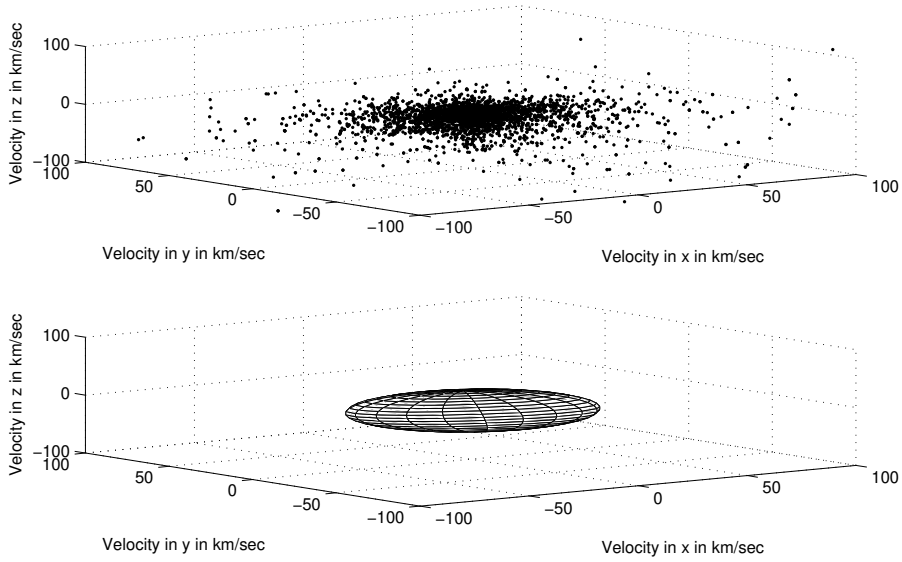

Fig. 5. '.'=rectangular velocity of star (upper); velocity ellipsoid (lower).

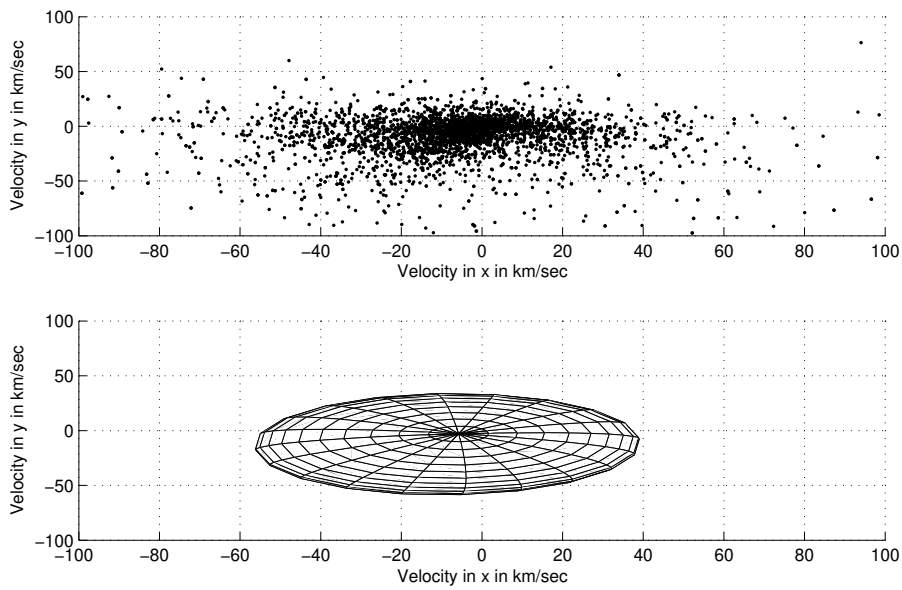

Fig. 6. Ellipsoid in $x - y$ plane.

the equations of condition. An inadequate reduction model, for example one in which some unknowns are strongly correlated, results in a high condition number for the matrix because of small singular values. The condition number of the matrix of the equations of condition for the G giants, however, is low, 22.8. The second check calculates Eichhorn's efficiency (Eichhorn 1990), a parameter that varies from 0 to 1 with 0 indicating redundancy in the parameters and 1 that all parameters are necessary. The efficiency of 0.94 indicates that *all* of the variables in the model are necessary and with little correlation among themselves.

The first solution for the G giants was calculated from all of the equations of condition. These solutions calculated residuals needed to find discordant data. For the G stars the criterion was five times the mean absolute deviation (MAD) of the residuals. This eliminated 168 of the 6,808 equations of condition, a 2.5%

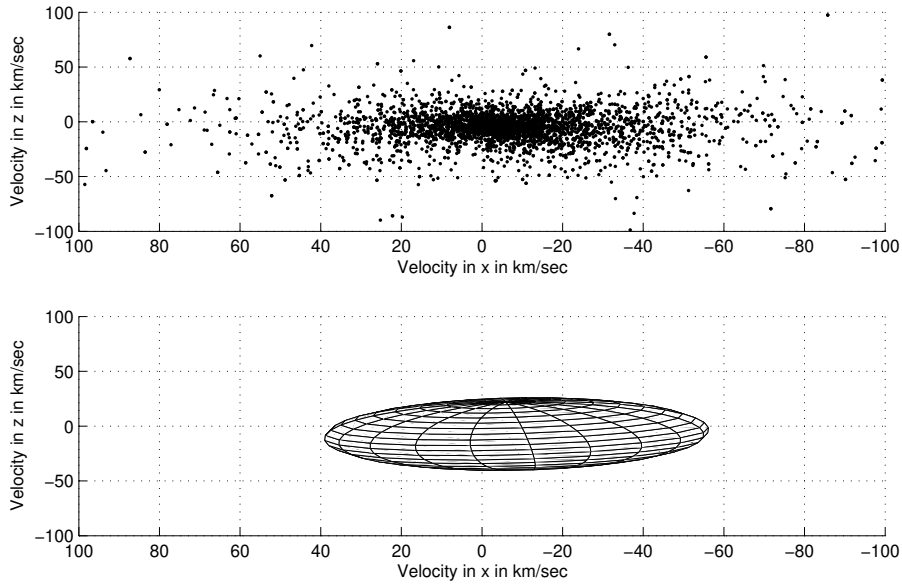

Fig. 7. Ellipsoid in $x - z$ plane.

trim. I have used this elimination criterion in the past, generally with good results, but a further reason exists to justify its use. For the G giants there is a 19.0% chance that the original residuals are random, as calculated by a runs test, but a 78.7% chance that the trimmed residuals are random. Eliminating some of the residuals, therefore, increases the randomness of the sample.

Table 1 shows the solution for the kinematical unknowns and Table 2 for the coefficients and orientation of the velocity ellipsoid for the G stars. For convenience the components for the displacement tensor are converted to the more familiar form of the solar motion, Oort constants, the deviation l_1 between the longitude of the geometric center and the kinematic center of the Galaxy, and K term. Also shown is the circular velocity V_0, found from the relation $V_0 = (A - B)R_0$, where R_0 is the distance to the centre of the Galaxy. Kerr & Lynden-Bell (1986) determine a value of 8.5 ± 1.1 kpc for R_0. Perryman (2008, App. A), however, after a survey of recent determinations feels that 8.2 kpc is a better determination. The mean error for V_0 comes from the procedure given in Branham (2008) and uses 8.2 kpc for R_0 with the same mean error as given by Kerr & Lynden-Bell (1986).

The orientation of the velocity ellipsoid in space and in the $x - y$, $x - z$, and $y - z$ planes is shown in Figures 5–8 for the G giants. (Because of the density of data points, it proved impossible to plot both the stars and the velocity ellipsoid on one graph because the stars blotted out the ellipsoid; therefore a subgraph was used for the stars and another for the ellipsoid.)

7. DISCUSSION

The distribution of the residuals from the kinematical solution, after eliminating discordant residuals, is seen in the histogram of Figure 9. As mentioned in the previous section, 168 of the residuals were eliminated, a 2.5% trim. The distribution is somewhat skewed, coefficient of skewness 0.09, more platykurtic, kurtosis of 1.42, than the normal distribution, kurtosis of 3, and more lighter tailed, Hogg's Q factor of 0.36, than a normal distribution, Q=2.58. The Q factor is defined as

$$Q = \frac{(U_{0.05} - L_{0.05})}{(U_{0.5} - L_{0.5})}, \tag{5}$$

where U_α and L_α are averages of the respective upper and lower 100α of the data (Stigler 1977). A runs test, however, reveals 3,350 runs out of an expected 3,404. The residuals, therefore, can be considered random. To be specific, there is a 19.0% chance that the residuals are taken randomly from a normal distribution.

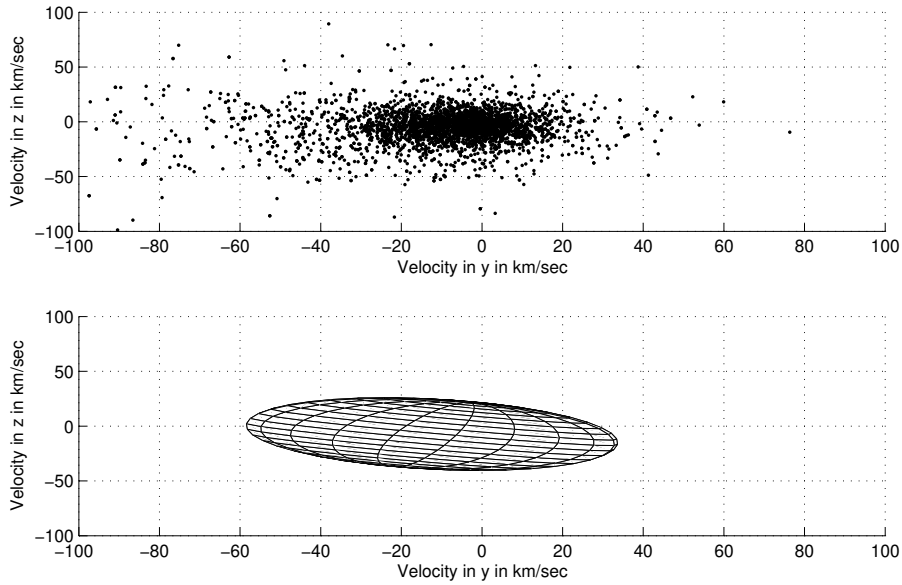

Fig. 8. Ellipsoid in $y - z$ plane.

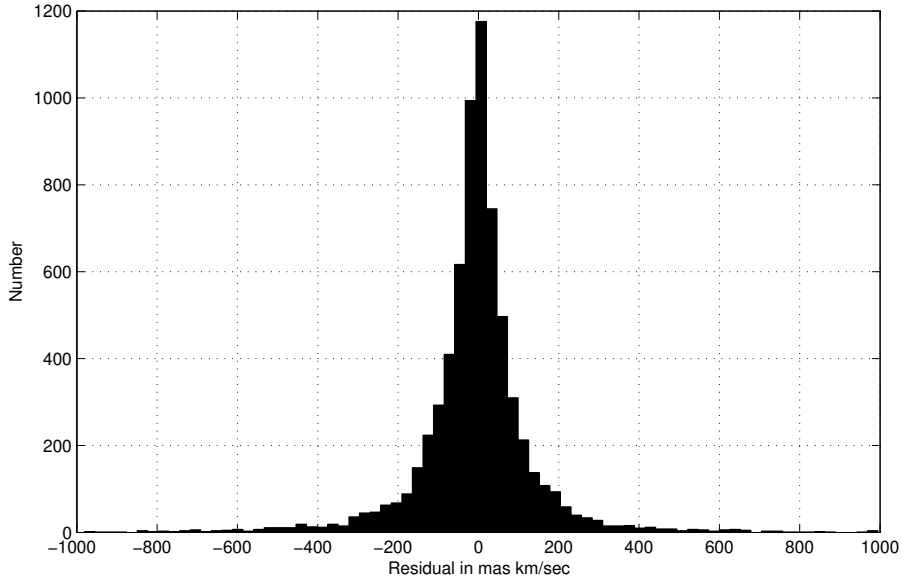

Fig. 9. Histogram of residuals from kinematical solution.

Because we generally use a 5% to 10% limit before rejecting the null hypothesis that a distribution is in fact not random, we infer that although the actual distribution deviates from normality the residuals conform to the null hypothesis of being random. If the runs test is applied separately to the equations of condition arising from the tangential velocities and those from the radial velocities, the former show 3,032 runs out of an expected 3,075 and the latter 303 runs out of an expected 329. This demonstrates that the tangential velocities seem of higher quality than the radial velocities, 31.2% probability of randomness versus 4.6%, but because they are used conjointly the residuals remain relatively random. All of this confirms, along with the singular values and Eichhorn's efficiency, that the reduction model suffers no serious defects and that inclusion of the K_1 incompleteness factor seems unnecessary.

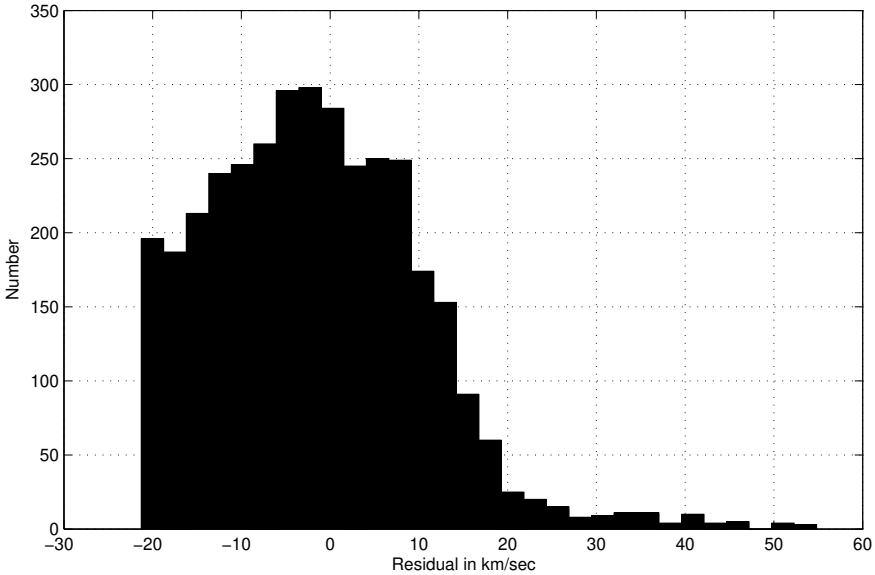

Fig. 10. Residuals in velocity for G giants.

TABLE 3

RECENT DETERMINATIONS OF THE SOLAR VELOCITY

Reference	Class	$-X$ (km s^{-1})	$-Y$ (km s^{-1})	$-Z$ (km s^{-1})	S_0 (km s^{-1})
Branham (2008)	M III	8.99 ± 0.42	20.40 ± 0.40	4.80 ± 0.39	24.20 ± 0.70[a]
Yuan et al. (2008)	O-B5	9.17 ± 0.40	8.66 ± 0.38	5.83 ± 0.34	13.90 ± 0.38[b]
Yuan et al. (2008)	K-M III	18.46 ± 0.32	17.70 ± 0.32	6.32 ± 0.32	20.61 ± 0.32[c]
Aumer & Binney (2009)	mixture IV, V	9.96 ± 0.33	5.25 ± 0.54	7.07 ± 0.34	13.29 ± 0.72
Branham (2009a)	B69 III	9.58 ± 0.39	11.94 ± 0.41	6.03 ± 0.33	16.40 ± 0.40[a]
Branham (2009a)	A III	9.85 ± 0.59	8.00 ± 0.58	5.80 ± 0.52	13.95 ± 0.58[a]
Branham (2009b)	K III	7.53 ± 0.26	19.11 ± 0.26	7.41 ± 0.22	21.83 ± 0.26[a]
Bobylev & Bajkova (2010)	Galactic masers	5.5 ± 2.2	11.0 ± 1.7	8.5 ± 1.2	15.0 ± 3.0
Branham (2010)	F III	10.84 ± 0.49	12.62 ± 0.49	8.14 ± 0.44	16.72 ± 0.41[a]
Schönrich et al. (2010)	F-G V	$11.1^{+0.69}_{-0.75}$	$12.24^{+0.47}_{-0.47}$	$7.25^{+0.37}_{-0.36}$	...
Shen & Zhang (2010)	Galactic Cepheids	12.58 ± 1.09	14.52 ± 1.06	8.98 ± 0.98	21.21 ± 1.81[d]

[a]Mean error calculated from equations (25) and (26) in Branham (2006).

[b]For heliocentric distance 0.2–3 kpc.

[c]For heliocentric distance 0.2–1 kpc.

[d]For heliocentric distance 0.2–3 kpc.

For the residuals from the velocity ellipsoid the situation becomes different, as Figure 10 shows. The residuals deviate even more from a normal distribution, coefficient of skewness 3.62, platykurtic, kurtosis 0.59, and light tailed, Q factor of 0.25. They are, however, even more random than the residuals from the kinematical solution, 1,784 runs out of an expected 1,813. There is thus a 33.7% probability that the residuals are random. This is the principal justification for use of the SVD to calculate the velocity ellipsoid.

Regarding recent determinations of the kinematical parameters Perryman (2008, p. 502) gives his Table 9.3 with pre-2007 results while Table 3 shows some post-2008 values. If we look at the 33 values for the solar velocity in both tables, without discriminating among spectrum-luminosity classes nor weighting by number of stars, there is a range from a minimum of 11.8 km s^{-1} to a maximum of 24.6 with mean 18.29 and standard deviation 3.74. The value in Table 1 falls well within this range. With respect to the Oort constants and

TABLE 4

RECENT DETERMINTIONS OF OORT CONSTANTS AND AUXILIARY QUANTITIES

Reference	Class	A (km s^{-1} kpc^{-1})	B (km s^{-1} kpc^{-1})	$A - B$	$-(A + B)$
Branham (2008)	M III	16.86 ± 2.78	-6.34 ± 2.56	23.20 ± 7.79[a]	-10.52 ± 8.82[a]
Yuan et al. (2008)	O-B5	15.33 ± 0.94	-15.12 ± 0.71	30.45 ± 1.18[b]	-0.21 ± 1.18[b]
Yuan et al. (2008)	K-M III	15.86 ± 1.30	-14.57 ± 1.01	30.44 ± 1.65[c]	1.29 ± 1.65[c]
Bobylev & Bajkova (2010)	Galactic masers	17.8 ± 0.8	-13.2 ± 1.5	31.1 ± 1.7	4.6 ± 1.7
Branham (2009a)	B69 III	11.77 ± 1.66	-9.05 ± 1.38	20.82 ± 3.83[a]	-2.72 ± 1.04[a]
Branham (2009a)	A III	11.48 ± 5.45	-8.29 ± 4.23	19.77 ± 12.09[a]	-3.19 ± 7.44[a]
Branham (2009b)	K III	13.08 ± 1.72	-10.21 ± 1.47	23.29 ± 2.20[a]	2.86 ± 0.82[a]
Branham (2010)	F III	14.85 ± 7.47	-10.85 ± 6.83	23.35 ± 4.07[a]	-4.75 ± 4.63[a]
Shen & Zhang (2010)	Galactic Cepheids	17.42 ± 1.17	-12.46 ± 0.86	29.88 ± 1.45	-4.96 ± 1.45[d]

[a]Mean error calculated from equations (25) and (26) in Branham (2006).
[b]For heliocentric distance 0.2–3 kpc.
[c]For heliocentric distance 0.2–1 kpc.
[d]For heliocentric distance 0.2–3 kpc.

TABLE 5

VELOCITY DISPERSIONS FOR THE GIANT STARS

Spectral type	σ_x (km s^{-1})	σ_y (km s^{-1})	σ_z (km s^{-1})	Number of stars
O-B5	32.44 ± 5.04	26.16 ± 2.75	18.71 ± 2.39	107 total space motion
B6-9	39.25 ± 3.29	10.83 ± 1.16	14.07 ± 0.85	147 total space motion
A	26.95 ± 4.26	23.08 ± 2.14	16.46 ± 0.55	144 total space motion
F	36.89 ± 1.90	24.66 ± 1.16	17.97 ± 0.81	222 total space motion 369 tangential velocity
G	51.78 ± 0.55	42.81 ± 0.32	28.45 ± 0.22	658 total space motion 2417 tangential velocity
K	50.58 ± 0.99	42.42 ± 1.13	32.92 ± 0.56	880 total space motion
M	57.40 ± 1.67	45.86 ± 1.63	33.84 ± 1.02	480 total space motion

associated quantities such as $A - B$ and $-(A + B)$, the former equal to V_0/R_0 and the latter to (dV/dR), Perryman's Table 9.3 shows determinations up to 2007 and Table 4 post-2008 determinations, a total of 28. We see that A ranges from a minimum of 9.6 km s^{-1} kpc^{-1} to a maximum of 19 with a mean of 14.52 and a standard deviation of 2.52, again without discriminating as to number of stars, spectrum or luminosity class, or other indicators. The value given in Table 1 coincides well with this mean. For B the corresponding values are minimum of -24 km s^{-1} kpc^{-1}, maximum of -6.34, mean -12.63, and standard deviation of 3.30. Once again, the value for B given in Table 1 shows no anomaly. The only quantity that shows a possibly discrepant value is the K term, putatively significant only for the early stars, with determinations falling near 5 km s^{-1}, and close to 0 for later spectral types. The value in Table 1, large and moreover negative, seems discrepant. Its mean error, however, is also large and furthermore Branham (2009a) has shown that this term is sensitive to errors in the data; little credence, therefore, should be placed on its value. In a recent paper McMillan & Binney (2010) find that the most probable range for V_0/R_0 falls between 29.9 km s^{-1} kpc^{-1} and 31.6 km s^{-1} kpc^{-1}. Many of the values in Perryman's Table 9.3 and Table 3 fall outside of this range which, however, merely shows that quantities such as the distance to the centre of the Galaxy and the Sun's circular velocity are difficult to determine.

About the velocity ellipsoid little can be said because the only previous study of all of the G giants is that of Parenago (Delhaye 1965, p. 64), which used fewer stars, 345, and a different reduction method, the method of moments (Trumpler & Weaver 1962, pp. 283–286). The dispersions of the velocity ellipsoid are higher than those Parenago found, but this is a consequence of use of the SDP method; see Branham (2004).

Some insight, however, can be gained if we take these results not in isolation but rather conjointly with my previous studies of the giant stars. Because all of these studies use the same reduction method, variations caused by differences in the calculation of the velocity ellipsoid, such as use of the method of moments, will be minimized. Table 5 shows the velocity dispersions for all of the giant stars from O to M.

Two conclusions follow from an examination of Table 5. There is a clear break in all of the velocity dispersions between the F and the G giants. Dehnen & Binney (1998) confirmed this break, known as Parenago's discontinuity, for the main sequence stars, but it appears as if the giant stars also show the discontinuity. Use of the SVD to include stars for which only tangential velocities are available, the second conclusion, seems justified on more than just a statistical basis. Neither the F giants compared with earlier spectral types that use only total space motions nor the G giants with later spectral types exhibit glaring discrepancies, indicating that the tangential velocities are integrated well with the total space motions.

8. CONCLUSIONS

Semi-definite programming proves itself once again a useful tool for problems of Galactic kinematics by allowing one to combine a solution for the kinematical parameters such as the Oort constants with one for the coefficients of the velocity ellipsoid. The singular value decomposition allows one to incorporate stars for which only tangential velocities but no radial velocities are available into the calculation of the velocity ellipsoid. When applied to the G III stars the calculated solutions appear concordant with what others have found. A comparison with giant stars of other spectral types confirms that Parenago's discontinuity exists for the giant stars as well as main sequence stars.

REFERENCES

Airy, G. 1854, AJ, 4, 24

Aumer, M., & Binney, J. J. 2009, MNRAS, 397, 1286

Bobylov, V. V., & Bajkova, A. T. 2010, MNRAS, 408, 1788

Barbier-Brossat, M., & Figon, P. 2000, A&AS, 142, 217

Bochanski, J. J., Hawley, S. L., & West, A. 2011, AJ, 141, 98

Branham, R. L., Jr. 1990, Scientific Data Analysis (New York: Springer)

_____. 2003, Ap&SS, 288, 417

_____. 2004, A&A, 421, 977

_____. 2006, MNRAS, 370, 1393

_____. 2008, RevMexAA, 44, 29

_____. 2009a, MNRAS, 396, 1473

_____. 2009b, RevMexAA, 45, 215

_____. 2010, MNRAS, 409, 1269

Calafiore, G. 2002, IEEE Trans. Sys., Man Cyber., Part A, 32, 269

Dehnen, W., & Binney, J. J. 1998, MNRAS, 298, 387

Delhaye, J. 1965, in Galactic Structure, ed. A. Blaauw & M. Schmidt (Chicago: Chicago Univ. Press), 61

Eichhorn, H. 1990, in Errors, Bias and Uncertainties in Astronomy, ed. C. Jaschek & F. Murtagh (Cambridge: Cambridge Univ. Press), 149

ESA 1997, The Hipparcos and Tycho Catalogues, ESA SP-1200 (Noordwijik: ESA)

Fuchs, B., et al. 2009, AJ, 137, 4149

Høg, E., et al. 2000, The Tycho-2 Catalogue of the 2.5 Million Brightest Stars, CD-Rom version (Washington, DC: U. S. Naval Observatory)

Kerr, F. J., & Lynden-Bell, D. 1986, MNRAS, 221, 1023

McMillan, P. J., & Binney, J. J. 2010, MNRAS, 402, 934

Nagy, T. A. 1991, Documentation for the Machine-Readable Version of the Wilson General Catalogue of Stellar Radial Velocities, CD-Rom version (Lanham, MD: ST Systems Corp.)

Ogorodnikov, K. F. 1965, Dynamics of Stellar Systems (Oxford: Pergamon)

Perryman, M. 2008, Astronomical Applications of Astrometry (Cambridge: Cambridge Univ. Press)

Pourbaix, D. 1998, A&AS, 131, 377

Shen, M., & Zhang, H. 2010, Chin. J. Astron. Astrophys., 34, 89

Smart, W. M. 1968, Stellar Kinematics (New York: Wiley)

Smith, H., Jr., & Eichhorn, H. 1996, MNRAS, 281, 211

Stigler, S. M. 1977, Annals of Statistics, 5, 1055

Schönrich, R., Binney, J. J., & Dehnen, W. 2010, MNRAS, 403, 1829

Trumpler, R. J., & Weaver, H. F. 1962, Statistical Astronomy (New York: Dover)

van Leeuwen, F. 2007, Hipparcos, the New Reduction of the Raw Data (New York: Springer)

Vandenberghe, L., & Boyd, S. 1996, SIAM Review, 38, 49

Wonnacott, T. H., & Wonnacott, R. J. 1972, Introductory Statistics (2nd ed., New York: Wiley)

Yuan, F.-T., Zhu, Z., & Kong, D.-L. 2008, Chin. J. Astron. Astrophys., 8, 714

Richard L. Branham, Jr.: Instituto Argentino de Nivología, Glaciología y Ciencias Ambientales, C.C. 330, 5500 Mendoza, Argentina (richardbranham_1943@yahoo.com).

Revista Mexicana de Astronomía y Astrofísica, **47**, 211–217 (2011)

SPECKLE INTERFEROMETRY AT THE OBSERVATORIO ASTRONÓMICO NACIONAL. III

V. G. Orlov, V. V. Voitsekhovich, C. A. Guerrero, F. Ángeles,
A. Farah Simon, E. Luna, and R. Vázquez Robledo

Instituto de Astronomía
Universidad Nacional Autónoma de México, Mexico

Received 2011 March 10; accepted 2011 April 6

RESUMEN

Se presentan las mediciones interferométricas de motas de estrellas binarias realizadas durante agosto de 2010 con el telescopio 1.5 m y en noviembre de 2010 con el telescopio de 2.1 m del Observatorio Astronómico Nacional en SPM (Mexico). Los resultados reportados aquí son 238 mediciones de 225 pares con una magnitud límite de $V = 12.2$. De éstas, 211 parejas presentan separaciones de menos de $1''$. El error medio obtenido en la separación es de $0''.02$ y en el ángulo de posición de $1.5°$. Algunos de los ángulos de posición se determinaron con los $180°$ usuales de ambigüedad.

ABSTRACT

We present speckle interferometric measurements of binary stars performed during August of 2010 with the 1.5 m telescope and during November of 2010 with the 2.1 m telescope of the Observatorio Astronómico Nacional at SPM (Mexico). We report here the results of 238 measurements of 225 pairs with a primary limiting magnitude of $V = 12.2$; 211 of them have separations less than $1''$. The mean error in separation is $0''.03$ and $1.5°$ in position angle. Some of the position angles were determined with the usual $180°$ ambiguity.

Key Words: binaries: visual — stars: fundamental parameters — techniques: high angular resolution — techniques: interferometric

1. INTRODUCTION

This is the third paper in the serie of publications presenting the results of speckle interferometric observations of binary stars performed with telescopes of the Observatorio Astronómico Nacional (OAN) of the Instituto de Astronomía Universidad Nacional Autónoma de México. Regular speckle interferometric measurements of binary stars have been made with telescopes of the OAN since 2008 (Orlov et al. 2009). This paper presents the results of double star observations carried out with the 1.5 m and the 2.1 m Telescopes of Sierra San Pedro Mártir National Astronomical Observatory (OAN-SPM) in August and November of 2010. For these observations we developed a new detector. This detector is a combination of the CCD camera Watec 120N with a third generation image intensifier. The third generation image intensifier also allows us to carry out near infrared speckle interferometric observations. The results reported here consist of 238 measures of 225 pairs with a primary limiting magnitude of $V = 12.2$; 211 of them have separations of less than $1''$. In these speckle observations we confirmed and measured 38 binaries first detected by Hipparcos. The paper concludes with a tabulation of the observational results. The analysis of specklegram has been performed using the technique described by Tokovinin, Mason, & Hartkopf (2010).

2. BRIEF DESCRIPTION OF THE EQUIPMENT

The observations were performed with the CCD camera Wat-120N which is optically connected with the 18 mm third-generation image intensifier. Because the Watec CCD device Wat-120N is primarily designed for amateur astronomers, its limiting sensitivity (0.00002 lx) is not enough for speckle interferometry, so we had to use the third-generation image intensifier. We describe some technical details

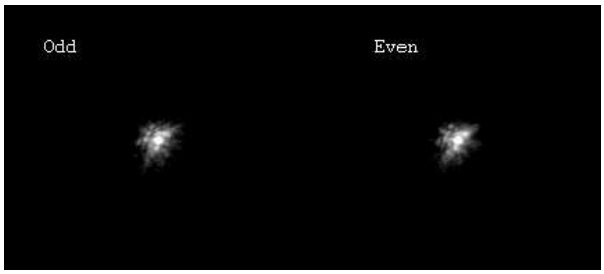

Fig. 1. Odd and even half frames taken with good seeing conditions.

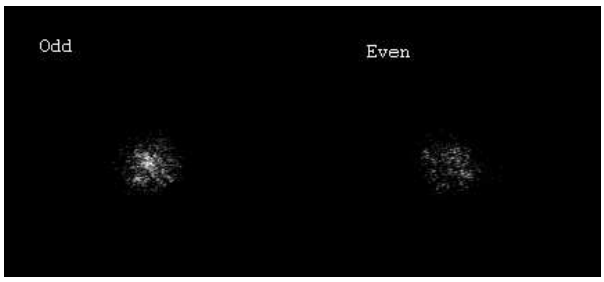

Fig. 2. Odd and even half frames taken with bad seeing conditions.

related to our CCD camera. The Wat-120N is an interline CCD camera where each single frame is a combination of two half-frames. One half-frame contains odd lines while the second one consists of the even lines. One half-frame is taken every 1/50th of a second. As one can see in Figure 1, in the case of good seeing conditions there are no difference between odd and even half frames. So, we can make the data processing for a complete frame 720×480. If the seeing conditions are not so good (Figure 2), the half-frames are very different. In this case we have to perform the data processing for the odd and even half-frames separately. Also we have to note that the Wat-120N does not have square pixels; this has to be taken into account during data processing.

The other disadvantage of Wat-120N is a manual control. We developed a simple Ethernet controller to resolve this problem. The set of our camera controls consists of three parts: gain control, gamma control, and on/off image intensifier switcher. The gain control has 8 values from 0 to 7 (Figure 3, the value 7 corresponds to the maximum gain). The gamma control allows three modes: linear (Off), low (Lo) and high (Hi). Two modes Lo and Hi are not linear and, if one needs measure accurate magnitude differences of components, they are not used during data recording. The last control is a switch on/off for the image intensifier.

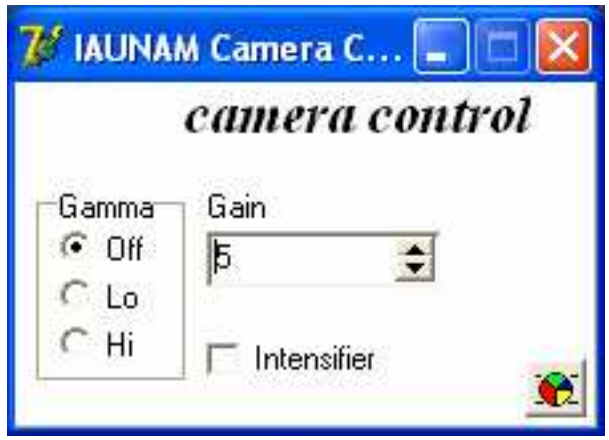

Fig. 3. Ethernet camera control.

3. OBSERVATIONS AND RESULTS

Data were recorded during the two observation campaigns carried out in August and November 2010. In August observations of 105 stars were performed at the OAN-SPM 1.5 m telescope. The atmospheric conditions (seeing and transparency) were excellent. For three nights in November 2010 we observed 120 stars with the 2.1 m telescope of OAN-SPM under poor atmospheric conditions. All the measurements were made through the R filter with a 640/130 nm bandpass window. In these speckle observations we measured 38 new binaries detected by Hipparcos (ESA 1997). For each star, a typical observing procedure involved the accumulation of one set of 998 frames (1996 half-frames). One frame consists of a two-dimensional 440×400 array of 8-bit numbers. After the calibration we determined that the pixel scales are equal to $0.039''$/px and $0.038''$/px for the 2.1 m telescope and for the 1.5 m telescope, respectively. Tables 1 and 2 contain the results of the measurements of binary stars performed at the 1.5 m and 2.1 m telescopes. The format for the presentation of these measurements is the same as in our previous publication (Orlov et al. 2010). The first column contains the epoch-2000 coordinates in the format used in the Washington Double Star (WDS) Catalog (Worley & Douglass 1997). The second column gives the name of the star or the discoverer designation. The third column gives the epoch of the observation in fractional Besselian years. The two following columns contain the measured position angles given in degrees and the angular distances in arcseconds. The last three columns show ephemerides calculated for the date of observation and references to publications in which orbital elements can be found (Hartkopf & Mason 2003).

TABLE 1

SPECKLE MEASUREMENTS ON THE 1.5 M TELESCOPE

WDS ($\alpha, \delta J2000.0$)	Disc. Name	Date Besselian	P.A. (deg)	Sep. (arcsec)	P.A. Orb. (deg)	Sep. Orb. (arcsec)	Reference
00008+1659	BAG 18	2010.6349	0.7	0.63			
00024+1047	A 1249	2010.6349	72.9	0.21	74.5	0.16	Zirm (2003)
00039+2759	A 429	2010.6349	331.4	0.53			
00039+2759 AC	A 429	2010.6349	289.4	5.26			
00061+0943	HDS 7	2010.6350	178.4	0.19			
00073+2058	HDS 12	2010.6350	191.3	1.35			
00074+2029	KU 3	2010.6350	76.2	0.92			
00090+2339	HU 402	2010.6350	68.7	0.56			
00095+1907	COU 247	2010.6350	249.9	0.30	258.0	0.37	Zirm (2003)
00260+1905	HDS 59	2010.6350	264.7	0.79			
00262+2827	COU 446	2010.6350	312.9	0.85			
00279+2334	BU 779	2010.6350	246.4	0.62			
00287+2134	HU 601	2010.6350	307.4	0.63			
00295+1501	HEI 200	2010.6350	62.9	0.76			
00307+1339	HDS 66	2010.6350	267.3	0.98			
00324+2147	HDS 72	2010.6351	39.4	0.22			
00445+1956	TDS1595	2010.6351	273.3	0.84			
00470+2315	HU 413	2010.6351	313.7	0.35	317.2	0.38	Olevic (2002)
00487+1841	BU 495	2010.6351	253.9	0.28	250.4	0.31	Scardia et al. (2000)
00511+2853	COU 447	2010.6351	39.4	0.84			
00536+1911	COU 252	2010.6351	96.9	0.31			
00557+1706	HEI 94	2010.6351	255.2	1.04			
01007+1659	HEI 96	2010.6351	68.2	0.38			
01024+0504	HDS 135	2010.6351	90.7	0.65	91.1	0.66	Balega et al. (2006)
01028+0214	A 2308	2010.6351	292.2	0.36	293.0	0.27	Baize (1984)
01041+2635	COU 351	2010.6351	245.9	0.77			
01055+2107	AG 14	2010.6351	315.2	0.76	263.5	0.55	Heintz (1998)
01093+2428	COU 78	2010.6351	358.2	0.76			
01166+1831	HDS 169	2010.6351	240.5	0.61			
17452+2107	COU 630	2010.6352	115.2	0.22			
17453+1750	TDT 488	2010.6352	9.7	0.74			
17470+2915	TDS 881	2010.6352	243.2	1.01			
17472+1502	HU 1288	2010.6352	163.2	0.40			
17502+2704	TDT 526	2010.6352	147.2	0.83			
17506+1517	FOX 22	2010.6352	339.2	0.95			
17513+1723	TDT 536	2010.6352	62.2	1.04			
17571+1547	MCT 10	2010.6352	281.2	1.07			
18031+2702	TDT 653	2010.6352	26.4	0.74			
18032+2603	HO 565	2010.6352	91.4	0.19			
18086+1700	HDS2555	2010.6352	111.7	0.48			
18086+1838	HU 314	2010.6352	79.2	0.27			
18088+1923	TDT 707	2010.6352	68.2	0.61			
18303+1907	COU 508	2010.6352	254.4	0.89			
18312+2516	A 248	2010.6352	34.2	0.48			
18382+1426	HU 675	2010.6352	61.2	0.25			
18389+2324	TDT 972	2010.6352	48.7	0.85			
18396+2356	TDT 980	2010.6352	101.9	0.25			
18406+2636	COU 641	2010.6352	54.2	0.57			
18421+2753	TDT1009	2010.6352	268.4	0.58			
18443+2720	TDS 941	2010.6352	92.4	0.85			
19073+2432	A 262	2010.6352	266.9	0.17			
19224+2517 Aa, Ab	TDT1405	2010.6353	159.9	0.61			
19266+2619	HDS2763	2010.6353	209.2	0.76			
19276+1806	TDT1471	2010.6353	105.2	0.59			
19282+1507	TDT1476	2010.6353	330.4	0.73			
19284+2734	TDT1480	2010.6353	167.4	0.66			
19409+1523	HEI 74	2010.6353	109.9	0.86			
19421+1533	HU 1305	2010.6353	102.2	0.42			
19464+2438	TDT1727	2010.6353	222.7	0.61			
19477+1913	TDT1759	2010.6344	354.2	0.65			

TABLE 1 (CONTINUED)

WDS ($\alpha, \delta J2000.0$)	Disc. Name	Date Besselian	P.A. (deg)	Sep. (arcsec)	P.A. Orb. (deg)	Sep. Orb. (arcsec)	Reference
20216+2346	STF2672	2010.6344	345.7	0.69			
20227+2837	COU1169	2010.6344	64.4	0.26			
20227+2930	TDT2218	2010.6344	292.4	0.41			
21067+2321	TDT2755	2010.6344	215.7	0.84			
21068+2306	HU 364	2010.6345	96.7	0.21			
21083+2913	COU1331	2010.6345	36.2	0.30			
21085+2332	TDT2781	2010.6345	317.9	0.75			
21091+1906	COU 329	2010.6345	99.9	0.64			
21091+2922	COU1332	2010.6345	21.2	0.23			
21096+2632	COU 529	2010.6345	218.7	0.36			
21106+1650	HU 367	2010.6345	339.2	0.30			
21107+1334	HEI 186	2010.6345	262.2	0.17			
21109+2925	BAG 29	2010.6345	279.7	0.24			
21115+2144	COU 227	2010.6345	112.9	0.51	213.0	0.13	Couteau (1995)
21125+2821	HO 152	2010.6345	135.4	0.22	132.8	0.27	Scardia et al. (2002)
21461+2448	TDT3149	2010.6345	218.4	0.65			
21466+1929	COU 431	2010.6345	183.2	0.46			
21468+2718	HO 608	2010.6346	127.4	0.57			
21481+2100	HU 378	2010.6346	297.4	0.18			
21488+2439	TDT3169	2010.6346	350.2	0.82			
21500+2157	TDT3184	2010.6346	170.7	2.56			
21521+2748	HO 171	2010.6346	341.7	0.73			
22196+2107	HU 383	2010.6346	29.9	0.36			
22202+2931	BU 1216	2010.6346	278.2	0.91			
22217+1125	TDT3484	2010.6346	256.7	0.26			
22392+2014	HU 393	2010.6347	226.4	0.87			
22396+2822	A 413	2010.6347	14.9	1.09			
22457+2924	HO 481	2010.6347	287.2	0.44			
22474+1749	WSI 91	2010.6347	113.7	0.26			
22479+1259	HU 985	2010.6347	136.4	0.70	139.6	0.67	Seymour et al. (2002)
23024+1837	HU 398	2010.6347	287.9	0.47	293.3	0.45	Baize (1981)
23038+2851	TDT3868	2010.6347	10.2	0.17			
23039+2512	COU 142	2010.6347	190.4	0.50			
23361+2027	TDT4118	2010.6347	1.9	0.58			
23368+2346	HU 498	2010.6348	298.2	0.67			
23379+2510	COU 441	2010.6348	10.7	0.69			
23380+1253	A 1241	2010.6348	9.9	0.62			
23401+1258	HU 1325	2010.6348	30.2	0.83	31.6	0.63	Olevic & Jovanovic (2001)
23401+1258	HU 1325				26.0	0.84	Scardia (2003)
23431+1150	A 1242	2010.6348	337.7	0.99	337.4	0.96	Ling (2004)
23435+1652	HEI 196	2010.6348	167.4	0.83			
23465+1705	EGB 8	2010.6348	86.4	1.07			
23470+1726	TDT4190	2010.6348	33.9	0.55			
23475+1729	TDT4195	2010.6348	315.2	0.70			
23486+1622	HEI 91	2010.6348	152.7	0.68			
23491+1915	COU 343	2010.6349	102.7	0.17			
23504+2620	COU 545	2010.6349	315.7	0.73			

4. CONCLUSION

We have presented the results of binary star observations focused on binaries from the WDS catalogue. In particular, we have been interested in new binaries discovered by Hipparcos. We confirmed 38 new binaries detected by Hipparcos. The main aim of this study was in the selection of binaries with a fast relative motion allowing to obtain candidates for determinations of new orbits. From our observation results we can also conclude that our new detector based on Wat-120N CCD is suitable for speckle observations with the OAN-based telescopes.

The speckle interferometry program at the OAN telescopes is supported by the Dirección General de Asuntos del Personal Académico (Universidad Nacional Autónoma de México, Mexico) under projects IN104910 and IN113308 (PAPIIT).

TABLE 2

SPECKLE MEASUREMENTS ON THE 2.1 M TELESCOPE

WDS ($\alpha, \delta J2000.0$)	Disc. Name	Date Besselian	P.A. (deg)	Sep. (arcsec)	P.A. Orb. (deg)	Sep. Orb. (arcsec)	Reference
00004+2749	TDS1238	2010.8836	87.9	0.85			
00008+1659	BAG 18	2010.8836	0.9	0.59			
00055+3406	HU 1201	2010.8919	304.2	0.21	307.19	0.192	Zirm (2003)
00085+3456	HDS 17	2010.8919	78.9	0.12	79.71	0.126	Cvetkovic (2010)
00260+1905	HDS 59	2010.8836	263.7	0.84			
00271+1852	TDS 19	2010.8836	137.4	0.90			
00295+1501	HEI 200	2010.8836	60.7	0.77			
00307+1339	HDS 66	2010.8836	266.9	0.93			
00312+0237	TDS1505	2010.8836	76.2	0.76			
00324+2147	HDS 72	2010.8836	38.9	0.21			
00344+2411	COU 350	2010.8837	140.9	0.94			
00353+2456	TDS1533	2010.8837	28.7	0.77			
00364+1213	A 807	2010.8837	233.9	0.86			
00374+0900	A 808	2010.8837	181.4	0.23			
00404+2504	COU 75	2010.8837	52.2	0.48			
00429+2047	A 2205	2010.8837	6.9	0.34	4.37	0.306	Baize (1989)
00487+1841	BU 495	2010.8837	247.7	0.28	249.789	0.314	Scardia et al. (2000)
01014+1155	BU 867	2010.8837	354.2	0.63	354.475	0.626	Hartkopf et al. (2008)
01046+2558	COU 253	2010.8837	95.9	0.95			
01055+2107	AG 14	2010.8837	314.7	0.76	263.073	0.549	Heintz (1998)
01072+3839	A 1516	2010.8920	4.7	0.22	355.60	0.145	Hartkopf et al. (2000)
01080+1204	A 2101	2010.8837	258.9	0.64			
01093+2428	COU 78	2010.8837	357.9	0.89			
01106+4917	COU2156	2010.8920	161.9	0.45			
01112+4113	A 655	2010.8920	353.9	0.33	349.24	0.317	Cvetkovic & Novakovic (2006)
01148+6056	BU 1100	2010.8920	353.4	0.33	351.21	0.268	Muller (1955)
01148+6056	BU 1100				153.72	0.199	Starikova (1977)
01178+4945	HU 520	2010.8920	167.4	0.33			
01251+4537	A 939	2010.8921	194.9	0.23	226.87	0.175	Starikova (1983)
01283+4247	AC 14	2010.8838	91.4	0.78			
01283+4247	AC 14	2010.8921	91.4	0.75			
01449+1951	A 2322	2010.8921	208.2	1.26			
01502+2702	BU 1313	2010.8921	153.7	0.53			
01510+2551	COU 452	2010.8921	179.2	0.23			
01513+6021	A 951	2010.8921	225.9	0.43			
01535+4437	STF3113	2010.8838	278.2	0.66			
01550+5817	A 954	2010.8921	198.7	0.63			
01551+5958	A 955	2010.8838	106.4	1.00			
01573+4812	A 818	2010.8838	204.7	0.28			
01584+5154	COU2559	2010.8838	65.4	0.40			
01586+3334	HDS 267	2010.8838	161.7	0.26			
01586+3334	HDS 267	2010.8922	165.7	0.23			
01588+3826	TDS2077	2010.8838	237.2	0.41			
02016+4107	COU1510	2010.8838	133.4	0.41			
02019+4831	COU2009	2010.8839	60.2	0.56			
02063+4936	COU2561	2010.8839	123.4	0.77			
02085+5852	HDS 284	2010.8839	77.7	0.22			
02085+5852	HDS 284	2010.8922	76.7	0.24			
02279+4523	COU2011	2010.8922	59.7	0.34			
02314+4234	A 660	2010.8922	311.4	0.52			
02323+3542	A 1927	2010.8922	192.2	0.81			
02382+4604	A 1278	2010.8922	311.7	0.22	286.29	0.231	Hartkopf & Mason (2001)
02417+5529	A 1280	2010.8923	12.7	0.33			
02454+5634 Aa, Ab	MLR 599	2010.8923	359.7	0.23			
03032+4121	COU1381	2010.8839	71.2	0.24			
03041+5040	COU2567	2010.8839	62.2	0.41			
03058+4818	COU2016	2010.8839	58.7	0.15			
03061+5144	COU2454	2010.8839	24.9	0.41			
03068+5813	TDS2446	2010.8839	351.4	0.77			

TABLE 2 (CONTINUED)

WDS ($\alpha, \delta J2000.0$)	Disc. Name	Date Besselian	P.A. (deg)	Sep. (arcsec)	P.A. Orb. (deg)	Sep. Orb. (arcsec)	Reference
03076+5230	MLR 658	2010.8839	80.2	0.40			
03081+4327	COU1679	2010.8839	1.9	0.50			
03084+4736	COU2017	2010.8839	9.4	0.28			
03129+5126	COU2568	2010.8839	309.4	0.40			
03138+3733 Aa, Ab	COU1075	2010.8839	40.4	0.89			
03141+5023	HU 543	2010.8840	106.9	0.29			
03150+3543	HO 502	2010.8840	15.2	0.84			
03250+4013	HU 1058	2010.8923	112.4	0.82			
03264+3520	HDS 430	2010.8923	278.2	0.23			
03279+4551	COU1687	2010.8840	290.4	0.77			
03279+4614	COU1686	2010.8840	262.7	0.53			
03354+3529	POP 83	2010.8923	265.9	0.51			
03484+5202	HU 546	2010.8840	26.2	0.30	28.527	0.358	Hartkopf & Mason (2009)
03499+4314	COU1691	2010.8840	318.4	0.38			
03503+4403	COU1692	2010.8840	37.9	0.53			
03522+5357	MLR 665	2010.8840	335.4	0.37			
03546+4554	TDS 121	2010.8840	113.4	0.97			
03586+4605	COU1696	2010.8840	139.2	0.86			
03594+4321	A 1708	2010.8840	338.2	0.82			
04016+5044	COU2458	2010.8841	141.2	0.65			
04017+5611	HDS 507	2010.8841	133.4	0.45			
04035+4211	A 1709	2010.8923	222.7	1.01			
04050+4936	COU2267	2010.8841	106.9	0.42			
04081+3407	COU1082	2010.8923	57.9	0.33			
04081+4535	COU2025	2010.8923	339.2	0.33			
04159+3142	STT 77	2010.8924	294.2	0.53	295.60	0.550	Starikova (1985)
04284+4914	HDS 575	2010.8924	315.7	0.45			
04302+5343	A 1300	2010.8841	148.2	0.85			
04306+5014	HU 550	2010.8841	298.4	0.53			
04308+4550	A 1007	2010.8841	161.9	0.27			
04310+4159	HDS 583	2010.8924	116.7	0.21			
04378+5249	MLR 696	2010.8841	66.2	1.05			
04381+5707	HDS 598	2010.8924	333.9	0.23			
04430+5712	A 1014	2010.8924	17.4	0.34	18.19	0.346	Brendley & Hartkopf (2007)
04477+4014	A 1545	2010.8924	95.7	0.45			
04542+4935 B	STF 603	2010.8925	105.9	1.13			
04542+4935 A	STF 603	2010.8925	99.4	2.18			
04599+4319	A 1551	2010.8841	273.4	0.23			
05038+3813	TDS3054	2010.8841	4.2	0.26			
05044+2139	COU 154	2010.8869	303.9	0.17			
05044+2938	A 1024	2010.8869	332.4	0.73			
05047+4458	A 1022	2010.8842	342.2	0.62			
05057+4516	COU2463	2010.8842	40.9	0.53			
05061+4222	COU2464	2010.8842	181.4	0.59			
05078+3723	COU1529	2010.8842	358.2	0.59			
05085+3755	COU1531	2010.8925	45.7	0.22			
05106+4924	HDS 684	2010.8925	57.2	0.46			
05119+4459	TDS3105	2010.8842	214.2	0.65			
05133+4940	COU2578	2010.8842	109.4	0.47			
05140+3655	POP 140	2010.8925	166.4	0.32			
05195+3809	COU1870	2010.8925	19.2	0.43			
05208+3329	COU1231	2010.8925	165.9	0.64			
05240+3238	COU1090	2010.8925	233.9	0.22			
05267+3857	HDS 714	2010.8925	262.4	0.45			
05310+2635	COU 574	2010.8869	136.2	0.32			
05319+2141	COU 268	2010.8869	164.2	0.72			
05326+4422	HDS 729	2010.8926	163.7	0.22			
05350+1838	A 2354	2010.8870	310.9	0.43			
05357+2054	COU 270	2010.8870	42.4	0.71			
06000+4643	A 1727	2010.8842	247.4	0.62			
06016+4111	COU2049	2010.8843	233.9	1.28			

TABLE 2 (CONTINUED)

WDS ($\alpha, \delta J2000.0$)	Disc. Name	Date Besselian	P.A. (deg)	Sep. (arcsec)	P.A. Orb. (deg)	Sep. Orb. (arcsec)	Reference
06025+3620	HU 1236	2010.8843	37.2	0.41			
06049+3211	HU 827	2010.8843	74.4	0.23			
06060+2331	HU 450	2010.8870	244.2	0.44			
06065+1832	A 2444	2010.8870	181.4	0.12			
06073+1848	COU 471	2010.8870	159.2	0.34			
06087+1724	STF 849	2010.8870	241.4	0.91			
06097+1630	A 2514	2010.8870	102.7	0.24			
06097+2914	A 54	2010.8870	332.4	0.55			
06117+2846	A 55	2010.8870	259.7	0.43			
06142+1217	TDS3652	2010.8870	17.9	0.43			
06150+1649	A 2044	2010.8871	34.9	0.34			
06152+2917	COU1103	2010.8871	51.9	0.23			
06185+2241	HDS 863	2010.8871	50.7	0.22			

REFERENCES

Baize, P. 1981, A&AS, 44, 199

_____. 1984, A&AS, 56, 103

_____. 1989, A&AS, 78, 125

Balega, I. I., Balega, Y. Y., Hofmann, K.-H., Malogolovets, E. V., Schertl, D., Shkhagosheva, Z. U., & Weigelt, G. 2006, A&A, 448, 703

Brendley, M., & Hartkopf, W. I. 2007, IAUDS Inf. Circ. 163

Couteau, P. 1995, VizieR Online Data Catalog 1209, `http://cdsarc.u-strasbg.fr/viz-bin/Cat?I/209A`

Cvetković, Z., & Novaković, B. 2006, Serb. Astron. J., 173, 73

Cvetkovic, Z. 2010, IAUDS Inf. Circ. 172

ESA 1997, The Hipparcos and Tycho Catalogues, ESA SP-1200 (Noordwijik: ESA)

Hartkopf, W. I., & Mason, B. D. 2001, IAUDS Inf. Circ. 145

_____. 2003, Sixth Catalog of Orbits of Visual Binary Stars (Washington: USNO), `http://ad.usno.navy.mil/wds/orb6.html`

_____. 2009, AJ, 138, 813

Hartkopf, W. I., Mason, B. D., & Rafferty, T. 2008, AJ, 135, 1334

Hartkopf, W. I., et al. 2000, AJ, 119, 3084

Heintz, W. D. 1998, ApJS, 117, 587

Ling, J. F. 2004, IAUDS Inf. Circ. 154

Muller, P. 1955, J. Obs., 38, 58

Olevic, D. 2002, IAUDS Inf. Circ. 147

Olevic, D., & Jovanovic, P. 2001, Serb. Astron. J., 163, 5

Orlov, V. G., Voitsekhovich, V. V., Mendoza-Valencia, G. A., Svyryd, A., Rivera, J. L., Ortiz, F., & Guerrero, C. A. 2009, RevMexAA, 45, 155

Orlov, V. G., Voitsekhovich, V. V., Rivera, J. L., Guerrero, C. A., & Ortiz, F. 2010, RevMexAA, 46, 245

Scardia, M. 2003, IAUDS Inf. Circ. 149

Scardia, M., Prieur, J.-L., Aristidi, E., & Koechlin, L. 2000, Astron. Nachr., 321, 255

Scardia, M., Prieur, J.-L., Koechlin, L., & Aristidi, E. 2002, IAUDS Inf. Circ. 146

Seymour, D., Mason, B. D., Hartkopf, W. I., & Wycoff, G. L. 2002, AJ, 123, 1023

Starikova, G. A. 1977, Astron. Tsirk. 961, 7

_____. 1983, Soviet Astron. Lett., 9, 189

_____. 1985, Trudy Gos. Astron. Inst. Sternberga, 57, 243

Tokovinin, A., Mason, B. D., & Hartkopf W. I. 2010, AJ, 139, 743

Worley, C. E., & Douglass, G. G. 1997, A&AS, 125, 523

Zirm, H. 2003, IAUDS Inf. Circ. 151

F. Ángeles, A. Farah Simon, C. A. Guerrero, E. Luna, V. G. Orlov, R. Vázquez Robledo, and V. V. Voitsekhovich: Instituto de Astronomía, Universidad Nacional Autónoma de México, Apdo. Postal 70-264, Cd. Universitaria, 04510 México D.F., México (fernando.angeles@gmail.com, farah, cguerrero@astro.unam.mx, eala@astrosen.unam.mx, orlov, rvazquez@astro.unam.mx, vvv.spm@gmail.com).

Revista Mexicana de Astronomía y Astrofísica, **47**, 219–234 (2011)

UPPER MAIN SEQUENCE STARS WITH ANOMALOUS ABUNDANCES. THE HGMN STARS HR 3273, HR 8118, HR 8567 AND HR 8937

C. Saffe, N. Núñez, and H. Levato

Instituto de Ciencias Astronómicas, de la Tierra y del Espacio (ICATE)
and Facultad de Ciencias Exactas, Físicas y Naturales
Universidad Nacional de San Juan, Argentina

Received 2010 December 13; accepted 2011 April 14

RESUMEN

Este trabajo es parte de un estudio para verificar posibles tendencias de las abundancias en estrellas HgMn con los parámetros estelares, rotación y edad. Presentamos un análisis de las estrellas HR 3273, HR 8118, HR 8567 y HR 8937. Utilizamos espectros echelle tomados con el telescopio de 2.1 m del CASLEO y modelos de atmósferas de ATLAS9. El He resultó por debajo del valor solar para las estrellas HgMn. El O resultó levemente sobreabundante en HR 3273 y HR 8567. MgII resultó por debajo excepto para HR 8118. El SiII resultó aproximadamente solar en HR 8118 y HR 8937, y por debajo en HR 3273 y HR 8567. El Fe resultó levemente sobreabundante en HR 8118 y HR 8937 y subabundante en HR 3273 y HR 8567. Las especies Sc, Ti, Cr, Mn, Sr, Y y Zr resultaron sobreabundantes mientras que el Ni resultó estar por debajo del valor solar.

ABSTRACT

This work is part of our current study for verifying a possible relation between abundances of HgMn stars with stellar parameters, rotation and age. We present an analysis of the stars HR 3273, HR 8118, HR 8567 and HR 8937. We used echelle spectra taken with the CASLEO 2.1 m telescope and ATLAS9 model atmospheres. HeI was underabundant for the HgMn stars. O was slightly underabundant in HR 3273 and HR 8567. MgII was underabundant except for HR 8118. SiII was close to solar in HR 8118 and HR 8937, and underabundant in HR 3273 and HR 8567. Fe was slightly underabundant in HR 3273 and HR 8567, and slightly overabundant in HR 8118 and HR 8937. The species Sc, Ti, Cr, Mn, Sr, Y and Zr were overabundant while Ni was underabundant.

Key Words: stars: chemically peculiar — stars: individual (HR 3273, HR 8118, HR 8567, HR 8937)

1. INTRODUCTION

The mercury-manganese (HgMn) stars belong to a group of chemically peculiar (CP) stars observed in the upper main sequence. Their hydrogen spectral types are usually B7-B9 with effective temperatures between 10000 K and 15000 K. HgMn stars show typically intensified lines of Hg (up to ∼5 dex), Mn (up to ∼3 dex) and a deficiency of He. This group shows an unusually high proportion of multiple systems: more than two thirds of them are spectroscopic binaries (SBs), many of which are double-lined systems (e.g., Hubrig & Mathys 1995). They are usually slow rotators (e.g., Abt, Chaffee, & Suffolk 1972) and they show no evidence of large-scale organized magnetic fields (e.g., Auriére et al. 2007, 2010; Makaganiuk et al. 2011).

The relation of the anomalous abundances and stellar parameters is not totally clear. Some authors found no correlation between the total HgII abundance and the effective temperature (e.g., Smith 1997; Woolf & Lambert 1999), while Dolk, Wahlgren, & Hubrig (2003) found a possible correlation for a sample of 31 HgMn stars. On the other hand, Smith & Dworetsky (1993) and later Jomaron, Dworetsky,

TABLE 1

OBSERVATIONAL DATA FOR THE SAMPLE OF HGMN STARS

Parameter	HR 3273	HR 8118	HR 8567	HR 8937	References
$B-V$	−0.08	−0.08	−0.04	−0.10	R1,R6,R8
$U-B$	−0.38	−0.32	−0.37	−0.37	R1,R6
V	6.42	6.76	6.36	4.37	R1,R6,R9
$b-y$	−0.020	−0.028	−0.018	−0.046	R2
m_1	0.090	0.117	0.101	0.125	R2
c_1	0.710	0.801	0.678	0.677	R2
β	2.704	2.780	2.737	2.776	R2
J	6.515	6.848	6.410	4.477	R7
H	6.607	6.925	6.493	4.669	R7
K	6.585	6.907	6.467	4.611	R7
Sp. Type	B9p (HgMn)	B9p Hg(Mn?)	B8(Mn), HgMn	B9.5 IVp (HgMn)	R3,R4,R5 R10, R11

References: R1: Cousins & Stoy (1962), R2: Hauck & Mermilliod (1998), R3: Andersen & Nordström (1977), R4: Renson & Manfroid (2009), R5: Wolff & Wolff (1974), R6: Corben & Stoy (1968) , R7: Cutri et al. (2003), R8: Crawford (1963), R9: Corben (1971), R10: Cowley et al. (1969), R11: Houk (1982).

& Allen (1999) found a dependence between MnI and MnII abundances and temperature. The authors suggest that difussion takes place in the atmospheres of these stars, but probably affected by other factors such as rotation and evolutionary state. This research is part of our current program for deriving elemental abundances among field CP stars and members of open clusters. The motivation of our work is to derive abundances for a sample of HgMn stars to determine possible relations with their fundamental parameters and other factors such as rotation, evolutionary state and age. In particular in this paper we report the results of four CP stars of the HgMn class, HR 3273, HR 8118, HR 8567 and HR 8937.

The star HR 3273 was classified as an HgMn star by Andersen & Nordström (1977). They studied ∼70 bright southern stars using coudé spectrograms of 20 Å/mm, taken with the ESO 1.5 m telescope at La Silla, Chile. The authors identified HR 3273 as a B9p (HgMn) star, with no definite variation in their spectra. UBV photoelectric photometry was published by Cousins & Stoy (1962). $uvby-\beta$ photometry was provided by Hauck & Mermilliod (1998), Eggen (1977) and Gronbech & Olsen (1976). JHK infrared photometry was presented by Cutri et al. (2003).

The star HR 8118 was classified as Hg(Mn?) star in the spectroscopic study of the Bright Star Catalogue by Cowley et al. (1968). They identified the line HgII $\lambda\lambda$3984 in the spectra taken at the Yerkes observatory with a dispersion of 125 Å/mm. Then the star was listed and classified as B9p Hg(Mn?) in the study of A bright stars (Cowley et al. 1969). UBV photometry was obtained by Crawford (1963) and Corben (1971). $uvby-\beta$ photometry was published by Gronbech & Olsen (1977) and Hauck & Mermilliod (1998).

The star HR 8567 was classified as HgMn star by Wolff & Wolff (1974). They studied 194 stars of types B4-B9 and identified in their sample 24 HgMn stars. The authors used UV spectrograms with a dispersion of 50 Å/mm in the region 3440–3500 Å. In this spectral range there are several strong lines of MnII. HR 8567 was classified as B8(Mn) star in the catalog of Renson & Manfroid (2009) and listed as HgMn star in the catalog of Schneider (1981). UBV photoelectric photometry was published by Rybka (1969) and Corben & Stoy (1968). $uvby-\beta$ photometry was obtained by Hauck & Mermilliod (1998), Gronbech & Olsen (1976) and Eggen (1977), and JHK infrared photometry was presented by Cutri et al. (2003).

The star HR 8937 was classified as B9p by Bertaud (1958) and then listed as B9.5 IVp (HgMn) in the Michigan Catalogue of Two Dimensional Spectral Types (Houk 1982). UBV photoelectric photometry have been provided by Abt & Golson (1962) and Irwin (1961). $uvby$ photometry was published by Crawford, Barnes, & Golson (1970) and Hauck & Mermilliod (1998), and their β photometric index were determined by Strauss & Ducati (1981).

Table 1 presents some relevant observational data for the sample of HgMn stars, HR 3273, HR 8118, HR 8567 and HR 8937.

2. OBSERVATIONAL MATERIAL AND LINE IDENTIFICATIONS

The stellar spectra of the stars were obtained at Complejo Astrónomico El Leoncito (CASLEO) between April 21 and 23, 2004. We used the *Jorge Sahade* 2.15 m telescope that fed the EBASIM echelle spectrograph through an optical fiber. The spectra were recorded on a TEK1024 (1024 × 1024 pixels) CCD detector. The EBASIM spectrograph uses gratings as cross dispersers. We have used one grating with 226 lines mm^{-1} centered at ∼5000 Å. Three spectra of each star were obtained, covering the visual range ∼λλ3800–5900 Å. The S/N ratio of the spectra is around 250 and the resolving power of the spectrograph is approximately 40000. Table 2 gives the spectral coverage of the 55 orders of the EBASIM spectrograph[1]. It contain echelle orders overlapping in ∼λλ3762–5644 Å and increasing gaps of 1–4 Å for $\lambda \gtrsim 5645$ Å.

The spectra were reduced using IRAF[2] standard procedures for echelle spectra. We applied bias and flat corrections and then normalized order by order with the *continuum* task, using 7–9 order Chebyshev polynomials. We also corrected the scattered light in the spectrograph (*apscatter* task). We fitted the background with a linear function on both sides of the echelle apertures, using the task *apall*. Extensive description of the characteristics of the reduction technique and some results obtained with the observational material, have been previously published (e.g., Saffe & Levato 2009). The equivalent widths were measured by integrating the profiles across the stellar metallic lines using the *splot* task. There are no differences among the equivalent width measurements of the same lines in different spectra.

We used Gaussian profiles to fit the stellar lines. This is an interactive process in which the IRAF user marks two continuum points in the spectra and then the program fits a single line profile (splot task). IRAF uses a fixed linear continuum through the stellar line. The fitting uses an interactive algorithm based on the Levenberg-Marquardt method. The successive iterations tend to improve the fit by varying the parameters along the gradient of improvement in the χ^2 function. The final fit is overplotted on the spectrum of the star and the user decides if the fit is satisfactory or not. The center, continuum at the center, core intensity, integrated flux, equivalent width and FWHMs are printed and saved in a log file. All the parameters except the continuum are based on the fitted analytic profiles.

Pintado & Adelman (2003) compared EBASIM and DAO (Dominion Astrophysical Observatory) equivalent widths corresponding to echelle and coudé spectra, respectively. The scattered light is usually easier to measure in the latter case. They used Gaussian profiles for the EBASIM spectra and rotational profiles for the DAO spectra, due to the lower res-

TABLE 2

SPECTRAL COVERAGE FOR THE EBASIM ECHELLE SPECTROGRAPH USING THE GRATING OF 226 LINES mm^{-1}

Order	Range [Å]	Order	Range [Å]
1	3762–3798	29	4625–4670
2	3787–3823	30	4663–4708
3	3813–3849	31	4702–4748
4	3839–3875	32	4741–4788
5	3865–3902	33	4781–4828
6	3891–3929	34	4822–4869
7	3918–3956	35	4864–4911
8	3946–3984	36	4906–4954
9	3973–4012	37	4949–4998
10	4002–4041	38	4993–5042
11	4030–4070	39	5037–5087
12	4059–4099	40	5083–5133
13	4088–4129	41	5129–5180
14	4118–4159	42	5176–5227
15	4149–4190	43	5224–5276
16	4179–4221	44	5273–5325
17	4210–4252	45	5323–5375
18	4242–4284	46	5374–5426
19	4274–4317	47	5425–5478
20	4307–4350	48	5478–5533
21	4340–4383	49	5533–5588
22	4373–4417	50	5588–5644
23	4407–4451	51	5645–5701
24	4442–4486	52	5703–5760
25	4478–4522	53	5762–5820
26	4514–4558	54	5822–5881
27	4550–4594	55	5884–5943
28	4587–4632		

[1]Due to modifications in the configuration of the EBASIM spectrograph, the spectral coverage could slightly vary in different observing runs.

[2]IRAF is distributed by the National Optical Astronomical Observatories which is operated by the Association of Universities for Research in Astronomy, Inc., under a cooperative agreement with the National Science Foundation.

olution of the EBASIM data. For 170 unblended lines of the star α Sex in the region 3840–4930 Å, they obtained nearly the same scale for the equivalent widths. Then, they did not apply any additional correction to the equivalent widths of the EBASIM spectra. However, we caution that the comparison done in Pintado & Adelman (2003) needs to be extended and made more robust. The authors plan to extend it with high S/N (> 500) spectra of sharp-lined stars.

The stellar lines of the HgMn stars were identified using the same procedure of previous papers (Saffe, Levato, & López-García 2004, 2005; Saffe & Levato 2009). We used the general references of *A Multiplet Table of Astrophysical Interest* (Moore 1945) and *Wavelengths and Transition Probabilities for Atoms and Atomic Ions*, Part 1 (Reader et al. 1980) as well as the more specialized references for P II (Svendenius, Magnusson, & Zetterberg 1983), Mn II (Iglesias & Velasco 1964), Fe II (Dworetsky 1971; Johansson 1978; Guthrie 1985) and Y II (Nilsson, Johansson, & Kurucz 1991). The final line list is similar to those used in recent papers of HgMn stars (Zavala et al. 2007; Adelman & Yüce 2010).

3. ATMOSPHERIC PARAMETERS

An estimate of the effective temperature and gravity was done by Woolf & Lambert (1999), who used the Strömgren $uvby-\beta$ photometry and the calibration of Moon & Dworetsky (1985). For HR 3273, the authors derived 12350 K and 3.28 dex for $T_{\rm eff}$ and $\log g$, respectively. Glagolevskij (1994) used the Shallis-Blackwell method and derived two temperatures from the parameters Q and X (reddening free index and multicolor photometry parameter). For HR 8118 they obtained 11900 K and 11500 K, while for HR 8937 they obtained 12400 and 12300 K, using the Q and X parameters, respectively. Dolk et al. (2003) derived a temperature and gravity using *uvby* photometric data but with the calibration of Napiwotzki, Shonberner, & Wenske (1993). For HR 8567, they obtained 11977 K and 4.06 dex, while for HR 8937 they derived 12476 K and 4.13 dex for $T_{\rm eff}$ and $\log g$, respectively.

We compared the observed Hγ profiles with synthetic spectra of the Hγ region calculated with SYNTHE (Kurucz & Avrett 1981) using Kurucz ATLAS9 (Kurucz 1995, private communication) model atmospheres with [M/H]=0.0, i.e. solar abundance, which seems to be adequate for these stars. However it is difficult to obtain accurate Balmer line profiles in this region from echelle spectra covering several orders. Thus, we estimated $T_{\rm eff}$ and $\log g$ using the $uvby-\beta$ mean colors of Hauck & Mermilliod (1998) with the calibration of Napiwotzki et al. (1993), and then we corrected the $T_{\rm eff}$ values according to Adelman & Rayle (2000). These values are presented in the first two columns of Table 3. Next we adjusted the surface gravity to get ionization equilibrium from FeI and FeII. A similar strategy was applied by Adelman & Yüce (2010) in the derivation of the fundamental parameters. The final adopted values of the fundamental parameters are shown in Table 3.

TABLE 3

TEMPERATURE AND GRAVITY DERIVED FOR THE HGMN STARS

Star	$uvby-\beta$ $T_{\rm eff}$	$uvby-\beta$ $\log g$	Adopted $T_{\rm eff}$	Adopted $\log g$
HR 3273	12253	3.32	12253	3.42
HR 8118	11381	4.01	11381	4.11
HR 8567	12315	3.78	12315	3.68
HR 8937	12088	4.28	12088	4.28

We fitted a synthetic spectrum to ∼20 Fe lines in order to derive an estimation of the rotational velocities of the HgMn stars. We used the program SYNTHE (Kurucz & Avrett 1981) and the command *broaden* to reproduce the instrumental broadening of the EBASIM spectrograph, adopting a resolving power of $R \sim 40000$. The value of R is approximate, and thus the derived rotational velocities should be taken with caution. The final $v \sin i$ values are obtained using the average and standard deviation of the lines. We derived rotational velocities of 20 ± 2 km s^{-1}, 30 ± 1 km s^{-1}, 22 ± 1 km s^{-1} and 24 ± 2 km s^{-1} for the stars HR 3273, HR 8118, HR 8567 and HR 8937, respectively. The HgMn stars of our sample are not extremely slow rotators.

4. ABUNDANCE ANALYSES

To derive the abundances of the chemical species we used the WIDTH9 code (Kurucz 1995, private communication) and equivalent widths measured in the spectra of the stars. The program also requires the selection of a model atmosphere and the atomic data for the lines (oscillator strength, excitation potentials, damping constants, etc.). The code calculates a theoretical equivalent width for an initial input abundance (taken from the model atmosphere) and compares this value with the measured EW. WIDTH9 computes basically the line profile and the curve of growth. Then it modifies the abundance iteratively to achieve a difference between theoretical and measured equivalent width < 0.01 mÅ. The process is repeated for each measured spectral line.

TABLE 4

DETERMINATION OF MICROTURBULENT VELOCITY FROM FEII LINES

Star	Species	n	ξ_1 km s^{-1}	$\log N/N_T$	ξ_2 km s^{-1}	$\log N/N_T$	gf-values
HR 3273	FeII	64	0.3	-4.75 ± 0.22	0.0	-4.74 ± 0.27	N4+KX+MF
		37	0.9	-4.87 ± 0.24	0.0	-4.80 ± 0.28	N4+MF
	adopted ξ:	0.3 km s^{-1}					
HR 8118	FeII	63	1.0	-4.36 ± 0.21	0.0	-4.28 ± 0.28	N4+KX+MF
		37	1.2	-4.41 ± 0.24	0.0	-4.27 ± 0.26	N4+MF
	adopted ξ:	0.5 km s^{-1}					
HR 8567	FeII	56	0.0	-4.91 ± 0.21	0.0	-4.91 ± 0.28	N4+KX+MF
		33	0.5	-4.99 ± 0.24	0.0	-4.98 ± 0.26	N4+MF
	adopted ξ:	0.1 km s^{-1}					
HR 8937	FeII	80	0.9	-4.32 ± 0.21	0.0	-4.27 ± 0.28	N4+KX+MF
		39	1.1	-4.40 ± 0.24	0.0	-4.29 ± 0.26	N4+MF
	adopted ξ:	0.5 km s^{-1}					

Note: the source of gf values are KX (Kurucz & Bell 1995), MF (Fuhr, Martin, & Wiese 1988) and N4 (Fuhr & Wiese 2006).

The adopted metal line damping constants were the default semi-classical approximations except for those of neutral and singly-ionized Ca-Ni lines, whose values are based on the data of Kurucz & Bell (1995). For the lines of CII, multiplet 6, and MgII, multiplet 4, the adopted values for Stark broadening were based on data of Sahal-Brechot (1969), and for SiII and CaII, the damping constants are those of Lanz, Dimitrijevic, & Artru (1988), and Chapelle & Sahal-Brechot (1970) respectively. We prefer this choice of gf values to the VALD database (Piskunov 1996) to ensure homogeneity with our previous work.

To determine the abundances we need an initial estimation of the microturbulent velocity (ξ). For this estimation we have used the standard method. We computed abundances from the FeII lines for a range of possible microturbulent velocities (ξ). For determining the final values (Table 4), we looked for the conditions that the abundances of FeII were not dependent on the equivalent widths (ξ_1) or that they minimize the rms scatter of the abundances (ξ_2). Values for each species were derived using lines with gf values from 3 different sources: KX values (Kurucz & Bell 1995), MF values (Fuhr et al. 1988) and N4 values (Fuhr & Wiese 2006). The sources of gf values shown in the last column of Table 4 determine the number of lines, n. The values derived for the microturbulence using the FeII lines are 0.32 km s^{-1}, 0.55 km s^{-1}, 0.13 km s^{-1} and 0.52 km s^{-1}, for the HgMn stars HR 3273, HR 8118, HR 8567 and HR 8937, respectively. Once a ξ value has been fixed the abundances corresponding to all chemical species measured are determined using the WIDTH9 code.

In our abundance determination we did not include seriously blended lines. To give an idea of the sensitivity of our results, raising the temperature of HR 3273 by ∼4% (500 K) increases the average abundance by ∼2%, and raising the surface gravity by ∼15% (0.5 dex) increases the average abundance by ∼0.5%. Table 5 shows the sensivity of the results for the abundances to these changes.

We present in the Table 6 the He/H ratios derived comparing the observed HeI line profiles with synthetized spectra. We used the program SYNTHE under the LTE condition; the results were convolved with the rotational velocity of the star and the instrumental broadening of the spectrograph. The mean derived He/H values are 0.07, 0.09, 0.08 and 0.03, for the stars HR 3273, HR 8118, HR 8567 and HR 8937, respectively.

Previous works in literature derived the Hg abundance taking into account the isotopic and hyperfine structure, using higher resolution spectra and S/N than ours (Woolf & Lambert 1999; Dolk et al. 2003). They determined the isotopic mixture for the line HgII $\lambda\lambda$3984 using similar values of $T_{\rm eff}$ and $\log g$. We adopted the Hg abundance derived by these authors for HR 3273 (-5.25 ± 0.32 dex), HR 8567 (-5.58 ± 0.37 dex) and HR 8937 (-4.23 ± 0.43 dex). These values are comparable to those derived using the equivalent width of $\lambda\lambda$ 3984, and LTE model atmosphere, i.e. -4.83 dex, -5.39 dex and -4.06 dex,

TABLE 5

SENSITIVITY OF THE DERIVED ABUNDANCES OF HR 3273 TO CHANGES IN EFFECTIVE TEMPERATURE AND SURFACE GRAVITY

HR 3273 Element	$\log N/H$ for adopted model	$\log N/H$ for 500 K hotter model	$\log N/H$ for 0.5 dex greater model
CII	−3.61	−3.96	−3.57
OI	−3.23	−3.15	−3.27
MgI	−5.17	−4.68	−5.26
MgII	−5.11	−5.02	−5.08
AlII	−6.80	−6.83	−6.70
SiII	−4.92	−4.95	−4.89
PII	−5.97	−6.13	−5.89
SII	−4.99	−5.28	−4.91
CaII	−5.57	−5.31	−5.70
ScII	−8.03	−7.72	−8.00
TiII	−6.35	−6.06	−6.30
CrII	−5.53	−5.32	−5.45
MnI	−4.63	−4.13	−4.68
MnII	−4.68	−4.52	−4.59
FeI	−4.34	−3.93	−4.37
FeII	−4.75	−4.67	−4.65
FeIII	−4.56	−4.81	−4.38
NiII	−6.74	−6.66	−6.57
YII	−7.68	−7.37	−7.64
ZrII	−7.79	−7.46	−7.72

TABLE 6

HE/H DETERMINATION FOR THE SAMPLE OF HGMN STARS

Line	HR 3273	HR 8118	HR 8567	HR 8937
3867	0.08	—	—	—
4026	0.07	0.09	0.09	0.03
4121	0.08	—	0.09	—
4471	0.06	0.09	0.07	0.03
4713	0.06	0.09	0.08	0.03
4921	—	—	0.09	—
Average	0.07±0.01	0.09	0.08±0.01	0.03

for HR 3273, HR 8567 and HR 8937, respectively, with a mean offset of −0.23 dex. For HR 8118 we used our estimation based on the equivalent width of $\lambda\lambda$ 3984 (−5.03 dex) and then we added the mean offset (−0.23 dex), obtaining finally −5.26 dex for the Hg abundance of this star. This is not a perfect solution as some very sharp-lined HgMn stars have $\lambda\lambda$ 3984 lines with a unique distribution of Hg isotopes.

5. DISCUSSION

HR 3273, HR 8118, HR 8567 and HR 8937 are main sequence stars with anomalous abundances, i.e. different from solar values. The comparison of derived and solar abundances for the HgMn stars is presented in the Table 7. We included the rms of the average abundance for each species and the number of lines n involved in the average. Solar abundances have been taken from Grevesse, Noels, & Sauval

TABLE 7

COMPARISON OF DERIVED AND SOLAR ABUNDANCES

	HR 3273		HR 8118		HR 8567		HR 8937		Sun
Species	$\log N/N_H$	n	$\log N/N_H$	n	$\log N/N_H$	n	$\log N/N_H$	n	$\log N/N_H$
HeI	-1.12 ± 0.06	5	-1.01 ± 0.01	3	-1.04 ± 0.05	5	-1.47 ± 0.04	3	-1.01
CII	-3.61 ± 0.11	2	-3.10 ± 0.02	2	-3.82 ± 0.27	3	-3.24 ± 0.03	2	-3.45
OI	-3.23	1	-3.71	1	-3.09	1			-3.13
MgI	-5.17	1	-4.96 ± 0.02	2	-5.14	1	-5.01 ± 0.01	2	-4.42
MgII	-5.11 ± 0.03	2	-4.54 ± 0.10	3	-4.91 ± 0.03	2	-4.73 ± 0.15	3	-4.42
AlII	-6.80	1	-5.47	1	-6.52	1			-5.53
SiII	-4.92 ± 0.22	8	-4.61 ± 0.17	6	-4.78 ± 0.20	7	-4.52 ± 0.18	8	-4.45
PII	-5.97	1					-5.37	1	-6.55
SII	-4.99 ± 0.14	7	-4.45 ± 0.19	5	-4.73 ± 0.18	7	-5.09 ± 0.09	3	-4.67
CaII	-5.57	1	-6.18	1	-5.35	1	-5.93	1	-5.64
ScII	-8.03	1	-7.02	1	-7.62	1			-8.83
TiII	-6.35 ± 0.24	34	-6.11 ± 0.22	34	-5.97 ± 0.23	32	-6.60 ± 0.23	26	-6.98
CrI			-5.20	1					-6.33
CrII	-5.53 ± 0.23	37	-5.19 ± 0.19	23	-5.34 ± 0.21	32	-5.73 ± 0.25	30	-6.33
MnI	-4.63 ± 0.22	7	-5.54 ± 0.18	3	-4.20 ± 0.26	14	-4.67 ± 0.19	11	-6.61
MnII	-4.68 ± 0.21	39	-5.26 ± 0.32	12	-4.25 ± 0.23	41	-4.46 ± 0.21	39	-6.61
FeI	-4.34 ± 0.02	2	-4.27 ± 0.35	19	-4.78 ± 0.24	3	-4.30 ± 0.40	18	-4.50
FeII	-4.75 ± 0.21	64	-4.31 ± 0.19	63	-4.91 ± 0.21	56	-4.29 ± 0.20	80	-4.50
FeIII	-4.56	1					-4.35	1	-4.50
NiII	-6.74 ± 0.30	2	-6.06 ± 0.21	2	-6.79 ± 0.25	2			-5.75
SrII			-8.43	1	-8.35	1	-6.30	1	-9.03
YII	-7.68 ± 0.26	5	-6.32 ± 0.24	9	-7.40 ± 0.16	8	-6.37 ± 0.20	11	-9.76
ZrII	-7.79 ± 0.05	2	-7.06 ± 0.16	13	-7.59 ± 0.32	2	-7.72 ± 0.14	6	-9.40
BaII			-9.17	1					-9.87
HgII	-5.25	1	-5.03	1	-5.58	1	-4.23	1	-10.83
$T_{\rm eff}$	12253		11381		12315		12088		
$\log g$	3.42		4.11		3.68		4.28		

(1996). We also present in Tables 8–11 the line by line abundance values derived for the sample of HgMn stars. The columns shown are the code of the species, the name of the element, multiplet number, wavelength of the line, $\log gf$ value, reference for the $\log gf$ value, equivalent width and abundance of the line. In Figure 1 we show the abundance anomalies relative to solar as a function of the atomic number. The HgMn stars are presented as crosses (HR 3273), empty triangles (HR 8118), empty circles (HR 8567) and empty squares (HR 8937). For comparison purposes we show the abundances of four other HgMn stars, depicted as filled circles (HR 4817), filled triangles (π Boo), filled hexagons (μ Lep) and filled squares (28 Her). These data are taken from Adelman & Pintado (1997). From the values presented in Table 7 and Figure 1, our sample of HgMn stars shows an abundance pattern similar to other HgMn stars. However there are some differences in particular cases.

The star HR 3273 shows a relatively low abundance of SiII (8 lines) compared to other HgMn stars. In the star HR 8567, the abundance of CrII (32 lines) is relatively high compared to other HgMn stars. The CrII lines $\lambda\lambda$4588, 4634 and 5237, for instance, are intense in the spectra. The Mn and Hg abundances are similar to other HgMn stars. The abundance of CII in HR 8118 and HR 8937 is also relatively high. However, this value is based on few lines, and assumes the LTE approximation. For star HR 8937, the abundance of SrII is high compared to other HgMn stars. However, this value is derived

TABLE 8

LINE ABUNDANCES OF HR 3273

Code	Species	Mult.	λ(Å)	$\log gf$	Ref.	$W_{\rm eq}$	$\log(N/N_T)$
6.01	C II	4	3918.97	−0.53	WF	19	−3.72
6.01	C II	4	3920.68	−0.23	WF	30	−3.49
8.00	O I	12	5330.73	−0.87	WF	22	−3.22
12.00	Mg I	2	5183.60	−0.16	WS	6	−5.17
12.01	Mg II	10	4390.57	−0.53	WS	23	−5.14
12.01	Mg II	9	4427.99	−1.21	WS	6	−5.07
13.01	Al II	2	4663.05	−0.28	FW	5	−6.80
14.01	Si II	1	3853.66	−1.44	LA	50	−5.18
14.01	Si II	1	3856.02	−0.49	LA	96	−5.10
14.01	Si II	1	3862.59	−0.74	LA	90	−4.97
14.01	Si II	3.01	4075.45	−1.40	SG	14	−4.85
14.01	Si II	3.01	4076.78	−1.67	SG	13	−4.61
14.01	Si II	3	4128.05	0.38	LA	120	−4.54
14.01	Si II	3	4130.89	0.53	LA	91	−5.06
14.01	Si II	5	5041.02	0.29	SG	60	−5.07
15.01	P II	15	4602.07	0.74	WS	8	−5.97
16.01	S II	44	4153.07	0.62	WS	11	−4.94
16.01	S II	44	4162.66	0.78	WS	12	−4.99
16.01	S II	9	4815.55	0.18	WM	9	−5.26
16.01	S II	7	4925.34	−0.47	WS	7	−4.77
16.01	S II	15	5014.04	0.03	KX	8	−4.99
16.01	S II	39	5212.62	0.24	WS	6	−4.91
16.01	S II	38	5320.72	0.46	WS	6	−5.08
20.01	Ca II	1	3933.66	0.13	WM	212	−5.57
21.01	Sc II	7	4246.82	0.24	LD	40	−8.03
22.01	Ti II	34	3900.54	−0.45	MF	55	−6.38
22.01	Ti II	34	3913.46	−0.53	MF	50	−6.50
22.01	Ti II	31	3932.02	−1.78	MF	10	−6.49
22.01	Ti II	11	4012.38	−1.61	MF	35	−6.11
22.01	Ti II	87	4028.34	−1.00	MF	14	−6.69
22.01	Ti II	87	4053.82	−1.21	MF	22	−6.22
22.01	Ti II	105	4163.64	−0.40	MF	35	−6.34
22.01	Ti II	20	4287.87	−2.02	MF	19	−5.91
22.01	Ti II	19	4294.09	−1.11	MF	37	−6.33
22.01	Ti II	41	4300.04	−0.77	MF	58	−5.97
22.01	Ti II	41	4301.92	−1.16	MF	20	−6.70
22.01	Ti II	41	4312.86	−1.16	MF	27	−6.49
22.01	Ti II	41	4320.95	−1.87	MF	17	−6.07
22.01	Ti II	51	4394.06	−1.59	MF	6	−6.86
22.01	Ti II	19	4395.03	−0.66	MF	49	−6.41
22.01	Ti II	61	4395.84	−2.17	MF	8	−6.14
22.01	Ti II	61	4409.24	−2.64	KX	5	−5.90
22.01	Ti II	115	4411.07	−1.06	MF	10	−6.25
22.01	Ti II	40	4417.71	−1.43	MF	21	−6.39
22.01	Ti II	19	4443.80	−0.70	MF	45	−6.50
22.01	Ti II	19	4450.48	−1.45	MF	16	−6.58
22.01	Ti II	31	4468.49	−0.60	MF	44	−6.60
22.01	Ti II	115	4488.32	−0.82	MF	17	−6.18
22.01	Ti II	31	4501.27	−0.75	MF	41	−6.56
22.01	Ti II	50	4533.96	−0.77	MF	57	−5.97
22.01	Ti II	41	4563.76	−0.96	MF	35	−6.46
22.01	Ti II	82	4571.97	−0.53	MF	53	−6.19
22.01	Ti II	59	4657.20	−2.15	MF	7	−6.23
22.01	Ti II	92	4779.98	−1.37	MF	13	−6.28
22.01	Ti II	82	4805.09	−1.10	MF	17	−6.39
22.01	Ti II	14	4911.20	−0.34	MF	17	−6.65
22.01	Ti II	86	5129.16	−1.39	MF	9	−6.53
22.01	Ti II	86	5185.90	−1.35	MF	17	−6.24
22.01	Ti II	7	5188.69	−1.21	MF	17	−6.52
24.01	Cr II	167	3865.60	−0.78	KX	32	−5.84
24.01	Cr II	130	3866.52	−2.07	KX	4	−5.86
24.01	Cr II	129	3911.32	−2.06	KX	9	−5.56
24.01	Cr II	183	3979.50	−0.73	KX	30	−5.79
24.01	Cr II	183	4012.50	−0.89	KX	37	−5.44
24.01	Cr II	19	4051.93	−2.19	KX	22	−5.80
24.01	Cr II	19	4054.08	−2.48	KX	24	−5.46
24.01	Cr II	26	4072.56	−2.41	KX	10	−5.76
24.01	Cr II	165	4082.28	−1.23	KX	13	−5.99
24.01	Cr II	26	4086.13	−2.42	KX	8	−5.83
24.01	Cr II	26	4132.42	−2.35	KX	11	−5.73
24.01	Cr II	162	4145.78	−1.16	KX	25	−5.66
24.01	Cr II	26	4179.42	−1.77	KX	23	−5.84
24.01	Cr II	31	4261.91	−1.53	KX	46	−5.40
24.01	Cr II	31	4275.57	−1.70	KX	42	−5.36
24.01	Cr II	44	4554.99	−1.38	MF	47	−5.42
24.01	Cr II	39	4565.74	−2.11	MF	25	−5.36
24.01	Cr II	44	4588.20	−0.63	MF	79	−5.05
24.01	Cr II	44	4592.05	−1.22	MF	42	−5.72
24.01	Cr II	44	4616.63	−1.29	MF	43	−5.64
24.01	Cr II	44	4618.80	−1.11	MF	60	−5.22
24.01	Cr II	44	4634.07	−1.24	MF	55	−5.27
24.01	Cr II	30	4836.23	−2.25	MF	24	−5.31
24.01	Cr II	30	4848.23	−1.14	MF	51	−5.63
24.01	Cr II	30	4884.61	−2.08	MF	19	−5.63
24.01	Cr II	190	4912.46	−0.95	KX	17	−5.53
24.01	Cr II	43	5232.50	−2.09	KX	15	−5.67
24.01	Cr II	43	5237.33	−1.16	MF	52	−5.42
24.01	Cr II	23	5246.77	−2.45	MF	20	−5.31
24.01	Cr II	23	5249.44	−2.43	KX	13	−5.54
24.01	Cr II	43	5274.96	−1.29	KX	48	−5.43
24.01	Cr II	43	5279.88	−2.10	MF	34	−5.05
24.01	Cr II	43	5280.05	−2.01	KX	36	−5.08
24.01	Cr II	43	5308.44	−1.81	MF	25	−5.61
24.01	Cr II	43	5310.70	−2.28	MF	17	−5.39
24.01	Cr II	43	5313.59	−1.65	MF	33	−5.54
24.01	Cr II	43	5334.87	−1.56	KX	34	−5.59
25.00	Mn I	2	4030.75	−0.47	MF	15	−4.91
25.00	Mn I	2	4033.06	−0.62	MF	19	−4.62
25.00	Mn I	2	4034.48	−0.81	MF	9	−4.84
25.00	Mn I	5	4041.35	0.29	MF	13	−4.69
25.00	Mn I	28	4462.03	0.32	MF	9	−4.47
25.00	Mn I	21	4762.37	0.42	MF	21	−4.19
25.00	Mn I	16	4783.43	0.04	MF	7	−4.69
25.01	Mn II	I	3859.21	−2.56	KX	11	−4.91
25.01	Mn II	I	3878.99	−1.71	KX	40	−4.73
25.01	Mn II	I	3917.32	−1.15	KX	29	−4.97
25.01	Mn II	I	3930.95	−2.15	KX	13	−4.68
25.01	Mn II	I	3952.42	−1.50	KX	12	−4.78
25.01	Mn II	I	3986.58	−2.60	KX	14	−4.70
25.01	Mn II	I	4000.05	−1.21	KX	26	−4.58
25.01	Mn II	I	4081.44	−2.24	KX	28	−4.27
25.01	Mn II	I	4087.91	−2.91	KX	7	−4.81
25.01	Mn II	I	4136.90	−1.29	KX	59	−4.21
25.01	Mn II	I	4140.44	−2.46	KX	17	−4.67
25.01	Mn II	2	4174.32	−3.55	KX	44	−4.62
25.01	Mn II	I	4184.45	−1.95	KX	22	−4.72
25.01	Mn II	I	4200.27	−1.74	KX	32	−4.64
25.01	Mn II	2	4205.38	−3.38	KX	51	−4.54
25.01	Mn II	I	4240.39	−2.07	KX	25	−4.51
25.01	Mn II	7	4244.25	−2.39	KX	33	−4.34
25.01	Mn II	I	4251.73	−1.06	KX	52	−4.68
25.01	Mn II	2	4260.46	−4.25	KX	15	−4.77
25.01	Mn II	I	4377.74	−2.14	KX	20	−4.95
25.01	Mn II	I	4393.38	−2.32	KX	15	−4.94
25.01	Mn II	I	4403.51	−1.80	KX	11	−5.08
25.01	Mn II	I	4478.64	−0.95	KX	40	−4.92
25.01	Mn II	I	4497.94	−2.59	KX	9	−4.98
25.01	Mn II	I	4503.20	−2.16	KX	15	−4.82
25.01	Mn II	I	4689.55	−2.54	KX	11	−4.56
25.01	Mn II	I	4702.73	−2.34	KX	10	−4.78
25.01	Mn II	I	4717.26	−1.86	KX	15	−4.86
25.01	Mn II	I	4730.40	−2.15	KX	40	−4.33
25.01	Mn II	I	4749.11	−2.00	KX	16	−4.85
25.01	Mn II	I	4764.73	−1.35	KX	62	−4.37
25.01	Mn II	I	4791.78	−1.72	KX	29	−4.69
25.01	Mn II	I	4806.82	−1.56	KX	46	−4.72
25.01	Mn II	I	4830.06	−1.85	KX	25	−4.70
25.01	Mn II	I	4839.74	−1.86	KX	19	−4.87
25.01	Mn II	I	4842.32	−2.01	KX	25	−4.53
25.01	Mn II	I	5102.52	−1.93	KX	27	−4.63
25.01	Mn II	I	5177.65	−1.77	KX	44	−4.24
25.01	Mn II	I	3902.36	−2.72	KX	13	−4.57
26.00	Fe I	43	4132.06	−0.68	N4	4	−4.31
26.00	Fe I	1146	5383.37	0.65	N4	3	−4.36

TABLE 8 (CONTINUED)

Code	Species	Mult.	λ(Å)	$\log gf$	Ref.	$W_{\rm eq}$	$\log(N/N_T)$
26.01	Fe II	38	3935.96	−1.86	N4	18	−4.78
26.01	Fe II	3	3938.29	−4.07	N4	11	−4.72
26.01	Fe II	190	3938.97	−1.85	N4	16	−4.71
26.01	Fe II	127	4024.55	−2.44	N4	11	−4.99
26.01	Fe II	172	4048.83	−2.14	N4	23	−4.34
26.01	Fe II	28	4122.67	−3.38	N4	15	−4.82
26.01	Fe II	27	4233.17	−1.81	N4	77	−4.36
26.01	Fe II	27	4273.33	−3.34	N4	11	−4.95
26.01	Fe II	28	4296.57	−3.01	N4	24	−4.81
26.01	Fe II	27	4303.18	−2.61	N4	51	−4.38
26.01	Fe II	27	4351.77	−2.08	N4	44	−5.16
26.01	Fe II	J	4357.58	−2.10	KX	11	−4.59
26.01	Fe II	27	4385.39	−2.57	N4	34	−4.92
26.01	Fe II	27	4416.83	−2.60	N4	33	−4.92
26.01	Fe II	37	4489.18	−2.97	N4	23	−4.83
26.01	Fe II	37	4491.40	−2.70	N4	24	−5.04
26.01	Fe II	38	4508.29	−2.21	N4	42	−4.99
26.01	Fe II	37	4515.34	−2.48	N4	34	−4.99
26.01	Fe II	37	4520.22	−2.60	N4	33	−4.91
26.01	Fe II	38	4522.63	−2.03	N4	47	−5.03
26.01	Fe II	38	4541.52	−3.05	N4	17	−4.92
26.01	Fe II	37	4555.89	−2.29	N4	42	−4.94
26.01	Fe II	38	4576.34	−3.04	N4	17	−4.93
26.01	Fe II	37	4582.84	−3.10	N4	15	−4.94
26.01	Fe II	38	4583.84	−2.02	N4	60	−4.62
26.01	Fe II	D	4596.02	−1.84	N4	12	−4.69
26.01	Fe II	38	4620.52	−3.28	N4	15	−4.76
26.01	Fe II	37	4629.34	−2.37	N4	38	−4.98
26.01	Fe II	186	4635.32	−1.65	N4	22	−4.65
26.01	Fe II	28	4666.76	−3.33	N4	11	−4.90
26.01	Fe II	43	4731.45	−3.13	N4	17	−4.82
26.01	Fe II	J	4913.29	0.01	KX	11	−4.69
26.01	Fe II	J	4951.58	0.18	KX	14	−4.69
26.01	Fe II	J	4977.04	0.04	KX	11	−4.65
26.01	Fe II	J	4990.51	0.18	KX	13	−4.72
26.01	Fe II	J	4993.36	−3.65	MF	6	−4.88
26.01	Fe II	J	5001.96	0.90	KX	30	−4.86
26.01	Fe II	J	5004.20	0.50	KX	18	−4.85
26.01	Fe II	J	5018.44	−1.22	MF	88	−4.44
26.01	Fe II	J	5021.59	−0.30	KX	11	−4.37
26.01	Fe II	J	5022.79	−0.02	KX	12	−4.60
26.01	Fe II	J	5035.71	0.61	KX	27	−4.63
26.01	Fe II	J	5061.72	0.22	KX	11	−4.88
26.01	Fe II	J	5070.90	0.24	KX	11	−4.88
26.01	Fe II	J	5075.76	0.28	KX	12	−4.78
26.01	Fe II	J	5093.58	0.11	KX	12	−4.65
26.01	Fe II	J	5097.27	0.31	KX	25	−4.37
26.01	Fe II	J	5106.11	−0.28	KX	10	−4.38
26.01	Fe II	J	5145.77	−0.40	KX	8	−4.33
26.01	Fe II	J	5150.49	−0.12	KX	11	−4.46
26.01	Fe II	J	5169.03	−0.87	MF	90	−4.72
26.01	Fe II	J	5199.12	0.10	KX	7	−4.92
26.01	Fe II	J	5216.85	0.81	KX	19	−5.01
26.01	Fe II	J	5228.90	−0.30	KX	7	−4.49
26.01	Fe II	J	5232.79	−0.06	KX	14	−4.37
26.01	Fe II	J	5234.62	−2.05	MF	45	−4.84
26.01	Fe II	J	5247.95	0.55	N4	18	−4.74
26.01	Fe II	J	5254.93	−3.23	KX	11	−4.79
26.01	Fe II	J	5257.12	0.03	KX	9	−4.66
26.01	Fe II	J	5260.25	1.07	KX	33	−4.82
26.01	Fe II	J	5272.40	−2.03	MF	16	−4.44
26.01	Fe II	J	5276.00	−1.94	MF	45	−4.96
26.01	Fe II	J	5291.67	0.58	KX	17	−4.86
26.01	Fe II	J	5339.59	0.54	KX	17	−4.80
26.02	Fe III	4	4419.60	−2.22	KX	7	−4.56
28.01	Ni II	12	4015.47	−2.42	KX	4	−6.44
28.01	Ni II	11	4067.03	−1.29	KX	12	−7.03
39.01	Y II	6	3950.35	−0.49	HL	12	−7.90
39.01	Y II	6	3982.59	−0.49	HL	11	−7.96
39.01	Y II	14	4124.90	−1.50	HL	4	−7.25
39.01	Y II	22	4900.12	−0.09	HL	14	−7.74
39.01	Y II	20	5205.72	−0.34	HL	12	−7.57
40.01	Zr II	16	3998.95	−0.67	GB	6	−7.84
40.01	Zr II	30	4045.64	−0.60	KX	8	−7.74
80.01	Hg II	–	3983.94	−1.73	DW	83	−4.83

from one line and should be taken with caution. For HR 8937 we adopted the Hg abundance derived by Dolk et al. (2003). They found an abundance of -4.23 ± 0.43 dex, i.e., a relatively high value. We compared this value with an estimation using the equivalent width of $\lambda\lambda$3984 and derived −4.06 dex, i.e. also a high abundance for HgII in this star.

For star HR 8118, the abundances of CII, AlII and ScII seem to be relatively high compared to other HgMn stars. However, these values are based on the measurement of few lines (2, 1 and 1, respectively) and should be taken with caution. On the other hand, the abundances of CrII, YII and ZrII are also relatively high, from a greater number of lines (23, 9 and 13, respectively). We caution that this star has the highest $v \sin i$ in our sample (30 ± 1 km s^{-1}) which suggest that high abundance values in different species might be due to blends with another lines. However this effect is not clearly seen in the FeII abundances (63 lines), and thus the CrII abundance could be real. A comparison of higher resolution spectra with synthetic spectra is needed to verify the abundance of Cr, Y and Zr in this star.

HeI was slightly underabundant for the sample of HgMn stars and underabundantin HR 8937. O was slightly underabundant in the stars HR 3273 and HR 8567. MgII was underabundant, except for HR 8118 (which is close to the solar value). SiII was close to solar in HR 8118 and HR 8937, and underabundant in HR 3273 and HR 8567. Fe was slightly underabundant in HR 3273 and HR 8567, and slightly overabundant in HR 8118 and HR 8937. The species Sc, Ti, Cr, Mn, Sr, Y and Zr were overabundant while Ni was underabundant.

As we said in the Introduction, our purpose is to discuss the possible trend of the abundances of the critical elements in HgMn stars with stellar parameters. Papers in the literature show that the abundances of some elements seem to correlate with the effective temperature (e.g., Smith & Dworetsky 1993; Smith 1997; Woolf & Lambert 1999; Jomaron et al. 1999; Dolk et al. 2003). However, it is not clear (for instance) how the abundances are corre-

TABLE 9

LINE ABUNDANCES OF HR 8118

Code	Species	Mult.	λ(Å)	log gf	Ref.	W_{eq}	log(N/N_T)
6.01	C II	4	3918.97	−0.53	WF	16	−3.12
6.01	C II	4	3920.68	−0.23	WF	23	−3.09
12.00	Mg I	2	5172.68	−0.38	WS	28	−4.98
12.00	Mg I	2	5183.60	−0.16	WS	41	−4.93
12.01	Mg II	5	3848.21	−1.59	WS	31	−4.42
12.01	Mg II	10	4390.57	−0.53	WS	50	−4.65
12.01	Mg II	9	4427.99	−1.21	WS	18	−4.55
13.01	Al II	2	4663.05	−0.28	FW	25	−5.47
14.01	Si II	1	3853.66	−1.44	LA	64	−4.66
14.01	Si II	1	3856.02	−0.49	LA	120	−4.78
14.01	Si II	1	3862.59	−0.74	LA	95	−4.85
14.01	Si II	3.01	4075.45	−1.40	SG	19	−4.38
14.01	Si II	3	4130.89	0.53	LA	123	−4.54
14.01	Si II	5	5041.02	0.29	SG	81	−4.47
16.01	S II	44	4145.06	0.23	KX	6	−4.33
16.01	S II	44	4153.07	0.62	WS	8	−4.51
16.01	S II	44	4162.66	0.78	WS	13	−4.31
16.01	S II	9	4815.55	0.18	WM	6	−4.78
16.01	S II	7	5032.43	0.18	WS	12	−4.30
20.01	Ca II	1	3933.66	0.13	WM	249	−6.18
21.01	Sc II	7	4246.82	0.24	LD	89	−7.03
22.01	Ti II	34	3900.54	−0.45	MF	75	−6.13
22.01	Ti II	34	3913.46	−0.53	MF	75	−6.07
22.01	Ti II	31	3932.02	−1.78	MF	33	−6.08
22.01	Ti II	87	4028.34	−1.00	MF	42	−6.25
22.01	Ti II	105	4163.64	−0.40	MF	57	−6.05
22.01	Ti II	33	4227.33	−2.36	KX	11	−6.20
22.01	Ti II	20	4287.87	−2.02	MF	26	−6.05
22.01	Ti II	41	4290.22	−1.12	MF	72	−5.62
22.01	Ti II	19	4294.09	−1.11	MF	66	−5.85
22.01	Ti II	41	4300.04	−0.77	MF	78	−5.77
22.01	Ti II	41	4301.92	−1.16	MF	51	−6.24
22.01	Ti II	41	4307.87	−1.29	MF	57	−5.92
22.01	Ti II	41	4312.86	−1.16	MF	50	−6.25
22.01	Ti II	104	4386.85	−1.26	MF	28	−5.95
22.01	Ti II	51	4394.06	−1.59	MF	20	−6.58
22.01	Ti II	19	4395.03	−0.66	MF	73	−6.07
22.01	Ti II	61	4395.84	−2.17	MF	14	−6.19
22.01	Ti II	61	4409.52	−2.57	KX	12	−5.89
22.01	Ti II	115	4411.07	−1.06	MF	20	−6.11
22.01	Ti II	40	4417.71	−1.43	MF	46	−6.10
22.01	Ti II	19	4450.48	−1.45	MF	32	−6.46
22.01	Ti II	31	4468.49	−0.60	MF	68	−6.28
22.01	Ti II	31	4501.27	−0.75	MF	65	−6.25
22.01	Ti II	50	4533.96	−0.77	MF	80	−5.63
22.01	Ti II	41	4563.76	−0.96	MF	64	−6.02
22.01	Ti II	82	4571.97	−0.53	MF	73	−5.95
22.01	Ti II	59	4657.20	−2.15	MF	18	−6.07
22.01	Ti II	92	4779.98	−1.37	MF	26	−6.20
22.01	Ti II	82	4805.09	−1.10	MF	40	−6.11
22.01	Ti II	114	4874.01	−0.79	MF	18	−6.45
22.01	Ti II	114	4911.20	−0.34	MF	29	−6.57
22.01	Ti II	86	5129.16	−1.39	MF	26	−6.25
22.01	Ti II	86	5185.90	−1.35	MF	36	−6.04
22.01	Ti II	7	5188.69	−1.21	MF	43	−6.16
24.00	Cr I	7	5208.43	0.16	MF	21	−5.20
24.01	Cr II	129	3911.32	−2.06	KX	17	−5.18
24.01	Cr II	183	3979.50	−0.73	KX	44	−5.40
24.01	Cr II	19	4051.93	−2.19	KX	41	−5.34
24.01	Cr II	26	4072.56	−2.41	KX	36	−4.94
24.01	Cr II	165	4082.28	−1.23	KX	25	−5.60
24.01	Cr II	26	4132.42	−2.35	KX	13	−5.64
24.01	Cr II	162	4145.78	−1.16	KX	45	−5.09
24.01	Cr II	26	4179.42	−1.77	KX	39	−5.44
24.01	Cr II	31	4275.57	−1.70	KX	56	−4.98
24.01	Cr II	44	4554.99	−1.38	MF	62	−5.01
24.01	Cr II	44	4588.20	−0.63	MF	87	−4.97
24.01	Cr II	44	4592.05	−1.22	MF	63	−5.14
24.01	Cr II	44	4616.63	−1.29	MF	63	−5.08
24.01	Cr II	178	4697.60	−1.88	MF	15	−5.07
24.01	Cr II	30	4812.34	−1.80	MF	42	−5.29
24.01	Cr II	30	4848.23	−1.14	MF	65	−5.26
24.01	Cr II	30	4884.61	−2.08	MF	35	−5.20
24.01	Cr II	190	4901.62	−0.83	KX	28	−5.28
24.01	Cr II	43	5232.50	−2.09	KX	34	−5.08
24.01	Cr II	23	5246.77	−2.45	MF	25	−5.14
24.01	Cr II	23	5249.44	−2.43	KX	25	−5.16
24.01	Cr II	43	5308.44	−1.81	MF	46	−5.02
24.01	Cr II	43	5310.70	−2.28	MF	29	−5.03
25.00	Mn I	2	4033.06	−0.62	MF	24	−5.29
25.00	Mn I	2	4034.48	−0.81	MF	9	−5.63
25.00	Mn I	16	4754.04	−0.09	MF	3	−5.69
25.01	Mn II	I	4136.90	−1.29	KX	17	−5.49
25.01	Mn II	I	4184.45	−1.95	KX	12	−5.01
25.01	Mn II	7	4244.25	−2.39	KX	9	−5.11
25.01	Mn II	I	4251.73	−1.06	KX	17	−5.69
25.01	Mn II	2	4260.46	−4.25	KX	11	−4.94
25.01	Mn II	I	4478.64	−0.95	KX	14	−5.69
25.01	Mn II	I	4702.73	−2.34	KX	9	−4.72
25.01	Mn II	I	4730.40	−2.15	KX	13	−5.13
25.01	Mn II	I	4755.72	−1.24	KX	37	−5.27
25.01	Mn II	I	4806.82	−1.56	KX	13	−5.69
25.01	Mn II	I	5177.65	−1.77	KX	18	−4.97
25.01	Mn II	I	4238.79	−3.63	KX	14	−5.43
26.00	Fe I	45	3815.84	0.23	N4	31	−4.79
26.00	Fe I	4	3859.91	−0.71	N4	27	−4.73
26.00	Fe I	43	4132.06	−0.68	N4	26	−3.96
26.00	Fe I	152	4187.04	−0.55	N4	19	−3.87
26.00	Fe I	152	4187.80	−0.55	N4	12	−4.13
26.00	Fe I	152	4198.30	−0.72	N4	7	−4.21
26.00	Fe I	522	4199.10	0.16	N4	29	−3.97
26.00	Fe I	152	4222.21	−0.97	N4	9	−3.85
26.00	Fe I	693	4227.43	0.27	N4	12	−4.50
26.00	Fe I	152	4250.12	−0.41	N4	17	−4.07
26.00	Fe I	42	4250.79	−0.71	N4	15	−4.28
26.00	Fe I	42	4271.76	−0.16	N4	17	−4.80
26.00	Fe I	41	4383.54	0.20	N4	30	−4.79
26.00	Fe I	41	4404.75	−0.14	N4	22	−4.64
26.00	Fe I	554	4736.77	−0.75	N4	6	−3.84
26.00	Fe I	318	4920.50	0.07	N4	13	−4.47
26.00	Fe I	383	5232.94	−0.06	N4	24	−3.93
26.00	Fe I	1146	5383.37	0.65	N4	11	−4.39
26.00	Fe I	686	5586.76	−0.14	N4	15	−3.89
26.01	Fe II	127	3845.18	−2.29	KX	17	−4.73
26.01	Fe II	29	3872.77	−3.32	KX	31	−4.18
26.01	Fe II	173	3906.04	−1.83	N4	32	−4.22
26.01	Fe II	38	3935.96	−1.86	N4	36	−4.05
26.01	Fe II	3	3938.29	−4.07	N4	21	−4.24
26.01	Fe II	190	3938.97	−1.85	N4	24	−4.26
26.01	Fe II	28	4122.67	−3.38	N4	25	−4.36
26.01	Fe II	27	4233.17	−1.81	N4	87	−4.05
26.01	Fe II	27	4273.33	−3.34	N4	37	−3.98
26.01	Fe II	28	4296.57	−3.01	N4	46	−4.06
26.01	Fe II	27	4303.18	−2.61	N4	53	−4.27
26.01	Fe II	27	4351.77	−2.08	N4	58	−4.64
26.01	Fe II	J	4357.58	−2.10	KX	8	−4.52
26.01	Fe II	27	4385.39	−2.57	N4	52	−4.28
26.01	Fe II	27	4416.83	−2.60	N4	43	−4.52
26.01	Fe II	37	4489.18	−2.97	N4	40	−4.20
26.01	Fe II	37	4491.40	−2.70	N4	39	−4.49
26.01	Fe II	38	4508.29	−2.21	N4	52	−4.60
26.01	Fe II	37	4515.34	−2.48	N4	55	−4.23
26.01	Fe II	37	4520.22	−2.60	N4	41	−4.55
26.01	Fe II	38	4522.63	−2.03	N4	58	−4.60
26.01	Fe II	38	4541.52	−3.05	N4	29	−4.41
26.01	Fe II	37	4555.89	−2.29	N4	52	−4.52
26.01	Fe II	38	4576.34	−3.04	N4	30	−4.41
26.01	Fe II	37	4582.84	−3.10	N4	22	−4.56
26.01	Fe II	38	4583.84	−2.02	N4	75	−4.11
26.01	Fe II	D	4596.02	−1.84	N4	18	−4.25
26.01	Fe II	38	4620.52	−3.28	N4	22	−4.38
26.01	Fe II	37	4629.34	−2.37	N4	66	−4.01
26.01	Fe II	186	4635.32	−1.65	N4	32	−4.12
26.01	Fe II	28	4666.76	−3.33	N4	18	−4.47

TABLE 9 (CONTINUED)

Code	Species	Mult.	λ(Å)	$\log gf$	Ref.	$W_{\rm eq}$	$\log(N/N_T)$
26.01	Fe II	43	4731.45	−3.13	N4	27	−4.37
26.01	Fe II	J	4826.68	−0.44	KX	5	−4.40
26.01	Fe II	J	4951.58	0.18	KX	14	−4.44
26.01	Fe II	J	4984.47	0.01	KX	12	−4.32
26.01	Fe II	J	4990.51	0.18	KX	15	−4.35
26.01	Fe II	J	4993.36	−3.65	MF	10	−4.49
26.01	Fe II	J	5001.96	0.90	KX	39	−4.34
26.01	Fe II	J	5004.20	0.50	KX	22	−4.43
26.01	Fe II	J	5018.44	−1.22	MF	106	−4.04
26.01	Fe II	J	5035.71	0.61	KX	28	−4.34
26.01	Fe II	J	5045.11	−0.13	KX	8	−4.40
26.01	Fe II	J	5061.72	0.22	KX	12	−4.52
26.01	Fe II	J	5070.90	0.24	KX	13	−4.50
26.01	Fe II	J	5075.76	0.28	KX	17	−4.29
26.01	Fe II	J	5082.23	−0.10	KX	9	−4.33
26.01	Fe II	J	5093.58	0.11	KX	21	−4.00
26.01	Fe II	J	5097.27	0.31	KX	32	−3.85
26.01	Fe II	J	5145.77	−0.40	KX	10	−3.93
26.01	Fe II	J	5149.46	0.40	KX	25	−4.12
26.01	Fe II	J	5160.84	−2.64	KX	10	−4.05
26.01	Fe II	J	5169.03	−0.87	MF	111	−4.31
26.01	Fe II	J	5216.85	0.81	KX	22	−4.57
26.01	Fe II	J	5234.62	−2.05	MF	58	−4.34
26.01	Fe II	J	5247.95	0.55	N4	18	−4.44
26.01	Fe II	J	5251.23	0.42	N4	21	−4.22
26.01	Fe II	J	5254.93	−3.23	KX	19	−4.28
26.01	Fe II	J	5257.12	0.03	KX	12	−4.20
26.01	Fe II	J	5260.25	1.07	KX	39	−4.38
26.01	Fe II	J	5272.40	−2.03	MF	14	−4.27
26.01	Fe II	J	5276.00	−1.94	MF	58	−4.45
26.01	Fe II	J	5291.67	0.58	KX	22	−4.37
26.01	Fe II	J	5339.59	0.54	KX	25	−4.22
28.01	Ni II	11	3849.55	−1.88	KX	21	−5.85
28.01	Ni II	11	4067.03	−1.29	KX	26	−6.27
38.01	Sr II	1	4215.52	−0.17	WM	35	−8.43
39.01	Y II	6	3950.35	−0.49	HL	65	−6.35
39.01	Y II	6	3982.59	−0.49	HL	62	−6.47
39.01	Y II	14	4124.90	−1.50	HL	42	−6.20
39.01	Y II	5	4422.58	−1.27	HL	53	−6.13
39.01	Y II	22	4854.86	−0.38	HL	48	−6.80
39.01	Y II	22	4900.12	−0.09	HL	74	−5.99
39.01	Y II	20	4982.13	−1.29	HL	30	−6.51
39.01	Y II	20	5200.41	−0.57	HL	59	−6.10
39.01	Y II	20	5289.82	−1.85	HL	20	−6.30
40.01	Zr II	17	3915.96	−0.82	KX	28	−7.22
40.01	Zr II	16	3958.23	−0.31	KX	44	−7.14
40.01	Zr II	30	3991.15	−0.25	KX	45	−7.07
40.01	Zr II	16	3998.95	−0.67	GB	41	−6.90
40.01	Zr II	54	4018.37	−0.99	KX	12	−7.41
40.01	Zr II	42	4034.10	−1.55	BG	8	−7.17
40.01	Zr II	29	4090.53	−1.10	GB	18	−7.15
40.01	Zr II	41	4149.22	−0.03	BG	52	−6.94
40.01	Zr II	29	4156.28	−0.71	GB	32	−7.13
40.01	Zr II	97	4186.67	−0.58	KX	20	−7.10
40.01	Zr II	99	4231.67	−1.02	KX	13	−6.91
40.01	Zr II	130	4494.42	−0.48	KX	20	−6.85
40.01	Zr II	129	4661.78	−0.80	KX	12	−6.83
56.01	Ba II	1	4934.07	0.00	WM	10	−9.17
80.01	Hg II	–	3983.94	−1.73	DW	59	−5.03

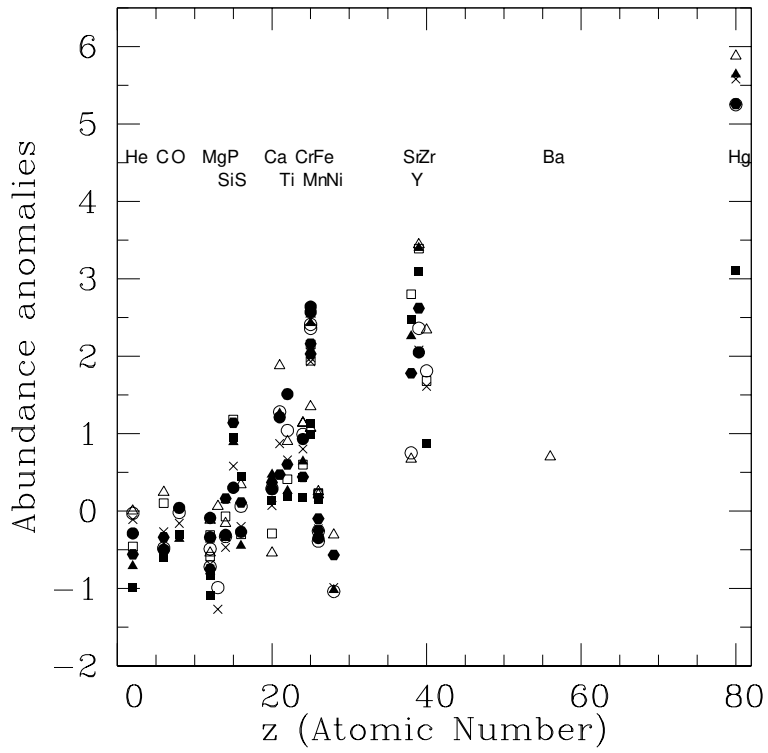

Fig. 1. Abundance anomalies relative to solar as a function of the atomic number. The HgMn stars are presented as crosses (HR 3273), empty triangles (HR 8118), empty circles (HR 8567) and empty squares (HR 8937). For comparison purposes we show the abundances of four other HgMn stars, depicted as filled circles (HR 4817), filled triangles (π Boo), filled hexagons (μ Lep) and filled squares (28 Her). Data taken from Adelman & Pintado (1997).

TABLE 10

LINE ABUNDANCES OF HR 8567

Code	Species	Mult.	λ(Å)	$\log gf$	Ref.	$W_{\rm eq}$	$\log(N/N_T)$
6.01	C II	4	3918.97	−0.53	WF	15	−3.76
6.01	C II	4	3920.68	−0.23	WF	26	−3.53
6.01	C II	6	4267.26	0.72	WF	15	−4.19
8.00	O I	12	5330.73	−0.87	WF	28	−3.09
12.00	Mg I	2	5183.60	−0.16	WS	8	−5.14
12.01	Mg II	10	4390.57	−0.53	WS	31	−4.95
12.01	Mg II	9	4427.99	−1.21	WS	10	−4.88
13.01	Al II	2	4663.05	−0.28	FW	8	−6.52
14.01	Si II	1	3853.66	−1.44	LA	56	−4.99
14.01	Si II	1	3856.02	−0.49	LA	107	−4.89
14.01	Si II	1	3862.59	−0.74	LA	88	−4.98
14.01	Si II	3.01	4075.45	−1.40	SG	16	−4.72
14.01	Si II	3.01	4076.78	−1.67	SG	19	−4.35
14.01	Si II	3	4130.89	0.53	LA	114	−4.73
14.01	Si II	5	5041.02	0.29	SG	73	−4.77
16.01	S II	44	4153.07	0.62	WS	12	−4.79
16.01	S II	44	4162.66	0.78	WS	14	−4.82
16.01	S II	9	4815.55	0.18	WM	13	−4.93
16.01	S II	1	4991.97	−0.65	WS	7	−4.45
16.01	S II	15	5014.04	0.03	KX	14	−4.47
16.01	S II	7	5032.43	0.18	WS	15	−4.71
16.01	S II	39	5212.62	0.24	WS	4	−4.93
20.01	Ca II	1	3933.66	0.13	WM	280	−5.35
21.01	Sc II	7	4246.82	0.24	LD	54	−7.61
22.01	Ti II	34	3900.54	−0.45	MF	66	−5.97
22.01	Ti II	34	3913.46	−0.53	MF	70	−5.78
22.01	Ti II	31	3932.02	−1.78	MF	23	−5.99
22.01	Ti II	87	4028.34	−1.00	MF	31	−6.19
22.01	Ti II	105	4163.64	−0.40	MF	48	−5.96
22.01	Ti II	41	4290.22	−1.12	MF	54	−5.74
22.01	Ti II	19	4294.09	−1.11	MF	61	−5.55
22.01	Ti II	41	4301.92	−1.16	MF	35	−6.28
22.01	Ti II	41	4312.86	−1.16	MF	43	−6.04
22.01	Ti II	94	4316.79	−1.42	MF	11	−6.31
22.01	Ti II	41	4320.95	−1.87	MF	38	−5.49
22.01	Ti II	104	4386.85	−1.26	MF	29	−5.62
22.01	Ti II	19	4395.03	−0.66	MF	65	−5.83
22.01	Ti II	61	4395.84	−2.17	MF	14	−5.86
22.01	Ti II	115	4411.07	−1.06	MF	20	−5.84
22.01	Ti II	40	4417.71	−1.43	MF	40	−5.88
22.01	Ti II	19	4443.80	−0.70	MF	58	−6.06
22.01	Ti II	19	4450.48	−1.45	MF	25	−6.29
22.01	Ti II	31	4468.49	−0.60	MF	61	−6.04
22.01	Ti II	115	4488.32	−0.82	MF	24	−5.94
22.01	Ti II	50	4533.96	−0.77	MF	65	−5.67
22.01	Ti II	41	4563.76	−0.96	MF	54	−5.86
22.01	Ti II	59	4657.20	−2.15	MF	11	−5.98
22.01	Ti II	92	4779.98	−1.37	MF	27	−5.84
22.01	Ti II	82	4805.09	−1.10	MF	32	−5.97
22.01	Ti II	114	4874.01	−0.79	MF	12	−6.38
22.01	Ti II	114	4911.20	−0.34	MF	27	−6.32
22.01	Ti II	113	5072.29	−0.75	MF	11	−6.44
22.01	Ti II	86	5129.16	−1.39	MF	21	−6.06
22.01	Ti II	86	5185.90	−1.35	MF	30	−5.84
22.01	Ti II	7	5188.69	−1.21	MF	35	−5.99
22.01	Ti II	70	5226.54	−1.30	MF	26	−6.15
24.01	Cr II	167	3865.60	−0.78	KX	50	−5.26
24.01	Cr II	129	3911.32	−2.06	KX	13	−5.32
24.01	Cr II	183	3979.50	−0.73	KX	36	−5.58
24.01	Cr II	19	4051.93	−2.19	KX	30	−5.55
24.01	Cr II	26	4072.56	−2.41	KX	25	−5.16
24.01	Cr II	165	4082.28	−1.23	KX	16	−5.83
24.01	Cr II	26	4086.13	−2.42	KX	15	−5.48
24.01	Cr II	181	4127.06	−1.77	KX	10	−5.40
24.01	Cr II	26	4132.42	−2.35	KX	15	−5.54
24.01	Cr II	26	4179.42	−1.77	KX	29	−5.63
24.01	Cr II	31	4275.57	−1.70	KX	51	−5.02
24.01	Cr II	191	4465.73	−1.18	KX	9	−5.65
24.01	Cr II	44	4554.99	−1.38	MF	50	−5.25
24.01	Cr II	39	4565.74	−2.11	MF	33	−5.08
24.01	Cr II	44	4588.20	−0.63	MF	80	−4.96
24.01	Cr II	44	4592.05	−1.22	MF	54	−5.28
24.01	Cr II	44	4616.63	−1.29	MF	50	−5.34
24.01	Cr II	44	4634.07	−1.24	MF	62	−4.96
24.01	Cr II	178	4697.60	−1.88	MF	9	−5.31
24.01	Cr II	30	4812.34	−1.80	MF	30	−5.53
24.01	Cr II	30	4836.23	−2.25	MF	31	−5.06
24.01	Cr II	30	4848.23	−1.14	MF	54	−5.46
24.01	Cr II	30	4884.61	−2.08	MF	24	−5.43
24.01	Cr II	190	4912.46	−0.95	KX	19	−5.43
24.01	Cr II	43	5232.50	−2.09	KX	21	−5.42
24.01	Cr II	43	5237.33	−1.16	MF	59	−5.11
24.01	Cr II	23	5249.44	−2.43	KX	16	−5.40
24.01	Cr II	43	5274.96	−1.29	KX	49	−5.35
24.01	Cr II	43	5308.44	−1.81	MF	37	−5.19
24.01	Cr II	43	5310.70	−2.28	MF	20	−5.25
24.01	Cr II	43	5313.59	−1.65	MF	43	−5.18
24.01	Cr II	43	5334.87	−1.56	KX	40	−5.37
25.00	Mn I	2	4030.75	−0.47	MF	31	−4.50
25.00	Mn I	2	4033.06	−0.62	MF	49	−3.76
25.00	Mn I	2	4034.48	−0.81	MF	16	−4.63
25.00	Mn I	5	4035.72	−0.19	KX	12	−4.33
25.00	Mn I	5	4041.35	0.29	MF	30	−4.25
25.00	Mn I	5	4058.93	−0.45	MF	8	−4.25
25.00	Mn I	23	4235.14	−0.26	KX	14	−3.81
25.00	Mn I	28	4455.01	−0.39	KX	11	−3.76
25.00	Mn I	28	4462.03	0.32	MF	11	−4.46
25.00	Mn I	22	4470.14	−0.44	MF	5	−4.16
25.00	Mn I	21	4709.71	−0.34	MF	6	−4.14
25.00	Mn I	16	4754.04	−0.09	MF	14	−4.32
25.00	Mn I	21	4761.51	−0.14	MF	8	−4.20
25.00	Mn I	16	4783.43	0.04	MF	17	−4.30
25.01	Mn II	I	3878.99	−1.71	KX	55	−4.16
25.01	Mn II	I	3917.32	−1.15	KX	43	−4.47
25.01	Mn II	I	3930.95	−2.15	KX	23	−4.29
25.01	Mn II	I	3952.42	−1.50	KX	23	−4.35
25.01	Mn II	I	3986.58	−2.60	KX	28	−4.20
25.01	Mn II	I	3995.31	−2.44	KX	24	−4.52
25.01	Mn II	I	4000.05	−1.21	KX	40	−4.11
25.01	Mn II	I	4081.44	−2.24	KX	41	−3.83
25.01	Mn II	I	4087.91	−2.91	KX	12	−4.47
25.01	Mn II	I	4140.44	−2.46	KX	26	−4.35
25.01	Mn II	2	4174.32	−3.55	KX	58	−4.08
25.01	Mn II	I	4180.06	−2.83	KX	13	−4.46
25.01	Mn II	I	4184.45	−1.95	KX	38	−4.18
25.01	Mn II	I	4200.27	−1.74	KX	48	−4.06
25.01	Mn II	2	4205.38	−3.38	KX	66	−3.92
25.01	Mn II	I	4240.39	−2.07	KX	40	−4.01
25.01	Mn II	7	4244.25	−2.39	KX	44	−3.95
25.01	Mn II	I	4251.73	−1.06	KX	61	−4.29
25.01	Mn II	2	4260.46	−4.25	KX	25	−4.41
25.01	Mn II	I	4377.74	−2.14	KX	29	−4.64
25.01	Mn II	I	4391.96	−2.89	KX	12	−4.45
25.01	Mn II	I	4393.38	−2.32	KX	31	−4.36
25.01	Mn II	I	4403.51	−1.80	KX	23	−4.59
25.01	Mn II	I	4478.64	−0.95	KX	56	−4.34
25.01	Mn II	I	4497.94	−2.59	KX	16	−4.59
25.01	Mn II	I	4503.20	−2.16	KX	26	−4.43
25.01	Mn II	I	4509.22	−3.60	KX	8	−3.97
25.01	Mn II	17	4510.21	−0.72	KX	17	−3.98
25.01	Mn II	I	4689.55	−2.54	KX	24	−4.02
25.01	Mn II	I	4702.73	−2.34	KX	15	−4.50
25.01	Mn II	I	4717.26	−1.86	KX	27	−4.43
25.01	Mn II	I	4730.40	−2.15	KX	52	−3.90
25.01	Mn II	I	4749.11	−2.00	KX	23	−4.57
25.01	Mn II	I	4791.78	−1.72	KX	41	−4.28
25.01	Mn II	I	4806.82	−1.56	KX	66	−3.93
25.01	Mn II	I	4830.06	−1.85	KX	39	−4.23
25.01	Mn II	I	4839.74	−1.86	KX	32	−4.43
25.01	Mn II	I	4842.32	−2.01	KX	39	−4.05
25.01	Mn II	I	5102.52	−1.93	KX	48	−3.91
25.01	Mn II	I	5307.35	−2.07	KX	17	−4.25
25.01	Mn II	I	3902.36	−2.72	KX	13	−4.53
26.00	Fe I	4	3859.91	−0.71	N4	10	−4.68

TABLE 10 (CONTINUED)

Code	Species	Mult.	λ(Å)	$\log gf$	Ref.	$W_{\rm eq}$	$\log(N/N_T)$
26.00	Fe I	20	3872.50	−0.93	N4	3	−4.54
26.00	Fe I	41	4383.54	0.20	N4	6	−5.10
26.01	Fe II	127	3845.18	−2.29	KX	8	−5.24
26.01	Fe II	38	3935.96	−1.86	N4	12	−4.96
26.01	Fe II	190	3938.97	−1.85	N4	11	−4.88
26.01	Fe II	28	4122.67	−3.38	N4	9	−4.99
26.01	Fe II	27	4273.33	−3.34	N4	8	−5.02
26.01	Fe II	28	4296.57	−3.01	N4	15	−5.03
26.01	Fe II	27	4303.18	−2.61	N4	46	−4.47
26.01	Fe II	27	4351.77	−2.08	N4	35	−5.35
26.01	Fe II	27	4385.39	−2.57	N4	28	−5.03
26.01	Fe II	27	4416.83	−2.60	N4	26	−5.05
26.01	Fe II	37	4489.18	−2.97	N4	18	−4.89
26.01	Fe II	37	4491.40	−2.70	N4	18	−5.16
26.01	Fe II	38	4508.29	−2.21	N4	32	−5.23
26.01	Fe II	37	4515.34	−2.48	N4	26	−5.14
26.01	Fe II	37	4520.22	−2.60	N4	22	−5.15
26.01	Fe II	38	4522.63	−2.03	N4	40	−5.17
26.01	Fe II	38	4541.52	−3.05	N4	13	−4.98
26.01	Fe II	37	4555.89	−2.29	N4	34	−5.10
26.01	Fe II	38	4576.34	−3.04	N4	13	−5.00
26.01	Fe II	37	4582.84	−3.10	N4	11	−5.07
26.01	Fe II	38	4583.84	−2.02	N4	51	−4.83
26.01	Fe II	D	4596.02	−1.84	N4	8	−4.84
26.01	Fe II	38	4620.52	−3.28	N4	8	−5.03
26.01	Fe II	37	4629.34	−2.37	N4	31	−5.10
26.01	Fe II	186	4635.32	−1.65	N4	17	−4.77
26.01	Fe II	28	4666.76	−3.33	N4	10	−4.90
26.01	Fe II	43	4731.45	−3.13	N4	10	−5.05
26.01	Fe II	J	4908.15	−0.30	KX	8	−4.50
26.01	Fe II	J	4951.58	0.18	KX	12	−4.76
26.01	Fe II	J	4984.47	0.01	KX	6	−4.92
26.01	Fe II	J	4990.51	0.18	KX	8	−4.94
26.01	Fe II	J	4993.36	−3.65	MF	4	−4.95
26.01	Fe II	J	5001.96	0.90	KX	28	−4.85
26.01	Fe II	J	5004.20	0.50	KX	14	−4.96
26.01	Fe II	J	5018.44	−1.22	MF	77	−4.68
26.01	Fe II	J	5022.79	−0.02	KX	8	−4.78
26.01	Fe II	J	5032.71	0.11	KX	14	−4.52
26.01	Fe II	J	5035.71	0.61	KX	21	−4.79
26.01	Fe II	J	5061.72	0.22	KX	7	−5.06
26.01	Fe II	J	5070.90	0.24	KX	6	−5.16
26.01	Fe II	J	5075.76	0.28	KX	8	−4.95
26.01	Fe II	J	5082.23	−0.10	KX	5	−4.80
26.01	Fe II	J	5093.58	0.11	KX	11	−4.64
26.01	Fe II	J	5145.77	−0.40	KX	5	−4.49
26.01	Fe II	J	5149.46	0.40	KX	14	−4.76
26.01	Fe II	J	5150.49	−0.12	KX	9	−4.50
26.01	Fe II	J	5169.03	−0.87	MF	81	−4.89
26.01	Fe II	J	5199.12	0.10	KX	5	−5.08
26.01	Fe II	J	5203.64	−0.05	KX	6	−4.81
26.01	Fe II	J	5216.85	0.81	KX	17	−5.00
26.01	Fe II	J	5234.62	−2.05	MF	37	−5.02
26.01	Fe II	J	5247.95	0.55	N4	22	−4.55
26.01	Fe II	J	5260.25	1.07	KX	30	−4.84
26.01	Fe II	J	5272.40	−2.03	MF	14	−4.46
26.01	Fe II	J	5276.00	−1.94	MF	34	−5.21
26.01	Fe II	J	5291.67	0.58	KX	13	−4.94
28.01	Ni II	11	3849.55	−1.88	KX	9	−6.54
28.01	Ni II	11	4067.03	−1.29	KX	11	−7.03
38.01	Sr II	1	4215.52	−0.17	WM	21	−8.35
39.01	Y II	6	3950.35	−0.49	HL	21	−7.55
39.01	Y II	6	3982.59	−0.49	HL	19	−7.62
39.01	Y II	5	4422.58	−1.27	HL	7	−7.43
39.01	Y II	22	4854.86	−0.38	HL	12	−7.59
39.01	Y II	22	4900.12	−0.09	HL	24	−7.38
39.01	Y II	20	5119.11	−1.36	HL	4	−7.14
39.01	Y II	20	5200.41	−0.57	HL	14	−7.28
39.01	Y II	20	5205.72	−0.34	HL	20	−7.24
40.01	Zr II	16	3998.95	−0.67	GB	5	−7.91
40.01	Zr II	42	4161.21	−0.72	BG	15	−7.26
80.01	Hg II	–	3983.94	−1.73	DW	50	−5.39

lated with stellar rotation. If difussion is operating in the atmospheres, probably one should expect that abundance anomalies should decrease with increasing rotational velocity. In fact, CP stars are rarely found having rotational velocities larger than ∼120 km s^{-1}. Finding a trend or its absence will be important in the context of the diffusion theory, which is the best explanation today for the spectroscopic characteristics of CP stars.

The authors acknowledge the use of the CCD and data reduction acquisition system supported by US NSF Grant AST 90-15827 to R. M. Rich. The authors thank Drs. R.L. Kurucz and I. Hubeny for making their codes available to them. This work was partially supported by a grant PICT 20269 from Agencia Nacional de Promoción Científica y Tecnológica.

REFERENCES

Abt, H., & Golson, J. 1962, ApJ, 136, 35
Abt, H., Chaffee, F. H., & Suffolk, G. 1972, ApJ, 175, 779
Adelman, S. J., & Pintado, O. 1997, A&AS, 125, 219
Adelman, S. J., & Rayle, K. E. 2000, A&A, 355, 308
Adelman, S. J., & Yüce, K. 2010, Astron. Nachr., 331, 785
Andersen, J., & Nordström, B. 1977, A&AS, 29, 309
Auriére, M., et al. 2007, A&A, 475, 1053
Auriére, M., et al. 2010, A&A, 523, 40
Bertaud, C. 1958, J. Obs., 42, 45
Corben, P. M. 1971, Mon. Not. Astron. Soc. S. Afr., 30, 37
Corben, P. M., & Stoy, R. H. 1968, Mon. Not. Astron. Soc. S. Afr., 27, 11
Cousins, A., & Stoy, R. 1962, Royal Greenwich Obs. Bull., 64, 103
Cowley, A. P., Cowley, C. R., Hiltner, W., Jaschek, M., & Jaschek, C. 1968, PASP, 80, 746
Cowley, A. P., Cowley, C. R., Jaschek, M., & Jaschek, C. 1969, AJ, 74, 375
Crawford, D. L. 1963, ApJ, 137, 530
Crawford, D. L., Barnes, J. V., & Golson, C. 1970, AJ, 75, 624
Cutri, R., et al. 2003, he IRSA 2MASS All-Sky Point Source Catalog, NASA/IPAC Infrared Science Archive http://irsa.ipac.caltech.edu/applications/Gator/
Chapelle, J., & Sahal-Brechot, S. 1970, A&A, 6, 415

TABLE 11

LINE ABUNDANCES OF HR 8937

Code	Species	Mult.	λ(Å)	log gf	Ref.	W_{eq}	log(N/N_T)
6.01	C II	4	3918.97	−0.53	WF	19	−3.21
6.01	C II	4	3920.68	−0.23	WF	24	−3.27
12.00	Mg I	2	5172.68	−0.38	WS	15	−5.01
12.00	Mg I	2	5183.60	−0.16	WS	22	−5.02
12.01	Mg II	5	3848.21	−1.59	WS	25	−4.51
12.01	Mg II	10	4390.57	−0.53	WS	35	−4.88
12.01	Mg II	9	4427.99	−1.21	WS	11	−4.80
14.01	Si II	1	3853.66	−1.44	LA	69	−4.59
14.01	Si II	1	3856.02	−0.49	LA	122	−4.76
14.01	Si II	1	3862.59	−0.74	LA	103	−4.76
14.01	Si II	3.01	4075.45	−1.40	SG	17	−4.52
14.01	Si II	3.01	4076.78	−1.67	SG	17	−4.23
14.01	Si II	3	4128.05	0.38	LA	145	−4.27
14.01	Si II	3	4130.89	0.53	LA	128	−4.56
14.01	Si II	5	5041.02	0.29	SG	90	−4.44
15.01	P II	15	4602.07	0.74	WS	11	−5.37
16.01	S II	44	4153.07	0.62	WS	4	−5.13
16.01	S II	44	4162.66	0.78	WS	7	−4.96
16.01	S II	9	4815.55	0.18	WM	5	−5.17
20.01	Ca II	1	3933.66	0.13	WM	232	−5.93
22.01	Ti II	34	3900.54	−0.45	MF	47	−6.76
22.01	Ti II	34	3913.46	−0.53	MF	49	−6.65
22.01	Ti II	87	4028.34	−1.00	MF	16	−6.70
22.01	Ti II	105	4163.64	−0.40	MF	30	−6.55
22.01	Ti II	19	4294.09	−1.11	MF	36	−6.44
22.01	Ti II	41	4300.04	−0.77	MF	54	−6.22
22.01	Ti II	41	4301.92	−1.16	MF	16	−6.90
22.01	Ti II	41	4312.86	−1.16	MF	26	−6.58
22.01	Ti II	19	4395.03	−0.66	MF	47	−6.58
22.01	Ti II	61	4395.84	−2.17	MF	6	−6.34
22.01	Ti II	51	4399.77	−1.27	MF	16	−6.75
22.01	Ti II	40	4417.71	−1.43	MF	16	−6.62
22.01	Ti II	19	4443.80	−0.70	MF	37	−6.81
22.01	Ti II	19	4450.48	−1.45	MF	13	−6.76
22.01	Ti II	31	4468.49	−0.60	MF	37	−6.89
22.01	Ti II	115	4488.32	−0.82	MF	11	−6.48
22.01	Ti II	31	4501.27	−0.75	MF	33	−6.85
22.01	Ti II	50	4533.96	−0.77	MF	51	−6.28
22.01	Ti II	41	4563.76	−0.96	MF	31	−6.63
22.01	Ti II	82	4571.97	−0.53	MF	47	−6.47
22.01	Ti II	59	4657.20	−2.15	MF	9	−6.17
22.01	Ti II	92	4779.98	−1.37	MF	9	−6.53
22.01	Ti II	82	4805.09	−1.10	MF	13	−6.61
22.01	Ti II	114	4911.20	−0.34	MF	9	−7.05
22.01	Ti II	86	5185.90	−1.35	MF	22	−6.14
22.01	Ti II	7	5188.69	−1.21	MF	14	−6.72
24.01	Cr II	167	3865.60	−0.78	KX	25	−5.92
24.01	Cr II	167	3905.64	−0.90	KX	43	−5.30
24.01	Cr II	129	3911.32	−2.06	KX	9	−5.43
24.01	Cr II	183	3979.50	−0.73	KX	15	−6.15
24.01	Cr II	19	4051.93	−2.19	KX	9	−6.16
24.01	Cr II	26	4072.56	−2.41	KX	11	−5.57
24.01	Cr II	162	4145.78	−1.16	KX	16	−5.85
24.01	Cr II	31	4261.91	−1.53	KX	46	−5.31
24.01	Cr II	31	4275.57	−1.70	KX	28	−5.64
24.01	Cr II	44	4554.99	−1.38	MF	31	−5.76
24.01	Cr II	44	4558.65	−0.66	MF	64	−5.51
24.01	Cr II	39	4565.74	−2.11	MF	13	−5.63
24.01	Cr II	44	4588.20	−0.63	MF	65	−5.50
24.01	Cr II	44	4592.05	−1.22	MF	30	−5.94
24.01	Cr II	44	4616.63	−1.29	MF	24	−6.06
24.01	Cr II	44	4618.80	−1.11	MF	45	−5.65
24.01	Cr II	44	4634.07	−1.24	MF	39	−5.68
24.01	Cr II	30	4812.34	−1.80	MF	11	−6.11
24.01	Cr II	30	4824.13	−1.22	MF	48	−5.55
24.01	Cr II	30	4836.23	−2.25	MF	12	−5.61
24.01	Cr II	30	4848.23	−1.14	MF	31	−6.11
24.01	Cr II	105	4876.40	−1.46	KX	35	−5.68
24.01	Cr II	30	4884.61	−2.08	MF	8	−5.94
24.01	Cr II	43	5232.50	−2.09	KX	15	−5.50
24.01	Cr II	23	5246.77	−2.45	MF	16	−5.29
24.01	Cr II	43	5274.96	−1.29	KX	24	−6.01
24.01	Cr II	43	5308.44	−1.81	MF	20	−5.61
24.01	Cr II	43	5310.70	−2.28	MF	8	−5.63
24.01	Cr II	43	5313.59	−1.65	MF	19	−5.82
24.01	Cr II	43	5334.87	−1.56	KX	19	−5.90
25.00	Mn I	2	4030.75	−0.47	MF	27	−4.98
25.00	Mn I	2	4033.06	−0.62	MF	47	−4.26
25.00	Mn I	2	4034.48	−0.81	MF	19	−4.86
25.00	Mn I	5	4035.72	−0.19	KX	10	−4.80
25.00	Mn I	5	4041.35	0.29	MF	26	−4.71
25.00	Mn I	22	4414.89	−0.29	MF	7	−4.51
25.00	Mn I	16	4754.04	−0.09	MF	12	−4.72
25.00	Mn I	21	4761.51	−0.14	MF	5	−4.74
25.00	Mn I	21	4765.85	−0.08	MF	11	−4.45
25.00	Mn I	21	4766.42	0.10	MF	11	−4.62
25.00	Mn I	16	4783.43	0.04	MF	15	−4.72
25.01	Mn II	I	3859.21	−2.56	KX	10	−4.80
25.01	Mn II	I	3878.99	−1.71	KX	40	−4.61
25.01	Mn II	I	3917.32	−1.15	KX	35	−4.65
25.01	Mn II	I	3952.42	−1.50	KX	15	−4.53
25.01	Mn II	I	3986.58	−2.60	KX	18	−4.41
25.01	Mn II	I	3995.31	−2.44	KX	17	−4.65
25.01	Mn II	I	4000.05	−1.21	KX	31	−4.31
25.01	Mn II	I	4081.44	−2.24	KX	32	−4.02
25.01	Mn II	I	4087.91	−2.91	KX	9	−4.51
25.01	Mn II	I	4110.62	−1.51	KX	34	−4.68
25.01	Mn II	I	4140.44	−2.46	KX	18	−4.50
25.01	Mn II	I	4184.45	−1.95	KX	28	−4.38
25.01	Mn II	I	4200.27	−1.74	KX	39	−4.28
25.01	Mn II	2	4205.38	−3.38	KX	57	−4.25
25.01	Mn II	I	4240.39	−2.07	KX	29	−4.25
25.01	Mn II	7	4244.25	−2.39	KX	37	−4.10
25.01	Mn II	2	4260.46	−4.25	KX	19	−4.49
25.01	Mn II	I	4377.74	−2.14	KX	22	−4.73
25.01	Mn II	I	4391.96	−2.89	KX	7	−4.58
25.01	Mn II	I	4393.38	−2.32	KX	20	−4.61
25.01	Mn II	I	4403.51	−1.80	KX	20	−4.58
25.01	Mn II	I	4478.64	−0.95	KX	49	−4.51
25.01	Mn II	I	4497.94	−2.59	KX	10	−4.74
25.01	Mn II	I	4500.54	−2.07	KX	15	−4.77
25.01	Mn II	I	4503.20	−2.16	KX	19	−4.55
25.01	Mn II	I	4689.55	−2.54	KX	15	−4.22
25.01	Mn II	I	4702.73	−2.34	KX	13	−4.49
25.01	Mn II	I	4717.26	−1.86	KX	19	−4.56
25.01	Mn II	I	4730.40	−2.15	KX	46	−4.03
25.01	Mn II	I	4749.11	−2.00	KX	17	−4.64
25.01	Mn II	I	4791.78	−1.72	KX	29	−4.56
25.01	Mn II	I	4806.82	−1.56	KX	55	−4.30
25.01	Mn II	I	4830.06	−1.85	KX	30	−4.41
25.01	Mn II	I	4839.74	−1.86	KX	21	−4.65
25.01	Mn II	I	4842.32	−2.01	KX	25	−4.38
25.01	Mn II	I	5102.52	−1.93	KX	40	−4.08
25.01	Mn II	I	5307.35	−2.07	KX	11	−4.39
25.01	Mn II	I	3902.36	−2.72	KX	10	−4.59
25.01	Mn II	I	3926.11	−2.42	KX	26	−4.08
26.00	Fe I	45	3815.84	0.23	N4	19	−4.80
26.00	Fe I	20	3825.88	−0.04	N4	20	−4.80
26.00	Fe I	4	3859.91	−0.71	N4	14	−4.79
26.00	Fe I	20	3865.52	−0.98	N4	18	−3.88
26.00	Fe I	20	3872.50	−0.93	N4	12	−4.17
26.00	Fe I	43	4071.74	−0.02	N4	12	−4.78
26.00	Fe I	152	4198.30	−0.72	N4	8	−3.89
26.00	Fe I	522	4199.10	0.16	N4	18	−4.01
26.00	Fe I	42	4271.76	−0.16	N4	11	−4.74
26.00	Fe I	41	4383.54	0.20	N4	19	−4.79
26.00	Fe I	41	4404.75	−0.14	N4	16	−4.51
26.00	Fe I	318	4920.50	0.07	N4	22	−3.90
26.00	Fe I	289	4957.30	−0.41	N4	9	−3.90
26.00	Fe I	318	4957.60	0.23	N4	9	−4.58
26.00	Fe I	325	5192.34	−0.42	N4	8	−3.86
26.00	Fe I	383	5232.94	−0.06	N4	17	−3.86
26.00	Fe I	1146	5383.37	0.65	N4	12	−4.10
26.00	Fe I	686	5586.76	−0.14	N4	8	−3.96

TABLE 11 (CONTINUED)

Code	Species	Mult.	λ(Å)	log gf	Ref.	W_{eq}	log(N/N_T)
26.01	Fe II	127	3845.18	−2.29	KX	13	−4.82
26.01	Fe II	173	3906.04	−1.83	N4	28	−4.29
26.01	Fe II	38	3935.96	−1.86	N4	24	−4.37
26.01	Fe II	3	3938.29	−4.07	N4	13	−4.39
26.01	Fe II	90	3938.97	−1.85	N4	20	−4.34
26.01	Fe II	28	4122.67	−3.38	N4	20	−4.41
26.01	Fe II	27	4233.17	−1.81	N4	83	−4.02
26.01	Fe II	27	4273.33	−3.34	N4	20	−4.36
26.01	Fe II	28	4296.57	−3.01	N4	33	−4.32
26.01	Fe II	27	4303.18	−2.61	N4	57	−4.01
26.01	Fe II	27	4351.77	−2.08	N4	50	−4.74
26.01	Fe II	J	4357.58	−2.10	KX	9	−4.45
26.01	Fe II	27	4385.39	−2.57	N4	45	−4.37
26.01	Fe II	27	4416.83	−2.60	N4	40	−4.49
26.01	Fe II	37	4472.93	−3.53	N4	13	−4.38
26.01	Fe II	37	4489.18	−2.97	N4	31	−4.34
26.01	Fe II	37	4491.40	−2.70	N4	36	−4.46
26.01	Fe II	38	4508.29	−2.21	N4	50	−4.53
26.01	Fe II	37	4515.34	−2.48	N4	42	−4.51
26.01	Fe II	37	4520.22	−2.60	N4	38	−4.54
26.01	Fe II	38	4522.63	−2.03	N4	56	−4.55
26.01	Fe II	38	4541.52	−3.05	N4	28	−4.35
26.01	Fe II	37	4555.89	−2.29	N4	51	−4.44
26.01	Fe II	38	4576.34	−3.04	N4	26	−4.40
26.01	Fe II	37	4582.84	−3.10	N4	22	−4.48
26.01	Fe II	38	4583.84	−2.02	N4	69	−4.15
26.01	Fe II	D	4596.02	−1.84	N4	18	−4.24
26.01	Fe II	38	4620.52	−3.28	N4	20	−4.35
26.01	Fe II	37	4629.34	−2.37	N4	50	−4.39
26.01	Fe II	186	4635.32	−1.65	N4	29	−4.20
26.01	Fe II	28	4666.76	−3.33	N4	18	−4.37
26.01	Fe II	43	4731.45	−3.13	N4	22	−4.41
26.01	Fe II	J	4908.15	−0.30	KX	10	−4.17
26.01	Fe II	J	4913.29	0.01	KX	14	−4.32
26.01	Fe II	J	4951.58	0.18	KX	18	−4.32
26.01	Fe II	J	4977.04	0.04	KX	17	−4.16
26.01	Fe II	J	4984.47	0.01	KX	12	−4.33
26.01	Fe II	J	4990.51	0.18	KX	15	−4.41
26.01	Fe II	J	4993.36	−3.65	MF	7	−4.55
26.01	Fe II	J	5001.96	0.90	KX	44	−4.25
26.01	Fe II	J	5004.20	0.50	KX	24	−4.43
26.01	Fe II	J	5015.75	−0.05	KX	24	−3.86
26.01	Fe II	J	5018.44	−1.22	MF	102	−3.99
26.01	Fe II	J	5021.59	−0.30	KX	6	−4.44
26.01	Fe II	J	5022.79	−0.02	KX	19	−4.17
26.01	Fe II	J	5030.63	0.40	KX	21	−4.44
26.01	Fe II	J	5035.71	0.61	KX	31	−4.32
26.01	Fe II	J	5045.11	−0.13	KX	9	−4.38
26.01	Fe II	J	5061.72	0.22	KX	16	−4.41
26.01	Fe II	J	5067.89	−0.20	KX	8	−4.35
26.01	Fe II	J	5070.90	0.24	KX	18	−4.36
26.01	Fe II	J	5075.76	0.28	KX	15	−4.44
26.01	Fe II	J	5082.23	−0.10	KX	9	−4.39
26.01	Fe II	J	5093.58	0.11	KX	22	−4.01
26.01	Fe II	J	5097.27	0.31	KX	31	−3.95
26.01	Fe II	J	5106.11	−0.28	KX	13	−4.02
26.01	Fe II	J	5117.03	−0.13	KX	8	−4.41
26.01	Fe II	J	5145.77	−0.40	KX	12	−3.92
26.01	Fe II	J	5149.46	0.40	KX	28	−4.09
26.01	Fe II	J	5150.49	−0.12	KX	12	−4.18
26.01	Fe II	J	5160.84	−2.64	KX	10	−4.03
26.01	Fe II	J	5169.03	−0.87	MF	106	−4.26
26.01	Fe II	J	5180.31	0.04	KX	5	−4.77
26.01	Fe II	J	5199.12	0.10	KX	21	−4.03
26.01	Fe II	J	5203.64	−0.05	KX	16	−4.07
26.01	Fe II	J	5216.85	0.81	KX	28	−4.45
26.01	Fe II	J	5223.26	−0.41	KX	7	−4.17
26.01	Fe II	J	5228.90	−0.30	KX	12	−3.99
26.01	Fe II	J	5232.79	−0.06	KX	16	−4.07
26.01	Fe II	J	5234.62	−2.05	MF	57	−4.22
26.01	Fe II	J	5247.95	0.55	N4	31	−4.08
26.01	Fe II	J	5251.23	0.42	N4	30	−3.98
26.01	Fe II	J	5254.93	−3.23	KX	13	−4.44
26.01	Fe II	J	5257.12	0.03	KX	12	−4.30
26.01	Fe II	J	5260.25	1.07	KX	46	−4.25
26.01	Fe II	J	5272.40	−2.03	MF	18	−4.09
26.01	Fe II	J	5276.00	−1.94	MF	52	−4.51
26.01	Fe II	J	5291.67	0.58	KX	37	−3.95
26.01	Fe II	J	5306.18	0.09	N4	23	−3.87
26.01	Fe II	J	5339.59	0.54	KX	30	−4.11
26.02	Fe III	4	4419.60	−2.22	KX	3	−4.35
38.01	Sr II	1	4215.52	−0.17	WM	81	−6.30
39.01	Y II	6	3950.35	−0.49	HL	52	−6.51
39.01	Y II	6	3982.59	−0.49	HL	54	−6.45
39.01	Y II	14	4124.90	−1.50	HL	29	−6.29
39.01	Y II	5	4235.73	−1.50	HL	34	−6.26
39.01	Y II	5	4422.58	−1.27	HL	35	−6.49
39.01	Y II	22	4854.86	−0.38	HL	37	−6.81
39.01	Y II	22	4900.12	−0.09	HL	59	−6.18
39.01	Y II	20	4982.13	−1.29	HL	19	−6.53
39.01	Y II	20	5200.41	−0.57	HL	48	−6.15
39.01	Y II	20	5205.72	−0.34	HL	54	−6.10
39.01	Y II	20	5289.82	−1.85	HL	10	−6.35
40.01	Zr II	17	3915.96	−0.82	KX	6	−7.86
40.01	Zr II	16	3958.23	−0.31	KX	15	−7.85
40.01	Zr II	30	3991.15	−0.25	KX	16	−7.77
40.01	Zr II	16	3998.95	−0.67	GB	16	−7.45
40.01	Zr II	41	4149.22	−0.03	BG	24	−7.69
40.01	Zr II	41	4208.98	−0.46	BG	13	−7.70
80.01	Hg II	–	3983.94	−1.73	DW	128	−4.06

Dolk, L., Wahlgren, G. M., & Hubrig, S. 2003, A&A, 402, 299

Dworetsky, M. M. 1971, PhD Thesis, University of California, USA

Eggen, O. 1977, PASP, 89, 205

Fuhr, J. R., Martin, G. A., & Wiese, W. L. 1988, J. Phys. Chem. Ref. Data, 17, Suppl. 4

Fuhr, J. R., & Wiese, W. L. 2006, J. Phys. Chem. Ref. Data, 35, 1669

Glagolevskij, Yu. V. 1994, Bull. Spec. Astrophys. Obs., 38, 152

Grevesse, N., Noels, A., & Sauval, A. 1996, in ASP Conf. Ser. 99, Cosmic Abundances, ed. S. Holt & G. Sonneborn (San Francisco: ASP), 117

Gronbech, B., & Olsen, E. H. 1976, A&AS, 25, 213

_____. 1977, A&AS, 27, 443

Guthrie, B. N. 1985, MNRAS, 216, 1

Hauck, B., & Mermilliod, M. 1998, A&AS, 129, 431

Houk, N. 1982, Michigan Catalogue of Two-Dimensional Spectral Types for the HD Stars, Vol. 3 (Ann Arbor: Univ. Michigan Dept. Astron.)

Hubrig, S., & Mathys, G. 1995, in ASP Conf. Ser. 81, Laboratory and Astronomical High Resolution Spectra, ed. A. J. Sauval, R. Blomme, & N. Grevesse (San Francisco: ASP), 555

Iglesias, L., & Velasco, R. 1964, Publ. Inst. Opt. Madrid, No. 23

Irwin, J. B. 1961, ApJS, 6, 253

Johansson, S. 1978, Phys. Scr., 18, 217

Jomaron, C. M., Dworetsky, M. M., & Allen, C. S. 1999,

MNRAS, 303, 555
Kurucz, R. L., & Avrett, E. H. 1981, SAO Spec. Rep., 391
Kurucz, R. L., & Bell, B. 1995, Atomic Line Data, Kurucz CD-ROM No. 23 (Cambridge: SAO)
Lanz, T., Dimitrijevic, M. S., & Artru, M. C. 1988, A&A, 192, 249
Makaganiuk, V., et al. 2011, A&A, 525, 97
Moon, T. T., & Dworetsky, M. 1985, MNRAS, 217, 305
Moore, C. E. 1945, A Multiplet Table of Astrophysical Interest (Princeton: Princeton Univ. Obs.)
Napiwotzki, R., Shonberner, D., & Wenske, V. 1993, A&A, 268, 653
Nilsson, A., Johansson, S., & Kurucz, R. L. 1991, Phys. Scr., 44, 226
Pintado, O. I., & Adelman, S. J. 2003, A&A, 406, 987
Piskunov, N. E. 1996, in ASP Conf. Ser. 108, Model Atmosphere and Spectrum Synthesis, ed. S. J. Adelman, F. Kupka, & W. W. Weiss (San Francisco: ASP), 307
Reader, J., Corliss, C. H., Wiese, W. L., & Martin, G. A. 1980, Wavelengths and Transition Probabilities for Atoms and Atomic Ions, Part 1 (NSRDS-NBS 68; Washington: NBS)
Renson, P., & Manfroid, J. 2009, A&A 498, 961
Rybka, E. 1969, Acta Astron., 19, 229
Saffe, C., & Levato, H. 2009, RevMexAA, 45, 171
Saffe, C., Levato, H., & López-García, Z., 2004, RevMexAA, 40, 231
_____. 2005, RevMexAA, 41, 415
Sahal-Brechot, S. 1969, A&A, 2, 322
Schneider, H. 1981, A&AS, 44, 137
Smith, K. C. 1997, A&A, 319, 928
Smith, K. C., & Dworetsky, M. M. 1993, A&A, 274, 335
Strauss, F. M., & Ducati, J. R. 1981, A&AS, 44, 337
Svendenius, N., Magnusson, C. E., & Zetterberg, P. O. 1983, Phys. Scr., 27, 339
Woolf, V. M., & Lambert, D. L. 1999, ApJ, 521, 414
Wolff, S., & Wolff, R. 1974, ApJ, 194, 65
Zavala, R. T., et al. 2007, ApJ, 655, 1046

C. Saffe, N. Núñez and H. Levato: Instituto de Ciencias Astronómicas, de la Tierra y del Espacio, C.C 467, 5400, San Juan, Argentina. CS and HL are members of the Carrera del Investigador Científico, Consejo Nacional de Investigaciones Científicas y Técnicas de la República Argentina (csaffe, nnunez, hlevato@icate-conicet.gob.ar).

Revista Mexicana de Astronomía y Astrofísica, **47**, 235–253 (2011)

ON THE STELLAR AND BARYONIC MASS FRACTIONS OF CENTRAL BLUE AND RED GALAXIES

A. Rodríguez-Puebla,[1] V. Avila-Reese,[1] C. Firmani,[1,2] and P. Colín[3]

Received 2011 January 21; accepted 2011 April 14

RESUMEN

Con la técnica del empate de abundancias, las relaciones locales masa estelar y bariónica-masa de halo ($M_{\rm s}$–$M_{\rm h}$ y $M_{\rm b}$–$M_{\rm h}$) para galaxias *centrales* azules y rojas (GAs y GRs) se infieren por separado. Se hace uso de las funciones de masa estelar galáctica observadas de GAs y GRs y las respectivas relaciones masa de gas-$M_{\rm s}$. Las funciones de masa de halos asociados a las GAs y GRs centrales se toman de una descomposición adecuadamente obtenida de la función de halos distinguibles ΛCDM. Para $M_{\rm h} \gtrsim 10^{11.5}\ M_\odot$, la $M_{\rm s}$ de GRs tiende a ser mayor que la de GAs a una dada $M_{\rm h}$, pero no más que un factor ∼1.7. Para $M_{\rm h} \lesssim 10^{11.5}\ M_\odot$, esta tendencia se invierte. Para GAs (GRs): (a) el máximo de $f_{\rm s}$=$M_{\rm s}/M_{\rm h}$ es $0.021^{+0.016}_{-0.009}$ ($0.034^{+0.026}_{-0.015}$) y se alcanza a $\log(M_{\rm h}/M_\odot) = 12.0$ (= 11.9); (b) $f_{\rm s} \propto M_{\rm h}$ ($f_{\rm s} \propto {M_{\rm h}}^3$) hacia el lado de bajas masas, mientras que en el otro extremo $f_{\rm s} \propto {M_{\rm h}}^{-0.4}$ ($f_{\rm s} \propto {M_{\rm h}}^{-0.6}$). Las $f_{\rm b}$=$M_{\rm b}/M_{\rm h}$ de GAs y GRs son cercanas para $M_{\rm h} \gtrsim 10^{11.7}\ M_\odot$, y alcanzan valores máximos de $f_{\rm b} = 0.028^{+0.018}_{-0.011}$ y $f_{\rm b} = 0.034^{+0.025}_{-0.014}$. Hacia masas menores la dependencia de $f_{\rm b}$ sobre $M_{\rm h}$ es mucho más empinada para GRs que para GAs. Discutimos las diferencias encontradas para las relaciones $f_{\rm s}$–$M_{\rm h}$ y $f_{\rm b}$–$M_{\rm h}$ entre GAs y GRs a la luz de inferencias semi-empíricas de evolución galáctica.

ABSTRACT

Using the abundance matching technique, we infer the local stellar and baryonic mass-halo mass ($M_{\rm s}$–$M_{\rm h}$ and $M_{\rm b}$–$M_{\rm h}$) relations separately for *central* blue and red galaxies (BGs and RGs). The observational inputs are the SDSS central BG and RG stellar mass functions and the measured gas mass-$M_{\rm s}$ relations. For halos associated to central BGs, the distinct ΛCDM halo mass function is used and set up to exclude: (i) the observed group/cluster mass function and (ii) halos with a central major merger at resdshifts $z \leq 0.8$. For central RGs, the complement of this mass function to the total one is used. At $M_{\rm h} > 10^{11.5}\ M_\odot$, the $M_{\rm s}$ of RGs tend to be higher than those of BGs for a given $M_{\rm h}$, the difference not being larger than 1.7. At $M_{\rm h} < 10^{11.5}\ M_\odot$, this trend is inverted. For BGs (RGs): (a) the maximum value of $f_{\rm s} = M_{\rm s}/M_{\rm h}$ is $0.021^{+0.016}_{-0.009}$ ($0.034^{+0.026}_{-0.015}$) and it is attained at $\log(M_{\rm h}/M_\odot) = 12.0$ (= 11.9); (b) $f_{\rm s} \propto M_{\rm h}$ ($f_{\rm s} \propto {M_{\rm h}}^3$) at the low-mass end while at the high-mass end, $f_{\rm s} \propto {M_{\rm h}}^{-0.4}$ ($f_{\rm s} \propto {M_{\rm h}}^{-0.6}$). The baryon mass fractions, $f_{\rm b}$=$M_{\rm b}/M_{\rm h}$, of BGs and RGs reach maximum values of $f_{\rm b} = 0.028^{+0.018}_{-0.011}$ and $f_{\rm b} = 0.034^{+0.025}_{-0.014}$, respectively. At $M_{\rm h} < 10^{11.3}\ M_\odot$, the dependence of $f_{\rm b}$ on $M_{\rm h}$ is much steeper for RGs than for BGs. We discuss the differences found in the $f_{\rm s}$–$M_{\rm h}$ and $f_{\rm b}$–$M_{\rm h}$ relations between BGs and RGs in the light of semi-empirical galaxy evolution inferences.

Key Words: dark matter — galaxies: luminosity function, mass function

1. INTRODUCTION

The galaxy stellar and baryonic mass functions (*GSMF* and *GBMF*, respectively), inferred from the observed luminosity function and gas fraction-stellar mass ($f_{\rm g}$–$M_{\rm s}$) relation, contain key statistical in-

[1]Instituto de Astronomía, Universidad Nacional Autónoma de México, Mexico.

[2]Osservatorio Astronomico di Brera, Italy.

[3]Centro de Radioastronomía y Astrofísica, Universidad Nacional Autónoma de México, Mexico.

formation to understand the physical processes of galaxy formation and evolution. Within the context of the popular Λ Cold Dark Matter (ΛCDM) hierarchical scenario, dark matter halos are the sites where galaxies form and evolve (White & Rees 1978; White & Frenk 1991). Hence, a connection between *GBMF* or *GSMF* and the halo mass function (*HMF*) is expected. The result of such a connection is the galaxy stellar and baryonic mass-halo mass relations, $M_{\rm s}$–$M_{\rm h}$ and $M_{\rm b}$–$M_{\rm h}$, and their intrinsic scatters, both set by complex dynamical and astrophysical processes intervening in galaxy formation and evolution (see for recent reviews Baugh 2006; Avila-Reese 2007; Benson 2010). In this sense, the $M_{\rm b}/M_{\rm h}$ and $M_{\rm s}/M_{\rm h}$ ratios quantify the efficiency at which galaxy and star formation proceeds within a halo of mass $M_{\rm h}$. Therefore, the empirical or semi-empirical inference of the $M_{\rm b}$–$M_{\rm h}$ and $M_{\rm s}$–$M_{\rm h}$ relations and their scatters (locally and at other epochs) is nowadays a challenge of great relevance in astronomy.

For simplicity, in statistical studies like those related to the *GSMF*, galaxies are labelled by their mass alone. However, according to their observed properties, correlations, and evolution, galaxies show a very different nature, at least for the two major groups in which they are classified: the rotationally-supported disk star-forming (late-type) and the pressure-supported spheroid quiescent (early-type) galaxies. In the same way, the evolution of galaxies is expected to differ if they are centrals or satellites. The main intrinsic processes of galaxy evolution are associated to central galaxies, while satellite galaxies undergo several *extra* astrophysical processes because of the influence of the environment of the central galaxy/halo system in which they were accreted. Hence, if the $M_{\rm b}$–$M_{\rm h}$ or $M_{\rm s}$–$M_{\rm h}$ relations are used for constraining galaxy formation and evolution processes, these relations are separately required for at least the two main families of late- and early-type galaxies and should take into account whether the galaxy is central or satellite. Fortunately, in the last years there appeared several studies in which a decomposition of complete *GSMF*s by color, concentration or other easily measurable indicators of the galaxy type was carried out (e.g., Bell et al. 2003; Shao et al. 2007; Bernardi et al. 2010). Furthermore, in a recent work Yang, Mo, & van den Bosch (2009, hereafter YMB09) used the Sloan Digital Sky Survey (SDSS) data to obtain the *GSMF*s of both central and central + satellite galaxies separated in each case into blue and red objects.

With the advent of large galaxy surveys, a big effort has been made to constrain the $z \sim 0$ *total* $M_{\rm s}$–$M_{\rm h}$ relation (i) *directly* by estimating halo masses with galaxy-galaxy weak lensing, with kinematics of satellite galaxies or with X-ray studies; and (ii) *indirectly* by linking observed statistical galaxy properties (e.g., the galaxy stellar mass function *GSMF*, the two-point correlation function, galaxy group catalogs) to the theoretical *HMF* (for recent reviews and additional references see Moster et al. 2010; Behroozi, Conroy, & Wechsler 2010, hereafter BCW10; More et al. 2011). While the latter approach does not imply a measure-based determination of halo masses, it is simpler from a practical point of view, as it allows to cover larger mass ranges, and can be extended to higher redshifts than the former approach (see recent results in Conroy & Wechsler 2009; Moster et al. 2010; Wang & Jing 2010; BCW10). Besides, both the weak lensing and satellite kinematics methods in practice are (still) statistical in the sense that one needs to stack large number of galaxies in order to get sufficient signal-to-noise. This introduces a significant statistical uncertainty in the inferred halo masses.

The indirect approach for linking galaxy and halo masses spans a large variety of methods, among which the halo occupation distribution (Peacock & Smith 2000; Berlind & Weinberg 2002; Kravtsov et al. 2004) and the conditional luminosity function formalisms (Yang, Mo, & van den Bosch 2003; Yang et al. 2004) can be mentioned. These formalisms introduce *a priori* functional forms with several parameters that should be constrained by the observations. Therefore, the final inferred $M_{\rm s}$–$M_{\rm h}$ relation is actually model-dependent and yet sometimes poorly constrained due to degeneracies in the large number of parameters. A simpler and more empirical method –in the sense that it uses only the *GSMF* (or luminosity function) as input and does not require to introduce any model– has been found to give reasonable results. This indirect method, called the abundance matching technique (hereafter AMT; e.g., Marinoni & Hudson 2002; Vale & Ostriker 2004; Conroy, Wechsler, & Kravtsov 2006; Shankar et al. 2006; Conroy & Wechsler 2009; Baldry, Glazebrook, & Driver 2008; Guo et al. 2010; Moster et al. 2010; BCW10), is based on the assumption of a monotonic correspondence between $M_{\rm s}$ and $M_{\rm h}$; in the limit of zero scatter in the $M_{\rm s}$–$M_{\rm h}$ relation, the halo mass $M_{\rm h}$ corresponding to a galaxy of stellar mass $M_{\rm s}$, is found by matching the observed cumulative *GSMF* to the theoretical cumulative *HMF*.

In this paper we apply the AMT in order to infer the local $M_{\rm s}$–$M_{\rm h}$ relation for *central blue and red* galaxies separately, which requires as input *both* the

observed central blue and red *GSMF*s, taken here from YMB09. Note that in order to infer the $M_{\rm s}$–$M_{\rm h}$ relation of galaxy subpopulations (e.g., blue/red or central/satellite ones) solely from the overall *GSMF*, models for each subpopulation should be introduced, which greatly increases the uncertainty of the result. Regarding the *HMF*s to be matched with the corresponding observed central *GSMF*s, the theoretical *HMF* is decomposed into two functions –associated to halos hosting blue and red galaxies– based on empirical facts: blue galaxies are rare as central objects in groups/clusters of galaxies, and they should not have undergone late major mergers because of the dynamical fragility of disk (blue) galaxies. Nowadays, it is not clear whether or not the $M_{\rm s}$–$M_{\rm h}$ relation varies significantly with galaxy color or type. Previous studies that discussed this question were based on direct methods: the weak lensing (Mandelbaum et al. 2006) and satellite kinematics (More et al. 2011) techniques. The uncertainties in the results of these studies are still large, and can be subject to biases intrinsic to the sample selection and to effects of environment.

We also estimate here the galaxy baryon mass-halo mass relations, $M_{\rm b}$–$M_{\rm h}$[4], where $M_{\rm b}$= $M_{\rm s}$+ $M_{\rm g}$, by using the *GSMF*s combined with average observational determinations of the galaxy gas mass, $M_{\rm g}$, as a function of $M_{\rm s}$. The galaxy baryonic mass fraction, $f_{\rm b}$= $M_{\rm b}/M_{\rm h}$, and its dependence on mass is important for constraining models and simulations of galaxy evolution, and is also a key input for some approaches, implemented to model the most generic population of galaxies, namely *isolated (central) disk galaxies* (e.g., Mo, Mao, & White 1998; Firmani & Avila-Reese 2000; van den Bosch 2000; Stringer & Benson 2007; Dutton et al. 2007; Gnedin et al. 2007; Dutton & van den Bosch 2009). In these and other studies, it was shown that several disk galaxy properties, correlations, and their scatters depend (or are constrained) by $f_{\rm b}$. In a similar way, the $f_{\rm b}$–$M_{\rm h}$ dependence is expected to play some role in the results of structural and dynamical models of spheroid-dominated galaxies.

In § 2 we describe the method and the data input. The stellar/baryon mass-halo mass relations for the total, blue and red (sub)samples are presented in § 3. In § 4 we compare our results with other observational works, and discuss whether they are consistent or not with expectations of semi-empirical inferences. The summary and our conclusions are given in § 5.

[4]We assume that the galaxy baryonic mass is included in the halo (virial) mass $M_{\rm h}$.

2. THE METHOD

The AM statistical technique is based on the hypothesis of a one-to-one monotonic increasing relationship between $M_{\rm s}$ (or $M_{\rm b}$) and $M_{\rm h}$. Therefore, by matching the *cumulative* galaxy stellar and halo mass functions, for a given $M_{\rm s}$ a unique $M_{\rm h}$ is assigned:

$$\int_{M_{\rm h}}^{\infty} \phi_h(M'_h)dM'_h = \int_{M_{\rm s}}^{\infty} \phi_s(M'_s)dM'_s, \qquad (1)$$

where ϕ_h is the overall *HMF* (distinct + subhalos) and ϕ_s is the overall *GSMF*; *distinct* halos are those not contained inside more massive halos. It is reasonable to link central galaxies with distinct halos. Therefore, in the case of using the *GSMF* for only central galaxies, the distinct *HMF* should be used for the matching. Since the main purpose of this paper is the inference of the $M_{\rm s}$–$M_{\rm h}$ (and the corresponding $M_{\rm b}$–$M_{\rm h}$) relation for blue (red) galaxies, (i) a *GSMF* that separates galaxies by color is necessary (the data to be used here are discussed in § 2.1), and (ii) a criterion to select the halos that will likely host blue (red) galaxies shall be introduced (see § 2.2.1).

In this paper we will not carry out an exhaustive analysis of uncertainties in the inference of the $M_{\rm s}$–$M_{\rm h}$ relation with the AMT. This was extensively done in BCW10 (see also Moster et al. 2010). In BCW10 the uncertainty sources are separated into three classes: uncertainties (i) in the observational inference of *GSMF*, (ii) in the dark matter HMF, which includes uncertainties in the cosmological parameters, and (iii) in the matching process arising primarily from the intrinsic scatter between $M_{\rm s}$ and $M_{\rm h}$.

2.1. *Galaxy and Baryonic Stellar Mass Functions*

In the last years, complete galaxy luminosity functions (and therefore, *GSMF*s) were determined for local samples covering a large range of luminosities (masses). The stellar mass is inferred from (multi) photometric and/or spectral data (i) by using average stellar mass-to-light ratios, depending only on color (inferred from application of stellar population synthesis –SPS– models to galaxy samples with independent mass estimates, e.g., Bell et al. 2003), or (ii) by applying directly the SPS technique to each sample galaxy, when extensive multi-wavelength and/or spectral information is available.

In both cases, a large uncertainty is introduced in the inference of $M_{\rm s}$ due to the uncertainties in the IMF, stellar evolution, stellar spectral libraries, dust extinction, metallicity, etc. Bell et al. (2003) estimated a scatter of ≈0.1 dex in their $M_{\rm s}/L$ ratios

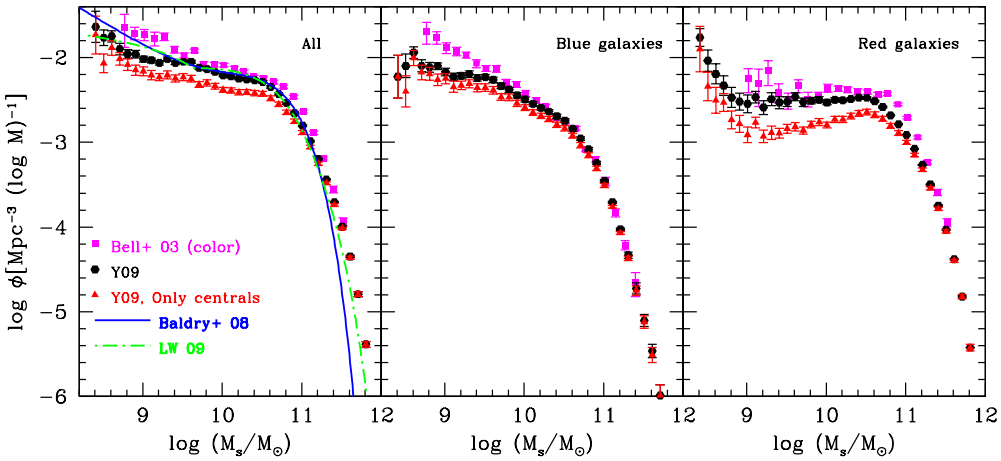

Fig. 1. Left panel: Different local *GSMF*s for *all* galaxies. The reported data in Bell et al. (2003, pink squares) and YMB09 (black hexagons) are plotted directly, while for Baldry et al. (2008, blue solid line) and Li & White (2009, dot-dashed green line), the best fits these authors find to their samples are plotted. Red triangles show the data from YMB09 corresponding to the *GSMF* of central-only galaxies. Middle and right panels: Data corresponding to the decomposition of the *GSMF* into blue and red galaxies, respectively, from Bell et al. (2003) and for the all and central-only galaxies from YMB09. The color figure can be viewed online.

in infrared bands. Conroy, Gunn, & White (2009) carried out a deep analysis of propagation of uncertainties in SPS modelling and concluded that $M_{\rm s}$ at $z \sim 0$ carry errors up to ∼0.3 dex (but see Gallazzi & Bell 2009). Here, we will consider an overall systematic uncertainty of 0.25 dex in the $M_{\rm s}$ determination (see BCW10).

Most of the current local *GSMF*s were inferred from 2dF Galaxy Redshift Survey, Two Micron All-Sky Survey (2MASS) and SDSS (e.g., Cole et al. 2001; Bell et al. 2003; Baldry et al. 2006). The low-mass completeness limit due to missing low surface brightness galaxies occurs at $\sim 10^{8.5}$ $M_{\rm s}$ (Baldry et al. 2008). An upturn of the *GSMF* close to this end (below $M_{\rm s} \sim 10^9$ $M_\odot$) was confirmed in several recent works (Baldry et al. 2008; YMB09; Li & White 2009). Due to this upturn, a better fit to the *GSMF*s is obtained by using a double or even triple Schechter function. Since the low-mass end of the *GSMF* is dominated by late-type galaxies, this upturn plays an important role in the $M_{\rm s}$–$M_{\rm h}$ relation of late-type galaxies at low masses.

For our purposes, observational works where the *GSMF* is decomposed into late- and early-types galaxies are required. Such a decomposition has been done, for example, in Bell et al. (2003), who combined 22679 SDSS Early Data Release and 2MASS galaxies, and used two different criteria, color and concentration, to split the sample into two types of galaxies. A much larger sample taken from the NYU-VAGC based on the SDSS DR4 has been used by YMB09 (see also Yang, Mo, & van den Bosch 2008), who split the sample into *blue and red* sub-samples according to a criterion in the ${}^{0.1}(g-r)-M_r$ diagram. In both works, $M_{\rm s}$ is calculated from the $r-$band magnitude by using the corresponding color-dependent $M_{\rm s}/L_r$ ratio given in Bell et al. (2003). In YMB09 each color subsample is in turn separated into central and satellite galaxies according to their memberships in the constructed groups, where the central galaxy is defined as the most massive one in the group and the rest as satellite galaxies.

In Figure 1, the Bell et al. (2003) and YMB09 *GSMF*s are reproduced by using the data sets reported in these papers. In the left panel, the full samples from each work (solid squares and solid hexagons, respectively) are plotted, as well as the case of central-only galaxies from YMB09 (solid triangles); both *GSMF*s and the other ones plotted in this figure are normalised to $h = 0.7$ and to a Chabrier (2003) IMF. In the central and right panels, the corresponding blue (late-type) and red (early-type) sub-samples are plotted with the same symbols as in the left panel. For the Bell et al. (2003) sub-samples, only those separated by their color criterion are plotted. Both *GSMF*s corresponding to the full and blue sub-samples are in good agreement for $M_{\rm s} \gtrsim 10^{9.5}$ $M_\odot$. For lower masses, the Bell et al. (2003) *GSMF*'s are higher. On one hand, the Bell et al. (2003) sample is much smaller than the

YMB09 one (therefore its cosmic variance is more significant). On the other hand, the redshift completeness and M_s limit in YMB09 are treated with updated criteria.

In Figure 1 we also plot fits to the overall *GSMF* presented in Baldry et al. (2008, double Schechter function, solid blue line) and in Li & White (2009, triple Schechter function, dashed green line) for new SDSS releases and by using directly SPS models to estimate M_s for each galaxy. These fits agree well with the YMB09 data in the mass range $9.2 \lesssim \log(M_s/M_\odot) \lesssim 11.2$. For smaller masses, the Baldry et al. (2008) fit tends to be steeper while the Li & White (2009) fit tends to be shallower than the YMB09 data. For larger masses, both fits decrease faster with M_s than the YMB09 data. All these (small) differences are due to the different methods used to estimate M_s, as well as the different volumes and limit corrections of the samples (see Baldry et al. 2008, YMB09, and Li & White 2009 for discussions).

The split into two colors of the sample used by YMB09 is a rough approximation to the two main families of disk- and spheroid-dominated galaxies. It is well known that the morphological type correlates with the galaxy color, though with a large scatter. There is for example a non-negligible fraction of galaxies (mostly highly inclined) that are red but of disk-like type (e.g., Bernardi et al. 2010). However, given that here we consider a partition of the overall sample just in two groups, we believe that it is reasonable to assume as a first approximation that the color criterion for the partition will provide at this level a result similar to that of a morphological criterion.

For the YMB09 sample, the blue and red galaxies are ≈55% and ≈45%, respectively, for $M_s \gtrsim 3 \times 10^8\ M_\odot$. Red galaxies dominate the total *GSMF* at large masses. At $M_s \approx 2 \times 10^{10}\ M_\odot$ the abundances of red and blue galaxies are similar and at lower masses the latter are increasingly more abundant than the former as M_s is smaller. For $M_s \lesssim 10^9\ M_\odot$, the abundance of red galaxies, mainly central ones, steeply increases towards smaller masses. The existence of this peculiar population of faint central red galaxies is discussed in YMB09. Wang et al. (2009) suggested that these galaxies are hosted by small halos that have passed through their massive neighbors, and the same environmental effects that cause satellite galaxies to become red are also responsible for the red colors of such galaxies. However, as these authors showed, even if the environmental effects work, there are in any case over 30% of small halos that are completely isolated, so that these effects cannot be invoked for them.

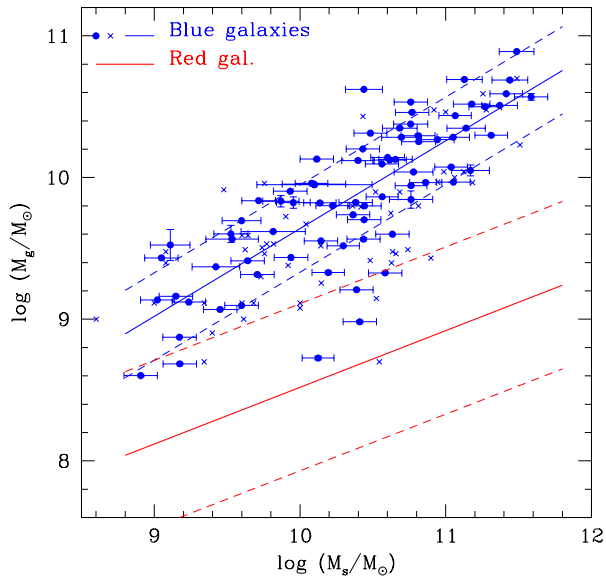

Fig. 2. Gas mass vs stellar mass for a sample of disk high and low surface brightness galaxies collected and homogenised by Avila-Reese et al. (2008, blue dots with error bars) and for a sample of disk galaxies presented by McGaugh (2005, blue crosses). The solid blue line is the orthogonal linear doubly-weighted regression to the data from the former authors and the dashed lines show an estimate of the intrinsic scatter around the fit. The solid red line is an estimate of the M_g–M_s correlation for red galaxies using our fit to blue galaxies and the ratio of blue-to-red atomic gas fraction determined in Wei et al. (2010), see text. The color figure can be viewed online.

In the YMB09 sample, around 70% of the galaxies are central. As mentioned in the § 1, the inference of the M_s–M_h relation for central-only galaxies is important for studies aimed to constrain galaxy formation and evolution in general; satellite galaxies are interesting on its own but they lack generality because their evolution and properties are affected by extra environmental processes.

In what follows, the YMB09 *GSMF* provided in tabular form and split into blue/red and central/satellite galaxies will be used for applying the AMT. Our main goal is to infer the M_s–M_h relation for central blue (late-type) and red (early-type) galaxies.

We will infer also the corresponding M_b–M_h (baryonic) relations. The blue and red *GBMF*s are estimated from the blue and red *GSMF*s, respectively, where in order to pass from M_s to M_b, the cool (atomic and molecular) gas mass, M_g, corre-

sponding on average to a given $M_{\rm s}$ is taken from the empirical blue and red $M_{\rm g}$–$M_{\rm s}$ relations. In Figure 2 a compilation of observational estimates is plotted in the $M_{\rm s}$–$M_{\rm g}$ plane for a sample of disk galaxies that includes low surface brightness galaxies from Avila-Reese et al. (2008; blue dots with error bars; they added H_2 mass contribution by using an estimate for the H_2-to-HI mass ratio as a function of galaxy type), and for another galaxy sample from McGaugh (2005; blue crosses; no H_2 contribution is considered and their dwarf galaxies were excluded). An orthogonal linear doubly-weighted regression to the data from Avila-Reese et al. (2008) gives:

$$\frac{M_{\rm g}}{10^{10}M_\odot} = 0.43 \times \left(\frac{M_{\rm s}}{10^{10}M_\odot}\right)^{0.62}. \qquad (2)$$

This fit is plotted in Figure 2 with its corresponding estimated scatter (≈0.3 dex; blue solid and dashed lines). This is the relation and its scatter used to calculate $M_{\rm b}$ and the blue *GBMF*. A similar relation has been inferred by Stewart et al. (2009). The gas fractions in red galaxies are much smaller than in blue galaxies. For sub-samples of blue and red galaxies, Wei et al. (2010) reported for each one the atomic gas fractions versus $M_{\rm s}$ (molecular gas was not included). The ratio of their fits to these data as a function of $M_{\rm s}$ is used here to estimate from equation 2 (blue galaxies) the corresponding average $M_{\rm g}$ for red galaxies as a function of $M_{\rm s}$. The red solid line shows the obtained relationship. As an approximation to the scatter (short-dashed lines), the average scatter reported for red galaxies in Wei et al. (2010) is adopted here.

2.2. *Halo and sub-halo mass functions*

A great effort has been made in the last decade to determine the *HMF* at $z = 0$ and at higher redshifts by means of N-body cosmological simulations. A good fit to the results, at least for low redshifts, is the universal function derived from a Press-Schechter formalism (Press & Schechter 1974) generalized to the elliptical gravitational collapse (Sheth & Tormen 1999, hereafter S-T). In fact, Tinker et al. (2008) have shown that at a high precision level, the *HMF* may change for different cosmological models and halo mass definitions as well as a function of z. For our purposes and for the cosmology used here, the S-T approximation provides a good description of the $z = 0$ *HMF* of distinct halos:

$$\phi_h(M_h)dM_h = A\left(1+\frac{1}{\nu^{2q}}\right)\sqrt{\frac{2}{\pi}}\frac{\bar{\rho}_M\nu}{M_h^2}\left|\frac{d\ln\sigma}{d\ln M_h}\right|\exp\left[-\frac{\nu^2}{2}\right]dM_h, \qquad (3)$$

where $A = 0.322$, $q = 0.3$, $\nu^2 = a(\delta_c/D(z)\sigma(M_{\rm h}))$ with $a = 0.707$; $\delta_c = 1.686\Omega_m^{0.0055}$ is the linear threshold in the case for spherical collapse in a flat universe with cosmological constant, $D(z)$ is the growth factor and $\sigma(M_{\rm h})$ is the mass power spectrum variance of fluctuations linearly extrapolated to $z = 0$. The halo (virial) mass, $M_{\rm h}$ is defined in this paper as the mass enclosed within the radius where the overdensity is $\bar{\rho}_{\rm vir} = \Delta$ times the *mean matter* density, $\bar{\rho}_M$; $\Delta \approx 340$ according to the spherical collapse model for the cosmology used here. The cosmological parameters assumed here are close to those of WMAP5 (Komatsu et al. 2009): $\Omega_M = 0.27, \Omega_\Lambda = 1 - \Omega_m = 0.73, h = 0.70, \sigma_8 = 0.8$.

The distinct *HMF* should be corrected when a *GSMF* corresponding to *all* galaxies is used in the AMT. In this case, satellite galaxies are included in the *GSMF*. Therefore, subhalos should be taken into account in the *HMF*. The subhalo fraction is no more than ≈20% of all the halos at $z = 0$ (e.g., Shankar et al. 2006; Conroy et al. 2006; Giocoli et al. 2010; BCW10). When necessary, we correct the S-T *HMF* for (present-day) subhalo population by using the fitting formula to numerical results given in Giocoli et al. (2010):

$$\frac{dn(m_{\rm sub})}{d\ln m_{\rm sub}} = A_0 m_{\rm sub}^{\eta-1}\exp\left[-\left(\frac{m_{\rm sub}}{m_0}\right)^\gamma\right], \qquad (4)$$

with $\eta = 0.07930$, $\log A_0 = 7.812$, $\log(m_0/M_\odot) = 13.10$ and $\gamma = 0.407$.

The upper panel of Figure 3 shows the (distinct) S-T *HMF* (solid line), the sub-halo *HMF* (short-long-dashed line), and the distinct+subhalo *HMF* (dash-dotted line). The correction by sub-halos in the abundance is small at low masses and negligible at high masses. When the *GSMF* refers only to central galaxies –which is the case in this paper– then it is adequate to use the distinct *HMF* for the AMT, i.e. *the subhalo abundance correction is not necessary.*

2.2.1. *Halos hosting blue and red galaxies*

In the AMT, the cumulative *GSMF* and *HMF* are matched in order to link a given $M_{\rm s}$ to $M_{\rm h}$. When a subsample of the total *GSMF* is used –as is the case for inferring the $M_{\rm s}$–$M_{\rm h}$ relation of only late- or early-type galaxies– it would not be correct to use the total *HMF* for the matching. This function, in the ignorance of which is the mass function of halos hosting blue (red) galaxies, at least should be re-normalised (decreased uniformly) by the same fraction corresponding to the decrease of the subsample *GSMF* with respect to the total *GSMF*. In

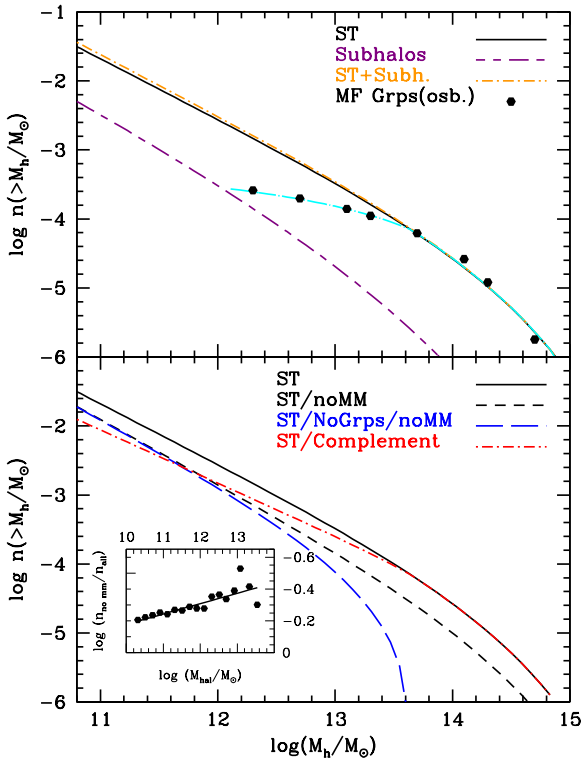

Fig. 3. Upper panel: Distinct S-T *HMF* for the cosmology adopted in this paper (solid black line), sub-halo mass function at $z = 0$ according to Giocoli et al. (2010, short-long-dashed purple line), and the sum of both (dot-dashed orange line). The solid dots are measures of the group/cluster mass function according to Heinämäki et al. (2003) and adequately corrected to our definition of virial halo mass; the dot-long-dashed cyan line is a eye-fit to the data. Lower panel: The same distinct S-T *HMF* (solid black line) shown in the upper panel but (i) excluding the halos that suffered late major mergers –since $z = 0.8$– (short-dashed black line) and (ii) excluding these halos and those of observed groups/clusters (long-dashed blue line). The latter is the *HMF* to be assigned to the sub-sample of central blue galaxies. The complement of this function to the total (S-T) one (dot-dashed red line) is the *HMF* to be assigned to the sub-sample of central red galaxies. The inset shows the ratio of number densities of halos that did not suffer major mergers since $z = 0.8$ to all the (distinct) halos according to measures in a cosmological N-body simulation (Colín et al. 2011, in preparation, see text). The fit to this ratio (solid line in the inset) is what has been used to correct the S-T *HMF* for halos thad did not suffer late major mergers. The color figure can be viewed online.

YMB09, ≈55% (≈45%) of the galaxies are in the blue (red) sub-samples for $M_s \gtrsim 3 \times 10^8\ M_\odot$. We may go one step further by proposing general observational/physical conditions for halos to be the hosts of blue (late-type) or red (early-type) galaxies. Note that the division of galaxies we do here is quite broad –just into two groups– and therefore very general conditions are enough.

Halos that host central blue and red galaxies are expected to have (i) a different environment, and (ii) a different merger history. We take into account these two factors in order to roughly estimate the *HMF* of those halos that will host today central blue and red galaxies.

Environment.- Blue (late-type) galaxies are rare in the centers of groups and clusters of galaxies (high-density environments; e.g., Norberg et al. 2001; Zehavi et al. 2005; Li et al. 2006; de Lapparent & Slezak 2007; Padilla, Lambas, & González 2010; Blanton & Moustakas 2009, and references therein). For example, in the SDSS YMB09 sample that we use here (see also Weinmann et al. 2006), among the groups with 3 or more members, the fraction of those with a central blue galaxy is only ≈20%, and most of these central galaxies have actually low masses. Therefore, cluster- and group-sized halos (more massive than a given mass) cannot be associated to central blue galaxies when using the AMT. This means that the halo mass function of groups/clusters of galaxies should be excluded from the theoretical *HMF* (Shankar et al. 2006).

Heinämäki et al. (2003) determined the *HMF* of groups with 3 or more members and with a number density enhancement $\delta n/n \geq 80$ from the Las Campanas Redshift Survey. The authors estimated the corresponding group virial mass on the basis of the line-of-sight velocity and harmonic radius of the group, in such a way that this mass was defined at the radius where $\delta n/n = 80$. The observational galaxy overdensity $\delta n/n$ is related to the mass overdensity $\delta\rho/\rho$ roughly through the bias parameter b: $\delta\rho/\rho = (1/b)\times\delta N/N$, where $b \approx 1/\sigma_8$ (Martínez et al. 2002). Hence, for $\sigma_8 = 0.8$, $\delta\rho/\rho \approx 64$; since the group selection was carried out in Tucker et al. (2000), where an Einstein-de Sitter cosmology was used, then $\rho = \rho_{\rm crit}$ in this case. In our case, the halo virial mass is defined at the radius where $\delta\rho/\rho \approx 340$ (see § 2.2); in terms of $\rho_{\rm crit}$, our overdensity is $340 \times \Omega_M = 92$. Therefore, the halo virial masses in Heinämäki et al. (2003) should be slightly larger than those used here. For the NFW halos of masses larger than $\sim 10^{13}\ M_\odot$, the differences are estimated to be factors of 1.10–1.20. We correct the group masses of Heinämäki et al. (2003) by 15%. In the upper panel of Figure 3, the corrected group (halo) mass function is reproduced (solid dots) and a eye-fit to them is plotted (dot-dashed cyan line).

Merger history.- Disk (blue, late-type) galaxies are dynamically fragile systems and thus they are not expected to survive strong perturbations such as those produced in major mergers or close interactions. However, as several theoretical studies have shown (e.g., Robertson et al. 2004; Governato, Mayer, & Brook 2008), when the mergers are gas-rich ('wet') and/or occur at early epochs (in fact, both facts are expected to be correlated), it is highly probable that a gaseous disk is regenerated or formed again with the late accreted gas. Therefore, a reasonable restriction for halos that will host disk galaxies is that they did not undergo *central* major mergers since a given epoch (at earlier epochs, while the central major merger may destroy the disk, a new gaseous disk can be formed later on). Based on numerical simulations, Governato et al. (2008) suggested that a 'wet' major merger of disk galaxies at $z \sim 0.8$ has still a non-negligible probability of rebuilding a significant disk by $z \sim 0$. We will assume here that halos whose *centers* have a major merger at $z < 0.8$ will not host a disk galaxy.

In Colín et al. (2011, in preparation) the present-day abundance fraction of halos with no *central* major merger since $z = 0.8$ was measured as a function of $M_{\rm h}$ from an N-body ΛCDM cosmological high-resolution simulation with $\Omega_m = 0.24$, $\Omega_\Lambda = 0.76$, and $\sigma_8 = 0.75$ (box size and mass per particle of 64 h^{-1} Mpc and $1.64 \times 10^7 h^{-1}$ $M_\odot$, respectively). The friends-of-friends (FOF) method with a linking-length parameter of 0.17 was applied for identifying halos. The mass ratio to define a major merger was $q = M_{\rm h,2}/M_{\rm h,1} > 0.2$ and the merger epoch was estimated as the time when the center of the accreted halo arrived at the center of the larger halo by dynamical friction; this epoch is calculated as the cosmic time when both FOF halos have "touched" plus the respective dynamical friction (merging) time as given by the approximation of Boylan-Kolchin, Ma, & Quataert (2008). The fraction of halos that did not suffer a major merger since $z = 0.8$ with respect to all the halos as a function of $M_{\rm h}$ measured in Colín et al. (2011, in preparation) is used here to correct our distinct S-T *HMF*. This measured fraction is shown in the inset in the lower panel of Figure 3; the solid line is a linear fit by eye in the log-log plot: $\log(n_{\rm noMM}/n_{\rm all}) = 0.472 - 0.065 \log(M_{\rm h}/M_\odot)$. As it is seen, the fraction slightly decreases with mass, which is consistent with the idea that larger mass halos are assembling later with a significant fraction of their masses being acquired in late major mergers. After the correction mentioned above, we get the mass function of halos that did not suffer a central major merger ($q > 0.2$) since $z = 0.8$ (short-dashed black line in the lower panel of Figure 3).

The final corrected HMFs.- The function obtained after (i) subtracting from the distinct S-T *HMF* the group mass function and (ii) excluding halos that did not suffer a late central major merger is plotted in Figure 3 (blue long-dashed line). This mass function is proposed here to correspond to halos that today host blue galaxies. The overall number fraction of these halos with respect to the distinct ones (described by the S-T *HMF*) is ∼58%, which is roughly consistent with the fraction of blue galaxies in the YMB09 sample. The *HMF* corresponding to the complement is plotted in Figure 3 as the red dot-dashed curve. By exclusion, this *HMF* will be associated with the *GSMF* of the red central galaxy sub-sample for deriving the $M_{\rm s}$–$M_{\rm h}$ relation of red galaxies.

3. RESULTS

3.1. *The overall, central, and satellite stellar-halo mass relations*

In Figure 4, the $M_{\rm s}$–$M_{\rm h}$ relation obtained by using the Li & White (2009) *GSMF* (see § 2.1 and Figure 1) and the S-T *HMF* corrected to include sub-halos is plotted (long-dashed blue line). The relation given by BCW10, who also used as input the Li & White (2009) *GSMF*, is shown (short-dashed red line). Both curves are almost indistinguishable, showing an excellent consistency of our results with those of BCW10, in spite of the differences in some of the methodological aspects.

Further, we plot in Figure 4 the $M_{\rm s}$–$M_{\rm h}$ relation as above but using now the total YMB09 *GSMF* (dot-dashed pink line). This relation is similar to the one inferred using the Li & White (2009) *GSMF*. For $\log(M_{\rm h}/M_\odot) \gtrsim 12$, the former slightly shifts with mass to higher values of $M_{\rm s}$ for a given $M_{\rm h}$ than the latter (at $\log(M_{\rm h}/M_\odot) = 13.5$ the difference is no larger than 0.08 dex in $\log M_{\rm s}$). Such a shift is explained by the (small) systematical difference between the YMB09 and Li & White (2009). *GSMF*s at masses larger than $\log(M_{\rm s}/M_\odot) \sim 11$ (see § 2.1 and Figure 1).

In Figure 4, the $M_{\rm s}$–$M_{\rm h}$ relations given in Baldry et al. (2008, dot-dashed orange line), Moster et al. (2010, short-long-dashed line) and Guo et al. (2010, dotted green line) are also plotted. When necessary, we have corrected the stellar masses to the Chabrier IMF, and the halo masses to the definition of virial mass used here (see § 2.2). As mentioned above, Baldry et al. (2008) corrected their *HMF* to exclude groups/clusters of galaxies (something that we do

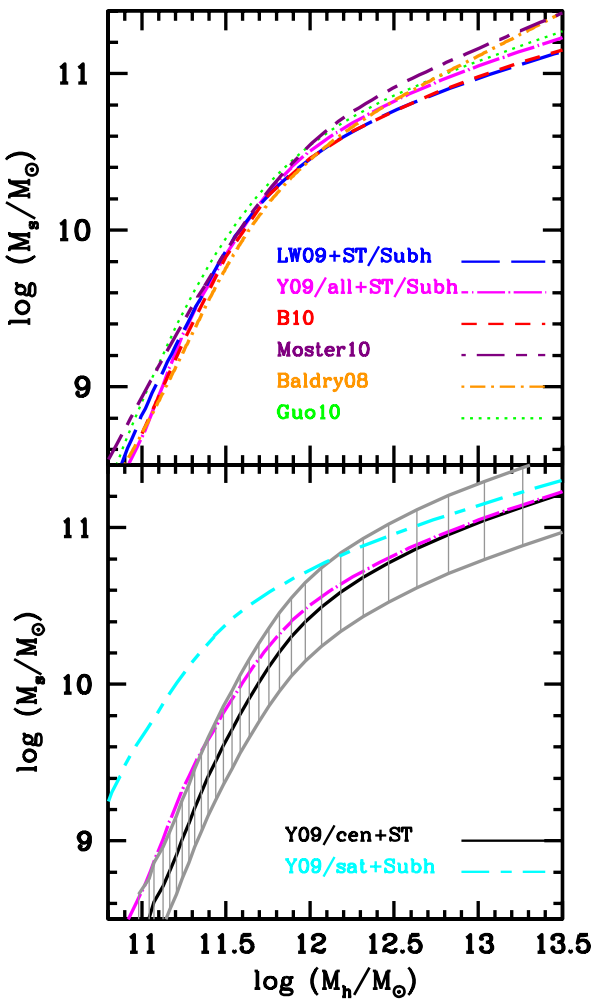

Fig. 4. Upper panel: Stellar mass vs halo mass as inferred here by using the Li & White (2009) overall *GSMF* and the S-T *HMF* increased by the subhalo population (long-dashed blue line) to be compared with the BCW10 inference, who used the same *GSMF* (short-dashed red line). The dot-dashed pink line shows the same M_s vs M_h inference but using the overall YMB09 *GSMF*. Different determinations of the overall M_s–M_h relation by other authors (indicated in the panel), who took into account in different ways the issue of group/cluster masses (see text) are also plotted. Lower panel: Same M_s–M_h relation as in the upper panel (dot-dashed pink line) but for the central-only YMB09 *GSMF* and the S-T (distinct) *HMF* (solid line). The grey curves connected by vertical lines show the estimated 1σ uncertainty for the latter case. The M_s–M_h relation inferred for the only satellite YMB09 *GSMF* and the Giocoli et al. (2010) $z = 0$ sub-halo mass function is plotted as a short-long-dashed cyan line. The color figure can be viewed online.

but only for the central blue galaxies, see § 2.2.1 and the result below). As seen in Figure 4, their correction produces a steeper M_s–M_h relation at the high-mass side than in our case. Moster et al. (2010) and Guo et al. (2010) constrained the M_s–M_h relation by assigning stellar masses to the halos and subhalos of an N-body cosmological simulation in such a way that the total *GSMF* was reproduced. Therefore, by construction, their M_s–M_h relations take into account the group/cluster halo masses issue. The M_s–M_h relations in both works are also slightly steeper than ours at high masses but shallower on average than that of Baldry et al. (2008). Note that in BCW10 the scatter in M_s at fixed M_h was taken into account but the group/cluster halo masses issue was not.

The M_s–M_h relation using the YMB09 *GSMF* only for central galaxies and the distinct (S-T) *HMF* is plotted in the lower panel of Figure 4 (solid black line). At large masses, this relation is quite similar to that for all galaxies/satellites and halos/subhalos (dot-dashed pink line). This is because at large masses the great majority of galaxies are centrals and the correction for sub-halos is negligible (see Figures 1 and 3). At lower masses, the exclusion of satellites and sub-halos implies a lower M_s for a given M_h. This is because the *GSMF* decreases more than the *HMF* as the mass is smaller when passing from the total (galaxy and halo) samples to the central-only galaxy/distinct halo samples. The physical interpretation of this result could be that satellite galaxies of a given M_s have less massive halos than central galaxies, due to tidal stripping. The M_s–M_h relation derived only for the satellites YMB09 *GSMF* and the Giocoli et al. (2010) $z = 0$ sub-halo *HMF* is plotted in the lower panel of Figure 4 (short-long-dashed cyan line).

3.1.1. *Uncertainties*

The uncertainty (standard deviation) in the M_s–M_h relation obtained using the YMB09 central *GSMF* and the distinct S-T *HMF* (solid line), is plotted in Figure 4 (grey curves connected by vertical lines). As remarked in § 2, we did not take into account all possible uncertainty sources in the M_s–M_h relation but have just considered the two following ones:

(i) The systematic uncertainty in stellar mass estimates, which is an uncertainty in the *GSMF*. We assume for this uncertainty a scatter of 0.25 dex (Gaussian-distributed) independent of mass, and propagate it to the M_s–M_h relation (it is by far the dominant source of error in the relation obtained with the AMT, see below and BCW10).

(ii) The intrinsic scatter in stellar mass at a fixed halo mass, which is an uncertainty in the process

of matching abundances. To take into account this scatter in $M_{\rm s}$ at fixed $M_{\rm h}$ a probability density distribution should be assumed. The convolution of this distribution with the true or intrinsic *GSMF* gives the measured *GSMF*. The cumulative true *GSMF* is then the one used for the AM (BCW10). The observational data allow to estimate the scatter in luminosity (or $M_{\rm s}$) and to date it appears to be independent of $M_{\rm h}$ (More et al. 2009; YMB09). In BCW10 a log-normal mass-independent scatter in $M_{\rm s}$ of 0.16 ± 0.04 is assumed. Here, we follow the overall procedure of BCW10 for taking into account this scatter.

We also explored the effect of (iii) the statistical uncertainty in the number density of the *GSMF* (as given in YMB09), but we found that the effect is negligible as compared to the one produced by item (i) (see also BCW10, their § 4.3.1). The effect of the intrinsic scatter in $M_{\rm s}$ for a given $M_{\rm h}$ is also very small in the overall scatter of the $M_{\rm s}$–$M_{\rm h}$ relation but it affects the high mass end of the calculated $M_{\rm s}$–$M_{\rm h}$ relation, where both the *GSMF* and *HMF* decay exponentially, since there are more low mass galaxies that are scattered upward than high mass galaxies that are scattered downward (BCW10). For instance, at $M_{\rm h} = 10^{13.5}\ M_{\odot}$, the stellar mass after including this scatter is 1.2 times smaller. The contribution from all other sources of error, including uncertainties in the cosmological model, is much smaller, ranging from 0.02 to 0.12 dex at $z = 0$.

From Figure 4 we see that the 1σ uncertainty in the $M_{\rm s}$–$M_{\rm h}$ relation is approximately 0.25 dex in $\log M_{\rm s}$ without any systematic dependence on $M_{\rm h}$, in good agreement with previous results (BCW10; Moster et al. 2010). This uncertainty is larger than the differences between the $M_{\rm s}$–$M_{\rm h}$ average relations found by different authors, including those that use the indirect AMT but with different *GSMF*s, methodologies, and corrections, and those who use more sophisticated formalisms (see for comparisons and discussions BCW10 and More et al. 2011). On one hand, this shows that most methods and recent studies aimed at relating halo masses to observed galaxies as a function of their stellar masses are converging to a relatively robust determination. On the other hand, this result suggests that attaining a higher precision in estimating $M_{\rm s}$ from observations is the crucial task for lowering the uncertainty in the inference of the $M_{\rm s}$–$M_{\rm h}$ relation.

3.2. *The stellar-halo mass relations for central blue and red galaxies*

The upper and lower left panels of Figure 5 show the mean $M_{\rm s}$–$M_{\rm h}$ and $f_{\rm s}$–$M_{\rm h}$ relations for: all central galaxies (solid line, as in Figure 4), central blue (short-dashed line), and central red (long dashed line) galaxies. In order to infer these relations for blue galaxies, the central blue YMB09 *GSMF* and the distinct (S-T) *HMF* corrected for excluding halos (i) associated to observed groups/clusters of galaxies and (ii) that suffered central major mergers since $z = 0.8$ (see § 2.2.2) were used. In the case of red galaxies, the central red YMB09 *GSMF* and the *HMF* complementary to the one associated to blue galaxies were used.

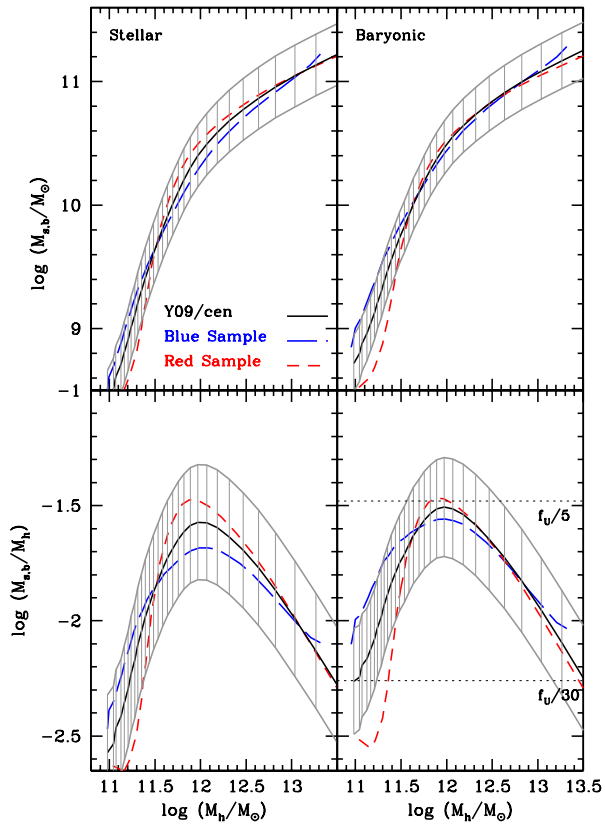

Fig. 5. Left panels: Mean $M_{\rm s}$–$M_{\rm h}$ (top) and $f_{\rm s}$–$M_{\rm h}$ (bottom) relations of all central (solid black line), blue central (long-dashed blue line), and red central (short-dashed red line) galaxies as inferred here using the YMB09 data. The grey curves connected by vertical lines show the 1σ uncertainty for the all-galaxies case; similar uncertainty regions around the main relations are found for the blue and red sub-samples (see Figure 8). Right panels: Same as in left panels but for $M_{\rm b}$ instead of $M_{\rm s}$. Dotted lines: $f_{\rm b} = f_U/5$ and $f_U/30$, where $f_U = 0.167$ is the universal baryon fraction. The color figure can be viewed online.

The shaded area in Figure 5 is the same 1σ uncertainty shown in Figure 4 for the overall central sample. The uncertainties corresponding to the $M_{\rm s}$–

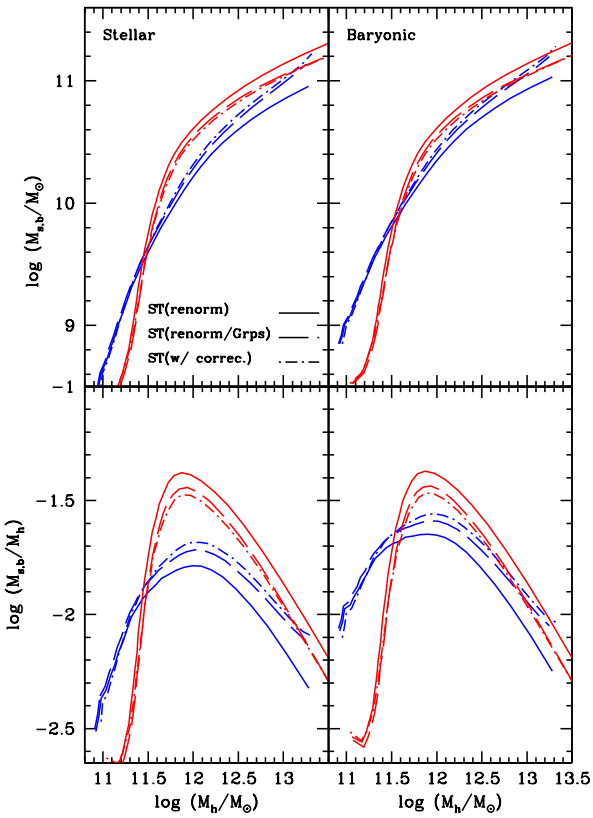

Fig. 6. Left panels: Mean $M_{\rm s}$–$M_{\rm h}$ (top) and $f_{\rm s}$–$M_{\rm h}$ (bottom) relations of central blue (blue lines) and red (red lines) galaxies when (i) no systematical corrections to the corresponding "blue" and "red" *HMF*s were applied apart from re-normalisations in the global abundance (see text, solid lines), (ii) the *HMF*s were corrected by group/cluster abundances and re-normalised (long-dashed lines), and (iii) the *HMF*s were corrected both by group/cluster abundances and late major mergers (as in Figure 4, dot-dashed lines). Right panels: Same as in left panels but for $M_{\rm b}$ instead of $M_{\rm s}$. The color figure can be viewed online.

$M_{\rm h}$ and $f_{\rm s}$–$M_{\rm h}$ relations for the blue and red galaxy sub-samples would be close to the one of the total sample if the corrections made to the *HMF* did not introduce an extra uncertainty. In fact this is not true, in particular for the group/cluster mass function introduced to correct the *HMF* associated to blue galaxies. Unfortunately, the work used for this correction does not report uncertainties. Hence, the uncertainties calculated here for the blue and red samples (shown explicitly in Figure 8 below) could be underestimated, specially at large masses.

In the mass range $11.5 \lesssim \log(M_{\rm h}/M_\odot) \lesssim 13.0$, the $M_{\rm s}$–$M_{\rm h}$ and $f_{\rm s}$–$M_{\rm h}$ relations for central blue (red) galaxies lie slightly below (above) the relations corresponding to the overall sample. For masses below these ranges, the trends invert. The $f_{\rm s}$–$M_{\rm h}$ curves for blue and red sub-samples peak at $\log(M_{\rm h}/M_\odot) = 11.98$ and 11.87, with values of $f_{\rm s} = 0.021^{+0.016}_{-0.009}$ and $f_{\rm s} = 0.034^{+0.026}_{-0.015}$, respectively. The corresponding stellar masses at these peaks are $\log(M_{\rm s}/M_\odot) = 10.30 \pm 0.25$ for blue galaxies and $\log(M_{\rm s}/M_\odot) = 10.40 \pm 0.25$ for red galaxies. These masses are around 0.23 and 0.30 times the characteristic stellar mass $M^\star \approx 10^{10.93}\ M_\odot$ of the overall YMB09 *GSMF*, respectively. The maximum difference between the blue and red mean $M_{\rm s}$–$M_{\rm h}$ relations is attained at $\log(M_{\rm h}/M_\odot) \approx 11.9$; at this mass, the $f_{\rm s}$ value of the former is 1.7 times smaller than the $f_{\rm s}$ of the latter. For larger masses this difference decreases.

At the low-mass end, roughly $f_{\rm s} \propto M_h$ ($\propto M_s^{0.5}$) and $f_{\rm s} \propto M_h^{3.0}$ ($\propto M_s^{0.8}$) for the blue and red samples, respectively, while at the high-mass end, $f_{\rm s} \propto M_h^{-0.4}$ ($\propto M_s^{-0.7}$) and $f_{\rm s} \propto M_h^{-0.6}$ ($\propto M_s^{-1.5}$), respectively.

It is important to note that the differences between blue and red $M_{\rm s}$–$M_{\rm h}$ relations at almost all masses are within the 1σ uncertainty of our inferences. We conclude that the $M_{\rm s}$–$M_{\rm h}$ ($f_{\rm s}$–$M_{\rm h}$) relation does not depend significantly on galaxy color (type). If anything, the mean $f_{\rm s}$–$M_{\rm h}$ relation of red galaxies is narrower and more peaked than the one of blue galaxies. In the mass range where the abundances of blue and red galaxies are closer ($10.0 < \log(M_{\rm s}/M_\odot) < 10.7$), the intrinsic scatter around the $M_{\rm s}$–$M_{\rm h}$ relation would slightly correlate with color in the sense that the redder (bluer) the galaxy, the larger (smaller) its $M_{\rm s}$ for a fixed $M_{\rm h}$, with a maximum average deviation from the mean due to color no larger than ∼0.1 dex. For masses smaller than $M_{\rm s} \approx 10^{9.7}\ M_\odot$, the correlation of the scatter with color would invert.

The (slight) differences between blue and red $M_{\rm s}$–$M_{\rm h}$ ($f_{\rm s}$–$M_{\rm h}$) relations can be understood basically by the differences in the respective cumulative *GSMF*s and, at a minor level, by the differences of the corresponding *HMF*s for each case. The sharp peak in the red $f_{\rm s}$–$M_{\rm h}$ relation is associated to the turn-over at $M_{\rm s} \sim 10^{10.5}\ M_\odot$ in the *GSMF* of red galaxies (see Figure 1).

In order to estimate the influence of the corrections introduced to the *HMF* for blue (red) galaxies, we have redone the analysis using the original distinct (S-T) *HMF* without any correction but re-normalised to obtain the same fraction of halos as the fraction implied by the *GSMF* of blue (red) galaxies with respect to the total *GSMF*. The results

TABLE 1

FIT PARAMETERS

Parameter	All	Blue	Red
$\log M_{0,h}$	11.97	11.99	11.87
$\log M_s^*$	10.40	10.30	10.40
β	0.34	0.37	0.18
α	1.45	0.90	1.50
γ	0.90	0.90	0.90
a $(M_s < M_s^*)$	0.000	0.125	0.000
a $(M_s > M_s^*)$	0.095	0.125	0.093

are shown in Figure 6, with solid curves of blue color (blue galaxies) and red color (red galaxies). For comparison, the corresponding relations plotted in Figure 5 are reproduced here (dot-dashed blue and red lines, respectively). One sees that the corrections to the *HMF* we have introduced for associating halos to the blue and red galaxy sub-samples act in the direction of reducing the differences among them in the $M_{\rm s}$–$M_{\rm h}$ ($f_{\rm s}$–$M_{\rm h}$) relations, specially for larger masses. The group/cluster mass function correction to the *HMF* hosting central blue galaxies is the dominant one. The dashed blue and red curves show such a case, where only this correction (and a small re-normalisation) is applied.

3.2.1. *Analytical fits to the stellar-halo mass relations*

From the comparison of the *GSMF* and *HMF* it is easy to deduce that high- and low-mass galaxies have significantly different $M_{\rm s}$–$M_{\rm h}$ scalings, a fact attributed to the different feedback/gas accretion mechanisms dominating in large and small systems (see e.g., Benson et al. 2003). The transition point between the low- and high-mass scalings defines a characteristic halo mass $M_{0,h}$ and an associated stellar mass M_s^*. Therefore, it was common to describe the $M_{\rm s}$–$M_{\rm h}$ relation as a double-power law with the turnover point at $M_{0,h}$. However, BCW10 have argued recently that a power-law at the high-mass side is conceptually a bad description for the $M_{\rm s}$–$M_{\rm h}$ relation and proposed a modification to it. Our results show indeed that a power-law is not sufficient to describe the high-mass side of the $M_{\rm s}$–$M_{\rm h}$ relations.

We have found that a good analytical description to the overall, blue, and red mean $M_{\rm s}$–$M_{\rm h}$ relations inferred here can be obtained for the inverse of the relations ($M_{\rm h}$ as a function of $M_{\rm s}$, as in BCW10), by proposing a power-law dependence for low masses and a sub-exponential law for high masses (see BCW10). The functional form that fits

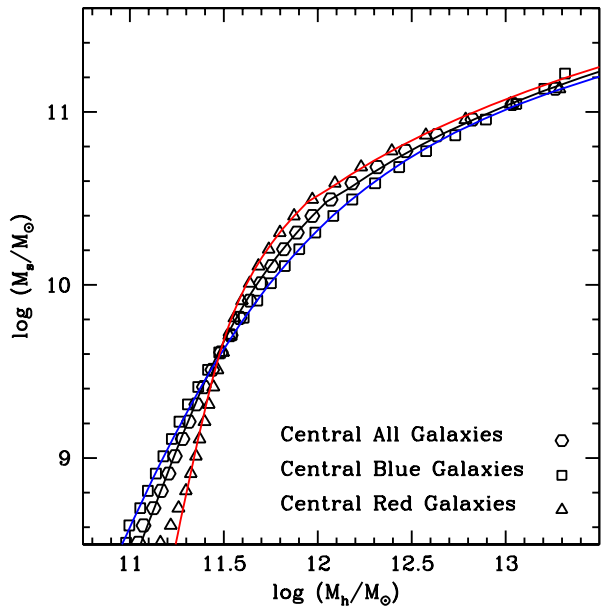

Fig. 7. Analytical fits given by equation (5) and Table 1 compared to the mean $M_{\rm s}$–$M_{\rm h}$ relation obtained here for all central galaxies (black solid line) and the central blue (blue solid line) and red (red solid line) galaxy sub-samples. The color figure can be viewed online.

well the three $M_{\rm h}$–$M_{\rm s}$ relations is:

$$M_h = \frac{M_{0,h}}{2^\gamma}\left[\left(\frac{M_s}{M_s^*}\right)^{\beta/\gamma} + \left(\frac{M_s}{M_s^*}\right)^{\alpha/\gamma}\right]^\gamma 10^{a(M_s/M_s^*-1)}, \tag{5}$$

where β regulates the behavior of the relation at masses $M_{\rm s} < M_s^*$, α together with the sub-exponential term ($a < 1$) regulate the behavior at masses $M_{\rm s} > M_s^*$, and γ regulates the transition of the relation around M_s^*. In Table 1 are given the values of all the parameters that best fit our results for the (central) overall, blue, and red $M_{\rm s}$-$M_{\rm h}$ relations. Note that a assumes two different values depending on whether the mass is smaller or larger than M_s^*.

Figure 7 shows the three mean $M_{\rm s}$–$M_{\rm h}$ relations obtained here and the functional form given in equation (5) with the corresponding parameters reported in Table 1. The functional form is an excellent fit to the overall and blue $M_{\rm s}$–$M_{\rm h}$ relations at all masses and to the red $M_{\rm s}$–$M_{\rm h}$ relation for masses larger than $M_{\rm h} \approx 10^{11.3}$ $M_\odot$.

3.3. *The baryonic-halo mass relations for central blue and red galaxies*

The right upper and lower panels of Figure 5 show the mean $M_{\rm b}$–$M_{\rm h}$ and $f_{\rm b}$–$M_{\rm h}$ relations, as in the left panels, for all central galaxies (solid line),

central blue (long-dashed blue line), and central red (short-dashed red line) galaxies. The blue and red *GBMF*s were calculated from the corresponding *GSMF*s and adding to $M_{\rm s}$ the respective gas mass, $M_{\rm g}$ (see § 2.1). The total *GBMF* is the sum of both of them. The error in $M_{\rm b}$ was calculated as the sum in quadrature of the errors in $M_{\rm s}$ and $M_{\rm g}$. This error, together with the intrinsic scatter in $M_{\rm s}$ (see § 2.2), both propagated to the $M_{\rm b}$–$M_{\rm h}$ relation, account for an uncertainty (standard deviation) of ∼0.23 dex in $\log M_{\rm b}$ at all masses (grey curves connected by vertical lines in Figure 5).

The baryonic mass fraction, $f_{\rm b}$, for blue galaxies is larger than the corresponding stellar one, $f_{\rm s}$, in particular at smaller halo masses. At $M_{\rm h} \approx 10^{11}\ M_\odot$, $f_{\rm b}$ is a factor 2.4 times higher than $f_{\rm s}$, while the peak of $f_{\rm b} = 0.028^{+0.018}_{-0.011}$ (at $M_{\rm h} = 10^{12.0}\ M_\odot$) is only 1.3 times larger than the peak of $f_{\rm s}$ (at $M_{\rm h} = 10^{12.0}\ M_\odot$). For larger masses, the difference between $f_{\rm b}$ and $f_{\rm s}$ decreases, while for smaller masses, the lower is $M_{\rm h}$, the larger is $f_{\rm b}$ compared to $f_{\rm s}$. For red galaxies, $f_{\rm s}$ and $f_{\rm b}$ are very similar, some differences being observed only at the lowest masses.

For masses larger (smaller) than $M_{\rm h} \approx 10^{11.6}\ M_\odot$, the differences between the $M_{\rm b}$–$M_{\rm h}$ ($f_{\rm b}$–$M_{\rm h}$) relation of blue and red galaxies become smaller (larger) than in the case of stellar masses (see § 3.2 and left panels of Figure 5). In general, the $f_{\rm b}$ bell-shaped curve for red galaxies is more peaked and narrower than the one for blue galaxies.

For blue galaxies, roughly $f_{\rm b} \propto {M_{\rm h}}^{0.7}$ (${M_{\rm b}}^{0.4}$) at the low-mass end, and $f_{\rm b} \propto {M_{\rm h}}^{-0.5}$ (${M_{\rm b}}^{-0.8}$) at the high-mass end. For red galaxies, roughly $f_{\rm b} \propto {M_{\rm h}}^{2.9}$ (${M_{\rm b}}^{0.8}$) at the low-mass end, and $f_{\rm b} \propto {M_{\rm h}}^{-0.6}$ (${M_{\rm b}}^{-1.5}$) at the high-mass end. For halos of masses $M_{\rm h} \approx 10^{11.0}\ M_\odot$ and $M_{\rm h} \approx 10^{13.2}\ M_\odot$, the baryon fraction for blue (red) galaxies decreases to values $f_{\rm b} \approx 0.004$ and 0.0085 ($f_{\rm b} \approx 0.0031$ and 0.0071), respectively. Therefore, for all masses, $f_{\rm b} \ll f_U$, where $f_U \equiv \Omega_b/\Omega_M$ is the universal baryon mass fraction; for the cosmology used here, $f_U = 0.167$.

4. DISCUSSION

4.1. *Comparison with other work*

As discussed in § 3.1 (see Figure 4), our inference of the local overall $M_{\rm s}$–$M_{\rm h}$ relation is in general in good agreement with several recent works that make use of the AMT (e.g., Baldry et al. 2008; Guo et al. 2010; Moster et al. 2010; BCW10). The aim in this paper is to estimate the $M_{\rm s}$–$M_{\rm h}$ and $M_{\rm b}$–$M_{\rm h}$ relations for blue (late-type) and red (early-type) central galaxies separately. We found that the differences between the means of the obtained relations for blue and red galaxies are within the 1σ uncertainty (see Figure 5). In more detail, the mean stellar and baryonic mass fractions ($f_{\rm s}$ and $f_{\rm b}$) as a function of $M_{\rm h}$ for red galaxies are narrower and more peaked than those for blue galaxies in such a way that for a given mass range (11.5–13.0 and 11.5–12.5 in $\log(M_{\rm h}/M_\odot)$ for the stellar and baryonic cases, respectively) the former are higher than the latter, and outside these ranges the trend is inverted, especially at the low-mass side.

There are only a few previous attempts to infer the halo masses of central galaxies as a function of mass (luminosity) *and* galaxy type (Mandelbaum et al. 2006; More et al. 2011). These works use direct techniques (see Introduction), which are, however, limited by low signal-to-noise ratios, especially for less massive systems, so that the halo mass determinations are reliable only for galaxies with $M_{\rm s} \gtrsim 10^{10}\ M_\odot$. These techniques are galaxy-galaxy weak lensing and kinematics of satellite galaxies around central galaxies. In order to overcome the issue of low signal-to-noise ratios in the current measures, large samples of galaxies are stacked together in bins of similar properties (e.g., luminosity, $M_{\rm s}$, galaxy type) obtaining in this way higher (statistically averaged) signals of the corresponding measures (the tangential shear in the case of lensing and the weighted satellite velocity dispersion in the case of satellite kinematics). Besides, estimates of $M_{\rm h}$ with these sophisticated techniques are subject to several assumptions, among them, those related to the internal halo mass distribution. It is usual to assume the Navarro, Frenk, & White (1997) density profile with the mean concentration for a given mass as measured in N-body cosmological simulations.

It is not easy to achieve a fair comparison of the results obtained with the AM formalism and those with the direct methods. We have inferred the mean (and scatter) of $\log M_{\rm s}$ as a function of $M_{\rm h}$, while the weak lensing and satellite kinematics techniques constrain $M_{\rm h}$ as a function of $M_{\rm s}$ (see e.g., More et al. 2011); besides, the former calculates the mean of $M_{\rm h}$ (and its scatter) in a linear scale instead of a logarithmic one. These different ways of defining the relationship between stellar and halo masses, depending on the shapes and scatters of the corresponding relations, diverge less or more among them. In BCW10 (see their Figure 10), it was shown that at low masses ($\log(M_{\rm h}/M_\odot \lesssim 12$, $\log(M_{\rm s}/M_\odot) \lesssim 10.5$), averaging $\log M_{\rm s}$ as a function of $M_{\rm h}$ or $\log M_{\rm h}$ as a function of $M_{\rm s}$ give equivalent results for the AMT, but at high masses, where the $M_{\rm s}$–$M_{\rm h}$ relation becomes much

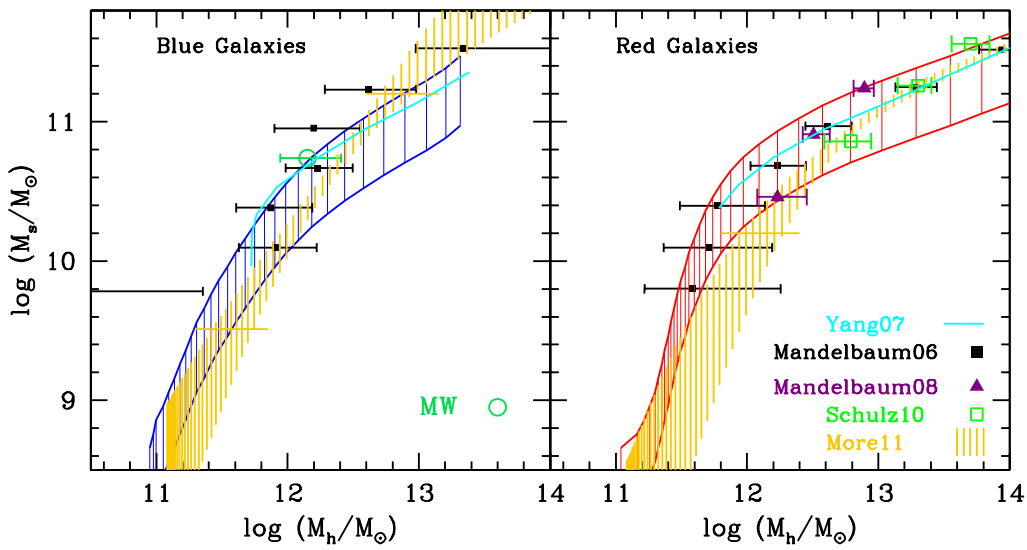

Fig. 8. Comparison with other observational inferences. Left panel: $M_{\rm s} - M_{\rm h}$ relation for blue (late-type) galaxies. The blue curves connected by vertical lines encompass the $\pm 1\sigma$ interval inferred here. We also reproduce the inferences using galaxy-galaxy weak lensing by Mandelbaum et al. (2006, black squares), galaxy groups (Yang et al. 2007, cyan solid line), and satellite kinematics (More et al. 2011, orange vertical lines). Estimates for the Milky Way are plotted (open circle with error bar). Right panel: $M_{\rm s} - M_{\rm h}$ relation for red (early-type) galaxies. The red curves connected by vertical lines encompass the $\pm 1\sigma$ interval inferred here. Other determinations as in the left panel but for early-type galaxies are plotted. More recent inferences with the weak lensing technique by Mandelbaum et al. (2008, filled violet triangles) and by Schulz et al. (2010, open green squares) are also plotted. The color figure can be viewed online.

shallower, this relation becomes steeper (higher stellar mass at a fixed halo mass) for the latter case with respect to the former one.

In Figure 8, the results from Mandelbaum et al. (2006) are reproduced, left panel for central late-type galaxies and right panel for central early-type galaxies (solid squares with error bars). The error bars are 95 percent confidence intervals (statistical). Mandelbaum et al. (2006) have used the (de Vaucouleours/exponential) bulge-to-total ratio, frac_deV, given in the SDSS PHOTO pipeline as a criterion for late- (frac_deV<0.5) and early-type (frac_dV≥ 0.5) separation. This criterion of course is not the same as the color used in YMB09, but there is a correlation between both of them in such a way that a comparison between our results and those of Mandelbaum et al. (2006) is qualitatively possible. Note that we have decreased the halo masses of Mandelbaum et al. (2006) by $\approx$15% on going from their to our definition of halo virial mass. In more recent works, Mandelbaum, Seljak, & Hirata (2008) and Schulz, Mandelbaum, & Padmanabhan (2010) reported a new weak lensing analysis for the massive central early-type galaxies using the seventh SDSS data release (DR7) and a more sophisticated criteria for selecting the early-type lens population. Their results are plotted in the right panel of Figure 8 with solid triangles and open squares, respectively.

In the case of the satellite kinematics determinations of $M_{\rm h}$ by More et al. (2011), the same SDSS sample and similar recipes as in YMB09 for calculating $M_{\rm s}$, classifying galaxies into blue and red, and finding central and satellites galaxies were used. More et al. (2011) applied their analysis to constrain the mean $\log M_{\rm h}$ as a function of $M_{\rm s}$, but also presented the constraints of their model for the mean of $\log M_{\rm s}$ as a function of $M_{\rm h}$. Their results for the latter case, kindly made available to us in electronic form by Dr. S. More, are reproduced in Figure 8 as the shaded (orange) regions which represent the 68% confidence intervals. On going from their to our definitions of halo mass and IMF, their $M_{\rm h}$ and $M_{\rm s}$ were decreased by $\approx$15% and $\approx$25%, respectively. The dotted horizontal lines in each panel show the approximate range in $M_{\rm s}$ where the determinations are reliable according to More et al. (2011, see their Figure 11).

In More et al. (2011) are also reported results for the average $M_{\rm h}$ as a function of $M_{\rm s}$ split into central blue and red galaxies corresponding to the galaxy group analysis by Yang et al. (2007). The solid (cyan) curves in Figure 8 reproduce these results.

Finally, the standard $\pm 1\sigma$ deviation intervals that we have obtained from the AMT are reproduced in Figure 8 for central blue and red galaxies (solid blue and red curves connected by vertical lines, respectively). Note that in the determinations with direct methods, the systematic uncertainty in $M_{\rm s}$, which is the main source of error in the AMT, was not taken into account.

Our inference for early-type (red) galaxies is consistent (within the uncertainties, errors, and different ways of presenting the constraints) with the weak lensing results of Mandelbaum et al. (2006) and Schulz et al. (2010), and with the galaxy group analysis of Yang et al. (2007) as reported in More et al. (2011), for all the masses reported in each one of these papers. With respect to the satellite kinematics analysis by More et al. (2011), their mean halo masses for $M_{\rm s} \sim 5 \times 10^9 - 10^{11}\ M_\odot$ (for smaller masses their uncertainties are very large) are larger than ours (and those of Mandelbaum et al. 2006) by factors around 2. For larger masses, all determinations agree roughly with our results. In fact, there is some indication that satellite kinematics yields halo masses around low mass central galaxies that are systematically larger than most other methods, specially for red central galaxies (Skibba et al. 2011; but see More et al. 2011 for a discussion).

For late-type (blue) galaxies, our results are in reasonable agreement with those of Mandelbaum et al. (2006) for masses $M_{\rm s} \lesssim 10^{10.8}\ M_\odot$. At higher masses, their results imply halo masses for a given $M_{\rm s}$ smaller than ours, with the difference increasing with increasing stellar mass. The discrepancy would be weaker taking into account that the mean $M_{\rm s}$–$M_{\rm h}$ relation in our case becomes steeper when calculating $M_{\rm h}$ as a function of $M_{\rm s}$. On the other hand, it must be said that the number statistics becomes poor for massive late-type galaxies, resulting in a stacked weak lensing analysis with large error bars. For example, in the two most massive bins in the Mandelbaum et al. (2006) sample (the two uppermost points in Figure 8), only 5 and 11 percent of the galaxies are classified as late types. Future weak lensing work should confirm whether high-mass late-type galaxies do or do not have such relatively small halos as found in Mandelbaum et al. (2006). Regarding the comparison with the satellite kinematics inferences of More et al. (2011), the agreement is reasonable at least up to $M_{\rm s} \approx 10^{11}\ M_\odot$, though the relation inferred by these authors is less curved than ours. For larger masses, these authors caution that their results become very uncertain, as in the weak lensing case, because of poor statistics of massive blue galaxies. The galaxy groups inference (Yang et al. 2007), in the mass range allowed by this technique, gives halo masses slightly smaller than the means of our inference for a given $M_{\rm s}$.

In general, most techniques for inferring the relationship between stellar and halo masses of galaxies agree among them within factors up to 2–3 in $M_{\rm h}$ (BCW10; More et al. 2011; Dutton et al. 2010). This seems to be also the case for samples partitioned into late- and early-type galaxies, as shown here. However, beyond the detailed comparison between our results and those obtained with direct techniques, it seems that there is a systematic qualitative difference: in our case, at a given halo mass (for $10^{11.5}\ M_\odot \lesssim M_{\rm h} \lesssim 10^{13.0}\ M_\odot$), blue centrals, on average, have lower stellar masses than red centrals, while in the case of determinations with direct techniques, the opposite occurs, at least for masses larger than $M_{\rm h} \sim 10^{12}\ M_\odot$ (Mandelbaum et al. 2006; More et al. 2011; see also Figures 5 and 8).

A partial source of bias contributing to this difference could be that in the weak lensing and satellite kinematics techniques the same concentration for halos hosting late- and early-type galaxies is assumed. If halos of late- (early-)type galaxies are less (more) concentrated than the corresponding average, then for the same measure (shear or satellite velocity dispersion), the halo masses are expected to be higher (lower) than the obtained ones. Therefore, the differences found (Mandelbaum et al. 2006 and More et al. 2011) in the mass halos of late- and early-type galaxies of a given $M_{\rm s}$ would decrease or even invert their sense.

While it is difficult to make any robust statement about possible systematics in each technique regarding late and early types, we ask ourselves what should be modified in our assumptions in order to invert the behavior of the $M_{\rm s}$–$M_{\rm h}$ relations with galaxy type (color) obtained here. We have shown in Figure 6 that our corrections to the *HMF* had the effect of bringing the $M_{\rm s}$–$M_{\rm h}$ relations of blue and red galaxies into closer agreement at large masses. One possibility in order not only to bring the relations into closer agreement but to invert them is to make even steeper (shallower) the *HMF* corresponding to blue (red) galaxies, mainly at the high-mass end (see Figure 3, lower panel). This would imply, for instance, a larger correction to the *HMF* due to groups than that made by us. The group/cluster mass function used by us (Heinämäki et al. 2003) is one of the most general ones found in the literature; it includes all kinds of groups/clusters with 3 or more members and $\delta N/N \geq 80$. The authors note that their sam-

ple is complete down to a dynamical mass roughly equivalent to $M_{\rm h} = 5\times10^{13}\ M_\odot$. It could be that the abundance of groups of lower masses is larger than that given in Heinämäki et al. (2003), though it is difficult to accept that blue galaxies are completely absent in the centers of small and loose groups of a few (> 2) members.

Last but not least, in Figure 8 we include observational estimates for our Galaxy (open circle). The uncertainties in the estimates of $M_{\rm h}$ for the Milky Way are still large but better than most of the determinations for other individual galaxies. For recent reviews on different results see Guo et al. (2010) and Dutton et al. (2010). In Figure 8 we plot a recent estimate of $M_{\rm h}$ based on observations of 16 high velocity stars (Smith et al. 2007). These authors find $M_{\rm h} = 1.42^{+1.14}_{-0.54} \times 10^{12}\ M_\odot$, which is in good agreement with several previous works (e.g., Wilkinson & Evans 1999; Sakamoto, Chiba, & Beers 2003; Li & White 2008), though results from Xue et al. (2008) suggest lower values (but see a recent revision by Przybilla et al. 2010). For its $M_{\rm h}$, the $M_{\rm s}$ of the Milky Way seems to be at the high extremum of blue galaxies, close to values typical of red galaxies. It should be said that it is an open question whether the Milky Way is an average galaxy or not. In the stellar Tully-Fisher and radius–$M_{\rm s}$ relations (e.g., Avila-Reese et al. 2008), the Milky Way is shifted from the average to the high-velocity and low-radius sides, respectively.

4.2. *Interpretations and consistency of the results*

Although our main result is that the differences between the $M_{\rm s}$–$M_{\rm h}$ and $M_{\rm b}$–$M_{\rm h}$ relations for central blue and red galaxies are marginal (within the uncertainties of our determinations), we will explore whether such differences are expected or not. For this it is important to approach the problem from an evolutionary point of view.

In Firmani & Avila-Reese (2010, hereafter FA10), the determinations of the $M_{\rm s}$–$M_{\rm h}$ relation for all galaxies at different redshifts, out to $z = 4$ (BCW10), and the average ΛCDM individual halo mass aggregation histories (MAHs) were used to determine the individual *average* $M_{\rm s}$ growth of galaxies in general as a function of mass (called in that paper as Galaxian Hybrid Evolutionary Tracks, GHETs). It was found that the more massive the galaxies, the earlier transit from their active (star-forming, blue) regime of $M_{\rm s}$ growth to a passive (red) phase (population 'downsizing'), while their corresponding halos continue growing, more efficiently at later epochs the more massive they are ('upsizing'). The inferred trend for the transition stellar mass is $\log(M_{\rm tran}/M_\odot) \approx 10.30 + 0.55z$. Therefore, galaxies of mass $M_{\rm s} \approx 10^{10.3}\ M_\odot$ are on average becoming passive (red) today. For $M_{\rm s} \gtrsim M_{\rm tran}$, the larger the mass, the redder will be the galaxy on average. The opposite applies for $M_{\rm s} \lesssim M_{\rm tran}$, the smaller the mass, the bluer will be the galaxy. Interestingly enough, $M_{\rm s} \approx 10^{10.3}\ M_\odot$ is roughly the mass where the overall YMB09 blue and red *GSMF*s cross: for masses larger than this crossing mass, $M_{\rm cross}$, redder galaxies become more and more abundant than bluer ones and the inverse happens at smaller masses (see Figure 1).

Galaxies that are transiting from active to passive at $z \sim 0$ (those around $M_{\rm tran} \approx 10^{10.3}\ M_\odot$) have probably been subject recently to a process that induced an *efficient* transformation of the available gas into stars in such a way that their stellar populations started to redden passively. Hence, for a given $M_{\rm h}$, they are expected to have a higher $M_{\rm s}$ (or $f_{\rm s}$) than those galaxies of similar mass that did not suffer (yet?) the above process (bluer ones). The relatively small difference in $f_{\rm s}$ for blue and red galaxies we have found here (whose maximum is attained around $M_{\rm tran} \sim M_{\rm cross}$, Figure 5) would imply that the scatter around $M_{\rm tran}$ is moderate.

Galaxies more massive than $M_{\rm tran}$ (or $M_{\rm cross}$), according to the evolutionary analysis by FA10, underwent the process of efficient gas consumption into stars (and the further cessation of $M_{\rm s}$ growth) earlier on average than more massive galaxies, while their halos continue growing. Therefore, one expects that the more massive the galaxy, the redder and the lower its stellar (and baryonic) mass fraction $f_{\rm s}$ will be on average. The few blue massive galaxies may have slightly smaller stellar masses (lower $f_{\rm s}$) than the corresponding red ones because they should have transformed gas into stars less efficiently in the past. Therefore, by including gas, i.e. when passing to $f_{\rm b}$ the difference between blue and red massive galaxies at large masses should become negligible. This is indeed what happens (see Figure 5).

Galaxies less massive than $M_{\rm tran}$ (or $M_{\rm cross}$) at $z \sim 0$, according to FA10, are in general the more actively assembling their stellar masses the smaller they are ('downsizing' in specific SFR), while their dark halo mass growth is already very slow. This implies the existence in the galaxies of relatively larger reservoirs of cold gas the smaller they are (gas not related to the halo-driven infall) because the SF has been delayed in the disk and/or cold gas is being lately (re)accreted into the galaxy. However, if for some reason the gas reservoir in these galaxies is lost,

then the galaxy will redden and its baryonic and stellar mass fractions will be smaller than those of the galaxies that were able to keep their gas reservoir (the majority), in agreement with our inferences here (Figure 5).

5. SUMMARY AND CONCLUSIONS

By means of the AM technique and using the central blue and red *GSMF*s, constructed from the local SDSS sample by YMB09, we have inferred the local $M_{\rm s}$–$M_{\rm h}$ (or $f_{\rm s}$–$M_{\rm h}$) relations for *central* galaxies and for the sub-samples of blue and red galaxies. To derive the relations for the sample of blue galaxies, (i) the mass function of observed groups/clusters of galaxies is subtracted from the distinct (S-T) *HMF* (blue, late-type galaxies are not observed in the centers of groups and clusters), and (ii) halos that suffered a major merger since $z = 0.8$ are excluded. For red galaxies, the *HMF* is assumed to be the complement of the "blue" one, with respect to the overall (distinct) *HMF*. We consider as sources of uncertainty in our analysis only the systematical error in assigning stellar masses to galaxies (0.25 dex) and the intrinsic statistical scatter in stellar mass at a fixed halo mass (0.16 dex). By using the observational $M_{\rm g}$–$M_{\rm s}$ relation and its scatter, we transited from $M_{\rm s}$ to $M_{\rm b}$ ($= M_{\rm s} + M_{\rm g}$) in the *GSMF* and estimated the overall blue and red *GBMF*s, which were used to obtain the corresponding baryonic $M_{\rm b}$–$M_{\rm h}$ (or $f_{\rm b}$–$M_{\rm h}$) relations using the AM technique.

The $M_{\rm s}$–$M_{\rm h}$ relation obtained here agrees rather well with previous studies (see Figure 4). The small differences found in this work can be explained mainly in terms of the different *GSMF*s used in each study, and to a lesser extent by variations in the methodology. The 1σ uncertainty in the obtained $M_{\rm s}$–$M_{\rm h}$ relation is ≈ 0.25 dex in log $M_{\rm s}$. The $M_{\rm s}$–$M_{\rm h}$ relation of central galaxies lies below (lower $M_{\rm s}$ for a given $M_{\rm h}$) the overall one by a factor ~ 1.6 at $M_{\rm h} = 10^{11}\ M_\odot$ and by less than 5% for $M_{\rm h} > 10^{13}\ M_\odot$.

Our main result refers to the calculation of the *central* $M_{\rm s}$–$M_{\rm h}$ and $M_{\rm b}$–$M_{\rm h}$ relations for the two broad populations into which the galaxy sample can be divided: blue (late-type) and red (early-type) galaxies. We highlight the following results from our analysis:

• At $M_{\rm h} \gtrsim 10^{11.3}\ M_\odot$ the mean stellar mass fraction $f_{\rm s}$ of blue galaxies is smaller than that of red galaxies, the maximum difference being attained at $M_{\rm h} \approx 10^{11.7}\ M_\odot$; at this mass, the $f_{\rm s}$ of red galaxies is 1.7 times that of blue galaxies (see Figure 5). At larger masses, the difference decreases until it disappears. At $M_{\rm h} \lesssim 10^{11.3}\ M_\odot$ the trend is reversed as blue galaxies tend to have higher values of $f_{\rm s}$ than red ones. In the case of the baryonic mass fractions, $f_{\rm b}$, the same trends of the stellar relations remain but at $M_{\rm h} \gtrsim 10^{11.3}\ M_\odot$ the difference in $f_{\rm b}$ between blue and red galaxies is small, while for smaller masses, the difference increases.

• The $M_{\rm s}$–$M_{\rm h}$ and $M_{\rm b}$–$M_{\rm h}$ (or $f_{\rm s}$–$M_{\rm h}$ and $f_{\rm b}$–$M_{\rm h}$) relations of central blue and red sub-samples do not differ significantly from the respective relations of the overall central sample, and these differences are within the 1σ uncertainty of the inferences (Figure 5). For blue (red) galaxies, the maximum value of $f_{\rm s}$ is $0.021^{+0.016}_{-0.009}$ ($0.034^{+0.026}_{-0.015}$) and is attained for halos of mass $M_{\rm h} = 10^{11.98}\ M_\odot$ ($M_{\rm h} = 10^{11.87}\ M_\odot$); the corresponding stellar mass is $M_{\rm s} = 10^{10.30\pm0.25}\ M_\odot$ ($M_{\rm s} = 10^{10.40\pm0.25}\ M_\odot$), which is around 0.23 (0.30) times $M^\star$, the Schechter fit characteristic mass of the overall *GSMF* of YMB09. For smaller and larger masses, $f_{\rm s}$ significantly decreases.

• We have compared our results with the few observational inferences of the $M_{\rm s}$–$M_{\rm h}$ relation for blue (late-type) and red (early-type) galaxies that exist in the literature. Although these studies estimate halo masses using direct techniques (weak lensing and galaxy satellite kinematics), they are still limited by the stacking approach they need to apply (due to the low signal-to-noise ratio of individual galaxies) and by the large uncertainties owing to the unknown systematics. The overall differences among the different studies (including ours) amount to factors of up to 2–4 at a given mass (these factors being much smaller at other masses) for most methods (Figure 8). For blue galaxies, all methods agree reasonably well for low masses ($M_{\rm h} \lesssim 3 \times 10^{12}\ M_\odot$), but for higher masses, our inference implies larger halos for a given $M_{\rm s}$ than the results from direct techniques. For red galaxies, at high masses ($M_{\rm h} \gtrsim 3 \times 10^{12}\ M_\odot$), all methods agree reasonably well, but at lower masses, the satellite kinematics technique produces halo masses, for a given $M_{\rm s}$, larger than those obtained by other methods.

• According to our results, for $M_{\rm h} \lesssim 10^{11.3}\ M_\odot$, the intrinsic scatter of the $M_{\rm s}$–$M_{\rm h}$ relation should slightly anti-correlate with galaxy color (for a fixed $M_{\rm h}$, the bluer the galaxy, the higher its $M_{\rm s}$), while for more massive systems, the correlation should be direct (for a fixed $M_{\rm h}$, the redder the galaxy, the higher its $M_{\rm s}$). For massive blue galaxies to have had higher higher $f_{\rm s}$ values than red ones as the results from direct techniques suggest, the *HMF* halos hosting blue (red) galaxies should have been even steeper

(shallower) than what we have proposed here; this seems too extreme.

• The maximum baryon mass fraction of blue and red galaxies are $f_{\rm b} = 0.028^{+0.018}_{-0.011}$ and $f_{\rm b} = 0.034^{+0.025}_{-0.014}$, respectively, much smaller than $f_U = 0.167$ in both cases, and these maxima are attained at $M_{\rm h} \approx 10^{12}\ M_\odot$. At large masses $f_{\rm b}$ decreases approximately as $f_{\rm b} \propto {M_{\rm h}}^{-0.5}({M_{\rm b}}^{-0.8})$ for blue galaxies and as $f_{\rm b} \propto {M_{\rm h}}^{-0.6}({M_{\rm b}}^{-1.5})$ for red galaxies, in such a way that from $M_{\rm h} \approx 5 \times 10^{12}\ M_\odot$ on, blue galaxies have on average slightly larger values of $f_{\rm b}$ than red ones. At low masses, the $f_{\rm b}$ of red galaxies strongly decreases as the mass decreases $f_{\rm b} \propto {M_{\rm h}}^{2.9}({M_{\rm b}}^{0.8})$, while for blue galaxies, due to the increasing gas fractions the smaller the mass, $f_{\rm b}$ decreases more slowly than $f_{\rm s}$, as $f_{\rm b} \propto {M_{\rm h}}^{0.7}$ $(\propto {M_{\rm b}}^{0.4})$.

The AM technique has been revealed as a relatively simple but powerful method for connecting empirically galaxies to dark halos. Here we extended this technique towards inferences for the blue and red galaxy sub-populations separately. By introducing a minimum of assumptions –otherwise the method becomes close to a semi-analytical model– we have found that the stellar and baryon mass-halo mass relations of blue and red galaxies do not differ significantly among them and from the overall ones. The maximum differences occur around the peak of these relations, $M_{\rm h} \approx 10^{12}\ M_\odot$, and are consistent qualitatively with the inference that the galaxies in these halos are transiting from an active to a quiescent regime of $M_{\rm s}$ growth (FA10). Those that transited recently did so because they had an efficient process of gas consumption into stars and further cessation of $M_{\rm s}$ growth; therefore, they should be redder and have higher $f_{\rm s}$ values than those that have not transited. For larger and smaller masses than $M_{\rm h} \approx 10^{12}\ M_\odot$, the differences decrease and even invert, something that is also consistent with the inferences by FA10, based on the semi-empirical determinations of the evolution of the overall $M_{\rm s}$–$M_{\rm h}$ relation.

We thank the referee for his/her useful comments and suggestions. We are grateful to Dr. S. More for sending us in electronic form the data plotted in Figure 8. A.R-P. acknowledges a graduate student fellowship provided by Conacyt. We thank PAPIIT-Universidad Nacional Autónoma de México grant IN114509 and Conacyt grant 60354 for partial funding, as well as a bilateral DFG-Conacyt grant through which we got access to results from N-body numerical simulations performed by Dr. S. Gottloeber.

REFERENCES

Avila-Reese, V. 2007, in Ap&SS Proc., Stellar and Galactic Connections Between Particle Physics and Astrophysics, ed. A. Carramiñana et al. (Berlin: Springer), 115 (arXiv:astro-ph/0605212v1)
Avila-Reese, V., Zavala, J., Firmani, C., & Hernández-Toledo, H. M. 2008, AJ, 136, 1340
Baldry, I. K., Balogh, M. L., Bower, R. G., Glazebrook, K., Nichol, R. C., Bamford, S. P., & Budavari, T. 2006, MNRAS, 373, 469
Baldry, I. K., Glazebrook, K., & Driver, S. P. 2008, MNRAS, 388, 945
Baugh, C. M. 2006, Rep. Prog. Phys., 69, 3101
Behroozi, P. S., Conroy, C., & Wechsler, R. H. 2010, ApJ, 717, 379 (BCW10)
Bell, E. F., McIntosh, D. H., Katz, N., & Weinberg, M. D. 2003, ApJS, 149, 289
Benson, A. J. 2010, Phys. Rep., 495, 33
Benson, A. J., Bower, R. G., Frenk, C. S., Lacey, C. G., Baugh, C. M., & Cole, S. 2003, ApJ, 599, 38
Berlind, A. A., & Weinberg, D. H. 2002, ApJ, 575, 587
Bernardi, M., Shankar, F., Hyde, J. B., Mei, S., Marulli, F., & Sheth, R. K. 2010, MNRAS, 404, 2087
Blanton, M. R., & Moustakas, J. 2009, ARA&A, 47, 159
Boylan-Kolchin, M., Ma, C.-P., & Quataert, E. 2008, MNRAS, 383, 93
Chabrier, G. 2003, PASP, 115, 763
Cole, S., et al. 2001, MNRAS, 326, 255
Conroy, C., Gunn, J. E., & White, M. 2009, ApJ, 699, 486
Conroy, C., & Wechsler, R. H. 2009, ApJ, 696, 620
Conroy, C., Wechsler, R. H., & Kravtsov, A. V. 2006, ApJ, 647, 201
de Lapparent, V., & Slezak, E. 2007, A&A, 472, 29
Dutton, A. A., Conroy, C., van den Bosch, F. C., Prada, F., & More, S. 2010, MNRAS, 407, 2
Dutton, A. A., & van den Bosch, F. C. 2009, MNRAS, 396, 14
Dutton, A. A., van den Bosch, F. C., Dekel, A., & Courteau, S. 2007, ApJ, 654, 27
Firmani, C., & Avila-Reese, V. 2000, MNRAS, 315, 457
_____. 2010, ApJ, 723, 755 (FA10)
Gallazzi, A., & Bell, E. F. 2009, ApJS, 185, 253
Giocoli, C., Tormen, G., Sheth, R. K., & van den Bosch, F. C. 2010, MNRAS, 404, 502
Gnedin, O. Y., Weinberg, D. H., Pizagno, J., Prada, F., & Rix, H.-W. 2007, ApJ, 671, 1115
Governato, F., Mayer, L., & Brook, C. 2008, in ASP Conf. Ser. 396, Formation and Evolution of Galaxy Disks, ed. J. G. Funes, S. J., & E. M. Corsini (San Francisco: ASP), 453
Guo, Q., White, S., Li, C., & Boylan-Kolchin, M. 2010, MNRAS, 367
Heinämäki, P., Einasto, J., Einasto, M., Saar, E., Tucker, D. L., & Müller, V. 2003, A&A, 397, 63

Komatsu, E., et al. 2009, ApJS, 180, 330
Kravtsov, A. V., Berlind, A. A., Wechsler, R. H., Klypin, A. A., Gottlöber, S., Allgood, B., & Primack, J. R. 2004, ApJ, 609, 35
Li, C., Kauffmann, G., Jing, Y. P., White, S. D. M., Börner, G., & Cheng, F. Z. 2006, MNRAS, 368, 21
Li, C., & White, S. D. M. 2009, MNRAS, 398, 2177
Li, Y.-S., & White, S. D. M. 2008, MNRAS, 384, 1459
Mandelbaum, R., Seljak, U., & Hirata, C. M. 2008, JCAP, 8, 6
Mandelbaum, R., Seljak, U., Kauffmann, G., Hirata, C. M., & Brinkmann, J. 2006, MNRAS, 368, 715
Marinoni, C., & Hudson, M. J. 2002, ApJ, 569, 101
Martínez, H. J., Zandivarez, A., Merchán, M. E., & Domínguez, M. J. L. 2002, MNRAS, 337, 1441
McGaugh, S. S. 2005, ApJ, 632, 859
Mo, H.J., Mao, S., & White, S.D.M. 1998, MNRAS, 295,319
More, S., van den Bosch, F. C., Cacciato, M., Mo, H. J., Yang, X., & Li, R. 2009, MNRAS, 392, 801
More, S., van den Bosch, F. C., Cacciato, M., Skibba, R., Mo, H. J., & Yang, X. 2011, MNRAS, 410, 210
Moster, B. P., Somerville, R. S., Maulbetsch, C., van den Bosch, F. C., Macciò, A. V., Naab, T., & Oser, L. 2010, ApJ, 710, 903
Navarro, J. F., Frenk, C. S., & White, S. D. M. 1997, ApJ, 490, 493
Norberg, P., et al. 2001, MNRAS, 328, 64
Padilla, N., Lambas, D. G., & González, R. 2010, MNRAS, 409, 936
Peacock, J. A., & Smith, R. E. 2000, MNRAS, 318, 1144
Press, W. H., & Schechter, P. 1974, ApJ, 187, 425
Przybilla, N., Tillich, A., Heber, U., & Scholz, R.-D. 2010, ApJ, 718, 37
Robertson, B., Yoshida, N., Springel, V., & Hernquist, L. 2004, ApJ, 606, 32
Sakamoto, T., Chiba, M., & Beers, T. C. 2003, A&A, 397, 899
Schulz, A. E., Mandelbaum, R., & Padmanabhan, N. 2010, MNRAS, 408, 1463
Shankar, F., Lapi, A., Salucci, P., De Zotti, G., & Danese, L. 2006, ApJ, 643, 14
Shao, Z., Xiao, Q., Shen, S., Mo, H. J., Xia, X., & Deng, Z. 2007, ApJ, 659, 1159
Sheth, R. K., & Tormen, G. 1999, MNRAS, 308, 119 (S-T)
Skibba, R. A., van den Bosch, F. C., Yang, X., More, S., Mo, H., & Fontanot, F. 2011, MNRAS, 410, 417
Smith, M. C., et al. 2007, MNRAS, 379, 755
Stewart, K. R., Bullock, J. S., Barton, E. J., & Wechsler, R. H. 2009, ApJ, 702, 1005
Stringer, M. J., & Benson, A. J. 2007, MNRAS, 382, 641
Tinker, J., et al. 2008, ApJ, 688, 709
Tucker, D. L., et al. 2000, ApJS, 130, 237
Vale, A., & Ostriker, J. P. 2004, MNRAS, 353, 189
van den Bosch, F. C. 2000, ApJ, 530, 177
Wang, L., & Jing, Y. P. 2010, MNRAS, 402, 1796
Wang, Y., et al. 2009, ApJ, 697, 247
Wei, L. H., Kannappan, S. J., Vogel, S. N., & Baker, A. J. 2010, ApJ, 708, 841
Weinmann, S. M., van den Bosch, F. C., Yang, X., & Mo, H. J. 2006, MNRAS, 366, 2
Wilkinson, M. I., & Evans, N. W. 1999, MNRAS, 310, 645
White, S. D. M., & Frenk, C. S. 1991, ApJ, 379, 52
White, S. D. M., & Rees, M. J. 1978, MNRAS, 183, 341
Xue, X. X., et al. 2008, ApJ, 684, 1143
Yang, X., Mo, H. J., Jing, Y. P., van den Bosch, F. C., & Chu, Y. 2004, MNRAS, 350, 1153
Yang, X., Mo, H. J., & van den Bosch, F. C. 2003, MNRAS, 339, 1057
_____. 2008, ApJ, 676, 248
_____. 2009, ApJ, 695, 900 (YMB09)
Yang, X., Mo, H. J., van den Bosch, F. C., Pasquali, A., Li, C., & Barden, M. 2007, ApJ, 671, 153
Zehavi, I., et al. 2005, ApJ, 630, 1

A. Rodríguez-Puebla & V. Avila-Reese: Instituto de Astronomía, Universidad Nacional Autónoma de México, Apdo. Postal 70-264, 04510, México, D.F., Mexico (apuebla@astroscu.unam.mx).
C. Firmani: Osservatorio Astronomico di Brera, via E.Bianchi 46, I-23807 Merate, Italy.
P. Colín: Centro de Radioastronomía y Astrofísica, Universidad Nacional Autónoma de México, Apdo. Postal 72-3 (Xangari), Morelia, Michoacán 58089, Mexico.

Revista Mexicana de Astronomía y Astrofísica, **47**, 255–259 (2011)

SPECTRAL MORPHOLOGY AND ROTATION IN THE OPEN CLUSTER NGC 6025

Mónica Grosso and Hugo Levato

Instituto de Ciencias Astronómicas, de la Tierra y del Espacio (ICATE)
Consejo Nacional de Investigaciones Científicas y Técnicas, CONICET
Universidad Nacional de San Juan, Argentina

Received 2011 January 19; accepted 2011 April 19

RESUMEN

Hemos clasificado espectralmente a los probables miembros más brillantes del cúmulo abierto NGC 6025 y hemos calculado sus velocidades de rotación. Encontramos un módulo de distancia de 9.80 ± 0.06 (error probable) y derivamos una edad de 84 millones de años para este cúmulo. La estrella más brillante de NGC 6025, HD 143448 fue clasificada como B1Ve y es una estrella azul desubicada (*blue straggler*) tal como fue propuesto por otros autores (ver Mermilliod 1982). Hemos encontrado tres estrellas peculiares (dos de Si y una de Hg-Mn?) y dos binarias de dos espectros, una de ellas previamente estudiada pero probablemente no miembro del cúmulo. Otra estrella del campo tiene emisión, pero probablemente tampoco es miembro del cúmulo. El promedio de la rotación axial para los miembros de este cúmulo es 73% del promedio de rotación de las estrellas de campo de igual temperatura.

ABSTRACT

We have performed spectral classification and measurements of the axial rotation velocity for the brightest stars in the region of the open cluster NGC 6025. A distance modulus of 9.80 ± 0.06 (pe) and an age of 84 million years were derived. The brightest star of the cluster, HD 143448 was classified as B1Ve and it is a blue straggler as proposed by other authors (see Mermilliod 1982). We found three peculiar stars (two Si and one Hg-Mn?). Another star in the field shows emission but is probably a non-member. We also found two SB2 binaries. The average axial rotation for the cluster members seems to be 73% of the average rotation of the field stars with the same temperature.

Key Words: Hertzsprung-Russell and C-M diagrams — open clusters and associations: individual (NGC 6025) — stars: rotation

1. INTRODUCTION

The galactic cluster NGC 6025 was studied several decades ago in two papers. Feinstein (1971) provided for the first time, UBV photoelectric measurements and derived a distance modulus of 9.4 ± 0.1 and an age of 10^8 years. Four years later Kilambi (1975) published *ubvy* photoelectric and UBV photographic data and obtained 9.7 ± 0.1 for the distance modulus and an age of 9×10^7 years. This author also derived the luminosity function and showed that this cluster has fractionally more bright members than does the Pleiades cluster. There is no spectroscopic study on NGC 6025 even as basic as an MK spectral classification of its members. Paunzen et al. (2001) classified star number 20 in a paper devoted to spectral classification of candidates for λ Bootis stars. There are also some papers in the literature that include NGC 6025 in statistical studies of open clusters (see Kharchenko et al. 2009).

In this paper we classify in the MK system the stars that have been considered to be members in previous papers although we use the new SPM4 Catalogue (van Altena et al. 2010, private communication) to confirm membership. We include other stars in the field of the cluster and we estimate the spectral types of 33 stars and the rotational velocities for 27.

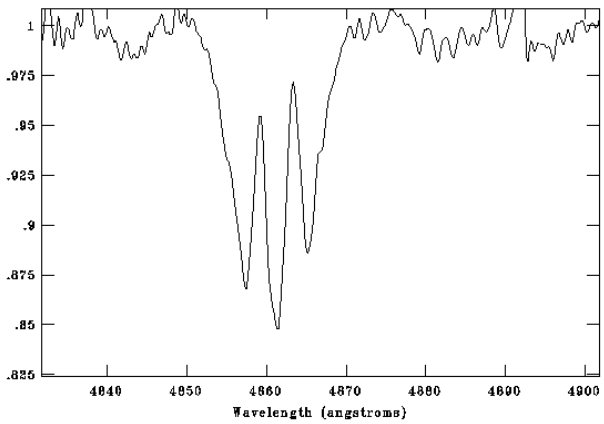

Fig. 1. Hβ profile in the spectrum of HD 143448.

2. OBSERVATIONS AND REDUCTION

The sample contains stars brighter than 11.3 magnitude in the V band. The observations were collected with the Jorge Sahade 2.15 m telescope at Complejo Astronómico El Leoncito, San Juan, Argentina. We used a REOSC spectrograph in simple and cross dispersion mode. The spectra cover the range 3600–6000 Å with a resolution around 3.6 Å/2px for simple dispersion and 0.28 Å/2px and a spectral range between 3700–5700 Å for cross dispersion. The detector was a CCD TEK of 1024 × 1024 pixels, of size 0.024 mm, thinned and back illuminated. Data reduction was carried out using IRAF tasks. The S/N for spectra in cross dispersion was about 100 and 200 for the classification spectra.

2.1. *MK classification*

The spectral classification in the MK system was derived using the WINMK code version 2.4 developed by Richard Gray at the Appalachian State University, USA[1]. The classification was carried out by comparison with MK standard stars taken with the same equipment and conditions and using the MK technique (Gray & Corbally 2009).

2.2. *Comments about some stars*

Star number 1 is a blue straggler with emission in Hβ and we have classified its spectrum as B1Ve. This star was previously classified by Morris (1961) as B3 IV and by Garrison, Hiltner, & Schild (1977) as B1.5 V. The profile of Hβ is similar in all 5 echelle spectra of star number 1 that we have taken and it is shown in Figure 1.

Star 6 shows emission in Hβ but it is probably a non-member of the cluster according to its absolute proper motion, although its position in the HR diagram fits well (see below). The classification spectrum of Star 11 shows Hg II λ 3984 and probably but less clear Mn II λ 4206. Star 25 is a Bp star of the Silicon type with λ 4200 well seen at the classification dispersion. Star 59 is also a Bp star of the Silicon type but with lower excitation level. Star 10 is an SB2 and eclipsing binary (González & Levato 2010, private communication). Star 26, HD 143511, was extensively studied by González & Levato (2006) and it is an SB2 and also an eclipsing binary with a period of 5.53546 days. It is probably a non-member of the cluster according to its absolute proper motion. Kilambi found stars 4, 6, 10 and 60 to have the Stromgreen m_1 index larger than normal. Additional features for each star are included in the notes to Table 1.

2.3. *Proper motions*

We have included in Table 1 the absolute proper motions in RA and DEC in mas yr^{-1}, taken from the SPM4 (van Altena et al. 2010, private communication) which contains 100 million stars. This catalogue is an excellent tool, among other purposes to decide about membership to open clusters. From the proper motion point diagram shown in Figure 2, it is clear that stars 6, 11, 15, 21 and 26 are probable non-members of the cluster. All of them have proper motions differing by more than 3σ from the average absolute proper motion of the cluster. We have used this criterion to decide about membership from the proper motion data.

3. RESULTS

3.1. *Reddening and distance*

The spectral types and the projected rotational velocities derived in this paper are listed in Table 1. The first column shows Feinstein's identification, the second is the HD number when available, or the CPD number. Columns 3 and 4 list the proper motions taken from van Altena et al. (2010, private communication), Column 5 lists the V magnitude taken from Feinstein (1971), Column 6 the MK types derived in the present paper, and Column 7 the projected axial rotation velocity also derived in this paper (see below). Comments have been included at the end of the table. They include conclusions about membership and the Hipparcos parallaxes available for five stars of the sample. Using the intrinsic $B-V$ for each MK type taken from the calibration published by Allen (2001) and using the observed $B-V$ taken from Feinstein (1971) we derived and interstellar extinction of 0.55 mag. adopting $A_v =$

[1] www1.appstate.edu/dept/physics/MK/xmk22.htm.

TABLE 1

RESULTS FOR THE OPEN CLUSTER NGC 6025

N	HD/CPD	μ_α [mas yr^{-1}]	μ_δ [mas yr^{1}]	V [mag]	ST	$v \sin\ i$ [km s^{-1}]
1[a]	143448	−1.49	−4.53	7.3	B1Ve	195
2[b]	143449	−2.34	−3.93	8.11	B5IV	65
3[c]	143413	−1.59	−7.00	8.42	B7 IV	240
4[d]	−60 6332	−5.46	−8.19	9.73	B8 V	60
5	−60 6316	0.98	0.33	10.23	B9 V	60
6[e]	143288	−0.65	27.21	8.96	B6 Ve	215
7[f]	143340	−2.30	−4.50	8.05	B5 IV	60
8	−60 6325	−6.07	−6.10	8.86	B6 V	200
10[g]	−60 6335	0.89	−3.46	10.8	A2:+A2:	20;20
11[h]	143287	−25.52	−12.15	8.34	B9 IVp(Hg−Mn?)	70
12[j]	143309	5.65	0.26	9.3	B6 V	10
13	−60 6319	−3.30	−4.96	9.62	B8 V	185
14[k]	−60 6322	1.85	0.68	9.85	B8.5 V	15
15[l]	−60 6327	−12.39	−29.72	9.63	F0 V	120
16	−60 6339	2.30	−3.99	9.88	B8 V	270
17[m]	−60 6343	−2.84	−11.15	11.17	B6/B7 V::	70
20	−60 6340	1.35	−7.86	11.25	A1V	···
21[n]	−60 6341	−16.76	−9.01	9.98	F5::	20
22[o]	143388	−1.44	5.89	9.15	B5 V	15
23	−60 6336	−3.66	−3.88	10.59	A0 V	60
24	−59 6562	−0.99	−3.76	10.06	B9 V	···
25	143412	−0.44	−3.56	9.7	B8 IIIpSiλ 4200	···
26[p]	143511	−8.02	−20.66	8.31	A0 V+A0 V:	25;25
29	−60 6313	−8.20	−6.75	10.69	B9 V	125
30	−60 6321	−5.77	−6.17	10.88	B9.5 V	···
34	−60 6362	−6.23	−0.69	10.51	B9 V	···
35	−60 6329	−1.35	4.31	10.97	A0 V	···
37	143220	−1.33	1.54	10.15	A3 III	15
38	−60 6311	−2.09	−4.61	10.68	A0 V	···
39[q]	−60 6342	−5.39	1.39	11.24	F0 V	···
43	143123	0.59	−5.43	9.34	B5 V	10
47	−60 6352	−3.74	−6.30	11.01	A1 V	···
59	143447	−1.67	−6.37	10.69	B9.5 p Si	···
60	−59 6578	−3.27	−3.97	10.48	B9.5 V	85
64	−60 6297	−7.91	−1.94	11.71	···	50
65	−60 6298	−4.98	−8.12	10.86	A0V	80
66	−60 6296	−4.29	−3.33	10.87	B9.5 V	80

Additional comments on individual stars:

[a]Variable (MQ TrA) between 7.2 and 7.3 mag in V. Blue struggler (see Mermilliod 1982). Parallax from Hipparcos (HIP 78682): 0.79 mas.
[b]Parallax from Hipparcos (HIP 78683): 0.64 mas.
[c]Parallax from Hipparcos (HIP 78659): 0.86 mas.
[d]m1 large as measured by Kilambi (1975). SB1.
[e]Probably a non-member due to its p.m. Emmission in Hβ.
[f]HIP 78643. Parallax 2.42 mas in new reduction (van Leeuwen 2007).
[g]SB2 (González & Levato 2010, private communication). $\delta V = 45$ km s^{-1} - m1 large.
[h]HIP 78604. parallax 3.58 mas. non-member according to its pm.
[j]Is it a variable (V350 Nor) between 9.2 and 9.310 V magnitude. It was classified by Houk & Cowley (1975) B9/B9 Ib/II.
[k]Radial velocity variable (González & Levato 2010, private communication).
[l]Probably non-member. Source proper motion.
[m]Spectral type not in the MK system. Only high resolution spectrum available.
[n]Probably non-member due to its proper motion.
[o]Radial velocity variable (González & Levato 2010, private communication).
[p]SB2, eclipsing binary, $P = 5.5354$ days. Probably non-member due to its pm.
[q]Probably non-member due to its spectroscopic parallax.

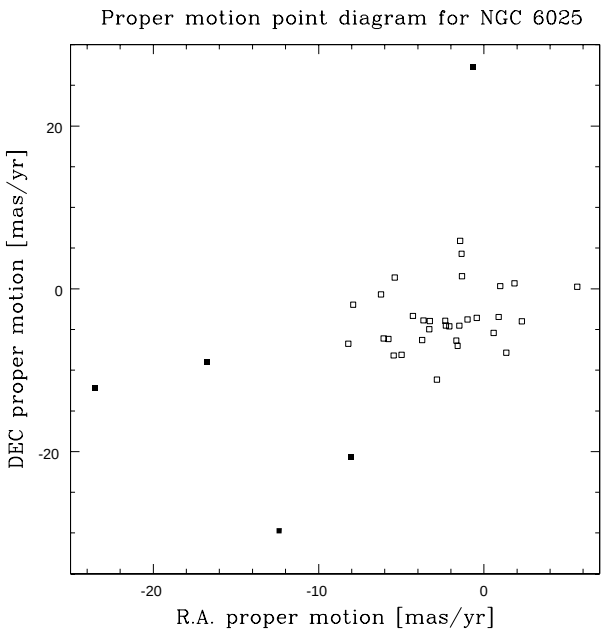

Fig. 2. Proper Motion point diagram for the stars in NGC 6025. Filled squares are non-members according with the 3σ criterium.

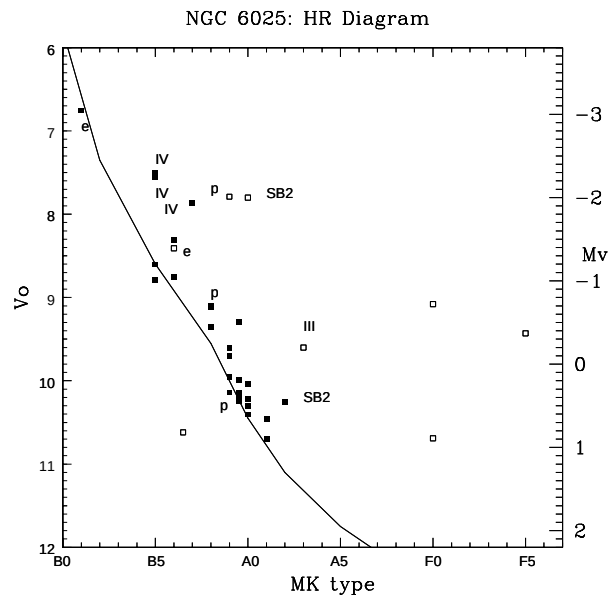

Fig. 3. Observed HR diagram for NGC 6025. Filled squares are probable members while open squares are non-members.

$3.3E(B-V)+0.28(B-V)E(B-V)+0.04E(B-V)^2$ from Allen (2001). Using the calibration between M_v and MK spectral types published by Allen (2001) we derived a true distance modulus for each star and obtained an average true distance modulus for the cluster $(m_v - M_v) = 9.80 \pm 0.06$ (pe of the mean which corresponds to 912 pc) using only the probable members as indicated in Table 1. We have not included neither CP, Be, giants nor binaries in the calculation. It is interesting to note the uncertainties in the Hipparcos parallaxes for stars 1, 2, and 3 that imply distances larger than 1 kpc. The errors in their parallaxes quoted in the Hipparcos catalogue are as large as the parallaxes themselves. We also want to point out a significant difference in the absolute visual magnitude vs MK type calibration between Allen (2001) and Gray & Corbally (2009) for the range B8-A2, which is an important range in this cluster. The visual absolute magnitude difference for the A0 V reaches 0.75 magnitudes, but it is 0.6 magnitudes for A2 V, in the sense that Allen's calibration is brighter than Gray & Corbally's. For late A stars the calibrations agree. To choose one or the other calibration to derive the spectroscopic distance of NGC 6025 is important, because the distance may increase or decrease by almost 50%. We have used Allen (2001) in order to keep consistency with our previous results on open cluster classification. The HR diagram for NGC 6025 is presented in Figure 3 where the absolute magnitude scale was drawn for a distance modulus of 9.8 mag. The main sequence has been taken from Allen (2001). Emission line stars, evolved stars, binaries and Bp-Ap stars were labeled. Probable non-members as indicated in Table 1 were plotted as open squares in Figure 3.

3.2. *Age*

We checked the age, taking into account that the earliest type on the main sequence of the cluster is B6 V. This implies a mass of 5.2 solar masses according to the calibration by Allen (2001). In such a case, the maximum age of the cluster should be 88 million years old using Schaller et al.'s (1992) results. This agrees quite well with the old determination by Kilambi (1975) (90 million years). We also checked the age using the isochrone grids calculated by Girardi et al. (2000). We plotted isochrones for solar composition on a $B-V$ vs Mv HR diagram and the best fit corresponds to log(age) = 7.9 (80 million years). So we have adopted 84 ± 4 million years as the most probable age determined in this paper (log(age) = 7.92).

3.3. *Axial Rotational velocities*

For the determination of the projected rotation velocities we have used as standards those from the Slettebak's system (Slettebak 1975). Calibration curves were constructed between the $fwhm$ of the

lines λ 4471 of HeI and λ 4481 of MgII against the $v \sin i$ for the selected standards. Linear regression lines were obtained for the spectral ranges B2–B5, B5–B7, B8–A2, A2–A5, A7–F2 for λ 4471 for the first two ranges and λ 4481 for all ranges except the first one. We have calculated the mean percentage of projected rotation velocities for the members of NGC 6025 with respect to field stars of the same types. These mean values were adopted from Abt & Morrell (1995) and Abt, Levato, & Grosso (2002). The extreme values of $v \sin\ i$ observed for cluster members are 10 km s^{-1} and 270 km s^{-1} for the minimum and maximum respectively. The cluster members seem to rotate with 73% $\pm$ 9% of the rotation of field stars of same temperatures.

4. CONCLUSIONS

We have derived a distance of 912 pc for NGC 6025, somewhat larger than previous determinations. We have found two peculiar stars of the silicon type among its members. We found a Hg-Mn? peculiar object in the region but it is probably a non-member. We found that the average axial rotation of the main sequence cluster members of NGC 6025 is less than 75% of that of the field stars of the same temperatures. This may be due to the presence of spectroscopic binaries in a larger proportion than among field stars (see Abt 2009). A thorough spectroscopic study to determine the spectroscopic binaries among the upper main sequence of NGC 6025 is under way.

The CCD and data acquisition system at CASLEO has been partly financed by R. M. Rich through U.S. NSF grant AST-90-15827. This research was partially supported by a grant PIP1113 from the National Research Council (CONICET). We thank Richard Gray who provided the WINMK version 2.4 code. Our appreciation also to W. van Altena for making available to us the SPM4 Catalogue before publication. This research has made use of the WEBDA database, operated at the Institute for Astronomy of the University of Vienna. We appreciate very much the support of CASLEO personnel in the observing process.

REFERENCES

Abt, H. 2009, PASP, 121, 1307
Abt, H., Levato, H., & Grosso, M. 2002, ApJ, 573, 359
Abt, H., & Morrell, N. 1995, ApJS, 99, 135
Allen, C. W. 2001, in Allen's Astrophysical Quantities, ed. A. N. Cox (4th ed.; New York: Spring-Verlag), 387
Feinstein, A. 1971, PASP, 83, 800
Garrison, R. F., Hiltner, W. A., & Schild, R. E. 1977, ApJS, 35, 111
Girardi, L. O., Bressan, A., Bertelli, G., & Chiosi, C. 2000, A&A, 141, 371
González, J. F., & Levato, H. 2006, A&A, 448, 283
Gray, R., & Corbally, C. 2009, Stellar Spectral Classification (Princeton: Princeton Univ. Press)
Houk, N., & Cowley, A. P. 1975, Michigan Catalogue of Two Dimensional Spectral Types for HD Stars, Vol. 1 (Ann Arbor: University of Michigan)
Kharchenko, N. V., Berczik, P., Petrov, M. I., Piskunov, A. E., Rser, S., Schilbach, E., & Scholz, R.-D. 2009, A&A, 495, 807
Kilambi, G. 1975, PASP, 87, 975
Mermilliod, J. C. 1982, A&A, 109, 37
Morris, P. 1961, MNRAS, 122, 325
Paunzen, E., Duffee, B., Heiter, U., Kuschnig, R., & Weiss, W. W. 2001, A&A, 373, 625
Schaller, G., Schaerer, D., Meynet, G., & Maeder, A. 1992, A&AS, 96, 269
Slettebak, A., Collins, G. W., Parkinson, T. D., Boyce, P. B., & White, N. M. 1975, ApJS, 29, 137
van Leeuwen, F. 2007, Hipparcos the New Reduction of the Raw Data (New York: Springer)

Mónica Grosso and Hugo Levato: Instituto de Ciencias Astronómicas de la Tierra y del Espacio, Casilla de Correo 49, CP 5400, San Juan, Argentina (mgrosso, hlevato@icate-conicet.gob.ar).

Revista Mexicana de Astronomía y Astrofísica, **47**, 261–275 (2011)

WIND STRUCTURE OF THE WOLF-RAYET STAR EZ CMA=HD 50896

Aaron Flores,[1] Gloria Koenigsberger,[2] Octavio Cardona,[3] and Lelio de la Cruz[1]

Received 2011 March 22; accepted 2011 May 9

RESUMEN

Presentamos los resultados del análisis de la línea de N V 4604 observada en espectros de la estrella Wolf-Rayet HD 50896 obtenidos en 1991, 1999, 2005 y 2009. Mostramos que la variabilidad de esta línea es consistente con un modelo en el que la opacidad del viento sufre cambios cíclicos con un periodo de 3.76 d o bien con un modelo de un viento con estructura cuadrupolar donde cada sector tiene una opacidad distinta.

ABSTRACT

The Wolf-Rayet star HD 50896 (EZ CMa=WR6) is well-known for the emission-line profile variability that occurs on a 3.7-day timescale. In particular, the shape of the N V 4604-21 doublet changes from a P Cygni profile to one in which no blue-shifted absorption component is present. In this paper we use spectroscopic observations obtained in 1991, 1999, 2005 and 2009 to glean physical conditions within the stellar wind that may give rise to these changes. We find that variations in the opacity at a distance $r/R_{\rm max} \sim 0.3$–0.5 of the stellar surface can produce the observed effects. Here, $R_{\rm max}$ is the extent of the N V line-forming region. The results are consistent either with a scenario in which the opacity of the inner wind region of HD 50896 undergoes cyclical variations over the 3.76 d period or with a quadrupolar wind distribution in which the sectors having different opacities rotate in and out of our line-of-sight on this periodic timescale.

Key Words: stars: individual (EZ CMa = HD 50896) — stars: winds, outflows — stars: Wolf-Rayet

1. INTRODUCTION

Classical Wolf-Rayet (WR) stars (van der Hucht et al. 1981) are the evolved remnants of massive O-type stars and are believed to be the last stable evolutionary phase of a star before it explodes as a supernova or, possibly, a "collapsar" (Crowther 2007). The WR stars are often found in binary systems in which the companion is also a massive O-type star. Van den Heuvel (1976) noted that after the more massive star in a massive binary system has become a supernova, leaving a neutron star or black hole remnant, its companion should eventually become a WR star. Hence, a number of *WR+cc* systems should be observable at any given time. The WN5-type star HD 50896 (EZ CMa=WR6; van der Hucht et al. 1981) was the first WR star to be proposed to fit this evolutionary scenario. Firmani et al. (1979, 1980) detected periodic ($P = 3.76$ d) emission-line profile variability which, when combined with the fact that HD 50896 is surrounded by a ring nebula (S308) and that it lies high above the galactic plane[4], led them to conclude that HD 50896 is a binary system with a low-mass companion. Shortly thereafter, linear polarization (McLean 1980) and photometric (Cherepashchuk 1981) observations confirmed the $P = 3.76$ day periodicity. Subsequent period determinations by Lamontange, Moffat, & Lamarre (1986) and Georgiev et al. (1999) gave, respectively $P = 3.766 \pm 0.001$ d and $P = 3.765 \pm 0.001$ d.

Two criteria were used by Firmani et al. (1979, 1980) to determine the original period: (a) the shape of the He II 4686 line profiles, particularly the lo-

[1]Facultad de Ingeniería, Universidad Autónoma del Carmen, Campeche, Mexico.

[2]Instituto de Ciencias Físicas, Universidad Nacional Autónoma de México, Mexico.

[3]Instituto Nacional de Astrofísica Óptica y Electrónica, Puebla, Mexico.

[4]Suggesting it is a "runaway" system as a consequence of the supernova "kick".

cation of superposed emission-like spikes that were either at line center, or "blueward", or "redward" of this location; and (b) the strength of the N V 4604-21 P Cygni absorptions. Georgiev et al. (1999) showed that the variations in this high ionization N V doublet retained coherence over ∼14 years of observations, with a period $P = 3.765$ d. However, although the variability in other lines and in photometric data is always consistent with the 3.76 d period, it is often not coherent over timescales of several weeks or longer (Drissen et al. 1989). Hence, the binary nature of HD 50896 has been questioned.

Another problem with the *WR+cc* scenario for HD 50896 is the absence of significant X-ray variability. Stevens & Willis (1988) and Skinner, Itoh, & Nagase (1998) showed that the observed levels of X-ray emission were far too low to be attributable to accretion onto a neutron star or black hole. On the other hand, Skinner et al. (2002) concluded that the presence of a low-mass companion upon which the WR wind collides would be consistent with the low X-ray emission levels. Hence, the binary scenario is still a viable one. However, even under the binary hypothesis, a physical mechanism by which the line-profile variability occurs is still not identified.

In this investigation we focus on one of the physical mechanisms that may produce the observed line-profile variations in HD 50896. Specifically, we will analyze the N V 4604 line profiles in order to determine the type of wind structure variations that may produce the observed variability. In § 2 we describe the observations; § 3 contains a description of the N V variability; § 4 describes the line-fitting technique; § 5 contains a discussion; and § 6 the conclusions.

2. OBSERVATIONS

The new observations were carried out during three epochs in 1999, 2005 and 2009 (hereafter referred to as OGH I, OGH II and OGH III, respectively), with the 2.1 m telescope of the Observatorio Astronómico Guillermo Haro (OGH), using a Boller & Chivens spectrograph, with a 830 grooves mm^{-1} grating in the second order, and a slit aperture of 250 μm. A Schott BG18 blocking filter was placed at the slit entrance, thus removing light at $\lambda < 4000$ Å. For the first and second epochs, we used a CCD with a 1024×1024 Tek chip and for the third epoch a CCD with 1300×1300 BestArray chip. The reciprocal dispersion for the first and second epochs was 0.31 Å/pix, and the spectral window was $\lambda\lambda$4463–4778 Å, while for the third epoch, the corresponding parameters were 0.26 Å/pix, and $\lambda\lambda$4470–4810 Å.

Data reduction was performed using standard procedures in the Image Reduction and Analysis Facility (IRAF) version 2.14.1 package[5], which included bias subtraction, flat field correction, cosmic ray deletion, and wavelength calibration. The wavelength calibration was performed using a He-Ar comparison lamp, yielding an uncertainty of 0.34 Å in wavelength measurements for the OGH II and OGH III epochs. For the OGH I epoch, due to a problem with the comparison lamp spectrum, the wavelength calibration was deficient, leading to uncertainties twice as large. Individual spectra have S/N∼110 at the continuum level, with the average spectra per night having S/N $\sim \sqrt{n}110$, where $n = 3,...,35$ is the number of spectra averaged. The individual spectra were normalized to the continuum level after interpolating a third-order Legendre polynomial function to line-free spectral regions.

One of the noteworthy features of these observations is the fact that each set was obtained over seven or eight consecutive nights, thus covering two contiguous 3.76-day cycles. On each night, between 3 and 35 spectra were obtained within time intervals ranging from one to six hours. The three sets of data are comprised of 151 spectra. Table 1 contains the journal of observations. Column 1 lists the identification number of the spectrum, Column 2 the mean Julian Date −2445000, Column 3 the date of observations, Column 4 the number of spectra obtained over the night, Column 5 the timespan (in hours) over which these spectra were collected and Column 6 the phase computed with $P = 3.7650$ d and $T_0 = 2443199.53$ from Georgiev et al. (1999).

The above data sets were complemented with a set of nightly average spectra obtained in the Observatorio Astronómico Nacional San Pedro Mártir (SPM) during 1991 January (Piceno 2003; Vázquez 2003; Morel et al. 1998; Georgiev et al. 1999). The date of observation, number of spectra averaged, and nightly timespan covered by these spectra are listed in Table 2. The SPM data set covers 13 consecutive nights. Only one spectrum was obtained on nights "a" and "d" due to bad weather; the first of these is a useful spectrum having S/N ∼ 100. On night "d" the spectrum has S/N ∼ 35 and was not used for the analysis presented in this paper. This set provides spectra for three consecutive cycles in the 3.76 d period.

[5]IRAF is distributed by the National Optical Astronomy Observatory, which is operated by the Association of Universities for Research in Astronomy, Inc., under cooperative agreement with the National Science Foundation.

TABLE 1

JOURNAL OF OBSERVATIONS FOR THE OGH SPECTRA AND LINE FIT PARAMETERS[a]

ID	JD	Day	n	Δt	ϕ	$V_{\max}$	X_0	X_1	R_1	X_2	R_2	X_3	R_3	X_4	Type
OGH I (Jan-Feb 1999)															
b24	1202.80	24	9	1.0	0.71	40	0.1	90	1.25	380	1.90	210	3.1	10.	a
b25	1203.73	25	35	6.0	0.96	34	0.1	40	1.38	370	2.10	160	2.9	10.	a
b26	1204.82	26	3	0.5	0.25	34	0.1	45	1.25	320	2.00	180	2.6	10.	a
b27	1205.71	27	25	5.0	0.48	40	0.1	45	1.45	710	2.00	60	2.7	0.1	s
b28	1206.76	28	15	2.0	0.76	34	0.1	50	1.25	310	1.90	220	2.4	70	a
b30	1208.70	30	19	2.7	0.28	38	0.1	40	1.30	410	1.88	180	2.95	60	a
b31	1209.70	31	10	2.0	0.54	42	0.1	45	1.30	640	1.90	40	2.7	0.1	s
b2	1211.70	02	35	6.0	0.07	38	0.1	46	1.40	500	2.00	70	3.0	0.1	w
OGH II (Nov 2005)															
n19	3693.84	19	8	1.0	0.37	34	20.	50	1.35	320	1.9	140	3.1	50.	a
n20	3694.96	20	10	2.7	0.64	36	0.1	55	1.30	360	1.95	75	2.7	0.1	w
n21	3695.97	21	15	2.2	0.91	35	20.	50	1.25	370	1.85	110	3.1	50.	a
n22	3696.98	22	20	5.0	0.17	40	0.1	45	1.40	650	1.85	20	2.7	0.1	s
n23	3697.96	23	7	1.0	0.44	35	0.1	50	1.25	270	1.70	140	3.8	50	a
n24	3698.95	24	5	1.0	0.70	33	0.1	60	1.35	340	1.95	33	2.9	80	w
n25	3699.98	25	10	2.7	0.97	33	0.1	40	1.40	400	2.20	93	2.9	0.8	w
n26	3700.87	26	20	5.0	0.21	40	0.1	45	1.40	700	1.85	8	2.7	0.1	s
OGH III (Feb 2009)															
d02	4864.82	02	15	1.0	0.36	33	0.1	60	1.46	400	2.05	73	2.9	0.1	w
d03	4865.74	03	20	2.7	0.60	38	0.1	43	1.40	520	2.00	40	2.7	0.1	s
d04	4866.77	04	14	2.2	0.88	34	0.1	60	1.30	280	1.90	140	2.8	40	a
d05	4867.75	05	22	5.0	0.14	38	10.	60	1.40	420	1.80	90	2.8	1	w
d06	4868.77	06	20	1.0	0.41	36	10.	60	1.39	400	2.0	60	3.0	0.1	w
d07	4869.78	07	15	1.0	0.68	35	0.1	45	1.40	400	2.00	45	2.7	0.1	s
d08	4870.71	08	6	2.7	0.92	34	0.1	60	1.38	250	1.80	110	3.0	60	a

[a]Mean Julian dates (-2450000) for the time interval (Δt) over which the data n spectra were collected. Phase (ϕ) is computed with the Georgiev et al. (1999) ephemeris. The fit parameters are described in the text. For all cases, $R_{\max} = 4.2\ R_*$, $R_a = 3.9\ R_*$ and $V_{\rm th} = 50$ km s^{-1}.

TABLE 2

JOURNAL OF OBSERVATIONS FOR THE SPM SPECTRA AND LINE FIT PARAMETERS[a]

ID	JD	n	Δt	Phase	$V_{\max}$	X_0	X_1	R_1	X_2	R_2	X_3	R_3	X_4	Type
a	280.9	1	–	0.63	36	0.1	47	1.21	410	2.02	30	2.9	0.1	s
b	281.8	22	4.5	0.87	37	0.1	59	1.40	510	2.05	18	3.0	0.1	s
c	282.8	34	6.1	0.14	34	0.1	90	1.40	250	1.95	130	3.2	9	a
e	284.8	30	5.7	0.67	31	0.1	10	1.20	330	2.2	58	2.9	1	w
f	285.8	22	5.1	0.93	37	0.1	67	1.36	460	2.02	20	2.8	0.1	s
g	286.8	32	4.9	0.20	34	0.1	90	1.27	220	1.85	130	3.2	9	a
h	287.8	35	4.5	0.47	31	0.1	30	1.30	290	2.1	78	2.9	1	w
i	288.7	7	0.6	0.70	31	0.1	30	1.40	340	2.2	58	3.0	1	w
j	289.8	34	5.5	0.00	35	20	51	1.35	390	2.12	37	2.8	0.1	s
k	290.7	7	3.4	0.24	34	0.1	90	1.35	260	1.7	120	3.5	9	a
l	291.8	40	4.4	0.53	31	0.1	30	1.40	340	2.24	60	3.0	1	w

[a]Mean JD's are -2448000. Other parameters as in Table 1.

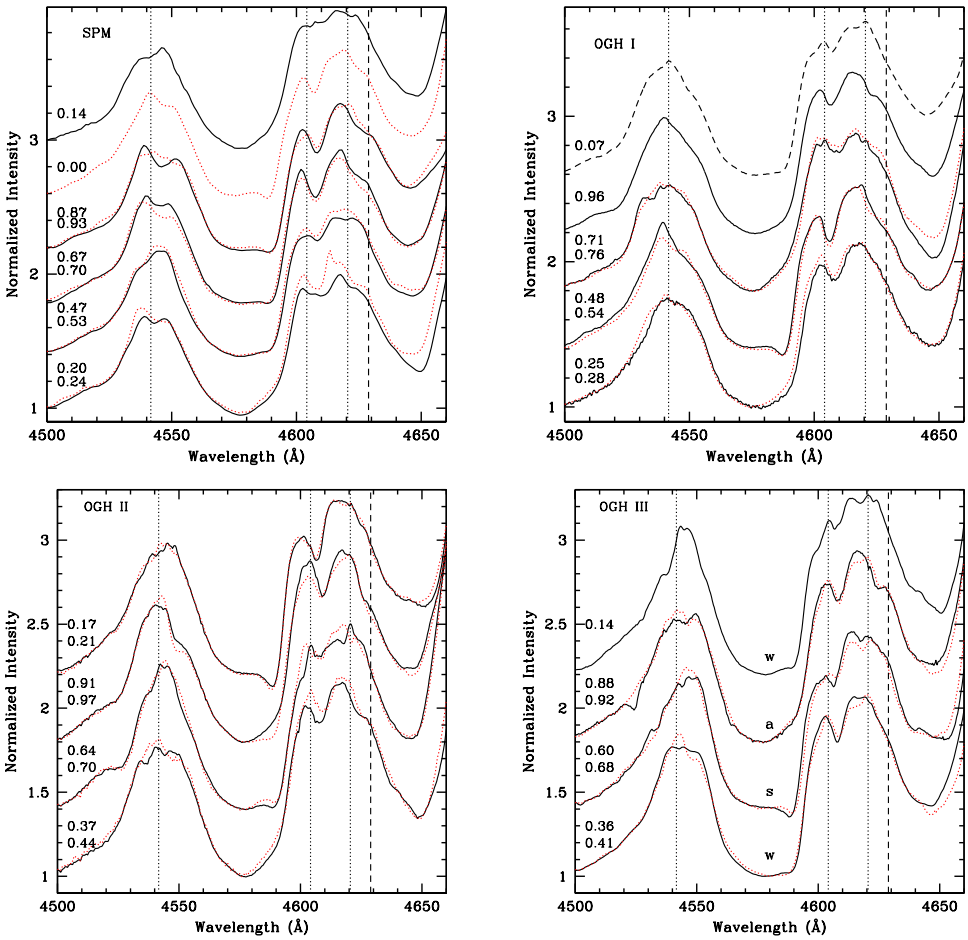

Fig. 1. Spectra from 1991 (SPM; top left), 1999 (OGH I; top right), 2005 (OGH II; bottom left) and 2009 (OGH III; bottom right). Spectra from the first 3.76 d cycle are shown with a continuous line, those from the second cycle are shown with dots, with spectra of similar orbital phases having the same vertical shift in the plot. Orbital phases with the Georgiev et al. (1999) ephemeris are listed. Vertical dotted lines indicate laboratory wavelengths of He II 4541.59, N V 4604.14 and N V 4620.50; the dashed line marks the location of O V 4628.87, a possible contributor to the blend. The letters *s*, *w* and *a* in the OGH III panel label the type of P Cygni absorption (see text). The color figure can be viewed online.

3. N V LINE-PROFILE VARIABILITY

Figure 1 shows the spectral region containing the He II 4542 and the N V 4604-21 doublet for the four epochs of observations. Spectra are displaced vertically to allow a clear view of their characteristics at different phases. Given that the observations of all four epochs were carried out over at least two 3.765 d cycles, two spectra per epoch at similar phases are generally available. The spectrum from the second cycle is plotted with dots. Phases were computed using the Georgiev et al. (1999) ephemeris and are listed.

The variations in the N V 4604-21 doublet can be described primarily in terms of the occasional presence of a prominent P Cygni absorption component which at other times is absent, and an intermediate state in which the absorption is weak. Although the same type of variability is present in all epochs, a comparison of the four panels in Figure 1 leads to the conclusion that a particular profile shape does not always appear in the same 3.76 d phase interval. For example, the P Cygni absorption component is strong at $\phi \sim 0.9 - 1.0$ in the SPM data, at $\phi \sim 0.5$ in the OGH I data; at $\phi \sim 0.2$ in the OGH II data, and $\phi \sim 0.6 - 0.7$ in the OGH III spectra. Hence, the presence of a strong P Cygni absorption does not correlate with phase for spectra separated in time by a few years, as are our data. However, on timescales of less than a couple of weeks, a phase-dependence does exist.

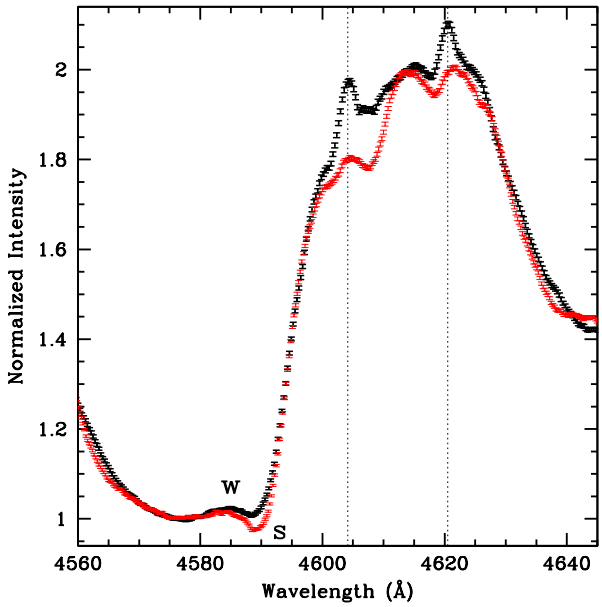

Fig. 2. Comparison between spectrum n20 and spectrum d07 illustrating the difference between the *weak* (w; black) and *strong* (s; red) types of absorption in N V 4604. Error bars indicate the uncertainties associated with each spectrum, as determined from the corresponding S/N ratios. The color figure can be viewed online.

TABLE 3

DAY-TO-DAY P CYGNI TYPE FOR EACH EPOCH[a]

Epoch	Type											
1991	s	s	a	-	w	s	a	w	w	s	a	w
1999	-	-	a	a	a	s	a	-	a	s	-	w
2005	-	-	a	w	a	s	a	w	w	s	-	-
2009	-	-	-	-	w	s	a	w	w	s	a	-

[a]Each entry of the table corresponds to one night of observations, and they are listed sequentially starting at the left with the first night of data. The letters indicate whether the N V 4604 profile has a *strong*, *weak* or *absent* P Cygni absorption component. The nights of each epoch have been aligned so that the *s* spectra all lie along the same columns. A dash indicates no data available for the given night.

We assign a classification of *strong*, *weak*, or *absent* to the type of line-profile observed. The distinction between the three types of profiles is most clearly seen at λ 4590 Å in Figure 1. The *weak* profiles have intensities that are very close to the continuum level, the *strong* profiles are below the continuum, and the *absent* profiles lie significantly above it. The continuum level lies at intensity level unity, by definition from the spectrum normalization process. Examples of the *strong* and the *weak* type profiles are shown in Figure 2. In Tables 1 and 2 each spectrum has been characterized with the letters *s*, *w* or *a* in accordance with this classification. Using this description for the N V profiles, the day-to-day variability pattern of the four epochs may be compared. Table 3 illustrates this variability pattern for each epoch individually (the different rows) and for the entire set by aligning the first *s* spectrum of the OGH data sets with the second *s* of the SPM set in the same column. Table 3 shows that the four epochs follow the same sequence that repeats with the 3.76 d period: $s \rightarrow a \rightarrow w/a \rightarrow a/w$, where a/w and w/a indicate that either *a* or *w* are present in the column.

Figure 1 also shows that part of the variability is due to the appearance of narrow emission peaks. A clear example of such features at the rest wavelength of He II 4642, N V 4604 and N V 4621 can be seen in the phase interval 0.64–0.70 of the OGH II spectra (see also Figure 2). Thus, in addition to the changing P Cyg absorption, the line-profile variability involves the presence of narrow, superposed emissions. The fact that they are located at the laboratory wavelength indicates that they originate in material that is flowing perpendicular to our line-of-sight.

Figure 3 again shows the spectral region containing He II 4542 and the N V 4604-21 doublet for the four epochs of observations. In this case, the first spectrum plotted from bottom to top is the first spectrum in the series having a *strong* N V 4604 P Cygni absorption component. In the SPM data set, we chose spectrum 'b' of the series because on night 'a' only 1 spectrum was obtained[6]. The second spectrum from bottom up, plotted with a +0.5 shift in the intensity scale, is the one obtained during the following night of observation; the third and fourth spectra correspond to the subsequent 2 nights, each with a corresponding additional +0.5 shift in the intensity scale. The fifth spectrum of the series is overlaid with the first, this time with a dotted line instead of a continuous line; similarly, with the following spectra of the series. This figure confirms the similarity between the four epochs' N V line profile variabiity, but it also shows that small changes in the line shapes are present for spectra of similar phases separated by a single 3.76 d cycle. The magnitude of these small changes may be evaluated from the ratios

[6]We do note, however, that spectrum 'a' has an *s*-type profile which apparently breaks the pattern described above.

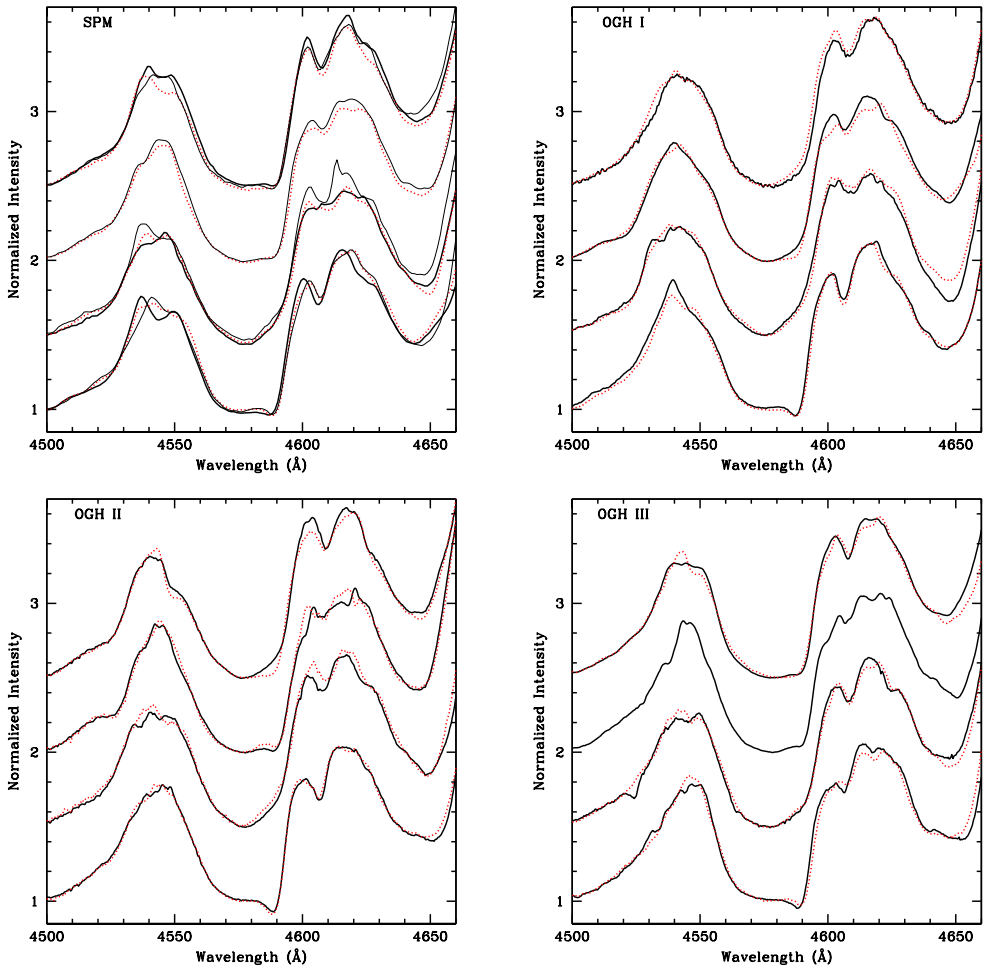

Fig. 3. Data from SPM (top left), OGH I (top right), OGH II (bottom left) and OGH III (bottom right) as in Figure 1 but here the spectra lying lowest in each plot are those in which N V 4604 has a *strong* P Cygni absorption component. Subsequent spectra stacked vertically correspond to the following nights of observation. Spectra of similar phases from contiguous cycles are superposed using different line types: the first cycle is plotted with thick lines, the second cycle with dots and the third cycle with thin lines. The *strong*-type profiles are always followed on the next night by an *absent*-type profile. The color figure can be viewed online.

of the spectra, and, for example, the changes seen in the OGH II spectra at phases 0.91 and 0.97 at 4585–4610 Å region lie in the range ∼5–8%. Given that S/N $\sim 110n^{1/2}$ in these spectra and that each of the spectra is the average of $n > 5$ individual exposures, most of these changes are well above what would be expected from random fluctuations.

4. LINE FITTING PROCEDURE

The periodic line profile variations can be interpreted within three general scenarios. The first is one in which the intrinsic wind structure of the WR star changes over the 3.76 d period; in the second scenario, it is anisotropic, for example, having quadrants with different velocity gradients or ionization fractions. In the third scenario, the inner portions of the wind have a stationary structure, but the outer regions do not, either because of some intrinsic instability or because of the perturbation from a companion. In this paper we focus on the first interpretation because it is the one that requires the smallest number of assumptions.

The line-profiles were modeled using the radiation transfer code described by Auer & Koenigsberger (1994). This is a simple code which computes the line profile produced in a wind having either a linear or a β-velocity law and an opacity distribution with arbitrary characteristics. The algorithm assumes spherical symmetry and uses the

TABLE 4

DESCRIPTION OF INPUT PARAMETERS FOR LINE FITS[a]

Parameter	Value	Description
$R_{\rm max}$	4.2	Maximum extent of line-forming region, in units of R_*
$V_{\rm max}$	–	Terminal wind speed, in units of $V_{\rm th}$
$V_{\rm th}$	50	Thermal velocity, in km s^{-1}
R_a	3.9	Extent of linear acceleration region, in units of R_*
R_i	–	Radius of the *i-th* region
X_0	–	Opacity parameter at R_*
X_i	–	Opacity parameter at R_i

[a]In Column 2 we list the values of those parameters that were held constant.

Sobolev approximation only in those portions of the wind where the approximation is valid. Where the Sobolev approximation breaks down (i.e., where the wind velocity gradient is small compared to the local Doppler velocities) it computes the radiative transfer precisely. A description of the input parameters is given in Table 4. The line is assumed to arise in a region whose maximum extent is $R_{\rm max}$. In the linear approximation, R_a is the distance over which the velocity increases; and R_i, with $i = 1,2, ...,n$ are the radii of regions within the wind having different opacities. All distances are given in units of the stellar radius, R_*, which is the hydrostatic radius. The opacity in the different regions is parametrized with the opacity factor, X, which is a nondimensional parameter that enters into the line-profile calculation through the optical depth, τ, defined as

$$\tau = \int \frac{X(r)}{[v(r)/v_{\rm th}](r/R_*)^2}\varphi[x - v_z(z)]d(z/R_*), \quad (1)$$

where $v(r)$ is the wind velocity law, $v_{\rm th}$ is the Doppler velocity, v_z is the projection of the wind velocity along the line of sight from the star to the observer in Doppler units, φ is the line profile function, x is the non-dimensional line frequency, and z is the coordinate along the line of sight. The maximum speed attained in the line-forming region is $V_{\rm max}$. It is specified in the code in units of $v_{\rm th}$.

The code allows the value of $X(r)$ to be specified for an arbitrary number of radial positions within the line-forming region. We represent its different values as X_i for the corresponding regions R_i. Note that by defining wind regions R_i with different X_i values, we are assuming that the excitation and/or ionization structure can change with distance from the stellar core.

Our analysis will be restricted to the "blue" wing of the N V 4604 line because its P Cygni absorption component is formed in the column of wind material that lies along the line of sight from the observer to the continuum emitting core. Hence, it describes the behavior of wind material whose location is constrained, thus simplifying the interpretation. In addition, it is not contaminated by other lines. This is unlike its centrally-located emission which is blended with the P Cygni absorption produced by the neighboring N V 4620 Å doublet member.

We used a linear velocity law of the form $v(r) = v_0 r$ because a standard β-velocity law failed completely to describe the observed line profiles. A β-law predicts a strong and sharp P Cygni absorption at the wind terminal speed ($\sim$1900 km s^{-1}) which is not observed. This problem can be avoided if the line opacity goes to zero in the region where the wind velocity tends asymptotically to v_∞. Hence, we opted to use a velocity law in which the wind accelerates linearly up to R_a, and then expands at a constant speed thereafter. The form of the velocity law in the code is $v(r) = V_{\rm max} r/R_a$, so the velocity at the stellar surface is $v(R_*) = V_{\rm max}/R_a$.

We chose to fix the value of $R_{\rm max} = 4.2$ based on the deduced ionization structure of HD 50896's wind from Hillier (1988; Figure 2) which shows that this is the extent of the region where the abundance of NV dominates over that of N IV. We also fixed $v_{\rm th} = 50$ km s^{-1}. This value was chosen in part because the ionization potential of NV is 98 eV which, under equilibrium conditions, corresponds to a thermal speed of 37 km s^{-1}, and in part because the code does not include turbulent broadening in the calculation and the added velocity serves to increase the Sobolev length accordingly. Since the velocities are given in units of $v_{\rm th}$, the product $V_{\rm max}\ v_{\rm th} = v_\infty$ is constrained by the observations. We also fixed the value of the acceleration radius, $R_a = 3.9\ R_*$.

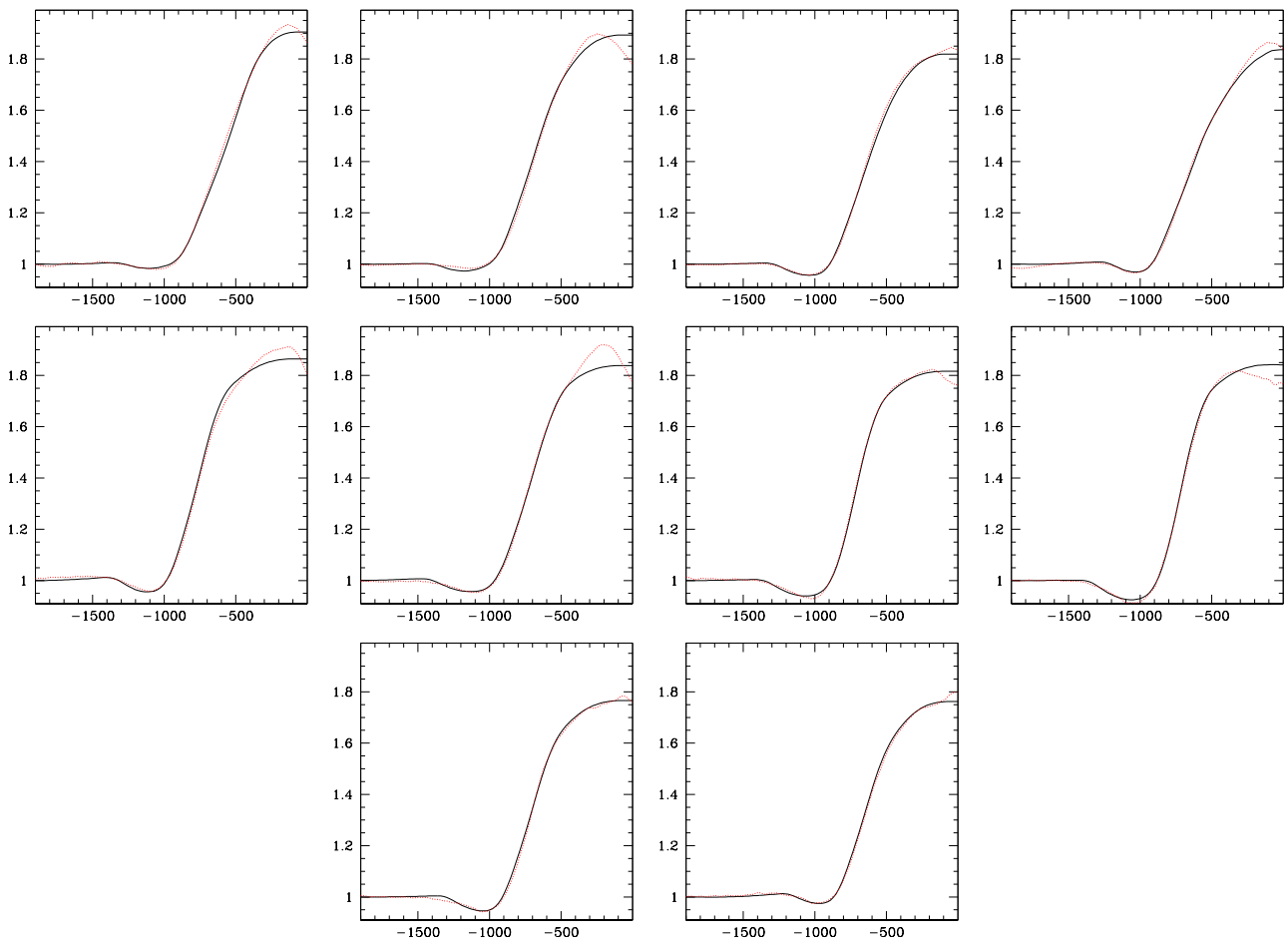

Fig. 4. Comparison of model calculations of the N V 4604 blue wing with the observations (dots) for the *strong* profiles. From left to right and from top to bottom: a, b, f, j, b27, b31, n22, n26, d03, d07. The abscissa is velocity in km s^{-1} with respect to the rest wavelength of N V 4604, the ordinate is normalized intensity. The color figure can be viewed online.

Values smaller than this lead to a sharp, blueshifted absorption component originating in the wind region that is moving at V_∞, and these absorptions are not present in the observations.

It is important to note that, with the above parameters fixed, there are different combinations of $V_{\rm max}$, X_i and R_i which lead to very similar model line profiles. Thus, the line fits of Figures 4–6 are not unique. However, once $v_{\rm th}$ is specified, $V_{\rm max}$ is constrained to values that are consistent with V_∞. Once $V_{\rm max}$ is fixed, the blue wing of the line profile is extremely sensitive to the values of X_2, X_3, R_2, and R_3 and we are unable to find different combinations of these parameters which yield the same line-profile.

The detailed shape of the P Cygni profile depends strongly on the velocity gradient and on the opacity within the accelerating region. After numerous experiments, we found it necessary to define at least three sub-regions within the accelerating region of the wind, each having different opacities. Keeping $R_{\rm max} = 4.2\ R_*$, $R_a = 3.9\ R_*$ and $v_{\rm th} = 50$ km s^{-1} constant, we fitted each line individually in an iterative manner by varying only the values of X_i, R_i and $V_{\rm max}$. As noted above, $V_{\rm max}$ is limited by the terminal wind speed, so the range of values over which it can be varied is not very broad. However, it is important to note that a small variation in $V_{\rm max}$ modifies the velocity gradient and, hence, the Sobolev optical depth. Thus, variations in $V_{\rm max}$ that are within the uncertainties of the measured V_∞ lead to noticeable differences in the line profiles.

In general, a good fit was achieved after ∼30 iterations. A second pass on the entire set of profiles, with ∼10–20 iterations each, yielded model profiles that differed from the observations within the noise

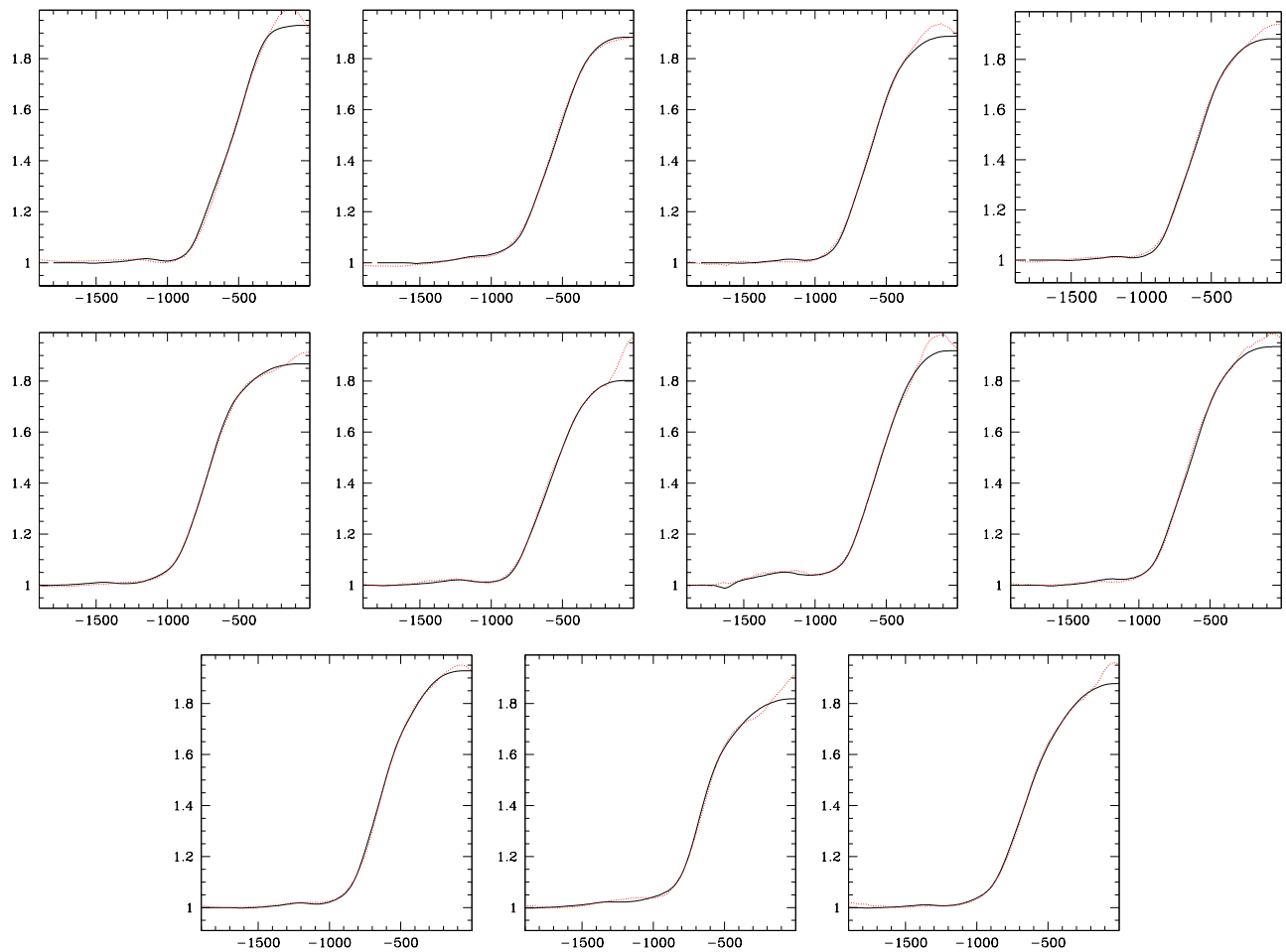

Fig. 5. Same as previous figure for the *weak* profiles. From left to right and top to bottom: e, h, i, l, b2, n20, n24, n25, d02, d05, d06. The color figure can be viewed online.

levels. The results are illustrated in Figures 4, 5, 6, where we grouped the profiles according to whether the P Cygni absorption is strong, weak or absent, respectively. In all cases, the fit to the blue wing, including the P Cyg absorption is excellent. We did not attempt to fit the centrally-located emission because it has contributions from the neighboring N V 4620, and it would be necessary to model the line transfer in the doublet. Thus, the model does not generally fit the observations around the emission maximum[7].

We examined the uncertainty in the model fits by determining the change in the input parameters needed to produce a difference of 3% in the profile with respect to the best fit model. In Figure 7 we plot the best-fit model for spectrum *n22* and the results obtained by changing the $V_{\rm max}$, X_i and R_i input parameters one at a time. The range in these parameters is $V^0_{\rm max} \pm 1.2$, $X^0_i \pm 10$, and $R^0_i \pm 0.05$, where the 0-superindex indicates the best-fit values.

The optical depth along any ray depends on both the projected velocity gradient and the opacity at each particular line-of-sight velocity component. Hence, it is *a priori* difficult to determine the effects of modifying each of the free parameters of the calculation. Within the parameter space listed in Table 4, only a a few guiding rules were found during the line-fitting process. For example, the slope of the line profile within the velocity range −800 to −200 km s^{-1} is strongly influenced by the choice of R_2. The location and strength of the P Cygni absorption component is determined to a large extent by the values of $V_{\rm max}$, X_3 and R_3. Increasing the

[7]It is interesting to note, however, that the model generally under-predicts the emission intensity, consistent with the fact that the contribution from the N V 4620 emission will add on to the λ4604 emission and approach the value of the observed intensity.

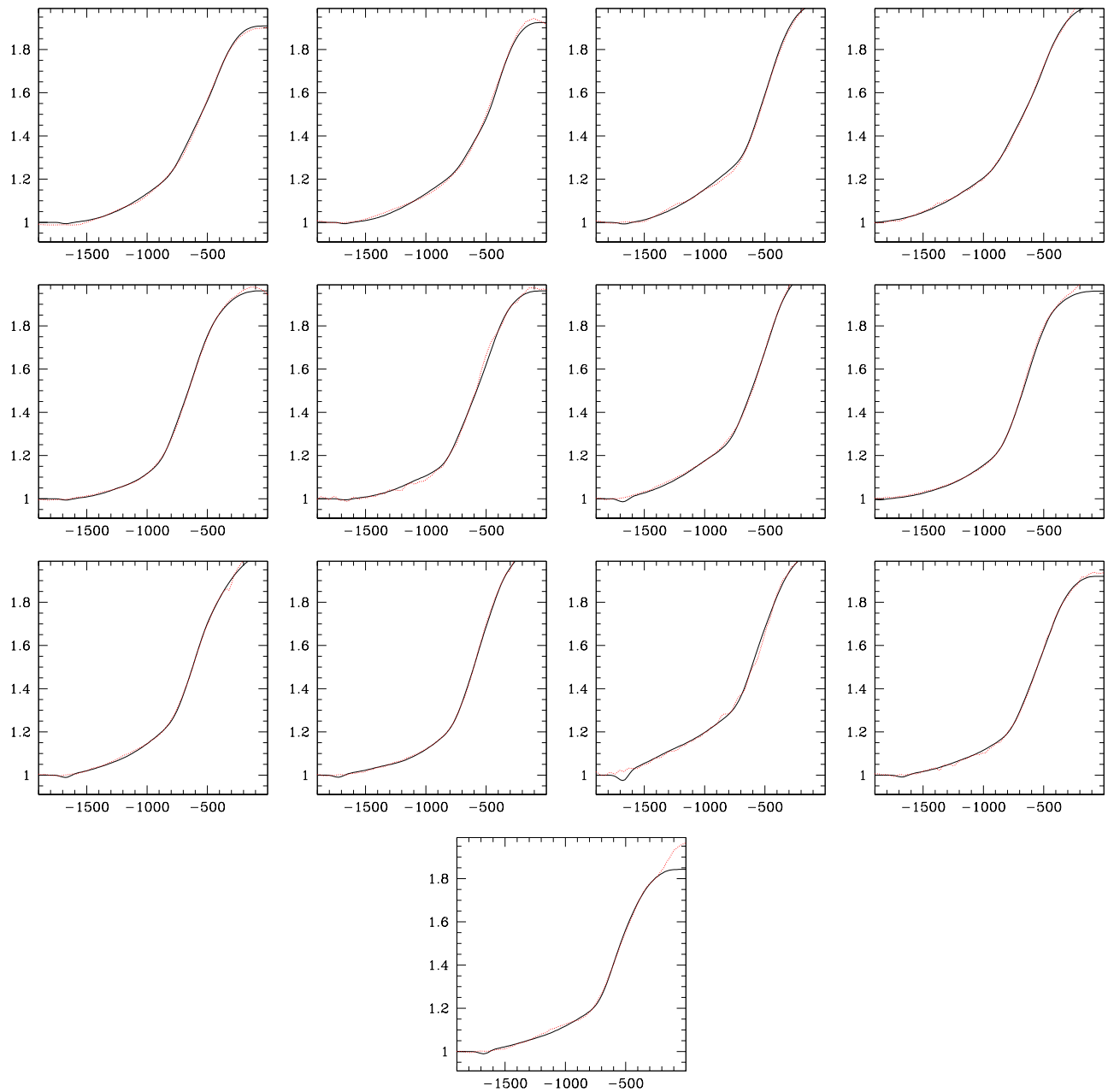

Fig. 6. Same as the previous figure for the *absent* profiles. From left to right and from top to bottom: c, g, k, b24, b25, b26, b28, b30, n19, n21, n23, d04, d08. The color figure can be viewed online.

value of X_3 and X_4 leads to an overall increase in the line strength. Changing the value of R_1 affects the strength of the emission component at small line-of-sight velocities. The values of X_0 and X_1 need to be smaller than that of X_3 to keep the line from being too strong at small velocities.

The input parameters that yielded the best fit to the P Cygni absorption of each spectrum are listed in Tables 1 and 2. The four regions into which the wind was divided are identified by their maximum extent, R_i, $i = 1,..,4$. The results of the fits provide the values of R_i and their corresponding X_i values. The first region extends from R_* to R_1, where $0.30 \leq R_1/R_{\rm max} \leq 0.35$. The second region extends to R_2, where $0.43 \leq R_2/R_{\rm max} \leq 0.52$. The third region extends to R_3, where $0.57 \leq R_3/R_{\rm max} \leq 0.74$. The fourth region extends to $R_{\rm max}$ and includes the portion of the wind that expands at a constant speed.

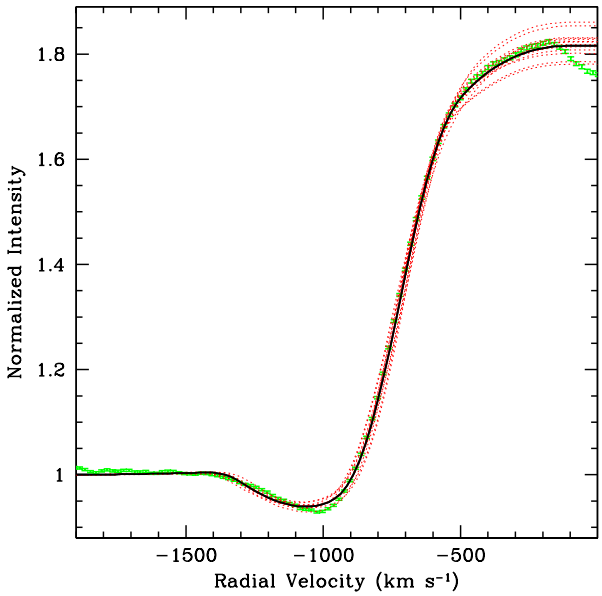

Fig. 7. Effects of changing the input parameters, one by one, on the shape of the line profile. The thick continuous line is the best-fit model. Dotted lines are the models with a different value for one of the following input parameters: $V_{\max}$, X_1, X_2, X_3, R_1, R_2, R_3. The observed spectrum (n22) is plotted as individual (green) points with error bars corresponding to S/N∼490. The "dip" in the observed line profile at ∼0 km s^{-1} is the P Cyg absorption component of the neighboring N V 4620 Å line. The color figure can be viewed online.

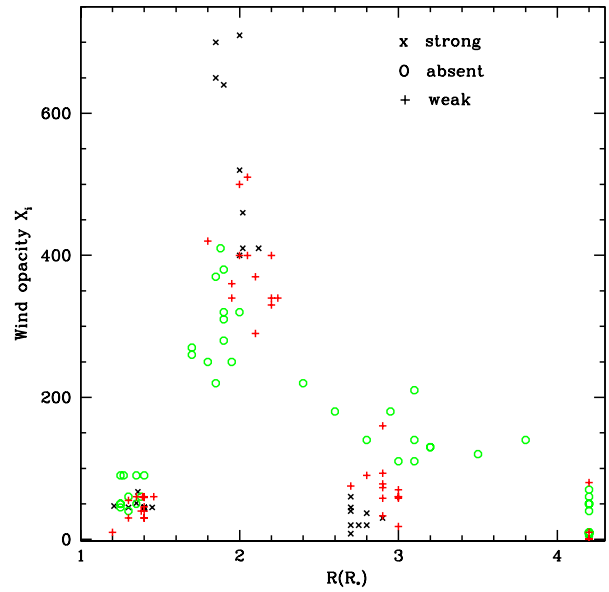

Fig. 8. Opacity parameter values (X_i, i = 1, 2, 3, 4) and their corresponding wind regions(R_i) derived from the line-profile fits. The different symbols indicate the different types of profiles: cross (s), plus sign (w) and circle (a). The color figure can be viewed online.

5. WIND STRUCTURE

Figure 8 shows the plot of the opacity parameter values, X_i, and the corresponding radial extent, R_i, derived from the line fits. The different symbols correspond to the three types of line profiles, *strong*, *weak* and *absent*, which henceforth will be referred to as s, w and a. The first noteworthy feature of this plot is that the opacity is, in general, small within the region closest to the star, ∼1.5 R_*. This is consistent with the NV/NVI $\ll$ 1 abundance ratio in the innermost wind region (Hillier 1988; Figure 2). The opacity then rises significantly in R_2, and then declines again in R_3 and R_4. Thus, the dominant opacity involved in the formation of the N V 4604 line is that of the wind material located in the R_2 region, but with the a profiles having a significant contribution from material in R_3. The second feature is the marked difference in the behavior of the opacity factor in the a profiles from that of the s/w profiles. The former have smaller values of X_2 and larger values of X_3 than the latter.

Given that similar profiles may be obtained with different combinations of $V_{\max}$, X_i and R_i, a second set of model fits was computed with $V_{\max}$ = const = 40, in order to illustrate the impact on the results. The fits were performed for the s and a profiles, since the w profiles are intermediate between these two. Figure 9 illustrates the difference between the results obtained above leaving $V_{\max}$ as a parameter to be fit (left) and holding $V_{\max}$ constant (right). The clear separation of the X_i, $i = 1, 2$ values for the s and a profiles persists as does the trend for a larger average value of R_3 in the a profiles.

We now examine the 3.76 d phase dependence of the model fit parameters. In Table 3 we listed the night-to-night sequence of profile types for each epoch of observations. Table 5 shows the same description as Table 3, but the letters s, a, w are here listed in sets of four, corresponding to four consecutive nights of observation (Columns 2–5). In this representation it is evident that for each epoch the profile shape cycles through the type s (day 1), a (day 2) and w/a (days 3 and 4), where w/a means either a w or an a type. Columns 6–10 and 11–14 of Table 5 list the corresponding values of the opacity parameters X_2 and X_3, respectively, in the same representation of sets of four nights. For each epoch, the column corresponding to the s profiles has the largest X_2 value and smallest X_3 value. This table clearly shows the 3.76 d cyclical pattern for

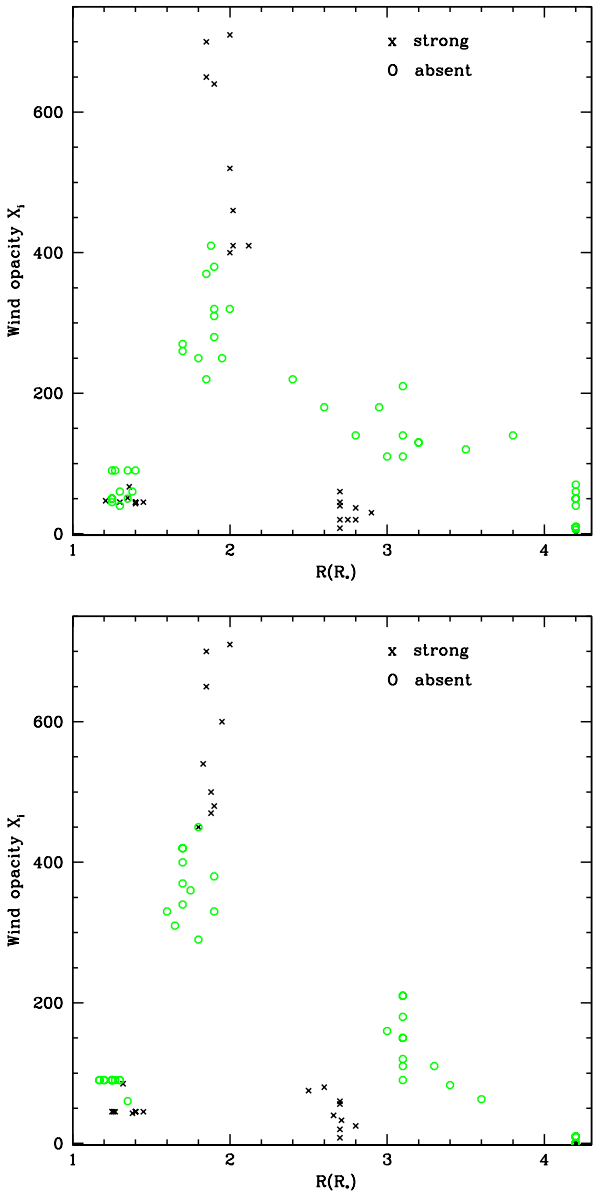

Fig. 9. Top: Same as previous figure, but showing only the values for the s and a profiles. Bottom: the same information, but this time from the model runs in which $V_{\max}$ was held constant and the fits were performed for only the X_i and R_i values. The color figure can be viewed online.

each epoch, which is also illustrated in Figure 10. Phases were all computed with the same ephemeris from Georgiev et al. (1999). This figure also shows that the phases of maximum X_2 and the amplitude of the variations differ from epoch to epoch. There is no significant difference in this figure if we plot the results obtained from the fits where $V_{\max}$ was held constant.

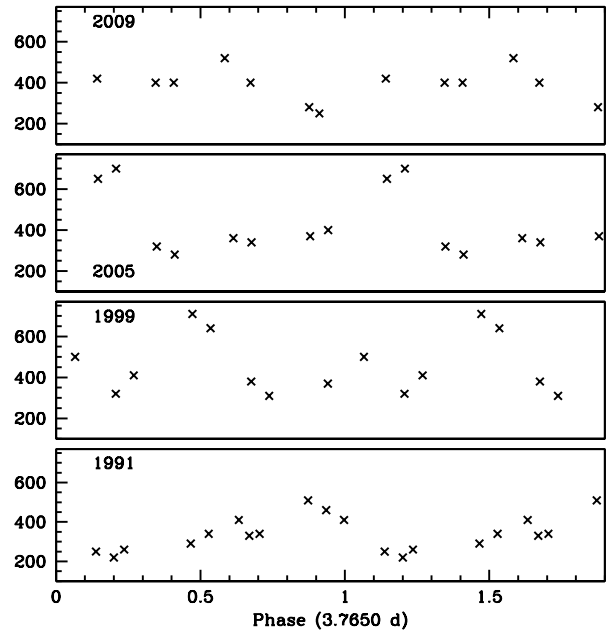

Fig. 10. Opacity parameter X_2 from the line-fits plotted as a function of 3.7650 d phase for each of the 4 observation epochs. A modulation is present in each epoch, but it is not coherent from one opoch to the next. Same data are plotted twice.

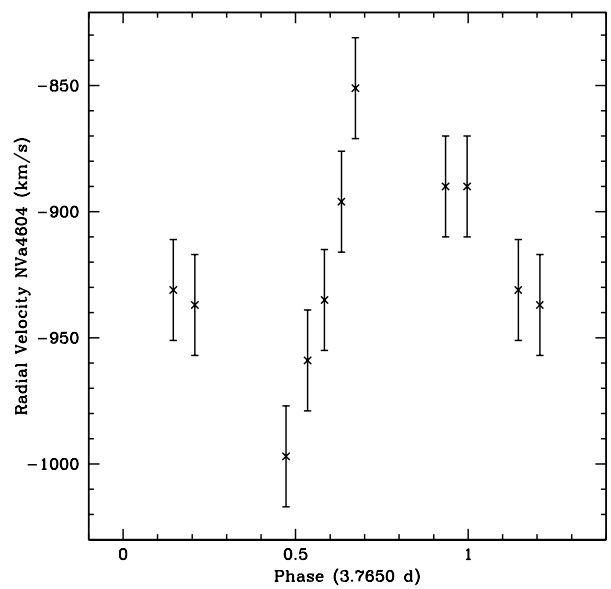

Fig. 11. Radial velocity variations of the N V 4604 P Cygni absorption component in the *strong* profiles plotted as a function of the 3.7650 d phase. A coherent variation over the 18 years of observations covered by these spectra is present.

TABLE 5

PROFILE TYPES IN GROUPS OF FOUR[a]

Epoch	Type				X_2				X_3			
	s	a	–	w	510	250	–	330	18	130	–	58
1991	s	a	w	w	460	220	290	340	20	130	78	58
	s	a	w	–	390	260	340	–	37	120	60	–
	–	a	a	a	–	380	370	320	–	210	160	180
1999	s	a	–	a	710	310	–	410	60	220	–	180
	s	–	w	–	640	–	500	–	40	–	70	–
	–	a	w	a	–	320	360	370	–	140	75	110
2005	s	a	w	w	650	270	360	400	20	140	33	93
	s	–	–	–	700	–	–	–	8	–	–	–
	–	–	–	w	–	–	—	400	–	–	–	73
2009	s	a	w	w	520	280	420	400	20	140	90	60
	s	a	–	–	400	250	–	–	45	110	–	–

[a]Columns 2–5: Same information as given in Table 3 but here organized in sets of four sequential nights per row. For all epochs there is a sequence: *s* (day 1) → *a* (day 2) → *w/a* (days 3 and 4). Second block of 4 columns: opacity parameter X_2 from the line fits; third block of 4 columns: opacity parameter X_3.

Given the above results we are led to conclude that the wind cycles through different opacity states over the 3.76 d period. These different states may be due to variations in the excitation/ionization structure or in the mass-loss rate, or a combination of the two. Such variations could be a consequence of pulsations in the underlying core. Piceno (2003) found periodic variation in the equivalent width of He II 4541 on timescales of 0.023 d, 0.044 d and 0.43 d on different nights of observation in the 1991 SPM data set, but not in the whole set of data, thus leaving an open question on the presence of possible non-radial pulsations. The precise mechanism by which the pulsations couple to the wind is still another open question (Townsend 2007).

An intriguing result concerns the radial velocity variations of the P Cygni absorption component of the *s* profiles. The centroid of these features was measured with a Gaussian fit from the location where the absorption meets the continuum level on the "blue" to the position of the emission component where the velocity is -500 km s^{-1}. In Figure 11 the derived RVs from the nine *s*-type profiles obtained over the 18 years of observation are plotted as a function of the 3.76 d phase computed with the Georgiev et al. (1999) ephemeris. The error bars correspond to the measurement uncertainties, estimated to be ± 30 km s^{-1}. This figure shows a clear modulation. Thus, although the data points are too few for a strong conclusion to be drawn, this result does suggest the presence of an underlying "clock" that retains coherence over very long timescales. It also indicates that it may be necessary to use only the *s* profiles to study the source of the "clock".

6. DISCUSSION AND CONCLUSIONS

In this paper we used the N V 4604 line observed in HD 50896 spectra obtained over 18 years to explore the possible wind structure variations that may lead to the observed changes in the shape of this line. We find that the variability in the P Cygni absorption component can be explained in terms of changes in the opacity structure of the wind. Specifically, changes in the relative opacities in regions $R_2 \sim 0.47\ R_{\rm max}$ and $R_3 \sim 0.65\ R_{\rm max}$, where $R_{\rm max}$ is the maximum extent of the N V 4604 line-forming region. Both these regions lie in the accelerating portion of the wind, according to the linear velocity law used to fit the profiles. The *strong* P Cygni absorptions are visible when the opacity in region R_2 is larger than in R_3. When this ratio is inverted, the P Cygni absorptions vanish. Evidence of opacity enhancements has previously been found in other objects, such as the O7.5-star 68 Cyg (Prinja & Howarth 1988).

The temporal sequence for the appearance of the profiles is such that a profile with a strong P Cygni absorption is followed one night later by one in which

the absorption is absent. On the following two nights the profile may have either a weak or an absent absorption. On only one occasion (epoch 1991) there are *strong* profiles on two consecutive nights. Since the opacity depends on the mass-loss rate and on the ionization structure of the wind, its variation implies changes in these parameters.

The terminal velocity of HD 50896 is estimated at -1900 km s^{-1} (Prinja, Barlow, & Howarth 1990; Howarth & Schmutz 1992). However, St-Louis et al. (1993) report that the most conspicuous absorption-line variability takes place between about -1800 and -2800 km s^{-1} for the major UV P Cygni lines. This implies that most of the variability occurs at speeds exceeding the normal maximum outflow velocity of the wind. The N V 4604 line does not provide information on these very large speeds, but it does tell us that the instability appears to be present at lower speeds as well. Given that UV lines arise from atomic transitions that are more optically thick, they are able to probe lower density regions of the wind. Such low density regions having high velocities are predicted to occur as a result of radiative instabilies (Owocki, Castor, & Rybicki 1988). Thus, the *absent* type N V 4604 profiles may occur when the radiative instabilities are more prevalent. We speculate that the *strong* type profiles might correspond to a more stable state of the wind, when fewer shocks are present. St-Louis et al. (1993) also concluded that the radiative instabilities probably play an important role in governing the line-profile variations that are observed in the UV.

One intriguing aspect of these perturbations is that significant changes in the line-profiles are observed on timescales of $\sim$1 day and no shorter. St-Louis et al. (1993) show how the UV P Cygni lines undergo changes on a day-to-day timescale. This is in contrast with, for example, the opacity enhancements mentioned above for 68 Cyg, where variations on timescales as short as 1 hr were observed (Prinja & Howarth 1988). Also relevant to this discussion is the presence of relatively narrow emission-like features ("sub-peaks") superposed on the broad He II emission lines. Variable sub-peak structure in WR stars is generally associated with the presence of an inhomogeneous stellar wind. However, Drissen et al. (1989) concluded from their polarimetric data that the smaller-scale "blob" activity observed in other WRs is quite low in HD 50896. Hence, the variability of HD 50896 seems to originate in what might be described as organized episodes of unstable and stable states, rather than the random-like inhomogeneities that are present in many other WRs. Also important to note is that at least one other WN-type star, WR1 (HD 4004) displays a variability similar to that of HD 50896 (Flores et al. 2007), so HD 50896 is not unique (see, also, St-Louis et al. (2009) for a discussion of varibility in several other WR stars). Also, in the WN5 binary V444 Cygni, the N V 4603-21 doublet undergoes phase-dependent variations qualitatively similar to those of HD 50896. Specifically, the P Cygni absorptions are deepest during one orbital phase interval (primary eclipse), becoming weaker in the neighborhood of the secondary minimum, and disappearing completely at secondary eclipse (Münch 1950). This suggests that the weak P Cygni absorptions are indicative of a perturbed wind structure[8] which, in the case of V444 Cyg, probably results from a combination of irradiation and surface distortion due to tidal effects. In the case of HD 50896, the profiles with an absent P Cygni absorption are more prevalent than in V444 Cyg, indicating that the perturbation causing the absorption to vanish occurs more frequently.

The model we have applied to fit the line profiles is one based on the simplest set of assumptions; that is, we assume that the line profile variability is caused by variations in the wind properties, specifically, the opacity. Because we fit only the blue wing of the line profile, our conclusion applies, strictly speaking, primarily to the column of wind that is projected onto the continuum-emitting core. Hence, we are unable to distinguish between a cyclical (in time) variation of the entire wind structure and the variations that would be caused by different zones of the stellar wind (each with different properties) entering and leaving our line-of-sight due to stellar rotation.

Matthews et al. (1992) suggested a model consisting of two oppositely-directed jets, emerging at an angle with respect to the observer's line-of-sight. They suggested that as the star rotates, the jets would alternately come into and out of the line-of-sight, thus producing the observed variability. Although the origin of such jets remains obscure, the general concept of a quadrupole-like wind structure may have a physical basis. Koenigsberger, Moreno, & Harrington (2010) proposed that the perturbations produced by the tidal forces in the eccentric binary system HD 5980 could lead to a variable wind structure as the system goes from periastron to apastron. Furthermore, since the tidal effects are stronger in the quadrant facing the companion than in the adjacent quadrants, the tidal perturbations

[8]The absent absorptions are attributed to the physical eclipse by Marchenko et al. (1997).

could, in principle, lead to a quadrupole-like wind distribution, independently of the eccentricity of the orbit. Demonstrating that a quadrupolar wind distribution in a rotating star reproduces the observed line-profile variations requires the use of a model that allows for departures from spherical symmetry.

In conclusion, we find that the N V 4604 line-profile variability may be understood in terms of a variable wind structure which involves changes in the N V opacity. The mechanism causing this variability remains to be determined.

GK acknowledges support from PAPIIT/Universidad Nacional Autónoma de México grant and computing support from Ulises Amaya. AF acknowledges the sabbatical stay in the INAOE and support from Conacyt under the target financed project 121166 "Spectroscopy Variations of Wolf-Rayet Stars", and by the UNACAR grant 1320.

REFERENCES

Auer, L. H., & Koenigsberger, G. 1994, ApJ, 436, 859
Cherepashchuk, A. 1981, MNRAS, 194, 755
Crowther, P. 2007, ARA&A, 45, 177
Drissen, L., Robert, C., Lamontagne, R., Moffat, A. F. J., St-Louis, N., van Weeren, N., & van Genderen, A. M. 1989, ApJ, 343, 426
Firmani, C., Koenigsberger, G., Bisiacchi, G. F., Moffat, A. F. J., & Isserstedt, J. 1980, ApJ, 239, 607
Firmani, C., Koenigsberger, G., Bisiacchi, G. F., Ruiz, E., & Solar, A. 1979, in IAU Symp. 83, Mass Loss and Evolution of O-Type Stars, ed. P. S. Conti & C. W. H. de Loore (Dordrecht: Reidel), 421
Flores, A., Koenigsberger, G., Cardona, O., & de la Cruz, L. 2007, AJ, 133, 2859
Georgiev, L. N., Koenigsberger, G., Ivanov, M. M., St.-Louis, N., & Cardona, O. 1999, A&A, 347, 583
Hillier, D. J. 1988, ApJ, 327, 822
Howarth, I. D., & Schmutz, W. 1992, A&A, 261, 503
Koenigsberger, G., Moreno, E., & Harrington, D. M. 2010, in ASP Conf. Ser. 425, Hot and Cool: Bridging Gaps in Massive Star Evolution, ed. C. Lietherer, P. Bennett, & J. van Loon (San Francisco: ASP), 209
Lamontagne, R., Moffat, A. F. J., & Lamarre, A. 1986, AJ, 91, 925
Marchenko, S. V., Moffat, A. F. J., Eenens, P. R. J., Cardona, O., Echevarría, J., & Hervieux, Y. 1997, ApJ, 485, 826
Matthews, J. M., St.-Louis, N., Moffat, A. F. J., Drissen, L., Koenigsberger, G., Cardona, O., & Niemela, V. S. 1992, in ASP Conf. Ser. 22, Nonisotropic and Variable Outflows from Stars, ed. L. Drissen, C. Leitherer, & A. Nota (San Francisco: ASP), 130
McLean, I. S. 1980, ApJ, 236, L149
Morel, T., St-Louis, N., Moffat, A. F. J., Cardona, O., Koenigsberger, G., & Hill, G. M. 1998, ApJ, 498, 413
Münch, G. 1950, ApJ, 112, 266
Owocki, S. P., Castor, J. I., & Rybicki, G. B. 1988, ApJ, 335, 914
Piceno, A. 2003, M. Sc. Thesis, INAOE, Puebla, Mexico
Prinja, R. K., Barlow, M. J., & Howarth, I. D. 1990, ApJ, 361, 607
Prinja, R. K., & Howarth, I. D. 1988, MNRAS, 233, 123
Skinner, S. L., Itoh, M., & Nagase, F. 1998, New Astron., 3, 37
Skinner, S. L., Zhekov, S. A., Güdel, M., & Schmutz, W. 2002, ApJ, 579, 764
Stevens, I. R., & Willis, A. J. 1988, MNRAS, 234, 783
St-Louis, N., Chené, A.-N., Schnurr, O., & Nicol, M.-H. 2009, ApJ, 698, 1951
St-Louis, N., Howarth, I. D., Willis, A. J., Stickland, D. J., Smith, L. J., Conti, P. S., & Garmany, C. D. 1993, A&A, 267, 447
Townsend, R. 2007, in AIP Conf. Proc. 948, Unsolved Problems in Stellar Physics, ed. R. Stancliffe, G. Houdek, R. Martin, & C. Tout (Melville, NY: AIP), 345
van den Heuvel, E. P. J. 1976, in IAU Symp. 73, Structure and Evolution of Close Binary Systems, ed. P. Eggleton, S. Mitton, & J. Whelan (Dordrecht: Reidel), 35
van der Hucht, K. A., Conti, P. S., Lundstrom, I., & Stenholm, B. 1981, Space Sci. Rev., 28, 227
Vázquez, G. 2003, M. Sc. Thesis, INAOE, Puebla, Mexico

O. Cardona: Instituto Nacional de Astrofísica Óptica y Electrónica, Luis Enrique Erro 1, Tonantzintla, Puebla, Mexico (ocardona@inaoep.mx).
L. de la Cruz and A. Flores: Facultad de Ingeniería, Universidad Autónoma del Carmen, Calle 56, 4. Cd. del Carmen, Campeche, Mexico (aflores, ldelacruz@pampano.unacar.mx).
G. Koenigsberger: Instituto de Ciencias Físicas, Universidad Nacional Autónoma de México, Ave. Universidad S/N, Col. Chamilpa, Cuernavaca 62210, Mexico (gloria@fis.unam.mx).

Revista Mexicana de Astronomía y Astrofísica, **47**, 277–288 (2011)

VARIABLE JETS WITH NON-TOP HAT EJECTION CROSS SECTIONS: A MODEL FOR THE KNOTS OF THE HH 34 JET

A. C. Raga,[1] A. Noriega-Crespo,[2] P. Kajdic,[3] F. De Colle,[4] D. López-Cámara,[1] and A. Esquivel[1]

Received 2010 December 15; accepted 2011 May 9

RESUMEN

Calculamos modelos axisimétricos, con una variación sinusoidal (de un modo) y un perfil de sección recta inicial de velocidad. Encontramos que para cocientes de velocidad borde a centro decrecientes, uno obtiene superficies de trabajo con choques de proa con alas progresivamente más extendidas. Estas alas producen emisión de [S II] que parcialmente llena las regiones entre los nudos en los mapas de emisión predichos. Luego calculamos modelos de 3 modos (con parámetros apropiados para el chorro HH 34), y comparamos los mapas de emisión predichos con imágenes del archivo del HST de HH 34. Encontramos que un modelo con cociente de velocidades borde a centro moderado produce estructuras de nudos con morfologías y variabilidades temporales muy parecidas a las observadas en HH 34.

ABSTRACT

We compute axisymmetric, single-sinusoidal mode variable ejection models with a non-top hat ejection velocity cross section. We find that for decreasing edge-to-center velocity ratios one obtains internal working surfaces with progressively more extended bow shock wings. These wings produce [S II] emission which partially fills in the inter-knot regions in predicted intensity maps. We then compute 3-mode models (with parameters appropriate for the HH 34 jet), and compare predicted intensity maps with archival HST images of HH 34. We find that a model with a moderate edge-to-center velocity ratio produces knot structures with morphologies and time-variabilites with clear similarities to the observations of HH 34.

Key Words: ISM: jets and outflows — ISM: kinematics and dynamics — stars: mass-loss — stars: pre-main sequence

1. INTRODUCTION

Rees (1978) first suggested that a variability in the ejection might be responsible for the structure observed in extragalactic jets. This idea was then pursued numerically by Wilson (1984), who modeled extragalactic jets with "twin-lobe" structures.

Raga et al. (1990) proposed an ejection variability as a mechanism for explaining the chains of knots observed along HH jets such as HH 34 (Reipurth et al. 1986) and HH 111 (Reipurth 1989). This proposed model was strengthened by the fact that later ground-based (Reipurth & Heathcote 1992; Reipurth, Raga, & Heathcote 1992) and HST images (Reipurth et al. 2002, 1997) showed that some of the knots along the HH 34 and HH 111 jets have bow-like morphologies.

This model has been explored analytically (e.g., Cantó, Raga, & D'Alessio 2000) and numerically (e.g., De Colle, Raga, & Esquivel 2008). Different effects in variable ejection jets have been studied, such as:

- different forms of the ejection variability (Hartigan & Raymond 1993; Tesileanu et al. 2009),
- the added presence of a precession (Raga & Biro 1993; Smith & Rosen 2005),
- variable jets with magnetic fields (Gardiner & Frank 2000; De Colle et al. 2008),
- variable jets in a sidewind (Esquivel et al. 2009).

[1]Instituto de Ciencias Nucleares, Universidad Nacional Autónoma de México, Mexico.
[2]Spitzer Science Center, California Institute of Technology, CA, USA.
[3]Instituto de Geofísica, Universidad Nacional Autónoma de México, Mexico.
[4]Astronomy and Astrophysics Department, University of California, Santa Cruz, CA, USA.

In the present paper, we focus on the effect on a variable ejection jet of a non-top hat ejection velocity cross section. An analytic model for the effect of a centrally peaked ejection velocity cross section was presented by Raga, Cantó, & Cabrit (1998). These authors show that for decreasing edge-to-center ejection velocity ratios the internal working surfaces (resulting from the ejection time-variability) become progressively more curved. This effect might produce emitting knots with a closer resemblance to some of the bow-shaped knots observed in HH jets.

Some numerical simulations of variable ejection jets have incorporated a non-top hat ejection velocity cross section. For example, Völker et al. (1999) used a quadratic ejection velocity cross section with a factor of 1/2 edge-to-center velocity ratio in variable ejection models. Some of the more recent papers of this group also describe models which incorporate a (presumably quadratic) non-top hat ejection velocity cross section (Rosen & Smith 2003, 2004; Smith & Rosen 2005) with a edge-to-center velocity ratio of 0.7 or 0.8. Dennis et al. (2008) present constant ejection jet models with a quadratic ejection velocity cross section with an edge-to-center ratio of 0.9. Raga et al. (1998) describe an analytic model for leading and internal working surfaces in jets with arbitrary ejection (density and velocity) cross sections, but only present a single numerical simulation of the leading head of a jet with a quadratic velocity cross section with an edge-to-center velocity ratio of 0.8. Raga et al. (2009) also computed variable jet models with a quadratic velocity cross section, and find that even jets with an edge-to-center velocity ratio of 0.8 differ substantially from initially top hat jets. Finally, the paper of Frank et al. (2000) appears to be the only study of a jet with a non-quadratic radial dependence of the ejection velocity. Somewhat surprisingly, a systematic numerical study of the effect on variable jets of different edge-to-center ejection velocity ratios has not yet been made.

In this paper, we present a set of eight axisymmetric, variable jet models (with a sinusoidal ejection variability) in which we explore the effect of varying the edge-to-center ejection velocity ratio. In order to illustrate the possible relevance of non-top hat cross sections for modelling HH jets, we then present a comparison between intensity maps predicted from the models and red [S II] images of the HH 34 jet.

For this purpose, we compute non-top hat, ejection models with the three-mode sinusoidal variability empirically determined for HH 34 by Raga et al. (2002). We explore a set of different edge-to-center ejection velocity ratios, and compare the predicted intensity maps with archival HST images of the HH 34 jet.

The paper is organized as follows. In § 2, we give a short description of the archival HST images of HH 34. In § 3, we describe the single-mode, non-top hat jet models. In § 4, we compare the intensity maps predicted from non-top hat, three-mode models with the HST images of HH 34. Finally, the results are summarized in § 5.

2. THE ARCHIVAL HST IMAGES OF HH 34

The *Hubble Space Telescope* (HST) Wide Field Planetary Camera 2 (WFPC2) data of HH 34 have been retrieved from the *Hubble Legacy Archive* (HLA), for two epochs (1998 & 2007). The processing of the HLA data uses a new calibration pipeline that includes an improved handling of the UV contamination, bias variations and other artifacts[5]. Furthermore, the WFPC2 HLA data have been resampled onto a uniform grid to correct for geometric distorsions, an essential step to determine, for instance, the proper motions of knots along the jet between the two epochs.

The 1998 images were described in detail by Reipurth et al. (2002). The HH 34 archival images from 2007 to our knowledge have not been presented anywhere, and we therefore describe them briefly. The data were obtained during the HST Cycle 16 (October 30, 2007) and belong to program 11179 (PI. P. Hartigan) on the dynamics of clumpy supersonic flows in stellar jets. Like in the 1998 observations (Reipurth et al. 2002) the data were obtained using the standard WFPC2 narrow band filters of Hα (F656N) and [S II]λ 6716+30 (F673N). The final images are the result of multiple co-added exposures (eight for both Hα & [S II]) which are used to mitigate the effects of cosmic rays, and with a total integration time of 9600 sec for each filter.

3. NON-TOP HAT, SINGLE MODE JETS

We have computed a set of models with a time-dependent ejection velocity of the form:

$$v_j(r,t) = \left[v_0 + v_1 \sin\left(\frac{2\pi t}{\tau}\right)\right]\left[1-(1-\sigma)\left(\frac{r}{r_j}\right)^2\right], \quad (1)$$

where t is the time, r is the cylindrical radius (measured across the initial cross secion of the jet), v_0 is the mean axial velocity of the jet, v_1 is the half-amplitude of the axial velocity variability and $\sigma = v_{\rm edge}/v_{\rm axis}$ is the ratio between the ejection velocity at the edge of the jet ($v_{\rm edge}$, at $r = r_j$) and

[5]See e.g. `http://hla.stsci.edu/hla_faq.html#WFPC2`.

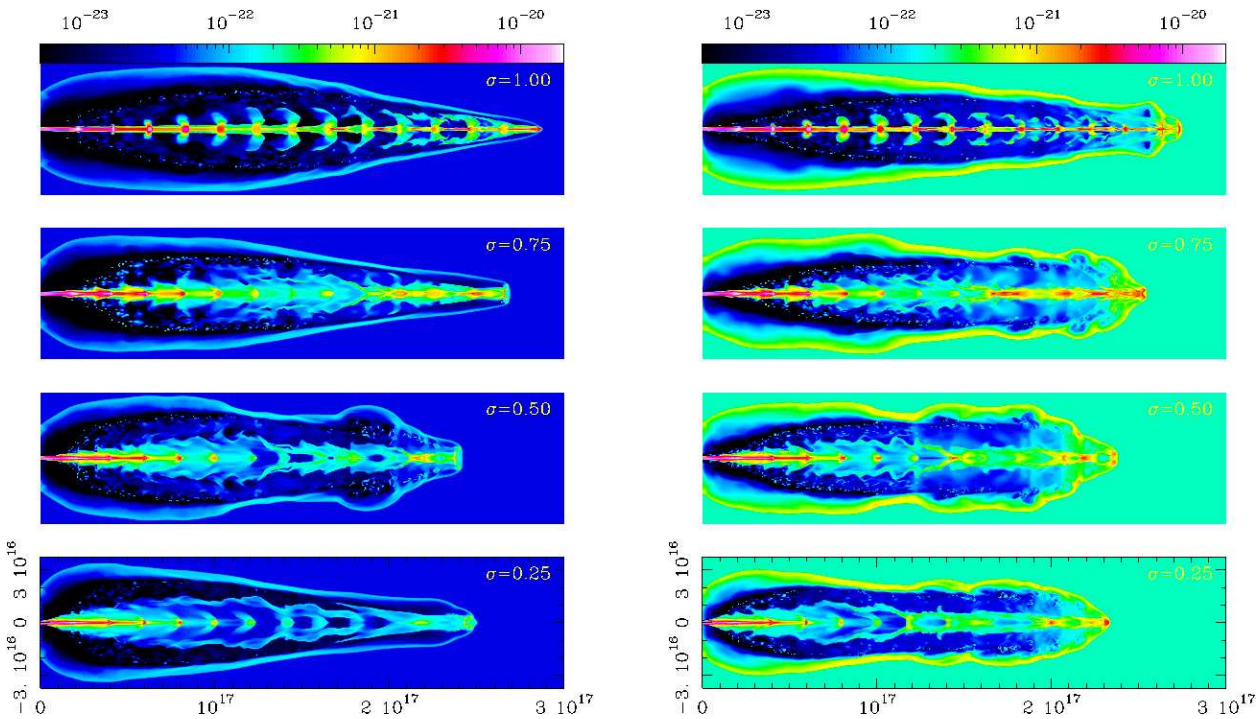

Fig. 1. Density stratifications obtained from the single-sinusoidal mode variable jet models (see § 3). The models of jets moving into an environment with $n_a = 15$ cm^{-3} are shown at $t = 350$ yr integration time (left column) and the models with $n_a = 100$ cm^{-3} are shown at $t = 400$ yr (right column). The results are labeled with the value of σ (the edge-to-center ejection velocity ratio) of each model. The full computational domain is shown on both sides of the symmetry axis (the axes are labeled in cm). The densities are depicted with the logarithmic color scheme given (in g cm^{-3}) by the top bar. The color figure can be viewed online.

the velocity along the jet axis ($v_{\rm axis}$, at $r = 0$). In other words, the ejection velocity has a single-mode, sinusoidal ejection velocity variability, and a center-to-edge, quadratic radial dependence.

When calculating variable ejection jet models, it is of course possible to include a time-variability in the initial density and/or temperature of the jet. Such variabilities, however, lead to the production of shocks with velocities of the order of the initial sound speed (typically of $\approx$ a few km s^{-1} for HH jets). Because of this, if one wants to model the emission along HH jets (which is formed in shocks with velocities $\sim$10 $\rightarrow$ 100 km s^{-1}), it is clear that an ejection velocity variability with a highly supersonic amplitude has to be included.

We have run two sets of four models (each set corresponding to environments with different densities, see below) with edge-to-center ejection velocity ratios $\sigma = 1.0$ (top hat), 0.75, 0.5 and 0.25. The models have the same ejection variability, with $v_0 = 250$ km s^{-1}, $v_1 = 30$ km s^{-1} and $\tau = 30$ yr. The ejection density and temperature have top-hat profiles with $n_j = 5000$ cm^{-3} and $T_j = 1000$ K (respectively). For the surrounding, homogeneous environment, we have considered a $T_a = 1000$ K temperature, and two possible densities: $n_a = 15$ and 100 cm^{-3}. It is assumed that both the jet and the environment are initially neutral except for C and S, which are assumed to be singly ionized. The jets have a $r_j = 10^{15}$ cm initial radius.

The gas-dynamic equations are integrated together with a set of rate equations for H, He, C, N, O and S ions, with an axisymmetric version of the "yguazú-a" adaptive grid code. The resulting, non-equilibrium ionization has been used to compute the energy loss term (included in the energy equation). The version of the code used is identical to the one described in detail by Kajdic, Velázquez, & Raga (2006) and by Raga et al. (2007). For the present calculations, we use a 6-level, binary adaptive grid which would fill the domain with 4096×512 (axial $\times$ radial) points at the highest grid resolution. The cylindrical domain has an on-axis reflection condition, an inflow condition for $r \leq r_j$ and a reflection condition for $r > r_j$ on the injection ($x = 0$) plane, and outflow conditions at the remaining two bound-

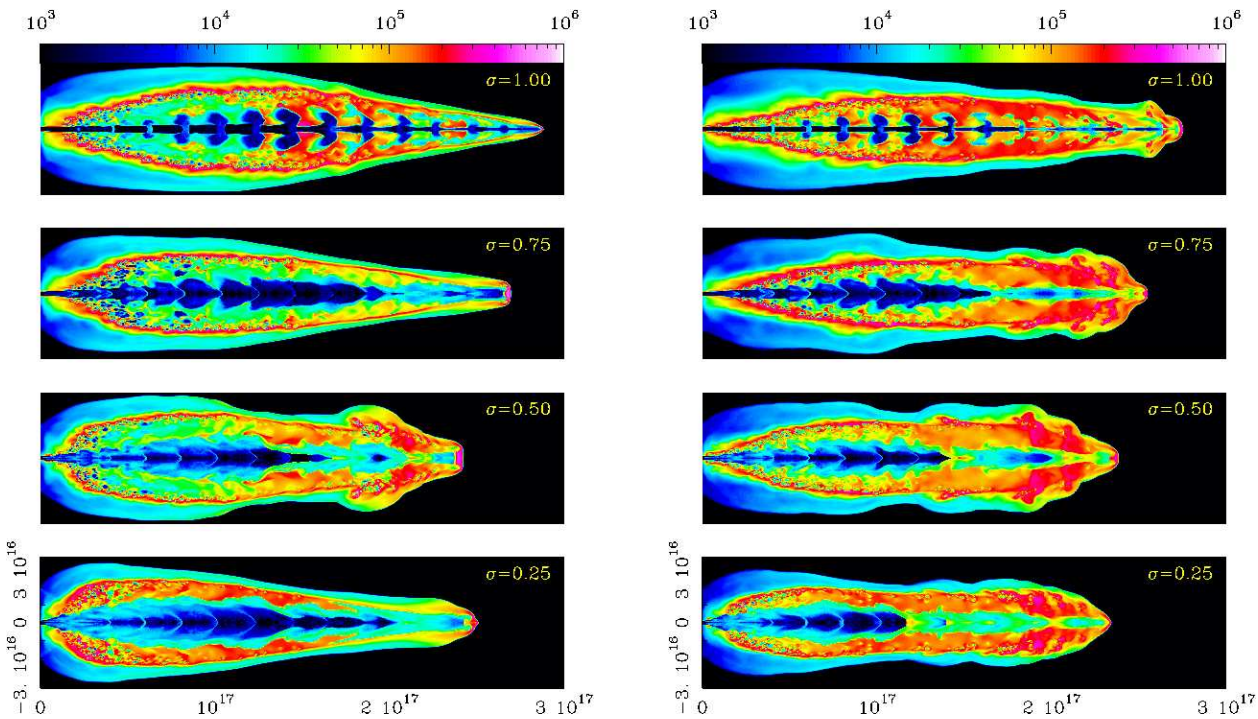

Fig. 2. Temperature stratifications obtained from the single-sinusoidal mode variable jet models (see § 3). The models of jets moving into an environment with $n_a = 15$ cm^{-3} are shown at a $t = 350$ yr integration time (left column) and the models with $n_a = 100$ cm^{-3} are shown at $t = 400$ yr (right column). The results are labeled with the value of σ (the edge-to-center ejection velocity ratio) of each model. The temperatures are depicted with the logarithmic color scheme given (in K) by the top bar. The color figure can be viewed online.

aries of the $(30, 3.75) \times 10^{16}$ cm (axial × radial) computational domain.

The density and temperature stratifications obtained from the four $n_a = 15$ cm^{-3} models after a $t = 350$ yr time-integration and the four $n_a = 100$ cm^{-3} models at $t = 400$ yr are shown in Figures 1 and 2. The models show a leading jet head and a series of travelling "internal working surfaces" (IWS) which are formed as a result of the ejection time-variability.

We first note that the knots within $\approx 10^{17}$ cm from the source have very similar structures in the $n_a = 15$ and 100 cm^{-3} models. From this, we conclude that the precise value of the environmental density does not have a strong effect on the sequence of knots close to the outflow source (see Figures 1 and 2). It is clear, however, that the value of n_a does have (as expected) an important effect on the structure and propagation of the leading head of the jet.

On the other hand, it is clear from Figures 1 and 2 that the value chosen for the edge-to-center ejection velocity ratio σ does have a strong effect on the structure of the IWS. For $\sigma = 1$, the working surfaces have compact, dense regions within the jet beam, which eject low density material out into the cocoon of the jet. For lower values of σ, the IWS have clear, bow-shaped morphologies, with densities that fall away from the symmetry axis (see Figure 1).

The value of σ also has a strong effect on the resulting temperature stratifications. For $\sigma = 1$, a relatively hot cocoon (with $T \sim 3 \rightarrow 20 \times 10^4$ K) is in contact with the jet beam. For lower values of σ, a lower temperature region (with $T \sim 10^4$ K) buffers the jet beam from the hot cocoon (this cool region is most clearly seen in the $\sigma = 0.25$ model, see Figure 2).

In Figure 3, we show the [S II] 6716+6730 emission maps predicted from the four $n_a = 15$ cm^{-3} models for $t = 350$ yr. These maps have been computed solving the appropriate 5-level atom problem, and integrating the resulting emission coefficient along lines of sight. It has been assumed that the outflow axis lies on the plane of the sky.

The maps shown in Figure 3 display the region close to the outflow source. It is clear that for $\sigma = 1$ the emission from the IWS is concentrated in compact "knots", with only very faint "wings" seen in

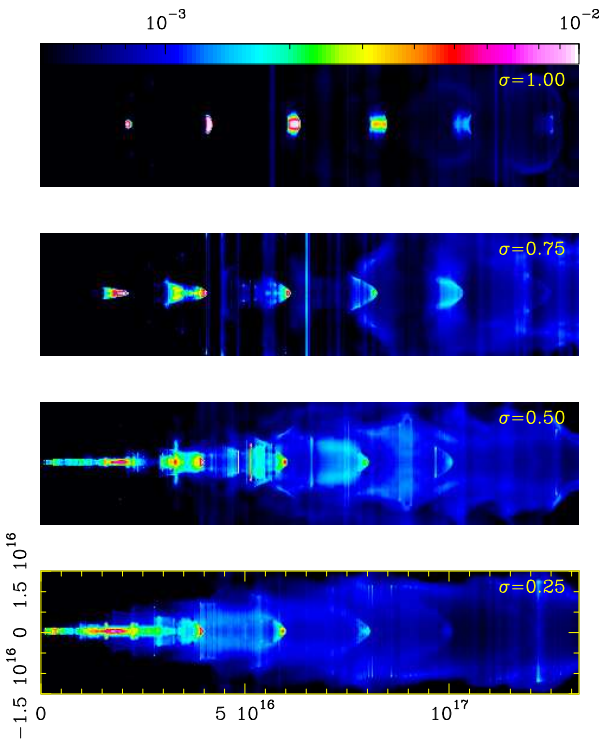

Fig. 3. [S II] 6716+30 intensity maps predicted from the four single-mode jet models with $n_a = 15$ cm^{-3} (see § 3) for a $t = 350$ yr integration time. The maps have been computed assuming that the outflow axis lies on the plane of the sky. Only a region close to the jet source is shown (compare with the full computational domain shown in Figures 1 and 2). The intensities are shown with a logarithmic color scheme given (in erg s^{-1} cm^{-2} sterad^{-1}) by the top bar. The color figure can be viewed online.

the knots with $x > 10^{17}$ cm. For lower values of σ, the emission knots have bow-wings of increasing intensity. The emission from these bow-wings partially fills in the gaps corresponding to the inter-knot regions (these gaps are clearly seen in the $\sigma = 1$ model, see Figure 3).

With these models we therefore show that the edge-to-center ejection velocity ratio σ has a strong effect on the morphology of the IWS (which results from the ejection velocity time-variability). For $\sigma = 1$ (i.e., for a top-hat jet, see equation 1), the [S II] emission of the IWS has a morphology of compact clumps, with low-emission gaps between the clumps. For lower values of σ, the emission from the IWS develops progressively more extended bow wings, which partially fill in the gaps between the successive knots. Therefore, by tuning the value of σ it is possible to produce knots with different morphologies, which could then be compared with the emission observed in specific HH jets. An attempt to do this is presented in the following section.

4. THREE-MODE MODEL FOR HH 34

Raga & Noriega-Crespo (1998) and Raga et al. (2002) proposed a three-mode ejection velocity variability for modelling the structure of the southern lobe of the HH 34 outflow. In particular, Raga et al. (2002) used radial velocity and proper motion observations of HH 34 to derive a variability of the form:

$$v_c(t) = v_0 + v_1 \sin\left(\frac{2\pi t}{\tau_1} + \phi_1\right) + v_2 \sin\left(\frac{2\pi t}{\tau_2} + \phi_2\right) + v_3 \sin\left(\frac{2\pi t}{\tau_3}\right), \quad (2)$$

with $v_0 = 270$ km s^{-1}, $v_1 = 70$ km s^{-1}, $\tau_1 = 1400$ yr, $\phi_1 = -0.80$ rad, $v_2 = 25$ km s^{-1}, $\tau_2 = 270$ yr, $\phi_2 = -0.85$ rad, $v_3 = 10$ km s^{-1} and $\tau_3 = 27$ yr. This function represents the past time-variability of the ejection of HH 34, with $t = 0$ representing the present time. Negative values of t represent the times at which the material presently observed along the HH 34 jet was ejected from the source.

We then choose an ejection velocity v_j with this three-mode variability, modulated with a quadratic center-to-edge profile:

$$v_j(r,t) = v_c(t)\left[1 - (1-\sigma)\left(\frac{r}{r_j}\right)^2\right], \quad (3)$$

where $v_c(t)$ is given by equation (2) and σ is the center-to-edge ejection velocity ratio (see equation 1).

Following Raga et al. (2002), we choose time-independent, top-hat ejection density and temperature cross sections with $n_j = 5000$ cm^{-3} and $T_j = 1000$ K (respectively), and a $r_j = 5 \times 10^{15}$ cm jet radius. The jet moves into a homogeneous environment with $n_a = 15$ cm^{-3} and $T_a = 1000$ K.

The computational domain has an (axial × radial) extent of $(16.8, 2.1) \times 10^{17}$ cm, resolved with 4096×512 grid points at the highest resolution of the 6-level, binary adaptive grid. The setup of the three-mode models is otherwise identical to the one of the single-mode models described in § 3.

We have then computed three models, with center-to-edge ejection velocity cross sections with $\sigma = 1$, 0.75 and 0.5. The simulations were all started at $t = -3000$ yr, and allowed to evolve until $t = 300$ yr.

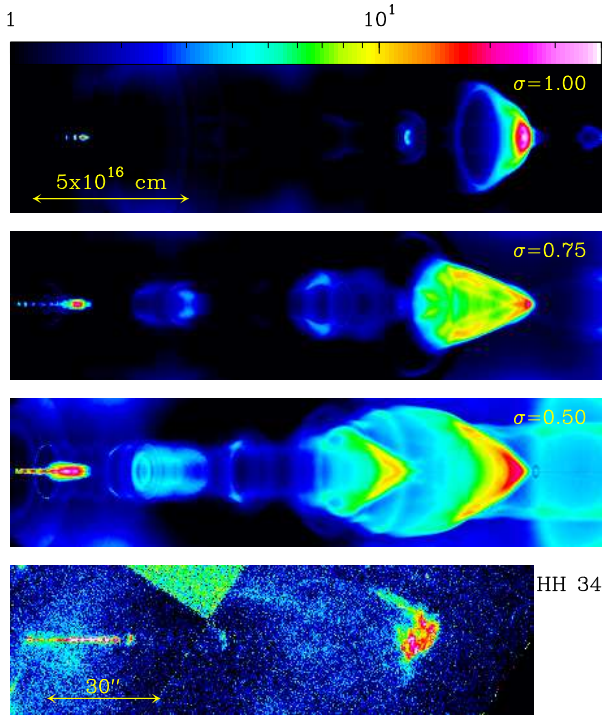

Fig. 4. [S II] 6716+30 intensity maps predicted from the three 3-mode jet models for a time $t = 0$ (the integration was started at $t = -3000$ yr, see § 4). The bottom frame shows the [S II] image obtained with the HST in 1998 (see § 2). The predicted maps have been computed assuming that the outflow axis lies at a 30° angle with respect to the plane of the sky (as appropriate for HH 34), and show a $(10.69, 2.67) \times 10^{17}$ cm domain. The HH 34 [S II] map has been scaled to the same scale as the predicted maps, assuming a distance of 450 pc (the displayed region has a vertical size of 39″.6). The source of HH 34 is on the left of the chain of aligned knots. The intensities are shown with a logarithmic color scheme covering a dynamic range of 40 (see the top bar), scaled so that in the four maps the brighter regions start to saturate at the highest depicted intensity. The color figure can be viewed online.

In Figure 4, we present the [S II] 6716+30 intensity maps predicted from these three models for $t = 0$ (i.e., for years ∼1990–1994 at which the data analyzed by Raga et al. 2002 were obtained). These maps were computed assuming a 30° angle between the jet axis and the plane of the sky, corresponding to the approximate orientation of the HH 34 outflow (see Heathcote & Reipurth 1992). Together with the predicted maps, we show an archival [S II] HST image of the southern lobe of the HH 34 outflow, rotated so that the outflow axis is parallel to the abscissa. The physical size of the domains of the synthetic and observed maps are identical (assuming a 450 pc distance to HH 34).

For all of the computed models, emission structures with a qualitative resemblance to HH 34 are obtained. The four models show a large bow shock at a distance from the source comparable to HH 34S, a chain of knots close to the source, and a few broader, faint condensations between the chain of knots and the large bow shock. These three main features are in qualitative agreement with the observed structure of the HH 34 jet.

It is clear from Figure 4 that the shape of the large bow shock is more flat-topped in the $\sigma = 1$ model than in the $\sigma = 0.75$ and 0.5 models, in which the bow shock has a more conical morphology. Also, in the $\sigma = 1$ model (presented previously by Raga et al. 2002), the [S II] emission from the chain of knots is fainter than the emission from the large bow shock. The $\sigma = 0.75$ and 0.5 models show a comparable peak [S II] emission in the main bow shock and in the brighter knots in the chain, in better qualitative agreement with the [S II] image of HH 34.

Figures 5, 6 and 7 show the time-evolution of the [S II] emission of the chain of knots for the $\sigma = 1$, 0.75 and 0.5 models (respectively), at 100 yr intervals. In the 300 yr time-sequence obtained from the $\sigma = 1$ model (Figure 5), we see either one or two groups of compact knots. The predicted emission is qualitatively different from the emission from the HH 34 jet (bottom panel), in which the inter-knot regions show considerably brighter emission. Also, some of the observed knots have bow shapes which are not seen in the maps predicted from the $\sigma = 1$ model.

The time-sequence of [S II] intensity maps obtained from the $\sigma = 0.75$ model (Figure 6) does show bow-shaped knots. The inter-knot regions show brighter emission, in better qualitative agreement with the HH 34 jet observation.

The emission maps obtained from the $\sigma = 0.5$ model show groups of knots having less contrast between the knot and inter-knot emission than the HH 34 jet. Because of this, we conclude that the $\sigma = 0.75$ model produces the best qualitative agreement with the structure of knots along the HH 34 jet. In the following, we therefore focus on the $\sigma = 0.75$ model.

In Figures 8 and 9 we show a sequence of intensity maps with a time-interval of 10 yr, together with the 1998 and 2007 HST [S II] images (see § 2). From these figures, it is clear that the knots along the HH 34 jets have changed quite strongly over a

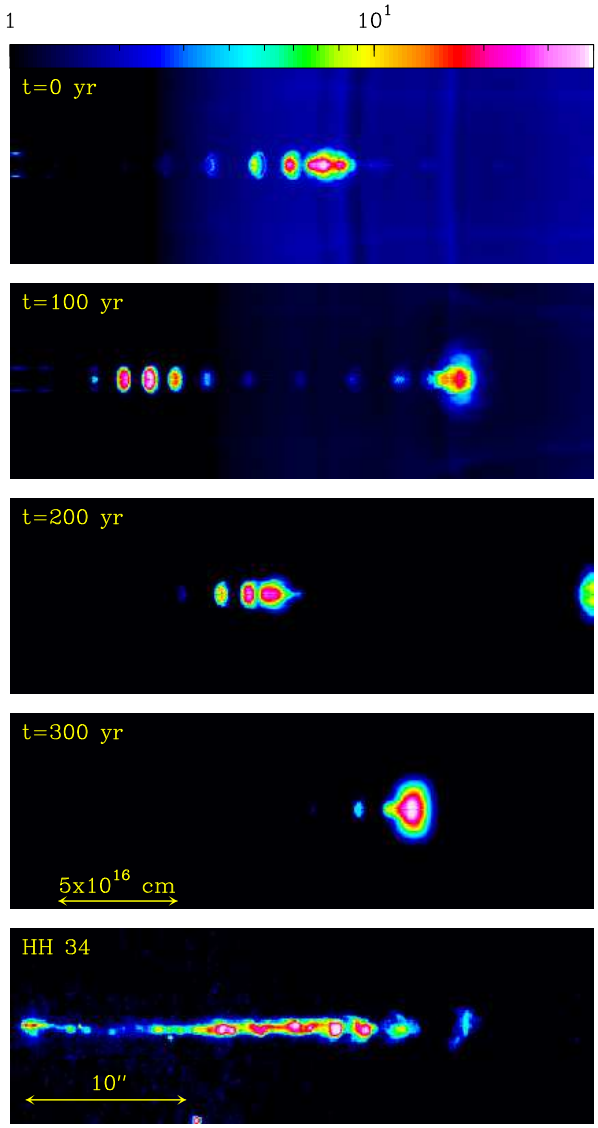

Fig. 5. [S II] 6716+30 intensity maps predicted from the $\sigma = 1$, 3-mode jet model for times $t = 0$, 100, 200 and 300 yr (the integration was started at $t = -3000$ yr, see § 4). The bottom frame shows the [S II] image obtained with the HST in 1998 (see § 2). The predicted maps have been computed assuming that the outflow axis lies at a 30° angle with respect to the plane of the sky (as appropriate for HH 34), and show a region with the source on the left and an axial extent of 2.46×10^{17} cm. The HH 34 [S II] map has been scaled to the same scale as the predicted maps, assuming a distance of 450 pc (the displayed region has a horizontal size of 36″.5). The intensities are shown with a logarithmic color scheme covering a dynamic range of 40 (see the top bar), scaled so that in the four maps the brighter regions start to saturate at the highest depicted intensity. The color figure can be viewed online.

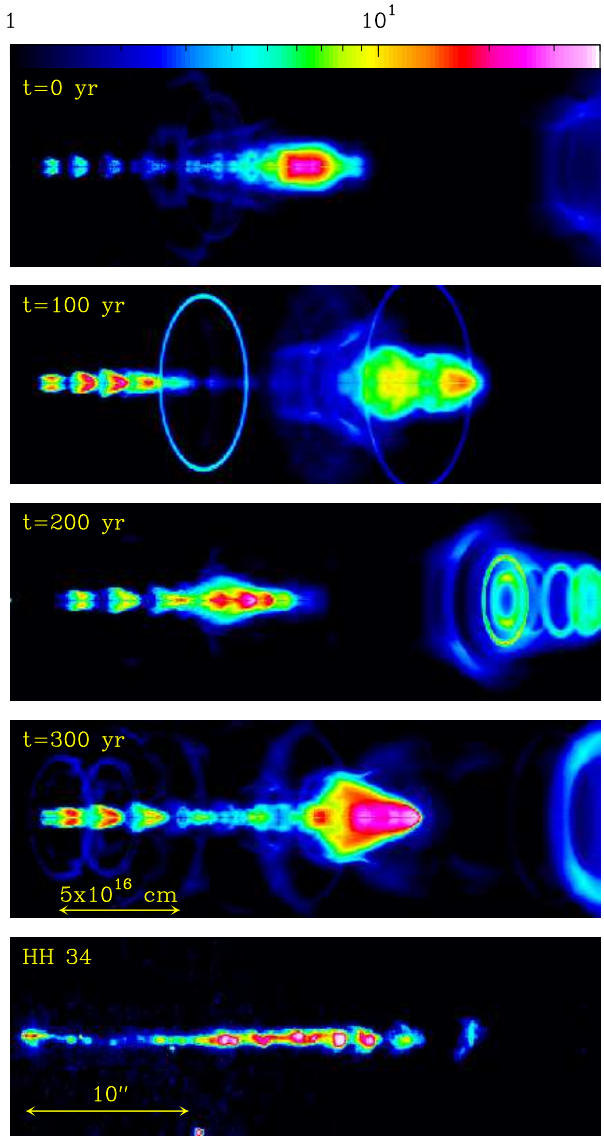

Fig. 6. The same as Figure 5 but for the $\sigma = 0.75$, 3-mode jet model (see § 4). The color figure can be viewed online.

13 yr time-span, with some of the knots becoming relatively fainter and other knots becoming brighter.

These changes are clearly seen in Figure 10, which shows intensity vs. position traces (obtained by integrating across the HH 34 jet and subtracting the adjacent background). It is clear that the $x < 2''$ region (where x is the distance from the source) has become considerably brighter, that the knots in the $10'' < x < 30''$ region have had clear variations (several of the knots having become fainter and others brighter).

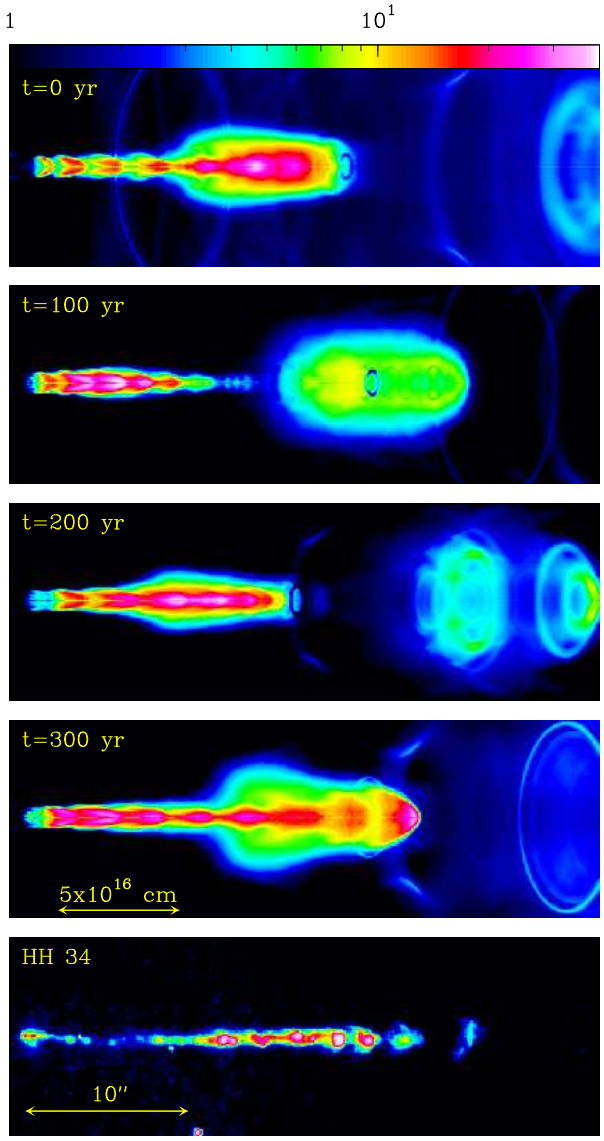

Fig. 7. The same as Figures 5 and 6 but for the $\sigma = 0.5$, 3-mode jet model (see § 4). The color figure can be viewed online.

In order to quantify these variations, we have defined segments along the [S II] tracings, incorporating the emission of the better defined knots. The positions and lengths of these segments were defined on the 1998 image (top frame of Figure 10), and were displaced 0″.7 in the $+x$ direction for calculating the knot intensities in the 2007 frame (except for the segment incorporating the emission around the outflow source, which was not displaced). This displacement corresponds to the average motion of the knots along the HH 34 axis between the two epochs (corresponding to a proper motion of ≈170 km s^{-1}, consistent with previous measurements of proper motions in this outflow). In the bottom frame of Figure 10, we plot the 2007/1998 intensity ratios for the successive knots (defined above), showing that some of the knots have had intensity variations of up to a factor of ∼2.

From Figures 8 and 9 we notice that intensity variabilities similar to the observed ones are also seen in the predicted intensity maps over 10–20 yr time-intervals. For example, from $t = -60$ to $t = -50$ yr and $t = -40$ yr we see that the main knots have intensity changes (with the brightest knot becoming fainter, and some of the other knots brighter). Also, a systematic brightening of the region close to the source is seen from the $t = 0$ to the $t = 60$ yr time-frames, with clear changes over each decade.

None of the predicted intensity maps show [S II] emission structures that one could even attempt to compare quantitavely with the HH 34 knots. However, it is clear that several of the time-frames from the model do show structures which resemble the observed knots (see Figures 8 and 9).

5. CONCLUSIONS

We have presented a systematic study of the effect of having a non-top hat velocity cross section in the ejection of a variable jet. We have chosen a parabolic velocity cross section, with an edge-to-center velocity ratio $\sigma = 0.25 \rightarrow 1.0$.

For a jet with a single-mode, sinusoidal ejection velocity variability (see equation 1), we find that for larger edge-to-center velocity contrasts (i.e., for lower σ values) the internal working surfaces develop bow shapes with progressively more extended wings. These bow wings appear as extensions to the [S II] emission from the knots, filling in the gaps between the knots (see Figure 3).

We then compute a model with the three sinusoidal modes deduced from observations of the HH 34 jet by Raga et al. (2002). We find that a model with $\sigma = 0.75$ produces a chain of knots close to the source which better resembles the HH 34 [S II] emission than models with $\sigma = 1$ (i.e., with a top-hat ejection cross section) and with $\sigma = 0.5$ (this model producing a chain of knots with a too low intensity contrast between the knots and the inter-knot regions).

Finally, we present a time-sequence of the [S II] emission of the knots predicted from the $\sigma = 0.75$, three-mode model, and compare the maps with two epochs of HST images of HH 34 (with a ≈10 yr time interval). We find that the model predicts knot structures with reasonable qualitative similarity to

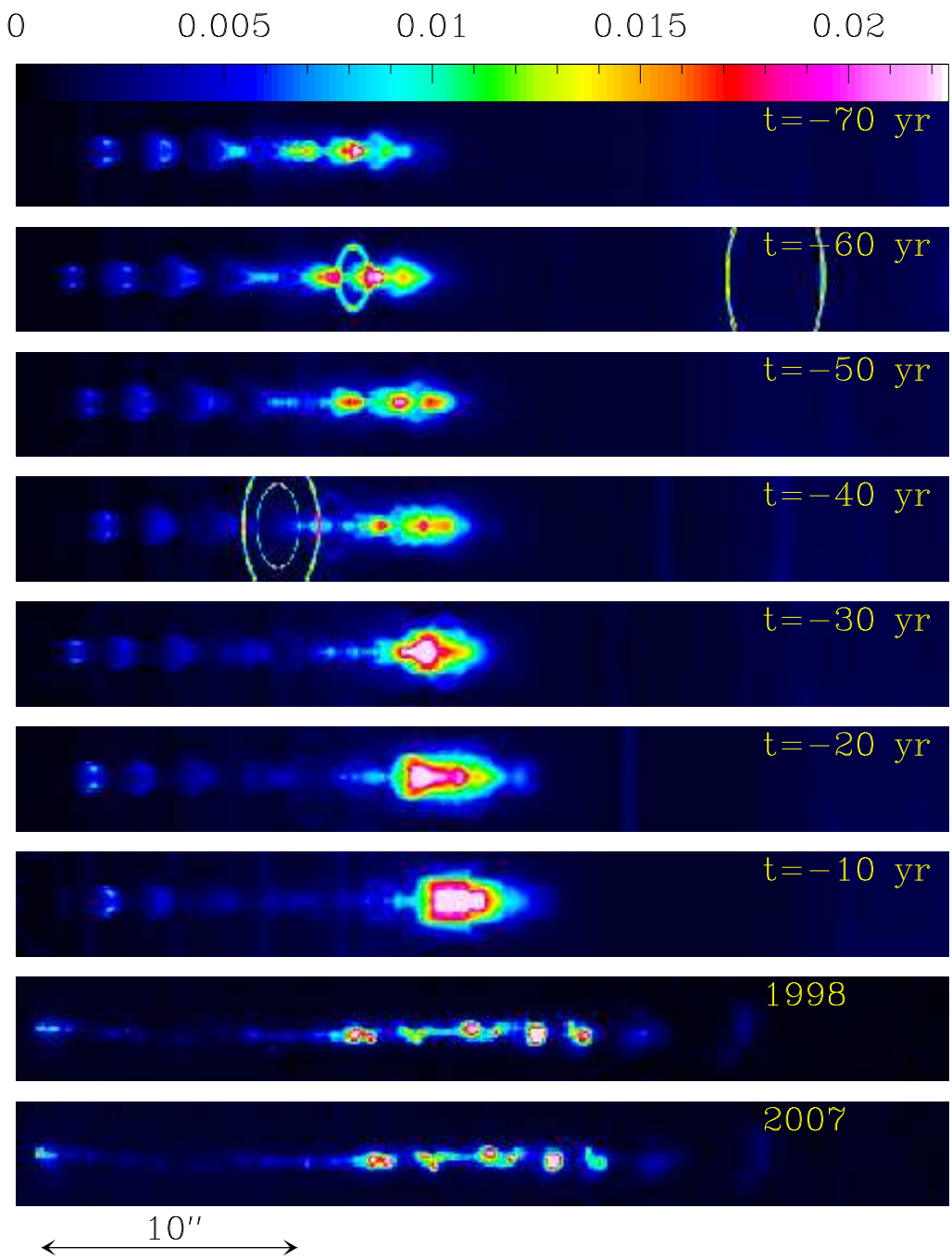

Fig. 8. [S II] 6716+30 intensity maps predicted from the $\sigma = 0.75$, 3-mode jet model for times $t = -70$ to -10 yr, at 10 yr intervals (the integration was started at $t = -3000$ yr, see § 4). The two bottom frames show the [S II] images obtained with the HST in 1998 and 2007 (see § 2). The predicted maps have been computed assuming that the outflow axis lies at a 30° angle with respect to the plane of the sky (as appropriate for HH 34), and show a region with the source on the left and an axial extent of 2.46×10^{17} cm. The HH 34 [S II] maps has been scaled to the same scale as the predicted maps, assuming a distance of 450 pc (the displayed region has a horizontal size of 36″.5). The intensities of the predicted maps are shown with a linear color scheme (given in erg s^{-1} cm^{-2} sterad^{-1} by the top bar), and the HH 34 maps are shown with a linear color scheme with a maximum value corresponding to 0.2 counts per second per pixel. The color figure can be viewed online.

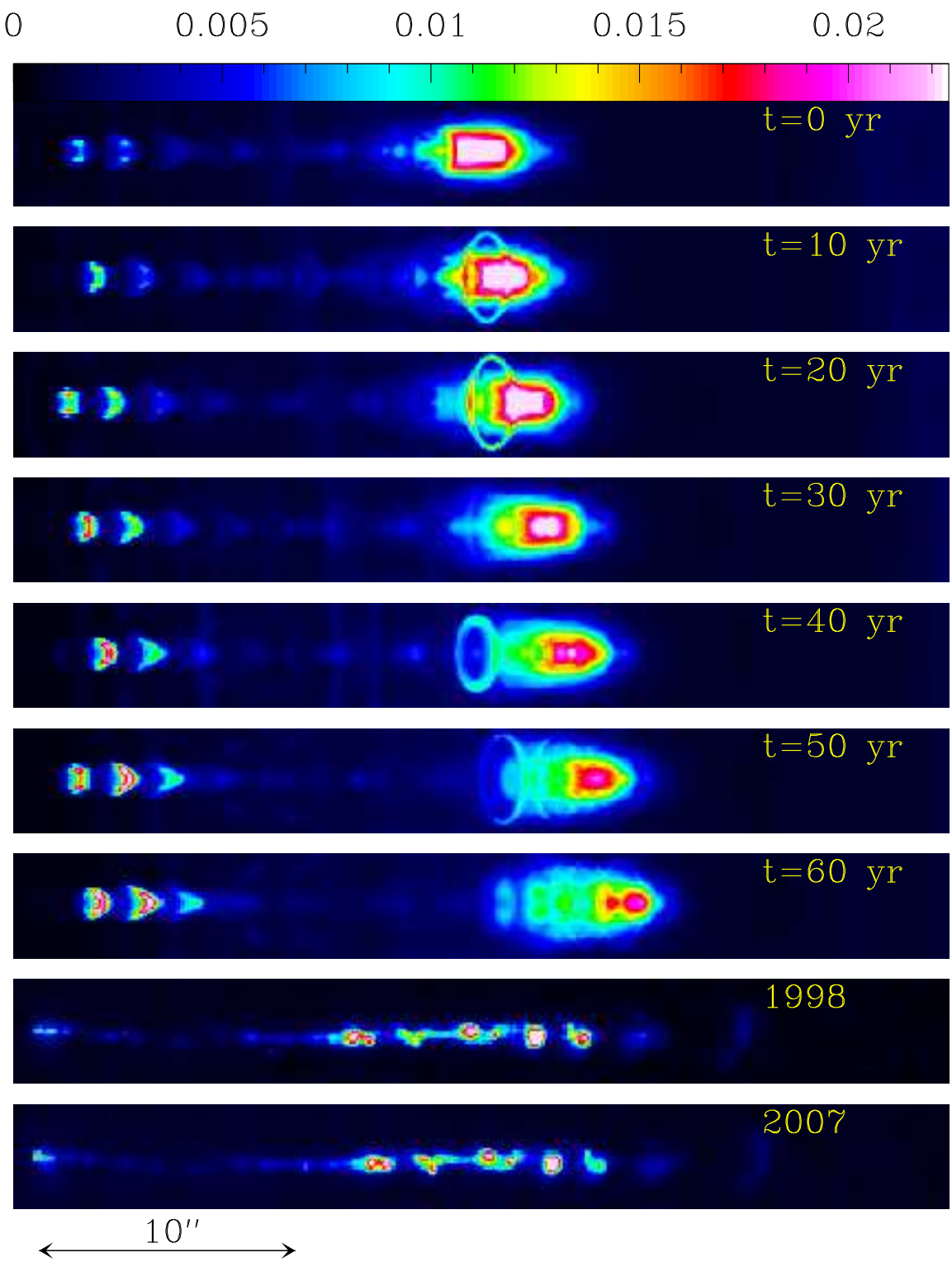

Fig. 9. The same as Figure 9, but with the intensity maps predicted from the $\sigma = 0.75$, 3-mode jet model for the times $t = 0$ to 60 yr, at 10 yr intervals (see § 4). The color figure can be viewed online.

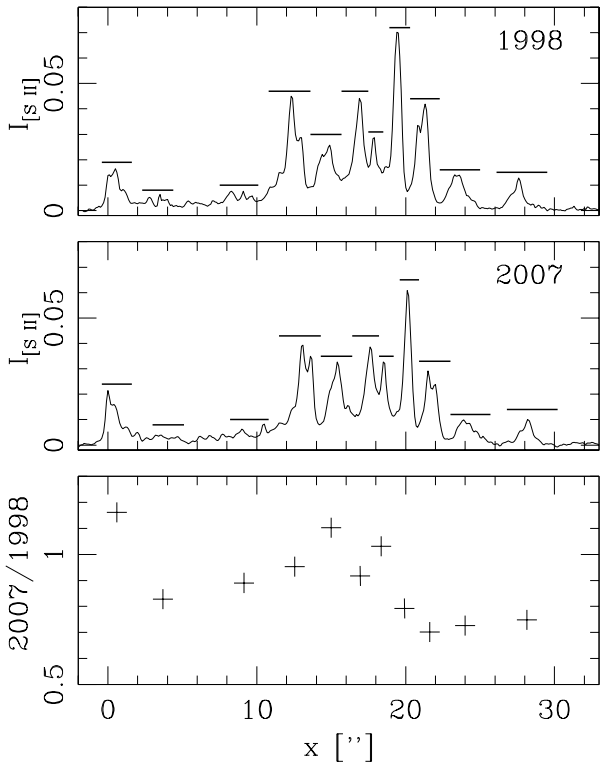

Fig. 10. [S II] tracings along the HH 34 jet for the 1998 (top) and 2007 (center) epochs, obtained by averaging over 3″ across the jet axis. The adjacent background emission has been subtracted. We have integrated the intensity over segments along the tracings. The lenghts and positions of the segments are shown on the two intensity tracings, with a displacement of +0″.7 along the x-axis for the 2007 epoch, (except for the segment incorporating the source, which was not displaced). The ratios between the integrated intensities (in the segments defined above) in the two epochs are shown in the bottom plot. The x-axis is the distance (in arcseconds) from the HH 34 source.

the HH 34 jet, and that the predicted structures show variabilities over ≈10 yr intervals which are consistent with the observed variability of the knots in HH 34.

The success we have obtained in reproducing the chain of knots within the first ∼1′ of the HH 34 jet is limited, as we are clearly not yet able to even attempt to carry out a quantitative comparison between the predicted and the observed emission structures. Nevertheless, the results are reasonably encouraging, because the predicted knot structures do show general morphologies and time-variabilities which appear to be consistent with the properties of the HH 34 knots. Also, the simulations approximately reproduce the shape of the HH 34S bow shock, and the intensity contrast between this bow shock and the chain of aligned knots. In particular, we find that including a non-top hat ejection velocity cross section (with a moderate edge-to-center velocity ratio) improves the qualitative similarity between predicted and observed knot structures. If this result is to be taken at face value, it would imply that the HH 34 jet has a centrally peaked velocity profile, with a drop of ∼25% towards the edge of the jet (this outer edge representing a sharp boundary at which the jet beam is interrupted).

This result, however, is uncertain. It has been shown that the presence of a toroidal magnetic field (De Colle et al. 2008), and/or the presence of a multi-mode (possibly chaotic) ejection variability can lead to the formation of elongated IWS (De Colle 2011). In future work, it will be necessary to explore whether or not these possibilities produce knot morphologies and time-variations similar to the ones observed in the HH 34 jet.

This work is part of an ongoing effort to attempt to reproduce the observational chatacteristics of a set of specific HH jets with variable jet models. We have previously presented models for HH 34 (Raga & Noriega-Crespo 1998; Raga et al. 2002; Masciadri et al. 2002a), HH 111 (Masciadri et al. 2002b), HH 32 (Raga et al. 2004), HH 30 (Esquivel, Raga, & De Colle 2007), the DG Tau microjet (Raga et al. 2001) and the photoionized jet HH 444 (López Martín et al. 2001; Raga, Riera, & González-Gómez 2010). This kind of comparison between predictions from numerical simulations and observations should eventually provide the grounds for deciding which HH objects have emitting structures that are definitely the result of an ejection time-variability. It should also provide constraints on models for the ejection of HH jets and at the same time give us an understanding of the mechanisms by which the emitting structures are formed.

As a final point, we should note that our study of non-top hat ejection velocity jets is limited to quadratic cross sections. The choice of a quadratic velocity cross section is to some extent natural, because it can be thought of as a second order Taylor series of an arbitrary, flat-topped function. For this reason, most of the previous papers on HH jet models with non-top hat velocity cross sections have considered quadratic profiles (for example, Völker et al. 1999; Rosen & Smith 2003, 2004). Another natural choice for the functional form of the ejection velocity cross section would be a Gaussian, as this is the form of the velocity cross section of turbulent labo-

ratory jets. However, for the edge-to-center velocity ratios σ used in the present paper, the deviations between a Gaussian and a quadratic cross section are not very large (they are smaller than 6, 14 and 21% for $\sigma = 0.75$, 0.5 and 0.25, respectively). We would therefore not expect to obtain significantly different results for Gaussian cross sections.

This work was supported by the Conacyt grants 61547, 101356 and 101975. We acknowledge the support of E. Palacios of the ICN-Universidad Nacional Autónoma de México computing staff. We also thank an anonymous referee for helpful comments.

REFERENCES

Cantó, J., Raga, A. C., & D'Alessio, P. 2000, MNRAS, 313, 656
De Colle, F. 2011, in IAU Symp. 275, Jets at all Scales, ed. G. A. Romero, R. A. Sunyaev, & T. Belloni (Cambridge: Cambridge Univ. Press), 392
De Colle, F., Raga, A. C., & Esquivel, A. 2008, ApJ, 689, 302
Dennis, T. J., Cunningham, A. J., Frank, A., Balick, B., Blackman, E. G., & Mitran, S. 2008, ApJ, 679, 1327
Esquivel, A., Raga, A. C., Cantó, J., & Rodríguez-González, A. 2009, A&A, 507, 855
Esquivel, A., Raga, A. C., & De Colle, F. 2007, A&A, 468, 613
Frank, A., Lery, T., Gardiner, T. A., Jones, T. W., & Ryu, D. 2000, ApJ, 540, 342
Gardiner, T. A., & Frank, A. 2000, ApJ, 545, L153
Hartigan, P., & Raymond, J. C. 1993, ApJ, 409, 705
Heathcote, S., & Reipurth, B. 1992, AJ, 104, 2193
Kajdic, P., Velázquez, P. F., & Raga, A. C. 2006, RevMexAA, 42, 217
López-Martín, L., Raga, A. C., López, J. A., & Meaburn, J. 2001, A&A, 371, 1118
Masciadri, E., de Gouveia Dal Pino, E. M., Raga, A. C., & Noriega-Crespo, A. 2002a, ApJ, 580, 950
Masciadri, E., Velázquez, P. F., Raga, A. C., Cantó, J., & Noriega-Crespo, A. 2002b, ApJ, 573, 260
Raga, A. C., & Biro, S. 1993, MNRAS, 264, 758
Raga, A. C., Cabrit, S., Dougados, C., & Lavalley, C. 2001, A&A, 367, 959
Raga, A. C., Cantó, J., Binette, L., & Calvet, N. 1990, ApJ, 364, 601
Raga, A. C., Cantó, J., & Cabrit, S. 1998, A&A, 332, 714
Raga, A. C., Cantó, J., De Colle, F., Esquivel, A., Kajdic, P., Rodríguez-González, A., & Velázquez, P. F. 2009, in Protostellar Jets in Context, ed. K. Tsinganos, T. Ray, & M. Stute (Berlin: Springer), 295
Raga, A. C., De Colle, F., Kajdic, P., Esquivel, A., & Cantó, J. 2007, A&A, 465, 879
Raga, A. C., & Noriega-Crespo, A. 1998, AJ, 116, 2943
Raga, A. C., Riera, A., & González-Gómez, D. I. 2010, A&A, 517, 20
Raga, A. C., Riera, A., Masciadri, E., Beck, T., Böhm, K. H., & Binette, L. 2004, AJ, 127, 1081
Raga, A. C., Velázquez, P. F., Cantó, J., & Masciadri, E. 2002, A&A, 395, 647
Rees, M. J. 1978, MNRAS, 184, 61
Reipurth, B. 1989, Nature, 340, 42
Reipurth, B., Bally, J., Graham, J. A., Lane, A. P., & Zealy, W. J. 1986, A&A, 164, 51
Reipurth, B., Hartigan, P., Heathcote, S., Morse, J. A., & Bally, J. 1997, AJ, 114, 757
Reipurth, B., & Heathcote, S. 1992, A&A, 257, 693
Reipurth, B., Heathcote, S., Morse, J., Hartigan, P., & Bally, J. 2002, AJ, 123, 362
Reipurth, B., Raga, A. C., & Heathcote, S. 1992, ApJ, 392, 145
Rosen, A., & Smith, M. D. 2003, MNRAS, 343, 181
_____. 2004, MNRAS, 347, 1097
Smith, M. D., & Rosen, A. 2005, MNRAS, 357, 579
Tesileanu, O., Massaglia, S., Mignone, A., Bodo, G., & Bacciotti, F. 2009, A&A, 507, 581
Völker, R., Smith, M. D., Suttner, G., & Yorke, H. W. 1999, A&A, 343, 953
Wilson, M. J. 1984, MNRAS, 209, 923

F. De Colle: Astronomy and Astrophysics Department, University of California, Santa Cruz, CA 95064, USA (fabio@ucolick.org).
P. Kajdic: Instituto de Geofísica, Universidad Nacional Autónoma de México, 04510 D.F., Mexico (primoz@geofisica.unam.mx)
D. López-Cámara and A. C. Raga: Instituto de Ciencias Nucleares, Universidad Nacional Autónoma de México, Apdo. Postal 70-543, 04510 D.F., Mexico (raga@nucleares.unam.mx, diegorretas@gmail.com.)
A. Noriega-Crespo: Spitzer Science Center, California Institute of Technology, Pasadena, CA 91125, USA (alberto@ipac.caltech.edu).

Revista Mexicana de Astronomía y Astrofísica, **47**, 289–295 (2011)

AN INTEPRETIVE BALLISTIC MODEL FOR QUASI-SYMMETRIC BIPOLAR JET SYSTEMS

A. C. Raga,[1] A. Noriega-Crespo,[2] J. C. Rodríguez-Ramírez,[1] V. Lora,[3] K. R. Stapelfeldt,[4] and S. J. Carey[2]

Received 2011 April 10; accepted 2011 June 6

RESUMEN

Presentamos un modelo analítico, balístico para sistemas de chorros/contra-chorros cuasi-simétricos, considerando tanto el caso no relativista como el relativista. El modelo considera la presencia de asimetrías en el tiempo y en la velocidad de eyección, las cuales producen diferencias entre las posiciones de los nudos a lo largo del chorro y del contra-chorro. Un ajuste de las predicciones del modelo no relativista a observaciones de dos flujos HH cuasi-simétricos (HH 34 y HH 111) nos permite obtener las magnitudes de las asimetrías de tiempo y velocidad de eyección de estos sistemas.

ABSTRACT

We present an analytic, ballistic model for quasi-symmetric jet/counterjet systems, considering both the non-relativistic and the relativistic cases. The model considers the presence of ejection time and velocity asymmetries, which produce offsets between the positions of the knots in jet/counterjet pairs. A fit of the non-relativistic model predictions to observations of two quasi-symmetric HH outflows (HH 34 and HH 111) allows us to obtain the magnitudes of the ejection time and velocity asymmetries of these systems.

Key Words: Herbig-Haro objects — infrared: ISM — ISM: individual objects (HH 34, HH 111) — ISM: jets and outflows — stars: formation

1. INTRODUCTION

Many HH outflows do not have well defined symmetries between the red- and blue-shifted lobes. Examples of this are HH 32 (in which the red-shifted lobe is not well developed, see e.g., Curiel et al. 1997) and HH 262 (the outflow from the L1551 IRS5 source, which shows a very complex structure at all wavelengths, see e.g., López et al. 2008).

Other HH objects show at least some degree of similarity between the two outflow lobes. Gyul'budagyan (1984) presents a discussion of the partially symmetric bipolar structure of the HH 1/2 outflow. The deviations from perfect symmetry in bipolar HH outflows were discussed by Bally & Reipurth (2001) and Woitas et al. (2002), who studied the asymmetries in the ejection density and velocity between the two outflow lobes.

Some IR bipolar outflows from young stellar objects (YSOs) show a surprising degree of "knot by knot" symmetry between the two outflow lobes. Examples of this are HH 212 (see, e.g., Smith, O'Connell, & Davis 2007; Cabrit et al. 2007) and HH 211 (e.g., Lee et al. 2010). In the well studied HH 34 and HH 111 optical outflows, it has been noted that good jet/counterjet knot symmetries are also present, particularly when one combines optical with IR observations (in which the highly obscured counterjets are detected). This was seen in HH 111 by Gredel & Reipurth (1994) and in HH 34 by García López et al. (2008).

Recent IR images obtained with the IRAC camera of *Spitzer* of HH 34 (Raga et al. 2011) and HH 111 (Noriega-Crespo et al. 2011) give us the possibility of directly measuring the positions of the knots (relative to the source) along the jet and counterjet in a single image, and to carry out a quantitative analysis of the degree of symmetry in the

[1]Instituto de Ciencias Nucleares, Universidad Nacional Autónoma de México, Mexico.
[2]SPITZER Science Center, California Institute of Technology, CA, USA.
[3]Astronomisches Rechen-Institut Zentrum für Astronomie der Universität Heidelberg, Germany.
[4]Jet propulsion Laboratory, California Institute of Technology, CA, USA.

outflows. Such an analysis was not possible before because the HH 34 and 111 jets, counterjets, and outflow sources were not simultaneously detected in previous optical and/or near-IR images. Therefore, the *Spitzer* images open up a new possible analysis of HH outflows, because even though they have somewhat lower angular resolution than previous optical/IR images, they simultaneously show the source and the knots along the two outflow lobes.

Motivated by these new observations, in the present paper we develop a model of a jet with quasi-symmetric ejections of ballistic knots. The model predicts the behavior of the spatial offsets between jet/counterjet knot pairs as a function of increasing distance from the outflow source. The predicted dependence can then be compared with the knot positions measured in observed HH outflows in order to constrain the model parameters. A simpler model of this kind was described by Raga et al. (2011).

The paper is organized as follows. The ballistic, binary ejection model is described in § 2 (both the non-relativistic and the relativistic cases are considered). An application of the non-relativistic model to the observed positions of the jet/counterjet knots in HH 34 and 111 is described in § 3. Finally, the implications of the results are discussed in § 4.

2. A BALLISTIC, QUASI-SYMMETRIC BINARY EJECTION MODEL

2.1. *Non-relativistic flows*

Let us consider a non-relativistic, bipolar ejection with imperfect symmetry. In one direction (along the "jet"), a clump is ejected at a time τ with a velocity v_j (projected on the plane of the sky). In the opposite direction (along the "counterjet"), a clump is ejected at a time $\tau + \Delta\tau$, with a velocity $v_j - \Delta v$. If the parcels are ballistic, at a later time t they will be at distances x_j and x_{cj} (on the plane of the sky, along the jet and the counterjet, respectively) given by:

$$x_j = (t-\tau)v_j\,; \quad x_{cj} = (t-\tau-\Delta\tau)(v_j-\Delta v)\,. \quad (1)$$

From this equation, one obtains that the offset $\Delta x = x_j - x_{cj}$ (between the positions of the jet and counterjet knots) grows with distance from the source, following

$$\Delta x = x_j - x_{cj} = \Delta\tau v_j + \frac{\Delta v}{v_j} x_j\,, \quad (2)$$

where we have neglected the term $\Delta\tau\,\Delta v$ (which involves the product of the two perturbations).

Now, let us assume that we have an ensemble of knot pairs, with $\Delta\tau$ and Δv values uniformly distributed in intervals $[\tau_0 - \Delta\tau_0, \tau_0 + \Delta\tau_0]$ and $[v_0 - \Delta v_0, v_0 + \Delta v_0]$, respectively. In other words, we allow for an intrinsic asymmetry in the ejection velocity Δv and in the time-delay $\Delta\tau$ between the jet/counterjet ejections.

The ensemble average of equation (2) is:

$$<\Delta x> = \int_{v_0-\Delta v_0}^{v_0+\Delta v_0}\int_{\tau_0-\Delta\tau_0}^{\tau_0+\Delta\tau_0} \Delta x\,\frac{d\Delta\tau\,d\Delta v}{4\Delta\tau_0\Delta v_0}$$
$$= \tau_0 v_j + \left(\frac{v_0}{v_j}\right) x_j\,. \quad (3)$$

Therefore, the ensemble average of Δx as a function of x_j (where x_j is the distance to the successive knots measured along the jet) is a straight line with intercept a_1 and slope b_1 such that:

$$a_1 = \tau_0 v_j\,; \qquad b_1 = \frac{v_0}{v_j}\,. \quad (4)$$

We should note that if we have an error of magnitude Δx_s in the estimated position of the source, we will obtain $a_1 = \tau_0 v_j \pm \Delta x_s$.

Also of interest is the quadratic average:

$$<(\Delta x)^2> = \int_{v_0-\Delta v_0}^{v_0+\Delta v_0}\int_{\tau_0-\Delta\tau_0}^{\tau_0+\Delta\tau_0}\left[(\Delta\tau)^2 v_j^2 + \left(\frac{\Delta v x_j}{v_j}\right)^2 + 2\Delta\tau\Delta v x_j\right]\frac{d\Delta\tau\,d\Delta v}{4\Delta\tau_0\Delta v_0}$$
$$= v_j^2\left(\tau_0^2 + \frac{\Delta\tau_0^2}{3}\right) + \left(\frac{x_j}{v_j}\right)^2\left(v_0^2 + \frac{\Delta v_0^2}{3}\right) + \tau_0 v_0 x_j\,. \quad (5)$$

Therefore, the ensemble average of $(\Delta x)^2$ has a quadratic, $<(\Delta x)^2> = a_2 + b_2 x_j + c_2 x_j^2$ dependence with:

$$a_2 = v_j^2\left(\tau_0^2 + \frac{\Delta\tau_0^2}{3}\right)\,; \quad c_2 = \left(\frac{v_0}{v_j}\right)^2 + \frac{1}{3}\left(\frac{\Delta v_0}{v_j}\right)^2\,, \quad (6)$$

and with $b_2 = a_1 b_1$ given by the results of the fit to the $<\Delta x>$ vs. x_j dependence (see equations 4 and 5).

To summarize, if one observes an outflow in which pairs of jet/counterjet knots can be identified, one has to make fits to the Δx vs. x_j and $(\Delta x)^2$ vs. x_j dependencies (where $\Delta x = x_j - x_{cj}$, the observed positional asymmetry between the jet/counterjet knot pairs). If one has an independent estimate of the spatial velocity v_j of the knots, the coefficients of the fits (see equations 4 and 6) directly give us the mean and half width of the ejection time (τ_0 and $\Delta\tau_0$) and velocity (v_0 and Δv_0) distributions.

2.2. *Relativistic flows*

Let us now consider the problem of quasi-symmetric, binary ejections at relativistic velocities. In § 2.1 (in which we considered a non-relativistic flow), we did not introduce the effect of projection onto the plane of the sky because the distances from the source and the jet velocity have the same plane-of-the-sky projection (and therefore, one can work with the projected distances and velocities).

In the case of a relativistic binary ejection, the clump ejected along the jet at a time τ with an intrinsic velocity v_j will be at a time t at a projected distance (from the source):

$$x_j = \frac{(t-\tau)v_j \cos\phi}{1 - v_j \sin(\phi/c)}\,, \tag{7}$$

where ϕ is the angle (towards the observer) between the jet axis and the plane of the sky, and c is the speed of light.

The clump ejected along the counterjet at a time $t+\Delta\tau$ with a velocity $v_j - \Delta v$ will be at a time t at a projected distance:

$$x_{cj} = \frac{(t-\tau-\Delta\tau)(v_j-\Delta v)\cos\phi}{1+(v_j-\Delta v)\sin(\phi/c)}\,. \tag{8}$$

Combining equations (7-8) and expanding in a Taylor series up to first order in $\Delta\tau$ and Δv we obtain:

$$\Delta x = x_j - x_{cj} = \frac{\Delta\tau v_j \cos\phi}{1+v_j\sin(\phi/c)} + \left[\frac{2v_j\sin(\phi/c)}{(1+v_j\sin(\phi/c))} + \frac{(1-v_j\sin(\phi/c))(\Delta v/v_j)}{(1+v_j\sin(\phi/c))^2}\right]x_j\,. \tag{9}$$

Carrying out the ensemble averages described in § 2.1, we then derive:

$$<\Delta x> = A_1 + B_1 x_j\,;\;\; <(\Delta x)^2> = A_2 + B_2 x_j + C_2 x_j^2\,, \tag{10}$$

with

$$A_1 = \tau_0 v_j A\,, \qquad B_1 = B + C\frac{v_0}{v_j}\,,$$

$$A_2 = A^2\left(\tau_0^2 + \frac{\Delta\tau_0^2}{3}\right)v_j^2\,,\;\; B_2 = 2A(Bv_j + Cv_0)\tau_0\,,$$

$$C_2 = \frac{C^2}{v_j^2}\left(v_0^2 + \frac{\Delta v_0^2}{3}\right) + B^2 + 2BC\frac{v_0}{v_j}\,, \tag{11}$$

where A, B and C are the dimensionless functions

$$A = \frac{\cos\phi}{1+v_j\sin(\phi/c)}\,, \quad B = \frac{2v_j\sin(\phi/c)}{(1+v_j\sin(\phi/c))}\,,$$

$$C = \frac{1-v_j\sin(\phi/c)}{(1+v_j\sin(\phi/c))^2}\,. \tag{12}$$

A, B and C are functions of order unity (except when $1+v_j\sin(\phi/c) \ll 1$) for relativistic jets, with $v_j \sim c$. For $v_j \ll c$, they have limits $A = C = 1$ and $B = 0$. Inserting these values in equation (11) it is clear that we recover the non-relativistic equations (3–5) (considering that the velocities used in equation 11 correspond to the full spatial motion and not the projection on the plane of the sky considered in equations 3–5).

3. AN APPLICATION OF THE MODEL TO TWO HH JETS

3.1. *Results of the model fit*

We now apply the non-relativistic ballistic ejection model described in § 2.1 to two HH jets: HH 34 and HH 111. We first calculate least squares fits of the jet/counterjet knot offsets $\Delta x = x_j - x_{cj}$ and of $(\Delta x)^2$ as a function of distance x_j from the source. We then use the coefficients from the fits (together with an estimate of the knot velocities v_j) to constrain the ejection time ($\tau_0 \pm \Delta\tau_0$) and ejection velocity ($v_0 \pm \Delta v_0$) distributions resulting in the observed jet/counterjet asymmetries.

Given the fact that the distances and velocities along the jet/counterjet have identical projections onto the plane of the sky, we carry out the fitting procedure using the angular distances and proper motion velocities measured for the knot pairs. To obtain physical values from the angular distances and velocities, we assume a distance of 417 pc to HH 34 and 111 (see Menten et al. 2007).

3.2. *The observations*

The observations of HH 34 and HH 111 were downloaded from the *Spitzer* Heritage Archive[5]. They are part of our original General Observer (GO) program 3315 (PI Noriega-Crespo) obtained with the infared camera IRAC (Fazio et al. 2004) and the infrared photometer MIPS (Rieke et al. 2004) in March 28, 2005. The high quality of the archival images (Post Basic Calibrated Data or Post-BCD; S18.7 products) was enough for our purposes and no further processing was required. The HH 34 and HH 111 observations with IRAC were taken in its four channels (1, 2, 3, 4) = (3.6, 4.5, 5.8 & 8.0 μm) and with a total integration time per pixel of 360 sec, using 30 sec High Dynamic Range (HDR) exposures. The final images are sampled with 0.6″ per pixel,

[5] `http://sha.ipac.caltech.edu/applications/Spitzer/SHA`.

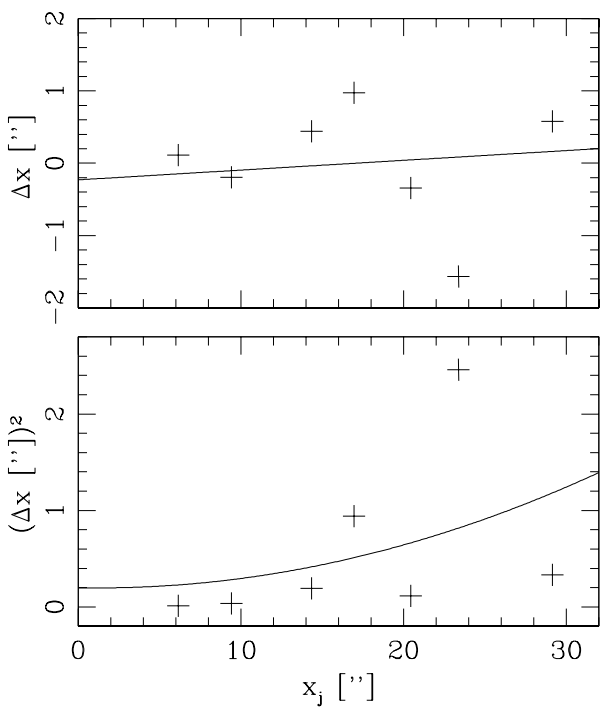

Fig. 1. Model fit to the HH 34 jet/counterjet knot pairs. We take the positions of the knots within 30″ from the outflow source (from Raga et al. 2011) and plot $\Delta x = x_j - x_{cj}$ (the jet/counterjet knot position offset, top graph) and $(\Delta x)^2$ (bottom graph) as a function of x_j. The straight line in the top graph and the curve in the bottom graph show the model fits, which result in the parameters given in Table 1.

nearly one third of the standard ∼2″ IRAC angular resolution.

As described in Raga et al. (2011) and Noriega-Crespo et al. (2011), given the collisional excitation characteristics of young stellar outflows like HH 34 and 111, the emission in the IRAC bandpasses is likely to be dominated by the pure rotational H_2 lines (e.g., Noriega-Crespo et al. 2004a,b; Looney, Tobin & Kwon 2007; Tobin et al. 2007; Ybarra & Lada 2009; De Buizer & Vacca 2010). Finally, in the HH 111 image we carried out astrometry of several field stars in order to correctly locate the position of the VLA 1 source (the source of the HH 111 outflow, see, e.g., Rodríguez et al. 2008).

3.3. *The HH 34 knots*

For the HH 34 outflow, we consider the 7 quasi-symmetric knot pairs detected in the *Spitzer* image of Raga et al. (2011). These knots lie at angular distances <30″ from the source, and have a clear correspondence between the jet and the counterjet.

TABLE 1

FITS TO THE HH 34/111 KNOTS

	HH 34	HH 111
a_1	$(-0.23 \pm 0.72)''$	$(2.19 \pm 0.85)''$
b_1	0.024 ± 0.039	0.027 ± 0.011
a_2	$(0.20 \pm 0.48)['']^2$	$(8.5 \pm 4.1)['']^2$
c_2	$(1.26 \pm 1.10) \times 10^{-3}$	$(0.93 \pm 0.42) \times 10^{-3}$
v_j	150 km s^{-1}	240 km s^{-1}
τ_0	(-3.0 ± 9.5) yr	(18.1 ± 7.0) yr
v_0	(2.0 ± 5.9) km s^{-1}	(6.5 ± 2.6) km s^{-1}
$\Delta\tau_0$	(8.8 ± 17.4) yr	(27.7 ± 20.5) yr
Δv_0	(9.0 ± 5.6) km s^{-1}	(10.9 ± 5.8) km s^{-1}

The results of the least squares fits to the Δx vs. x_j and $(\Delta x)^2$ vs. x_j dependencies are shown in Figure 1. The coefficients of the (linear Δx vs. x_j and quadratic $(\Delta x)^2$ vs. x_j) fits, together with the errors estimated through the fitting procedure, are given in Table 1.

Proper motion measurements (see, e.g., Reipurth et al. 2002) indicate that the knots close to the source of the HH 34 system have plane of the sky velocities $v_j \approx 150$ km s^{-1}. Using this velocity and the parameters derived from the fits, from equations (4–6) we obtain the mean values of the widths of the ejection time (τ_0 and Δv_0) and of the ejection velocity (v_0 and Δv_0) distributions. The resulting values (together with their uncertainties) are given in Table 1.

3.4. *The HH 111 knots*

Noriega-Crespo et al. (2011) present a *Spitzer* image of the HH 111 system. This system does not show such a clearly symmetric structure as the HH 4 outflow. This fact is illustrated in Figure 2.

From the observed jet and counterjet structures, we choose a set of 5 well defined knot pairs which appear to have clear jet/counterjet correspondences (see Figure 2). We then use these 5 knot pairs to obtain the Δx vs. x_j and $(\Delta x)^2$ vs. x_j dependencies. The fits to these dependencies are shown in Figure 3, and the resulting coefficients are given in Table 1.

From the values of the coefficients from the fits and a $v_j \approx 240$ km s^{-1} plane of the sky velocity (see, e.g., Hartigan et al. 2001), we obtain the parameters of the ejection time and velocity distributions (τ_0, $\Delta\tau_0$ and v_0, Δv_0, respectively). These parameters are given in Table 1.

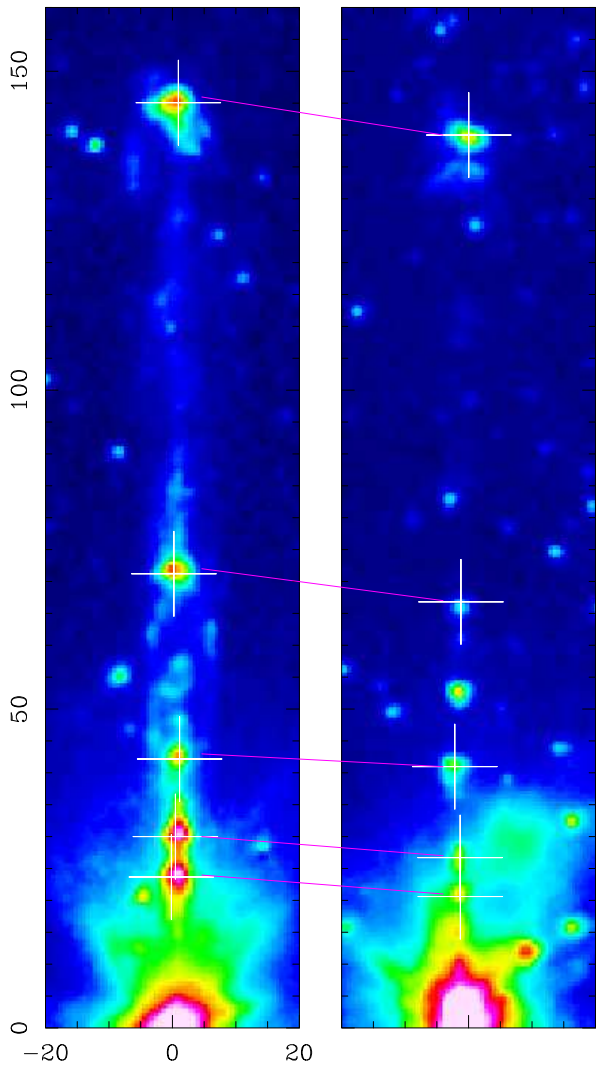

Fig. 2. The HH 111 *Spitzer* IRAC I2 band image of Noriega-Crespo et al. (2011), displayed in two frames. The left frame shows the E lobe, and the right frame the W lobe of HH 111. In both cases, the outflow axis has been rotated so that the outflow is parallel to the ordinate. In both frames, the source is placed at the origin of the reference system. The arrows indicate the chosen jet/counterjet knot pairs, and the crosses show the positions determined from parabolic fits to the emission peaks of the knots. The axes are labeled in arcseconds. The color figure can be viewed online.

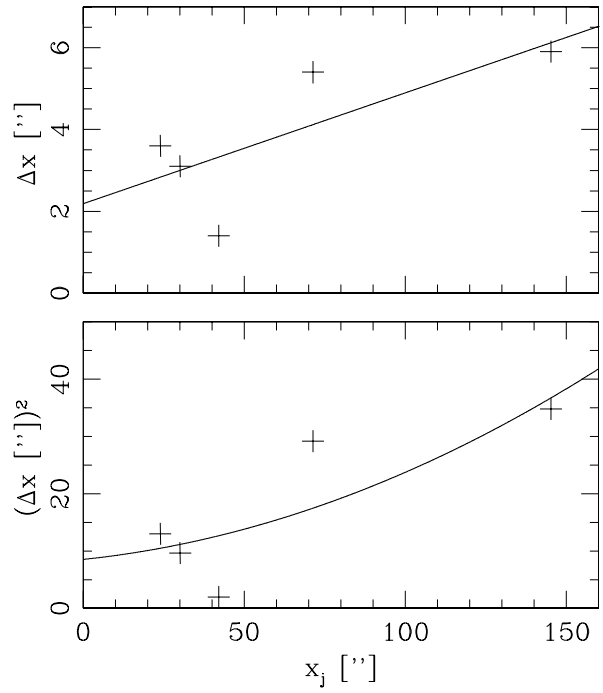

Fig. 3. Model fit to the HH 111 jet/counterjet knot pairs. We take the positions of the knot pairs shown in Figure 2 and plot Δx (top graph) and $(\Delta x)^2$ (bottom graph) as a function of x_j. The straight line in the top graph and the curve in the bottom graph show the model fits, which result in the parameters given in Table 1.

3.5. *Discussion*

From Table 1, we see that the ejection asymmetries deduced for the HH 34 and HH 111 outflows differ from each other in a significant way. If we look at the average values τ_0 and v_0 of the ejection time and velocity offsets (respectively), we find that:

- the knot structure of HH 34 implies ejection asymmetries with average time [$\tau_0 = (-3.0 \pm 9.5)$ yr] and velocity [$v_0 = (2.0 \pm 5.9)$ km s^{-1}] offsets which are not significantly different from zero,

- the positions of the knots of HH 111 imply non-zero average time [$\tau_0 = (18.2 \pm 7.1)$ yr] and velocity [$v_0 = (6.5 \pm 2.6)$ km s^{-1}] offsets.

As it is explained after equation (4), the non-zero value of τ_0 determined for HH 111 could be due to an error in the estimated position for the outflow source. For HH 111 the required offset would be $\Delta x_s = \tau_0 v_j \approx 2''.2$. Given the fact that we have located the source of HH 111 with an accuracy of better than one pixel ($\approx 0''.6$), it is clear that the average time offset that we find for the HH 111 ejections is not dominated by a possible error in the position of the outflow source. The $v_0 = (6.5 \pm 2.6)$ km s^{-1} average velocity offset also is undoubtedly a real effect.

For the widths of the ejection time and velocity offset distributions (see Table 1) we obtain that:

- HH 34 has a time offset distribution with a $\Delta\tau_0 = (8.9 \pm 17.3)$ yr width, which is not significantly different from zero. The velocity offset distribution has a $\Delta v_0 = (9.0 \pm 5.6)$ km s^{-1} width,
- HH 111 implies a time offset distribution with $\Delta\tau_0 = (27.7 \pm 20.5)$ yr and $\Delta v_0 = (10.9 \pm 5.8)$ km s^{-1}.

4. CONCLUSIONS

We have presented a simple, ballistic binary ejection model for interpreting the observed knot structures of quasi-symmetric bipolar outflows. In this model it is assumed that knots are ejected with small time ($\Delta\tau$) and velocity (Δv) offsets, which result in a slightly asymmetric propagation as the knots move away from the source. It is also assumed that these offsets have uniform distributions with mean values τ_0 and v_0 and half-widths $\Delta\tau_0$ and Δv_0 (for the time and velocity offsets, respectively). Under these assumptions, we show that the values of τ_0, v_0, $\Delta\tau_0$ and Δv_0 can be recovered from observations of the spatial jet/counterjet knot offsets $\Delta x = x_j - x_{cj}$ for a system of identifiable knot pairs.

We then apply this method to recent *Spitzer* observations of the HH 34 (Raga et al. 2011) and HH 111 (Noriega-Crespo et al. 2011) jet/counterjet systems. We find that the knots of the HH 34 outflow imply binary ejections with basically zero systematic jet/counterjet ejection times or velocities. The dispersion of the ejection times also lies below the errors due to small number statistics. However, the observed spatial distribution of the jet/counterjet knot offsets does imply a non-zero value for the width of the ejection velocity distribution [$\Delta v_0 = (9.0 \pm 5.6)$ km s^{-1}, see Table 1].

As noted by Raga et al. (2011), the good time coordination of the binary ejections of HH 34 imply that the triggering of the ejection events occurs in a compact region. Even though we are not able to obtain a well constrained value for the time-offsets between the jet and counterjet knots, we can take as an estimate either the value of τ_0 or of $\Delta\tau_0$ (both $\sim$5 yr, see Table 1). If we assume a (sound or Alfvén) wave propagation velocity $v_s \sim 3$ km s^{-1} for the jet formation region, this coordination timescale then implies a size $d \sim 3$ AU.

A clearly different result is obtained for HH 111. The jet/counterjet knot pairs of this system imply a clear bias towards one side, with the clumps in the W lobe being ejected on average a time $\tau_0 = (18.2 \pm 7.1)$ yr later and $v_0 = (6.5 \pm 2.6)$ km s^{-1} slower than the corresponding knots in the E lobe. The observations also imply non-zero widths for the ejection time and velocity distributions ($\Delta\tau_0 = (27.7 \pm 20.5)$ yr and $\Delta v_0 = (10.9 \pm 5.8)$ km s^{-1}, respectively, see Table 1).

For HH 111 we then conclude that an intrinsically asymmetric ejection is taking place, with one side producing faster and earlier ejections than the other. Such an effect is seen at least in one other YSO outflow: Curiel et al. (2006) present high resolution radio continuum maps at many epochs of the Cepheus A HW2 outflow, and they find that the knots are ejected $\sim$2 yr earlier in one of the two lobes. It appears that in HH 111 we are seeing a similar effect, but with a time-delay that is larger by one order of magnitude.

The systematic velocity offset ($v_0 \approx 6.5$ km s^{-1}, see Table 1) of the HH 111 jet/counterjet knots could actually be the result of a non-ballistic behavior of the motion. For example, if the knots along one of the outflow lobes were interacting directly with a denser medium, this interaction could lead to a lower velocity knot propagation velocity. However, as the knots are traveling into the wake of previous ejection episodes, such a direct knot/environment interaction seems unlikely. Also, the different velocities could in principle be the result of different orientations of the lobes with respect to the plane of the sky. However, the very small deviations from a straight path on the plane of the sky observed in HH 111 (see Noriega-Crespo et al. 2011) do not favor this scenario.

The asymmetries in the ejections of the HH 34 and 111 knots in principle provide constraints on the jet production model. However, in many cases it is not yet possible to apply these constraints because the present models for the production of outflows from young stars are either stationary (e.g., Salmeron, Königl, & Wardle 2011) or do not appear to incorporate the mechanism(s) that produce the knots observed along HH jets (e.g., Ramsey & Clarke 2011; Stute et al. 2010; Yamada et al. 2009). A recent analysis of models producing asymmetric ejections (as the result of the presence of a time-independent magnetospheric magnetic field with both a dipole and a quadrupole component) is given by Lovelace et al. (2010), who for some parameters obtain outflows that "flip-flop" with a period of $\sim$30 days. Given the fact that this predicted timescale is a factor of 10–100 times too small for explaining the asymmetries observed for the HH 34 and 111 knots, it is clear that if one is to rescue the ideas of Lovelace et al. (2010) it will be necessary to introduce other elements. A possibility would be the presence of a time-variability in the magnetospheric magnetic field, as explored by De Colle, García, &

Murphy (2008). The magnetospheric magnetic field could have time-dependencies on timescales similar to the solar cycle (i.e., with periods ∼20 yr).

From the observational point of view, significant progress will be possible through the analysis of other bipolar HH jets. Such studies should include both objects with good jet/counterjet symmetries (such as HH 211, see, e.g., Lee et al. 2010) and objects with evident asymmetries (such as HH 228, see Wang & Henning 2009).

Finally, in § 2.2 we have described a model for relativistic, quasi-symmetric binary ejections. An application of this model to observations of relativistic jets is left for a future paper.

This work was supported by the Conacyt grants 61547, 101356 and 101975.

REFERENCES

Bally, J., & Reipurth, B. 2001, ApJ, 546, 299
Cabrit, S., Codella, C., Gueth, F., Nisini, B., Gusdorf, A., Dougados, C., & Bacciotti, F. 2007, A&A, 468, L29
Curiel, S., Raga, A. C., Raymond, J. C., Noriega-Crespo, A., & Cantó, J. 1997, AJ, 114, 2736
Curiel, S., et al. 2006, ApJ, 638, 878
De Buizer, J. M., & Vacca, W. D. 2010, AJ, 140, 196
De Colle, F., Gracía, J., & Murphy, G. 2008, ApJ, 688, 1137
Fazio, G., et al. 2004, ApJS, 154, 10
García López, R., Nisini, B., Giannini, T., Eislöffel, J., Bacciotti, F., & Podio, L. 2008, A&A, 487, 1019
Gredel, R., & Reipurth, B. 1994, A&A, 289, L19
Gyul'budagyan, A. L. 1984, Astrophysics, 20, 75
Hartigan, P., Morse, J. A., Reipurth, B., Heathcote, S., & Bally, J. 2001, ApJ, 559, L157
Lee, C.-F., Hasegawa, T. I., Hirano, N., Palau, A., Shang, H., Ho, P. T. P., & Zhang, Q. 2010, ApJ, 713, 731
Looney, L. W., Tobin, J. J., & Kwon, W. 2007, ApJ, 670, L131
López, R., García-Lorenzo, B., Sánchez, S. F., Gómez, G., Estalella, R., & Riera, A. 2008, MNRAS, 391, 1107
Lovelace, R. V. E., Romanova, M. M., Ustyugova, G. V., & Koldoba, A. V. 2010, MNRAS, 408, 2083
Menten, K. M., Reid, M. J., Forbrich, J., & Brunthaler, A. 2007, A&A, 474, 515
Noriega-Crespo, A., et al. 2004a, ApJS, 154, 352
Noriega-Crespo, A., et al. 2004b, ApJS, 154, 402
Raga, A. C., Noriega-Crespo, A., Lora, V., Stapelfeldt, K. R., & Carey, S. J. 2011, ApJ, 730, L17
Ramsey, J. P., & Clarke, D. A. 2011, ApJ, 728, L11
Reipurth, B., Heathcote, S., Morse, J., Hartigan, P., & Bally, J. 2002, AJ, 123, 362
Rieke, G. H., et al. 2004, ApJS, 154, 25
Rodríguez, L. F., Torrelles, J. M., Anglada, G., & Reipurth, B. 2008, AJ, 136, 1852
Salmeron, R., Königl, A., & Wardle, M. 2011, MNRAS, 412, 1162
Smith, M. D., O'Connell, B., & Davis, C. J. 2007, A&A, 466, 565
Stute, M., Gracía, J., Tsinganos, K., & Vlahakis, N. 2010, A&A, 516, A6
Tobin, J. J., Looney, L. W., Mundy, L. G., Kwon, W., & Hamidouche, M. 2007, ApJ, 659, 1404
Wang, H., & Henning, T. 2009, AJ, 138, 1072
Woitas, J., Ray, T. P., Bacciotti, F., Davis, C. J., & Eislöffel, J. 2002, ApJ, 580, 336
Yamada, M., Machida, M. N., Inutsuka, S., & Tomisaka, K. 2009, ApJ, 703, 1141
Ybarra, J. E., & Lada, E. A. 2009, ApJ, 695, 120

S. J. Carey and A. Noriega-Crespo: Spitzer Science Center, California Institute of Technology, Pasadena, CA 91125, USA (carey, alberto@ipac.caltech.edu).
V. Lora: Astronomisches Rechen-Institut Zentrum für Astronomie der Universität Heidelberg, Mönchhofstr. 12-14 69120 Heidelberg, Germany (vlora@ari.uni-heidelberg.de).
A. C. Raga and J. C. Rodríguez-Ramírez: Instituto de Ciencias Nucleares, Universidad Nacional Autónoma de México, Apdo. Postal 70-543, 04510 D.F., Mexico (raga, juan.rodriguez@nucleares.unam.mx).
K. R. Stapelfeldt: Jet propulsion Laboratory, California Institute of Technology, MS 183-900, 4800 Oak Grove Drive, Pasadena, CA 91109, USA (krs@exoplanet.jpl.nasa.gov).

Revista Mexicana de Astronomía y Astrofísica, **47**, 297–307 (2011)

V1898 CYGNI: AN INTERACTING ECLIPSING BINARY IN THE VICINITY OF NORTH AMERICA NEBULA[1]

A. Dervişoğlu,[2] Ö. Çakırlı,[2,3] C. İbanoğlu,[2] and E. Sipahi[2]

Received 2011 April 12; accepted 2011 June 12

RESUMEN

Presentamos observaciones espectroscópicas de la binaria eclipsante tipo Algol, de doble línea, V1898 Cygni. El análisis de las curvas de luz en las bandas BV nos lleva a una determinación de los parámetros fundamentales de las componentes de V1898 Cygni. Los parámetros absolutos son: $M_1 = 6.054 \pm 0.037\ M_\odot$, $M_2 = 1.162 \pm 0.011\ M_\odot$, $R_1 = 3.526 \pm 0.009\ R_\odot$, $R_2 = 2.640 \pm 0.010\ R_\odot$, $T_{\rm eff_1} = 18000 \pm 600$ K, y $T_{\rm eff_2} = 6200 \pm 200$ K. Analizamos los residuos entre los tiempos observados y calculados para el eclipse medio y obtenemos una tasa de cambio del período de $\dot{P}/P = 6.68 \times 10^{-7}$ yr^{-1}. Estimamos una tasa de transferencia de masa de $1.88 \times 10^{-7}\ M_\odot$ por año. Utilizando las magnitudes infrarojas JHK y las correcciones bolométricas para la estrella primaria, calculamos la distancia al sistema V1898 Cyg como 501 ± 5 pc. Las componentes de los movimientos propios del sistema presentan alguna información sobre su pertenencia a la Nebulosa de Norteamérica.

ABSTRACT

We present spectroscopic observations of the double-lined Algol type eclipsing binary V1898 Cyg. Analyses of the BV light curves and RVs led to determination of the fundamental stellar parameters of the V1898 Cyg's components. The absolute parameters for the stars are derived as: $M_1 = 6.054 \pm 0.037\ M_\odot$, $M_2 = 1.162 \pm 0.011\ M_\odot$, $R_1 = 3.526 \pm 0.009\ R_\odot$, $R_2 = 2.640 \pm 0.010\ R_\odot$, $T_{\rm eff_1} = 18000 \pm 600$ K, and $T_{\rm eff_2} = 6200 \pm 200$ K. The residuals between the observed and computed times of mid-eclipses were analysed and a rate of the period change $\dot{P}/P = 6.68 \times 10^{-7}$ yr^{-1} was obtained; a mass transfer rate of $1.88 \times 10^{-7}\ M_\odot$ in a year is estimated. We have calculated the distance to the system V1898 Cyg as 501 ± 5 pc using the infrared JHK magnitudes and bolometric corrections for the primary star. The components of the system's proper motions present some indications about membership to the North America nebula.

Key Words: binaries: close — binaries: eclipsing — binaries: general — binaries: spectroscopic — stars: individual (V1898 Cyg)

1. INTRODUCTION

V1898 Cyg (HD 200776, BD +45° 3384, 2MASS J21035377+4619499, HIP 103968, $V = 7^m.81$, $(B - V) = +0^m.01$) was discovered to be a single-lined spectroscopic binary by Abt, Levy, & Gandet (1972). HD 200776 was included in the list of bright OB stars to be observed for the determination of galactic rotation constants and other galactic parameters. Their spectroscopic observations yield that HD 200776 is a spectroscopic binary with an orbital period of 2.9258 days. They also calculated the preliminary elements and mass function for the system. McCrosky & Whitney (1982) searched for photometric variations in some short-period spectroscopic binaries (including HD 200776) given in the Seventh Catalogue of the Orbital Elements of Spectroscopic Binary System (Batten, Fletcher, & Mann 1978). They observed abrupt drops, amounting to

[1]Based on observations collected at Catania Astrophysical Observatory (Italy) and TÜBİTAK National Observatory (Antalya, Turkey).

[2]Department of Astronomy and Space Sciences, Science Faculty, Ege University, Turkey.

[3]TÜBİTAK National Observatory, Akdeniz University Campus, Turkey.

$0^m.2 - 0^m.4$, in the brightness of the system which were inconsistent with the orbital period proposed by Abt et al. (1972). Photometric observations in the B and V-bandpass made by Halbedel (1985) revealed that HD 200776 is an eclipsing binary with both eclipses nearly identical, in contrast to the spectroscopic observations. He proposed a new orbital period of 3.0239 days, 3 percent longer than that given by Abt et al. (1972). Caton & Smith (2005, hereafter CS) published a new light curve and new times of mid-eclipses as well as a new orbital period of 1.5131273 days, nearly half that of given by Halbedel (1985). Later, Dallaporta & Munari (2006, hereafter DM) presented complete and accurate BV light curves of HD 200776 as well as three times for the mid-primary eclipse. Fortunately the same comparison star was used in the photometric observations of Halbedel (1985) and DM. No further spectroscopic observations were made for this eclipsing-spectroscopic binary after Abt et al. (1972).

The main aims of this study are: (1) to detect some lines of the secondary component; (2) to reveal radial velocities for both components; (3) to solve the radial velocity curves for the primary and secondary components on the basis of new observations in order to obtain accurate masses and radii; and (4) to determine the rotational velocities of the components and compare them with those expected for orbital synchronization.

2. SPECTROSCOPIC OBSERVATIONS

The spectra were obtained with several telescopes over the course of three years, beginning in 2007. Table 1 lists the full set of observations. The first set was observed with the Échelle spectrograph (FRESCO) at the 91 cm telescope of Catania Astrophysical Observatory. Spectroscopic observations were performed with the spectrograph fed by the telescope through an optical fibre (UV-NIR, 100 μm core diameter) and located, in a stable position, in the room below the dome level. Spectra were recorded on a CCD camera equipped with a thinned back-illuminated SITe CCD of 1k×1k pixels (size 24×24 μm). The cross-dispersed échelle configuration yields a resolution of about 22000, as deduced from the full width at half maximum of the lines of the Th-Ar calibration lamp. The spectra cover the wavelength range from 4300 to 6650 Å, split into 19 orders. In this spectral region, and in particular in the blue portion of the spectrum, there are several lines useful for measuring the radial velocity, as well as for spectral classification of the stars.

The system was also observed with the Turkish Faint Object Spectrograph Camera (TFOSC) attached to the 1.5 m RTT150 telescope on August 07–20, 2010 under good seeing conditions[4]. The wavelength coverage of each spectrum was 4100–9000 Å in 11 orders, with a resolving power of $\lambda/\delta\lambda$ 7000 at 6563 Å.

The electronic bias was removed from all spectra and we used the CRREJECT task of IRAF[5] for cosmic ray removal. The échelle spectra were extracted and wavelength calibrated by using a Fe-Ar and Th-Ar lamp source with help of the IRAF echelle package. The stability of the instruments was checked by cross-correlating the spectra of the standard star against each other using the FXCOR task in IRAF. The standard deviation of the differences between the velocities measured using FXCOR and the velocities in Nidever et al. (2002) was about 1.1 km s^{-1}.

Twenty-eight spectra of V1898 Cyg were collected during the two different seasons. Typical exposure times for the V1898 Cyg spectroscopic observations were between 2400 and 2600 s for the Catania telescope and 1200 s for the RTT150 telescope. The signal-to-noise ratio (S/N) achieved was between 70 and 115, and ∼150 depending on atmospheric condition. α Lyr (A0V), 59 Her (A3IV), ι Psc (F7V), HD 27962 (A2IV), and τ Her (B5IV) were observed during each run as radial velocity and/or rotational velocity templates. The average S/N at the continuum in the spectral region of interest was 150–200 for the standard stars.

3. SPECTROSCOPIC ANALYSIS

Double-lined spectroscopic binaries reveal two peaks in the cross-correlation function (CCF) between variable and the radial velocity template spectrum, which displace back and forth, as seen in Figure 1. The location of the peaks allows to measure the radial velocity of each component at the time of observation. The cross-correlation technique applied to digitized spectra is now one of the standard tools for the measurement of radial velocities in close binary systems.

The radial velocities of V1898 Cyg were obtained by cross-correlating échelle orders of the V1898 Cyg spectra with the spectra of the bright radial velocity standard stars α Lyr (A0V), 59 Her (A3IV) and ι Psc (F7V) (Nordström et al. 2004). For this purpose the IRAF task FXCOR was used.

[4]Further details on the telescope and the spectrograph can be found at `http://www.tug.tubitak.gov.tr`.

[5]IRAF is distributed by the National Optical Observatory, which is operated by the Association of the Universities for Research in Astronomy, inc. (AURA) under cooperative agreement with the National Science Foundation.

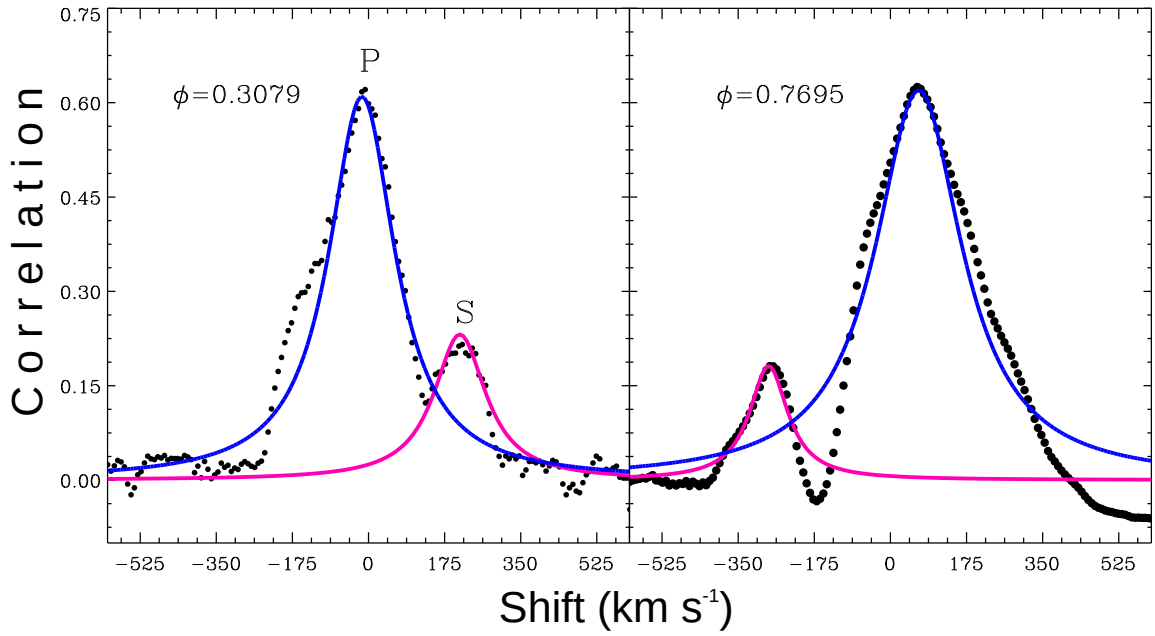

Fig. 1. Sample of Cross Correlation Functions (CCFs) between V1898 Cyg and the radial velocity template spectrum (Vega) at four different orbital phases. The color figure can be viewed online.

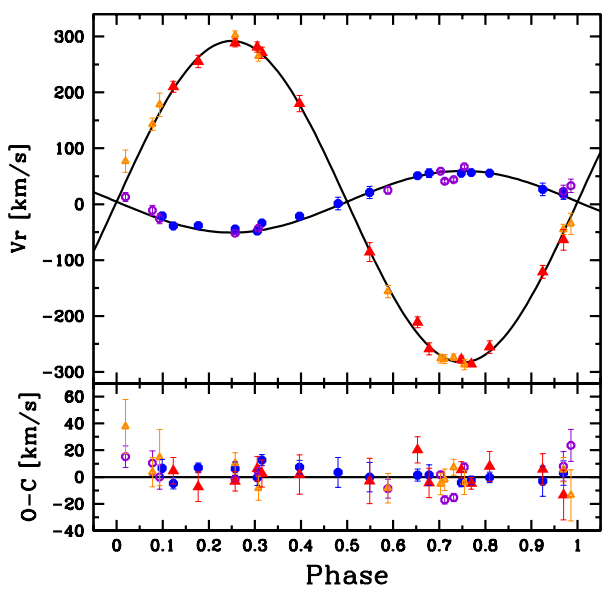

Fig. 2. Radial velocities of the primary (dots) and secondary stars (triangles) folded on an orbital period of 1.513126 days. The velocities obtained at the Catania observatory are indicated by filled symbols while those obtained at the National Observatory of Turkey by open symbols. The vertical lines show error bars of each radial velocity. The residuals between the observed and computed RVs are plotted in the lower panel. The color figure can be viewed online.

Figure 1 shows examples of CCFs of V1898 Cyg near the first and second quadrature. The two non-blended peaks correspond to each component of V1898 Cyg. We applied the cross-correlation technique to five wavelength regions with well-defined absorption lines of the primary and secondary components. These regions include the following lines: Si III 4568 Å, Mg II 4481 Å, He I 5016 Å, He I 4917 Å, He I 5876 Å. The stronger CCF peak corresponds to the more massive component that also has a larger contribution to the observed spectrum. To better evaluate the centroids of the peaks (i.e. the radial velocity difference between the target and the template), we adopted two separate Gaussian fits for the case of significant peak separation.

The radial velocity measurements, listed in Table 1 together with their standard errors, are weighted means of the individual values deduced from each order. The observational points and their error bars are displayed in Figure 2 as a function of orbital phase as calculated by means of the linear part of the ephemeris given in equation (2). The radial velocities of the secondary component of V1898 Cyg are presented for the first time in this study. The simultaneous analysis of both curves shows the semi-amplitude of the more massive, more luminous component to be $K_1 = 55.2 \pm 0.8$ km s^{-1} and $K_2 = 287.6 \pm 2.1$ km s^{-1} for the secondary component, with a systemic velocity of 4.4 ± 0.8 km $^{-1}$.

TABLE 1

RADIAL VELOCITIES OF THE V1898 CYG'S COMPONENTS[1]

HJD	Phase	Star 1			Star 2			Remarks
2400000+		$\mathbf{V}_p$	σ	O-C	$\mathbf{V}_s$	σ	O-C	
54327.55412	0.5489	21.1	10.9	0.0	−85.5	16.9	−3.0	a
54328.50480	0.1772	−38.1	3.6	6.9	255.3	11.1	−7.2	a
54329.46135	0.8093	55.5	3.9	−0.3	−255.5	11.1	8.0	a
54330.47685	0.4805	1.2	11.1	3.5	···	···	···	a
54331.44914	0.1231	−38.8	4.2	−4.7	210.1	9.9	4.7	a
54335.45358	0.7695	56.7	3.3	−2.5	−285.8	4.3	−4.8	a
54336.40281	0.3969	−21.5	5.1	7.3	179.9	14.6	1.9	a
54337.46485	0.0988	−21.1	6.6	6.5	···	···	···	a
54338.44704	0.7479	55.5	3.1	−4.1	−277.7	6.1	5.5	a
54360.40110	0.2571	−44.4	5.1	6.3	288.6	7.2	−3.2	a
54361.41090	0.9245	16.6	11.2	−3.0	−121.1	11.6	5.8	a
54362.55110	0.6780	55.5	7.7	1.4	−258.6	10.9	−4.3	a
54363.50010	0.3052	−47.9	5.9	−0.5	281.1	9.2	6.1	a
54364.50527	0.9695	18.0	9.1	3.1	−63.7	18.5	−13.4	a
54365.53939	0.6530	51.1	4.5	1.4	−211.1	9.8	20.3	a
54366.54137	0.3152	−33.5	4.1	12.6	270.9	10.1	2.6	a
55387.53130	0.0777	−11.0	9.0	10.4	143.0	11.0	3.6	b
55390.46920	0.0193	13.0	8.0	15.2	77.0	20.0	37.8	b
55390.58090	0.0932	−26.0	9.0	0.0	178.0	21.0	14.6	b
55391.50380	0.7031	59.0	2.0	1.8	−276.0	8.0	−5.2	b
55391.58150	0.7544	67.0	3.0	7.4	−287.0	9.0	−3.9	b
55392.41900	0.3079	−43.0	3.0	4.1	265.0	9.0	−8.3	b
55393.41980	0.9694	23.0	11.0	8.0	−45.0	9.0	5.5	b
55394.57290	0.7314	44.0	3.0	−15.2	−274.0	6.0	7.2	b
55396.47080	0.9857	33.0	12.0	23.6	−35.0	19.0	−13.6	b
55397.38320	0.5887	25.0	7.0	−8.6	−156.0	11.0	−8.3	b
55397.56950	0.7119	41.0	3.0	−17.0	−277.0	8.0	−2.0	b
55398.39480	0.2573	−52.0	2.0	−1.4	302.0	8.0	10.2	b

[1]The columns give the heliocentric Julian date, the orbital phase, the radial velocities of the two components with the corresponding errors and residuals.

Remarks: (a) Based on Catania and (b) on TUG observations.

3.1. *Spectral classification*

The spectral types of the stars can be found either from photometry or from spectroscopy or from both. The apparent visual magnitude and colors of V1898 Cyg were estimated by Hiltner (1956) as $V = 7^m.81$, $B - V = 0^m.01$, $U - B = -0^m.82$. However the apparent magnitudes are given by Reed (2003) as $7^m.0$, $7^m.80$ and $7^m.82$ in the U, B and V passbands, respectively. On the other hand, the $B - V$ color of the system out of eclipse was determined as $0^m.01$ by Halbedel (1985). We computed the $B-V$ color of the system at the maxima as $0^m.036$ using the data given by Dallaporta & Munari (2006). The combined spectral types are given as B1 IVp by Abt et al. (1972) and B2 III by Kennedy & Buscombe (1974). The infrared magnitudes of the system are given by Cutri et al. (2003) as $J = 7^m.697$, $H = 7^m.718$ and $K = 7^m.757$. Unfortunately, intermediate- and narrow-band photometric measurements are not available. Bessell, Castelli, & Plez (1998) derive reddening-independent Q-parameter from theoretical colors as $Q = (U-B) - 0.71\,(B-V)$. They also predict an interstellar reddening for the main-sequence OB stars as $E(B-V) = (B-V) - ((U-B) - 0.71(B-V))/3$. Using the observed $(U - B)$ and $(B - V)$ colors by Hiltner (1956) we find $E(B-V) = 0^m.28$, while Dal-

laporta & Munari (2006) estimate the reddening as $0^m.31$.

We computed the intrinsic colors of the primary component using the JHK magnitudes as $J-H = -0^m.021 \pm 0^m.044$ and $H-K = -0^m.039 \pm 0^m.033$. V1898 Cyg is located between supergiants and dwarfs in the infrared $(J-H)-(H-K)$ diagram (Tokunaga 2000). Using the the equations given by Straižys, Corbally, & Laugalys (2008) we estimated the interstellar reddening as $E(J-H) = 0^m.106 \pm 0^m.060$ and $E(H-K) = 0^m.052 \pm 0^m.060$. Using the transformation equation given by Bessell et al. (1998) we find $E(B-V) = 0^m.286$, in very good agreement with that found from the UBV colors. Since the observed common color index is $0^m.036$ one obtains an intrinsic $B-V$ color of $-0^m.25$ which corresponds to a B1V star in the calibrations of Papaj, Krelowski, & Wegner (1993).

We used our spectra to determine the spectral type of the primary component of V1898 Cyg. We followed the procedures of Hernández et al. (2004), choosing helium lines in the blue-wavelength region, where the contribution of the secondary component to the observed spectrum is almost negligible. From several spectra we measured EWs of HeI λ 4026, 4144, 4387, 4922 as 0.867 ± 0.044, 0554 ± 0.062, 0.497 ± 0.090, 0.768 ± 0.028 Å, respectively. Then we used the EW-spectral type diagrams given by Hernández et al. (2004). The EWs of the helium lines indicate that the spectral type of the primary component is $B1.8 \pm 0.6$ which is in a agreement with that obtained from infrared photometry. The calibration of Papaj et al. (1993) gives an effective temperature of 18700 K and $B-V$ of $-0^m.21$ for a B2V star, 16800 K and $-0^m.19$ for the same spectral type but for a giant star. Therefore, we estimated an effective temperature of 18000 ± 600 K for the primary component of V1898 Cyg.

3.2. *Reddening*

The measurement of reddening is a key step in determining the distance of stars. V1898 Cyg is located in the direction of the NAP, where reddening varies from one place to other. We estimated the reddening in the $B-V$ color as $0^m.29$ using the infrared colors. On the other hand we find $E(B-V) = 0^m.25$ for a star of type B2V and $E(B-V) = 0^m.23$ for a B2III star. The photometric and spectroscopic determinations of the interstellar reddening seem to be in a good agreement within a 3σ error. Our spectra cover the interstellar Na I (5890 and 5896 Å) doublet, which is an excellent estimator of the reddening as demonstrated by Munari & Zwitter (1997). They calibrated a tight relation linking the Na I D1 (5890 Å) equivalent widths with the $E(B-V)$ reddening. On spectra obtained at quadratures, lines from both components are un-blended with the interstellar ones, and they can therefore be accurately measured. We derive an equivalent width of 0.52 ± 0.06 Å for the Na I D1 line, which corresponds to $E(B-V) = 0^m.33 \pm 0.09$. Since the star is located nearly on the galactic plane ($l = 87°.60$, $b = -0°.34$) and near the edge of North America nebula (NAN) such a reddening at optical wavelengths is expected.

3.3. *Rotational velocity*

The width of the cross-correlation profile is a good tool for the measurement of $v \sin i$ (see, e.g., Queloz et al. 1998). The rotational velocities ($v \sin i$) of the two components were obtained by measuring the FWHM of the CCF peaks in nine high-S/N spectra of V1898 Cyg acquired close to the quadratures, where the spectral lines have the largest Doppler-shifts. In order to construct a calibration curve FWHM-$v \sin i$, we have used an average spectrum of HD 27962, acquired with the same instrumentation. Since the rotational velocity of HD 27962 is very low but not zero ($v \sin i \simeq 11$ km s^{-1}, e.g., Royer et al. (2002) and references therein), it could be considered as a useful template for A-type stars rotating faster than $v \sin i \simeq 10$ km s^{-1}. The spectrum of HD 27962 was synthetically broadened by convolution with rotational profiles of increasing $v \sin i$ in steps of 5 km s^{-1} and the cross-correlation with the original one was performed at each step. The FWHM of the CCF peak was measured and the FWHM-$v \sin i$ calibration was established. The $v \sin i$ values of the two components of V1898 Cyg were derived from the FWHM of their CCF peak and the aforementioned calibration relations, for a few wavelength regions and for the best spectra. This gave values of 110 ± 5 km s^{-1} for the primary star and 90 ± 9 km s^{-1} for the secondary star.

4. TIMES OF MINIMA AND THE ORBITAL PERIOD

Times of mid-eclipses were published by Halbedal (1985), CS, DM and Brát et al. (2008). These times of eclipses are presented in Table 2. The O-C(I) residuals are computed using the light curve elements given below,

$$\mathrm{MinI(HJD)} = 2\,450\,690.6948 + 1^d.51311 \times E\,, \quad (1)$$

where the orbital period is adopted from DM. The behavior of the deviations from the linear light curve

TABLE 2

TIMES OF MID-ECLIPSES FOR V1898 CYG AND THE O-C RESIDUALS (SEE TEXT)

Minimum time (HJD-2400000)	Epoch	O-C(I)	O-C(II)	O-C(III)	Ref.
45960.6758	−3126	−0.0371	0 .0139	0.0004	1
45963.6986	−3124	−0.0406	0.0105	−0.0030	1
46010.6101	−3093	−0.0355	0.0151	0.0018	1
46013.6351	−3091	−0.0367	0.0138	0.0006	1
50690.6948	0	0.0000	0.0010	0.0010	3
52169.7772	977.5	0.0174	0.0027	0.0014	3
52185.6636	988	0.0161	0.0013	0.0000	3
52895.3220	1457	0.0259	0.0036	0.0007	2
52901.3740	1461	0.0255	0.0031	0.0002	2
52928.6107	1479	0.0262	0.0035	0.0005	3
53207.7802	1663.5	0.0269	0.0013	−0.0025	3
53226.6966	1676	0.0294	0.0036	−0.0003	3
53246.3663	1689	0.0287	0.0027	−0.0013	2
53270.5757	1705	0.0284	0.0021	−0.0020	3
54443.2559	2480	0.0483	0.0096	0.0011	4
54443.2565	2480	0.0489	0.0102	0.0017	4
54691.4070	2644	0.0494	0.0080	−0.0016	4
54691.4089	2644	0.0513	0.0099	0.0003	4
54691.4097	2644	0.0521	0.0107	0.0011	4

References: (1) Halbedel (1985), (2) Dallaporta & Munari (2006), (3) Caton & Smith (2005), (4) Brát et al. (2008).

elements O-C(II) with respect to the epoch numbers suggests an upward curved parabola. Therefore, a parabolic fit to the data was adopted, which gives,

$$\mathrm{MinI(HJD)} = 2\,450\,690.6938(8) + 1^d.5131260(2) \times E + 1.38(13)10^{-9} \times E^2 \,. \quad (2)$$

The standard mean errors in the last digits are given in parentheses. The coefficient of the quadratic term is positive, which indicates that the orbital period of the system is increasing with the epoch number. Such a quadratic ephemeris appears to a very good representation of the orbital period change of V1898 Cyg, as well as other interacting Algols. This quadratic behaviour of the O-C(II) residuals, plotted in the upper panel of Figure 3, is an indication of the secular period increase for the system. In the bottom panel of Figure 3 the O-C(III) residuals with respect to ephemeris (2) are plotted, which illustrates a good agreement between the timings and the new ephemeris. It is known that the classical Algols have an evolved less massive component which fills its Roche lobe and transfers its mass to the more massive primary star through the Lagrangian L_1 point of the system. The orbital period of the system is increasing at an average rate of $\dot{P}/P = 6.68(\pm 0.63) \times 10^{-7}$ yr^{-1} which means that the orbital period has increased by about 0.38(±0.04) seconds in the last 24 years. The sum of the squares of residuals for the parabolic fit is 3.672×10^{-5} d^2. We limited times of mid-eclipses covering about 24 yrs. The time span of the observations is too short to reveal any abrupt period change caused by the fast mass transfer phenomenon. Of course, observations to be obtained in the coming years could indicate some hints about the nature of the orbital period change. Assuming a conservative mass transfer from the less massive component to the more massive primary star we estimate a transfer of $1.88(\pm 0.17) \times 10^{-7}$ $M_\odot$ in a year.

5. ANALYSIS OF THE LIGHT CURVES

Three light curves V1898 Cyg have been obtained and published. The first photometric observations were obtained by Halbedel (1985) between July and November, 1985. The second photometric observations were made by CS from August 22, 2001 to Oc-

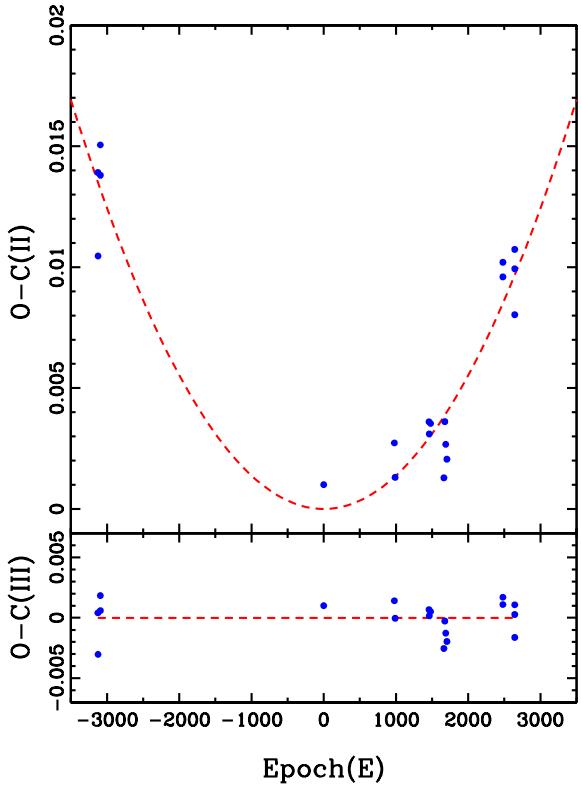

Fig. 3. The O-C(II) residuals plotted versus the epoch number for V1898 Cyg. A least-squares quadratic fit to the residuals is shown by the dashed line (upper panel). In the lower panel the O-C(III) residuals, the deviations from the quadratic fit, are also plotted. The color figure can be viewed online.

tober 26, 2004. The star was observed by DM from July 22, 2003 to September 17, 2004. Only the V-band light curve and observational data of CS were published. However, DM published the B and V light curves. The V light curves obtained in these studies are asymmetric in shape, and they differ from each other. The brightness of the system shows a fast decrease from phase 0.75 up to external contact. However, the increase in brightness following the primary eclipse is no steeper. The distortion of the light curve preceding the primary eclipse is larger in the CS light curve. A remarkable change in the light curve is seen at the phase interval between 0.09 and 0.42. The total brightness of the system in the V-bandpass at this phase interval is greater by about $0^m.03$ in the CS light curve than in DM's. However, CS report that the brightness of their primary comparison star showed light variations during the observations. Moreover the depth of the secondary eclipse is larger by about $0^m.007$ in the light curve of CS than in that of DM. We should note that there is also a slight asymmetry in both the DM's B- and V-passband light curves. This feature is attributed to the transfer of material from the cool secondary to the high temperature primary star which occults a small area of the primary star just before the deeper eclipse.

Acerbi & Barani (2007) analysed the DM's light curves. Since the spectroscopic mass-ratio was not available at that time, they started the analysis by deriving the photometric mass-ratio. Their preliminary analysis indicated that the mass-ratio for the system was about 0.30. Assuming an effective temperature of 20183 K for the primary component and that the secondary, less massive, star fills its corresponding Roche-lobe, i.e. a semi-detached configuration, they arrived at preliminary elements for the system. Their orbital parameters were: $i = 70°$, $r_1 = 0.3196$ and $r_2 = 0.2795$ and $T_2 = 7500$ K. Since the light curves were asymmetric they reported that the agreement between the computed and observed light curves was not very satisfactory: the sum of the squares of the residuals was about 0.814.

In order to analyse the light curves we choose the Wilson-Devinney (W-D) code implemented into the PHOEBE package tool by Prsa & Zwitter (2005). A preliminary analysis indicates that the system is a classical Algol, the secondary component filling its corresponding Roche lobe. Therefore Mode-5 is applied. The WD code is based on Roche geometry which is sensitive to the mass ratio which is taken from RV analysis as 0.192±0.002. Gravity-darkening exponents $g_1 = 1$, $g_2 = 0.32$ and bolometric albedos $\mathrm{Alb}_1 = 1$, $\mathrm{Alb}_2 = 0.5$ were set, i.e. the more massive star has a radiative envelope while the less massive secondary has a convective atmosphere. We used the non-linear square-root limb-darkening and the bolometric limb-darkening coefficients from the tables of Díaz-Cordovés, Claret, & Giménez (1995) and van Hamme (1993).

The orbital inclination (i), effective temperature of the secondary star (T_2), surface potential of the primary (Ω_1), phase shift ($\Delta\phi$), and fractional luminosity of the primary (L_1) were taken as adjustable parameters. The other parameters were fixed. The iterations were carried out automatically until convergence was achieved, and a solution was defined as the set of parameters for which the differential corrections were smaller than the probable errors. The final results obtained by separate analysis of three light curves are listed in Table 3 and the computed light curves are shown as continuous lines in Figure 4. The uncertainties assigned to the adjusted parameters are the internal errors provided directly

TABLE 3

RESULTS OF INDIVIDUAL LIGHT CURVE ANALYSES FOR V1898 CYG

Parameter	CS V	DM B	DM V
$i(^\circ)$	74.20±0.02	73.05±0.03	73.03±0.03
T_1 (K)		18000[Fix]	
T_2 (K)	6582±65	6205±76	6109±50
Ω_1	3.0887±0.0085	3.2885±0.0116	3.2784±0.0103
Ω_2		2.2122[Fix]	
$q_{\rm spec}$		0.1918[Fix]	
$L_1/(L_{1+2})$	0.9563±0.0013	0.9801±0.0017	0.9490±0.0016
r_1	0.3513±0.0013	0.3296±0.0013	0.3286±0.0012
r_2	0.2464±0.0012	0.2464±0.0012	0.2464±0.0012
$\Delta\phi$	0.0022±0.0001	0.0008±0.0001	0.0008±0.0001
$\Sigma(\rm res)^2$	0.1196	0.0109	0.0123

Ref: r_1, r_2: Relative volume radii, CS V: Caton & Smith's (2005) V-band light curve, DM B and DM V: The B- and V-band light curves of Dallaporta & Munari (2006). The errors quoted for the adjustable parameters are the formal errors determined by the WD-code.

TABLE 4

FUNDAMENTAL PARAMETERS OF V1898 CYG

Parameter	Primary	Secondary
Mass ($M_\odot$)	6.054±0.037	1.162±0.011
Radius ($R_\odot$)	3.526±0.009	2.640±0.010
$T_{\rm eff}$ (K)	18 000± 600	6 200±200
log ($L/L_\odot$)	3.071±0.029	0.957±0.085
log g (cgs)	4.125±0.002	3.660±0.004
Spectral type	B2IV±1	G2III±1
a ($R_\odot$)	10.714±0.022	
i ($^\circ$)	73.05±0.03	
d (pc)	501±5	
$(v \sin\ i)_{\rm obs}$ (km s^{-1})	110±5	90±9
$(v \sin\ i)_{\rm calc}$ (km s^{-1})	112.8±0.3	84.5±0.4
J, H, K_s (mag)*	7.697±0.035, 7.718±0.026, 7.757±0.020	
$\mu_\alpha \cos\delta$, μ_δ (mas yr^{-1})**	2.07±0.62, 0.81±0.53	

2MASS All-Sky Point Source Catalogue (Cutri et al. 2003).

Newly Reduced Hipparcos Catalogue (van Leeuwen 2007).

by the WD code. As seen in Table 3 the sum of the squares of the residuals is 0.0109 and 0.0123 for the B- and V-bandpass light curves, being 75-times smaller than those of the analysis made by Acerbi & Barani (2007) of the same data. In the bottom panel of Figure 4 the residuals between observed and computed intensities are also plotted. The residuals reveal that the binary model may represent the observed DM's light curves successfully. However, the computed light curve differs mostly from fourth contact to beginning of secondary eclipse in the CS light curve.

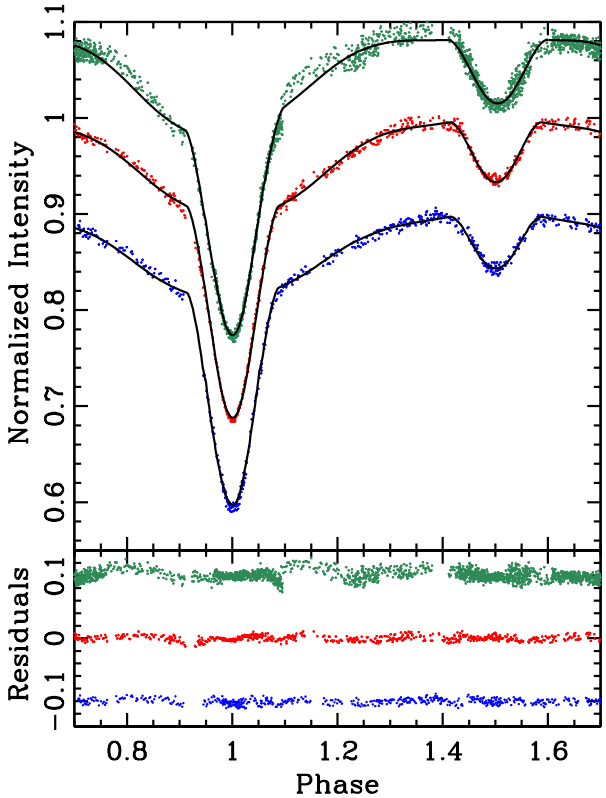

Fig. 4. Comparison of the observed and computed light curves of V1898 Cyg. From top to bottom the CS-V, DM-B and DM-V light curves, respectively. In the lower panel residuals have been plotted to show the goodness of the fits. The color figure can be viewed online.

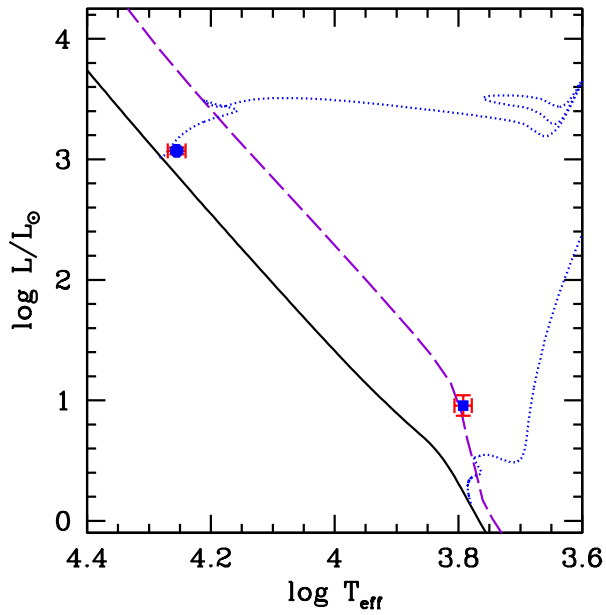

Fig. 5. Location of the two stellar components of V1898 Cyg in the log $T_{\rm eff}$ − log L diagram, together with evolutionary models for 1.15 and 6.0 $M_\odot$. The solid circle corresponds to the primary and the solid square to the secondary with error bars. The zero-age main-sequence (continuous line) and terminal-age MS (long-dashed-dotted line) are also plotted. The evolutionary tracks are shown by dotted lines. The color figure can be viewed online.

6. DISCUSSION AND CONCLUSION

Since the sum-of-squares in the analysis of CS light curve is too large when compared to the DM's light curves, and there is doubt about the light constancy of their primary comparison star, we take weighted mean orbital parameters obtained by the analysis of the DM's B and V light curves. The mean parameters obtained from the light curve analysis are: $i = 73^\circ.05 \pm 0.02$, $r_1 = 0.3291 \pm 0.0013$, $r_2 = 0.2464 \pm 0.0012$, $T_2 = 6200 \pm 200$ K. The fractional radius of the secondary component exceeds its corresponding Roche lobe radius by about 4%. Combining the results obtained from RVs analysis we have derived the astrophysical parameters of the components and other properties listed in Table 4. The mass and radius of the massive primary star are derived with an accuracy of 0.6 and 1.4 percent, while for the less massive donor star we obtain 0.4 and 0.5 percent. The observed and computed rotational velocities of the components are in good agreement, showing nearly synchronized rotation. In Figure 5, we plot the location of the V1898 Cyg stellar components in a log $T_{\rm eff}$ − log $L/L_\odot$ diagram. The evolutionary tracks for masses 6 and 1.16 $M_\odot$ are also shown in this figure. For constructing the solar metallicity evolutionary tracks, we used the Cambridge version of the STARS CODE which was originally developed by Eggleton (1971) and substantially updated by Eldridge & Tout (2004). The continuous and dashed lines from left to right show the zero-age and terminal-age main-sequences, respectively. While the primary star is located very close to the ZAMS the secondary, less massive star appears to have evolved up to the giant branch as is common in semi-detached Algol-type binaries. The appearance of the components in the HR diagram is common for the classical Algol-type binaries. The donor seems to have higher temperature and luminosity, and most of its atmospheric material has been transferred to its companion. Since the secondary component fills its Roche lobe it transfers its mass to the more massive component. Therefore the orbital period change is attributed to the mass transfer. However, the gainer

has climbed up to higher effective temperature and luminosity. In addition, V1898 Cyg is located in the diagram between the specific angular momentum and mass-ratio where angular momentum decreases faster (see İbanoğlu et al. 2006). The average distance to the system was calculated to be 501 ± 5 pc. However, the average distance to the system is estimated to be 621^{+443}_{-182} pc from the trigonometric parallax measured by the Hipparcos mission. The distance derived in this study is smaller by about 20 percent, but, most importantly, it has a very small uncertainty when compared with that measured by the Hipparcos mission.

The North America (NGC 7000) and Pelican (IC 5070) nebulae (NAP) are known to be the most nearby huge, extended HII regions where star formation with intermediate mass is still ongoing. The distance to this extended star-forming region has been estimated from 200 to 2000 pc (see for example, Bally & Reipurth 2003). While Herbig (1958) estimates a distance of 500 pc, Laugalys & Straižys (2002) derived a distance to NAP 600 ± 50 pc. If the star is a member of NAP complex, the distance to the star derived by us is in better agreement with that of Herbig, but also agrees with that proposed by Laugalys & Straižys (2002) within 2σ. Recently, Straižys et al. (2008) listed several OB stars in the vicinity of NAP, one of which is V1898 Cyg. The distance to the star estimated by us appears to confirm its membership to NAN. Proper motions for V1898 Cyg are given in the SIMBAD database as $\mu_\alpha \cos\delta = 2.07 \pm 0.62$ mas yr^{-1} and $\mu_\delta = 0.81 \pm 0.53$ mas yr^{-1}, with a space velocity of 45.3 km s^{-1}. We selected about 20 stars in the vicinity of V1898 Cyg listed by Laugalys & Straižys (2002) for comparing their mean proper motions with that of the variable. The velocities of the stars vary from 45 to -97 km s^{-1}, and the mean proper motions are: $\mu_\alpha \cos\delta = 0.48$, $\mu_\delta = -2.85$ mas yr^{-1}. It seems that one cannot definitely classify which stars actually belong to the NAP and which do not.

We thank Prof. G. Strazzulla, director of the Catania Astrophysical Observatory, and Dr. G. Leto, responsible for the M. G. Fracastoro observing station, for their warm hospitality and for allocating telescope time for the observations. We also thank TÜBİTAK National Observatory (TUG) for partial support in using RTT150 with project numbers 10ARTT150-483-0 and 09BRTT150-468-0. This research has been also supported by TÜBİTAK under project number 109T708 and INAF and Italian MIUR. This research has made use of the ADS and CDS databases, operated at the CDS, Strasbourg, France and ULAKBİM Süreli Yayınlar Kataloğu. The authors thank the anonymous referee for his/her valuable comments.

REFERENCES

Abt, H. A., Levy, S. G., & Gandet, T. L. 1972, AJ, 77, 138
Acerbi, F., & Barani, C. 2007, Open Eur. J. Variable Stars, 77, 1
Bally, J., & Reipurth, B. 2003, AJ, 126, 893
Batten, A. H., Fletcher, J. M., & Mann, P. J. 1978, Publ. Dom. Astrophys. Obs., 15, 121
Bessell, M. S., Castelli, F., & Plez, B. 1998, A&A, 337, 321
Brát L., et al. 2008, Open Eur. J. Variable Stars, 94, 1
Caton, D. B., & Smith, A. B. 2005, Inf. Bull. Variable Stars, 5699, 1 (CS)
Cutri, R. M., et al. 2003, The 2MASS All-Sky Catalog of Point Sources (Pasadena: NASA/IPAC Infrared Science Archive) `http://irsa.ipac.caltech.edu/applications/Gator`
Dallaporta, S., & Munari, U. 2006, Inf. Bull. Variable Stars, 5714, 1 (DM)
Díaz-Cordovés, J., Claret, A., & Giménez, A. 1995, A&AS, 110, 329
Eggleton, P. P. 1971, MNRAS, 151, 351
Eldridge, J. J., & Tout, C. A. 2004, MNRAS, 348, 201
Halbedel, E. M. 1985, Inf. Bull. Variable Stars, 2663, 1
Herbig, G. H. 1958, ApJ, 128, 259
Hernández, J., Calvet, N., Briceño, C., Hartmann, L., & Berlind, P. 2004, AJ, 127, 1682
Hiltner, W. A. 1956, ApJS, 2, 389
İbanoğlu, C., Soydugan, F., Soydugan, E., & Dervişoğlu, A. 2006, MNRAS, 373, 435
Kennedy, P. M., & Buscombe, W. 1974, MK Spectral Classifications, Published since Jaschek's La Plata Catalogue (Evanston: Northwestern University)
Laugalys, V., & Straižys, V. 2002, Baltic Astron., 11, 205
McCrosky, R. E., & Whitney, C. A. 1982, Inf. Bull. Variable Stars, 2186, 1
Munari, U., & Zwitter, T. 1997, A&A, 318, 269
Nidever, D. L., Marcy, G. W., Butler, R. P., Fischer, D. A., & Vogt, S. S. 2002, ApJS, 141, 503
Nordström, B., et al. 2004, A&A, 418, 989
Papaj, J., Krelowski, J., & Wegner, W. 1993, A&A, 273, 575
Prša, A., & Zwitter, T. 2005, ApJ, 628, 426
Reed, B. C. 2003, AJ, 125, 2531
Royer, F., Grenier, S., Baylac, M.-O., Gómez, A. E., & Zorec, J. 2002, A&A, 393, 897
Straižys, V., Corbally, C. J., & Laugalys, V. 2008, Baltic Astron., 17, 125
Queloz, D., Allain, S., Mermilliod, J.-C., Bouvier, J., & Mayor, M. 1998, A&A, 335, 183

Tokunaga, A. T. 2000, in Allen's Astrophysical Quantities, ed. A. N. Cox (4th ed.; Berlin: Springer-Verlag), 143
van Hamme, W. 1993, AJ, 106, 2096
van Leeuwen, F. 2007, A&A, 474, 653

A. Dervişoğlu, Ö. Çakırlı, C. İbanoğlu and E. Sipahi: Astronomy and Space Sciences, Science Faculty, Ege University, Dept., 35100 Bornova, İzmir, Turkey (ahmetdervisoglu@mail.ege.edu.tr).

Revista Mexicana de Astronomía y Astrofísica, **47**, 309–321 (2011)

$uvby-\beta$ PHOTOELECTRIC PHOTOMETRY OF THE OPEN CLUSTERS NGC 6811 AND NGC 6830[1]

J. H. Peña,[2] L. Fox Machado,[3] H. García,[4] A. Rentería,[2] S. Skinner,[2,5] A. Espinosa,[2] and E. Romero[2]

Received 2010 October 27; accepted 2011 June 15

RESUMEN

A partir de la fotometría fotoeléctrica $uvby-\beta$ de los cúmulos abiertos NGC 6811 (75 estrellas) y NGC 6830 (19 estrellas) realizamos la determinación de distancias y, por ende, la pertenencia de las estrellas a cada cúmulo. Asimismo, se determinaron la edad y el enrojecimiento de cada uno. Dado que recientemente se han determinado estrellas variables para el primero, realizamos un estudio de dichas variables.

ABSTRACT

From $uvby-\beta$ photometry of the open clusters NGC 6811 (75 stars), and NGC 6830 (19 stars) we were able to determine membership of the stars to each cluster, and fix the age and reddening for each. Since several short period stars have recently been found, we have carried out a study of these variables.

Key Words: open clusters and associations: individual (NGC 6811, NGC 6830) — techniques: photometric

1. INTRODUCTION

The study of open clusters and their short period variable stars is fundamental in stellar evolution. Because the cluster members are formed in almost the same physical conditions, they share similar stellar properties, such as age and chemical composition. The assumption of common age, metallicity and distance imposes strong constraints when modeling an ensemble of short period pulsators belonging to open clusters (e.g., Fox Machado et al. 2001, 2006). Thus, observational studies involving variable stars in open clusters have attracted more and more attention (e.g., Fox Machado et al. 2002; Li et al. 2002, 2004).

A series of papers (see Peña & Peniche 1994; Peña et al. 1998, 2003; Peña, Fox Machado, & Garrido 2007) study the physical nature of the short period variable stars in open clusters by means of Strömgren photometry, since, once their membership to the cluster has been established, their physical quantities can be unambiguously derived. In particular, the determination of physical parameters of cluster member stars from $uvby-\beta$ photometry can be done through a comparison with theoretical models (Lester, Gray, & Kurucz 1986, hereinafter LGK86).

As a continuation of our study, we now present observations of the open clusters NGC 6811 and NGC 6830. Both clusters have no previous published $uvby-\beta$ data.

Very recently, Luo et al. (2009) carried out a search for variable stars in the direction of NGC 6811 with CCD photometry in the B, and V bands. They detected a total of sixteen variable stars. Among these variables, twelve were catalogued as δ Scuti stars, while no variability type was assigned to the remaining stars. They claim that the twelve δ Scuti stars are all very likely members of the cluster, which makes this cluster an interesting target for asteroseismological studies. Moreover, NGC 6811 has been selected as a asteroseismic target of the Kepler space mission (Borucki et al. 1997). Therefore, deriving accurate physical parameters for the pulsating star members is very important.

For NGC 6811 Luo et al. (2009) estimated an age of $\log(t) = 8.76 \pm 0.009$ from theoretical isochrone fitting to the color magnitude diagram (CMD here-

[1]Based on observations collected at the San Pedro Mártir Observatory, Mexico.

[2]Instituto de Astronomía, Universidad Nacional Autónoma de México, Mexico.

[3]Observatorio Astronómico Nacional, Instituto de Astronomía, Ensenada, Mexico.

[4]Observatorio Astronómico de la Universidad Nacional Autónoma de Nicaragua, Nicaragua.

[5]Universidad Nacional de Panamá, Panama.

TABLE 1

LOG OF THE OBSERVING SEASONS

Epoch	Cluster	Initial date year mo day	Final date year mo day	Observers
2009 June	NGC 6811, NGC 6830	2009 06 24	2010 06 29	jhp, hg, arl
2010 August	NGC 6811	2010 08 03	2010 08 06	jhp, ss, er, ae

Observers: jhp, J. H. Peña; hg, H. García; arl, A. Rentería; ss, S. Skinner; er, E. Romero; ae, A. Espinosa.

after) and assuming a metallicity of $Z = 0.019$. They determined the distance modulus and color excess as 10.59 ± 0.09 and 0.12 ± 0.05, respectively.

To the best of our knowledge, no δ Scuti variable stars have been reported in NGC 6830 to date.

According to the compilation of data of open clusters in Paunzen & Mermilliod (2007, WEBDA), NGC 6811 has a distance [pc] of 1215; a reddening [mag] of 0.160; a distance modulus [mag] of 10.92; a log age 8.799 and no data on metallicity reported. NGC 6830 has the following: distance [pc] 1639; reddening [mag] 0.501; distance modulus [mag] 12.63; log age 7.572 with no determined metallicity.

2. OBSERVATIONS

These were all taken at the Observatorio Astronómico Nacional, Mexico in two different seasons, those of 2009 and 2010. The dates are listed in Table 1. The 1.5 m telescope to which a spectrophotometer was attached was utilized at all times. The first observing season was carried out over six nights from June–July 2009. The ID charts utilized were those of WEBDA. When the NGC 6811 data were reduced, there were several stars whose photometry showed large discrepancies with the literature. In view of this and due to the fact that several δ Scuti stars were recently discovered in this cluster (Luo et al. 2009), a second observing season was planned in 2010 to measure all of these stars in the $uvby - \beta$ system.

2.1. *Data acquisition*

The following procedure was utilized during all nights: each measurement consisted of at least five ten-second integrations of each star and one ten-second integration of the sky for the *uvby* filters and the narrow and wide filters that define Hβ. Individual uncertainties were determined by calculating the standard deviations of the fluxes in each filter for each star. The percent error in each measurement is, of course, a function of both the spectral type and the brightness of each star, but they were observed long enough to secure sufficient photons to get a S/N ratio of accuracy of $N/\sqrt{(N)}$ of 0.01 mag in most cases. Each night a series of standard stars was also observed to transform the data into the standard system. The reduction procedure was done with the numerical packages NABAPHOT (Arellano-Ferro & Parrao 1988) which reduce the data into a standard system, although some data were also taken from the *Astronomical Almanac* (2006) for the standard bright stars. The chosen system was that defined by the standard values of Olsen (1983) and the transformation equations are those defined by Grönbech, Olsen, & Strömgren (1976) and by Crawford & Mander (1966). In these equations, the coefficients D, F, H and L are the slope coefficients for $(b - y)$, m_1, c_1 and β, respectively. The coefficients B, J and I are the color terms of V, m_1, and c_1. The averaged transformation coefficients of each season determined from the mean of all nights are listed in Table 2 along with their standard deviations. Errors of the season were evaluated by means of the standard stars observed. These uncertainties were calculated through the differences in magnitude and colors, for (V, $b-y$, m_1, c_1 and β) as (0.020, 0.017, 0.011, 0.031, 0.011) respectively, which provide a numerical evaluation of our uncertainties. Emphasis is made on the large range of the standard stars in the magnitude and color values: V:(5.4, 8.7); $(b - y)$:(0.02, 0.80); m_1:(0.09, 0.67); c_1:(0.06, 1.12) and β:(2.53, 2.89).

The transformation equations used in the work have the following forms in which 'inst' stands for instrumental values and 'std' for photometric values in the standard system:

$$
\begin{aligned}
V &= \mathrm{A} + \mathrm{B}\ (b-y)(\mathrm{inst}) + y\ (\mathrm{inst}),\\
(b-y)\ (\mathrm{std}) &= \mathrm{C} + \mathrm{D}\ (b-y)(\mathrm{inst}),\\
m_1(\mathrm{std}) &= \mathrm{E} + \mathrm{F}\ m_1(\mathrm{inst}) + \mathrm{J}\ (b-y)(\mathrm{inst}),\\
c_1(\mathrm{std}) &= \mathrm{G} + \mathrm{H}\ c_1(\mathrm{inst}) + \mathrm{I}\ (b-y)(\mathrm{inst}),\\
\beta\ (\mathrm{std}) &= \mathrm{K} + \mathrm{L}\ \beta\ (\mathrm{inst}).
\end{aligned}
$$

TABLE 2

TRANSFORMATION COEFFICIENTS OBTAINED FOR THE TWO OBSERVING SEASONS

Season	B	D	F	J	H	I	L
2009	−0.005	0.975	1.002	0.037	1.008	−0.067	−1.397
σ	0.051	0.032	0.045	0.033	0.049	0.067	0.031
2010	0.002	0.962	1.021	0.025	0.991	−0.006	−1.309
σ	0.013	0.003	0.034	0.002	0.042	0.145	0.021

Table 3 lists the photometric values of the observed stars for the NGC 6811 cluster. In this table we list the following: Column 1, the ID number as in WEBDA, which follows Lindoff's nomenclature; Columns 2 to 6 the measured photometric values (N denotes the times each star was measured) the next five columns list the standard deviations from our photometry and the final columns, the spectral type for each star, determined from the $[m1]$ $[c1]$ diagram and from WEBDA and Becker (1947). The agreement between the spectral types deduced from the photometry with that reported by spectroscopic methods is interesting to note. Although there is consistency among the three values, there also is some disagreement among them. For example, W113 has spectroscopic types A4 and A8 from WEBDA and Becker (1947), respectively and there are some stars (W16 and W37) that are defined as early type stars from the spectroscopy and as later types from the photometry. Nevertheless, we note that, in general, the spectral types are coincident within the three mentioned sources. The remaining stars we classified do not have reported spectral classes. Table 4 lists in Column 1 the ID of WEBDA, Columns 2 to 6 the photometric values, Column 7 the spectral type derived from the photometry and Columns 8 and 9 the spectral types listed by WEBDA which are, respectively, Hoag & Applequist (1965) and Turner (1976).

2.2. *Comparison with other photometries*

Since no $uvby-\beta$ has been previously obtained for these clusters, a comparison of our values was made with the available UBV photometry reported in WEBDA.

NGC 6811. We compared our 2009 season photometry with that reported by WEBDA. The intersection of both sets is constituted of seventy five stars, some of them (four) showing a large difference, greater than 0.5 mag in V. There were some others (six) with differences larger than 0.1 mag. In view of this we planned and carried out a second campaign in 2010. Table 3 reports the mean values of the two observing campaigns; N indicates the number of measurements for each star. Among the stars with large differences found in the 2009 season and WEBDA, five were measured in both observational campaigns showing small differences between them. Hence, with high probability, the discrepancies cannot be attributed to our measurements because (i) these stars were measured in two different seasons one year apart by different observers and (ii) the measured standard stars show reasonable values when compared to the standard literature values. Hence, the differences can be due to either a misidentification of the star by previous authors or a variable nature of these stars. Despite these differences, a linear fit between both sets yields the equation $V_{(\mathrm{pp})} = 0.82+0.97\,V_{(\mathrm{WEBDA})}$ with a correlation coefficient of 0.97 and a standard deviation of 0.25. The color relationship yields $(b-y) = 0.06+0.57\,(B-V)$ with a correlation coefficient of 0.92 and a standard deviation of 0.09.

NGC 6830. This cluster was compared with those UBV values reported by WEBDA for a set constituted of only seven stars. The linear fit between both sets gave the equation $V_{(\mathrm{pp})} = 0.477 + 0.958 \times V_{(\mathrm{WEBDA})}$ with a correlation coefficient of 0.997 and a standard deviation of 0.080. The relationship in $B-V$ and $b-y$ gave $(b-y) = 0.117+0.573\times(B-V)$ with a correlation coefficient of 0.922 and a standard deviation of 0.022.

3. METHODOLOGY

In order to determine the physical characteristics of the stars in each cluster this procedure was followed.

The evaluation of the reddening was done by first establishing, as was stated above, to which spectral class the stars belonged: early (B and early A) or late (late A and F stars) types; the later class stars

TABLE 3

$uvby-\beta$ PHOTOELECTRIC PHOTOMETRY OF THE OPEN CLUSTER NGC 6811

WBD	V	$(b-y)$	m_1	c_1	bt	sV	sby	sm_1	sc_1	sbt	N	Spectral Type Photometry	Spectral Type WBD
4	12.681	0.259	0.127	0.861	2.706						1	A3V	A7
5	11.795	0.168	0.185	0.950	2.770	0.067	0.028	0.015	0.029	0.062	28	A5V	A2
6	14.463	0.786	0.291	0.554	2.538	0.076	0.111	0.108	0.226	0.071	3	>G	
7	14.381	0.399	0.125	0.388	2.588	0.201	0.071	0.221	0.104	0.020	3	F7V	
8	14.110	0.356	0.142	0.498	2.630	0.150	0.053	0.153	0.115	0.055	3	F7V	
9	12.081	0.166	0.218	0.959	2.790	0.080	0.015	0.029	0.067	0.077	3	Ap	A1
10	14.234	0.339	0.223	0.346	2.525	0.283	0.073	0.065	0.153	0.180	3	G2V	
12	14.363	0.455	0.148	0.387	2.540	0.098	0.067	0.057	0.142	0.094	3	G0V	
13	15.055	0.567	0.058	0.542	2.585	0.264	0.158	0.164	0.277	0.037	2	F7V	
14	13.672	0.765	0.399	0.174	2.510	0.182	0.029	0.041	0.022	0.040	2	>G	
16	12.196	0.235	0.165	0.927	2.781						1	A5V	A4
18	12.118	0.236	0.144	0.966	2.806						1	A5V	A4
22	13.034	0.522	0.267	0.230	2.529	0.019	0.018	0.005	0.023	0.039	2	K0V	
23	13.981	0.558	0.227	0.185	2.655						1	>G	
24	11.245	0.613	0.327	0.318	2.564	0.044	0.020	0.012	0.052	0.019	2	>G	G8
26	11.414	0.197	0.186	0.985	2.795						1	A5V	
31	13.308	0.327	0.131	0.635	2.760						1	F5V	
32	11.351	0.640	0.349	0.322	2.583						1	>G	G
33	11.917	0.232	0.149	0.950	2.771						1	A5V	A2
34	11.623	0.204	0.204	0.956	2.829						1	A5p	B9
35	13.859	0.325	0.206	0.406	2.559	0.084	0.071	0.052	0.071	0.020	2	G2V	
36	13.221	0.283	0.180	0.561	2.614	0.065	0.062	0.049	0.009	0.052	2	G0V	
37	11.113	0.182	0.181	0.933	2.766	0.034	0.013	0.006	0.023	0.040	29	A5V-F5Ib	
38	13.206	0.662	0.382	0.330	2.535	0.052	0.079	0.013	0.066	0.128	2	>G	
39	11.528	0.212	0.157	0.961	2.728	0.069	0.020	0.012	0.042		29	A5V	A4
40	13.070	0.111	0.147	0.632	2.673	0.127	0.062	0.073	0.100	0.071	2	A1V	
41	12.014	0.148	0.195	0.956	2.741	0.100	0.035	0.017	0.037		29	A5V	
42	12.568	0.190	0.184	0.829	2.698	0.172	0.055	0.028	0.049	0.059	29	A8V	
43	12.743	0.268	0.176	0.785	2.658	0.023	0.000	0.001	0.049	0.030	2	A8V	
44	12.046	0.169	0.182	0.935	2.757	0.082	0.033	0.016	0.032	0.029	29	A5V	
45	12.705	0.204	0.194	0.831	2.735	0.142	0.027	0.015	0.040	0.039	3	A8V	A5
46	12.958	0.329	0.116	0.533	2.645	0.058	0.006	0.017	0.047	0.043	3	F5V	
47	13.649	0.383	0.099	0.389	2.613	0.136	0.020	0.046	0.065	0.083	3	F5V	
49	12.422	0.218	0.142	0.978	2.822						1	A0V	A5
51	13.418	0.269	0.139	0.592	2.590	0.076	0.094	0.115	0.125	0.035	2	F5V	
53	12.754	0.178	0.191	0.898	2.774	0.076	0.020	0.030	0.045	0.085	3	A5V	
54	12.356	0.266	0.136	0.757	2.713	0.027	0.025	0.029	0.027	0.078	3	A8V	
56	12.160	0.247	0.149	0.787	2.691	0.013	0.025	0.024	0.055	0.037	2	A8V	
57	14.039	0.439	0.161	0.357	2.670	0.149	0.196	0.161	0.114	0.073	4	G0V	
58	14.350	0.622	0.219	0.151	2.650	0.187	0.231	0.122	0.256	0.132	3	K0V	
62	12.846	0.224	0.163	0.728	2.714						2	A8V	
63	15.234	0.979	0.846	0.714		0.193	0.569	0.401	0.677	0.294	2	>G	
64	13.609	0.352	0.088	0.557	2.897	0.041	0.016	0.056	0.021	0.366	2	F2V	
65	14.450	0.460	0.199	0.217	2.510	0.087	0.164	0.106	0.057	0.103	2	G2V	
68	10.850	0.272	0.152	0.869	2.737						1	A8V	A2
70	10.925	0.298	0.139	0.876	2.713						1	A5V	A4
71	13.716	0.388	0.154	0.473	2.551						1	G0V	A2
73	9.851	0.992	0.830	0.166	2.551						1	>G	K5
74	12.322	0.415	0.171	0.305	2.568	0.078	0.007	0.003	0.028	0.008	2	G0V	
77	13.860	0.257	0.206	0.461	2.650	0.120	0.040	0.041	0.028	0.025	2	G0V	
78	13.664	0.270	0.167	0.567	2.676	0.070	0.023	0.011	0.040	0.037	2	F7V	
79	10.393	0.935	0.719	0.146	2.519						1	>G	
82	13.025	0.705	0.341	0.333	2.546						1	>G	
85	12.860	0.308	0.134	0.545	2.684						1	F5V	
86	13.389	0.334	0.106	0.490	2.662						1	F2V	
87	12.622	0.380	0.206	0.399	2.617						1	G2V	
92	12.260	0.221	0.166	0.722	2.704						1	A8V	
99	11.962	0.168	0.184	0.957	2.817	0.036	0.036	0.028	0.028	0.078	2	A5V	B9
101	10.682	0.671	0.393	0.333	2.569						1	>G	
102	12.882	0.586	0.221	0.287	2.562						1	K0V	
105	12.419	0.230	0.241	0.850	2.802						1	Ap	A7
106	11.379	0.301	0.138	0.796	2.713						1	A8V	A3
107	12.726	0.419	0.123	0.414	2.640						1	F7V	
112	12.825	0.372	0.146	0.412	2.663						1	F9V	
113	11.471	0.233	0.144	0.990	2.767						1	A5V	A4
114	12.145	0.229	0.141	0.967	2.786	0.020	0.033	0.019	0.053	0.035	3	A5V	B7
115	11.551	0.220	0.169	0.787	2.759	0.135	0.040	0.023	0.076	0.025	3	A3V	A1
118	12.352	0.469	0.174	0.399	2.548						1	G2V	
122	12.825	0.372	0.146	0.412	2.663						1	F9V	
123	13.970	0.648	0.689	0.386	2.579						1	>G	
133	12.069	0.576	0.346	0.230	2.510						1	>G	G2
139	13.197	0.358	0.082	0.569	2.646						1	F2V	
146	12.504	0.353	0.151	0.475	2.650						1	F9V	
147	12.129	0.168	0.200	0.972	2.847						1	A5V	A4
178	9.909	1.039	0.839	0.225	2.835						1	>G	
218	12.087	0.194	0.157	0.982	2.858						1	A5V	A5
489	11.000	0.252	0.179	0.855	2.748						1	A5V	
491	13.681	0.240	0.241	0.857	2.889						1	Ap	
V17	15.009	0.560	0.067	0.157	2.468						1	F9V	

TABLE 4

$uvby-\beta$ PHOTOELECTRIC PHOTOMETRY OF THE OPEN CLUSTER NGC 6830

ID	V	$(b-y)$	m_1	c_1	β	SpTyp		sptp
						Phe	Spc	
5	9.849	0.266	0.013	0.554	2.721	B6V	B7 V	B5 III
7	11.176	0.353	0.007	0.822	2.689	B8V	A0 V	B7 III
8	11.540	0.373	−0.018	0.716	2.616	B7V	B7 IV	
49	10.956	0.456	0.103	0.875	2.751	AV5		
4	12.623	0.600	−0.100	0.471	2.685	B3V		
2258	13.003	0.546	0.086	0.484	2.721	F9V		
2257	12.166	0.390	−0.008	0.584	2.706	B7V		
26	12.309	0.564	0.160	0.255	2.661	G1V		
164	12.240	0.460	0.093	0.819	2.766	A8V		
25	12.465	0.333	0.012	0.661	2.718	B8V		
24	11.644	0.391	−0.034	0.612	2.635	B5V	B6 V	B6 IV
2	10.625	0.329	−0.017	0.606	2.603	B5V		
3	12.888	1.620	0.383	0.256	2.569	K G		
39	11.192	0.386	−0.051	0.681	2.668	B8I	B5 IV	
2275	11.909	1.160	0.306	−0.047	2.576	B7V		
13	12.787	0.767	0.134	0.380	2.605	K0V		
14	11.995	0.348	0.017	0.532	2.714	B6V	B6 V	B6 IV
15	12.659	0.407	−0.035	0.646	2.681	B6V		
16	12.456	0.408	0.108	0.807	2.794	K		

(later than G) were not considered in the analysis since no reddening determination calibration has yet been developed for MS stars. In order to determine the spectral type of each star, the location of the stars in the $[m_1]-[c_1]$ diagram was employed as a primary criteron. In Tables 3 and 4 the photometrically determined spectral class has been indicated. The determined spectral types compiled in the literature are also presented.

The reddening determination was obtained from the spectral types through Strömgren photometry. The application of the calibrations developed for each spectral type (Shobbrook 1984 for O and early A types and Nissen 1988 for late A and F stars) were considered. No determination of reddening was calculated for G and later spectral types. The results of applying such calibrations are shown in Tables 5 and 6 for NGC 6811 and NGC 6830, respectively. In Table 5, the following columns are presented: Column 1 the ID (WEBDA) for each star; Column 2, the reddening $E(b-y)$; Columns 3 to 5, the unreddened indexes $(b-y)_0$, m_0, and c_0; Column 6 the Hβ value; Columns 7 and 8 V_0, and the absolute magnitude, respectively. Columns 9 and 10 show the distance modulus and the distance in parsecs. The metallicity is presented in Column 11 and, finally, Column 12 lists the membership to the cluster, denoted by M (member) or NM (non-member). The membership was determined from the distance modulus or distance histograms. A Gaussian fit with a bin size of one was done to the bars in the histogram to all the stars and the obtained fit is presented, along with the uncertainties in each figure. Membership then was established from the above mentioned fit. Stars within a standard deviation value from the mean were considered to be members. Those with standard deviation values slightly larger than one sigma are considered to be stars with marginal membership. In the table, those stars that are considered to be members of the cluster are denoted by an 'm'. Marginal membership is indicated by a semi-colon, 'm:', those that were non-members are denoted by 'nm'. Table 6 is analogous. Probable members are denoted by a semicolon.

TABLE 5

REDDENING, UNREDDENED PARAMETERS AND DISTANCE FOR THE OPEN CLUSTER NGC 6811

ID	$E(b-y)$	$(b-y)_0$	m_0	c_0	β	V_0	M_V	DM	DST	[Fe/H]	Memb
112	0.082	0.290	0.171	0.396	2.663	12.47	3.82	8.7	537	0.1	NM
122	0.082	0.290	0.171	0.396	2.663	12.47	3.82	8.7	537	0.1	NM
107	0.108	0.311	0.155	0.392	2.640	12.26	3.47	8.8	574	−0.2	NM
31	0.134	0.193	0.171	0.608	2.760	12.73	3.47	9.3	713		M
489	0.072	0.180	0.201	0.841	2.748	10.69	1.32	9.4	749		M
146	0.052	0.301	0.167	0.465	2.650	12.28	2.82	9.5	780	0.0	M
68	0.085	0.187	0.177	0.852	2.737	10.48	1.01	9.5	786		M
34	0.099	0.105	0.234	0.936	2.829	11.20	1.57	9.6	842		M
105	0.093	0.137	0.269	0.831	2.802	12.02	2.16	9.9	938		M
85	0.055	0.253	0.150	0.534	2.684	12.63	2.71	9.9	964	−0.1	M
218	0.116	0.078	0.192	0.959	2.858	11.59	1.65	9.9	973		M
106	0.088	0.213	0.164	0.778	2.713	11.00	1.06	9.9	973	0.0	M
47	0.060	0.323	0.117	0.377	2.613	13.39	3.42	10.0	985	−0.7	M
37	0.024	0.158	0.188	0.928	2.766	11.01	0.87	10.1	1065		M
147	0.080	0.088	0.224	0.956	2.847	11.79	1.62	10.2	1080		M
70	0.089	0.209	0.166	0.858	2.713	10.54	0.31	10.2	1112	0.0	M
86	0.061	0.273	0.124	0.478	2.662	13.13	2.88	10.3	1120	−0.5	M
26	0.067	0.130	0.206	0.972	2.795	11.12	0.84	10.3	1140		M
99	0.053	0.115	0.200	0.946	2.817	11.73	1.42	10.3	1154		M
18	0.113	0.123	0.178	0.943	2.806	11.63	1.18	10.5	1233		M
115B	0.261	−0.041	0.247	0.737	2.759	10.43	−0.22	10.6	1345		M
16	0.088	0.147	0.192	0.909	2.781	11.82	1.15	10.7	1357		M
54	0.052	0.214	0.152	0.747	2.713	12.13	1.43	10.7	1384	−0.2	M
113	0.082	0.151	0.168	0.974	2.767	11.12	0.37	10.8	1409		M
92	0.000	0.226	0.166	0.722	2.704	12.26	1.49	10.8	1423	0.0	M
46	0.040	0.289	0.128	0.525	2.645	12.79	2.01	10.8	1431	−0.5	M
33	0.080	0.152	0.173	0.934	2.771	11.57	0.79	10.8	1431		M
114	0.090	0.139	0.168	0.949	2.786	11.76	0.87	10.9	1506		M
049B	0.244	−0.026	0.215	0.932	2.822	11.37	0.48	10.9	1513		M
5	0.015	0.153	0.189	0.947	2.770	11.73	0.78	11.0	1549		M
9	0.030	0.136	0.227	0.953	2.790	11.95	1.00	11.0	1551		M
62	0.008	0.216	0.165	0.726	2.714	12.81	1.72	11.1	1650	0.0	M
139	0.080	0.278	0.106	0.553	2.646	12.85	1.57	11.3	1808	−0.7	M
44	0.004	0.165	0.183	0.934	2.757	12.03	0.72	11.3	1824		M
53	0.023	0.155	0.198	0.893	2.774	12.66	1.31	11.4	1860		M
45	0.012	0.192	0.198	0.829	2.735	12.65	1.30	11.4	1863		M
78	0.004	0.266	0.168	0.566	2.676	13.65	2.27	11.4	1882	0.1	M:
39	0.028	0.184	0.165	0.955	2.728	11.41	−0.03	11.4	1938		NM
41	0.000	0.176	0.195	0.956	2.741	12.01	0.31	11.7	2192		NM
8	0.039	0.317	0.154	0.490	2.630	13.94	2.20	11.7	2230	−0.3	NM
56	0.013	0.234	0.153	0.784	2.691	12.11	0.36	11.8	2238	−0.1	NM
36	0.000	0.344	0.180	0.561	2.614	13.22	0.98	12.2	2805	−0.1	NM
42	0.000	0.231	0.184	0.829	2.698	12.57	0.22	12.4	2952	0.3	NM
004B	0.296	−0.037	0.216	0.805	2.706	11.41	−1.33	12.7	3532		NM
51	0.000	0.342	0.139	0.592	2.590	13.42	−0.09	13.5	5033	−0.6	NM
43	0.000	0.279	0.176	0.785	2.658	12.74	−0.77	13.5	5041	0.1	NM
040B	0.161	−0.050	0.195	0.601	2.673	12.38	−1.76	14.1	6728		NM
Mean value	0.074							10.42	1258	−0.3	
σ	0.057							0.61	339	0.3	

TABLE 6

REDDENING, UNREDDENED PARAMETERS AND DISTANCE FOR THE OPEN CLUSTER NGC 6830

ID	$E(b-y)$	$(b-y)_0$	m_0	c_0	β	V_0	M_V	DM	DST	[Fe/H]	Mbr
26	0.244	0.320	0.233	0.206	2.661	11.26	5.67	5.59	131	0.85	nm
2258	0.310	0.236	0.179	0.422	2.721	11.67	4.10	7.57	327		nm
13	0.371	0.396	0.245	0.306	2.605	11.19	3.43	7.76	357	0.46	nm
164	0.291	0.169	0.180	0.761	2.766	10.99	1.90	9.09	658		nm
5	0.326	−0.060	0.111	0.492	2.721	8.45	−0.65	9.10	661		m:
4	0.677	−0.077	0.103	0.342	2.685	9.71	−1.25	10.96	1559		m
14	0.412	−0.064	0.141	0.454	2.714	10.22	−0.76	10.98	1571		m
7	0.394	−0.041	0.125	0.747	2.689	9.48	−1.64	11.12	1676		m
2257	0.449	−0.059	0.127	0.499	2.706	10.23	−0.91	11.14	1692		m
39	0.436	−0.050	0.080	0.598	2.668	9.32	−1.89	11.21	1745		m
25	0.384	−0.051	0.127	0.588	2.718	10.81	−0.76	11.57	2063		m
15	0.461	−0.054	0.103	0.558	2.681	10.68	−1.49	12.16	2709		m
24	0.447	−0.056	0.100	0.527	2.635	9.72	−2.81	12.53	3200		m
2	0.385	−0.056	0.098	0.533	2.603	8.97	−4.40	13.37	4719		nm
8	0.420	−0.047	0.108	0.636	2.616	9.73	−4.08	13.81	5785		nm

4. ANALYSIS

In order to gain some insight into the clusters we must first find out which stars belong to each one. As was already mentioned, this is accomplished by constructing a histogram of the deduced distances. From the results listed in Tables 5 and 6 and shown in Figure 1, we can establish that NGC 6811 has a distinctive accumulation of thirty-seven stars at a distance modulus of 10.5 ± 1.0 mag, whereas NGC 6830 is merely an association of eight early type stars at DM 11.1 ± 1.6 mag, although emphasis should be made on the fact that we merely observed a small sample of stars in the direction of this cluster: nineteen of the brightest stars. According to the study of Netopil et al. (2007) four CP stars in NGC 6830 were found. Since Strömgren photometry is most suitable for this topic, we checked our measured stars for the Ap determination. Unfortunately, none of our measured stars lay in the regions defined by the boxes in the m_0, and c_0 diagram where the Ap stars should be, as in Golay's (1974, Figure 124). Hence, we cannot corroborate, nor discard the findings by Netopil et al. (2007). For NGC 6811 we determined four stars belonging to the Ap category, namely W9, W34, W105 and W491, all to the Sr-Cr-Eu class.

Age is fixed for the two determined clusters once we measured the hottest and hence the brightest stars for each one. The effective temperature of these hottest stars was determined by plotting the location of all stars on the theoretical grids of LGK86, once we evaluated the unreddened colors (Figure 2) for a solar chemical composition. We considered this metallicity based on the thirteen F type stars for which we determined the metallicity [Fe/H]; a mean value of -0.18 ± 0.30 was found. In the related figures, LGK86 in the upper left corner indicates that the grids were taken from the mentioned reference of LGK86 and the specified metalicity. We have utilized the $(b-y)$ vs. c_0 diagrams which allow the determination of the temperatures with an accuracy of a few hundreds of degrees. However, for NGC 6811, as can be seen in Figure 2, the stars are clustered together and the effective temperature cannot be easily determined. To measure the temperature with more accuracy, a plot of $(b-y)$ vs. β was constructed and compared with the theoretical grids of LGK86, Figure 3. The temperature for the hottest stars is around 11,700 K for NGC 6811, whereas for NGC 6830 it is much hotter (17,000 K). Once membership has been established, age is determined after calculating the effective temperature through the calibrations of Meynet, Mermilliod, & Maeder (1993) for open clusters; a log age of 8.266 (1.845×10^8 yr) is found from the relation $-3.611 \log\log T_{\rm eff} + 22.956$ valid in the range $\log\log T_{\rm eff}$ within the limits [3.98, 4.25] for NGC 6811; whereas for NGC 6830 the re-

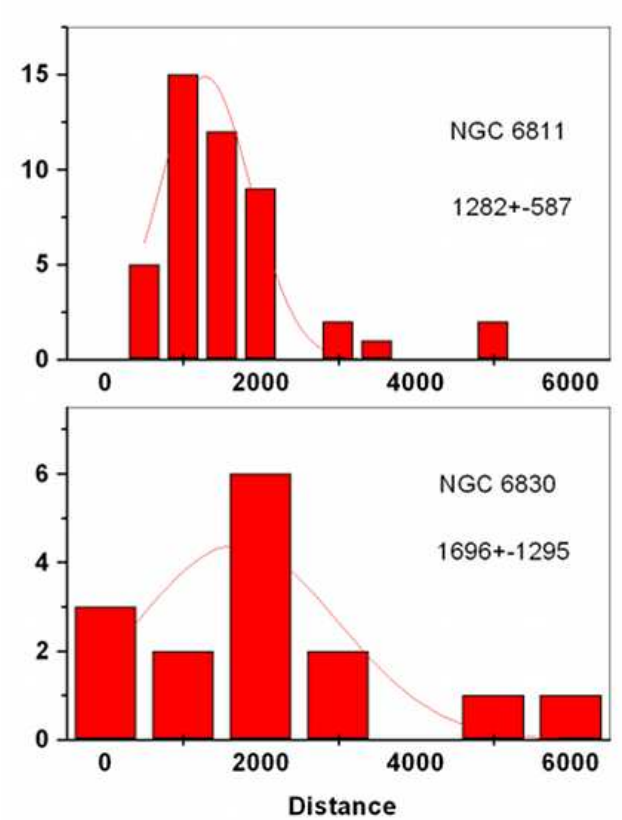

Fig. 1. Histogram of the distance modulus (X axis, in magnitudes) found for the B, A and F stars in the direction of NGC 6811 (top) and NGC 6830 (bottom).

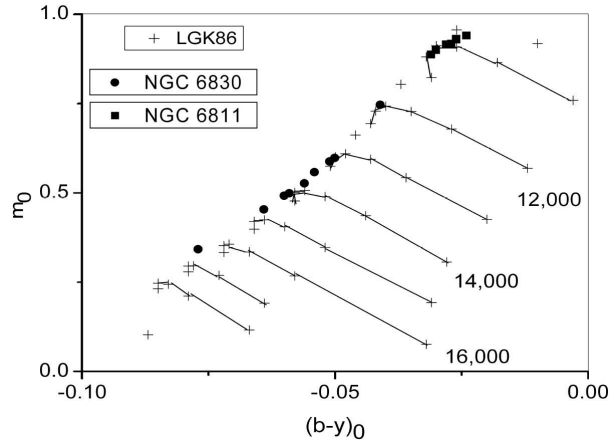

Fig. 2. Location of the unreddened points of the two clusters on the LGK86 grids. Squares: NGC 6811; dots: NGC 6830.

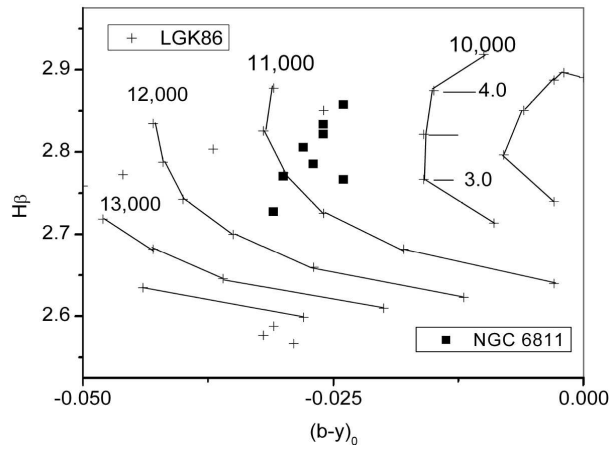

Fig. 3. Location of the unreddened points of the hot stars in the NGC 6811 cluster on the LGK86 grids.

lation $\log(\text{age}) = -3.499 \log\log T_{\text{eff}} + 22.476$ valid in the range [4.25, 4.56] yields log(age) of 7.69 (4.89×10^7 yr).

These determinations are confirmed by constructing the color-magnitude diagram of NGC 6811 and NGC 6830 which are shown in Figures 4 and 5, respectively. The unreddened magnitudes $[(b-y)_0,\ M_V]$ of cluster members taken from Tables 5 (NGC 6811) and 6 (NGC 6830) are shown with filled circles. In each plot two theoretical isochrones in the Strömgren photometric system are shown with solid and dashed lines. The metallicity and ages are indicated in the figures. The theoretical isochrones were obtained from the Padova database (Girardi et al. 2003). As can be seen, the isochrones match the observed color-magnitude diagram with the ages and distance derived in the present paper.

5. VARIABLE STARS IN NGC 6811

As was stated in the introduction, Luo et al. (2009) performed time-series photometric observations of the open cluster NGC 6811 to search for variable stars. These observations were carried out during five nights from June 6 to July 24, 2008 utilizing the 85 cm telescope of the Xonglong Station of the National Astronomical Observatories of the Chinese Academy of Sciences. The instrumentation they used was a 1024×1024 CCD camera with a field of view of $16.5' \times 16.5'$ with standard Johnson-Cousin-Bessell filters in B and V bands, with which they obtained 750 CCD frames in each band. Sixteen certain variable stars were detected or confirmed from that survey, namely V1–V7 and V10–V18 following the variable name list of van Cauteren et al. (2005) (see Table 1 by Luo et al. 2009). Among these, twelve stars were catalogued as Delta Scuti variables based upon the light curves (V1–V7 and V10–V14). The omitted variables, V8 and V9, were outside of their

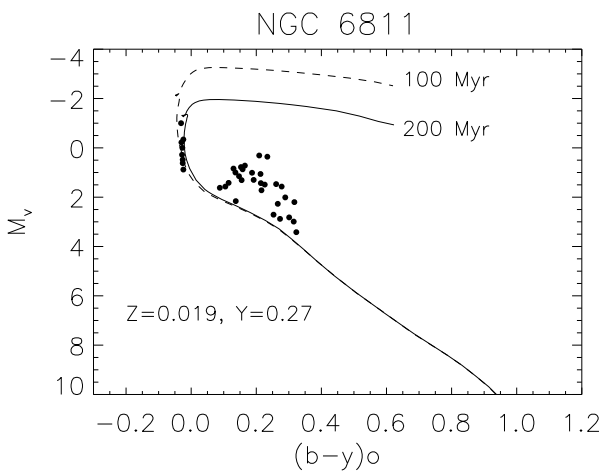

Fig. 4. Color-magnitude diagram of the NGC 6811 cluster considering only the cluster members. The target stars are represented by filled circles. Theoretical isochrones for 100 Myr (dashed line) and 200 Myr (solid line) computed with $Z = 0.019$ are shown.

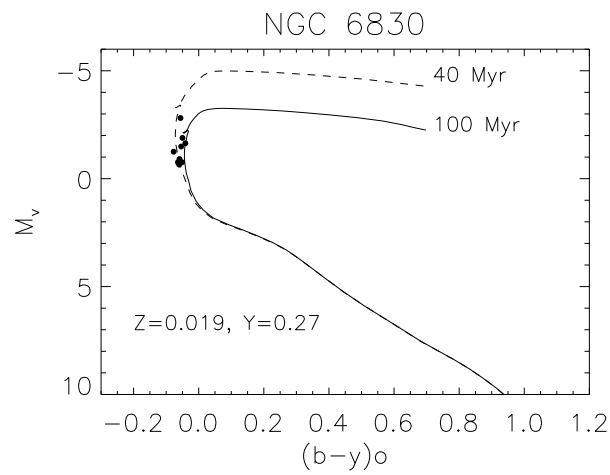

Fig. 5. Color-magnitude diagram of the NGC 6830 cluster considering only the cluster members. The target stars are represented by filled circles. Theoretical isochrones for 40 Myr (dashed line) and 100 Myr (solid line) computed with $Z = 0.019$ are shown.

field-of-view. In particular, Luo et al. (2009) discovered variability in V10–V18; four of them (V10, V12, V15, V16) had been just reported as suspected variables by Rose & Hintz (2007), while the variability of V1–V7 was discovered by van Cauteren et al. (2005). On the other hand, nine stars reported as variables by Rose & Hintz (2007) were not confirmed by Luo et al. (2009). One explanation provided for this inconsistency was that the amplitude of light variations was too low to be detected. Luo et al. 2009 also determined the membership probabilities of twelve variables (V1–V5 and V10–V16) through the proper-motion membership probabilities (PMP) listed by Sanders (1971). From these values they claim that with high probability all of the twelve stars (V1–V3, V5, V10–V16) are cluster members, except for V4. For the the stars without PMP data, namely V6, V7, V17 and V18, based on their position in the CMD diagram, they concluded that the first two are most likely members of the cluster whereas the last two are probably field stars.

On the night of August 6, 2010 (UT) we carried out a very short span of observations in differential photometric mode. The variables we considered were chosen due to their nearness and were, in the notation of Luo et al. (2009): V2, V4, V11 and V14 with W5 and W99 as reference and check stars. Although the time span we observed was too short to detect long period variation, the only star which showed a clear variation was V4, with two clearly discernible peaks of relatively large amplitude of variation, 0.188 mag, and a period of 0.025 d.

From our cluster membership determinations on a star-to-star basis, the conclusion we reach is slightly different from the previous assertions regarding variability. Memberships are determined for V1, V3, V4, V5, V10, V11, V13 and V16. Marginal membership for V12 and V14, non-membership for V15 and we were unable to determine membership for the remaining stars mainly because they do not belong to the spectral classes B, A or F but belong to a latter spectral type which makes them unlikely to be δ Scuti type variables. From the location of these variables in the theoretical grids of LGK86, Figures 6 and 7, we determine their temperatures.

6. CONFIDENCE OF THE RESULTS

As has been said in previous sections, the high accuracy of each observed star was attained by multiply observing each star in sequences of five 10 sec integrations. Hence, mean values and standard deviations were calculated to determine the signal/noise ratio. In all cases, enough star counts were secured to attain a signal to noise ratio large enough to achieve an accuracy better than 0.01 mag. Nevertheless, it is obvious that the brighter stars were more accurately observed than the fainter ones. Quoting Nissen (1988) "as expected from photon statistics considerations the average mean errors increase as we go to fainter magnitudes". Unfortunately, since the aim of this project was to observe as many stars as possible, most of them were observed only twice, and a few, only once. The uncertainties of the season were determined from the differences between

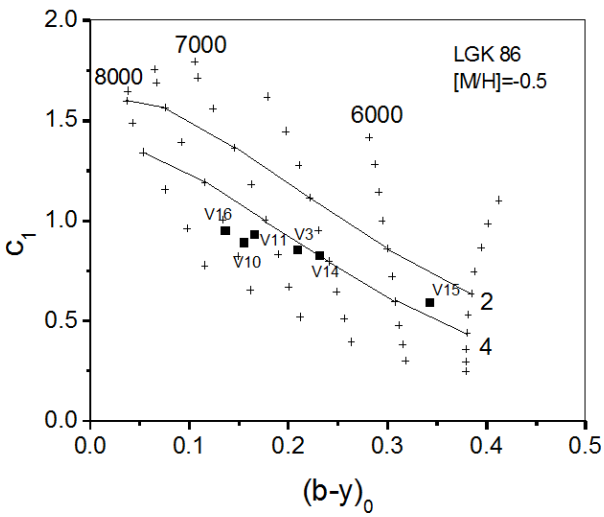

Fig. 6. Location of the δ Scuti stars of NGC 6811 on the theoretical grids of LGK86.

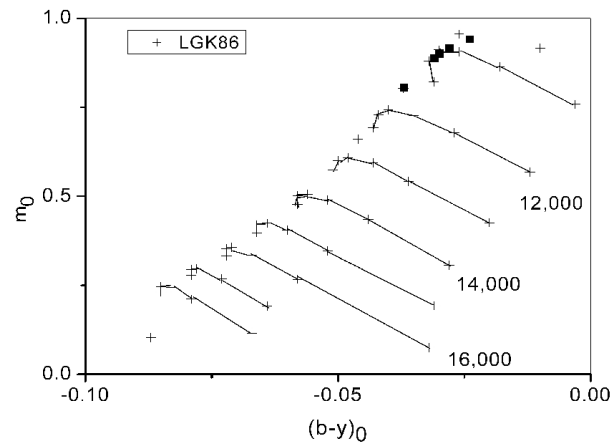

Fig. 7. Location of the hot variable stars of NGC 6811 on the theoretical grids of LGK86.

the derived magnitude of the standard stars vs. reported values in the literature. The average values of such differences are $\Delta(V,\ b-y,\ m_1,\ c_1) = (0.008,\ 0.005,\ -0.004,\ 0.012)$; on most nights at least ten standard stars were observed but this figure increased to 15 on some nights. The number of the whole sample of standards data points, due to the large time span of the season, was considerable, adding up to 80 points of standard stars.

To calculate the propagation of errors for the reddening (in Nissen's 1988 work, § 3), the intrinsic color index $(b-y)_0$ has served to determine the individual color excess, $E(b-y) = (b-y) - (b-y)_0$ and, as in his paper, assuming the photometric mean errors given for our observations, although larger than the work by Nissen (1988), we do expect a mean error $E(b-y)$ close to that derived by Nissen of 0.011 for F stars and of 0.009 for A stars, since our errors are not exceedingly different.

7. DISCUSSION

New $uvby-\beta$ photoelectric photometry has been acquired and is presented for the brightest stars in the direction of two open clusters NGC 6811 and NGC 6830. From the observed stars in the field, some were determined to be early type stars, either B or A. Using the calibrations to determine reddening and distance for these stars, distances for the clusters have been obtained. Unreddened indexes in the LGK86 grids allowed us to determine the effective temperature of the hottest stars and hence, the age of the cluster.

A brief discussion of each cluster is presented. Table 7 lists the previous knowledge and the newly determined characteristics of the clusters.

NGC 6811. Considering the classical UBV photometry compiled for this cluster, very little can be deduced about its properties. No clear distinction in the color-color diagram $B-V$ vs $U-B$ can be drawn; the same conclusion is reached from its HR diagram. From our results we have determined that 37 stars belong to the cluster. Since they are the brightest, the conclusion on the age, which agree with that previously determined, is also correct. We have found that the cluster is farther, its extinction is less and it is younger than previously assumed. The goodness of our method has been previously tested, as in the case of the open cluster Alpha Per (Peña & Sareyan 2006) against several sources which consider proper motion studies as well as results from the Hipparcos and Tycho data bases. Hence, we feel that our results throw new light regarding membership to this cluster.

There have been several previous works in which membership probabilities were considered. Table 8 lists the identification numbers from several studies, namely those of WEBDA, Luo et al. (2009), Sanders (1971), Becker (1947), Barkhatova, Zakharova, & Shashkina (1978) and more recently, the compilation by Kharchenko et al. (2005). We have repeated part of the information on the distance provided in Table 8 in order to support the conclusions based on the last columns of the table, which present the membership probability obtained in the present paper (PP), that of Sanders (1971) and those reported by the compilation of Kharchenko et al. (2005) based on

TABLE 7

COMPILED CHARACTERISTICS FOR NGC 6830 AND NGC 6811

Cluster	Source	log age	Reddening $E(B-V)$ [mag]	Distance [kpc]	Metallicity
NGC 6830	Barkhatova (1957)	–	–	1.68	–
	Hoag & Applequist (1965)	–	0.51	1.38	–
	Becker & Fenkart (1971)	–	0.58	1.47	–
	Moffat (1972)	8.0	0.56	1.70	–
	Glushkova et al. (1999)	–	0.12	1.24	–
	Dias et al. (2002)	7.57	0.50	1.64	–
	Kharchenko et al. (2005)	7.52	0.50	1.64	–
	Paunzen & Mermilliod (2007)	7.57	0.50	1.64	–
	PP	7.69	0.63	1.88	+0.13
NGC 6811	Luo et al. (2009)	8.76	0.12	1.31	+0.02
	Paunzen & Mermilliod (2007)	8.80	0.16	1.22	–
	PP	8.27	0.14	1.64	−0.02

studies of proper motion, photometry and position of the stars. Membership probabilities, if compared with those of Sanders' (1971), are in rough agreement: all but two stars (W92 and W146) that we assign cluster membership are not assigned as members according to Sanders' probabilities, but it is equally true that those which we define as non-members are determined to be members by Sanders (1971). When the comparison is done with those probabilities of the compilation of Kharchenko et al. (2005) the conclusions are equally in agreement. There are two stars, W18 and W45 we define as members that Kharchenko et al. (2005) find to be non-members from the proper motion studies but members with the other two criteria. In conclusion, the comparison of our results with the others support our findings particularly because the results obtained from $uvby-\beta$ photometry are more accurate.

The DM and reddening determined from our photometry, although discordant from those derived from UBV photometry, is in agreement with that of Glushkhova, Batyrshinova, & Ibragimov (1999) who, from radial velocity measurements for 60 late-type stars and $UBVRI$ photoelectric photometry refined the distance modulus of the cluster to be 10.47 ± 0.08 mag and $E(B-V)$ of 0.12 ± 0.02, in agreement with the values we derived.

We were able to determine membership to the NGC 6811 open cluster of several variable stars. We found that six stars V1, V4, V10, V11, V13 and V16 are cluster members. On the contrary, V12, V14 and V15 are definitely non-member stars. For the rest not much can be said. Accurate temperature determination was done for each star.

NGC 6830. Again, since no previous $uvby-\beta$ exists, knowledge of the cluster rests on UBV photometry. Both the color-color and the color-magnitude diagrams do not show a clear main sequence which make the distance, age and reddening determinations ambiguous. We only measured nineteen stars, but with this small sample we determined some clustering of stars. Our findings coincide, within the uncertainties, with the previous distance, reddening and age determinations. Of course, many more data are needed to unambiguously establish the true nature of this cluster, but we emphasize that, since we observed all the bright stars, our conclusions are correct.

We would like to thank the staff of the OAN and E. Romero for their assistance in securing the observations. This work was partially supported by PAPIIT IN110102 and IN114309. HG, ER, SS, AE and ARL thank the IA- Universidad Nacional Autónoma de México, for the opportunity to carry out the observations. JHP thanks the hospitality of the UNAN. Typing and proofreading were done by J. Orta, and J. Miller, respectively. C. Guzmán, F. Ruiz and A. Díaz assisted us in the computing. This research has made use of the Simbad databases operated at CDS, Strasbourg, France and NASA ADS Astronomy Query Form.

TABLE 8

CROSS ID AND MEMBERSHIP PROBABILITIES FOR THE OPEN CLUSTER NGC 6811

WBD	Luo et al. (2009)	Sanders (1971)	Becker (1947)	Barkhatova et al. (1978)	Kharchenko (2005)	Prob (Sanders)	Prob (Kharchenko) Pkin	Pph	Psp	mbr
112		177	51	1136		0				nm
122										nm
107		183	48			96				nm
31		102	15	1057		97				m
489	6	205		2080		89				m
146		187	42	1143		0				m
68		110	86	1065	78	97	0.9272	1	1	m
34		121	22	1084		96				m
105		185	47	1141		25				m
85		94	4	1041		95				m
218		192		1154		92				m
106		172	49	1133		97				m
47		158	35	1121		96				m
37	2	136	26	1104		96				m
147		189	43	1146		97				m
70	3	108	82	1063	76	96	0.9837	1	1	m
86		98	5	1050		89				m
26		86	10	1038	69	97	0.4193	1	1	m
99		159	29	1122		97				m
18	1	97	85	1049	73	97	0.0016	1	1	m
115		149	65			95				m
16		103	81	1059		90				m
54		147	68	1114		97				m
113	5	166	60	1126	98	93	0.8128	1	1	m
92		115	20	1071		0				m
46		160	36	1124		96				m
33	13	113	19	1066	79	95	0.9765	0.9971	1	m
114		146	66			96				m
49		165	46	1125	97	93	0.7504	1	1	m
5		127	25	1092	83	93	0.9227	0.7357	1	m
9	16	134	71	1101	86	88	0.9565	1	1	m
62		123	77	1087		97				m
139		131		1096		95				m
44	11	157	33	1120	95	96	0.9137	1	1	m
53	10	135	69	1105		94				m
45		155	34	1118	94	97	0.0001	0.6244	1	m
78		72	11	1023		95				m:
39	4	144	30	1112		54				nm
41		154	28	1117		0				nm
8				1106						nm
56		138	67	1108	89	0	0.7463	0.9707	1	nm
36		132		1099		97				nm
42	14	143	31	1111		90				nm
4	12	119	23	1077		95				nm
51	15	137	70	1109		97				nm
43		142	32	1110		96				nm
40										nm
6				1093						und
7				1102						und
10				1085						und
12				1078						und
13				1082						und
14		114	80	1067		0				und
22		84	18	1029		0				und
23	18		17	1053						und
24		95	14	1047	72	97	0.8117	1	1	und
32		106	16	1061		97				und
35		128		1095		80				und
38		150	27	1115		0				und
57		129	72	1097		79				und
58		130	73	1098		71				und
63										und
64										und
65		120	78	1081		96				und
71		77	100	1026	66	97	0.5865	1	1	und
73		64	101	1016	61	0	0.0646	1	1	und
74		74	13			0				und
77		67	12	1018		97				und
79		85	1	1031	68	0	0.4112	1	1	und
82		89	3	1036		27				und
87		100	7	1054		57				und
101		170	38	1131	87	97	0.8326	1	1	und
102		179	40	1137		0				und
145	64	1113		0						und
123				1051						und
133		92	2	1039	71	94	0.8766	1	1	und
178		76	99	1025	65	96	0.8519	0.9999	1	und
491	7	209				0				und
v17										und

REFERENCES

Arellano-Ferro, A., & Parrao, L. 1988, Reporte Técnico, 57 (México: IA-UNAM)

Barkhatova, K. A. 1957, Soviet Astron., 1, 822

Barkhatova, K. A., Zakharova, P. E., & Shashkina, L. P. 1978, AZh, 55, 56

Becker, W. 1947, Astron. Nachr., 275, 229

Becker, W., & Fenkart, R. 1971, A&AS, 4, 241

Borucki, W. J., Koch, D. G., Dunham, E. W., & Jenkins, J. M. 1997, in ASP Conf. Ser. 119, Planets Beyond the Solar System and the Next Generation of Space Missions, ed. D. Soderblom (San Francisco: ASP), 153

Crawford, D. L., & Mander, J. 1966, AJ, 71, 114

Dias, W. S., Alessi, B. S., Moitinho, A., & Lepine, J. R. D. 2002, A&A, 389, 871

Fox Machado, L., Pérez Hernández, F., Suárez, J. C., Michael, E., & Lebreton, Y. 2006, A&A, 446, 611

Fox Machado, L., et al. 2001, in Helio- and Asteroseismology at the Dawn of the Millennium, ed. A. Wilson (ESA SP-464; Noordwijk: ESA), 427

Fox Machado, L., et al. 2002, A&A, 382, 556

Girardi, L., et al. 2003, Mem. Soc. Astron. Italiana, 74, 474

Glushkova, E. V., Batyrshinova, V. M., & Ibragimov, M. A. 1999, Astron. Lett., 25, 86

Golay, M. 1974, Introduction to Astronomical Photometry (Dordrecht: Reidel)

Grönbech, B., Olsen, E. H., & Strömgren, B. 1976, A&AS, 26, 155

Hoag, A. A., & Applequist, N. L. 1965, ApJS, 12, 215

Kharchenko, N. V., Piskunov, A. E., Röser, S., Schilbach, E., & Scholz, R. D. 2005, A&A, 438, 1163

Lester, J. B., Gray, R. O., & Kurucz, R. I. 1986, ApJ, 61, 509 (LGK86)

Li, Z. P., et al. 2002, A&A, 395, 873

Li, Z. P., et al. 2004, A&A, 420, 283

Lindoff, U. 1972, A&A, 16, 315

Luo, Y. P., Zhang, X. B., Luo, C. Q., Deng, L. C., & Luo, Z. Q. 2009, New Astron., 14, 584

Meynet, G., Mermilliod, J. C., & Maeder, A. 1993, A&AS, 98, 477

Moffat, A. F. J. 1972, A&AS, 7, 355

Netopil, M., et al. 2007, A&A, 462, 591

Nissen, P. 1988, A&A, 199, 146

Olsen, E. H. 1983, A&AS, 54, 55

Paunzen, E., & Mermilliod, J. C. 2007, WEBDA: A Site Devoted to Stellar Clusters in the Galaxy and the Magellanic Clouds (Vienna: Institute of Astronomy of the University of Vienna) `http://www.univie.ac.at/webda/`

Peña, J. H., Fox Machado, L., & Garrido, R. 2007, RevMexAA, 43, 329

Peña, J. H., García-Cole, A., Hobart, M., De la Cruz, C., Plascencia, J. C., & Peniche, R. 2003, RevMexAA, 39, 171

Peña, J. H., & Peniche, R. 1994, RevMexAA, 28, 139

Peña, J. H., & Sareyan, J. P. 2006, RevMexAA, 42, 179

Peña, J. H., et al. 1998, A&AS, 129, 9

Rose, M. B., & Hintz, E. G. 2007, AJ, 134, 2067

Sanders, W. L. 1971, A&A, 15, 368

Shobbrook, R. R. 1984, MNRAS, 211, 659

Turner, D. G. 1976, AJ, 81, 1125

van Cauteren, P., Lampens, P., Robertson, C. W., & Strigachev, A. 2005, Commun. Asteroseismol., 146, 21

A. Espinosa, J. H. Peña, A. Rentería, E. Romero, and S. Skinner: Instituto de Astronomía, Universidad Nacional Autónoma de México, Apdo. Postal 70-264, México, D. F. Mexico (jhpena@astroscu.unam.mx).

L. Fox Machado: Observatorio Astronómico Nacional, Instituto de Astronomía, Universidad Nacional Autónoma de México, Apdo. Postal 877, 22800, Ensenada, B. C., Mexico (lfox@astrosen.unam.mx).

H. García: Observatorio Astronómico de la Universidad Nacional Autónoma de Nicaragua, Nicaragua.

Revista Mexicana de Astronomía y Astrofísica, **47**, 323–331 (2011)

THE COMETARY CAVITY CREATED BY AN ALIGNED STREAMING ENVIRONMENT/COLLIMATED OUTFLOW INTERACTION

D. López-Cámara,[1] A. Esquivel,[1] J. Cantó,[2] A. C. Raga,[1] P. F. Velázquez,[1] and A. Rodríguez-González[1]

Received 2011 May 20 ; accepted 2011 June 16

RESUMEN

Presentamos un modelo analítico de "capa delgada" de la interacción de un chorro bicónico y un medio ambiente en movimiento (alineado con la dirección del chorro), así como simulaciones numéricas (axisimétricas) de dicha interacción. Una situación similar, aunque en un escenario más complejo, ocurre en la cabeza de la estructura cometaria de Mira. Por esta razón, en la mayoría de las simulaciones numéricas exploramos parámetros que son consistentes con las observaciones del flujo bipolar de Mira B. Para estos parámetros la interacción es no-radiativa, lo que tiene como resultado una zona de interacción chorro/medio ambiente bastante ancha. A pesar de esto, encontramos que el modelo analítico de capa delgada describe de manera satisfactoria la morfología básica del flujo.

ABSTRACT

We present a "thin shell" model of the interaction of a biconical outflow and a streaming environment (aligned with the direction of the flow), as well as numerical (axisymmetric) simulations of such an interaction. A similar situation, although in a more complex setup, takes place at the head of the cometary structure of Mira. Thus, for most of the numerical simulations we explore parameters consistent with the observed bipolar outflow from Mira B. For these parameters, the interaction is non-radiative, so that a rather broad jet/streaming environment interaction region is formed. In spite of this, a reasonable agreement between the thin-shell analytic model and the numerical simulations is obtained.

Key Words: hydrodynamics — ISM: kinematics and dynamics — ISM: jets and outflows — stars: AGB and post-AGB — stars: mass-loss

1. INTRODUCTION

Prompted by the discovery by Martin et al. (2007) of a striking $\sim 2^\circ$ cometary tail attached to Mira, a series of theoretical and observational studies of this object have been made. Theoretical works include Wareing et al. (2007b); Raga et al. (2008); Raga & Cantó (2008); Esquivel et al. (2010), all of which are devoted to study the interaction between the post-AGB wind (from Mira A) and a streaming interstellar medium (ISM). This streaming medium corresponds to the motion of Mira through the galactic plane. Observations of the cometary tail have been done in several wavebands, including 21 cm (Matthews et al. 2008) and the IR (Ueta 2008).

Optical (Hα) observations by Meaburn et al. (2009) revealed a fast bipolar outflow, which probably arises from the less luminous component, Mira B. This outflow is embedded in the head of the cometary structure. It has radial velocities of ± 150 km s^{-1} (with respect to Mira), is relatively broad, and its projection onto the plane of the sky is approximately aligned with the direction of Mira's proper motion.

The mass loss rate from Mira A has estimated values from 10^{-7} to 10^{-5} $M_\odot$ yr^{-1} (Knapp & Morris 1985; Bowers & Knapp 1988). Part of this mass loss is accreted onto a disk around Mira B (and eventually onto Mira B itself). Ireland et al. (2007) estimated a $\sim 5\times 10^{-9}$ $M_\odot$ yr^{-1} accretion rate. Part of this accretion rate would then be redirected into the bipolar outflow from Mira B.

[1]Instituto de Ciencias Nucleares, Universidad Nacional Autónoma de México, Mexico.

[2]Instituto de Astronomía, Universidad Nacional Autónoma de México, Mexico.

In the Mira A/B system, we therefore appear to have a bipolar outflow from Mira B which first interacts with the wind from Mira A and at larger distances emerges from the wind into the streaming ISM region. However, in the present paper we consider the simpler problem of an aligned (bi-conical) bipolar outflow/streaming environment interaction (i.e., we neglect the presence of the wind from Mira A). This is a first step to modeling the high velocity outflow observed by Meaburn et al. (2009).

We present an analytic, stationary, thin shell model of the interaction of a bi-conical outflow and an aligned, streaming environment in § 2. Time-dependent, axisymmetric numerical simulations of this problem are described in § 3, and their results presented in § 4. With the simulations we show the characteristics of the flow in greater detail, and evaluate the level of agreement with the analytic, thin shell solution. Finally, the implications of this model for the interpretation of Mira's outflow are discussed in § 5.

2. THE ANALYTIC MODEL

Let us consider a source that ejects a bipolar, conical outflow (with a half-opening angle θ_j, velocity v_j and mass loss rate $\dot{M}_j$ for each outflow lobe), immersed in a uniform, streaming environment of density ρ_a, which travels parallel to the outflow axis at a velocity v_a. The situation is shown in the schematic diagram of Figure 1. We assume that, as the material from the outflow encounters the streaming environment, a thin shell of well mixed material is formed (the thick solid line shown in Figure 1). This layer has a bow shock shape $R(\theta)$, where R is the spherical radius and θ the angle measured from the z-axis, see Figure 1).

At a position θ along the bow shock, the material flowing along the thin shell has a mass rate:

$$\dot{M}(\theta) = \int_0^\theta d\dot{M}_j + \pi r^2 \rho_a v_a \,, \tag{1}$$

where the first term on the right represents the mass fed into the shell by the conical jet, and the second term is the mass from the streaming environment (with $r = R\sin\theta$ being the cylindrical radius, see Figure 1).

The radial momentum rate of the material in the shell is:

$$\dot{\Pi}_r(\theta) = \dot{M}(\theta)\, v_r(\theta) = \int_0^\theta v_j \sin\theta \, d\dot{M}_j \,, \tag{2}$$

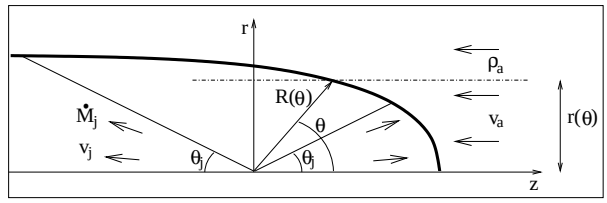

Fig. 1. Schematic diagram showing the interaction between a bi-conical outflow (of half-opening angle θ_j, velocity v_j and total mass loss rate $2\dot{M}_j$) with a streaming environment of density ρ_a and velocity v_a (aligned with the outflow axis).

with a contribution only from the jet. The axial momentum (along the z-direction) flowing along the shell is:

$$\dot{\Pi}_z(\theta) = \dot{M}(\theta)\, v_z(\theta) = \int_0^\theta v_j \cos\theta \, d\dot{M}_j - \pi r^2 \rho_a v_a^2 \,. \tag{3}$$

In equations (2) and (3), v_r and v_z are the r- and z-components of the velocity of the (well mixed) material flowing along the thin shell. One can also write an expression for the angular momentum rate of the material flowing along the shell:

$$\dot{J}(\theta) = \dot{M}(\theta)\, v_\theta(\theta) R(\theta) = \int_0^r r' v_a (2\pi 4' \rho_a v_a) dr'$$
$$= \frac{2}{3}\pi \rho_a v_a^2 R^3 \sin^3\theta \,, \tag{4}$$

where v_θ is the velocity in the θ-direction (of the material flowing along the thin shell), which is given by:

$$v_\theta = v_r \cos\theta - v_z \sin\theta \,. \tag{5}$$

Now, we consider a conical, bipolar outflow with a mass loss rate given by:

$$d\dot{M}_j = \begin{cases} \frac{\dot{M}_j}{1-\cos\theta_j} \sin\theta \, d\theta & \theta \le \theta_j \text{ or } \theta \ge \pi - \theta_j \,, \\ 0 & \theta_j < \theta < \pi - \theta_j \,. \end{cases} \tag{6}$$

With this form for $d\dot{M}_j$, it is possible to carry out the integrals in equations (1–3), allowing us to obtain the shape of the bow shock:

$$R(\theta) = R_0 \operatorname{cosec}\theta \times \sqrt{3\,(1 - \theta \operatorname{cotan}\theta)} \,; \;\; \theta \le \theta_j \,, \tag{7}$$

$$R(\theta) = R_0 \operatorname{cosec}\theta$$
$$\times \sqrt{3\,[\cos(\theta - \theta_j)\sin\theta_j \operatorname{cosec}\theta - \theta_j \operatorname{cotan}\theta]} \,;$$
$$\theta_j < \theta < \pi - \theta_j \,, \tag{8}$$
$$R(\theta) = R_0 \operatorname{cosec}\theta$$

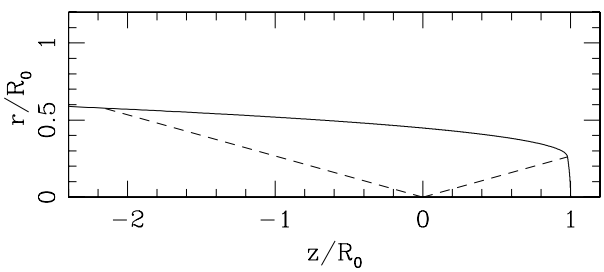

Fig. 2. Analytic solution for the shape of the bow shock produced by the interaction of a bi-conical outflow with an aligned, streaming environment. The outflow cones have a half-opening angle $\theta_j = 15°$, and their outer boundaries are shown by the dashed lines.

$$\times\sqrt{3\left[1+(\pi-\theta-2\theta_j+\sin 2\theta_j)\ \mathrm{cotan}\,\theta\right]}\,;$$

$$\pi-\theta_j \le \theta \le \pi\,, \tag{9}$$

where

$$R_0 \equiv \sqrt{\frac{\dot{M}_j v_j}{2\pi(1-\cos\theta_j)\rho_a v_a^2}}\,, \tag{10}$$

is the on-axis standoff distance between the bow shock and the jet source.

As an example, in Figure 2 we show the bow shock shape obtained from equations (7–9) for a bi-conical outflow with a half-opening angle $\theta_j = 15°$. The solution is quite flat-topped in the $\theta < \theta_j$ "head" region. For $\theta > \theta_j$ the solution first rapidly curves, and then straightens out into a slowly expanding bow shock wing.

3. THE NUMERICAL SIMULATIONS

We have computed seven different axisymmetric gasdynamic simulations of aligned bi-conical jet/streaming environment interactions with the WALICXE code, which is described in detail by Esquivel et al. (2010). The code integrates the gasdynamic equations with an approximate Riemann solver (in this case we used a hybrid HLL-HLLC algorithm, see Harten, Lax, & van Leer 1983; Toro, Spruce, & Speares 1994; Esquivel et al. 2010). A hydrogen ionization rate equation is solved along with the gasdynamic equations in order to include the radiative losses through a parametrized cooling function, that depends on the density, temperature and hydrogen ionization fraction (Raga & Reipurth 2004).

The WALICXE code has a block based adaptive grid, with blocks of a constant number of cells (in our case, of 24×24 cells), which are refined by successive factors of 2. Most of our simulations were run at a medium resolution (labeled "mr" in Table 1). These consist of two root blocks aligned in the axial direction, which are allowed to have 8 levels of refinement. The resolution at the finest level would correspond to 6144×3072 cells (axial and radial, respectively) in a uniform grid. In addition, we ran low and high resolution versions of model 1 (labeled "lr" and "hr" in Table 1). The low resolution run has 7 levels of refinement (3072×1536 cells in a uniform grid), while the high resolution run has 9 levels of refinement (12288×6144 cells in a uniform grid).

Models 1–6 have a computational box of the same size, $[2 \times 4]10^{18}$ cm (radial and axial). Therefore the "mr" runs have a maximum resolution of 6.51×10^{14} cm, and the "lr" and "hr" runs have resolutions of 1.30×10^{15} cm and 3.25×10^{14} cm, respectively. In model 7 we were more interested in resolving the structure at the head of the shock than in the long cometary tail. To achieve a higher resolution (6.51×10^{13} cm) with the same number of computational cells, in these models we have reduced the size of the computational box by a factor of 10.

The simulations were performed in a cylindrical computational grid with an axial extent $[z_{\rm min}, z_{\rm max}]$ (with the jet source placed at $z = 0$) and extending radially from the symmetry axis ($r = 0$, where a reflecting boundary condition is applied) out to $r_{\rm max}$. An inflow condition is applied in the positive z grid boundary, where a streaming environment is injected with a constant velocity in the $-z$ direction. Outflow boundaries were applied at the negative z grid boundary and at $r_{\rm max}$. In models 1–3 $z_{\rm min} = -2.8 \times 10^{18}$ cm and $z_{\rm max} = 1.2 \times 10^{18}$ cm, in models 4–6 $z_{\rm min} = -2.0 \times 10^{18}$ cm and $z_{\rm max} = 2.0 \times 10^{18}$ cm, in model 7 $z_{\rm min} = -2.8 \times 10^{17}$ cm and $z_{\rm max} = 1.2 \times 10^{17}$ cm.

The parameters of the simulations are summarized in Table 1. The jets are imposed in two cones with a half-opening angle Θ and an initial outer radius equal to $R_j = 10^{16}$ cm for models 1–6, and $R_j = 10^{15}$ cm for model 7. The outflows have a velocity v_j (see Table 1) and a temperature $T_j = 100$ K. The density inside the source follows a $\propto R^{-2}$ profile set by the mass loss rate $\dot{M}_j$. The environment has an initial temperature $T_a = 10^4$ K, a density n_a and a velocity v_a. The values for the parameters of models 1–6 are roughly consistent with the jet of Mira B while model 7 (with a denser streaming environment) was chosen to produce a more radiative interaction region. Both the jet and the environment are initially neutral, except for a seed electron density assumed to come from the presence of singly ionized carbon.

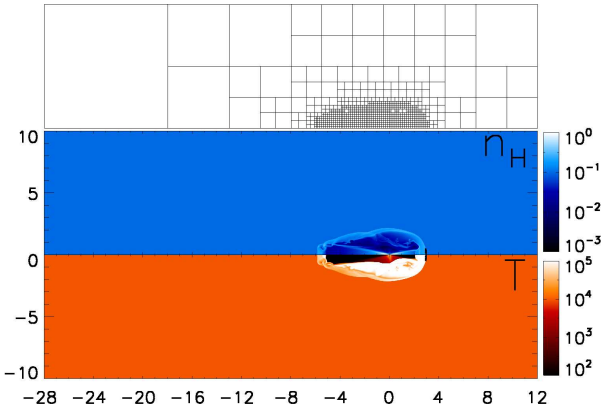

Fig. 3. Density (color scale given in cm^{-3}, middle panel) and temperature (color scale given in K, bottom panel) stratifications. The corresponding mesh configurations (on top of each density/temperature plot) are also shown, with each square representing a 24×24 grid point block. The results are for model 1 at $t = 1 \times 10^3$ yr. The axes are labeled in units of 10^{17} cm (the figure only shows the inner half of the radial extent, the rest is unperturbed). The color figure can be viewed online.

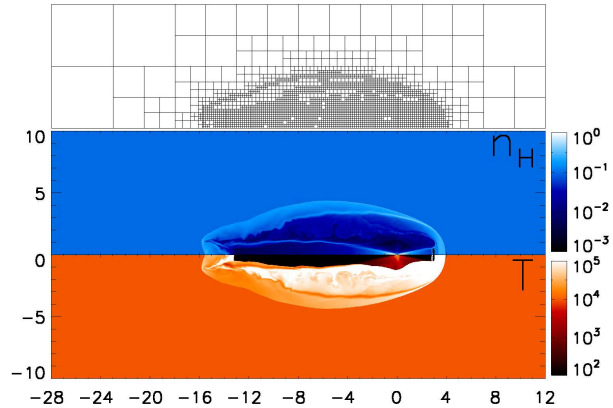

Fig. 4. Same as Figure 3 at $t = 3 \times 10^3$ yr. The color figure can be viewed online.

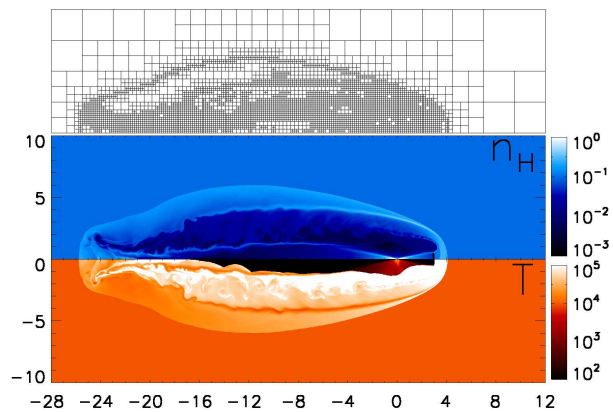

Fig. 5. Same as Figure 3 at $t = 5 \times 10^3$ yr. The color figure can be viewed online.

In Table 1 we have also included the corresponding value of the bow-shock standoff distance R_0 (see equation 10), and the cooling distances associated with the double shock structure at R_0. The cooling distance ${d_c}^f$ corresponds to the forward shock (with the streaming ambient medium), while ${d_c}^r$ corresponds to the cooling behind the reverse shock. In order to calculate these cooling distances, we have used the fit:

$$ {d_c}^i = \left(\frac{100\,\mathrm{cm}^{-3}}{n_0^i}\right)\left\{\left[3\times10^{11}\mathrm{cm}\right]\left(\frac{u_0^i}{100\,\mathrm{km\,s}^{-1}}\right)^{-6.4} + \left[8\times10^{13}\mathrm{cm}\right]\left(\frac{u_0^i}{100\,\mathrm{km\,s}^{-1}}\right)^{5.5}\right\}, \quad (11) $$

to the cooling distances to 10^4 K given in the tabulation of self-consistent preionization, plane-parallel shock models of Hartigan, Raymond, & Hartmann (1987). In equation (11), n_0 is the pre-shock atom+ion number density, and u_0 is the shock velocity.

4. RESULTS

In Figures 3–5, we show the time-evolution ($t = 1\times10^3$, 3×10^3, and 5×10^3 yr, respectively) obtained from model 1 (see Table 1). For each time, we show the corresponding mesh configuration, the density n_H (in cm^{-3}) and the temperature T (in K) (top, middle, and bottom panels, respectively). Thanks to the adaptive grid of the code we used less than 10% (for $t \times 10^3$ yr) and 20% (for $t > 10^3$ yr) of the finest grid in the domain, thus notably reducing the required computer time.

From the time-sequence shown in Figures 3–5, we see that the flow develops a cometary-shaped structure, due to the presence of the side-streaming environmental wind (which flows parallel to the z-axis, from right to left). The head of the cometary structure approaches the steady state star/bow shock stagnation distance R_0 (see § 2) at a time $t \approx 10^3$ yr.

In Figure 6, we show single time frames ($t = 5 \times 10^3$ yr) of the density and temperature stratifications (top and bottom parts, respectively, of each of the three panels) obtained from models 1 through 3 (see Table 1). In each plot we include the corresponding "thin shell" analytic solution (see § 2).

Even though models 1 through 3 differ in $\dot{M}_j$ and Θ (see Table 1), they result in basically the same flow morphology. Model 3 (which has the largest

TABLE 1

MODEL CHARACTERISTICS

Model	Θ [°]	v_j [km s^{-1}]	$\dot{M}_j$ [$M_\odot$ s^{-1}]	v_a [km s^{-1}]	n_a [cm^{-3}]	R_0 [10^{17} cm]	${d_c}^r/(R_0 \tan\Theta)$	${d_c}^f/(R_0 \tan\Theta)$	Resolution
1	10	200	1.00×10^{-10}	125	0.044	2.97	402.4	11.9	lr,mr,hr
2	20	200	3.97×10^{-10}	125	0.044	2.97	194.9	5.7	mr
3	30	200	8.82×10^{-10}	125	0.044	2.97	122.9	3.6	mr
4	10	200	1.00×10^{-9}	125	0.044	9.39	127.2	3.7	mr
5	20	200	3.97×10^{-9}	125	0.044	9.39	61.6	1.8	mr
6	30	200	8.82×10^{-9}	125	0.044	9.39	38.9	1.1	mr
7	10	40	1.00×10^{-10}	100	1.0	3.48	0.28	1.3	mr

mass loss rate and opening angle) has the broadest flow. Independently of the $\dot{M}_j$ and Θ values, all three models coincide with the theoretical stagnation point ($R_0 = 2.97 \times 10^{17}$ cm), and they also have tails with the same basic morphology. It is clear that the numerical simulations produce broad interaction regions, which are a direct result of the fact that the post-shock cooling distances (${d_c}^r$, and ${d_c}^f$, see Table 1) are not small compared to the width of the flows. We find that the thin layer analytic solution lies along a line dividing the computed flows into two regions: an internal low-density, hot region (corresponding to the jet cocoon) and a high-density external, cold region (corresponding to the shocked, streaming ambient medium).

The fact that the cooling distances are large compared to the cross section of the jet indicates that the flows are non-radiative. In this case it is remarkable that the analytical solution does successfully divide the hot/low-density from the cold/high-density regions. This is not necessarily expected, as the analytical model assumes that the material is well mixed in a thin layer, which would arise more naturally in radiative flows (where cooling occurs in a small region).

The density and temperature stratifications (at $t = 5 \times 10^3$ yr) for models 4–6 are shown in Figure 7. These models, with mass loss rates one order of magnitude larger than those of the first three models ($\sim 10^{-9}$ $M_\odot$ s^{-1}, for details see Table 1) have smaller cooling distances than models 1–3; however, they are still in the non-radiative regime. The three models roughly match the analytically derived stagnation point ($R_0 = 9.39 \times 10^{17}$ cm), and produce broader flows for larger values of the opening angle Θ.

In order to check how well the numerical simulations reproduce the theoretical stagnation point in the thin shell analytical solution from § 2, we show

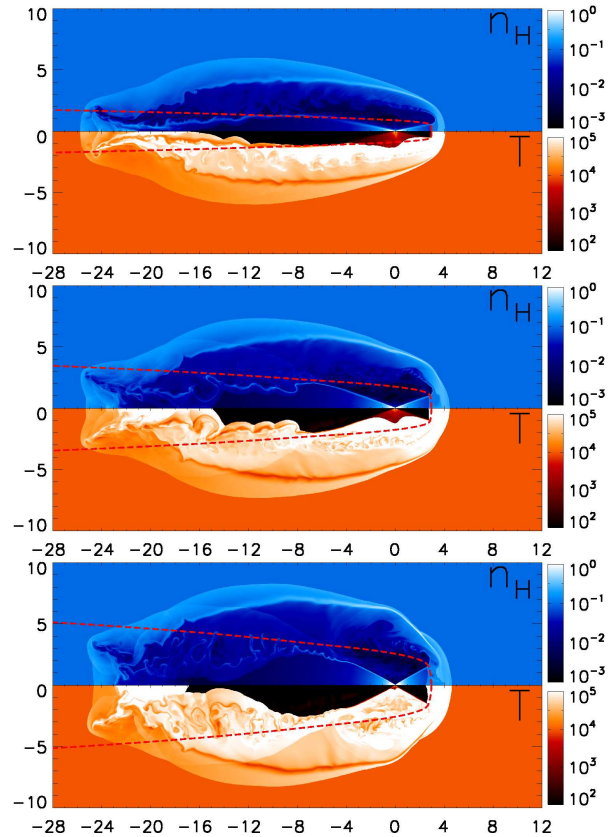

Fig. 6. Density stratifications (color scale given in cm^{-3}, blue panels); and temperature (color scale given in K, orange panels). Top, middle and bottom figures correspond to models 1, 2 and 3 (respectively). The integration time is $t = 5 \times 10^3$ yrs (top). The axes are labeled in units of 10^{17} cm. The broken line delimits the analytic solution proposed in § 2. The color figure can be viewed online.

a zoom of the density structures of the jet heads for all models in Figures 8–9. We find that a steady state is reached (with small discrepancies, more evident in models 4–7, Figure 9), with a shock structure approximately centered on the stagnation radius R_0

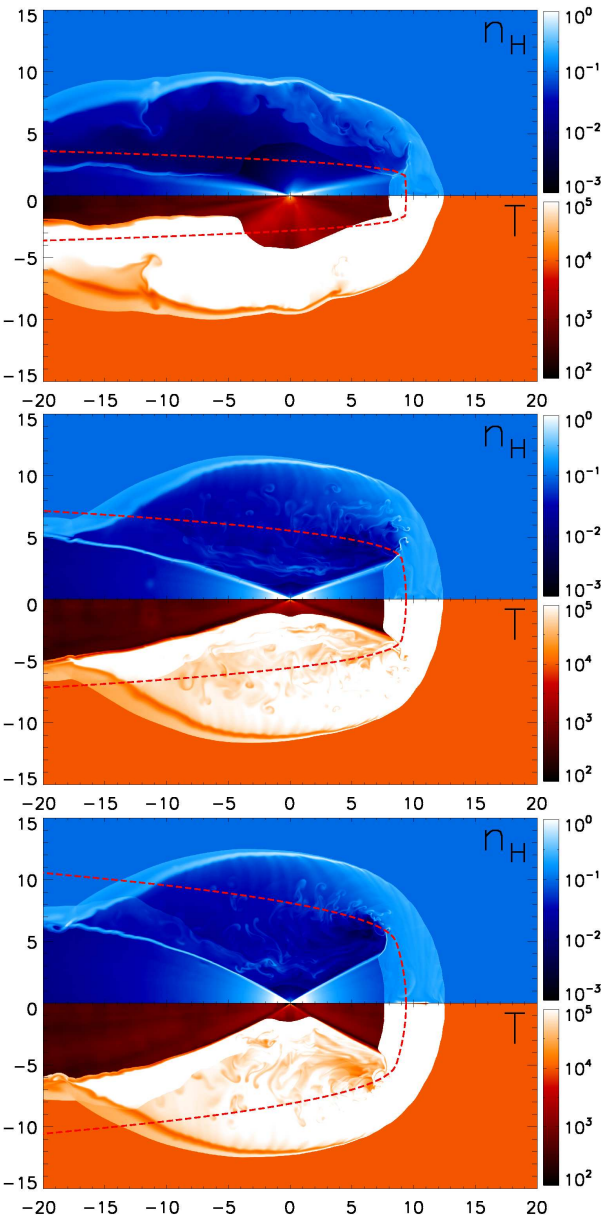

Fig. 7. Same as Figure 6 but for models 4, 5, and 6 (top, middle, and bottom respectively). The color figure can be viewed online.

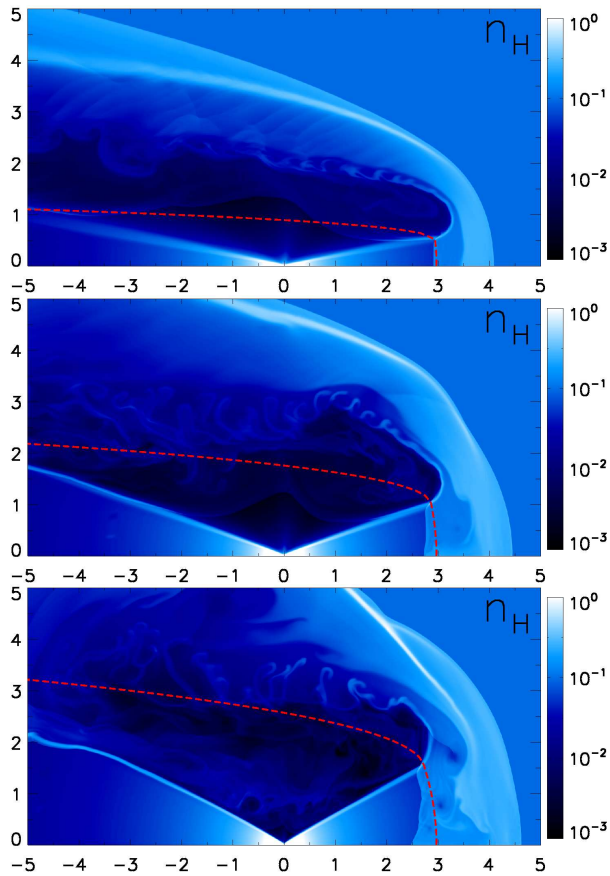

Fig. 8. Density stratifications (color scale given in cm^{-3}). Top, middle and bottom figures correspond to model 1 (and 2), 3 and 4, respectively. The integration time is $t = 5 \times 10^3$ yrs (top). The axes are labeled in units of 10^{17} cm. The broken line delimits the analytic solution proposed in § 2. The color figure can be viewed online.

(see Table 1). One can also see that the place at which the solution curves sharply coincides nicely with the end of the dense wall of the jet.

In order to illustrate the effect of the numerical resolution, we computed two extra simulations with the setup of model 1. The resulting density stratifications for an integration time $t = 5 \times 10^3$ yr, are shown in Figure 10.

Even though more complex structures are obtained for increasing resolutions, the basic morphology of the flow (stagnation point, cocoon size, density profile, etc.) is the same in all cases. Taking the number of grid points across the jet as an estimate of the Reynolds number of the simulation (Re), in these models we only reach Re $\sim R_j/\Delta x \approx 10^2$ (in our hr run). To avoid Reynolds number dependency, the simulations should have resolutions larger by a factor of at least two orders of magnitude, which is presently unattainable. However, from the results shown in Figure 8, it is clear that the mr resolution appears to produce the correct basic morphology for the flow. We must note that this result is similar to the one found by Wareing, Zijlstra, & O'Brien (2007a). In this study, the authors simulated the interaction of an AGB star moving through the ISM (with also Re $\sim 10^2$). The key result was that independently of the Reynolds number, the ISM ram pressure stripped material from

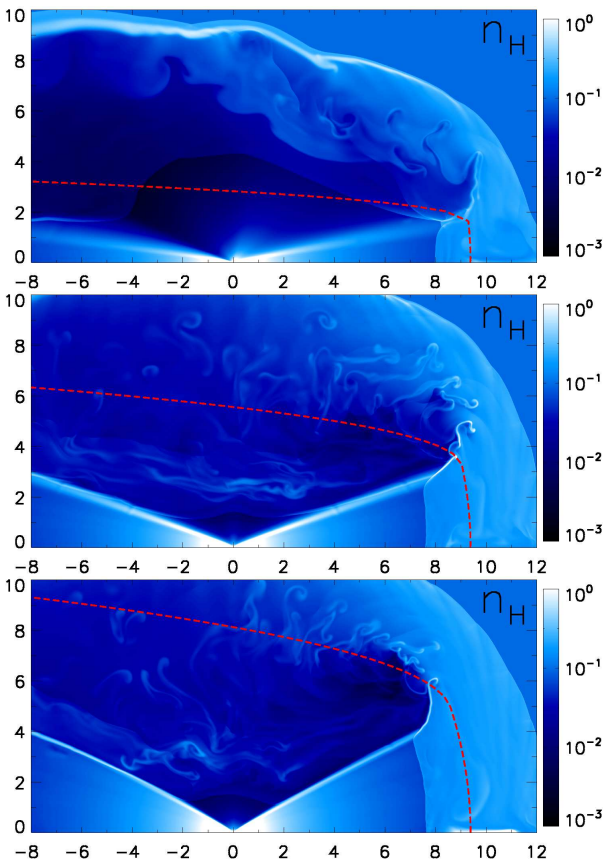

Fig. 9. Same as Figure 8 but for models 5, 6, and 7 (top, middle and bottom respectively). The color figure can be viewed online.

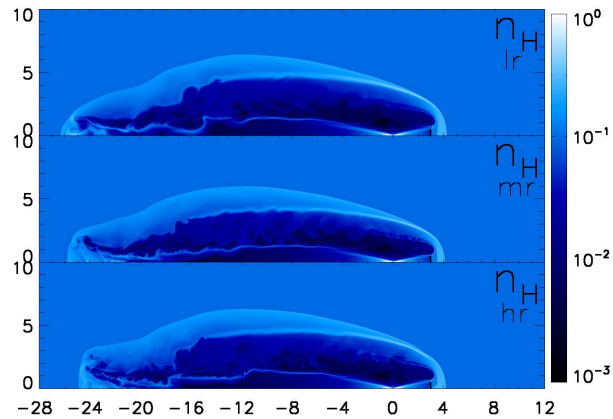

Fig. 10. Density stratifications (color scale given in cm^{-3}) for model 1 at $t = 3 \times 10^3$ yrs, for an "hr" resolution (top panel); "mr" resolution (middle panel); and "lr" resolution (bottom panel). The axes are labeled in units of 10^{17} cm. The color figure can be viewed online.

the head of the AGBs bow shock. Such stripping, as well as the presence of Rayleigh-Taylor instabilities, produced turbulent clump structures that eventually moved down-stream to the tail of the bow shock. This mechanism, although on a smaller scale, is also present in our simulations (see Figures 3–5).

As we have mentioned earlier, the analytic model assumes that the material of the environment and the jet mix well in a thin shell. Such a situation is more easily met in radiative flows, characterized by a thin cooling layer. However, our simulations with parameters appropriate for the jet of Mira B are basically non-radiative. In order to check what happens with a more radiative flow we ran model 7. In this model, the reverse shock is indeed radiative ($d_c{}^r < R_0 \tan\Theta$) while the cooling distance of the forward shock is of the order of the cross section of the jet ($d_c{}^f \sim R_0 \tan\Theta$) (see Table 1). This model has a 10 times smaller computational domain, and therefore a 10 times larger resolution than the mr models (see § 3). In Figure 11, we overlap the thin layer analytic solution on top of the density and temperature stratifications obtained from model 7 at various times ($v_a = 100$ km s^{-1}, and $v_j = 40$ km s^{-1}). For this model the stagnation point is $R_0 = 3.48 \times 10^{16}$ cm, and the cooling distances are $d_c{}^r = 0.28\, R_0 \tan\Theta$, and $d_c{}^f = 1.31\, R_0 \tan\Theta$. As can be seen from the time-sequence, a steady state is not reached in this model. The model develops a turbulent structure which is not stable, and the distance from the jet source to the bow-shock oscillates around R_0.

5. DISCUSSION

Motivated by the recently observed bipolar jet from Mira (Meaburn et al. 2009), we study the interaction of a steady bi-conical outflow with a streaming environment. We use this scenario to perform 2D axisymmetrical simulations and an analytical model of such an interaction.

We have studied the particular case in which the bi-conical jets are aligned with the streaming environment (as shown in Figure 1). This of course is an idealization of the situation which could possibly be found in Mira, which is unlikely to have a perfect alignment between the outflow axis and the direction of Mira's motion. It allows, however, simple axisymmetrical analytical and numerical solutions which are useful as a first exploration of the more complex, less symmetric problem of the jet in Mira B.

The proposed "thin shell" analytical solution, based on the momentum equilibrium between the outflow material from the conical jet and the ambient medium, traces the shape of the shock (see

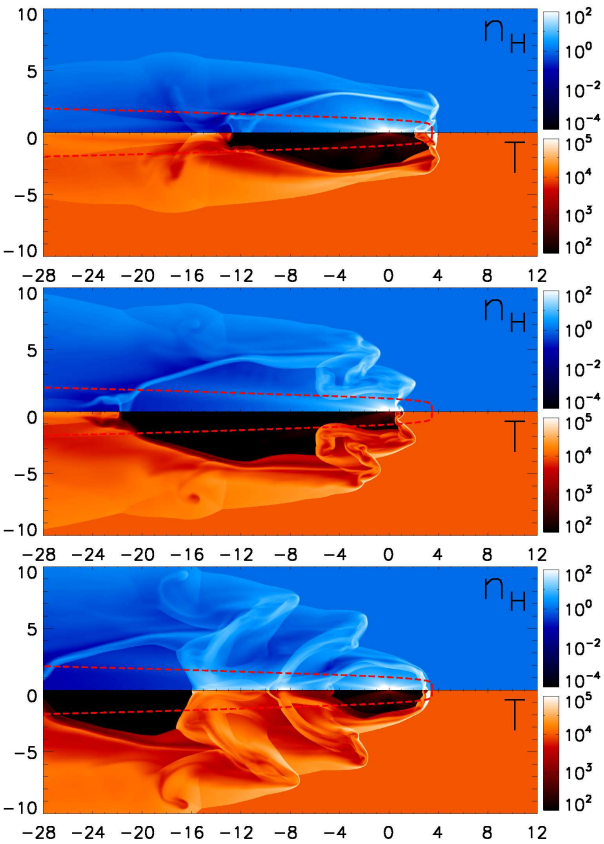

Fig. 11. Density stratifications (color scale given in cm^{-3}, blue panels); and temperature (color scale given in K, orange panels) of model 7 at $t = 10 \times 10^3$ yrs (top); $t = 18 \times 10^3$ yrs (middle); and $t = 24 \times 10^3$ yrs (bottom). The axes are labeled in units of 10^{16} cm. The broken line delimits the analytic solution proposed in § 2. The color figure can be viewed online.

equations 7–9). The model assumes that the interaction occurs in a very thin layer in which the material from the jet and the ISM mixes well. This situation is likely to occur in radiative flows, where the sizes of the cooling distances are small compared with the flow dimensions. This, however, is not the case for the resulting interaction of the outflow launched from Mira B and its surrounding environment.

The models reach a stationary state with a fixed stand-off distance between the jet head and the outflow source. This configuration might be relevant for the collimated outflow from Mira, in which the forward directed jet head has a very low proper motion with respect to Mira (see Meaburn et al. 2009).

We find that the non-radiative flow configurations (that result from the parameters deduced from the bipolar outflow from Mira) have broad interaction regions which approximately coincide with the predictions from the analytic model (in which a thin shell interaction is assumed). Also, the analytical solutions lie close to the contact discontinuity dividing the material in the jet cocoon from the shocked environment region.

We have tested the convergence of the numerical simulations for increasing resolutions. We find that at different resolutions we obtain similar large-scale flow structures, but with different structures at smaller scales (in which the Kelvin-Helmholtz instabilities associated with shear layers are active). Better convergence is expected only for resolutions higher by at least two orders of magnitude, in which the simulations would start to approach the "high Reynolds number regime" appropriate for the real, astrophysical flow.

We end by noting again that the present model of a bipolar jet/streaming ISM interaction is not completely consistent with the outflow from the Mira system (Meaburn et al. 2009). This is because in the binary Mira AB system, the mass loss rate from Mira A's uncollimated wind (with $\dot{M} \sim 10^{-6}\ M_\odot\ s^{-1}$, Ireland et al. (2007)) clearly dominates the interaction with the ambient medium. The mass loss from the bi-conical jet ($\dot{M}_j \sim 10^{-9}\ M_\odot\ s^{-1}$, inferred from Martin et al. (2007)), will simply modify the morphology created by the interaction from the isotropic wind and the ambient medium, except in the region in which the leading jet from Mira B emerges from the Mira A wind bubble. This is the region to which our model would in principle apply.

Future models of the outflow from Mira should include both the wind from the primary star and the collimated outflow from the secondary. This more complex flow will clearly be the topic of future papers on Mira's outflow/ISM interaction.

DLC work has been possible thanks to a DGAPA postdoctoral grant from the UNAM. We also acknowledge support from CONACyT grants 61547, 101256, and 101975. We thank Enrique Palacios and Martín Cruz for supporting the servers in which the calculations of this paper were carried out.

REFERENCES

Bowers, P. F., & Knapp, G. R. 1988, ApJ, 332, 299

Esquivel, A., Raga, A. C., Cantó, J., Rodríguez-González, A., López-Cámara, D., Velázquez, P. F., & De Colle, F. 2010, ApJ, 725, 1466

Harten, A., Lax, P. D., & van Leer, B. 1983, J. Soc. Industrial Appl. Math. Rev., 25, 357

Hartigan, P., Raymond, J. C., & Hartmann, L. W. 1987, ApJ, 316, 323

Ireland, M. J., et al. 2007, ApJ, 662, 651
Knapp, G. R., & Morris, M. 1985, ApJ, 292, 640
Martin, D. C., et al. 2007, Nature, 448, 780
Matthews, L. D., Libert, Y., Gérard, E., Le Bertre, T., & Reid, M. J. 2008, ApJ, 684, 603
Meaburn, J., López, J. A., Boumis, P., Lloyd, M., & Redman, M. P. 2009, A&A, 500, 827
Raga, A. C., & Cantó, J. 2008, ApJ, 685, L141
Raga, A. C., Cantó, J., De Colle, F., Esquivel, A., Kajdic, P., Rodríguez-González, A., & Velázquez, P. F. 2008, ApJ, 680, L45
Raga, A. C., & Reipurth, B. 2004, RevMexAA, 40, 15
Toro, E. F., Spruce, M., & Speares, W. 1994, Shock Waves, 4, 25
Ueta, T. 2008, ApJ, 687, L33
Wareing, C. J., Zijlstra, A. A., & O'Brien, T. J. 2007a, ApJ, 660, L129
Wareing, C. J., Zijlstra, A. A., O'Brien, T. J., & Seibert, M. 2007b, ApJ, 670, L125

A. Esquivel, D. López-Cámara, A. C. Raga, A. Rodríguez-González, and P. F. Velázquez: Instituto de Ciencias Nucleares, Universidad Nacional Autónoma de México, Apdo. Postal 70-543, Mexico 04510 D.F., Mexico (d.lopez, esquivel, raga, pablo, ary@nucleares.unam.mx).
J. Cantó: Instituto de Astronomía, Universidad Nacional Autónoma de México, Apdo. Postal 70-264, Mexico, 04510 D.F., Mexico.

Revista Mexicana de Astronomía y Astrofísica, **47**, 333–344 (2011)

THE PROPER MOTION OF THE LARGE MAGELLANIC CLOUD REVISITED

M. H. Pedreros[1,2]

Received 2011 March 2; accepted 2011 June 24

RESUMEN

El movimiento propio (PM) de la Nube Mayor de Magallanes (LMC) relativo a cuatro cuasares en el trasfondo de los respectivos campos, se ha determinado leyendo y reprocesando datos de las imágenes de dos estudios previos. El PM total del centro de masas de la LMC que se obtiene aquí es $\mu = (+1.94 \pm 0.08)$ mas yr^{-1}, con un ángulo de posición de $\theta = (61.5 \pm 3.2)^\circ$. Los nuevos resultados concuerdan razonablemente con aquellos obtenidos previamente por nuestro y otros grupos, y con varios modelos teóricos existentes. A partir de la velocidad radial del centro de la LMC obtenida de la literatura, en combinación con el vector velocidad transversal determinado de nuestra medición del PM en este trabajo, obtenemos la velocidad espacial del centro de la LMC. Usando esta última y suponiendo un potencial puntual de masa para la Galaxia, hemos estimado la cantidad de masa contenida dentro de 50 kpc desde el centro de la Galaxia.

ABSTRACT

The proper motion (PM) of the Large Magellanic Cloud (LMC) relative to four background quasi-stellar objects has been determined by reading and reprocessing image data from two previous studies. The total center of mass PM for the LMC obtained here is $\mu = (+1.94 \pm 0.08)$ mas yr^{-1}, with a position angle $\theta = (61.5 \pm 3.2)^\circ$. The new results agree reasonably well with those obtained previously by our group and by other groups, and with several existing theoretical models. From the radial velocity of the center of the LMC found in the literature, in combination with the transverse velocity vector determined from the PM measured in the present work, we obtain the space velocity of the LMC center. Using the latter and assuming a point-mass potential for the Galaxy, we have estimated the amount of mass contained within 50 kpc of the center of the Galaxy.

Key Words: astrometry — proper motions — Magellanic Clouds — quasars: general

1. INTRODUCTION

The present study is a follow-up of the works by Anguita, Loyola, & Pedreros (2000, hereafter ALP00), Pedreros, Anguita, & Maza (2002, hereafter PAM02), Pedreros, Costa, & Méndez (2006, hereafter PCM06) and Costa et al. (2009, hereafter CMP09), in which the PM of the LMC was determined using the "quasar method". This method, fully described in ALP00, PAM02 and PCM06, consists in using quasi-stellar objects (QSOs) in the background field of the LMC as fiducial reference points to determine the PM of the cloud. In this method, the position of the background QSOs is measured at different epochs with respect to a group of bona-fide field stars of the LMC (the Local Reference System, hereafter LRS). Because a QSO can be considered a fiducial

[1]Departamento de Física, Facultad de Ciencias, Universidad de Tarapacá, Arica, Chile.

[2]Visiting Astronomer, Cerro Tololo Inter-American Observatory, National Optical Astronomy Observatories, operated by the Association of Universities for Research in Astronomy, Inc. (AURA), under cooperative agreement with the National Science Foundation.

TABLE 1

PREVIOUS DETERMINATIONS OF THE LMC PROPER MOTION BY OUR GROUP USING THE QUASAR METHOD

Source	$\mu_\alpha \cos(\delta)$ mas yr^{-1}	μ_δ mas yr^{-1}	Weighted Mean from
ALP00 (LMC center)	$+1.7 \pm 0.2$	$+2.9 \pm 0.2$	Three fields
PAM02 (LMC center)	$+2.0 \pm 0.2$	$+0.4 \pm 0.2$	One Field
PCM06 (LMC center)	$+1.8 \pm 0.1$	$+0.9 \pm 0.1$	Four fields
CMP09 (LMC center)	$+1.82 \pm 0.13$	$+0.39 \pm 0.15$	One field

TABLE 2

OBSERVATIONAL MATERIAL FOR THE LMC QSO FIELDS

Field	Source	Epochs	Frames	Epoch Range
Q0459-6427	PAM02	9	45	1989.91−2001.96
Q0557-6713	ALP00	13	70	1989.02−2001.96
Q0558-6707	ALP00	9	48	1992.81−2001.96
Q0615-6615	ALP00	11	53	1989.90−2001.96

reference point, any motion detected will be a reflexion of the motion of the LRS, that is, those selected LMC stars present in each field.

As shown in Table 1, and despite the fact that basically the same set of images was used in the mentioned studies (excepting the case of CMP09, as explained in item 6 of § 6), there is a rather large discrepancy, particularly in DEC, between the PM of the LMC derived by ALP00 and that derived by PAM02 and PCM06, with ALP00-PCM06 differences of -0.1 mas yr^{-1} (0.7σ) in R.A., and $+2.0$ mas yr^{-1} (13σ) in DEC This puzzle prompted us to read and re-process directly the original images obtained by ALP00 and PAM02 along with those added in PCM06 and not taken into account in the two previously mentioned works. This is because, as mentioned in PCM06, all previous analyses were carried out using not the original image material but rather the (X, Y) coordinates processed by the original authors, with the exception of the newly processed data not included in ALP00 and those included in PAM02. Therefore the results reported here were determined using the (X, Y) coordinates directly obtained from the re-processing of the LMC images themselves of the QSO fields containing: Q0459-6427, Q0557-6713, Q0558-6707 and Q0615-6615 (in the same nomenclature used by PCM06). The original study of field Q0459-6427 was reported in PAM02, and those of Q0557-6713, Q0558-6707 and Q0615-6615 in ALP00 and PCM06. Table 2 summarizes the total observational material used in the present work. The new processing led to a different number of frames, from those for the same fields in PCM06, because of the deletion of one or two frames due to a bad quality image or other reasons, which became apparent with the new inspection of the images required for their new processing. In one case (Q0615 field) three frames were added to the previous sample, which were not considered before. We will refer to CMP09 in § 6, because it is a special case, with a different set of images.

2. OBSERVATIONS AND REDUCTIONS

The observational material used in this work was described in ALP00, PAM02 and PCM06 and was obtained at the Cassegrain focus of the CTIO 1.5 m telescope in its f/13.5 configuration. The CCD chips used in each epoch for each field are shown in Table 3. The same LRS stars and numbering were adopted as those used by ALP00 or PAM02. The number of LRS stars in each of the studied fields is 17, 23, 52 and 16, for the fields Q0459-6427, Q0557-6713, Q0558-6707 and Q0615-6615, respectively. Finding charts for the reference stars and the background QSO in each field can be found in ALP00 and PAM02.

TABLE 3

MEAN BARYCENTRIC POSITIONS OF QUASARS IN THE LMC

Epoch	$\Delta\alpha\cos(\delta)$ arcsec	σ mas	$\Delta\delta$ arcsec	σ mas	N	CCD chip
			Q0459-6427			
1989.908	8.433	1.0	−7.612	2.6	3	RCA No.5
1990.872	8.434	2.2	−7.620	5.9	3	Tek No. 4
1990.878	8.427		−7.620		1	RCA No.5
1993.800	8.429	0.9	−7.613	4.0	3	Tek1024 No.1
1993.953	8.437	1.1	−7.610	1.9	9	Tek1024 No.2
1994.916	8.427	1.3	−7.614	2.4	3	Tek1024 No.2
1996.860	8.429	3.8	−7.618	1.5	5	Tek2048 No.4
1998.880	8.424	1.4	−7.615	1.2	6	Tek1024 No.2
2000.010	8.421	0.7	−7.616	1.1	9	Tek1024 No.2
2001.961	8.422	1.5	−7.611	2.4	3	Tek1024 No.2
			Q0557-6713			
1989.024	0.048	0.9	−2.770	0.9	6	RCA No.5
1989.905	0.037	1.3	−2.772	1.8	8	RCA No.5
1990.873	−0.036	0.8	−2.772	0.8	5	Tek No. 4
1990.878	−0.045	3.7	−2.769	0.6	2	RCA No.5
1991.938	0.043	1.7	−2.772	1.0	6	Tek1024 No.1
1992.812	0.037	0.6	−2.776	1.5	5	Tek 2048 No.1
1993.055	0.034	2.1	−2.776	1.2	3	Tek1024 No.1
1993.800	0.042	0.0	−2.779	0.0	1	Tek1024 No.1
1993.953	0.036	0.8	−2.779	1.1	9	Tek1024 No.2
1994.119	0.032	1.0	−2.779	1.3	5	Tek1024 No.2
1994.917	0.034	0.8	−2.784	0.8	9	Tek1024 No.2
1996.861	0.031	0.7	−2.781	0.9	3	Tek 2048 No.4
1998.883	0.032	0.4	−2.789	0.8	6	Tek1024 No.2
2001.961	0.029	0.3	−2.786	0.8	3	Tek1024 No.2
			Q0558-6707			
1991.939	−12.230	1.3	−15.479	0.2	3	Tek1024 No.1
1992.813	−12.232	4.7	−15.475	4.3	4	Tek2048 No.1
1993.058	−12.229	0.5	−15.482	1.0	4	Tek2048 No.1
1993.952	−12.231	0.7	−15.480	1.8	6	Tek1024 No.2
1994.117	−12.240	1.4	−15.486	0.7	3	Tek1024 No.2
1994.918	−12.234	0.5	−15.485	1.1	7	Tek1024 No.2
1996.863	−12.235	1.8	−15.486	1.8	6	Tek2048 No.4
1998.886	−12.239	0.6	−15.489	0.8	3	Tek1024 No.2
1999.942	−12.240	0.9	−15.489	1.0	6	Tek1024 No.2
2001.958	−12.243	1.3	−15.485	1.2	6	Tek1024 No.2
			Q0615-6615			
1989.908	−7.294	3.3	−8.078	2.1	3	RCA No.5
1990.878	−7.297	3.7	−8.082	1.2	3	RCA No.5
1993.954	−7.286	2.5	−8.089	2.0	7	Tek1024 No.2
1994.920	−7.279	2.3	−8.090	1.1	4	Tek1024 No.2
1995.178	−7.277	1.0	−8.092	1.0	3	Tek1024 No.2
1996.069	−7.282	3.1	−8.090	3.3	3	Tek1024 No.2
1996.864	−7.280	2.6	−8.085	0.9	3	Tek2048 No.4
1997.194	−7.280	2.0	−8.090	2.9	5	Tek1024 No.2
1998.886	−7.273	2.8	−8.098	2.0	3	Tek1024 No.2
1999.942	−7.271	1.0	−8.093	1.4	3	Tek1024 No.2
2001.959	−7.269	1.3	−8.100	1.3	15	Tek1024 No.2

The method we used for the LMC PM determination was previously explained in PCM06. In brief, after obtaining the (x, y) coordinates of the QSO and the LMC field reference stars in each image (the LRS), using a sequence of DAOPHOT's routines (Stetson 1987), the coordinates were corrected for differential color refraction (DCR) and transformed to barycentric coordinates, that is, $(x - \overline{x}, y - \overline{y})$ coordinates relative to the average

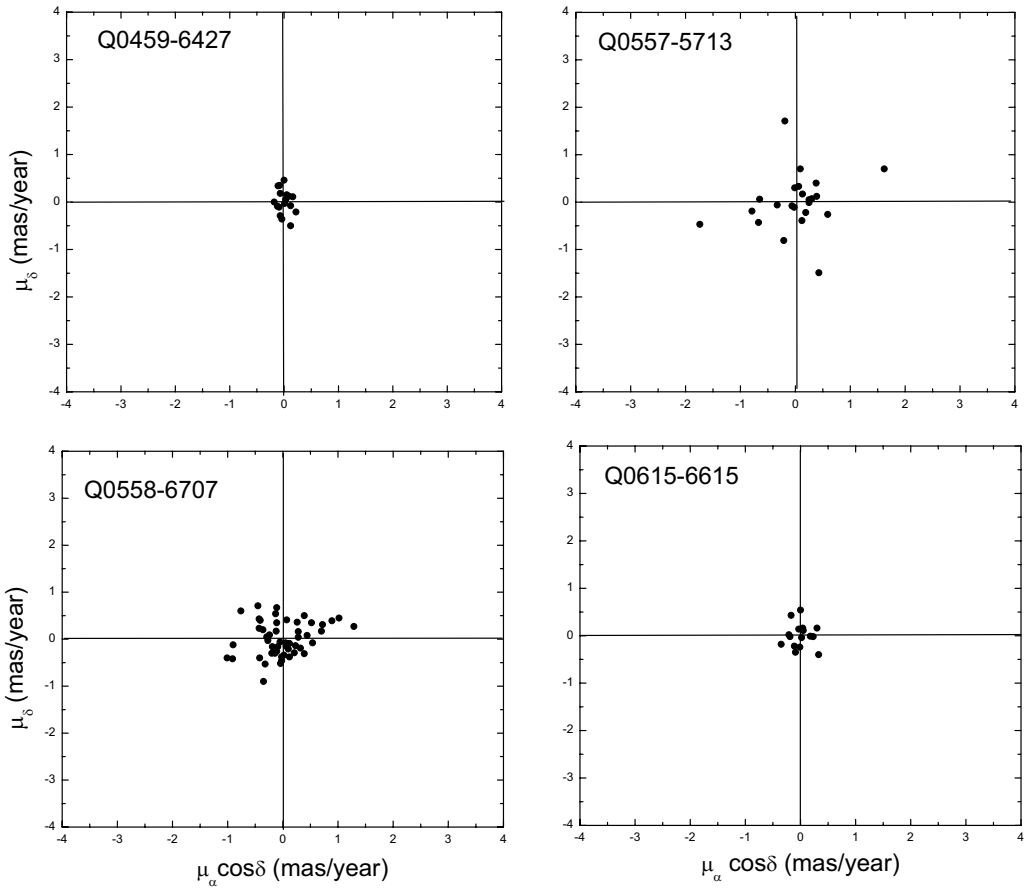

Fig. 1. Residual proper-motion maps for the reference stars. The dispersion around the mean is ±0.11, ±0.62, ±0.46, and ±0.19 mas yr^{-1} in R.A. ($\mu_\alpha \cos\delta$), and ±0.26, ±0.60, ±0.36, ±0.26 mas yr^{-1} in DEC (μ_δ), for Q0459-6427, Q0557-6713, Q0558-6707 and Q0615-6615, respectively.

$(\overline{x}, \overline{y})$ coordinates of the LRS stars in the image. Then, by averaging the barycentric coordinates of the best set of consecutive images taken for each QSO field throughout our program, a Standard Reference Frame (SRF) was defined for every field. Later on, all images of each field, taken at different epochs, were referred to its corresponding SRF (one per field). This registration process was done through a multiple regression analysis by fitting both sets of coordinates to a third degree polynomial of the form:

$$X = a_0 + a_1 x + a_2 y + a_3 x^2 + a_4 xy + a_5 y^2 + a_6 x^3 + a_7 x^2 y + a_8 xy^2 + a_9 y^3 \,,$$

$$Y = b_0 + b_1 x + b_2 y + b_3 x^2 + b_4 xy + b_5 y^2 + b_6 x^3 + b_7 x^2 y + b_8 xy^2 + b_9 y^3 \,,$$

where (X, Y) are the coordinates on the SRF system and (x, y) are the the observed barycentric coordinates. It was found that the above transformation equations yielded the best results for the registration into the SRF, showing no remaining systematic trends in the data. It must be noted here that in the previous studies of the fields mentioned above, quadratic and linear polynomials were adopted instead, for the registration into the SRF.

3. RESULTS

The results for the LRS stars are much improved (with the significant lower dispersion shown below), in comparison to those obtained by PCM06 and shown in their Tables 3–6. In Figure 1 we present the PM (μ) maps for the LRS stars obtained in this work. The dispersion around the mean in the figure turned out to be (in parentheses the values by PCM06) ±0.11 (±0.34), ±0.62 (±0.79), ±0.46 (±0.54), and ±0.19 (±0.41) mas yr^{-1}

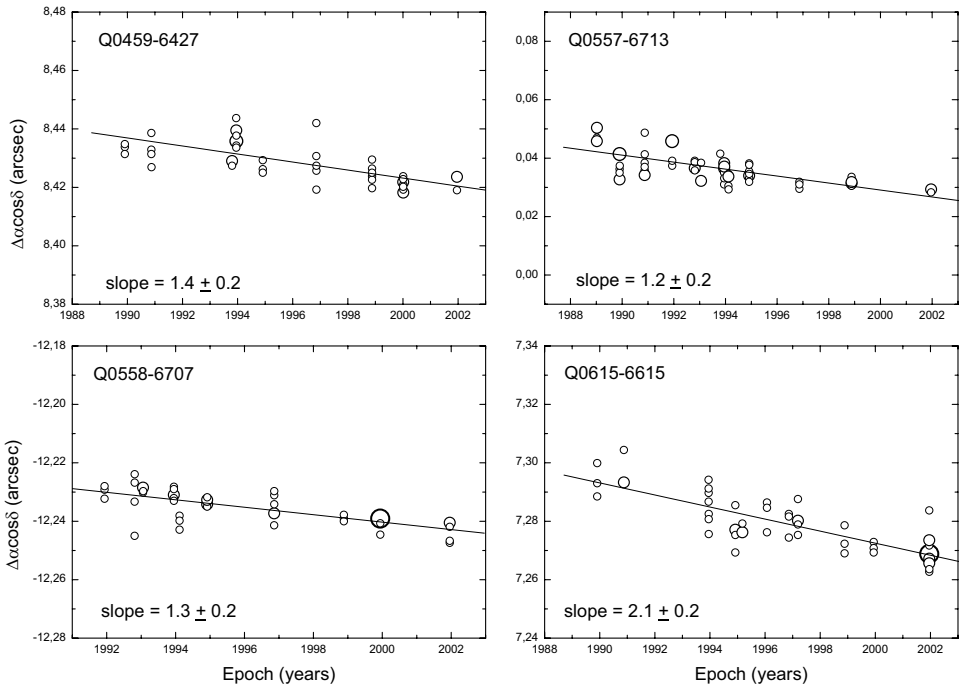

Fig. 2. Relative positions in R.A. ($\Delta\alpha\cos\delta$) vs. epoch of observation for the studied fields. The values of $\Delta\alpha\cos\delta$ represent the individual positions of the QSO on different CCD frames relative to the barycenter of the SRF. The point sizes are proportional to the number of times the measurement yielded the same coordinate value for a particular epoch (extra-small, small, medium, large and extra-large sizes indicate one to five measurements per epoch, respectively). The best-fit straight lines from linear regression analyses on the data are also shown.

in R.A., and ±0.26 (±0.52), ±0.60 (±0.71), ±0.36 (±0.58), ±0.26 (±0.62) mas yr^{-1} in DEC, for Q0459-6427, Q0557-6713, Q0558-6707 and Q0615-6615, respectively.

We believe the improvement is mainly due to the new third degree polynomial registration process used in the present work. It seems that the latter is quite adequate for the optics of the telescope we used, which, by the way, was never changed throughout the entire time baseline of this project. As stated in PCM06, we believe the scatter shown in the plots probably stems entirely from the random errors in the measurements and the registration process, and does not represent the actual velocity dispersion in the LMC.

In Figures 2 and 3 we present position vs. epoch diagrams for the QSO fields in R.A. ($\Delta\alpha\cos\delta$) and DEC ($\Delta\delta$), where $\Delta\alpha\cos\delta$ and $\Delta\delta$ represent the (X, Y) positions of the QSO on different CCD frames, relative to the barycenter of the SRF. These diagrams were obtained using individual position data for the QSO in each CCD image as a function of epoch. In Table 3 we give the mean barycentric positions of the QSOs per epoch, along with their mean errors (the errors of the averages). The heading N (sixth column) represents the sum of all data points (one per image) used to calculate the mean for each coordinate and corresponding epoch (first column). This sum is the same for both R.A. and DEC. Also shown (last column) are the CCD detectors used in each epoch. Symbol sizes in Figures 2 and 3 are proportional to the number of times the measurements yielded the same coordinate value for a particular epoch. The latter may be different for R.A. and DEC, since each point in Figures 2 and 3 represents a subset of data points in a small range of coordinates; thus, the number of points in the range may be different for R.A. and DEC, but the sum af all the points for a particular epoch is the same for both coordinates, as shown in Table 3. This is done to avoid point overlapping in the graph. The best-fit straight lines resulting from simple linear regression analysis on the data points are also shown. The negative values of the line slopes correspond to the PM of the barycenter of the LRS in each QSO field.

Table 4 summarizes our results for the (measured) PM of the LMC. Column 1 gives the quasar identification, Columns 2 and 3 the R.A. and DEC components (together with their standard deviations) of the LMC PM,

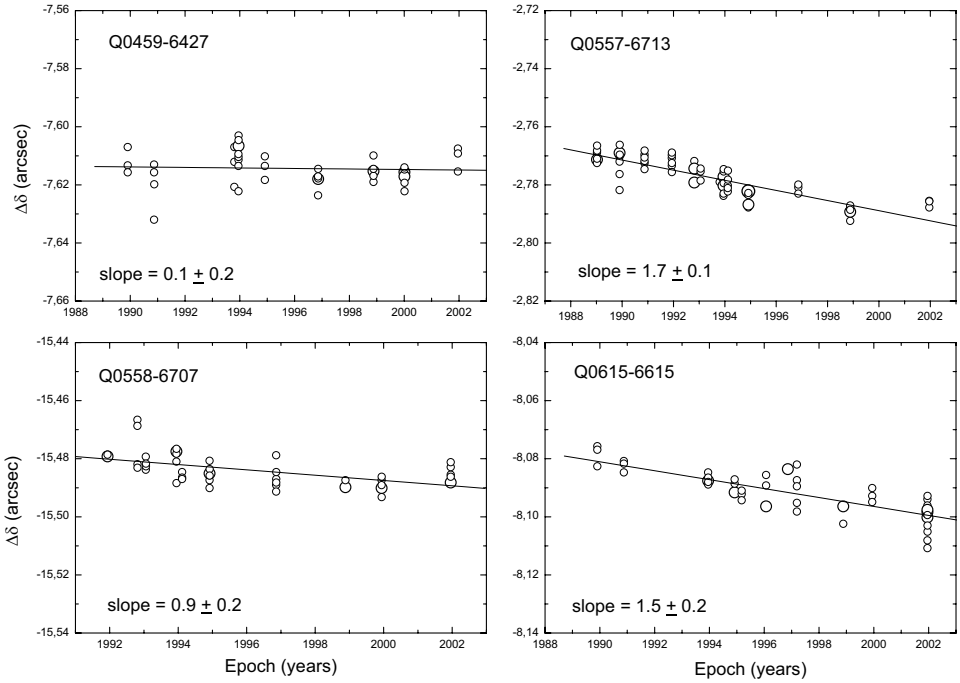

Fig. 3. Same as Figure 2 but for DEC ($\Delta\delta$).

TABLE 4

PROPER MOTION OF THE LMC (AS MEASURED)

Field ID	$\mu_\alpha \cos(\delta)$ mas yr^{-1}	μ_δ mas yr^{-1}	Frames	Epochs	Epoch Range
Q0459-6427	1.4 ± 0.2	0.1 ± 0.2	45	9	1989.91−2001.96
Q0557-6713	1.2 ± 0.2	1.7 ± 0.1	70	13	1989.02−2001.96
Q0558-6707	1.3 ± 0.2	0.9 ± 0.2	48	9	1992.81−2001.96
Q0615-6615	2.1 ± 0.2	1.5 ± 0.2	53	11	1989.90−2001.96

respectively, and, finally, Columns 4, 5, and 6 show the number of frames, the number of epochs, and the observation period, respectively. It should be noted that the rather small quoted errors for the PM come out directly from what the least-square fit yields as the uncertainty in the determination of the slope of the best fit line. The fact that the DEC component of the PM for Q0459-6427 in this table differs by more than 2σ from the rest, may be because this field is in a different location within the LMC relative to the rest of the fields, namely, to the NW of the LMC bar, whereas the other three fields are far to the NE of the LMC bar which means that it might be affected by local internal motions in the cloud of the type suggested by Piatek, Pryor, & Olszewski (2008). This topic probably deserves further studies on the dynamics of this LMC area (and others of similar type in it).

4. COMPARISON WITH PREVIOUS MEASUREMENTS

Table 5 lists the results of all the PM measurements that are known for the LMC with respect to either the center of the LMC or the corresponding field (indicated as "field"), with uncertainties of less than 1 mas yr^{-1} in both PM (μ) components, and the system of reference used in each case. The values for the LMC center are obtained by correcting the field PM for rotation of the LMC plane, and for perspective effects, as explained in

TABLE 5

HIGH PRECISION DETERMINATIONS OF THE PROPER MOTION FOR THE CENTER OF THE LMC

Source	LMC Adopted Parameters	$\mu_\alpha \cos(\delta)$ mas yr^{-1}	μ_δ mas yr^{-1}	Proper Motion System
Kroupa et al. (1994) (field)		+1.3 ± 0.6	+1.1 ± 0.7	PPM
Jones et al. (1994)	JKL94	+1.37 ± 0.28	−0.18 ± 0.27	Galaxies
Kroupa & Bastian (1997) (field)		+1.94 ± 0.29	−0.14 ± 0.36	Hipparcos
ALP00	JKL94	+1.7 ± 0.2	+2.9 ± 0.2	3 Quasars
PAM02	JKL94	+2.0 ± 0.2	+0.4 ± 0.2	1 Quasar
Drake et al. (2001)		+1.4 ± 0.4	+0.38 ± 0.25	Quasars
Kallivayalil et al. (2006)	vDM02	+2.03 ± 0.08	+0.44 ± 0.05	21 Quasars
PCM06 (weighted average)	JKL94	+1.8 ± 0.1	+0.9 ± 0.05	4 Quasars
Piatek et al. (2008)	vDM02	+1.956 ± 0.036	+0.435 ± 0.036	21 Quasars
CMP09	vDM02	+1.82 ± 0.13	+0.39 ± 0.15	1 Quasar
Vieira et al. (2010)	vDM02	+1.89 ± 0.27	+0.39 ± 0.27	SPM, Hipparcos
This work (weighted average)				
field		+1.42 ± 0.09	+1.32 ± 0.09	4 Quasars
	vDM02	+1.46 ± 0.09	+1.25 ± 0.08	4 Quasars
	JKL94	+1.71 ± 0.09	+0.92 ± 0.07	4 Quasars

the next section. The PM values shown in Table 5 for this work are those obtained using both the new input parameters for the LMC given by van der Marel et al. (2002, hereafter vDM02), and those given by Jones, Klemola, & Lin (1994, hereafter JKL94). This is done in order to facilitate comparison of our results with those by the rest of the authors. The adopted LMC parameters by these authors are:

LMC Center: (R.A., DEC) = $(81°.90, -69°.87)J2000.0$. Heliocentric distance of the LMC center: 50.1 kpc. Inclination of the disk: ($i = 34°.7$). P.A. of the descending node: ($-50°.1$), by vDM02.

LMC Center: (R.A., DEC) = $(80°.25, -69°.28)J1950.0$. Heliocentric distance of the LMC center: 50.1 kpc. Inclination of the disk: ($i = 27°.0$). P.A. of the descending node: ($-10°.0$), by JKL94.

Note that there is a significant difference between the values of the inclination of the disk and the P.A. of the descending node in both sets of parameters. This will notoriously affect the final results for the PM of the LMC center.

The total LMC PM values obtained here, for both vDM02 and JKL94 input parameters, amount to $\mu = (+1.92 \pm 0.08)$ mas yr^{-1}, with a position angle $\theta = 49°.2 \pm 3°.4$, and to $\mu = (+1.94 \pm 0.08)$ mas yr^{-1}, with a position angle $\theta = 61°.5 \pm 3°.2$, respectively. The position angle is measured eastward from the meridian joining the center of the LMC to the north pole.

The above total PM values are quite compatible with several theoretical models (Murai & Fujimoto 1980; Lin & Lynden Bell 1982; Shuter 1992; Gardiner, Sawa, & Fujimoto 1994), which predict a proper motion for the LMC in the range 1.5−2.0 mas yr^{-1}, but they are only marginally compatible with the $\theta \approx 90°$ position angle predicted by the same models.

As seen from Table 5, the values of the PM determined by our group (for the JKL94 input LMC parameters) confirm the results of the PCM06 study and show a reasonable agreement with some of the available data. Our "field" results agree particularly well with those of Kroupa, Röser, & Bastian (1994), who used the *Positions and Proper Motions Star Catalog* (Röser & Bastian 1993, PPM) as reference system. On the other hand, there is a significant discrepancy with ALP00's result in DEC, and some discrepancy with the one-field results by CMP09 for QJ0557-6713.

The rest of the PM values in Table 5, that have been recently determined by other groups using QSOs, depart from our values by about 2σ (especially in DEC), with ours being the highest PM values and those by Piatek et al. (2008) the lowest and more recent values for the measured PM. The latter values are also in good agreement with other recent determination (except with ours in DEC). A possible explanation for this departure is that, in both previous sets of data, there may be systematic effects still present (despite some of

TABLE 6

PROPER MOTION AND SPACE VELOCITY RESULTS FOR THE LMC VDM02 PARAMETERS AND $V_{\rm rot} = 50$ km s^{-1}

Parameter	Q0459-6427	Q0557-6713	Q0558-6707	Q0615-6615
$\Delta\mu_\alpha \cos\delta$, rotation correction (mas yr^{-1})	−0.17	0.17	0.17	0.17
$\Delta\mu_\delta$, rotation correction (mas yr^{-1})	−0.06	−0.14	−0.14	−0.15
$\mu_\alpha^{\rm Field} \cos\delta$, LMC centered (mas yr^{-1})	1.5 ± 0.2	1.0 ± 0.2	1.1 ± 0.2	1.9 ± 0.2
$\mu_\delta^{\rm Field}$, LMC centered (mas yr^{-1})	0.2 ± 0.2	1.9 ± 0.1	1.1 ± 0.2	1.7 ± 0.2
$\mu_\alpha^{\rm CM} \cos\delta$, LMC centered (mas yr^{-1})	1.4 ± 0.2	1.2 ± 0.1	1.2 ± 0.2	2.1 ± 0.2
$\mu_\delta^{\rm CM}$, LMC centered (mas yr^{-1})	0.4 ± 0.2	1.7 ± 0.1	0.9 ± 0.2	1.3 ± 0.1
$\mu_\alpha^{\rm GRF} \cos\delta$ (mas yr^{-1})	0.9 ± 0.1	0.7 ± 0.1	0.7 ± 0.1	1.6 ± 0.1
$\mu_\delta^{\rm GRF}$ (mas yr^{-1})	0.3 ± 0.2	1.6 ± 0.1	0.8 ± 0.2	1.1 ± 0.2
$\mu_l^{\rm GRF} \cos b$ (mas yr^{-1})	−0.4 ± 0.2	−1.7 ± 0.1	− 0.9 ± 0.2	−1.4 ± 0.2
$\mu_b^{\rm GRF}$ (mas yr^{-1})	0.9 ± 0.1	0.5 ± 0.1	0.6 ± 0.1	1.4 ± 0.1
Π, velocity component (km s^{-1})	189 ± 28	199 ± 20	178 ± 25	306 ± 26
Θ, velocity component (km s^{-1})	65 ± 50	369 ± 28	182 ± 45	278 ± 36
Z, velocity component (km s^{-1})	133 ± 29	54 ± 21	80 ± 25	247 ± 27
$V_{\rm gc,r}$, radial velocity (km s^{-1})	86 ± 25	138 ± 18	106 ± 22	123 ± 24
$V_{\rm gc,t}$, transverse velocity (km s^{-1})	224 ± 32	399 ± 28	246 ± 38	466 ± 31

them having been corrected). In our set of data, a clear example of this kind of effect is the differential color refraction (DCR) whereas in Piatek et al. (2008) data it is the CCD charge transfer inefficiency. However, as mentioned before, both of these effects were corrected in the corresponding studies. In any case, to the best of our knowledge, the PM values in the present work are not greately affected by DCR, since the working set of images were all selected from those with hour angles less than 1 hr (in absolute value). The ground-based equipment (and its setup) used in our case, was a very stable one, with an optics with a minimal field distortion and whose parameters, as far as we know, were kept unchanged in all of our observing runs. The previously mentioned factors were quite appropriate for this type of astrometric studies.

5. SPATIAL VELOCITY OF THE LMC AND MASS OF THE GALAXY

Using the PM of the LMC determined in § 3, and the radial velocity of the center of the LMC (adopted from the literature), V_r, we can calculate the radial and tangential components of the LMC velocity, as seen from the center of the Galaxy. To do this we have followed the procedure outlined by JKL94. As mentioned before, in the calculations we used two sets of basic LMC parameters, namely, that adopted by vDM02, and that given by JKL94 (see previous section), along with radial velocities $V_r = 262.1$ km s^{-1} and $V_r = 250$ km s^{-1}, respectively. The rotational velocities of the LMC plane adopted for the range of distances from our studied fields to the LMC center (see § 4.1 in CMP09) were both $V_{\rm rot} = 50$ km s^{-1} and $V_{\rm rot} = 120$ km s^{-1}. The two sets of parameters were used to allow an easier comparison of our results with those of the rest of the authors in Table 5 and for following discussions.

In order to calculate the tangential and radial components of the LMC spatial velocity as seen from the Galactic center and with respect to the Galactic Rest Frame (GRF), from the previously measured PM, we have followed a series of steps, which were carried out through an ad-hoc computer software written by the author (MHP). These include: a correction of the PM values for the rotation of the LMC plane; a transformation of the corrected PM into R.A. and DEC velocities centered on the field; a transformation of these two velocity components, into heliocentric (hc) galactic longitudinal and latitudinal velocity components for the center of the LMC; a transformation of the previous velocity components into their galactocentric (gc) counterparts which, in turn, were combined to derive the transverse velocity, ($V_{\rm gc,t}$) of the LMC center with respect to the Galactic center. Similarly, in order to obtain the galactocentric radial velocity ($V_{\rm gc,r}$) for the LMC center, we

TABLE 7

PROPER MOTION AND SPACE VELOCITY RESULTS FOR THE LMC
JLK94 PARAMETERS AND $V_{\rm rot} = 50$ km s^{-1}

Parameter	Q0459-6427	Q0557-6713	Q0558-6707	Q0615-6615
$\Delta\mu_\alpha \cos\delta$, rotation correction (mas yr^{-1})	−0.17	−0.11	−0.11	−0.12
$\Delta\mu_\delta$, rotation correction (mas yr^{-1})	−0.09	0.18	0.18	0.18
$\mu_\alpha^{\rm Field} \cos\delta$, LMC centered (mas yr^{-1})	1.5 ± 0.2	1.3 ± 0.2	1.4 ± 0.2	2.2 ± 0.2
$\mu_\delta^{\rm Field}$, LMC centered (mas yr^{-1})	0.2 ± 0.2	1.6 ± 0.1	0.7 ± 0.2	1.4 ± 0.2
$\mu_\alpha^{\rm CM} \cos\delta$, LMC centered (mas yr^{-1})	1.5 ± 0.2	1.5 ± 0.1	1.5 ± 0.2	2.4 ± 0.2
$\mu_\delta^{\rm CM}$, LMC centered (mas yr^{-1})	0.4 ± 0.2	1.3 ± 0.1	0.5 ± 0.2	0.9 ± 0.1
$\mu_\alpha^{\rm GRF} \cos\delta$ (mas yr^{-1})	1.0 ± 0.1	1.0 ± 0.1	1.0 ± 0.1	1.9 ± 0.1
$\mu_\delta^{\rm GRF}$ (mas yr^{-1})	0.3 ± 0.2	1.2 ± 0.1	0.4 ± 0.2	0.7 ± 0.2
$\mu_l^{\rm GRF} \cos b$ (mas yr^{-1})	−0.4 ± 0.2	−1.4 ± 0.1	−0.6 ± 0.2	−1.1 ± 0.2
$\mu_b^{\rm GRF}$ (mas yr^{-1})	0.9 ± 0.1	0.8 ± 0.1	0.9 ± 0.1	1.7 ± 0.1
Π, velocity component (km s^{-1})	189 ± 30	218 ± 21	195 ± 26	325 ± 27
Θ, velocity component (km s^{-1})	70 ± 53	291 ± 29	105 ± 46	193 ± 37
Z, velocity component (km s^{-1})	148 ± 30	124 ± 22	147 ± 26	313 ± 28
$V_{\rm gc,r}$, radial velocity (km s^{-1})	76 ± 27	114 ± 20	81 ± 24	97 ± 25
$V_{\rm gc,t}$, transverse velocity (km s^{-1})	239 ± 33	367 ± 27	253 ± 31	481 ± 30

applied the previous procedure to the radial velocity of each field (V_r), whose values were adopted in such a way as to reproduce the nominal radial velocity of the LMC center adopted from the literature. The transverse and radial components are finally combined to obtain the spatial velocity vector of the LMC center. The reader is referred to ALP00, PAM02 and PCM06 for more details of the procedure. The results from these calculations are listed in Tables 6 and 7. These two tables also show the equatorial and galactic coordinate components of the PM relative to the GRF (representing the motion of the cloud as seen from a reference point that is stationary with respect to the Galactic center and which is located at the instantaneous solar position), and the Π, Θ and Z galactocentric space velocity components of the LMC in a rectangular Cartesian coordinate system centered on the LMC (as defined by Schweitzer et al. (1995) for the Sculptor dwarf spheroidal galaxy and described by PCM06 for the LMC).

If we assume that the LMC is gravitationally bound to, and in an elliptical orbit, around the Galaxy, and that the mass of the Galaxy is contained within 50 kpc of the galactic center, we can calculate its lower mass limit through the following expression for a point-mass galactic potential:

$$M_{\rm G} = (r_{\rm LMC}/2G)[V_{\rm gc,r} + V_{\rm gc,\ t}(1 - r_{\rm LMC}^2/r_a^2)]/(1 - r_{\rm LMC}/r_a)\,,$$

where r_a is the LMC apogalacticon distance and $r_{\rm LMC}$ its present distance.

For $r_a = 300$ kpc (Galaxy's tidal radius), the two sets of LMC input parameters quoted above, respectively, and rotation velocities of 50 and 120 km s^{-1}, we obtain the results shown in Tables 8 and 9,

Values in Table 8 (for the vDM02 LMC input parameters) result in weighted averages of: $\langle M_{\rm G}\rangle = (6.6 \pm 0.7) \times 10^{11}\ M_\odot$ and $\langle M_{\rm G}\rangle = (8.8 \pm 0.8) \times 10^{11}\ M_\odot$, for the mass of our Galaxy enclosed within 50 kpc, for the two mentioned rotation velocities, respectively. Likewise, values shown in Table 9 (for the JKL94 LMC input parameters) resulted in weighted averages of: $\langle M_{\rm G}\rangle = (6.4 \pm 0.6) \times 10^{11}\ M_\odot$ and $\langle M_{\rm G}\rangle = (7.1 \pm 0.6) \times 10^{11}\ M_\odot$, respectively.

One of the reasons why there are a couple of velocities (mainly tangential velocities) and masses of the Galaxy, derived from our four QSO fields, whose differences are greater than 2σ in Tables 8 and 9, may be due to local internal motions in that area of the LMC, as those suggested by Piatek et al. (2008), especially considering that our four fields are located at the northern side of the LMC bar, albeit at twice the distance from the center of mass of the LMC as those used by the latter authors. This is the area on the LMC,

TABLE 8

MASS OF THE GALAXY FOR TWO LMC ROTATIONAL VELOCITIES (VDM02 PARAMETERS)

Parameter	Q0459-6427	Q0557-6713	Q0558-6707	Q0615-6615
For $V_{\rm rot} = 50$ km s^{-1}				
$V_{\rm gc,r}$, LMC galactocentric velocity (km s^{-1})	86 ± 25	138 ± 18	106 ± 22	123 ± 24
$V_{\rm gc,t}$, LMC galactocentric velocity (km s^{-1})	224 ± 32	399 ± 28	246 ± 38	466 ± 31
$M_{\rm G}$, mass of the Galaxy in $10^{11} \times M_\odot$	(3.9 ± 1.0)	(12 ± 2)	(4.9 ± 1.3)	(16 ± 2)
For $V_{\rm rot} = 120$ km s^{-1}				
$V_{\rm gc,r}$, LMC galactocentric velocity (km s^{-1})	91 ± 25	146 ± 18	114 ± 22	132 ± 24
$V_{\rm gc,t}$, LMC galactocentric velocity (km s^{-1})	283 ± 32	428 ± 28	256 ± 43	466 ± 33
$M_{\rm G}$, mass of the Galaxy in $10^{11} \times M_\odot$	(6.0 ± 1.3)	(14 ± 2)	(5.4 ± 1.5)	(16 ± 2)

TABLE 9

MASS OF THE GALAXY FOR TWO LMC ROTATIONAL VELOCITIES (JKL94 PARAMETERS)

Parameter	Q0459-6427	Q0557-6713	Q0558-6707	Q0615-6615
For $V_{\rm rot} = 50$ km s^{-1}				
$V_{\rm gc,r}$, LMC galactocentric velocity (km s^{-1})	76 ± 27	114 ± 20	81 ± 24	97 ± 25
$V_{\rm gc,t}$, LMC galactocentric velocity (km s^{-1})	239 ± 33	367 ± 27	253 ± 31	481 ± 30
$M_{\rm G}$, mass of the Galaxy in $10^{11} \times M_\odot$	(3.9 ± 1.1)	(9.2 ± 1.4)	(4.4 ± 1.1)	(16 ± 2)
For $V_{\rm rot} = 120$ km s^{-1}				
$V_{\rm gc,r}$, LMC galactocentric velocity (km s^{-1})	82 ± 27	103 ± 20	71 ± 24	87 ± 25
$V_{\rm gc,t}$, LMC galactocentric velocity (km s^{-1})	299 ± 34	343 ± 26	265 ± 27	488 ± 29
$M_{\rm G}$, mass of the Galaxy in $10^{11} \times M_\odot$	(6.1 ± 1.4)	(8.0 ± 1.2)	(4.8 ± 1.0)	(16 ± 2)

showing greater internal motions (Piatek et al. 2008). We remind the reader that in order to determine the mentioned velocities, we had to correct for perspective effects and assume a constant rotation velocity of the LMC plane for all the QSO fields, which would introduce an error in the center of mass PM and consequently in the derived tangential velocities, should local internal motions departing from the assumed constant rotation velocity be present. Another possible error factor (among several others) affecting the derived velocities and masses, especially in extreme cases as that for the field Q0615-6615, could be optical brightness variability, of the fiducial QSO, with time (observing epoch), which is known to occur in some QSOs (i.e. Geha et al. 2003), that could affect the QSO centering process, contaminating the PM results for that particular field. This variability hypothesis should be tested for this particular QSO.

Although slightly larger (specially those for $V_{\rm rot} = 120$ km s^{-1}), the quoted results are compatible with the theoretical 5.5×10^{11} $M_\odot$ value for the upper mass limit of the Galaxy (Sakamoto, Chiba, & Beers 2003), and with the assumption that the LMC is bound to the Galaxy.

6. CONCLUSIONS

1. Our results, obtained from re-processing the data directly from the original images in order to measure the PM of each LMC field relative to the QSO for different epochs, confirm the results by PCM06 obtained from the (X, Y) coordinates previously processed by the original authors in ALP00. This supports the idea mentioned in § 6.1 by PCM06, where they state that the "ALP00-PAM02 discrepancy" did not originate

in the data itself but rather in the data processing by ALP00. This is because in the present work we read the images anew and re-process them from scratch, obtaining basically the same results as those by PCM06.

2. Besides, the procedure to register the individal images into the Standard Frame of Reference, used in this work, through a third degree polynomial, yields basically the same results (although with lower errors) as those by PCM006, meaning that the above discrepancy does not arise from the registration process.

3. Our results here are in a better agreement with those by other authors, in particular with the result given by Kroupa et al. (1994), as well as with several theoretical models, when using the JKL94 LMC input parameters rather than the more recent ones by vDM02.

4. There might be systematic errors still present in some of the PM values using the "quasar method", in Table 5, which would account for some observed marginal differences (of the order of 2σ) in PM, especially in DEC.

5. In reference to the stream of galaxies orbiting around our Galaxy, which would include the LMC, SMC, Draco and Ursa Minor, and possibly Carina and Sculptor galaxies, proposed by Lynden-Bell & Lynden-Bell (1995), and according to the results in the present work, we can conclude that the LMC does not seem to be a member of the proposed stream, because our measured values for μ and θ are at least (considering both sets of LMC input parameters) 5.2σ and 8.9σ away from the predicted values of $\mu = +1.5$ mas yr^{-1} and $\theta = 90°$.

6. The marginal discrepancy of our results from those by CMP09 (especially in DEC) for the same QSO field, has so far no explanation. It might be interesting to note though, that between the present study and that by CMP09 there are important observing setup differences, among them, a different telescope, telescope setup and detector equipment as well as a different set of LRS stars, for the QJ0557-6713 field and, in the present work, a longer observing time baseline and a greater number of observing epochs, for the above field. It is also interesting to note that, despite the short baseline and the fact that only one LMC field was included in this study, the PM values determined by CMP09 are closer to recently measured values for the LMC center of mass than ours.

7. Summing up, our PM and space velocity values support the idea that the LMC is indeed gravitationally bound to our Galaxy.

M.H.P. is greatful of the support by the Universidad de Tarapacá research fund (project # 4721-09). The author wishes to thank to an anonymous referee for helpful suggestions which improved this paper. It is also a pleasure to thank T. Martínez for helping with data processing.

REFERENCES

Anguita, C., Loyola, P., & Pedreros, M. H. 2000, AJ, 120, 845 (ALP00)
Costa, E., et al. 2009, AJ, 137, 4339 (CMP09)
Drake, A. J., Cook, K. H., Alcock, C., Axelrod, T. S., Geha, M., & MACHO Collaboration 2001, Bull. Am. Astron. Soc., 33, 1379
Gardiner, L. T., Sawa, T., & Fujimoto, M. 1994, MNRAS, 266, 567
Geha, M., et al. 2003, AJ, 125, 1
Jones, B. F., Klemola, A. R., & Lin, D. N. C. 1994, AJ, 107, 1333 (JKL94)
Kallivayalil, N., van der Marel, R. P., Alcock, C., Axelrod, T., Cook, K. H., Drake, A. J., & Geha, M. 2006, ApJ, 638, 772
Kroupa, P., & Bastian, U. 1997, New Astron., 2, 77
Kroupa, P., Röser, S., & Bastian, U. 1994, MNRAS, 266, 412
Lin, D. N. C., & Lynden-Bell, D. 1982, MNRAS, 198, 707
Lynden-Bell, D., & Lynden-Bell, R. M. 1995, MNRAS, 275, 429
Murai, T., & Fujimoto, M. 1980, PASJ, 32, 581
Pedreros, M. H., Anguita, C., & Maza, J. 2002, AJ, 123, 1971 (PAM02)
Pedreros, M. H., Costa, E., & Méndez, R. A. 2006, AJ, 131, 1461 (PCM06)
Piatek, S., Pryor, C., & Olszewski, E. W. 2008, AJ, 135, 1024
Röser, S., & Bastian, U. 1993, Bull. Inf. CDS, 42, 11 (PPM)

Sakamoto, T., Chiba, M., & Beers, T. C. 2003, A&A, 397, 889
Schweitzer, A. E., Cudworth, K. M., Majewski, S. R., & Suntzeff, N. B. 1995, AJ, 110, 2747
Shuter, W. L. H. 1992, ApJ, 386, 101
Stetson, P. B. 1987, PASP, 99, 191
van der Marel, R. P., Alves, D. R., Hardy, E., & Suntzeff, N. B. 2002, AJ, 124, 2639 (vDM02)
Vieira, K., et al. 2010, AJ, 140, 1934

Mario H. Pedreros: Departamento de Física, Facultad de Ciencias, Universidad de Tarapacá, Casilla 7-D, Arica, Chile (mpedrero@uta.cl).

Revista Mexicana de Astronomía y Astrofísica, **47**, 345–356 (2011)

SPACE REDDENINGS FOR FIFTEEN GALACTIC CEPHEIDS

D. G. Turner,[1] R. F. MacLellan,[2] A. A. Henden,[3] and L. N. Berdnikov[4]

Received 2011 February 24; accepted 2011 June 27

RESUMEN

Derivamos enrojecimientos espaciales para 15 Cefeidas galácticas a partir de datos CCD $BV(RI)_C$ desenrojecidos para estrellas tipo AF en las vecindades inmediatas de esas variables, en conjunción con enrojecimientos 2MASS de estrellas tipo BAF en los mismos campos. Analizamos las soluciones potenciales de enrojecimiento utilizando el método de extinción variable para identificar estrellas con distancias y enrojecimientos similares a las de las Cefeidas, muchas de las cuales presentan excesos de color. Hemos modificado ligeramente la relación de color intrínseco $BV(RI)_C$ para enanas AF en nuestro análisis, de tal forma que los colores observados para estrellas no enrojecidas en la muestra queden descritos de forma apropiada.

ABSTRACT

Space reddenings are derived for 15 Galactic Cepheids from dereddening CCD $BV(RI)_C$ data for AF-type stars in the immediate vicinities of the variables, in conjunction with 2MASS reddenings for BAF-type stars in the same fields. Potential reddening solutions were analyzed using the variable-extinction method to identify stars sharing potentially similar distances and reddenings to the Cepheids, several of which have large color excesses. The intrinsic $BV(RI)_C$ color relation for AF dwarfs was modified slightly in the analysis in order to describe better the colors observed for unreddened stars in the samples.

Key Words: methods: observational — stars: variable: Cepheids — ISM: dust, extinction

1. INTRODUCTION

Because of the deleterious effects of interstellar reddening and extinction, it is difficult to establish an empirical picture of the Cepheid instability strip based entirely upon observations of Milky Way Cepheids. The use of extragalactic Cepheids is not necessarily a practical solution to the problem, since the available data for Milky Way Cepheids are generally more extensive and of greater precision, and the effects of internal reddening within other galaxies are not as well established as they are locally. Such considerations justify the continued use of the Galactic sample in studies aimed at establishing reliable intrinsic properties of classical Cepheid variables.

The determination of accurate reddenings for Cepheids has traditionally followed three different routes: (i) from field reddenings of specific objects (e.g., binary, cluster, association, or isolated Cepheids) based upon the analysis of photometric data for early-type stars sharing the same lines of sight, (ii) from observations mainly of bright Cepheids involving photometric parameters designed to be independent of interstellar reddening, and (iii) from using standard reddening laws and a calibrated intrinsic color relation (either observational or model generated) to deredden photometric observations for large samples of Cepheids. Methods (i) and (ii) are the most reliable means of establishing reddenings for individual Cepheids since method (iii) may entail use of period-color relations (e.g., Fernie 1990a,b), which do not account for the intrinsic spread in effective temperature of the Cepheid instability strip and may generate erroneous results (see Turner 1995).

For method (ii), spectroscopic indices related to stellar effective temperature and designed to be independent, or relatively independent, of interstellar and atmospheric extinction include the Γ-index (Kraft 1960; Spencer Jones 1989), which measures

[1]Saint Mary's University, Halifax, Nova Scotia, Canada.
[2]Queen's University, Kingston, Ontario, Canada.
[3]AAVSO, Cambridge, Massachusetts, USA.
[4]Sternberg Astronomical Institute, Moscow, Russia.

the depression of the G-band of CH (λ4305) relative to the local continuum, the β-index, which samples the strength of the Hβ Balmer line of hydrogen relative to the surrounding continuum, and the KHG-index of Brigham Young University (McNamara & Potter 1969; McNamara, Helm, & Wilcken 1970; Feltz 1972), which measures the strengths of Ca II K (λ3933), Balmer Hδ (λ4101), and the G-band through narrow band interference filters in a manner independent of extinction. A more recent technique (Sasselov & Lester 1990) involves the use of line depth ratios between C I and Si II lying on the Brackett continuum near 10728 Å. A similar technique was used by Krockenberger et al. (1998) using spectral lines falling in the red region of Cepheid spectra. Kovtyukh et al. (2008) have taken the technique to its ultimate level of sophistication by using high resolution optical spectra of Cepheids throughout their cycles, in conjunction with stellar atmosphere models, to track their changes in effective temperature, and thus intrinsic broad band color.

The use of close neighbours to deduce reddenings for Cepheids appears to date from its application to the blue companion of δ Cep by Eggen (1951); it has also been used recently for Cepheids studied with the *Hubble Space Telescope* (Benedict et al. 2007). But the existing sample includes only ∼40 Cepheids of known space reddening (Laney & Caldwell 2007). This study presents new space reddenings for 15 Galactic Cepheids derived from CCD $BV(RI)_C$ photometry for stars in the immediate fields of the variables. The goal is to test the feasibility of deriving Cepheid reddenings based upon only $BV(RI)_C$ observations for stars in the fields of the Cepheids, as well as to augment the limited sample of Cepheids with space reddenings. As demonstrated here, the methodology appears to provide useful results that extend the sample of Cepheids with independently derived reddenings.

2. OBSERVATIONAL DATA

The input data for the present study consist of observations of 15 Cepheid fields obtained with the 1.0 m Ritchey-Chrétien telescope of the U.S. Naval Observatory, Flagstaff Station. A Tektronix/SITe, 1024 × 1024 pixel, thinned CCD was used with Johnson system BV and Kron-Cousins system $(RI)_C$ filters to image the fields (e.g., Henden & Munari 2000). Several deep images were obtained for each field, from which average $BV(RI)_C$ magnitudes and colors, with typical uncertainties smaller than $\pm 0^m.01$, were extracted for all detectable stars using DAOPHOT (Stetson 1987). Since no U-band observations or spectral types are available for the stars in the survey fields, it was necessary to deduce individual reddenings from photometric analyses of two-color diagrams constructed from the $BV(RI)_C$ data. The data are available electronically from A.A.H. via ftp from the American Association of Variable Star Observers website[5].

An often-ignored feature of interstellar reddening is that no single relationship accurately describes it over all regions of the Galaxy (Wampler 1961, 1962; Mathis 1990; Turner 1976a,b, 1989, 1994). Regional variations in the reddening law depend directly upon direction viewed through the Milky Way, vary slowly with Galactic longitude, and are tied to differences in the distribution of particle sizes for dust lying along different lines of sight. The resulting Galactic longitude and latitude dependence of the extinction law affects interstellar reddening studies that implicitly use a relationship of fixed parameterization to describe the extinction in a particular color system, and should be most important for stars of large reddening. Several of the Cepheids in the present sample are heavily reddened, so the extinction laws for the fields of each object were established prior to the analysis by taking advantage of existing studies for regions reasonably close to the program objects (e.g., Johnson 1968; Turner 1976b, 1989, as well as other published studies by the lead author).

Specifically, a reddening slope E_{U-B}/E_{B-V} for the field of each program Cepheid was established from studies by Turner (1976b, 1989) for adjacent regions, and was linked to specific reddening slopes E_{V-I}/E_{B-V} and E_{R-I}/E_{B-V} on the Johnson system using regional reddening curves from Johnson (1968). Those were then converted to reddening slopes E_{V-I}/E_{B-V} and E_{R-I}/E_{B-V} on the Kron-Cousins system using the results of Fernie (1983) and Caldwell et al. (1993). To illustrate the methodology, the results for specific fields studied by Johnson (1968) and exhibiting a range of color excess ratios E_{U-B}/E_{B-V} are shown in Figure 1, where it can be noted that the I–band E_{V-I}/E_{B-V} reddening ratios appear to display no significant dependence on visible reddening slope E_{U-B}/E_{B-V}. The Cepheids studied here all lie in fields where the reddening slope does not vary significantly from the locally observed Galactic mean, so specifying the exact reddening ratio for each field proved to be only a minor concern.

3. METHOD OF ANALYSIS

This study presents new space reddenings for 15 Galactic Cepheids derived from two-color dia-

[5] ftp://www.aavso.org/public/calib/.

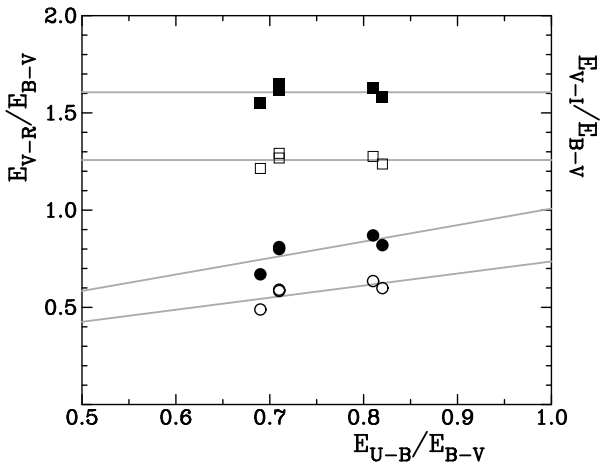

Fig. 1. Derived Johnson system (filled symbols) and Kron-Cousins system (open symbols) reddening ratios E_{V-R}/E_{B-V} (circles, lower) and E_{V-I}/E_{B-V} (squares, upper) for fields studied by Johnson (1968). Gray lines denote the implied dependences on reddening slope E_{U-B}/E_{B-V}.

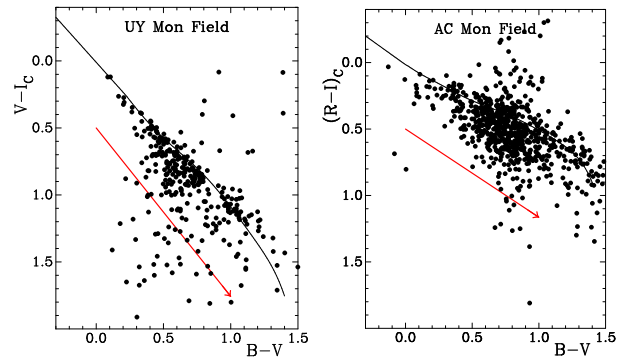

Fig. 2. Two-color diagrams, V–I_C versus B–V for the field of UY Mon (left), and $(R$–$I)_C$ versus B–V for the field of AC Mon (right), showing the intrinsic color relations adopted (solid curves). Reddening lines specific for the fields are shown separately in red for $E_{B-V} = 1.0$, with arrows denoting the direction of increasing reddening. The color figure can be viewed online.

grams, V–I_C versus B–V and $(R$–$I)_C$ versus B–V, constructed from CCD $BV(RI)_C$ photometry for stars in the fields of the variables. Reddening lines appropriate for each field were adopted as indicated above, specifically the adopted reddening slopes E_{U-B}/E_{B-V} were 0.73 for VY Sgr, AY Sgr, and V1882 Sgr, 0.75 for HZ Per and OT Per, 0.76 for FO Cas, IO Cas, EW Aur, YZ CMa, CN CMa, BD Pup, BE Pup, and LR Pup, and 0.77 for UY Mon and AC Mon. The reddening slopes E_{V-I}/E_{B-V} and E_{R-I}/E_{B-V} were next obtained through interpolation and computation with the data of Figure 1, resulting in values on the Kron-Cousins system of $E_{V-I}/E_{B-V} = 1.257$ for all fields and values of E_{R-I}/E_{B-V} of 0.689, 0.677, 0.670, and 0.664, respectively, for the Cepheid fields listed above. Examples are shown in Figure 2, where the derived reddening slopes for UY Mon and AC Mon are $E_{V-I}/E_{B-V} = 1.257$ and $E_{R-I}/E_{B-V} = 0.664$ according to the inferred reddening ratio $E_{U-B}/E_{B-V} = 0.73$. Note that the adopted field reddening lines are unchanging for E_{V-I}/E_{B-V} and exhibit only small variations for E_{R-I}/E_{B-V}.

Initial tests with two-color diagrams using intrinsic $BV(RI)_C$ colors for dwarfs from Caldwell et al. (1993) revealed small anomalies in the inferred E_{B-V} reddenings derived from the two diagrams, as well as an overabundance of unreddened and negatively-reddened stars relative to the intrinsic relation, not explainable as luminosity effects (Caldwell et al. 1993). Such non-physical results suggested the need for slight corrections to the intrinsic colors used with the present data sets, which are normalized to the Kron-Cousins system. Small adjustments to the intrinsic relations for late B-type and A-type dwarfs to make them bluer were therefore tried, using alternative intrinsic colors from Johnson (1966) adjusted to the Cape system (Fernie 1983). That produced greater consistency in the derived reddenings and better agreement for unreddened stars, and was adopted throughout the remainder of the study. The intrinsic colors corresponding to such changes are presented in Table 1 for reference purposes, where they are compared with the Caldwell et al. (1993, SAAO) colors for dwarfs, which were adopted for all other stars. Given that the analysis was restricted to stars that dereddened uniquely to the AF-dwarf relation, the modification affects the resulting space reddenings, but only to a minor extent. Likely B-type stars in the field of each Cepheid were only used when analyzing 2MASS colors for the stars.

Reddening lines run nearly parallel to the intrinsic relations for B-dwarfs and KM-dwarfs, particularly in V–I_C versus B–V diagrams, which is why the analysis was restricted to stars indicated to be likely AF-dwarfs, which are reasonably plentiful in each field. The slope of the intrinsic relation for AF-dwarfs relative to the effects of interstellar reddening in the $BV(RI)_C$ system results in sufficient separation, particularly in $(R$–$I)_C$ relative to B–V, to produce unique photometric dereddening solutions for

TABLE 1

INTRINSIC $BV(RI)_C$ COLORS FOR DWARFS

$(B–V)_0$	$(V–I)_0$	$(V–I)_0$ SAAO	$(R–I)_0$	$(R–I)_0$ SAAO	$(B–V)_0$	$(V–I)_0$	$(V–I)_0$ SAAO	$(R–I)_0$	$(R–I)_0$ SAAO
−0.24	−0.259	−0.237	−0.157	−0.158	+0.04	+0.055	+0.037	+0.040	+0.021
−0.23	−0.248	−0.221	−0.150	−0.146	+0.05	+0.066	+0.048	+0.046	+0.026
−0.22	−0.236	−0.206	−0.143	−0.134	+0.06	+0.077	+0.059	+0.053	+0.032
−0.21	−0.225	−0.193	−0.136	−0.123	+0.07	+0.088	+0.070	+0.059	+0.038
−0.20	−0.214	−0.181	−0.129	−0.114	+0.08	+0.100	+0.081	+0.066	+0.043
−0.19	−0.203	−0.170	−0.121	−0.105	+0.09	+0.111	+0.093	+0.072	+0.049
−0.18	−0.192	−0.159	−0.114	−0.097	+0.10	+0.122	+0.105	+0.078	+0.055
−0.17	−0.180	−0.149	−0.107	−0.089	+0.11	+0.133	+0.117	+0.084	+0.061
−0.16	−0.169	−0.140	−0.100	−0.082	+0.12	+0.144	+0.129	+0.090	+0.068
−0.15	−0.158	−0.131	−0.092	−0.076	+0.13	+0.156	+0.141	+0.095	+0.074
−0.14	−0.147	−0.122	−0.085	−0.070	+0.14	+0.167	+0.153	+0.101	+0.080
−0.13	−0.136	−0.114	−0.078	−0.064	+0.15	+0.178	+0.166	+0.106	+0.086
−0.12	−0.124	−0.106	−0.071	−0.059	+0.16	+0.189	+0.179	+0.112	+0.093
−0.11	−0.113	−0.098	−0.064	−0.053	+0.17	+0.200	+0.191	+0.117	+0.099
−0.10	−0.102	−0.090	−0.056	−0.048	+0.18	+0.212	+0.204	+0.122	+0.106
−0.09	−0.091	−0.082	−0.049	−0.043	+0.19	+0.223	+0.217	+0.127	+0.112
−0.08	−0.080	−0.074	−0.042	−0.039	+0.20	+0.234	+0.230	+0.133	+0.119
−0.07	−0.068	−0.066	−0.035	−0.034	+0.21	···	+0.243	+0.138	+0.125
−0.06	−0.057	−0.057	−0.028	−0.029	+0.22	···	+0.256	+0.143	+0.132
−0.05	−0.046	−0.049	−0.020	−0.024	+0.23	···	+0.269	+0.148	+0.138
−0.04	−0.035	−0.040	−0.013	−0.020	+0.24	···	+0.281	+0.154	+0.144
−0.03	−0.024	−0.031	−0.006	−0.015	+0.25	···	+0.294	+0.159	+0.151
−0.02	−0.012	−0.022	+0.001	−0.010	+0.26	···	+0.307	+0.164	+0.157
−0.01	−0.001	−0.013	+0.008	−0.005	+0.27	···	+0.320	+0.170	+0.164
+0.00	+0.010	−0.004	+0.015	+0.000	+0.28	···	+0.332	+0.175	+0.170
+0.01	+0.021	+0.006	+0.021	+0.005	+0.29	···	+0.345	+0.180	+0.176
+0.02	+0.032	+0.016	+0.027	+0.010	+0.30	···	+0.357	+0.185	+0.182
+0.03	+0.043	+0.026	+0.033	+0.016					

each star, and the use of two separate color-color diagrams provides independent estimates for the intrinsic color of each star, although greater precision is obtained with solutions from the $(R–I)_C$ versus $B–V$ diagram alone, because the angle between the intrinsic relation and typical reddening lines is larger. Infrared JHK_s observations exist for most stars (Cutri et al. 2003) from the Two Micron All Sky Survey (2MASS, Skrutskie et al. 2006), and confirm the adopted reddenings from $BV(RI)_C$ data, although the scatter in 2MASS JHK_s colors tends to be rather significant, larger than in UBV color-color diagrams (Turner 1976a).

Typical companions and progenitors of Cepheids are B-type stars (Turner 1984), which are rare enough that their occurrence in the field of a Cepheid raises the possibility of a physical association. AF-type stars, on the other hand, are a more common constituent of Galactic star fields (McCuskey 1965), so the possibility of their physical association with a nearby Cepheid is reduced, but not necessarily to zero. In many of our program fields some of the stars identified as likely AF-type may be associated with the Cepheid of interest, but that was not explored here since there are no catalogued star clusters in the fields, although the regions around UY Mon, BE Pup, YZ CMa, and VY Sgr appear to contain faint anonymous clusters, and BD Pup and FO Cas are located in bright groups of surrounding stars.

The additional scatter in Figure 2 illustrates some of the problems associated with dereddening stars in $BV(RI)_C$ color-color diagrams. Such scatter for a small proportion of stars is a common characteristic of color-color diagrams, including those in UBV and those used for 2MASS photometry, and is readily explained in most cases by observational error, typically one or more of the magnitudes in the observed colors falling too close to the survey limits. At bright magnitude limits the typical stars encountered in Galactic star fields are A dwarfs and

GK giants (McCuskey 1965), but the demographic changes as the magnitude limits increase, and faint, nearby degenerate stars and M dwarfs begin to compound the picture with their unusual colors and larger measuring uncertainties. Emission, binarity, overly bright stars suffering from image saturation, objects lying away from the main sequence (Caldwell et al. 1993), and low quality observations for faint stars all combine to generate scatter in such plots, but using two separate color-color diagrams and limiting the analysis to stars fainter than the bright survey limits and brighter than the faint survey limits assures that likely AF dwarfs are identified properly. They are the small fraction of objects that deredden uniquely to the intrinsic relation for such stars in Figure 2, as confirmed by their JHK_s colors.

The derived reddenings for stars analyzed in each field were adjusted to equivalent color excesses for a B0 star according to their inferred intrinsic colors and the dependence of reddening on intrinsic color summarized by Fernie (1963). Interstellar extinction affects the effective wavelengths of broad band BV filters differently according to the continuum of the star being observed, such that a typical Cepheid of, say, $(B-V)_0 = 0.60$ reddened by $E(B-V) = 0.90$ suffers identical extinction to a B0 dwarf star of $(B-V)_0 = -0.30$ reddened by $E(B-V) = 0.97$ (cf. η factor of Fernie 1963). Such adjustments are necessary when comparing reddenings of stars across a wide range of intrinsic color. Zero-age main sequence (ZAMS) values of M_V as a function of intrinsic $(B-V)_0$ color (Turner 1976a, 1979) were also assigned to each star from the photometric dereddening solutions in order to provide estimates, or at least underestimates, of apparent distance modulus, V–M_V, for the stars in each field. The stars were then plotted in a variable-extinction diagram, such as those for each field summarized in Figure 3, as a means of assessing the likely space reddening of each Cepheid. Figure 3 represents only a portion of each variable-extinction diagram, namely the most heavily-populated regions associated with the expected parameters for each Cepheid.

Mean $\langle B \rangle$ and $\langle V \rangle$ magnitudes are available for each Cepheid from Berdnikov (2007) and the present study, and rough estimates of reddening and luminosity were made from older, published period-color (e.g., Fernie 1990a,b) and period-luminosity (e.g., Turner 1992) relations, which do not differ substantially from more recent results (Turner 2001, 2010). It was then possible to establish roughly where in each variable-extinction diagram the parameters for the Cepheid should fall, keeping in mind that an extremely liberal interpretation of such "predictions" is essential to avoid biasing the results. Some of the sample Cepheids are suspected Type II objects or overtone pulsators, for example, which affects estimates of both reddening and luminosity. Generous uncertainties of ± 0.1 or more in E_{B-V} and ± 1 in M_V were therefore assumed in the analysis. Note that the "predictions" for IO Cas, FO Cas, and V1882 Sgr are inconsistent with expectations for classical Cepheids (they have larger predicted distance moduli than those for surrounding stars of similar reddening), which means that they are potential Type II objects. The situation for HZ Per, BD Pup, and OT Per is more ambiguous.

All such information is needed in order to establish which stars in the field of each Cepheid are useful for deriving its space reddening. In the case of UY Mon, for example, the estimated distance and reddening for the Cepheid associate it with the group of slightly reddened stars at $E_{B-V} \simeq 0.1$, $(V\text{–}M_V)_0 \simeq$ 11–12 ($d \simeq$ 1.6–2.5 kpc), but less distant and less reddened than stars of $E_{B-V} \simeq 0.5$, $(V\text{–}M_V)_0 \simeq$ 12.5–13 ($d \simeq$ 3–4 kpc), in its vicinity. The best match is therefore to the 4 stars within $5'$ of UY Mon that are reddened by $E_{B-V} \simeq 0.1$. Other cases are more complex because of the patchy reddening that permeates most fields, but have been resolved by considering only stars close to each Cepheid.

What appears to be a continuous run of reddening with distance in some fields results from the patchy extinction in each field combined with larger-than-average uncertainties in the inferred color excesses, E_{B-V}. The extinction associated with most Galactic star fields is typically associated with individual dust clouds dispersed along the line of sight (Turner 1994). But large uncertainties in reddening can confuse the picture. Figure 4 presents the results of a simulation of such circumstances in a field where the scatter in the color excesses is taken to be ± 0.05, with associated uncertainties in absolute magnitude of ± 0.5, both quantities being applied randomly to the test points. Star densities were assumed constant as a function of distance, and the input parameters included specific amounts of reddening and extinction arising in discrete dust clouds located along the line of sight at distances of 0.5 pc, 0.9 pc, and 1.1 pc, producing mean color excesses of $E_{B-V} = 0.2$, 0.5, and 0.7, respectively. An extinction law with $R = 3.0$ is depicted for the last group. The parameters, in particular the adopted scatter, were chosen in order to produce the greatest complexity in the resulting variable-extinction diagram. The resulting scatter produces results similar

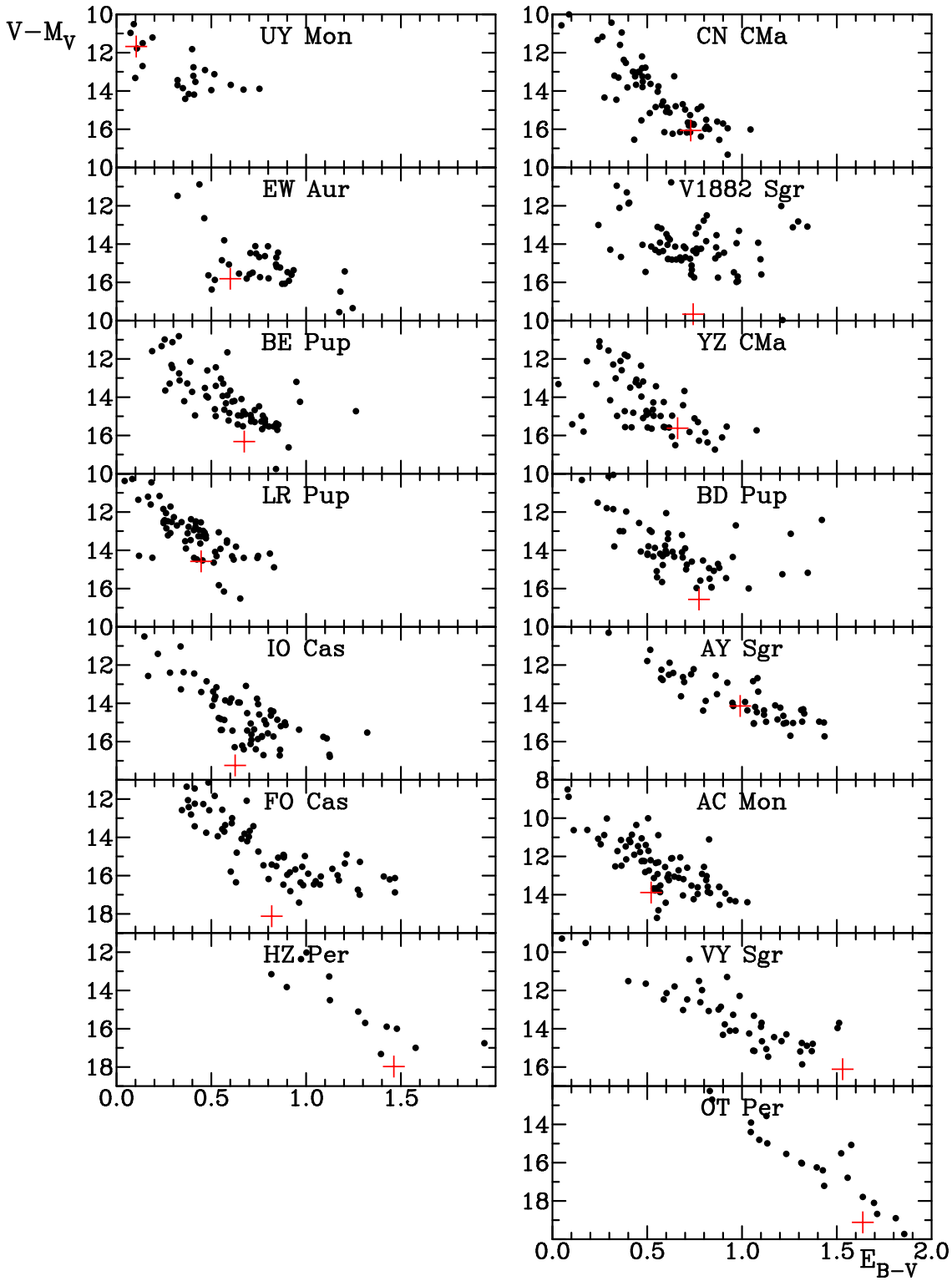

Fig. 3. Variable-extinction diagrams for the fields examined in this study, identified by the Cepheid of interest. Filled symbols denote AF stars near each Cepheid, and red plus signs are "predictions" for the Cepheid parameters. The color figure can be viewed online.

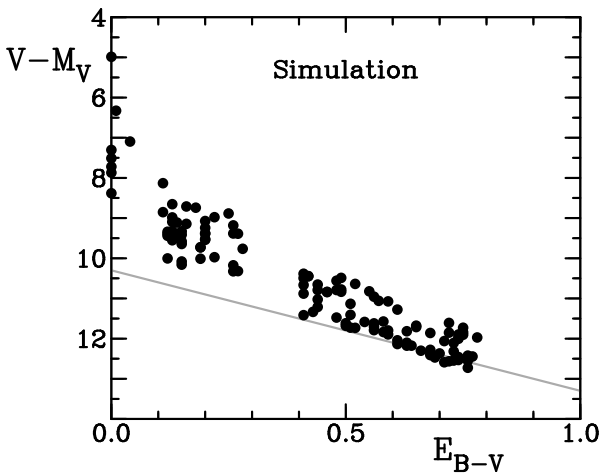

Fig. 4. A simulated variable-extinction diagram for a star field where the reddening increases with distance according to dust clouds producing $E_{B-V} = 0.20$, 0.50, and 0.70 located at distances of 0.5 kpc, 0.9 kpc, and 1.1 kpc, respectively, with associated uncertainties in E_{B-V} of ± 0.05 and in M_V of ± 0.5. The gray line denotes a standard reddening law of $R = A_V/E_{B-V} = 3.0$ for stars at a distance of 1.1 kpc.

to some of the variable-extinction diagrams of Figure 3.

The large range of inferred reddenings for field stars near each Cepheid was reduced further through an analysis of 2MASS observations (Cutri et al. 2003) for likely BAF-type stars in the same fields, analyzed in similar fashion to that employed by Turner et al. (2008) and Turner (2011). 2MASS observations were used separately without combination with the *BV(RI)*$_C$ photometry in order to avoid potential zero-point problems. The observed *J*–*H* and *H*–K_s colors for stars lying within 5′ of each Cepheid are shown in Figure 5, and were compared with the intrinsic relation for main-sequence stars in the 2MASS system (Turner 2011), adjusted with a reddening slope $E_{H-K}/E_{J-H} = 0.49$ from Turner (2011). Multiple solutions in some cases, e.g., UY Mon and HZ Per, were resolved with reference to the variable-extinction diagrams and "predicted" values, and best fits were made by trial and error by establishing reddenings for which likely BAF-type stars had colors distributed randomly about the reddened intrinsic relation.

The *JHK*$_s$ colors generate independent E_{B-V} reddenings for the stars in the Cepheid fields, with the advantage of being more closely tied to B-type stars in the fields, stars that lie blueward of the "kink" in the intrinsic relation and that may share a common origin with the Cepheid. The reddenings have slightly larger uncertainties because of larger photometric scatter in the observations (by factors of 3–5 relative to the *BV(RI)*$_C$ photometry) in combination with the correction from infrared to optical reddening. They are nevertheless crucial for narrowing the range of potential color excesses for some of the sample Cepheids, such as IO Cas. A few objects in the sample appear to be Type II Cepheids, but that does not affect the results. In most cases the implied reddening near the Cepheid is fairly evident.

4. RESULTS

The results of the variable-extinction studies of the sample Cepheids are presented in Table 2, which lists the inferred space reddening for each Cepheid derived from likely AF-type stars lying within different angular radii, from 2′ to 5′ distant, and the reddening inferred from 2MASS *JHK*$_s$ colors for stars within 5′ of the Cepheid. The adopted color excess in each case, Column 8, was the average for all AF-type stars lying within 5′ of the Cepheid and of comparable inferred distance, and the resulting reddening, which is equivalent to that for a star of spectral type B0, was converted in the last column of the table to a value appropriate for the derived intrinsic color of the Cepheid, again using the relationship of Fernie (1963). The number of stars used to obtain the space reddening is listed in the second last column of Table 2. In rich fields that number is of order ∼10–20, whereas in more poorly populated regions or fields with a larger spread in reddening, less than half a dozen reference stars were available. Two solutions are presented for UY Mon, for reasons indicated later, although the adopted solution for the Cepheid is the first.

It is worth noting that the 2MASS reddenings fall closer to the converted color excess for the Cepheid than to the B0-star reddenings. A reasonable explanation lies in the fact that the BAF-star reddenings in a 2MASS color-color diagram tend to be dominated by the AF stars, particularly likely F-type stars, since B-type stars are less common in the small fields analyzed and are potentially affected by circumstellar effects (Turner 2011). The 2MASS reddenings are also important for providing confirmation of the relationship used to convert B0-star color excesses to those appropriate for a star with the average unreddened colors of the Cepheid, which are very similar to F-type dwarfs in the 2MASS samples.

The derived intrinsic colors are presented in Table 3, which also provides in Column 3 the variable

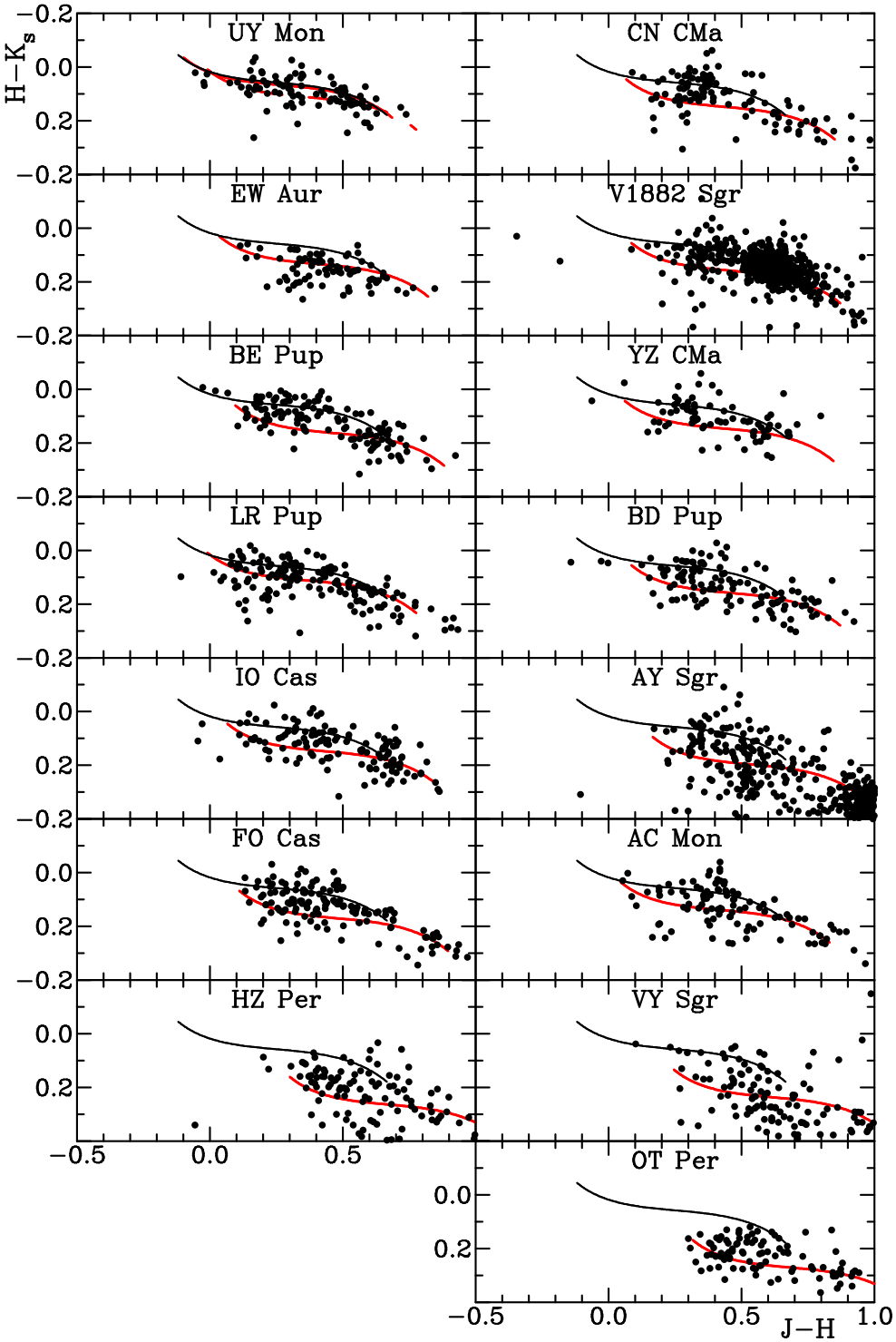

Fig. 5. 2MASS color-color diagrams, H–K_s versus J–H, for stars within 5′ of each Cepheid, from observations by Cutri et al. (2003). The intrinsic relation for main sequence stars is plotted as a black line, while red lines depict the adopted reddening for stars associated with the Cepheids, from Column 7 of Table 2. The dashed red line for UY Mon represents the alternate solution for that field. The color figure can be viewed online.

TABLE 2

SPACE REDDENINGS FOR CEPHEID FIELDS

Cepheid	log P	E_{B-V}(B0) $< 2'$	E_{B-V}(B0) $< 3'$	E_{B-V}(B0) $< 4'$	E_{B-V}(B0) $< 5'$	E_{B-V} 2MASS	E_{B-V}(B0) Adopted	No. Stars	E_{B-V}(Cδ)
UY Mon	0.380	···	0.09	0.09	0.12 ± 0.01	0.07 ± 0.07	0.12 ± 0.01	4	0.11 ± 0.01
UY Mon[1]	···	···	0.42	0.44 ± 0.03	0.43 ± 0.02	0.37 ± 0.07	0.43 ± 0.02	3	···
CN CMa	0.390	0.62 ± 0.02	0.65 ± 0.02	0.66 ± 0.02	0.67 ± 0.02	0.63 ± 0.12	0.67 ± 0.02	11	0.63 ± 0.02
EW Aur	0.425	0.52	0.63 ± 0.06	0.61 ± 0.04	0.61 ± 0.04	0.53 ± 0.08	0.61 ± 0.04	6	0.58 ± 0.03
V1882 Sgr	0.433	0.60 ± 0.01	0.68 ± 0.03	0.70 ± 0.02	0.68 ± 0.02	0.69 ± 0.05	0.68 ± 0.02	20	0.64 ± 0.01
BE Pup	0.458	0.80	0.72 ± 0.04	0.69 ± 0.03	0.68 ± 0.02	0.73 ± 0.12	0.68 ± 0.02	20	0.64 ± 0.02
YZ CMa	0.499	···	0.71 ± 0.10	0.64 ± 0.09	0.60 ± 0.03	0.61 ± 0.07	0.60 ± 0.03	10	0.56 ± 0.03
LR Pup	0.523	0.44	0.47 ± 0.02	0.46 ± 0.01	0.45 ± 0.01	0.37 ± 0.07	0.45 ± 0.01	14	0.42 ± 0.01
BD Pup	0.593	0.63 ± 0.03	0.71 ± 0.03	0.74 ± 0.03	0.72 ± 0.02	0.69 ± 0.08	0.72 ± 0.02	19	0.67 ± 0.02
IO Cas	0.748	0.74	0.64 ± 0.03	0.62 ± 0.03	0.63 ± 0.03	0.63 ± 0.08	0.63 ± 0.03	14	0.59 ± 0.02
AY Sgr	0.818	···	1.04 ± 0.02	1.02 ± 0.04	1.00 ± 0.03	0.97 ± 0.05	1.00 ± 0.03	8	0.94 ± 0.02
FO Cas	0.832	0.99	0.99	0.83 ± 0.07	0.82 ± 0.06	0.78 ± 0.14	0.82 ± 0.06	7	0.76 ± 0.05
AC Mon	0.904	···	0.61	0.61 ± 0.02	0.59 ± 0.02	0.56 ± 0.05	0.59 ± 0.02	5	0.55 ± 0.01
HZ Per	1.052	1.39	1.39	1.48 ± 0.07	1.48 ± 0.05	1.42 ± 0.10	1.48 ± 0.05	4	1.36 ± 0.04
VY Sgr	1.132	···	1.50	1.41 ± 0.04	1.35 ± 0.04	1.24 ± 0.15	1.35 ± 0.04	3	1.24 ± 0.04
OT Per	1.416	···	1.70	1.52 ± 0.11	1.52 ± 0.09	1.47 ± 0.12	1.52 ± 0.09	5	1.39 ± 0.08

[1]Alternate solution for stars of large reddening near UY Mon.

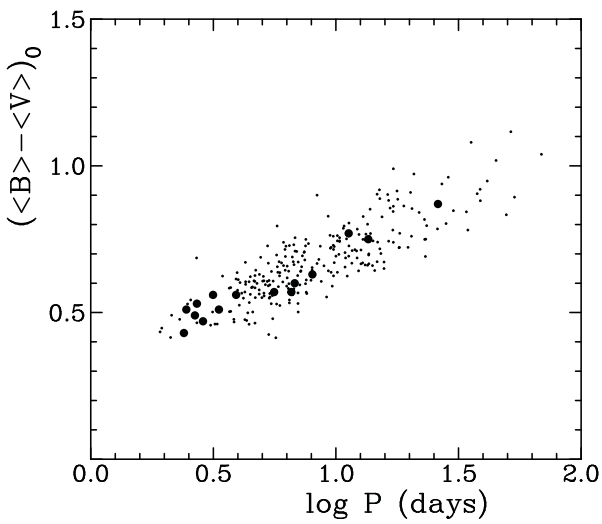

Fig. 6. Derived intrinsic $\langle B\rangle$–$\langle V\rangle$ colors for sample Cepheids (large symbols) relative to other Cepheids with derived reddenings (small symbols, Turner 2001), as a function of pulsation period.

star type designation for the object from the *General Catalogue of Variable Stars* (Samus et al. 2004). Type II Cepheids are designated as CWB for short period (1–8 days) BL Herculis variables, and CWA for longer period (8–20 days) W Virginis stars. The intrinsic $(\langle B\rangle$–$\langle V\rangle)_0$ colors are plotted in Figure 6 relative to a set of similar intrinsic colors calibrated relative to other Cepheids with field reddenings (binary, cluster or association members) and Cepheids with reddenings derived using reddening-free indices (Turner 2001).

All of the program stars studied here appear to have intrinsic colors consistent with those of classical Galactic Cepheids, despite remaining questions about the true population status for some of them. The spread in color at a given value of pulsation period P for the reference sample can be attributed to the natural width of the Cepheid instability strip, and in a few cases to erroneous reddenings. The location of individual Cepheids in our sample relative to the hot (blue) and cool (red) edges of the strip, if used in conjunction with light amplitude and rate of period change, provides useful information about what stage the Cepheids have reached in their evolution (Turner et al. 2006).

Figure 7 plots the inferred $(R$–$I)_J$ colors for our sample Cepheids relative to their $(\langle B\rangle$–$\langle V\rangle)_0$ colors, transposed from $(R$–$I)_C$ using the relationships of Fernie (1983). Included are inferred colors for AFGK supergiants from Johnson (1966), in similar fashion to the analysis of Dean et al. (1978). There is good agreement of the derived intrinsic colors for sample Cepheids with the colors expected for supergiant stars, with the exception of V1882 Sgr and YZ CMa. Both objects have faint optical companions that may contaminate the $(RI)_C$ photometry, so the results of Figure 7 do not necessarily indicate a significant difference in color between classical and Type II Cepheids. The data also indicate the general success of the procedure adopted in this study. The temperature spread of the instability strip is less marked in intrinsic $(R$–$I)_J$ and $(R$–$I)_C$ colors than in $(\langle B\rangle$–$\langle V\rangle)_0$ color, as expected.

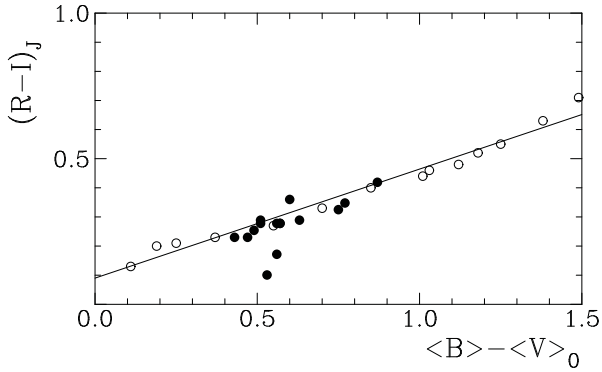

Fig. 7. Derived Johnson system $(R–I)_J$ colors for sample Cepheids (filled circles) relative to intrinsic $(\langle B\rangle–\langle V\rangle)_0$ colors, with derived colors for AFGK supergiants from Johnson (1966) plotted for reference purposes as open circles. The line is a fitted relation for the supergiants. The anomalous Cepheids are V1882 Sgr and YZ CMa.

TABLE 3

UNREDDENED $BV(RI)_C$ COLORS FOR SAMPLE CEPHEIDS

Cepheid	$\log P$	Type	$\langle B\rangle–\langle V\rangle$	$V–R_C$	$V–I_C$	Deduced Type
UY Mon	0.380	DCEPS	+0.43	+0.28	+0.51	DCEPS[1]
CN CMa	0.390	CWB:	+0.51	+0.33	+0.61	DCEP
EW Aur	0.425	DCEP	+0.49	+0.29	+0.54	DCEP
V1882 Sgr	0.433	CEP	+0.53	+0.30	+0.42	CWB
BE Pup	0.458	CWB:	+0.47	+0.29	+0.52	DCEP
YZ CMa	0.499	CWB:	+0.56	+0.28	+0.46	CWB?
LR Pup	0.523	CEP	+0.51	+0.32	+0.59	DCEP
BD Pup	0.593	DCEP	+0.56	+0.36	+0.63	DCEP
IO Cas	0.748	DCEP	+0.57	+0.36	+0.63	CWB?
AY Sgr	0.818	DCEP	+0.57	+0.31	+0.58	DCEP
FO Cas	0.832	DCEP	+0.60	+0.44	+0.78	CWB?
AC Mon	0.904	DCEP	+0.63	+0.35	+0.63	DCEP
HZ Per	1.052	DCEP	+0.77	+0.40	+0.73	DCEP
VY Sgr	1.132	DCEP	+0.75	+0.43	+0.74	DCEP
OT Per	1.416	DCEP	+0.87	+0.49	+0.88	DCEP

[1]Fundamental mode pulsation likely.

With regard to the variable star designations for specific objects in Table 3, the short period Cepheids UY Mon and CN CMa are solar-metallicity stars according to Diethelm (1990), who derived reddenings of $E_{B-V} = 0.15 \pm 0.08$ and 0.61 ± 0.10, respectively, for the stars from Walraven photometry. Both values are consistent with the present results, although of lower precision. UY Mon is an s-Cepheid, its light curve being indistinguishable from a sine wave, many of which are overtone pulsators, yet fundamental mode pulsation provides the simplest solution to the variable-extinction study presented here (Figure 3), provided it is a classical Cepheid. CN CMa is a suspected Type II Cepheid because of its unusually large amplitude for a short-period pulsator, but that designation is not consistent with its photometric solar metallicity (Diethelm 1990) or the variable-extinction analysis. Type II Cepheids are known to display a wide range of abundances, from solar to below solar (Harris 1981), so that is not necessarily a good criterion to decide Population type for CN CMa. A better case for it being a classical Cepheid lies in the variable-extinction results (Figure 3). Its $(RI)_C$ and $(RI)_J$ colors are also consistent with those of a classical Cepheid (Figure 7), which is the designation preferred here.

For four of the sample objects the field star variable-extinction data produce results indicating that the Cepheid's luminosity may have been overestimated in the analysis, i.e., it might be a Type II object. The Cepheids are V1882 Sgr, BE Pup, IO Cas, and FO Cas. The latter two objects are identified as classical Cepheids in the GCVS, so either the variable-extinction results for them are anomalous or the classification of the stars is erroneous. The latter possibility is suspected here, so their deduced types as Type II Cepheids in the last column of Table 3 reflect the results of the variable-extinction analysis. V1882 Sgr has the characteristic light curve of a Cepheid, but is of uncertain type. The variable-extinction results suggest that it is a Type II object, while its $V(RI)_C$ colors (Table 3) are slightly bluer than those of classical Cepheids in the sample, which may indicate a metal-poor object. The "CEP" designation for the star in the GCVS is presumably preliminary, and it appears likely to be a Type II object. Similarly, the variable-extinction results for BE Pup are consistent with either a classical or Type II Cepheid, while its $V(RI)_C$ colors (Table 3) are similar to those of classical Cepheids in the sample. BE Pup is also a double-mode pulsator (Wils & Otero 2004), which is suggestive of a classical Cepheid, our preferred designation.

YZ CMa is suspected to be a classical Cepheid according to the variable-extinction analysis, but its $V(RI)_C$ colors are also slightly bluer than those of other classical Cepheids. The "CWB": designation in the GCVS may therefore be correct, although further study is needed to resolve the question. In general, the studies summarized here consistently tend to identify most sample objects (11/15) as classical Cepheids. Two of the likely Type II objects, V1882 Sgr and YZ CMa, appear slightly bluer in $V–R_C$ and $V–I_C$ than other Cepheids in the sample, but the photometry for both stars may suffer from contamination by close companions, so their distinctive dif-

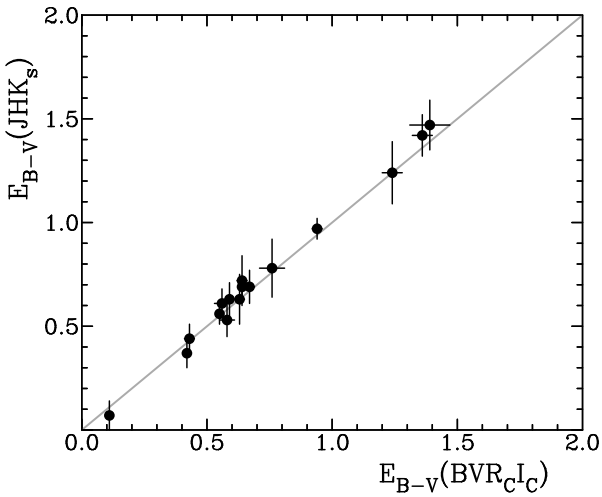

Fig. 8. Comparison of derived 2MASS reddenings, with their uncertainties, for the Cepheids in our sample with the color-corrected broad band $BV(RI)_C$ reddenings. The gray line represents expectations for an exact match.

ference in color cannot be considered definitive. Detailed atmospheric abundance studies of both stars should help to solidify their classifications and establish if there are obvious differences in color between classical and Type II Cepheids.

Figure 8 plots the inferred 2MASS reddenings for our sample Cepheids relative to their broad band $BV(RI)_C$ reddenings, where we have included the second result for the UY Mon field because of the obvious separation in Figures 3 and 5 of stars of small reddening from those of large reddening, for which separate solutions were obtained. The close agreement of both sets of reddenings in Figure 8 indicates that the two techniques are of comparable reliability for establishing field reddenings of Galactic objects, although there is clearly greater precision in the $BV(RI)_C$ color excesses.

5. DISCUSSION

The present study was undertaken as a feasibility test of the use of CCD $BV(RI)_C$ photometry for studying the space reddening of Galactic Cepheids. The $BV(RI)_C$ data by themselves were sometimes insufficient to define the field reddenings of each Cepheid unambiguously, but the addition of 2MASS reddenings and initial "predictions" guided the process successfully. The number of Galactic Cepheids of well-established field reddening has been increased from 40 (Laney & Caldwell 2007) to 55 by this study, and the sample now includes a few Type II Cepheids, some of which appear to display slightly bluer intrinsic $(V–R)_C$ and $(V–I)_C$ colors relative to their classical Cepheid cousins. A comparable test using reddenings derived from 2MASS JHK_s colors indicates that the 2MASS survey may also be suitable for the derivation of space reddenings, for a variety of stellar types and not just Cepheids. Further studies of that possibility have already been initiated (Majaess et al. 2008a,b).

The results of this study have already been used in a preliminary mapping of the Cepheid instability strip using Cepheid reddenings tied to space reddenings and spectroscopic reddenings of Galactic Cepheids (Turner 2001), the results of which can be seen in the data plotted in Figure 6. The addition of U-band observations would have assisted the analysis considerably, but it is important to note that accurate Johnson system U-band observations are difficult to obtain with some CCD/filter combinations (see comments by Turner 2011). Despite that, the success of the present study using both $BV(RI)_C$ and JHK_s photometry should spur further investigations that take advantage of existing survey photometry to study the reddening in interesting Galactic star fields.

The present study was supported in part by research funding awarded through the Natural Sciences and Engineering Research Council of Canada (NSERC), through the Russian Foundation for Basic Research (RFBR), and through the program of Support for Leading Scientific Schools of Russia. This publication makes use of data products from the Two Micron All Sky Survey, which is a joint project of the University of Massachusetts and the Infrared Processing and Analysis Center/California Institute of Technology, funded by the National Aeronautics and Space Administration and the National Science Foundation.

REFERENCES

Benedict, G. F., et al. 2007, AJ, 133, 1810
Berdnikov, L. N. 2007, `http://www.sai.msu.su/groups/cluster/CEP/PHE/`
Caldwell, J. A. R., Cousins, A. W. J., Ahlers, C. C., van Wamelen, P., & Maritz, E. J. 1993, South African Astron. Obs. Circ., 15, 1
Cutri, R. M., et al. 2003, The IRSA 2MASS All-Sky Point Source Catalog of Point Sources, NASA/IPAC Infrared Science Archive
Dean, J. F., Warren, P. R., & Cousins, A. W. J. 1978, MNRAS, 183, 569
Diethelm, R. 1990, A&A, 239, 186
Eggen, O. J. 1951, ApJ, 113, 367
Feltz, K. A., Jr. 1972, PASP, 84, 497

Fernie, J. D. 1963, AJ, 68, 780
_____. 1983, PASP, 95, 782
_____. 1990a, ApJS, 70, 153
_____. 1990b, ApJ, 354, 295
Harris, H. C. 1981, AJ, 86, 719
Henden, A. A., & Munari, U. 2000, A&AS, 143, 343
Johnson, H. L. 1966, ARA&A, 4, 193
_____. 1968, in Nebulae and Interstellar Matter, ed. B. L. Middlehurst & L. H. Aller (Chicago: Univ. Chicago Press), 167
Kovtyukh, V. V., Soubiran, C., Luck, R. E., Turner, D. G., Belik, S. I., Andrievsky, S. M., & Chekhonadskikh, F. A. 2008, MNRAS, 389, 1336
Kraft, R. P. 1960, ApJ, 131, 330
Krockenberger, M., et al. 1998, in ASP Conf. Ser. 154, Cool Stars, Stellar Systems, and the Sun, ed. R. A. Donahue & J. A. Bookbinder (San Francisco: ASP), 791
Laney, C. D., & Caldwell, J. A. R. 2007, MNRAS, 377, 147
Majaess D. J., Turner D. G., & Lane D. J. 2008a, MNRAS, 390, 1539
Majaess D. J., Turner D. G., Lane D. J., & Moncrieff, K. A. 2008b, J. Am. Ass. Variable Star Obs., 36, 90
Mathis, J. S. 1990, ARA&A, 28, 37
McCuskey, S. W. 1965, in Galactic Structure, ed. A. Blaauw & M. Schmidt (Chicago: Univ. Chicago Press), 1
McNamara, D. H., Helm, T. M., & Wilcken, S. K. 1970, PASP, 82, 293
McNamara, D. H., & Potter, D. 1969, PASP, 81, 545
Samus, N. N., et al. 2004, Combined Catalog of Variable Stars (Moscow: Inst. of Astronomy of Russian Academy of Sciences)
Sasselov, D. D., & Lester, J. B. 1990, ApJ, 360, 227
Skrutskie, M. F., et al. 2006, AJ, 131, 1163
Spencer Jones, J. H. 1989, MNRAS, 238, 269
Stetson, P. B. 1987, PASP, 99, 191
Turner, D. G. 1976a, AJ, 81, 97
_____. 1976b, AJ, 81, 1125
_____. 1979, PASP, 91, 642
_____. 1984, JRASC, 78, 229
_____. 1989, AJ, 98, 2300
_____. 1992, AJ, 104, 1865
_____. 1994, RevMexAA, 29, 163
_____. 1995, in ASP Conf. Ser. 83, Astrophysical Applications of Stellar Pulsation, ed. Stobie, R. S. & Whitelock, P.-A. (San Francisco: ASP), 256
_____. 2001, Odessa Astron. Publ., 14, 166
_____. 2010, Ap&SS, 326, 219
_____. 2011, RevMexAA, 47, 127
Turner, D. G., Abdel-Sabour Abdel-Latif, M., & Berdnikov, L. N. 2006, PASP, 118, 410
Turner, D. G., et al. 2008, MNRAS, 388, 444
Wampler, E. J. 1961, ApJ, 134, 861
_____. 1962, ApJ, 136, 100
Wils, P., & Otero, S. A. 2004, Inf. Bull. Variable Stars, 5501, 1

D. G. Turner: Department of Astronomy and Physics, Saint Mary's University, Halifax, Nova Scotia, B3H 3C3, Canada (turner@ap.smu.ca).
R. F. MacLellan, Department of Physics and Engineering Physics, Queen's University, Kingston, ON K7L 3N6 Canada (rmaclellan@bama.ua.edu).
A. A. Henden, American Association of Variable Star Observers, 49 Bay State Road, Cambridge, MA 02138, U.S.A. (arne@aavso.org)
L. N. Berdnikov, Sternberg Astronomical Institute, 13 Universitetskij prosp., Moscow 119992, Russia (leonid.berdnikov@gmail.com).

Revista Mexicana de Astronomía y Astrofísica, **47**, 357–360 (2011)

MISSING SEYFERT GALAXIES

Hrant M. Tovmassian[1] and O. Yam[2]

Received 2011 May 11; accepted 2011 July 1

RESUMEN

El objetivo de este trabajo es la estimación del número de galaxias Seyfert *faltantes* debido a la ocultación por el polvo del disco de las galaxias espirales. Comparamos la distribución de las inclinaciones de las galaxias anfitrionas de las Sy1s y Sy2s con la de la muestra de control de las galaxias espirales. Encontramos que el número relativo de galaxias Seyfert es mayor para las Seyfert vistas de frente, en las galaxias con $i < 30°$, y es menor en las galaxias muy inclinadas con $i > 61°$ que en las galaxias espirales sin núcleos activos. Concluimos que la diferencia observada se debe a la absorción de los núcleos Seyfert en el disco de polvo de las galaxias inclinadas. Estimamos que las Seyfert faltantes son alrededor del 100% para las Sy1y y del 50% para las Sy2s.

ABSTRACT

The aim of this work is to estimate the number of Seyfert nuclei missing in catalogs due to obscuration by the dust disc in host spiral galaxies. We compared the distribution of inclinations of host galaxies of Sy1s and Sy2s with that of in control sample of spiral galaxies, and found that the relative number of Seyferts is higher in almost face-on galaxies with $i < 30°$ and smaller in highly inclined, $i > 61°$, spiral galaxies without active nuclei. We conclude that the difference found is due to absorption of the Seyfert nuclei by the dust-disc of inclined galaxies. We estimate that about 100% and 50% of the observed Sy1s and Sy2s respectively are missing.

Key Words: galaxies: Seyfert

1. INTRODUCTION

According to the Unified scheme (Miller & Goodrich 1990; Antonucci 1993; Urry & Padovani 1995), the difference between Sy1 and Sy2 galaxies is caused by the orientation of the inner dust torus in relation to the observer. If the opening angle of the torus is pointing towards the observer, and the active galactic nuclei (AGN) with the broad line region (BLR) is directly seen, the galaxy is classified as Sy1. If the orientation of the torus is such that the BLR is hidden, and only the narrow line region is observable the galaxy is classified as Sy2. The ratio of the numbers of Sy1 and Sy2 galaxies determines the opening angle of the putative dust torus. In order to understand the nature of Seyferts it is also important to know the frequency of their occurrence among galaxies.

Numerous efforts have been made in compiling new a large list of Seyfert galaxies (e.g., Huchra 1977; Véron-Cetty & Veron 2010, and references therein). Some Seyfert nuclei, however, may not be revealed because they are hidden behind the galactic dust-disc. Indeed, Keel (1980), Kirhakos & Steiner (1990), McLeod & Rieke (1995) found, that Seyfert nuclei avoid edge-on galaxies. Malkan, Gorjian, & Tam (1998) also found dust lanes and patches in the central regions of Seyferts. Driver et al. (2008) showed that the role of absorption of starlight by dust grains in galactic discs is substantial. Therefore, the emission of the AGN may be completely hidden by the dust-disc in some highly inclined spiral galaxies, and a certain number of Seyferts may be missing. The real ratio of the numbers of Sy2 and Sy1 galaxies may be altered, and consequently the value of the opening angle of the dust-torus in the Unified scheme may be in error.

It has been suggested that the activity of the galactic nucleus may be triggered by dense envi-

[1]Instituto Nacional de Astrofísica Óptica y Electrónica, Puebla, Mexico.

[2]Depto. de Ciencias, Universidad de Quintana Roo, Mexico.

TABLE 1

THE NUMBER OF SPIRAL GALAXIES GALAXIES IN THREE BINS OF INCLINATION i

	$i \leq 30°$	$31° < i < 60°$	$i > 61°$	$i \leq 30°$	$31° < i < 60°$	$i > 61°$
Type	V-CV			SSRS2		
n	56	231	157	163	703	557
$n/n_{\rm total}$	0.13	0.52	0.35	0.12	0.49	0.39

ronments. However, contradictory results have also been obtained. Petrosian (1982), Dahari (1985), Laurikainen & Salo (1995), Dultzin-Hacyan et al. (1999), Storchi-Bergmann et al. (2001), Chatzichristou (2002), Sánchez & Gonzaléz-Serrano (2003), Kouluoridis et al. (2006) showed that Seyferts are found in more dense environments. Meanwhile, Viriani, De Robertis, & van Dalfsen (2000), Schmitt (2001, and references therein) did not find a relation between nuclear activity and environment. The discrepancy may be explained by the inclusion of galaxies with hidden Seyfert nuclei in the control samples.

The first attempt to estimate the number of missing Seyferts was made by Tovmassian (2001). In this paper we reconsider the problem, and estimate the number of missing Seyferts by the study of the distribution of inclinations of spiral galaxies in which Seyfert nuclei mainly reside. We take into account that, as Kinney et al. (2000) showed, the distribution of the angle β between the direction of the radio jet (or the dust torus axis) and the galaxy rotation axis is homogenous in the $0° - 90°$ range. This means that Seyferts should be observed in host galaxies with any inclination angle, if there are no biases in the catalogs. Kirhakos & Steiner (1990) suggested detecting the missing edge-on Seyferts on the basis of the IR and X-ray emission of galaxies. The presence of the broad line region (BLR) emission in some galaxies was detected by observation of the polarized emission scattered by particles located far from the nucleus of a galaxy. Such galaxies are called hidden Sy1s (Sy1h).

2. RESULTS AND DISCUSSION

2.1. *The data*

For our study we used the Sy1 and Sy2 galaxies from the 13-th Edition of the Catalogue of Quasars and Active Nuclei (Véron-Cetty & Véron 2010, hereafter VC-V) with magnitudes $V < 16^m$) and $z < 0.035$. Seyferts hosted in spiral galaxies of morphological types S0/a and later were included in the study. Morphological types of host galaxies of Seyferts were taken from the NED (The NASA/IPAC Extragalactic Database). In accordance with Meurs & Wilson (1984), Osterbrock & Shaw (1988), we joined galaxies with Sy1.2 and Sy1.5 types into the Sy1 category, and Sy1.8s and Sy1.9s into the Sy2 category. The sample of Sy1s includes galaxies of Sy1n type, and the sample of Sy2s includes galaxies classified as Sy1h (hidden Sy1). By cross-checking with the data in the NED we excluded from the studied sample those galaxies whose classification in the NED differed from those in the VC-V catalog. The compiled sample contains 79 Sy1s and 188 Sy2s.

For comparison we compiled two lists of spiral galaxies using the Revised Shapley-Ames catalog of bright galaxies (Sandage & Tammann 1981) and the Southern Sky Redshift Survey (SSRS2) (da Costa et al. 1998). From the latter catalog we used galaxies with radial velocities $V_r < 9000$ km s^{-1} and magnitudes $V < 15.5^m$. From both catalogs we selected spiral galaxies of morphological types from S0/a to Scd. The morphological types were taken from the NED. Galaxies with active galactic nuclei, such as Seyferts, LINERs or those having powerful radio emission were excluded. We did not include in the sample galaxies with any peculiar morphology or members of dense doubles.The compiled list from the Revised Shapley-Ames catalog contains 444 galaxies with measured a and b axes given in the NED. The corresponding list from the SSRS2 catalog consists of 1423 galaxies.

2.2. *Analysis and Results*

We calculated the inclinations i of the galaxies using their observed axial ratio b/a, and binned them in three intervals of inclination $i \leq 30°$, $31° < i < 60°$ and $i > 61°$. In Table 1 we present the numbers of spiral galaxies of the compiled lists from the Revised Shapley-Ames (1st row) and the SSRS2 (3rd row) catalogs in these intervals of inclination. The relative numbers for both catalogs in corresponding bins are given in Rows 2 and 4 of Table 1. Table 1

TABLE 2

THE NUMBERS AND RELATIVE NUMBERS OF SY1S AND SY2S GALAXIES IN THREE BINS OF INCLINATION i

Type	VC-V					
i	$N(< 30°)$	$N(31° - 60°)$	$N(> 61°)$	$N(< 30°)/N_t$	$N(31° - 60°)/N_t$	$N(> 61°)/N_t$
Sy1	20	49	10	0.25	0.62	0.13
Sy2	35	103	50	0.19	0.55	0.26

shows that the distribution of inclinations is not uniform which is evidence of the rather prolate space configuration of spiral galaxies (Vincent & Ryden 2005).

In the absence of biases one would expect the distribution of inclinations of the Seyferts to be the same as that of the normal galaxies, and they should also have about the same relative numbers in the three intervals of inclinations considered. However, we found that the distribution of inclinations of Seyfert galaxies differs from that of spiral galaxies not containing active nuclei (Table 2). A comparison of Table 1 and Table 2 shows that the relative number of both types of Seyferts in almost face-on galaxies ($i \leq 30°$) is higher than in the whole sample of spiral galaxies. The relative number of Seyferts in the second bin is about the same, as for spiral galaxies. At the same time, the relative number of galaxies in the third bin of highly inclined Seyfert host galaxies ($i \geq 61°$) is smaller than that of spirals.

2.3. *The number of missing Seyfert galaxies*

We suggest that the higher abundance of Seyferts seen in almost face-on host spiral galaxies and their paucity in galaxies with very high inclination (third bin) is due to absorption of the emission of the Seyfert nuclei by the dust disc of their host galaxies. In order to estimate the number of missing Seyferts we assume that the relative number of their host galaxies with $i \leq 30°$ ($b/a < 0.86$) must be equal to the corresponding value of spiral galaxies, i.e. about 0.125. Dividing the numbers of Sy1s and Sy2s with inclinations $i \leq 30°$ to the deduced relative number $n_i \leq 30°$ of spiral galaxies with inclinations in the same bin, we estimate the expected total number n_t of Sy1s and Sy2s correspondingly. Subtracting from the estimated total number n_t of Seyferts the corresponding observed number n_o, we find the number n_m of the missing Seyferts. The results of our accounting are presented in Table 3. In the sixth column the relative number n_m/n_t is given.

TABLE 3

NUMBER OF SY1S AND SY2S WITH INCLINATIONS OF THE HOST SPIRAL GALAXIES $i \leq 30°$, THEIR ESTIMATED TOTAL NUMBER, NUMBER OF MISSING ONES AND RELATIVE NUMBER OF MISSING SEYFERTS

	$n_{i \leq 30°}$	n_t	n_o	n_m	n_m/n_o
Sy1	20	160	79	81	1.02
Sy2	35	280	188	92	0.49

Table 3 shows that the number of missing Sy1s is about the same as the number of the known ones. The number of the missing Sy2s is about half of the known ones.

3. CONCLUSIONS

We compared the distribution of inclinations of the host galaxies of Sy1 and Sy2 galaxies from the VC-V catalog with that of the control sample of spiral galaxies not containing AGN from the Revised Shapley-Ames and the SSRS2 catalogs, and estimated the number of Seyferts in which the AGN is hidden by the absorbing dust in the disc of inclined galaxies. We find that about 100% of Sy1s and 50% of Sy2s are missing. The relatively smaller number of missing Sy2s might be expected, since the NLR of some of them are observed at large distances from the galactic plane, where absorption of the dust disc is smaller. The number of missing Seyferts is large and may influence the conclusions on the nature of these galaxies and on the mechanisms of their formation. The relative number of Seyferts among galaxies is thus higher than previously estimated. Taking into account the missing Seyferts increases the opening angle of the dust torus from 90° to 100°. When considering the influence of the environment in activating the Seyfert nuclei, it is necessary to be careful in compiling a control sample: the inclusion of large numbers of highly inclined galaxies in the

latter, strongly affected by the disc absorption, may result in erroneous conclusions.

We are grateful to the referee for a careful reading of the paper and valuable suggestions for its improvement. HMT thanks the IPAC (Pasadena, CA, USA) for hospitality. This research has made use of the NASA/IPAC Extragalactic Database (NED) which is operated by the Jet Propulsion Laboratory, California Institute of Technology, under contract with the National Aeronautics and Space Administration.

REFERENCES

Antonucci, R. 1993, ARA&A, 31, 473
Chatzichristou, E. 2002, ApJ, 581, 161
da Costa, L. N., et al. 1998, AJ, 116, 1
Dahari, O. 1985, ApJS, 57, 643
Driver, S. P., Popescu, C. C., Tuffs, R. J., Graham, A. W., Liske, J., & Baldry I. 2008, ApJ, 678, L101
Dultzin-Hacyan, D., Krongold, Y., Fuentes-Guridi, I., & Marziani, P. 1999, ApJ, 513, 111
Huchra, J. P. 1977, ApJS, 35, 171
Keel, W. C. 1980, AJ, 85, 198
Kinney, A. L., Schmitt, R. H., Clarke, C. J., Pringle, J. S., Ulvistad, J. S., & Antonucchi, R. R. J. 2000, ApJ, 537, 152
Kirhakos, S. D., & Stainer, J. E. 1990, AJ, 99, 1435
Koulouridis, E., Plionis, M., Chavushyan, V., Dultzin-Hacyan, D., Krongold, Y., & Goudis, C. 2006, ApJ, 639, 37
Laurikainen, E., & Salo, H. 1995, A&A, 293, 683
Malkan, M., Gorjian, V., & Tam, R. 1998, ApJS, 117, 25
McLeod, K. K., & Rieke, G. H. 1995, ApJ, 441, 96
Meurs, E. J. A., & Wilson, A. S. 1984, A&A, 136, 206
Miller, J. S., & Goodrich, R. W. 1990, ApJ, 355, 456
Osterbrock, D. E., & Shaw, R. A. 1988, ApJ, 327, 89
Petrosian, A. R. 1982, Astrofizika, 18, 548
Sánchez, S. F., & González-Serrano, J. I. 2003, A&A, 406, 435
Sandage, A., & Tammann, G. A. 1981, Revised Shapley-Ames Catalog of Bright Galaxies (Washington: Carnegie Inst. of Washington)
Schmitt, H. R. 2001, Bull. Am. Astron. Soc., 33, 834
Storchi-Bergman, T., González-Delgado, R. M., Schmitt, H. R., Cid-Fernandes, R., & Heckman, T. 2001, ApJ, 559, 147
Tovmassian, H. M. 2001, Astron. Nachr., 322, 87
Urry, C. M., & Padovani, P. 1995, PASP, 107, 803
Véron-Cetty, M.-P., & Véron, P. 2010, A&A, 518, 10 (VC-V)
Vincent, R. A., & Ryden, B. S. 2005, ApJ, 623, 137
Virani, S. N., De Robertis, M. M., & van Dalfsen, M. L. 2000, AJ, 120, 1739

Hrant M. Tovmassian: Instituto Nacional de Astrofísica Óptica y Electrónica, Apdo. Postal 51 y 216, C.P. 72000, Puebla, Puebla, Mexico (hrant@inaoep.mx).
O.Yam: Depto. de Ciencias, Universidad de Quintana Roo, Blvd. Bahía, 77019 Chetumal, Q. Roo, Mexico (oyam@uqroo.mx).

Revista Mexicana de Astronomía y Astrofísica, **47**, 361–383 (2011)

THE NATURE AND ORIGIN OF NARROW LINE AGN ACTIVITY IN A SAMPLE OF ISOLATED SDSS GALAXIES

R. Coziol,[1] J. P. Torres-Papaqui,[1] I. Plauchu-Frayn,[2] J. M. Islas-Islas,[1]
R. A. Ortega-Minakata,[1] D. M. Neri-Larios,[1] and H. Andernach[1]

Received 2011 May 26; accepted 2011 August 1

RESUMEN

Discutimos la naturaleza y origen de la actividad nuclear observada en una muestra de 292 galaxias con líneas de emisión angostas del SDSS, cuya formación y evolución se considera que ha ocurrido en aislamiento. La fracción de galaxias con un núcleo activo (AGNs) o de objetos de transición (TOs; un AGN con formación estelar circunnuclear) alcanza 64% de la muestra. Verificamos que la probabilidad de que una galaxia muestre un núcleo activo aumenta con la masa de su bulbo (Torres-Papaqui et al. 2011). También encontramos evidencia de que dicha tendencia es realmente un subproducto de la morfología, y sugiere que el fenómeno AGN está íntimamente ligado al proceso de formación de galaxias. Los AGNs con líneas de emisión angostas en nuestra muestra son consistentes con una versión a menor escala o menor energía de cuásares y AGNs con líneas de emisión anchas.

ABSTRACT

We discuss the nature and origin of the nuclear activity observed in a sample of 292 SDSS narrow-emission-line galaxies, considered to have formed and evolved in isolation. The fraction of Narrow Line AGNs (NLAGNs) and Transition type Objects (TOs; a NLAGN with circumnuclear star formation) amounts to 64% of the galaxies. We verify that the probability for a galaxy to show an AGN characteristic increases with the bulge mass of the galaxy (Torres-Papaqui et al. 2011), and find evidence that this trend is really a by-product of the morphology, suggesting that the AGN phenomenon is intimately connected with the formation process of the galaxies. The NLAGNs in our sample are consistent with a scaled-down or powered-down versions of quasars and Broad Line AGNs.

Key Words: galaxies: active — galaxies: formation

1. INTRODUCTION

Spectroscopic surveys, like the Sloan Digital Sky Survey (SDSS) (York et al. 2000; Stoughton et al. 2002), have revealed that a large fraction of galaxies in the nearby universe show emission lines consistent with some kind of nuclear activity. Using diagnostic diagrams that compare various emission line ratios, different classification criteria were proposed to classify these galaxies based on the possible sources of excitation of the gas (Baldwin, Phillips, & Terlevich 1981; Veilleux & Osterbrock 1987; Kewley et al. 2001; Kauffmann et al. 2003). These classification criteria imply that there are two possible main sources: thermal sources, which are associated with star forming activity, and non-thermal sources, which are produced by the accretion of matter onto a Super-Massive Black Hole (SMBH) in the nucleus of the galaxies–the so called Active Galactic Nuclei (AGNs).

The majority of the emission line galaxies in the SDSS turn out to be star forming galaxies (SFGs). However, recent studies (e.g., Miller et al. 2003; Martínez et al. 2010; Torres-Papaqui et al. 2011) inferred that the actual number of galaxies with a non-thermal ionization source in their nucleus could be much higher than previously believed, but the evidence was somewhat obscured by the large variation of characteristics presented by AGNs. For ex-

[1]Departamento de Astronomía, Universidad de Guanajuato, Guanajuato, Mexico.
[2]Instituto de Astrofísica de Andalucía (CSIC), Granada, Spain.

ample, in the Seyfert 1, where we can distinguish broad emission line components akin to what is observed in quasars (Osterbrock 1989; Weedman 1986; Krolik 1999), the presence of a SMBH seems indubitable. However, a significantly larger fraction of AGNs show only narrow emission lines. Also, many researchers have alluded to different characteristics for these Narrow Line AGNs (NLAGNs) by separating them into two main groups, the high ionization galaxies, generally called Seyfert 2 (Sy2), and the low ionization ones, called LINERs, which stands for Low Ionization Nuclear Emission-line Regions (Heckman 1980; Coziol 1996; Kewley et al. 2006). As a consequence, the source of ionization of NLAGNs, although clearly distinct from SFGs, is still an actively debated subject, and there is presently no consensus about their nature or evolutionary status.

It is usually admitted that both Sy2 and LINERs are phenomena that occur in early-type (Sa and Sb) spiral galaxies in the field, that is, galaxies forming in relatively low galactic density environments (Heckman 1980). On the other hand, there is growing evidence that NLAGNs in clusters and compact groups of galaxies differ from those in the field by their earlier morphological types and intrinsic low luminosities (Phillips 1986; Coziol et al. 1998a; Miller et al. 2003; Wake et al. 2004; Martínez et al. 2008, 2010; Torres-Papaqui et al. 2011). These differences seem to point to distinct formation mechanisms for galaxies in different environments, which could have also affected the formation and evolution of their black holes. For example, the Low Luminosity AGNs (LLAGNs) found in compact groups and clusters of galaxies appear to prefer massive bulge spiral galaxies or elliptical galaxies–galaxies which are poor in gas–and it is this actual scarcity of matter that can be accreted that is assumed to explain the low luminosity of these objects (Martínez et al. 2008; Torres-Papaqui et al. 2011). This explanation is fully consistent with the starving quasar model (Richstone et al. 1998; Gavignaud et al. 2008; Martínez et al. 2008, 2010), according to which a SMBH that had accreted at high rates in the past, producing a quasar-like activity, evolved as its reservoir of gas was depleted into a slowly accreting SMBH producing a LLAGN.

In order to test the idea of a variation of the AGN phenomenon in different environments we considered important to study galaxies for which the influence of their environment was minimal. These are galaxies that are relatively isolated–that is, they formed in low galactic density environments and evolved without major interactions with other galaxies.

2. DESCRIPTION OF THE SAMPLE AND DATA USED FOR ANALYSIS

Our sample of isolated galaxies was selected from the 2 Micron Isolated Galaxies catalogue (hereafter 2MIG), as compiled by Karachentseva et al. (2010). The 2MIG catalogue contains 3227 galaxies, covering the entire sky. All the galaxies have a near-infrared magnitude brighter than $K_s = 12$, and a projected image that extends across an angular diameter $a_K \geq 30''$. The isolation criterion used in this catalogue is the following: a galaxy is considered isolated when its nearest neighbor has a size within a factor 4 of the major-axis diameter of the target galaxy, and lies more than 20 diameters away from it. This criterion assures that a galaxy with a typical diameter of 20 kpc and peculiar velocity of the order of 150 km s^{-1} was not influenced by a similar type of galaxy during the last ∼3 Gyr (Turner et al. 1979).

To produce our sample, we have cross-correlated the positions of the galaxies in the 2MIG catalogue with spectroscopic targets in the Sloan Digital Sky Survey Data Release 7 (SDSS DR7) database (Abazajian et al. 2009). This resulted in 445 galaxies, which represents 88% of the galaxies in the 2MIG catalogue covered by the SDSS DR7. The remaining 12% are galaxies for which spectroscopic data were not obtained by SDSS, because they were too nearby or too bright.

Color images of the galaxies were obtained using the tool CHART of SDSS[3]. After visual inspection, we eliminated 28 galaxies with morphological peculiarities or possible faint companions, in apparent contradiction with the isolation assumption.

A preliminary examination of the spectra reveals that all these galaxies except one show emission lines. The only non-emission "isolated" galaxy is identified as SDSS J072635.39+431746.8. This is a nearby galaxy, $z = 0.0105$, with a possible E or S0 morphology. Being the only galaxy of its kind it was excluded from our study.

Also excluded from our analysis were two extremely blue S0-like galaxies, with spectra typical of late-type spirals–showing a recent and extremely intense level of star formation. A careful examination of their images suggested that they are low mass irregular or morphologically peculiar galaxies. Their positions in the standard diagnostic diagram reveal that they are HII galaxies–small mass and low gas metallicity starburst galaxies (see Coziol 1996).

Only five galaxies in our sample were found to have broad emission line components. The spectra

[3] http://cas.sdss.org/dr7/en/tools/chart/chart.asp.

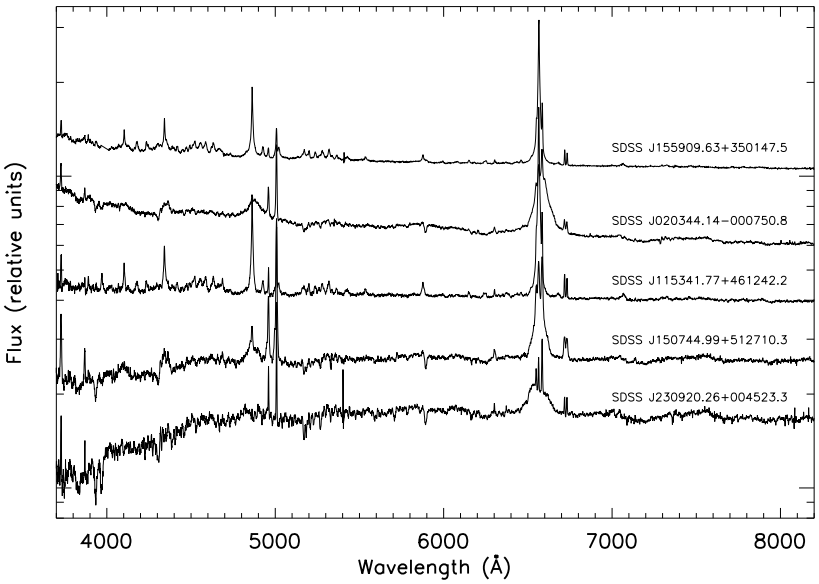

Fig. 1. Spectra of the broad line AGNs of our original sample of 2MIG galaxies. The flux scale is relative and was slightly displaced for clarity.

of these galaxies are presented in Figure 1. These galaxies were also discarded from our analysis.

We classified the 409 remaining galaxies as isolated Narrow Emission Lines Galaxies (NELGs). The spectra of these galaxies were subsequently corrected for Galactic extinction (Schlegel, Finkbeiner, & Davis 1998), shifted to their rest frame, resampled to $\Delta\lambda$=1 Å between 3400 and 8900 Å, and processed using the spectral synthesis code STARLIGHT (Cid Fernandes et al. 2005), which produces a stellar population template that fits the continuum of each galaxy. We ran STARLIGHT using a combination of $N_\star$ Simple Stellar Populations (SSPs) from the evolutionary synthesis models of Bruzual & Charlot (2003). The models were computed with the MILES library (Vazdekis et al. 2010), following Padova's evolutionary tracks with the initial mass function of Chabrier (2003). An SSP consists of $N_\star = 150$ elements, spanning six metallicities, $Z = 0.005$, 0.02, 0.2, 0.4, 1 and 2.5 $Z_\odot$, and 25 stellar population ages in the range from 1 Myr to 18 Gyr.

In the template-subtracted spectra, we measured automatically different important attributes of the spectral emission lines, like their flux and full width at half maximum (FWHM). Other important features retrieved from the stellar population templates fitted by STARLIGHT are the stellar velocity dispersions and the star formation history (SFH) of the host galaxies. The SFH map shows how the smoothed star formation rate (SFR) in a galaxy varies over a time period covering $\log(t) = 5.7$ yr to $\log(t) = 10.6$ yr (Asari et al. 2007).

2.1. *Morphologies and star formation history*

To determine the morphologies of the galaxies we used a composite method combining an eye estimate with the SFH. First, two of us (IP-F and RC) determined by eye the morphologies of the 409 isolated NELGs following the standard Hubble classification. Then, using only the galaxies with concordant morphologies–meaning the two observers gave exactly the same morphology–an average SFH prototype for each morphology class was created. Using these prototypes, the residuals of the SFH for each galaxy were calculated separately in three distinct time periods: Recent, $5.7 \leq \log(t/\mathrm{yr}) \leq 7.9$, Intermediate, $7.9 < \log(t/\mathrm{yr}) \leq 9.0$, and Old, $9.0 < \log(t/\mathrm{yr}) \leq 10.6$. A correction was then made to the eye morphology classification by choosing a morphology that minimized the variance of the residuals in each time period. For example, by eye we could have given the type S0 or Sa to a galaxy, but the residuals being minimal for Sa we adopted this last classification.

Once the morphologies were correctly adjusted to the SFH, we recalculated the prototypes by calculating the mean SFH in each morphological bin. Since we found the Sb and Sbc types to have SFH prototypes that are extremely similar and almost impossible to distinguish, we merged these two morphological bins together, keeping only the Sb identifi-

TABLE 1

EXAMPLES OF SPECTROSCOPIC CHARACTERISTICS OF THE ISOLATED NELGS[†]

Identification in SDSS	$\log\left(\frac{\mathrm{O[III]}}{\mathrm{H}\beta}\right)$	$\log\left(\frac{\mathrm{N[II]}}{\mathrm{H}\alpha}\right)$	Activity Type	$L_{\mathrm{H}\alpha}$ $L_\odot$	$\sigma_\star$ km s^{-1}	$\log(\lambda\ L_{5100})$ erg s^{-1}
SDSS J105809.84−004628.8	−0.364	−0.351	SFG	6.19	87	42.13
SDSS J113903.33−001221.6	0.228	0.060	AGN	6.05	144	42.56
SDSS J135807.05−002332.9	−0.604	−0.521	SFG	7.03	86	42.76
SDSS J142223.76−002315.5	−0.437	−0.494	SFG	5.50	81	41.16
SDSS J150654.85+001110.8	0.253	0.055	AGN	6.67	202	43.11
SDSS J113423.32−023145.5	0.363	0.238	AGN	6.23	136	43.00
SDSS J115425.04−021910.3	−0.275	−0.453	SFG	5.36	78	41.29
SDSS J122353.98−032634.4	−0.218	−0.148	TO	5.39	113	41.64
SDSS J124428.12−030018.8	−0.193	−0.300	TO	6.28	115	42.69
SDSS J170128.21+634128.0	−0.671	−0.375	SFG	7.20	99	42.52

[†]Full table available in electronic form at `http://www.astroscu.unam.mx/rmaa/RMxAA..47-2/RMxAA..47-2_rcoziol-tables.zip/`.

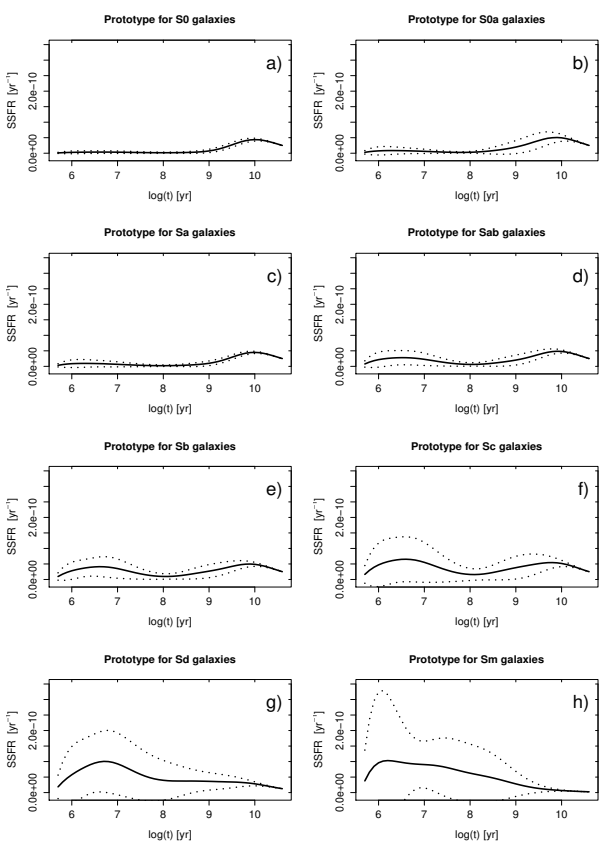

Fig. 2. SFH for the isolated NELGs. In each graph we show the mean prototype (solid line) and its dispersion at two sigma (dotted line). In order to use the same scale for all morphological classes, we have applied a factor of 0.5 and 0.1 to the SFH curves of the Sd and Sm, respectively.

cation. The final prototypes, including 327 (80%) of the 409 isolated NELGs, are presented in Figure 2. The prototypes suggest that S0, S0a, and Sa galaxies formed most of their stars in the past, $\log(t) > 9.0$ yr, while the Sab had a near constant star formation activity over the whole time lapse covered by STARLIGHT. This is also true for the Sb galaxies, but with a slightly larger dispersion. In the Sc galaxies, recent star formation activity becomes more important than in the past, but the dispersion also increases significantly the later the type. In Sd and Sm galaxies most of the stars appear to have formed recently, $\log(t) < 8.0$ yr. These results are in good agreement with similar studies based on integrated spectroscopy (e.g., Kennicutt 1992).

The remaining 20% galaxies were considered peculiar. Among these galaxies we count 36 late-type spirals (Sc or Sd) with a SFH typical of an Sa. These galaxies turned out to be cases where the fiber was covering only the innermost part of the galaxies. Also considered peculiar were 22 galaxies with a burst of star formation ∼100 Myr in the past. No external cause for the bursts could be determined, the galaxies being confirmed as isolated. Another 24 E or S0 galaxies were found to show a trace (not intense) of very recent star formation. All these peculiar galaxies were excluded from our analysis.

2.2. *Activity classification*

For our spectral activity analysis we further reduced our sample to 292 NELGs with a S/N ≥ 3 in the four most important emission lines: Hβ, [OIII]λ5007, Hα and [NII]λ6584. In Table 1 we com-

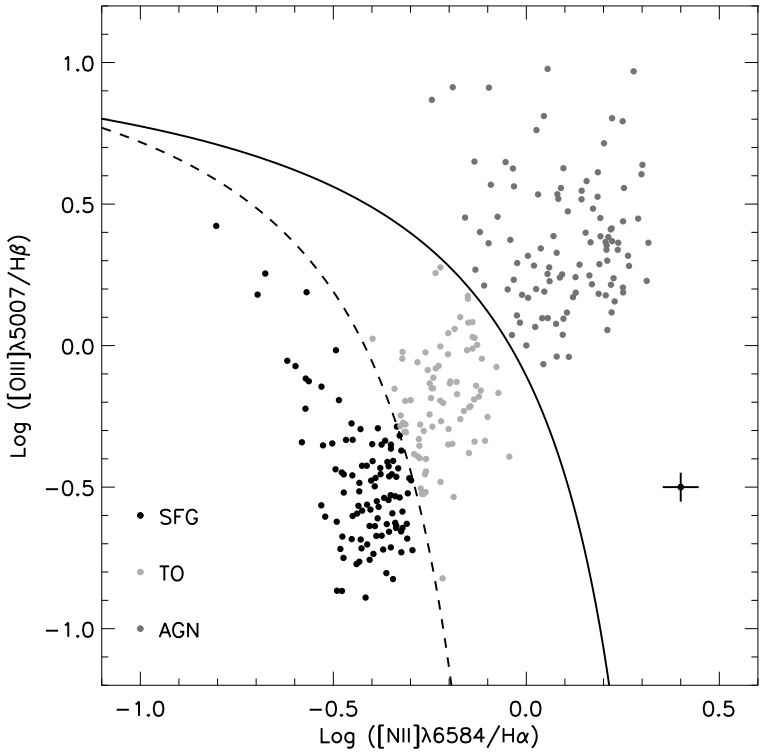

Fig. 3. Diagnostic diagram for the activity classification of the isolated NELGs. The separation between SFGs and TOs was suggested by Kauffmann et al. (2003) and the separation between TOs and AGNs by Kewley et al. (2006). Mean uncertainties on the line ratios are indicated as a cross on the lower right of diagram (not a datum). The color figure can be viewed online.

pile the spectroscopic characteristics of these galaxies as measured in the template subtracted spectra. Column 1 gives the SDSS identification of the galaxies. In Columns 2 and 3 we list the values of the two line ratios used to determine the activity type of the galaxies. The adopted classification is given in Column 4. In Column 5 we list the Hα emission line luminosity. In Column 6 we give the velocity dispersion of the stars, $\sigma_\star$, as deduced from the STARLIGHT template and corrected for the SDSS spectral resolution. Considering the size of the fiber used in SDSS ($3''$), this value can be taken as the stellar velocity dispersion of the bulge of the galaxy. Finally, in Column 7, we give the luminosity of the continuum at λ5100 Å as measured in the spectra before template subtraction.

We have identified the activity type of the 292 isolated NELGs in Figure 3, where we compare the two line ratios [OIII]λ5007/Hβ and [NII]λ6584/Hα. The typical low uncertainty levels on these ratios (cross in Figure 3) have practically no effect on our classification. We distinguish 105 SFGs (36.0%), 83 TOs (28.4%), and 104 AGNs (35.6%).

2.3. *Physical characteristics of the isolated NELGS*

We present the basic physical properties of the 292 isolated NELGs in Table 2. After the SDSS identification in Column 1, we list in Columns 2, 3 and 4 the right ascension, declination and redshift of the galaxies as listed in SDSS DR7. The results of our morphological classification are given in Column 5. Also from the SDSS DR7 database, we give in Columns 6 and 7 the Petrosian radii (in kpc) at 90% of the light distribution and the concentration index, CI, which is the ratio of the two Petrosian radii (CI $= R_{90\%}/R_{50\%}$). In Column 8 we list the luminosity in the K band as determined from 2MASS (K20 from 2MASS). In Column 9, we give the mean stellar age of the stellar populations consistent with the STARLIGHT template (Asari et al. 2007).

The K20 magnitudes from 2MASS were extracted from the extended sources catalog (Jarrett et al. 2000) by choosing the closest galaxy within 5 arcsecs of the best match. They were corrected for Galactic extinction at the position of the galaxies using the dust maps published in Schlegel et al. (1998). We also applied a k-correction using the method de-

TABLE 2

EXAMPLES OF BASIC PHYSICAL PROPERTIES OF THE ISOLATED NELGS

Identification in SDSS	RA (J2000) (degree)	DEC (J2000) (degree)	z	Morph.	$R_{90\%}$ kpc	CI	$\log(L_K)$ $L_\odot$	Mean (t_*) yr
SDSS J105809.84−004628.8	164.54102	−0.77468	0.0215	Sc	6.5	2.18	10.43	8.79
SDSS J113903.33−001221.6	174.76388	−0.20600	0.0181	Sab	8.6	3.06	10.77	9.82
SDSS J135807.05−002332.9	209.52940	−0.39248	0.0296	Sc	9.8	2.11	10.80	8.61
SDSS J142223.76−002315.5	215.59903	−0.38766	0.0055	Sd	4.6	1.90	10.01	7.81
SDSS J150654.85+001110.8	226.72857	0.18634	0.0351	Sa	12.1	2.72	11.19	9.60
SDSS J113423.32−023145.5	173.59719	−2.52933	0.0395	Sb	13.9	2.09	11.06	9.79
SDSS J115425.04−021910.3	178.60434	−2.31955	0.0080	Sd	4.5	2.12	9.78	8.05
SDSS J122353.98−032634.4	185.97495	−3.44292	0.0068	Sab	5.5	2.79	10.58	8.92
SDSS J124428.12−030018.8	191.11718	−3.00525	0.0239	Sc	8.6	2.65	10.61	9.17
SDSS J170128.21+634128.0	255.36758	63.69112	0.0163	Sc	5.5	1.76	10.42	7.89

†Full table available in electronic form at `http://www.astroscu.unam.mx/rmaa/RMxAA..47-2/RMxAA..47-2_rcoziol-tables.zip/`.

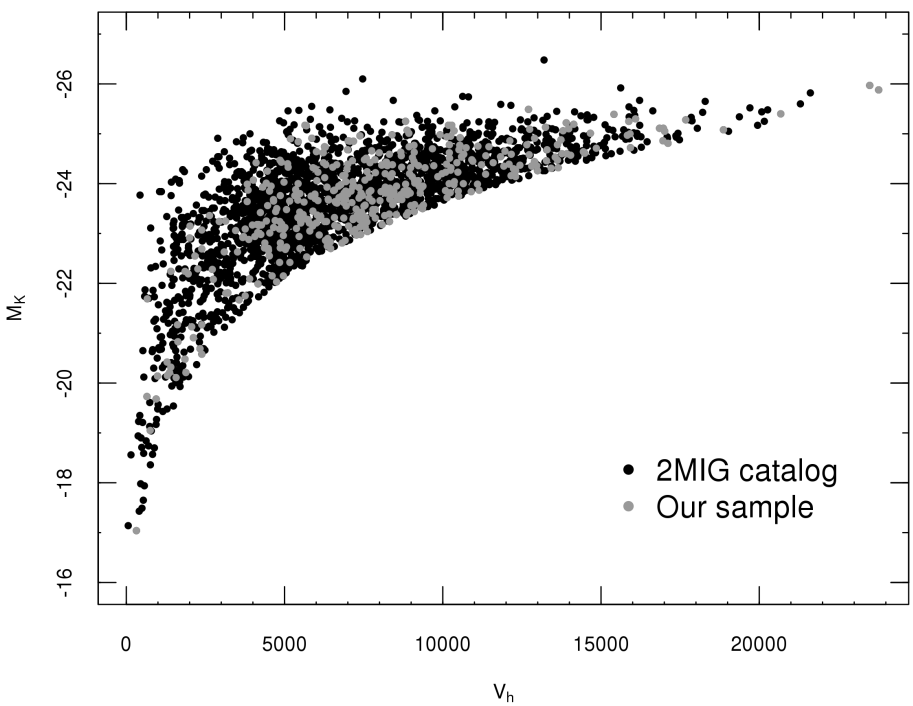

Fig. 4. Comparison of absolute K magnitude vs. heliocentric velocity for the 2MIG catalog and our subsample of 292 isolated NELGs. The color figure can be viewed online.

scribed in Kochanek et al. (2001). This method is reported to be valid for $z < 0.25$ and to be independent of the galaxy morphological type. The K band absolute magnitude was calculated using the standard relation:

$$M_K = m_K - 25 - 5\log(D_L) - A_K - k(z), \quad (1)$$

where m_K is the total apparent magnitude in K, A_K is the Galactic extinction, D_L is the luminosity distance in Mpc, calculated assuming $H_0 = 75$ km s^{-1} Mpc^{-1}, and $k(z) = -6.0\log(1+z)$ is the k-correction. From the magnitudes we deduce the K luminosities applying the relation:

$$\log(L_K/L_\odot) = 0.4(M_{\odot K} - M_K), \quad (2)$$

TABLE 3

DISTRIBUTION OF MORPHOLOGIES OF 292 ISOLATED NELGS

Morphology type	Number	Fraction %
S0	9	3.1
S0a	4	1.4
Sa	55	18.8
Sab	68	23.3
Sb	83	28.4
Sc	53	18.2
Sd	17	5.8
Sm	3	1.0

where $M_{\odot K} = 3.28$ is the absolute magnitude of the Sun in the K band (Binney & Merrifield 1998). From the uncertainties in the fluxes (Jarrett et al. 2000), a mean uncertainty of 6% is estimated for our K luminosities.

In Figure 4 we compare the distributions of the 2MASS absolute magnitudes in K and heliocentric radial velocities, as found in our subsample of 292 isolated NELGs and in the entire 2MIG catalogue. The distribution for the 2MIG catalogue is typical of a flux limited survey. The galaxies of our subsample are randomly distributed, suggesting they form a statistically fair sample of all the isolated galaxies in the 2MIG catalogue.

3. ANALYSIS

3.1. *Activity type vs. morphology*

We present the fractions of morphology types in our sample of 292 isolated NELGs in Table 3. The majority (70.5%) of these galaxies are classified as intermediate spirals (Sa-Sab-Sb). In Figure 5 we show how the distribution of activity type varies in the different morphology classes: AGNs and TOs are mostly found in early-type galaxies (S0-Sa), while the proportion of SFGs gradually increases in later types (Sab-Sm). This result is not new, but confirms the common view about AGNs in the field: they are mostly found in early-type spiral galaxies (e.g., Melnick, Terlevich, & Moles 1986; Osterbrock 1989; Blandford, Netzer, & Woltjer 1990).

In Table 4 we give our estimated masses for the bulges, $M_{\rm Bulge}$, as determined using the velocity dispersions, $\sigma_\star$, and applying the virial theorem. The box-whisker plots for the bulge masses of the galaxies separated by activity type are presented in Figure 6a. The median values are reported in Table 5. AGNs and TOs possess more massive bulges than SFGs. The trends observed for the AGNs and TOs are confirmed using a non-parametric statistical test (Kruskall-Wallis with Dunn's multiple comparison tests). The results of these tests are presented in Table A1 of the Appendix. The tests find the medians in the three samples to be significantly different at a level of confidence of 99%.

In Figure 6b we compare the bulge mass of galaxies with different morphologies. We also observe a significant difference, the bulge mass being larger in

TABLE 4

EXAMPLES OF MASSES OF ISOLATED NELGS†

Identification in SDSS	$\log(M)(M_\odot)$		
	$M_{\rm Bulge}$	$M_{\rm BH}$	M_B
SDSS J105809.84−004628.8	9.04		10.71
SDSS J113903.33−001221.6	9.40	6.41	10.55
SDSS J135807.05−002332.9	9.17		11.04
SDSS J142223.76−002315.5	8.39		10.17
SDSS J150654.85+001110.8	9.99	7.06	11.12
SDSS J113423.32−023145.5	9.69	6.74	11.22
SDSS J115425.04−021910.3	8.52		9.86
SDSS J122353.98−032634.4	8.77	5.70	10.28
SDSS J124428.12−030018.8	9.33	6.33	10.96
SDSS J170128.21+634128.0	9.03		10.77

†Full table available in electronic form at `http://www.astroscu.unam.mx/rmaa/RMxAA..47-2/RMxAA..47-2_rcoziol-tables.zip/`.

TABLE 5

MEDIAN MASSES AND CONCENTRATION INDICES

	$\log(M)(M_\odot)$			CI
	$M_{\rm Bulge}$	M_K	M_B	
AGN	9.64	10.90	10.92	2.41
TO	9.41	10.85	10.78	2.21
SFG	9.10	10.66	10.56	2.11
S0/S0a	9.73	10.98	10.94	3.21
Sa	9.72	10.91	11.00	2.87
Sab	9.46	10.82	10.78	2.62
Sb	9.39	10.94	10.77	2.34
Sc	9.10	10.66	10.58	2.12
Sd	8.44	9.86	9.66	2.07

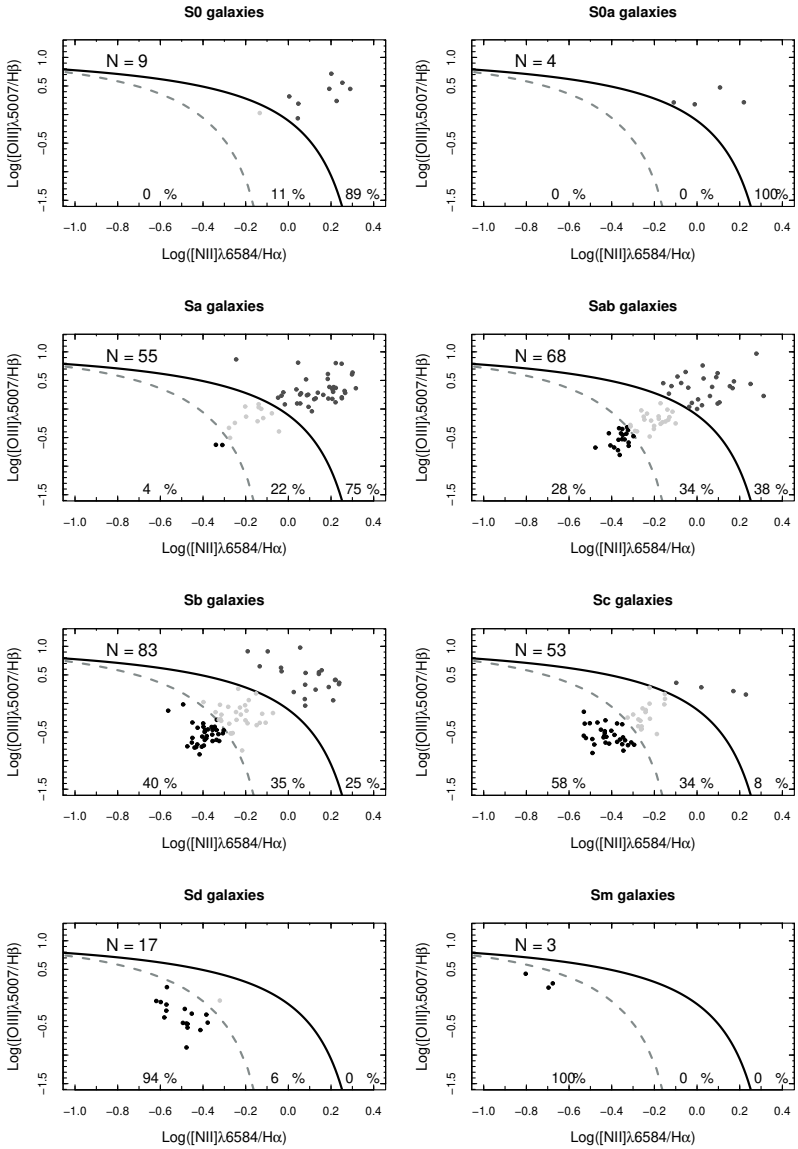

Fig. 5. Diagnostic diagrams for isolated NELGs with different morphologies. The separations and colors are as explained in Figure 3. The color figure can be viewed online.

earlier morphological types. This trend is also found to be statistically significant. The results for the tests, presented in Table A2 of the Appendix, show that the farther apart the morphological class, the more significant the difference in bulge mass. For example, the statistical tests reveal no difference between Sa and Sab, but a significant one between Sa and Sb. Similarly, no difference appears between Sab and Sb, but a significant one is found between Sab and Sc.

The above results lead to the question of whether the most important parameter is the mass of the bulge or the morphology of the galaxy. As a test, we compare the bulge masses in two statistical groups: Group 1 which is composed of Sa and Sab galaxies, and Group 2 which is composed of Sab and Sb. The box-whisker plots are drawn in Figure 7a for Group 1 and Figure 7b for Group 2. We find no significant difference in bulge mass between the different activity types in Group 1, while in Group 2 there is a significant difference only between the SFGs and AGNs. This is confirmed by the statistical tests in Table A1 of the Appendix. We conclude that the AGN activity is related to the bulge mass, but mostly because of the strong connection of this parameter with the morphology: the earlier the morphology, the larger

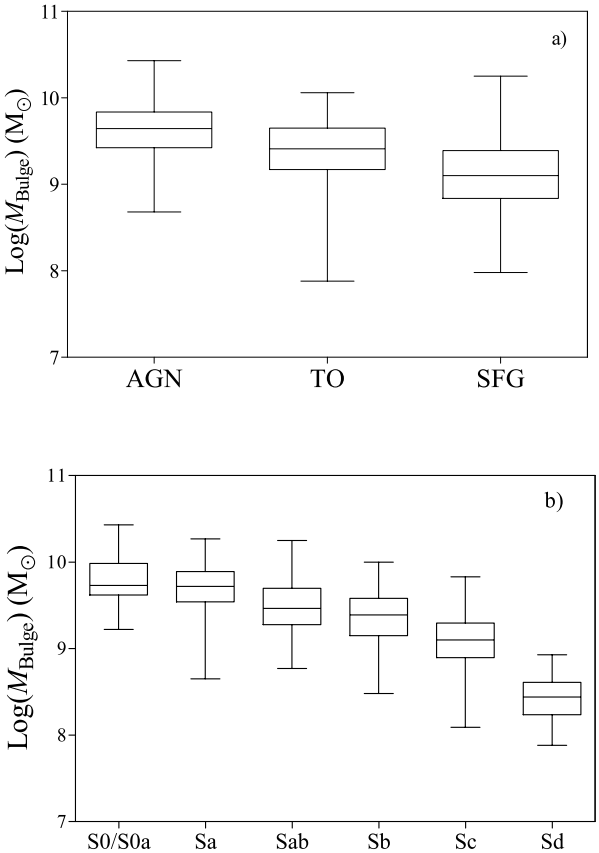

Fig. 6. Box-whisker plots for the bulge masses of galaxies as function of (a) activity type, (b) morphology. The middle line is the median, the box is limited by the percentiles and the whiskers indicate the full range of values.

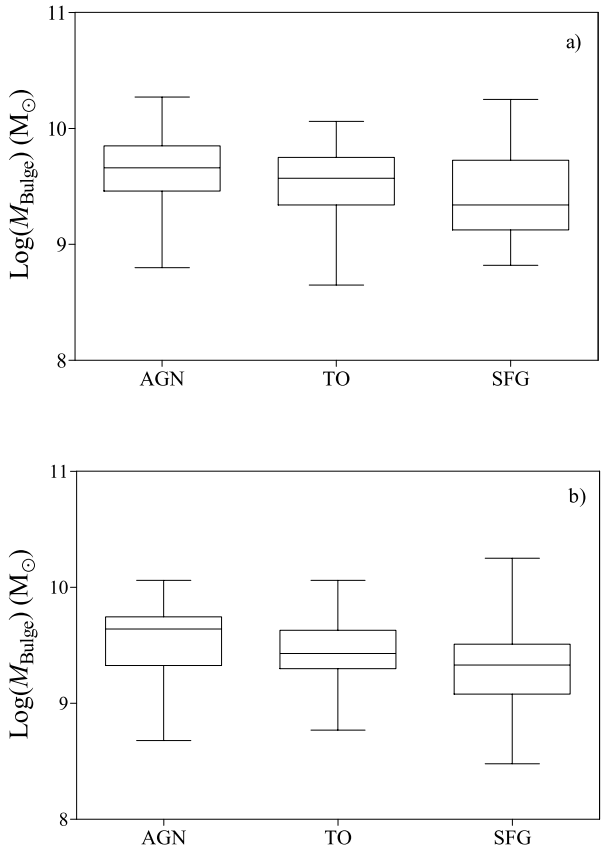

Fig. 7. Box-whisker plots for the bulge masses as found (a) in group 1 (Sa and Sab galaxies), and (b) in group 2 (Sab and Sb galaxies). Box-whiskers are defined as in Figure 6.

the bulge mass, and the higher the probability to see an AGN. This is also consistent with the diagnostic diagrams, which show a larger frequency of AGNs in earlier morphological types. In Group 1, the numbers of AGNs, SFGs and TOs are 67, 21 and 35, respectively, while in Group 2 these numbers change to 47, 53 and 51 respectively. For an increase by a factor of 2 in bulge mass, from Sa to Sb (the bulge mass increases by factor of 3.5 from AGN to SFG in Table 5), the number of AGNs slightly falls and the number of TOs and SFGs doubles.

The bulge mass being an important morphological parameter, the strong correlation found with AGN activity suggests this phenomenon is intimately connected with the formation process of the galaxies.

3.2. *Activity type vs. galaxy mass*

We have estimated the masses of our galaxies using two different methods. The first method is based on 2MASS K band luminosities (as compiled in Table 2), while the second is based on the absolute B magnitudes, which were obtained using the Johnson-B band magnitude synthesized from the SDSS magnitudes (Fukugita et al. 1996). The absolute magnitudes in B are compiled in Tables 6, 8 and 9, for the SFGs, AGNs, and TOs, respectively. The uncertainty is of the order of 0.05 mag. Being insensitive to dust extinction and to the morphological type of the galaxies the near-infrared emission is a better tracer of the stellar mass than the B magnitudes, for which we need to apply a correction depending on the morphology.

The K luminosities were transformed into masses using the mass-to-light ratio $M/L_K = 0.95$, as estimated by Bell et al. (2003). To transform the B absolute magnitudes into masses, we first corrected for galactic extinction and k-correction using the code developed by Blanton & Roweis (2007). Then we applied the different mass-to-light ratios for galaxies

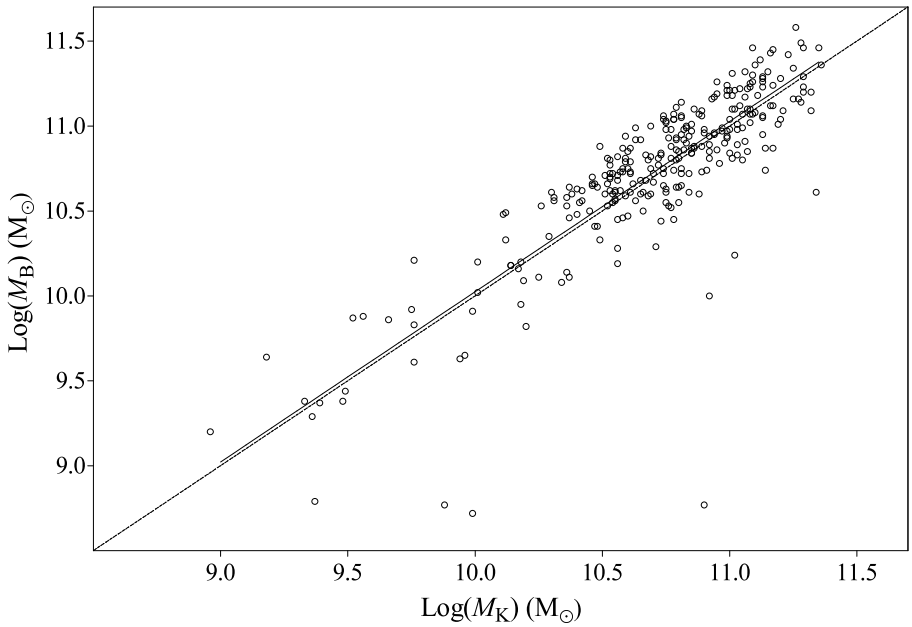

Fig. 8. Comparison of the two mass estimates. The dotted line is the one-to-one relation and the continuous line is a linear fit.

as published by Faber & Gallagher (1979). These ratios were adjusted for our adopted value of the Hubble constant. The B mass estimates appear in Column 4 of Table 4.

In Figure 8 we compare the two mass estimates. The linear relation fitted has a correlation parameter $r^2 = 0.72$, implying that 72% of the total variance of the B mass estimates is explained by the variation of the K mass estimates (and vice versa). The median values for the masses in the B and K bands are given in Table 5. They are in excellent agreement with those reported by Roberts & Haynes (1994) for galaxies having similar morphological types.

In Table 5 we see that both median masses, M_B and M_K, tend to increase from the SFGs to the AGNs. The general trend observed in the box-whisker plots presented in Figure 9 looks slightly more obvious using M_K than M_B. In Table A1 of the Appendix we see that using M_B the statistical tests detect a slightly more significant difference between the AGNs and SFGs than between the TOs and SFGs, while both differences are similarly statistically significant using M_K. No significant difference is observed between the AGNs and TOs.

In Figure 10 we compare the masses of the galaxies having different morphological types. Although we found a significant variation of the bulge mass with the morphology, the total mass M_B and M_K do not seem to vary as much between galaxies having different morphologies. In Table A2 of the Appendix, we find that the observed differences start to be statistically significant only when the comparison is done with the latest types, Sc for M_B, and even later, Sd, for M_K. We conclude that galaxies with different morphologies show only marginal differences in their total masses.

Based on our analysis, the trends observed between the AGN activity, the bulge mass and morphology does not appear to be "quantitative" (based on a difference in total mass), but more "qualitative", the AGN activity appearing more frequently when a higher fraction of the mass of the galaxy is in the form of a bulge. This seems to favor a mechanism based on different astration rates–defined as the efficiency with which a galaxy transforms its gas into stars (Sandage 1986). The higher the astration rate, the more massive the bulge and the higher the probability to observe an AGN.

3.3. *Relation with stellar populations*

In Figure 11 we compare the distributions of the mean ages of the stellar populations in galaxies showing different activity types. The stellar populations of the SFGs are dominated by young stars, with mean ages ranging from 0.32 to 1.0 Gyr. These values correspond to the 25 and 75 percentiles, respectively. The mean age of the stellar populations is observed to go up in the TOs, with values ranging

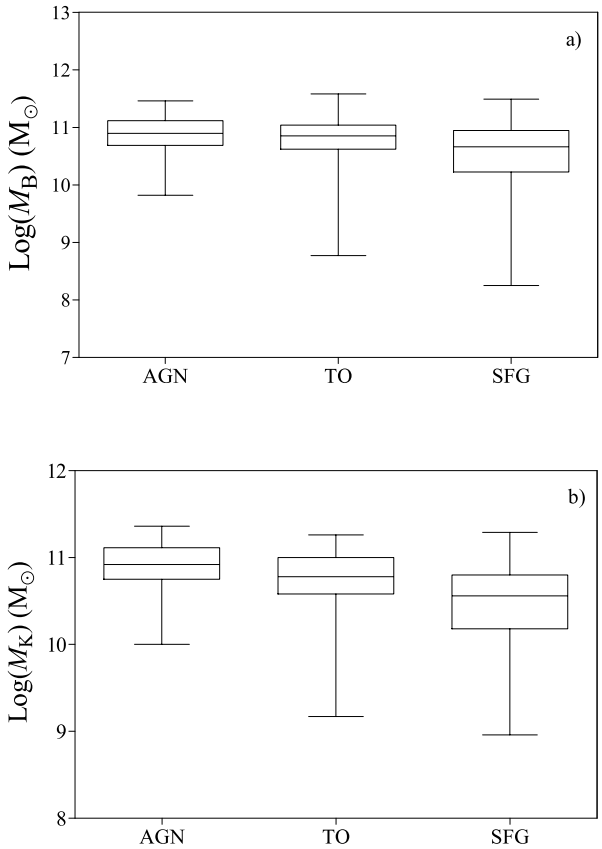

Fig. 9. Box-whisker plots for the total masses in galaxies showing different activity types; (a) M_B and (b) M_K.

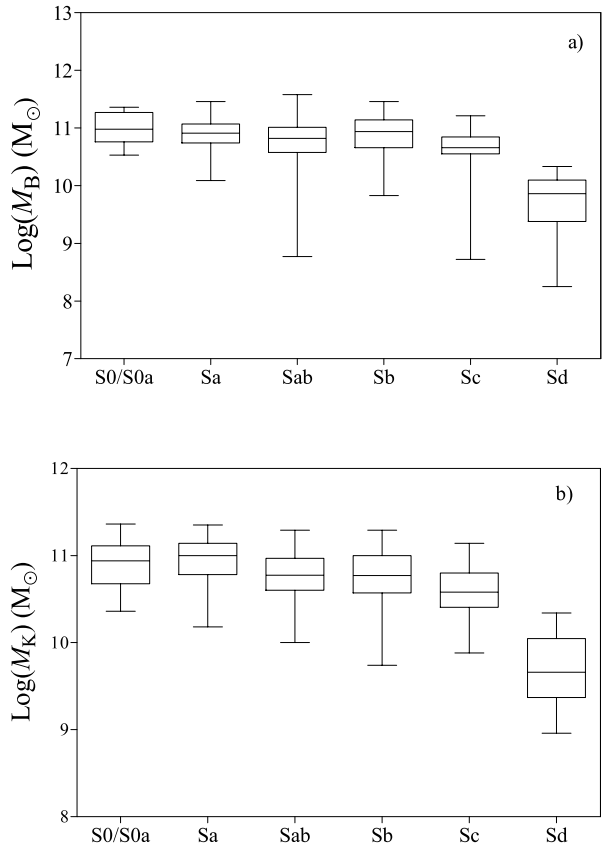

Fig. 10. Box-whisker plots for the total masses in galaxies having different morphologies; (a) M_B and (b) M_K.

from 0.5 to 3.2 Gyr, and to culminate in the AGNs with values ranging from 1.6 to 6.3 Gyr. Comparable results were encountered before by Boisson et al. (2000).

A strong connection is also found with the morphologies. In Figure 12 the morphologies were regrouped into three broad classes: Late (Sc, Sd, and Sm), Intermediate (Sa, Sab, and Sb), and Early (S0 and S0a). The SFGs show a mixture of Late and Intermediate morphologies, while the TOs have only Intermediate morphologies. The AGNs on the other hand have mostly Early morphologies.

The correlations between morphology, activity type and mean stellar ages of the stellar populations support a strong connection between the AGN activity and the formation process of the galaxies. In particular, the AGN phenomenon appears like a normal by-product of the formation process of galaxies that produces more massive bulges.

There are many structural similarities between the bulges of spiral galaxies and elliptical galaxies, suggesting similar formation mechanisms (e.g., Jablonka, Martin, & Arimoto 1996). In particular, elliptical galaxies are known to have endured higher astration rates than spiral galaxies when they formed

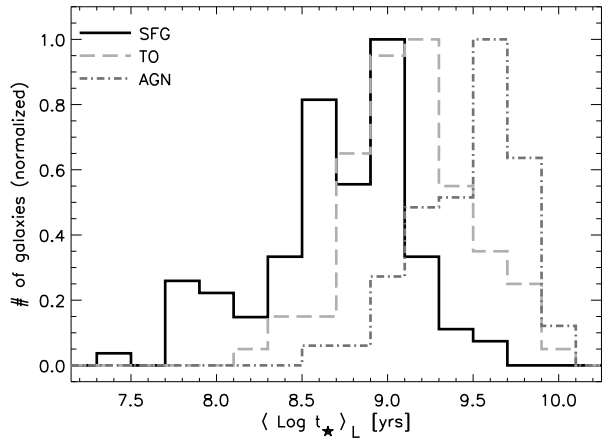

Fig. 11. Distributions of mean ages of stellar populations for galaxies with different activity types. The color figure can be viewed online.

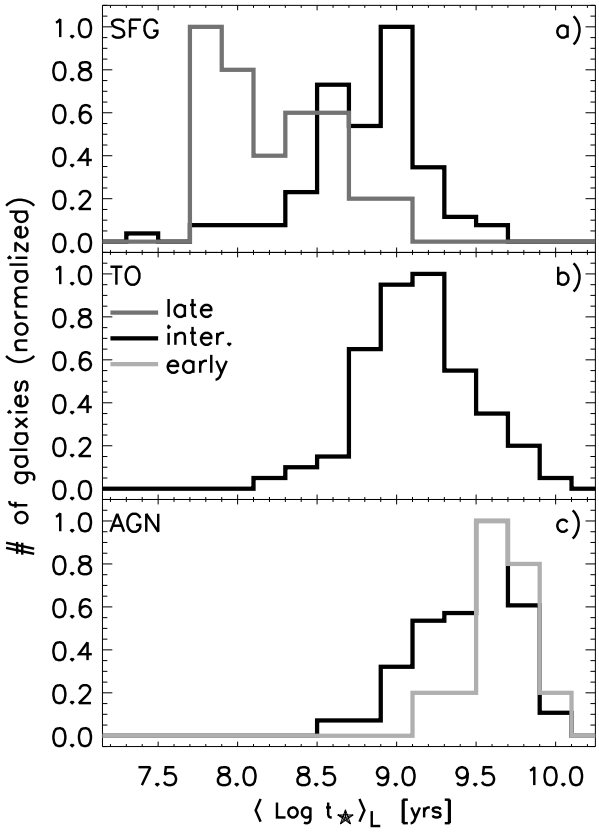

Fig. 12. Distributions of mean ages of stellar populations for galaxies with different activity types and different morphologies. The color figure can be viewed online.

(Sandage 1986), transforming almost all their gas into stars in a very short period of time. Assuming that galaxies form by a succession of star forming episodes–an assumption necessary to produce the mass-metallicity relation–galaxies with high astration rates would thus be expected to have formed most of their stars in the past because, the reservoir of gas being limited, the galaxy would have consumed it rapidly and stopped forming stars relatively early. This would explain the differences in mean ages for the stellar populations observed in our sample of isolated NELGs.

3.4. *Relation with gas metallicity*

After correcting for dust absorption, the metallicities of the gas in the SFGs were estimated using the empirical correlation found between log(O/H) and the emission-line ratio $R_3 = ([\mathrm{OIII}]\lambda4959 + [\mathrm{OIII}]\lambda5007)/\mathrm{H}\beta$ (Edmunds & Pagel 1984; Vacca & Conti 1992). The correlation originates from the cooling effect of oxygen: as the metallicity of the gas increases, the gas is cooled more efficiently, the temperature drops and the line ratio R_3 decreases (McCall, Rybski, & Shields 1985; Evans & Dopita 1985).

TABLE 6

EXAMPLES OF GAS METALLICITIES AND ABSOLUTE B MAGNITUDES OF SFGS†

Identification in SDSS	[O/H]	M_B
SDSS J105809.84−004628.8	0.26	−18.46
SDSS J135807.05−002332.9	0.43	−19.68
SDSS J142223.76−002315.5	0.31	−17.11
SDSS J115425.04−021910.3	0.20	−16.35
SDSS J170128.21+634128.0	0.47	−18.65
SDSS J214907.29+002650.3	0.51	−18.28
SDSS J235106.25+010324.1	0.48	−17.67
SDSS J021859.64+001948.0	0.44	−18.69
SDSS J025154.58+003953.3	0.29	−19.06
SDSS J003823.71+150222.4	0.38	−18.69

†Full table available in electronic form at `http://www.astroscu.unam.mx/rmaa/RMxAA..47-2/RMxAA..47-2_rcoziol-tables.zip/`.

The gas metallicities in the SFGs are compiled in Table 6, together with their absolute B magnitudes. We assume the solar metallicity is $12 + \log(\mathrm{O/H}) = 8.66 \pm 0.05$ (Asplund et al. 2004). The uncertainty in the metallicities is of the order of ± 0.2 dex (Edmunds & Pagel 1984). In Figure 13 we plot the gas metallicities in the SFGs against their absolute B magnitudes. The results are in excellent agreement with what is expected based on their late-type morphologies (Zaritsky, Kennicutt, & Huchra 1994). The results are also in good agreement with what was observed in Starburst Nucleus Galaxies (SBNGs): the gas in the late-type SBNGs is more metal rich than in the early-type SBNGs, due to their different formation processes (Coziol et al. 1998b).

The usual way to determine the metallicity of AGNs is to compare the observed line ratios with the outputs obtained using an ionization code like CLOUDY (Ferland et al. 1998). However, the results are usually ambiguous, with more than one possible solution (Nagao, Maiolino, & Marconi 2006). There maybe also other physical mechanisms, like shocks or special ionizing structures, that can complicate the interpretation based solely on photoionization model results (Viegas & de Gouveia dal Pino 1992; Cooke et al. 2000).

An excellent study was presented recently by Bennert et al. (2006). With the permission of the

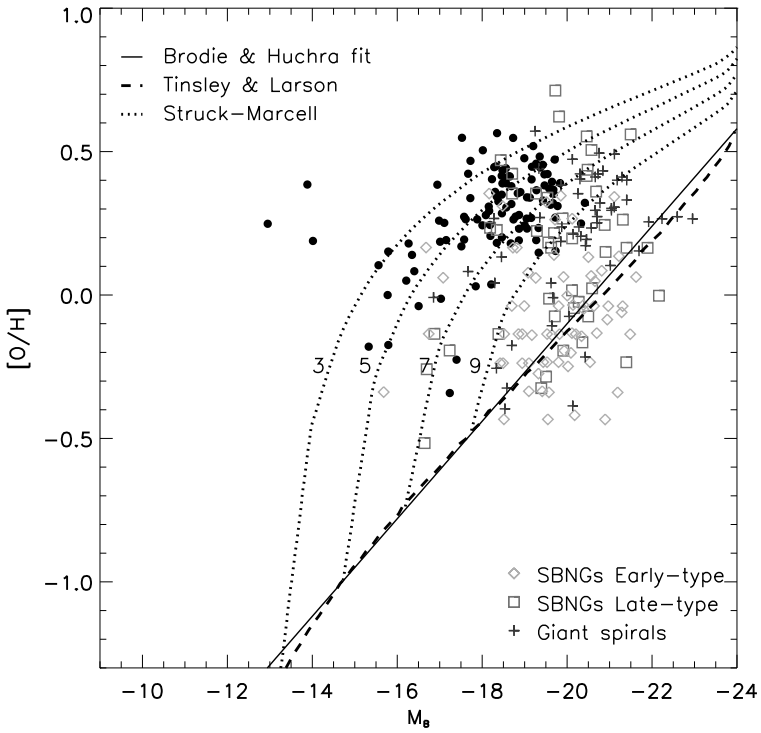

Fig. 13. Gas metallicities vs. absolute B magnitudes for the SFGs (filled dots). The giant spirals sample is taken from Zaritsky et al. (1994) and the SBNGs from (Coziol et al. 1998b). The continuous straight line is the Brodie-Huchra (1991) relation for elliptical galaxies. Also shown are two models of multiple mergers by Tinsley & Larson (1979) and Struck-Marcell (1981). The numbers indicate the approximate number of mergers necessary in the models to reproduce the metallicities. The color figure can be viewed online.

authors, we reproduce some of their results in Figure 14. The models discussed in their study apply exactly to our NELGs. From their study we can see that the line ratio [NII]/Hα is extremely sensitive to the abundance of nitrogen. One possible cause for the increase of nitrogen emission in the AGNs could be an excess of nitrogen (Osterbrock 1970; Storchi-Bergmann & Pastoriza 1989; Storchi-Bergmann 1991; Hamann & Ferland 1993). In the center of galaxies with massive bulges and old stellar populations, we do not expect the nitrogen abundance to follow the normal secondary relation (Zaritsky et al. 1994; Thurston, Edmunds, & Henry 1996; van Zee et al. 1998; Coziol et al. 1999).

In Figure 14 we also observe that, for any value in excess of nitrogen abundance, increasing the ionizing parameter, U, while keeping the metallicity constant causes the ratio [OIII]/Hβ to rise. But, if we increase U too much the ratio [NII]/Hα begins to decrease. In the same figure we observe that when we lower the metallicity while keeping U constant, both line ratios increase, which is consistent with the cooling effect of oxygen. However, if we decrease the metallicity too much, both line ratios eventually decrease. This behavior is consistent with a coupling effect between U and the metallicity (Evans & Dopita 1985): as the metallicity decreases, U increases and vice versa. Therefore, one can arbitrarily change one parameter or the other with almost the same effect.

In Figure 14 the TOs and AGNs trace a continuous sequence where the ratios [NII]/Hα and [OIII]/Hβ increase together. According to the CLOUDY models of Bennert et al. one way to explain this sequence would be to decrease the metallicity gradually while increasing the overabundance of nitrogen. Consistent with this model, we fitted on the TOs and AGNs distributions an empirical relation between the ratio [OIII]/Hβ and [NII]/Hα. We then searched for a calibration that would yield the same range in metallicities for the TOs as obtained using the model of Bennert et al. (2006), from 2.5 to 1 $Z_{\odot}$. As a first approximation we found that the R_3 calibration for the SFGs nearly reproduces these values. Extrapolating this calibration over the AGNs region suggests a decrease in metallicities for these objects from 1 $Z_{\odot}$ to 0.3 $Z_{\odot}$. Based on the models of

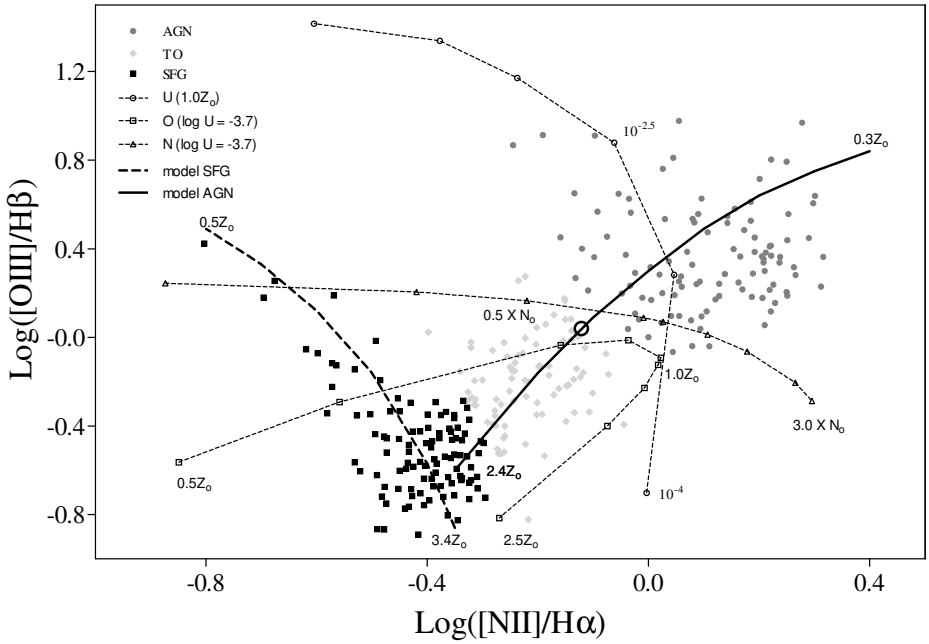

Fig. 14. Diagnostic diagram with three curves obtained by Bennert et al. (2006) using CLOUDY: U, varying the ionizing parameter at constant solar metallicity; O, varying the metallicity keeping U constant; N, varying the nitrogen abundance. Also shown is our calibration using R_3. The bold circle on this curve corresponds to 1.0 $Z_\odot$. The color figure can be viewed online.

Bennert et al. (2006), the ionizing parameter would increase from $10^{-3.5}$ to $10^{-2.5}$, which seems in good agreement with the values found by Baskin & Laor (2005), and the abundance of nitrogen would not exceed 2 times the solar value, which is a lower excess than suggested originally by Osterbrock (1970), but still fully consistent with what is observed in the bulges of normal galaxies (Thurston et al. 1996; van Zee et al. 1998; Coziol et al. 1999).

Our model suggests that there is an inversion in the metallicity-nitrogen abundance relation in the AGNs compared to that in the SFGs: in the SFGs, the nitrogen abundance increases with the metallicity, while in the TOs and AGNs the nitrogen abundance increases as the metallicity decreases (consistent with an excess in nitrogen abundance). For the TOs and AGNs the relation is:

$$[\mathrm{O/H}] = -0.52 + (\log([\mathrm{NII}]/\mathrm{H}\alpha) - 0.6)^2 . \quad (3)$$

For the SFGs the relation is:

$$[\mathrm{O/H}] = -[0.99 + 0.61/(\log([\mathrm{NII}]/\mathrm{H}\alpha) - 0.05)] . \quad (4)$$

To test our calibration, we searched the literature for NLAGNs for which the metallicity of the gas was previously estimated using CLOUDY, and could also be evaluated by our method (with reported spectrophotometry in the optical). We found very few examples, and all are Sy2 located in the upper part of our diagram in Figure 15, where we expect our calibration to yield the most discrepant results. The values obtained are compiled in Table 7.

TABLE 7

GAS METALLICITIES OF AGNS FROM THE LITERATURE, COMPARED TO THOSE OBTAINED USING OUR CALIBRATION

ID	$Z/Z_\odot$ (lit.)	$Z/Z_\odot$ (ours)	Literature sources
Mrk 78	0.30	0.30	(1)(2)
NGC 3393	0.10	0.21	(3)
NGC 1068	0.30	0.16	(4)
NGC 4507	0.50	0.27	(4)
NGC 5135	0.2-0.5	0.43	(4)
NGC 5506	0.50	0.23	(4)
Mrk 1388	0.70	0.23	(4)

(1)Ramos Almeida et al. 2006, (2) Ulrich 1971, (3) Cooke et al. 2000, (4) Nagao et al. 2006.

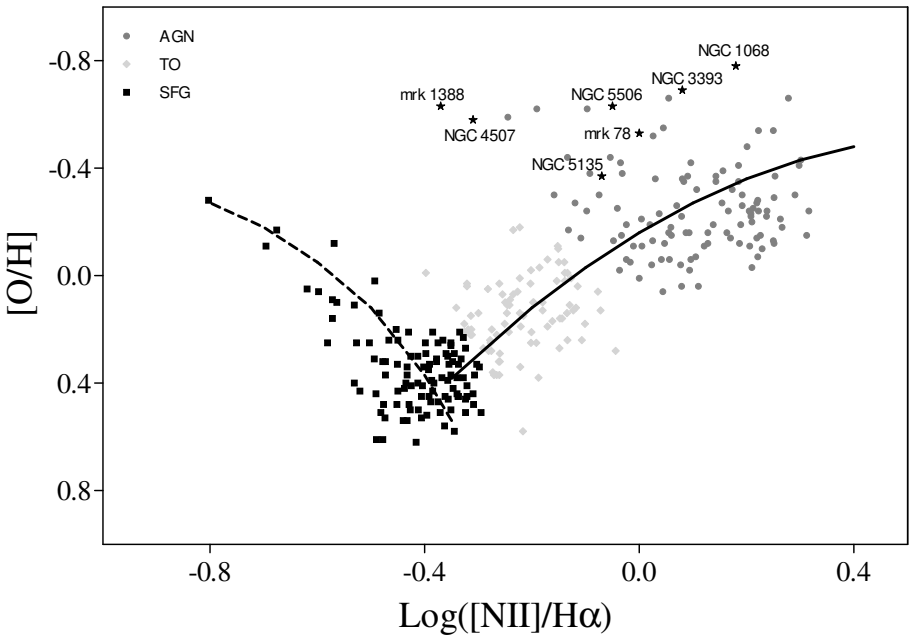

Fig. 15. Metallicity calibrated diagnostic diagram. The two empirical relations (equations 3 and 4) are also traced over the data. Also shown are Sy2 galaxies from the literature for comparison. The color figure can be viewed online.

Only the low metallicity solutions reported by Nagao et al. (2006) for their objects are consistent with our model. Surprisingly, the differences observed are not systematic, suggesting that other physical parameters (e.g., shocks, as we mentioned before, or special geometries, like an ionization cone or an obscuring torus) could also be important in these galaxies.

The above comparison suggests that the uncertainty in our metallicities is of the order of 0.3 dex, increasing to as much as 0.5 dex in some Sy2 like Mrk 1388. However, this galaxy appears to be an extreme case, for which we do not expect our calibration to apply. In Figure 15, most of the AGNs and TOs in our sample fall in a different regime than the AGNs from the literature used for the test (that is, the AGN in our sample fall in a different part of the diagnostic diagram, and they are clearly tracing a continuous relation). A better estimate of the uncertainty in the gas metallicities obtained with our method may be ∼0.2 dex, which is consistent with the variance of our fitted relation.

The gas metallicities as deduced from our calibration together with the B luminosities are presented in Table 8 for the AGNs, and in Table 9 for the TOs. In Figure 16 we show the box-whisker plots for the gas metallicities in galaxies having different activity types and different morphologies. The AGNs and TOs have lower gas metallicities than the SFGs and we find an excellent correlation with the morphological type of the galaxies, the metallicities increasing in the later types. The statistical tests (Table A1 and Table A2 in the Appendix) confirm the differences observed at a level of confidence of 99%.

In Figure 17 we compare the gas metallicities of the TOs and AGNs with those of the SFGs.

TABLE 8

EXAMPLES OF GAS METALLICITIES AND ABSOLUTE B MAGNITUDES OF AGNS[†]

Identification in SDSS	[O/H]	M_B
SDSS J113903.33−001221.6	−0.15	−18.06
SDSS J150654.85+001110.8	−0.16	−19.52
SDSS J113423.32−023145.5	−0.24	−19.75
SDSS J172613.73+620858.1	−0.19	−18.85
SDSS J173044.85+562107.1	−0.35	−19.25
SDSS J025017.75−083548.5	−0.20	−17.84
SDSS J032501.68−054444.8	−0.06	−18.25
SDSS J142757.71+625609.3	−0.22	−19.46
SDSS J114743.68+014934.3	−0.66	−19.12
SDSS J133548.24+025956.1	−0.36	−19.28

[†]Full table available in electronic form at `http://www.astroscu.unam.mx/rmaa/RMxAA..47-2/RMxAA..47-2_rcoziol-tables.zip/`.

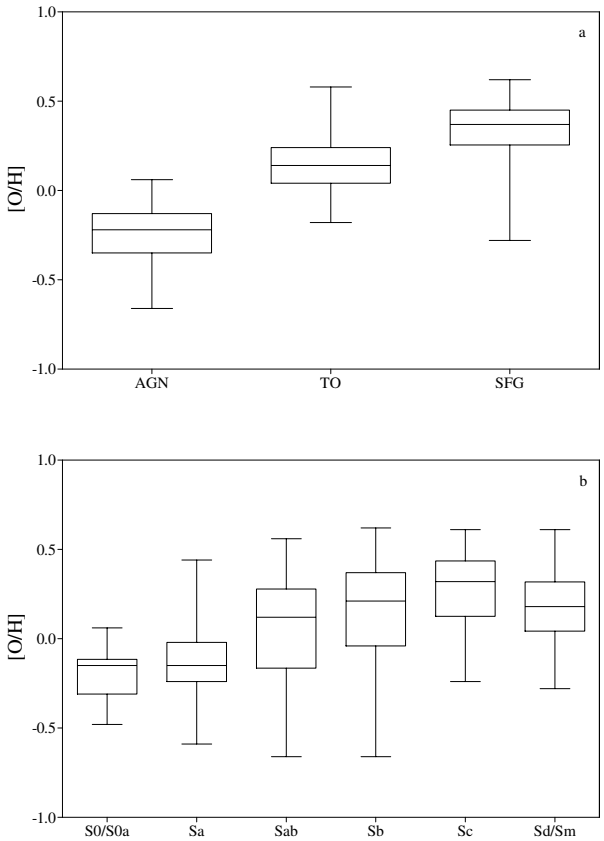

Fig. 16. Box-whisker plots for the gas metallicity variation in galaxies having (a) different activity types, and (b) different morphologies.

The AGNs seem to follow the Brodie-Huchra (1991) mass-metallicity relation for elliptical and bulge-dominated galaxies (Zaritsky et al. 1994; Coziol et al. 1998b). The TOs, on the other hand, with their intermediate morphologies, show also metallicities which are intermediate between those of the SFGs and the AGNs. The differences in metallicities observed between the SFGs, TOs and AGNs are in excellent agreement with the differences in mean ages of the stellar populations and bulge masses. All these parameters are consistent with higher astration rates for the AGNs as compared to the SFGs (Sandage 1986).

4. DISCUSSION

Our study suggests that the formation of a SMBH in the center of a galaxy is tightly connected with the formation process of its bulge (Häring & Rix 2004; Peterson et al. 2005; Gültekin et al. 2009). Some authors have even suggested that the formation of the bulge is a self-regulated process with strong feedback from the SMBH growing in its center (see Younger et al. 2008 and references therein). Our observations may support such interpretations.

TABLE 9

EXAMPLES OF GAS METALLICITIES AND ABSOLUTE B MAGNITUDES OF TOS[†]

Identification in SDSS	[O/H]	M_B
SDSS J122353.98−032634.4	0.16	−17.40
SDSS J124428.12−030018.8	0.14	−19.10
SDSS J224424.36−000943.5	0.24	−19.44
SDSS J020540.31−004141.4	0.21	−19.37
SDSS J031347.83+004139.7	0.10	−19.27
SDSS J032406.50−010328.2	0.03	−18.49
SDSS J012853.25+134737.6	0.02	−18.95
SDSS J030848.32−070226.1	0.28	−19.53
SDSS J033358.81−070826.6	0.10	−18.82
SDSS J090513.20−002947.8	−0.01	−17.82

[†]Full table available in electronic form at `http://www.astroscu.unam.mx/rmaa/RMxAA..47-2/RMxAA..47-2_rcoziol-tables.zip/`.

According to Aller & Richstone (2007) the gravitational binding energy is one key factor explaining the relation between the SMBH and the bulge mass. The gravitational binding energy is the negative of the gravitational potential energy. For a system of N particles, with an approximate mass $M = Nm_p$, where m_p is the mass of a proton, the binding energy per baryon is equal to:

$$U/N = GMm_p/R\,, \tag{5}$$

where G is the gravitational constant and R is the radius of the object. By definition, a SMBH represent a huge mass, which represents maybe only 1% to 0.1% of the bulge mass, but which is concentrated in an extremely small region of space at the center of mass of the galaxy. The formation of such a highly gravitationally bound object implies a significant increase in binding energy of the host galaxy itself.

The above description gives us a new test for the NLAGNs in our sample. If these galaxies host a SMBH in their center, we would expect them to show relatively high gravitational binding energies compared to, for example, the SFGs. To verify this assumption, we have used the masses as determined from the K magnitudes, M_K, and the Petrosian radii, $R_{90\%}$, reported in Table 2, to calculate the gravitational binding energy per baryon of all the galaxies in our sample. As expected, we observe in

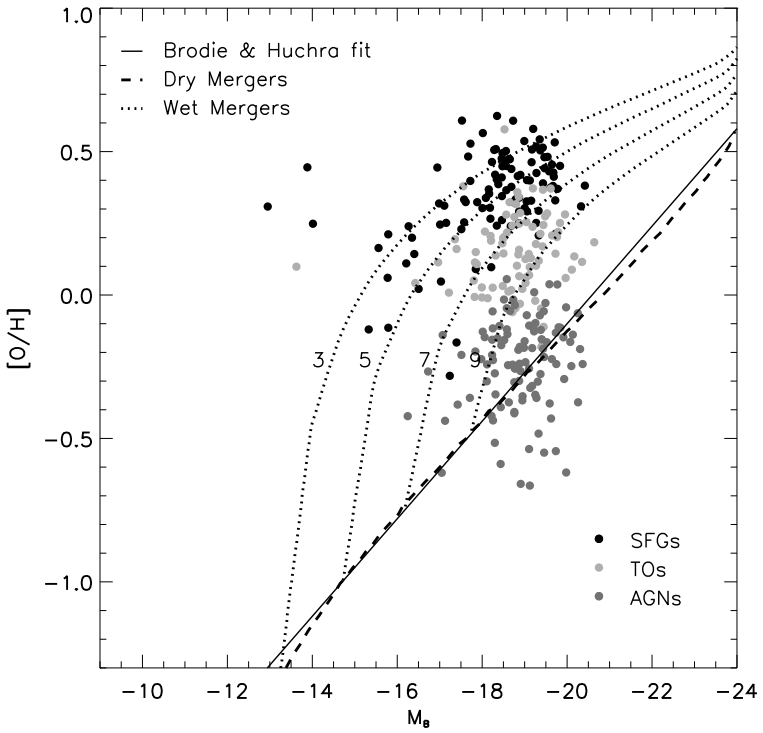

Fig. 17. Gas metallicities vs. absolute B magnitudes for all the isolated NELGs. The multiple merger model of Tinsley & Larson (1979) is identified as the dry merger scenario and the Struck-Marcell (1981) model is denoted as the wet merger scenario (see explanations in our discussion section). The color figure can be viewed online.

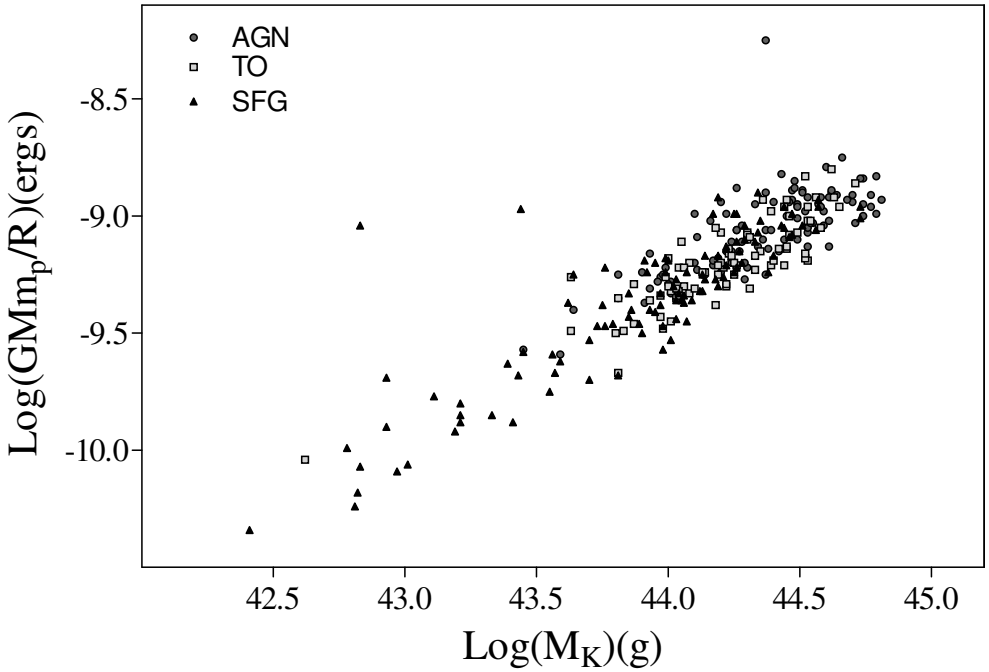

Fig. 18. Gravitational potential energy per baryon of the galaxies in our sample. The color figure can be viewed online.

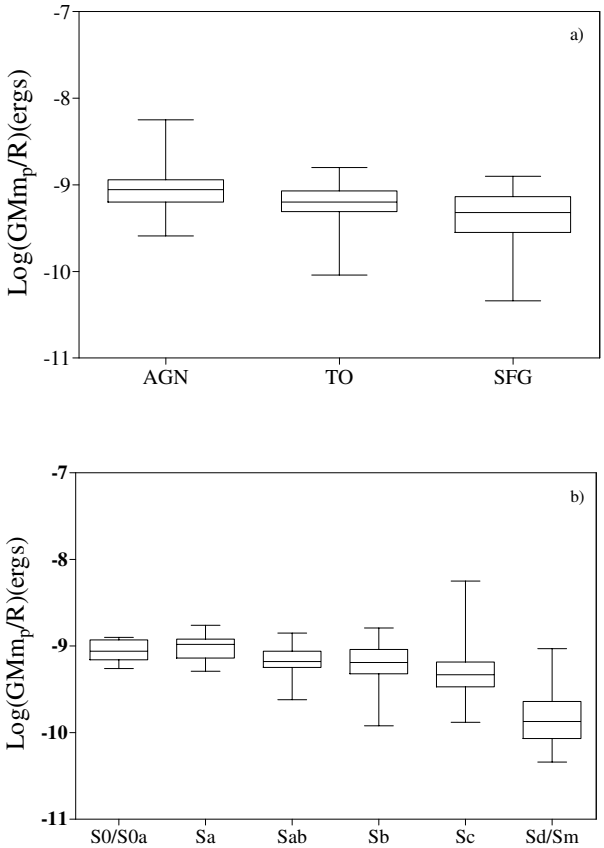

Fig. 19. Box-whisker plot of gravitational potential energy per baryon of the isolated NELGs, (a) with different activity types, (b) with different morphologies.

Figure 18 that the AGNs and TOs have higher gravitational binding energies than the SFGs. This trend is better seen in Figure 19a, which shows the box-whisker plots for the gravitational binding energies. The trend is also confirmed to be statistically significant in Table A1 of the Appendix.

The variation of gravitational binding energies with galaxy morphologies is shown in Figure 19b, and the trend is statistically tested in Table A2 of the Appendix. Galaxies with massive bulges, S0, S0a, and Sa, have comparable gravitational binding energies, which are significantly higher than those of galaxies having less massive bulges, Sab and later. These results are in good agreement with the hypothesis of a SMBH in the NLAGNs (and possibly also in the TOs).

4.1. *Masses of SMBHs vs. accretion rates*

Our analysis of the NLAGNs in our sample is consistent with the standard AGN interpretation: this phenomenon is the product of the accretion of matter onto a SMBH that developed at the same time as the massive bulge of the galaxy. According to this interpretation, the nearby NLAGNs in our sample are possibly scaled-down (and/or powered-down) versions of quasars and broad-line AGNs (BLAGNs). One good example is our own galaxy, with an intermediate Sb or SBb morphology (Binney & Merrifield 1998), where evidence was found in its center for both a SBMH, with a mass of the order of 3 or $\sim 4\times10^6$ $M_\odot$ (Genzel & Townes 1987; Ghez, Morris, & Becklin 2000; Schödel, Merritt, & Eckart 2009), and of recent star formation episodes (Figer et al. 2004), which suggests it could be classified as a LINER or a TO by outside observers.

In Häring & Rix (2004) a strong correlation was found between bulge mass and black hole mass (see also Gültekin et al. 2009, and references therein). In Shemmer et al. (2004) and Matsuoka et al. (2011), a strong correlation was also found between the black hole mass and the gas metallicity. These two correlations are fully consistent with our observations: while the formation of the SMBH follows (or self-regulates) the formation of the bulge, the gas metallicity, being a product of the evolution of the stars, also depends on the bulge formation through typically high astration rates (Sandage 1986). Based on these observations, we may therefore expect the NLAGNs to follow the same correlations as the quasars and BLAGNs.

To calculate the black hole masses, $M_{\rm BH}$, as reported in Column 3 of Table 4, we used the relation between the bulge mass and black hole mass as determined by Häring & Rix (2004). For the isolated NLAGNs we find a median value of 4.8×10^6 $M_\odot$, which is two to three orders below the value found in BLAGNs, but in good agreement with the black hole mass found in the center of our galaxy (Genzel & Townes 1987; Ghez et al. 2000; Schödel et al. 2009).

In Figure 20 we compare the gas metallicities and black hole masses for the NLAGNs of our sample with those measured in quasars and BLAGNs (Shemmer et al. 2004). The metallicities measured by Shemmer et al. (2004) were transformed to the units used in our study by Neri-Larios et al. (2011). The NLAGNs seem to continue the linear correlation found for the quasars and BLAGNs in the lower metallicity regime. A linear fit with a correlation coefficient of $r_{\rm Pearson} = 0.77$ and $r_{\rm Spearman} = 0.83$, both with chance probability $P(r_{\rm Pearson})$ and $P(r_{\rm Spearman})$ practically equal to zero, suggests the metallicity increases with the black hole mass as:

$$\log([{\rm O/H}]) = -2.56 + 0.3590 \times \log(M_{\rm BH})\,. \quad (6)$$

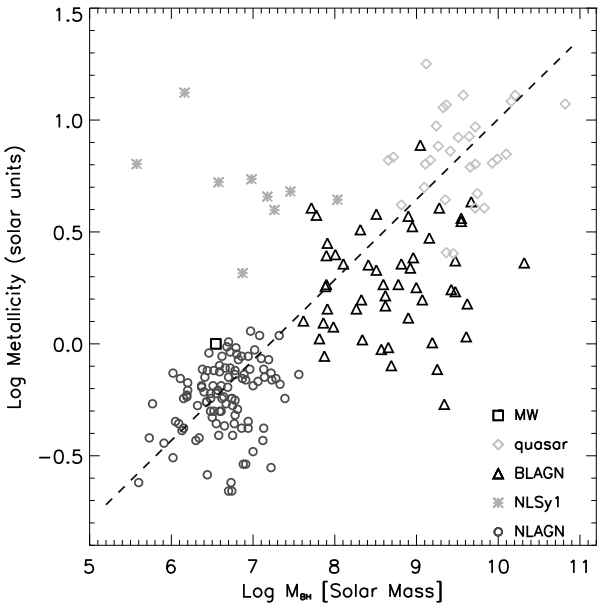

Fig. 20. Metallicities vs. black hole mass. The dashed line is our linear fitted correlation (excluding the NLSy1). The metallicity for the Milky Way is that of the Sun, which is now in better agreement with those of stars in its immediate neighborhood (Asplund et al. 2004). The color figure can be viewed online.

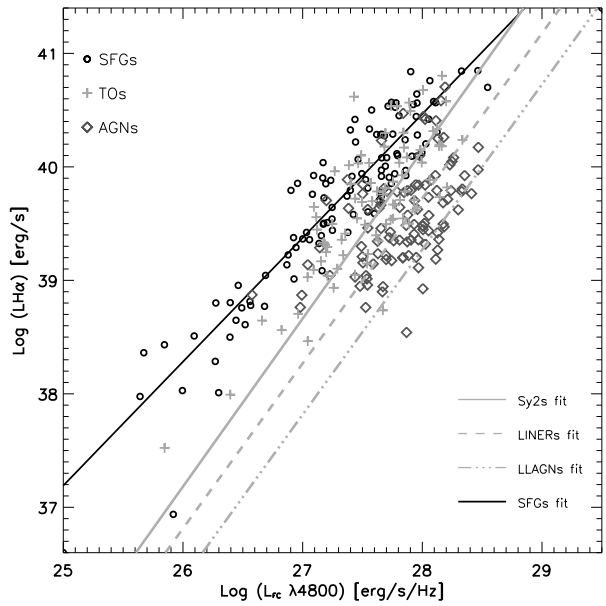

Fig. 21. Relation between ionization luminosity (Hα) and continuum luminosity (at 4800 Å). The different linear relations were determined by Torres-Papaqui et al. (2011) using a sample of 318486 SDSS galaxies. The SFGs follow a linear relation $L_{\mathrm{H}\alpha} \propto L_{4800}^{1.09\pm0.03}$, while the NLAGNs follow a steeper power law relation $L_{\mathrm{H}\alpha} \propto L_{4800}^{1.45\pm0.03}$. The color figure can be viewed online.

In Torres-Papaqui et al. (2011) it was shown that all the different kinds of NLAGNs (Seyfert 2, LINERS and LLAGNs) follow the same power law between the luminosity in Hα and luminosity at 4800 Å (Osterbrock 1989), while the SFGs follow a different, less steep, linear relation. In Figure 21 we verified that this also applies to the isolated NLAGNs of our sample. One can note also the intermediate position of the TOs, consistent with their being a mixture of SFGs and AGNs. This result suggests that we can use the black hole masses in conjunction with the luminosities at 5100 Å to estimate the accretion rates, as was done by Peterson et al. (2005).

In Figure 22, we follow the method of Peterson et al. (2005) to estimate the accretion rates of the NLAGNs of our sample. The SMBHs in the NLAGNs seem to accrete matter at relatively high rates of 0.1 times the Eddington limit. The isolated NLAGNs are consistent with scaled-down versions of quasars and BLAGNs, not powered-down versions: the lower luminosity is a result of smaller-mass black holes, not of lower accretion rates.

In Figure 23 we compare the gas metallicities and accretion rates of the NLAGNs of our sample with those found in quasars and BLAGNs, as determined in Neri-Larios et al. (2011) for the sample studied by Shemmer et al. (2004). Again, the NLAGNs seem to continue the linear correlation found for the quasars and BLAGNs in the lower metallicity regime. A linear fit with a correlation coefficient $r_{\mathrm{Pearson}} = r_{\mathrm{Spearman}} = 0.66$ with both chance probabilities practically equal to zero, suggests the metallicity increases with the accretion rate as:

$$\log([\mathrm{O/H}]) = 0.77 + 0.66 \times \log(L_{\mathrm{Bol}}/L_{\mathrm{Edd}})\,. \quad (7)$$

Although our results are fully consistent with the standard interpretation of NLAGNs as scaled-down versions of quasars and BLAGNs, we must state that there is an unfortunate uncertainty in the black hole masses we have determined. The fact is that there is no consensus in the literature about what is the correct relation to use. For practical reasons, we have used the relation proposed by Häring & Rix (2004) between the bulge mass and the black hole mass. However, in Gültekin et al. (2009) the relation proposed between black hole mass and velocity dispersion of the bulge yields masses which are ten times higher. The problem lies with what Häring & Rix (2004) called the "black hole sphere of influence". These authors argued that the black hole representing only a small fraction of the bulge mass (1% to

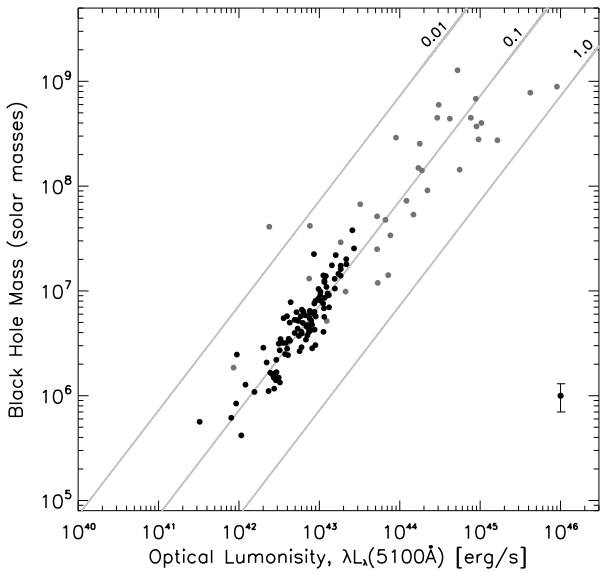

Fig. 22. Black hole mass as a function of continuum luminosity at 5100 Å for the NLAGNs compared to the BLAGNs studies in Peterson et al. (2005). The typical uncertainty for the NLAGNs is indicated by the red dot with error bars. The color figure can be viewed online.

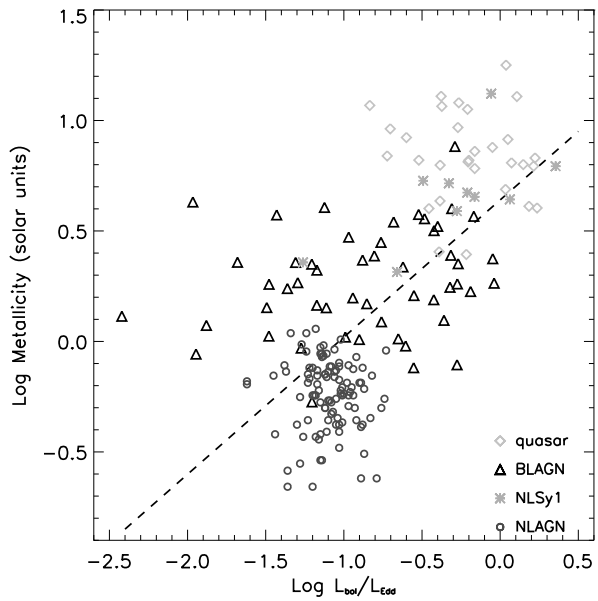

Fig. 23. Relation between metallicity and accretion rate. The NLAGNs are compared to the quasars and BLAGNs as studied by (Shemmer et al. 2004). The linear relation was fitted for all the galaxies (including the NLSy1). The color figure can be viewed online.

0.1%) cannot be responsible for the full value of the velocity dispersion, which explains why they apply a correction and obtain ten times smaller black hole mass values. In Gültekin et al. (2009), this correction is simply rejected as non valid, without further arguments.

If we adopt the relation of Gültekin et al. (2009), then the SMBH in the NLAGNs would be ten times more massive. In Figure 20, the relation between metallicity and black hole mass would be slightly steeper and the NLAGNs would differ significantly from the Milky Way. In Figure 22 the NLAGNs would not be scaled-down versions of BLAGNs but rather powered-down versions, that is, the SMBH of the NLAGNs would have masses comparable to those found in the BLAGNs but they would now be accreting at only 0.01 times the Eddington limit. Finally in Figure 23 the NLAGNs would fall farther to the left, but would still be in good agreement with the metallicity vs. accretion rate relation suggested by Shemmer et al. (2004).

5. SUMMARY AND CONCLUSION

We have constructed a sample of galaxies that have formed in low galactic density environments and have evolved in relative isolation. All these galaxies show a spiral disk and some kind of nuclear activity. Using a standard diagnostic diagram we have established that as many as 64% of these galaxies are classified as NLAGNs or TOs.

We have established a strong connection between the AGN phenomenon and the mass of the bulge, but have also found a strong correlation with the morphological type of the galaxies. This suggests that the AGN phenomenon is a "normal" occurrence related to the formation process of massive bulges in early-type spiral galaxies.

Consistent with this interpretation, our analysis suggests the AGNs and TOs have experienced during their formation higher astration rates than the SFGs–transforming their gas into stars more efficiently (Sandage 1986). Evidences favoring higher astration rates in AGNs than in SFGs are: (1) their older stellar populations; (2) their lower oxygen abundance and a possible excess of nitrogen. We also found the NLAGNs to have higher binding energies than the SFGs, suggesting they host a SMBH in their center.

Our results are in good agreement with the standard interpretation of NLAGNs, either as scaled-down (lower BH mass but same accretion rates) or powered-down (same BH mass but lower accretion rates) versions of quasars and BLAGNs. The NLAGNs also seem to follow the same relation between the BH mass, the accretion rate and the gas metallicity as the quasars and BLAGNs.

TABLE A1

DUNN'S POST TESTS FOR ACTIVITY TYPES VS. BULGE MASS, TOTAL MASS, METALLICITY AND GRAVITATIONAL BINDING ENERGY

	$M_{\rm Bulge}$		Group 1		Group 2		M_B		M_K		[O/H]		U/N	
	AGN	TO	AGN	TO	AGN	TO	AGN	TO	AGN	TO	AGN	TO	AGN	TO
AGN														
TO	***		ns		ns		ns		ns		***		***	
SFG	***	***	ns	ns	***	ns	***	**	***	***	***	***	***	**

We dedicate this article to the memory of Gabriel García Ruiz, night assistant and friend at the Observatorio Astronómico Nacional, San Pedro Mártir, Mexico, who died tragically while on duty at the end of 2010. The authors would also like to thank N. Bennert and S. Komossa for making their results of CLOUDY models available to us, and O. Shemmer for furnishing the data for the quasars and BLAGNs. T-P acknowledges PROMEP for support grant 103.5-10-4684 and I. P.-F. acknowledges a postdoctoral fellowship from Conacyt, Mexico No. 145727. This publication makes use of data products from the Two Micron All Sky Survey, which is a joint project of the University of Massachusetts and the Infrared Processing and Analysis Center/California Institute of Technology, funded by the National Aeronautics and Space Administration and the National Science Foundation. The SDSS is managed by the Astrophysical Research Consortium (ARC) for the Participating Institutions. The Participating Institutions are: the American Museum of Natural History, Astrophysical Institute Potsdam, University of Basel, University of Cambridge (Cambridge University), Case Western Reserve University, the University of Chicago, the Fermi National Accelerator Laboratory (Fermilab), the Institute for Advanced Study, the Japan Participation Group, the Johns Hopkins University, the Joint Institute for Nuclear Astrophysics, the Kavli Institute for Particle Astrophysics and Cosmology, the Korean Scientist Group, the Los Alamos National Laboratory, the Max-Planck-Institute for Astronomy (MPIA), the Max-Planck-Institute for Astrophysics (MPA), the New Mexico State University, the Ohio State University, the University of Pittsburgh, University of Portsmouth, Princeton University, the United States Naval Observatory, and the University of Washington.

APPENDIX – RESULTS OF STATISTICAL TEST

The statistical tests used in this study are the non-parametric Kruskal-Wallis test (KW), together with the Dunn's post tests. The KW test compares the medians in three or more unmatched groups of data and the post tests do multiple one-to-one comparisons. The P values reported in Tables A1 and A2 are codified in the following way: non significant difference, ns, significant, ** for $P < 0.01$, highly significant, *** for $P < 0.001$.

In Table A1, comparing the bulge mass in galaxies having different activity types, the post tests indicate that all three samples have different medians. In Group 1, no difference is found while in Group 2 only the AGNs differ from the SFGs.

In Table A2 we compare the bulge mass in galaxies having different morphologies; the post tests find highly significant differences between the most separated morphological classes. No differences are observed between the S0, S0a, Sa and Sab, the Sab and Sb, and the Sc and Sd. These tests suggest that the relation between bulge mass and activity type is a by-product of the morphology, consistent with the results for the diagnostic diagrams.

In Table A1 we verify that the total mass does not vary as strongly as the bulge mass in galaxies having different activity types. The same is true for the morphologies in Table A2. Therefore, the trend observed for the AGN activity is more qualitative than quantitative: it is not the mass of the galaxy that counts, but the fraction of mass that is in the form of a bulge.

In Table A1 we find significant differences in metallicities, the AGNs being less metal rich than the SFGs, and the TOs being intermediate. We also find a significant difference in metallicity between the early and late-type galaxies in Table A2, early-type galaxies being metal poor compared to late-type ones. These results are in good agreement with the difference in mean stellar population ages.

TABLE A2

DUNN'S POST TESTS FOR MORPHOLOGY VS. BULGE MASS, TOTAL MASS, METALLICITY AND GRAVITATIONAL BINDING ENERGY

	$M_{\rm Bulge}$					[O/H]					U/N				
	S0/S0a	Sa	Sab	Sb	Sc	S0/S0a	Sa	Sab	Sb		S0/S0a	Sa	Sab	Sb	Sc
Sa	ns					ns					ns				
Sab	ns	ns				ns	**				ns	***			
Sb	**	***	ns			**	***	ns			ns	***	ns		
Sc	***	***	***	**		***	***	***	ns		***	***	**	ns	
Sd	***	***	***	***	ns						***	***	***	***	ns

	M_B					M_K				
	S0/S0a	Sa	Sab	Sb	Sc	S0/S0a	Sa	Sab	Sb	Sc
Sa	ns					ns				
Sab	ns	ns				ns	ns			
Sb	ns	ns	ns			ns	**	ns		
Sc	**	**	ns	***		ns	***	ns	ns	
Sd	***	***	***	***	**	***	***	***	***	**

In Table A1 we find a strong relation between the gravitational binding energy and the AGN activity. This applies for galaxies having more massive bulges, Table A2. Since we find no such relation for the masses, these results are consistent with a strong dependence of the AGN phenomenon with the gravitational binding energy: the larger the gravitational binding energy, the larger the bulge mass and the higher the probability to find an AGN.

All these results favor an explanation in terms of astration rates: high astration rates produce massive bulges which increases the probability of finding an AGN.

REFERENCES

Abazajian, K. N., et al. 2009, ApJS, 182, 543
Aller, M. C., & Richstone, D. O. 2007, ApJ, 665, 120
Asari, N. V., et al. 2007, MNRAS, 381, 263
Asplund, M., Grevesse, N., Sauval, A. J., Allende Prieto, C., & Kiselman, D. 2004, A&A, 417, 751
Baldwin, J. A., Phillips, M. M., & Terlevich, R. 1981, PASP, 93, 5
Baskin, A., & Laor, A. 2005, MNRAS, 358, 1043
Bell, E. F., McIntosh, D. H., Katz, N., & Weinberg, M. D. 2003, ApJS, 149, 289
Bennert, N., Jungwiert, B., Komossa, S., Haas, M., & Chini, R. 2006, A&A, 446, 919
Binney, J., & Merrifield, M. 1998, Galactic Astronomy (Princeton: Princeton Univ. Press)
Blandford, R. D., Netzer, H., & Woltjer, L. 1990, Active Galactic Nuclei (Berlin: Springer-Verlag)
Blanton, M. R., & Roweis, S. 2007, AJ, 133, 734
Boisson, C., Joly, M., Moultaka, J., Pelat, D., & Serote Roos, M. 2000, A&A, 357, 850
Brodie, J. P., & Huchra, J. P. 1991, ApJ, 379, 157
Bruzual, G., & Charlot, S. 2003, MNRAS, 344, 1000
Chabrier, G. 2003, PASP, 115, 763
Cid Fernandes, R., Mateus, A., Sodré, L., Stasínska, G., & Gomes, J. M. 2005, MNRAS, 358, 363
Cooke, A. J., Baldwin, J. A., Ferland, G. J., Netzer, H., & Wilson, A. S. 2000, ApJS, 129, 517
Coziol, R. 1996, A&A, 309, 345
Coziol, R., Carlos Reyes, R. E., Considère, S., Davoust, E., & Contini, T. 1999, A&A, 345, 733
Coziol, R., Contini, T., Davoust, E., & Considère, S. 1998b, in ASP Conf. Ser. 147, Abundance Profiles: Diagnostic Tools for Galaxy History, ed. D. Friedli, M. Edmunds, C. Robert, & L. Drissen (San Francisco: ASP), 219
Coziol, R., Ribeiro, A. L. B., de Carvalho, R. R., & Capelato, H. V. 1998a, ApJ, 493, 563
Edmunds, M. G., & Pagel, B. E. P. 1984, MNRAS, 211, 507
Evans, I. N., & Dopita, M. A. 1985, ApJS, 58, 125
Faber, S. M., & Gallagher, J. S. 1979, ARA&A, 17, 135
Ferland, G. J., Korista, K. T., Verner, D. A., Ferguson, J. W., Kingdon, J. B., & Verner, E. M. 1998, PASP, 110, 761
Figer, D. F., Rich, R. M., Kim, S. S., Morris, M., & Serabyn, E. 2004, ApJ, 601, 319
Fukugita, M., Ichikawa, T., Gunn, J. E., Doi, M., Shimasaku, K., & Schneider, D. P. 1996, AJ, 111, 1748
Gavignaud, I., et al. 2008, A&A, 492, 637
Genzel, R., & Townes, C. H. 1987, ARA&A, 25, 377
Ghez, A. M., Morris, M., & Becklin, E. E. 2000, AGM, 16, 42

Gültekin, K., et al. 2009, ApJ, 698, 198
Hamann, F., & Ferland, G. 1993, ApJ, 418, 11
Häring, N., & Rix, H.-W. 2004, ApJ, 604, L89
Heckman, T. M. 1980, A&A, 87, 152
Jablonka, P., Martin, P., & Arimoto, N. 1996, AJ, 112, 1415
Jarrett, T. H., Chester, T., Cutri, R., Schneider, S., Skrutskie, M., & Huchra, J. P. 2000, AJ, 119, 2498
Karachentseva, V. E., Mitronova, S. N., Melnyk, O. V., & Karachentsev, I. D. 2010, Astrophys. Bull., 65, 1
Kauffmann, G., et al. 2003, MNRAS, 346, 1055
Kennicutt, R. C., Jr. 1992, ApJ, 388, 310
Kewley, L. J., Dopita, M. A., Sutherland, R. S., Heisler, C. A., & Trevena, J. 2001, ApJ, 556, 121
Kewley, L. J., Groves, B., Kauffmann, G., & Heckman, T. 2006, MNRAS, 372, 961
Kochanek, C. S., et al. 2001, ApJ, 560, 566
Krolik, J. H. 1999, Active Galactic Nuclei: from the Central Black Hole to the Galactic Environment (Princeton: Princeton Univ. Press)
Martínez, M. A., del Olmo, A., Coziol, R., & Focardi, P. 2008, ApJ, 678, L9
Martínez, M. A., del Olmo, A., Coziol, R., & Perea, J. 2010, AJ, 139, 1199
Matsuoka, K., Nagao, T., Marconi, A., Maiolino, R., & Taniguchi, Y. 2011, A&A, 527, 100
McCall, M. L., Rybski, P. M., & Shields, G. A. 1985, ApJS, 57, 1
Melnick, J., Terlevich, R., & Moles, M. 1986, in IAU Symp, 116, Luminous Stars and Associations in Galaxies, ed. C. W. H. DeLoore, A. Wilkis, & P. Laskarides (Dordrecht: Reidel), 505
Miller, C. J., Nichol, R. C., Gómez, P. L., Hopkins, A. M., & Bernardi, M. 2003, ApJ, 597, 142
Nagao, T., Maiolino, R., & Marconi, A. 2006, A&A, 447, 863
Neri-Larios, D. M., Coziol, R., Torres-Papaqui, J. P., Andernach, H., Islas-Islas, J. M., Plauchu-Frayn, I., & Ortega-Minakata, R. A. 2011, Narrow-Line Seyfert 1 Galaxies and their place in the Universe, ed. L. Foschini, M. Colpi, L. Gallo, D. Grupe, S. Komossa, K. Leighly, & S. Mathur (Trieste: PoS SISSA), id. 65 `http://pos.sissa.it/cgi-bin/reader/conf.cgi?confid=126`
Osterbrock, D. E. 1970, QJRAS, 11, 1990
_____. 1989, Astrophysics of Gaseous Nebulae and Active Galactic Nuclei (Mill Valley, CA: University Science Books)
Peterson, B. M., et al. 2005, ApJ, 632, 799
Phillips, M. M., Jenkins, C. R., Dopita, M. A., Sadler, E. M., & Binette, L. 1986, AJ, 91, 1062
Ramos Almeida, C., Pérez García, A. M., Acosta-Pulido, J. A., Rodríguez Espinosa, J. M., Barrena, R., & Manchado, A. 2006, ApJ, 645, 148
Richstone, D., et al. 1998, Nature, 395, 14
Roberts, M. S., & Haynes, M. P. 1994, ARA&A, 32, 115
Sandage, A. 1986, A&A, 161, 89
Schlegel, D. J., Finkbeiner, D. P., & Davis, M. 1998, ApJ, 500, 525
Schödel, R., Merritt, D., & Eckart, A. 2009, A&A, 502, 91
Shemmer, O., Netzer, H., Maiolino, R., Oliva, E., Croom, S., Corbett, E., & di Fabrizzio, L. 2004, ApJ, 614, 547
Storchi Bergmann, T. 1991, MNRAS, 249, 404
Storchi Bergmann, T., & Pastoriza, M. G. 1989, ApJ, 347, 195
Stoughton, C., et al. 2002, AJ, 123, 485
Struck-Marcell, C. 1981, MNRAS, 197, 487
Thurston, T. R., Edmunds, M. G., & Henry, R. B. C. 1996, MNRAS, 283, 990
Tinsley, B. M., & Larson, R. B. 1979, MNRAS, 186, 503
Torres-Papaqui, J. P., Coziol, R., Andernach, H., Islas-Islas, J. M., Ortega-Minakata, R. A., Neri-Larios, D. M., & Plauchu-Frayn, I. 2011, MNRAS, submitted
Turner, E. L., Aarseth, S. J., Blanchard, N. T., Mathieu, R. D., & Gott, J. R., III 1979, AJ, 228, 684
Ulrich, M.-H. J. 1971, ApJ, 163, 441
Vacca, W. D., & Conti, P. S. 1992, ApJ, 401, 543
van Zee, L., Salzer, J. J., Haynes, M. P., O'Donoghue, A. A., & Balonek, T. J. 1998, AJ, 116, 2805
Vazdekis, A., et al. 2010, MNRAS, 404, 1639
Veilleux, S., & Osterbrock, D. E. 1987, ApJS, 63, 295
Viegas, S. M., & de Gouveia dal Pino, E. M. 1992, ApJ, 384, 467
Wake, D. A., et al. 2004, ApJ, 610, L85
Weedman, D. W. 1986, Quasar Astronomy (Cambridge: Cambridge Univ. Press)
York, D. G., et al. 2000, AJ, 120, 1579
Younger, J. D., Hopkins, P. F., Cox, T. J., & Hernquist, L. 2008, ApJ, 686, 815
Zaritsky, D., Kennicutt, R. C., & Huchra, J. P. 1994, ApJ, 420, 87

H. Andernach, R. Coziol, J. M. Islas-Islas, D. M. Neri-Larios, R. A. Ortega-Minakata, and J. P. Torres-Papaqui: Departamento de Astronomía, Universidad de Guanajuato, Apdo. Postal 144, 36000 Guanajuato, Guanajuato, Mexico (heinz, coziol, jmislas, daniel, rene, papaqui@astro.ugto.mx).
I. Plauchu-Frayn: Instituto de Astrofísica de Andalucía (CSIC), E-18008, Granada, Spain (ilse@iaa.ee).

Revista Mexicana de Astronomía y Astrofísica, **47**, 385–399 (2011)

KINEMATICS FROM SPECTRAL LINES FOR AGN OUTFLOWS BASED ON TIME-INDEPENDENT RADIATION-DRIVEN WIND THEORY

J. M. Ramírez

Leibniz-Institut für Astrophysik Potsdam, Germany

Received 2011 January 17; accepted 2011 August 5

RESUMEN

Construimos un modelo de fotoionización dependiente de la velocidad para el absorbedor tibio de NGC 3783. Adoptando formas funcionales de la velocidad del flujo y su densidad del número de partículas con el radio, apropiadas para un viento acelerado por radiación, calculamos el nivel de ionización, la temperatura, el corrimiento Doppler y las profundidades ópticas de las líneas como función de la distancia. El modelo reproduce la relación observada entre la ionización del gas y el corrimiento del centroide de las líneas de absorción en NGC 3783. Este espectro requiere de la presencia de dos flujos: uno altamente ionizado responsable de las alas azules de las líneas de alto grado de ionización y al mismo tiempo las alas rojas de las líneas de menor grado de ionización; y uno de baja ionización que produce las alas azules de las líneas de oxígeno.

ABSTRACT

We build a bulk velocity-dependent photoionization model of the warm absorber of the Seyfert 1 galaxy NGC 3783. By adopting functional forms for the velocity of the flow and its particle density with radius, appropriate for radiation-driven winds, we compute the ionization, the temperature, the line Doppler shift, and the line optical depths as a function of distance. The model reproduces the observed relationship between the gas ionization and the velocity shift of the absorption line centroids in the X-ray spectrum of NGC 3783. The distribution of asymmetry seen in this spectrum requires the presence of two outflows: a higher ionization component responsible for the blue wings of the high ionization lines and the red wings of the low ionization oxygen lines, and a lower ionization flow that produces the blue wings of the oxygen lines.

Key Words: galaxies: Seyfert — quasars: absorption lines — quasars: individual (NGC 3783)

1. INTRODUCTION

X-ray (0.5–10 keV) *Chandra* spectra of type-I active galactic nuclei (AGN) often show the presence of absorption lines coming from H- and He-like ions of O, Ne, Mg, Si, S as well as from Fe XVII-Fe XXIII L-shell transitions. These lines are near the region of the bound-free absorption edges of O VII and O VIII at ∼0.8 keV, which are the hallmark of warm absorbers (George et al. 1998; Komossa 1999). In Seyfert 1 galaxies these absorption lines can be narrow (Seyfert 1 NALs) with full width at half maximum (FWHM) spanning ∼100–500 km s^{-1} (Kaspi et al. 2000), or broad (Seyfert 1 BALs) with FWHM ∼500–2000 km s^{-1} (Kaspi et al. 2001). The troughs of the lines are blue-shifted relative to rest frame of the host galaxy with velocities that go from several hundred to a few thousand km s^{-1} (Yaqoob et al. 2003), implying the presence of outflows that cover a wide range of velocities and ionization stages (Kaastra et al. 2000; Kaspi et al. 2002; Krolik & Kriss 2001; Różańska et al. 2006).

In Seyfert galaxies and quasars, absorption spectra show a range of ionization stages that arise from ionization parameters that span ξ∼10–1000 erg cm s^{-1} (Kaspi et al. 2002). Simultaneous UV and X-ray observations may enhance this range

even further (Shields & Hamann 1997; Gabel et al. 2005). The location of these absorbing material is uncertain. Models of X-ray absorbers in AGN place them in a wide range of distances from the central source, from winds originated at the accretion disk (Murray et al. 1995; Elvis 2000), out to the dusty (∼1 pc) torus (Krolik & Kriss 2001) and beyond the narrow-line region (e.g., Ogle et al. 2000).

In the Seyfert galaxy NGC 3783 the 900 ks *Chandra* spectrum of Kaspi et al. (2002) allows the precise measurements of radial velocities and widths of the lines. It is seen that the velocity shift of lines from Fe XXIII-Mg XII covers a range of ∼60–600 km s^{-1} while the low-ionized lines Si XIII-O VII cover velocities ∼500–1000 km s^{-1} (see Figure 6 in Ramírez, Bautista, & Kallman 2005). The average velocity of the warm absorber outflow of NGC 3783 is around ∼500 km s^{-1}. The spectrum also reveals that the line profiles are asymmetric (Kaspi et al. 2002), in such a way that approximately 90% of the lines have extended blue wings. Such asymmetries were quantified by Ramírez et al. (2005). In terms of ionization, mostly high ionization species are seen in the short-wavelength portion of the spectrum ∼4–12 Å. Here, resonant lines from Fe XXIII, Fe XXII, Fe XXI, S XVI, S XV, Si XIV, and Mg XII cover ionization parameters ξ from ∼630 to ∼150 erg cm s^{-1}. The longer wavelengths of the spectrum, ∼10–20 Å, are dominated by lower ionization lines from Si XIII, Fe XVIII, Ne X, Mg XI, Fe XVII, Ne IX, O VIII, and O VII that span ionization parameters ξ from ∼125 erg cm s^{-1} down to ∼8 erg cm s^{-1}.

Thus, photoionization modeling shows that the observed spectrum is hardly explained by a single ionization parameter. Rather two or three components are needed, and this has been the subject of well-detailed studies (Krongold et al. 2003; Netzer et al. 2003; Krongold et al. 2005). In these papers two/three components in pressure equilibrium are enough to account for all the charge states seen in the spectra. At the start of these simulations, the ionization parameter is not kept constant throughout the cloud but made to vary in a self-consistent way. On the other hand, Steenbrugge et al. (2003) used a nearly continuous distribution of ionization parameters that spans three orders of magnitude. In reality both approaches do not need to be contradictory. We just have to look at the possibility of introducing species between the components proposed by Krongold et al. (2003); Netzer et al. (2003); Krongold et al. (2005); and this immediately leads us to the discussion of whether the material absorbing is clumpy or not. And this is in part the goal of the present work. We present both possibilities, continuous *vs* clumpy flows, with their physical implications.

Although there is no evident correlation between the ionization of the absorption species and the velocity shifts of lines (Kaspi et al. 2002), Ramírez et al. (2005) suggested the possibility for such relationship to exist, as the lines are consistent with being originated from an outward flowing wind. In that work a wind velocity law was adopted (Castor, Abbott, & Klein 1975), with an ionization fraction that goes as a power-law of the ionization parameter $q \sim \xi^{\eta}$ with $\eta > 0$ for all ξ and all lines. Further, $q \sim \xi^{\eta}$ and an optical depth of the form proposed by the SEI method from Lamers, Cerruti-Sola, & Perinotto (1987) were used to fit the lines in the spectrum and to study the possible relationship between the profiles and the expansion velocity of the flow.

Here, in this theoretical approach no analytical dependence of q with ξ is assumed, but it is computed self-consistently using the photoionization code XSTAR with modifications of the optical depth of the lines to work with an expanding outflow.

It is the aim of the present paper to further study the wind scenario for the warm absorber of NGC 3783 by modeling a photoionized wind flow and trying to reproduce the main features in the spectrum in terms of both equivalent widths and line profiles. The model consists of a spherically symmetric gas flow with velocity increasing with radius according to the wind velocity law of Castor et al. (1975). The microphysics of the plasma is then solved in detail along the wind, and radiative transfer is treated for the flowing plasma including Doppler shift effects on the emerging spectrum. This kind of approach has been used previously in studies of the ionization and thermal properties of O stars by Drew (1989), on cataclysmic variables by Drew & Verbunt (1985) and in an evaluation of absorption line profiles from winds in AGN by Drew & Giddings (1982).

Self-consistent hydrodynamic modeling of AGNs has been performed in the past (see e.g., Murray et al. 1995) who qualitatively predict the same β-velocity law, where $v(r) \sim (1 - r_0/r)^{\beta}$, as adopted here. However, these models did not include a detailed treatment of the thermal and spectral processes that lead to synthetic spectra.

The present paper is organized as follows: In § 2 we discuss the statistical significance of the X-ray lines under study. Later in § 3, we present the theoretical method we have used in this work. In § 5 we present the main results of our work. We present

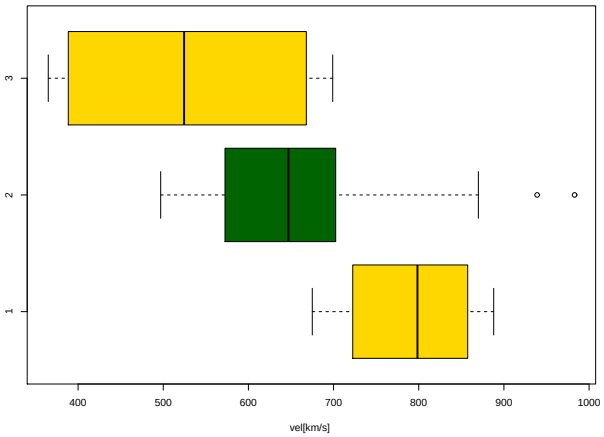

Fig. 1. Statistical significance of the shifting of the X-ray lines found in the spectrum of NGC 3783. Each box is made of five-number summaries: the smallest observation (sample minimum, which are the thin bars at the extreme left of each box), a lower quartile (Q1, which is the left thick border of each box), the median (Q2, black thick vertical line), the upper quartile (Q3, the right thick border of each box) and largest observation (sample maximun, which are the thin bars at the extreme right of each box).

the final physical solution in § 6. We summarize in § 7.

2. SIGNIFICANCE OF THE SHIFTING IN THE X-RAY LINES

Since our analysis searches for possible correlation between the ionization state of the ions forming the absorption lines observed in the X-ray spectrum of this object, and the Doppler velocity shift of those lines, we first study the statistical significance of this possible shifting. A convenient way to do this is through the separation of the ions into groups to search for the velocity shifting. We take all the ions we find in Table 3 (see Table 3 below). The line's centroids are taken from Kaspi et al. (2002). The ionization fraction curves for the classification are taken from Kallman & Bautista (2001); Bautista & Kallman (2001). Afterwards we collect them into three groups[1]: Group 1, representative of all ions of low ionization with ionization parameter $0 < \xi(\mathrm{erg\ cm\ s^{-1}}) < 10$; Group 2, $10 < \xi(\mathrm{erg\ cm\ s^{-1}}) < 250$, representative of intermediate ionization state; and Group 3, $250 < \xi(\mathrm{erg\ cm\ s^{-1}}) < 650$. A graphical way to represent this grouping scheme is shown in Figure 1. Each box is made of five-number summaries: the smallest observation (sample minimum, which is the thin bar at the extreme left of each box); a lower quartile (Q1), which is the left thick border of each box; the median (Q2), the black thick vertical line; upper quartile (Q3), the right thick border of each box and largest observation (sample maximum) which is the thin bar at the extreme right of each box. The first conclusion is that all three Q2s are different. It is clear that Groups 1 and 3 are different at $\gtrsim 1\sigma$. There is overlap between Groups 1 and 2 (possibly due to limited resolution of the instrument), but Groups 2 and 3 are different at $\gtrsim 1\sigma$. We continue our analysis bearing in mind these overlaps in the groups.

[1]We group and generate the figure using the statistical package R (`http://www.r-project.org`).

3. METHOD

Let us consider a radiation source with $L \sim 10^{44} - 10^{47}$ erg s^{-1}, arising from a supermassive ($\sim 10^8\ M_\odot$) black hole (BH). Material $\sim$0.1–1 pc from the BH only needs to absorb a small fraction of this energy to be accelerated to few thousand km s^{-1} in Seyfert galaxies and up to 0.1–0.2 c in high redshift Quasars (Arav, Li, & Begelman 1994; Ramírez 2008; Saez, Chartas, & Brandt 2009; Chartas et al. 2009). By conservation of mass the number density of hydrogen can be written, assuming spherical symmetry, as

$$n_H(r) = \frac{\dot{M}}{4\pi r^2 v(r) \mu m_H}, \tag{1}$$

where $\dot{M}$ is the mass-loss rate, $v(r)$ is the outflow speed at radius r, μ is the mean atomic weight per hydrogen atom and m_H is the hydrogen mass.

We adopted a velocity law $v(r)$ compatible with the predictions of the radiatively driven wind theory (Castor et al. 1975). The velocity law has two fundamental roles. The first is to shift the frequency of the absorbing lines according to the Doppler effect. The second is to dilute the gas density, affecting radiative transfer across the gas and consequently the ionization and thermal state of the gas. The velocity law varies with distance as

$$w(x) = w_0 + (1 - w_0)\left(1 - \frac{1}{x}\right)^{\beta}. \tag{2}$$

Here, w is the velocity normalized to the terminal velocity of the wind v_∞, w_0 is the velocity in the base of the wind and x is the distance normalized to the radius of the central core r/r_0. The parameter β is the quantity governing the slope of the velocity with the distance and its *ad hoc* value depends on the type of radiative force acting on the wind. Analysis of hot stars suggests that $0.5 \lesssim \beta \lesssim 1$ (Lamers et al. 1987). The evaluation of radiation-driven wind in AGNs of Drew & Giddings (1982),

and more recent dynamical calculations (e.g., Murray et al. 1995; Proga, Stone, & Kallman 2000), suggest that in AGNs $0.5 \lesssim \beta \lesssim 2$. We have computed models using velocity laws $\beta = 0.5, 1, 1.5$ and 2, representing a range from fast ($\beta = 0.5$) to slow winds ($\beta = 2$). We found that fast winds were not able to simultaneously cover the range in velocity and ionization state observed in the spectrum of NGC 3783, needed for the goal of this work, and that the best-fit velocity law was $\beta = 2$. This is why for the rest of this work we use $\beta = 2$. Then, we rewrite the number density in terms of the velocity law as,

$$n_H(x) = n_0 x^{-2} w^{-1}, \tag{3}$$

where $n_0 = \left(\frac{\dot{M}}{4\pi\mu m_H} r_0^{-2} v_\infty^{-1}\right)$. The absorbing line frequencies are shifted according to the Doppler relation,

$$w = \frac{c}{v_\infty}\left(1 - \frac{\lambda}{\lambda_0}\right), \tag{4}$$

where λ_0 is rest wavelength.

Our models are based on clouds illuminated by a point-like X-ray source. The input parameters are the source spectrum, the gas composition, the gas density $n_H(x)$, and the outflow velocity $w(x)$, where x is the position of each slab inside the cloud normalized to the radius of the most exposed face to the source, r_0. The source spectrum is described by the spectral luminosity $L_\epsilon = L f_\epsilon$, where L is the integrated luminosity from 1 to 1000 Ryd, and $\int_1^{1000\mathrm{Ryd}} f_\epsilon d\epsilon = 1$. This spectral function is taken to be a power law $f_\epsilon \sim \epsilon^{-\alpha}$, with $\alpha = 1$. The gas consists of the following elements, H, He, C, N, O, Ne, Mg, Si, S, Ar, Ca and Fe. We use solar abundances of Grevesse, Noels, & Sauval (1996), in all our models.

Thermal and statistical equilibrium in our models are computed with the code XSTAR (Kallman & Bautista 2001; Bautista & Kallman 2001). The code includes all relevant atomic processes and computes the equilibrium temperature and optical depths of the most prominent X-ray and UV lines identified in AGN spectra.

We consider two types of models, the single absorber model (SA) and the multicomponent model (MC). In both cases the absorption line profiles depend simultaneously upon the ionization and the kinematics of the absorbing gas.

3.1. *The Single absorber Model*

This model consists of a single extended cloud directly in the line of sight between the observer and the central source. Such a cloud flows away from the central source and towards the observed. For this model we make use of the Sobolev approximation for computing the line optical depths (Castor et al. 1975),

$$\tau_\nu(r) = \frac{\pi e^2}{mc} f \lambda_0 n_i(r) \left(\frac{dv}{dr}\right)^{-1}, \tag{5}$$

where f is the absorption oscillator strength, λ_0 (in cm) is the laboratory wavelength of the transition, n_i (in cm^{-3}) is the number density of the absorbing ion, and dv/dr is the velocity gradient in the wind. This gives us the relation between the outflow state and the radiation field. This is different from the calculation of the optical depth in the static case, which is directly proportional to the column density.

Inside the cloud we use a one-step forward differencing formula for the radiation transfer (Kallman & McCray 1982)

$$L_\nu(r + \Delta r) = L_\nu(r) e^{-\tau_\nu(r)} + 4\pi r^2 j_\nu(r) \frac{1 - e^{-\tau_\nu(r)}}{\kappa_\nu(r)}, \tag{6}$$

where $j_\nu(r)$ is the emission coefficient at radius r.

Under ionization equilibrium conditions the state of the gas depends just upon the shape of the ionizing spectrum and the ionization parameter ξ, that we define as in Tarter, Tucker, & Salpeter (1969)

$$\xi(r) = \frac{4\pi F(r)}{n_H(r)}, \tag{7}$$

where $F(r)$ is the total ionizing flux,

$$F(r) = \frac{1}{4\pi r^2} \int_1^{1000\mathrm{Ryd}} L_\nu(r) d\nu, \tag{8}$$

with $L_\nu(r)$ given by equation (6). The requirement that ξ spans various orders of magnitude, as observed, yields a cloud geometrically thick throughout most of the spectrum, i.e. a *photoionization bounded* cloud. For instance, a luminosity $L \sim 10^{44}$ erg s^{-1} and $\Delta\xi = \xi_2 - \xi_1 = \frac{L}{n}(\frac{1}{r_2^2} - \frac{1}{r_1^2}) = 10^3$ yield $n \sim 10^6$ cm^{-3} and the column density of the absorbing material is $N_H \sim n\Delta R \sim 9.7 \times 10^{24}$ cm^{-2}. This is a large value, such that even lines with moderately small oscillator strengths become saturated in the emergent spectrum, unless the metal abundances are reduced by several orders of magnitude with respect to solar.

In Figure 2 we compare the computed optical depth for the Ne X λ12.134 line in a stationary nebula with $L = 10^{44}$ erg s^{-1}, and constant density $n = 10^6$ cm^{-3} with a flow with $n(x) = 3.3 \times 10^6 x^{-0.5} w^{-1}$, a wind velocity function with $\beta = 2$, and $v_\infty =$

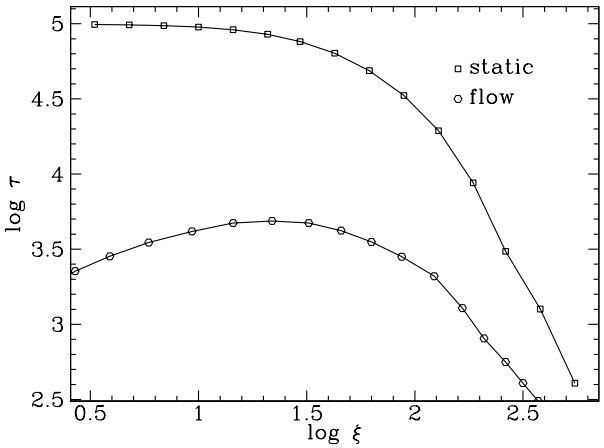

Fig. 2. Optical depth (τ) static case vs outflow model for the line Ne X λ12.134 (see text).

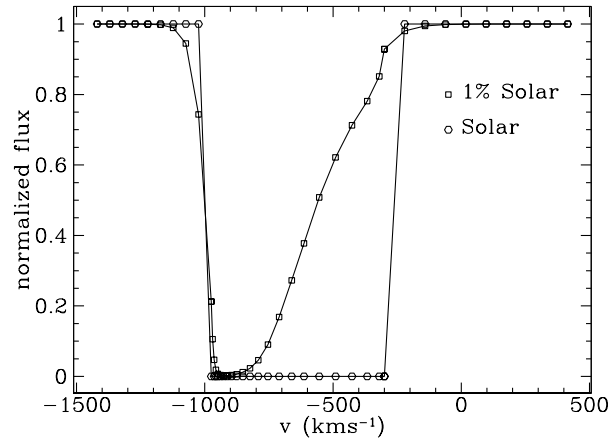

Fig. 3. Profile of the line Ne X λ12.134 formed by taking $F_\lambda(v) = F_c \times \exp[-\tau_\lambda(v)]$ as function of the velocity. The rectangle profile is made by a cloud with solar abundances (open circles). The profile with an extended red wing and a sharp blue wing is made by a cloud with 1% solar abundances (open square).

1000 km s^{-1}. In both cases we adopt a turbulence velocity of 200 km s^{-1} and solar abundances. In the stationary case, τ is proportional the column density of the absorbing material and can reach very large values. In the outflow model, τ peaks at $\log\xi \sim 1.3$ ($v \sim 890$ km s^{-1}) reaching $\sim$5000, that is, nearly two orders of magnitude smaller than in the stationary cloud for the same ξ. Such high optical depths are common to other lines in the X-ray band, like O VIII in the 14–20 Å and the line O VIII λ18.969. In such cases lines appear saturated in the absorption spectrum in contrast with observation. In Ramírez et al. (2005) we fitted the integrated optical depths of resonant lines in the spectrum of NGC 3783 and found $T_{\rm tot} \lesssim 1$ for most of the lines. We illustrate in Figure 3 the consequences of taking this model for the reproduction of the profile of the line Ne X λ12.134. In order to have a non-saturated line (as observed), we had to reduce the abundance to $\sim$1% solar, which has no physical motivation. We do not go further with this model, and present the clumpy (multicomponent) scenario in the next section.

3.2. *The Multicomponent Model*

Now, we examine the scenario in which the absorption profile seen in the X-ray and UV spectra of AGNs are made up of multiple components. The main difference between this model calculations and previous ones by other authors (e.g., Kaspi et al. 2002; Krongold et al. 2003; Różańska et al. 2006), is that in our model all the components are linked by a velocity law and a gas density distribution.

Each absorber is specified by an ionization parameter ξ, a column density N_H, an absorption covering factor, a gas density $n_H(r)$ and an outflow velocity $v(r)$ in order to shift the absorption lines according to the Doppler effect. Once the ionic fraction is calculated from the ionization equations, and the ionic levels computed, the opacity in each frequency bin is

$$\kappa_\nu \rho = \frac{\pi e^2}{m_e c} f_l n_l \left[1 - \frac{n_u g_l}{n_l g_u}\right] \phi(\Delta\nu), \qquad (9)$$

where κ_ν is the opacity at the frequency ν, $\rho = \mu m_H n_H$ is the mass density, f_l is the absorption oscillator strength, n_l, n_u (in cm^{-3}), g_l, g_u are the number density and the statistical weight of the lower and upper levels of the transition, respectively. We allow for the lines to have a finite width characterized by the line profile $\phi(\Delta\nu)$, with a width which is the greater one between the thermal and the turbulent motions. In all our models the turbulence velocity is assumed to be 200 km s^{-1}. The optical depth of a line in each component is

$$\tau_\nu = \int_{r_1}^{r_2} \kappa_\nu(r)\rho(r)dr, \qquad (10)$$

where r_2 and r_1 are the limits of the cloud.

It is important to highlight a special difference between the way we use the ionization parameter in the MC model and the way it is used in the SA model. Because the clouds intervening in this model are optically thin, the ionization parameter at the most exposed face of the cloud remains essentially constant through the cloud, i.e.

$$\xi(r) = \frac{4\pi F(r)}{n_H(r)}, \qquad (11)$$

where $F(r)$ is the total ionizing flux at the radius r.

When two or more outflows are put together they are assumed to be distributed such that the observed spectrum is the result of the addition of all components. Thus, the radiative flux in each bin of frequency for the composite spectrum is

$$F_\nu = \sum_{i=1}^{m} f_\nu(x_i), \tag{12}$$

where m is the number of absorbing clouds in the line-of-sight, $f_\nu(x_i)$ is the flux resulting from the pass of the continuum radiation through the absorbing cloud i, and x_i is the normalized spatial radius of the cloud.

In Ramírez et al. (2005), it is shown that in order to fit the line profiles in NGC 3783 a geometry for the gas distribution different from spherical is required. Such a deviation from spherical geometry has two effects. In the normalized notation the number density is

$$n_H(x) = n_0 x^{-2+\kappa} w^{-1}, \tag{13}$$

where $0 \leq \kappa \leq 2$. A positive value of κ implies that the gas flow dilutes more slowly than in a free spherical expansion, i.e. that there are sources of gas embedded in the flow, or that the flow is confined. A negative value corresponds to sinks of gas in the flow, or expansion of an initially confined flow in a flaring geometry.

Secondly, we allow the radiation flux to have a form

$$F = F_0 \times x^{-2-p}, \tag{14}$$

where p is an index to mimic a deviation of flux from the pure geometrical dilution case. This is expected if the medium between clouds has a significant optical depth (if p is positive) or if there are sources of radiation embedded in the flow (if p is negative).

4. ASSUMPTION ABOUT THE NUMBER DENSITY

Before going into the presentation of the results we would like to highlight important differences between the underlying physical/geometrical motivation of the present work and previous ones. After reviewing the single (geometrically thick) model and the clumpy (geometrically thin) model, we favored the latter, and require for the production of the line profile found in the spectrum of Seyfert galaxies that $\Delta R/R \ll 1$ (also based on results by Gabel et al. (2005) from UV data).

Based on UV CIII* density constraints (Gabel et al. 2005), the electron density for the absorber could be $n_e \approx 10^4$ cm^{-3}. With this (using equation 11 and $n_H \approx n_e/1.2$), the distance between the absorber and the central source is $R \approx 25$ pc ($\approx 10^{20}$ cm). As in Gabel et al. (2005), the low ionization species (XLI in that paper) seems to share the same kinematics with the UV absorber. Using a typical luminosity L for this object of $\approx 10^{44}$ erg s^{-1}, $n_H \approx 10^4$ cm^{-3}, and an ionization parameter of $\xi \approx 1$, $R \approx 10^{20}$ cm; similar to that computed by Gabel et al. (2005); but if we take $n_H \approx 10^{11}$ cm^{-3}, as is required for $\Delta R \ll R$, then $R \approx 10^{16.5}$ cm. This is not in contradiction with Krongold et al. (2005), where they set limits on the density and location of the absorber; with $n_e > 10^4$ cm^{-3}, and $D < 5.7$ pc. However, is clearly different from the computation made by Netzer et al. (2003), of $n_e < 5 \times 10^4$ cm^{-3} $D > 3.2$ pc for the $\log(U_{\rm ox}) = -2.4$ component, $n_e < 10^5$ cm^{-3} $D > 0.63$ pc for the $\log(U_{\rm ox}) = -1.2$ component, and $n_e < 2.5 \times 10^5$ cm^{-3} $D > 0.18$ pc for the $\log(U_{\rm ox}) = -0.6$ component. It is clear that some of the differences in the estimations can be due to differences in the nature of the physics behind the estimations. In Krongold et al. (2005) (and also Reeves et al. 2004, for the Fe K shell), the fundamental assumption behind the computation of n_e is that the absorber responds instantaneously to changes of flux of the ionizing source, while in Netzer et al. (2003) the estimations are based on temperature derived models, average recombination rates and no response to continuum variations on timescales of 10 days. And, for our purposes, this basically translates into differences between the two proposed physical mechanisms: thermally accelerated winds, which in principle have to consider a sublimination radius for the material not being evaporated, and radiatively accelerated winds with origin possibly in the accretion disk of subparsec scale; both are competitor theories in the explanation of the origen of the warm-absorber outflows.

5. RESULTS AND DISCUSSIONS

In Figure 4 we show the variation of the different variables governing the kinematics and the ionization structure of one of our models (model A). This is a wind with a velocity slope $\beta = 2$, $\kappa = 1.5$ and $p = 1.5$. The number of kinematic components m is 11. The assumed abundance is solar, as is given in Table 1, and each component has a column density $N_H = 5 \times 10^{20}$ cm^{-2}. In this model the variation in the ionization parameter is $\log \xi = 3.5 - (-0.65)$ [erg cm s^{-1}], where the "launching" ionization parameter is defined as $\log \xi_0 = 3.5$ [erg cm s^{-1}], and the variation in density $\log n_H = 11.4 - 10.26$ [cm^{-3}].

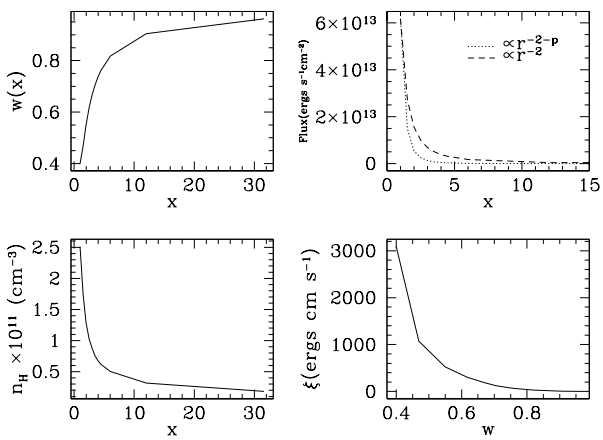

Fig. 4. Variation of the main kinematic and ionization variables for model A (see text). Upper left: Velocity law $w(x)$ for the model. Upper right: The ionizing radiative flux, decaying as $\propto r^{-2}$ (dashed line) and as $\propto r^{-2-p}$ (dotted line). Lower left: Variation of the density as function of x. Lower right: Variation of the ionization parameter (ξ) with the normalized velocity.

TABLE 1

COMPOSITION AND PARAMETER VALUES OF THE KINEMATIC MODEL A[a]

Element	Relative Abundance
H	1.0
He	0.1
C	0.3540E-03
N	0.9330E-04
O	0.7410E-03
Ne	0.1200E-03
Mg	0.3800E-04
Si	0.3550E-04
S	0.2140E-04
Ar	0.3310E-05
Ca	0.2290E-05
Fe	0.3160E-04

[a]In this model $w_0 = 0.4$, $v_\infty = 900$ km s^{-1}, $\log_{10} r_0 = 15.75$ [cm], $v_{\rm turb} = 200$ km s^{-1} and $N_H = 5\times10^{20}$ cm^{-2}.

We can see the variation with distance of the input parameters w, flux, n_H and ξ, for model A in Figure 4. In Figure 5 we plot the velocity shifts taken from the maximum line optical depths $\tau_{\rm max}$ of our model versus the line centroids measured by Kaspi et al. (2002) for NGC 3783 (see Table 3 in that paper).

We fit a linear model by robust regression using the M estimator (Huber 1964). The weights are included as the inverse of the variances, with the variance equal to $\Delta v = (v_{\rm lo}+v_{\rm hi})/2$, and $v_{\rm lo}$, and $v_{\rm hi}$ are the differences between centroid and lower and upper velocity limits of the measured lines given in Table 3 of Kaspi et al. (2002). The best-fit slope is 0.97 ± 0.31 (solid line in the figure), and the residual standard error (rms) is 15.4 for 25 degrees of freedom (dof). The agreement is encouraging, considering that no model has been suggested before to explain the possible correlation between the ionization parameter and the velocity shift seen in this Seyfert galaxy.

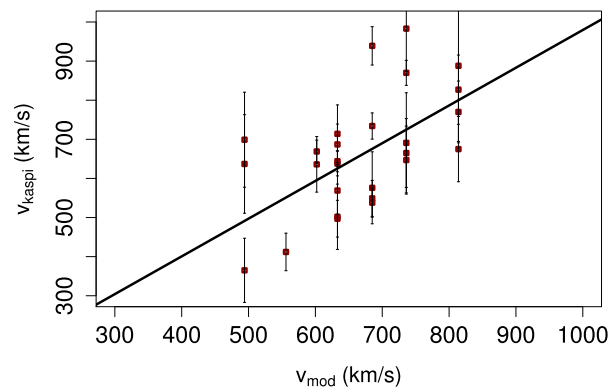

Fig. 5. Measured vs model predicted velocities for the group of unblended lines given in Table 2 of Ramírez et al. (2005). The measurements are taken from Kaspi et al. (2002). The solid line is the best line after a linear regression for model A.

Although the velocity shifts measured with respect to line minima are well explained by this model the distribution (in general) of the line profile shapes is not in agreement with that reported in Ramírez et al. (2005), for instance. From that study, most lines have extended blue wings. On the other hand, the model does predict the correct asymmetries for a few lines from highly ionized species, but the profiles of the lower ionizations lines exhibit more extended red wings, unlike the observations. The discrepancy between the modeled profile of the O VIII λ18.9 line and that observed in NGC 3783 is important. This is why we created model B.

In Figure 6 we present the variation of the variables governing the kinematics and the ionization structure of another model (model B). Here we change slightly the parameters $\log\xi_0$, and v_∞ (see Table 2 for details). The wind has the parameters $\beta = 2$, $\kappa = 1.5$ and $p = 1.5$. The number of kinematic components m is 11. The abundances and the column density are as in model A. In this model the variations in ionization parameter and density are $\log\xi = 3.00 - (-1.13)$ [erg cm s^{-1}] and

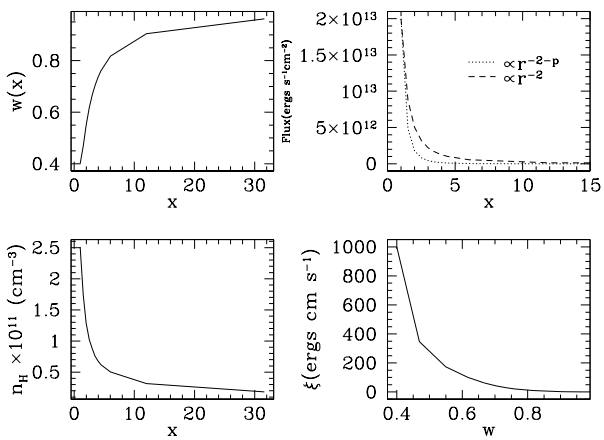

Fig. 6. Variation of the main kinematic and ionization variables for model B (see text). Upper left: Velocity law $w(x)$ for the model. Upper right: The ionizing radiative flux, decaying as $\propto r^{-2}$ (dashed line) and as $\propto r^{-2-p}$ (dotted line). Lower left: Variation of the density as function of x. Lower right: Variation of the ionization parameter (ξ) with the normalized velocity.

TABLE 2

COMPOSITION AND PARAMETER VALUES OF THE KINEMATIC MODEL B[a]

Element	Relative Abundance
H	1.0
He	0.1
C	0.3540E-03
N	0.9330E-04
O	0.7410E-03
Ne	0.1200E-03
Mg	0.3800E-04
Si	0.3550E-04
S	0.2140E-04
Ar	0.3310E-05
Ca	0.2290E-05
Fe	0.3160E-04

[a]In this model $w_0 = 0.4$, $v_\infty = 1100$ km s^{-1}, $\log_{10} r_0 = 15.75$ [cm], $v_{\rm turb} = 200$ km s^{-1} and $N_H = 5\times10^{20}$ cm^{-2}.

$\log n_H = 11.40 - 10.26$ [cm^{-3}]. We compare models A and B in terms of the variation of optical depth vs. velocity of the flows of three important lines, i.e, Si XIV λ6.182, Si XIII λ6.648 and Mg XII λ7.106. We could estimate the contribution of each cloud to the formation of the composite profiles of these lines. We note that model B is superior to model A in describing the low-velocity portion of the flow reflected by the high ionization lines seen in NGC 3783 (extended blue wings), but yields a worse description of the spectrum at the higher terminal velocities responsible for the center of the lines measured by Kaspi et al. (2002).

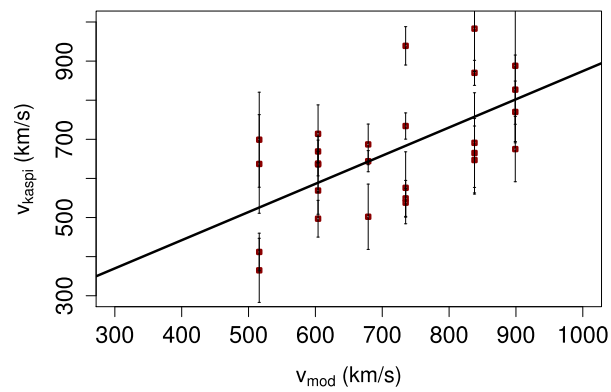

Fig. 7. Measured vs model predicted velocities for the group of unblended lines given in Table 2 of Ramírez et al. (2005). The measurements are taken from Kaspi et al. (2002). The solid line is the best line after a linear regression for model B.

Figure 7 shows the fit of a linear model by robust regression using the M estimator for model B. As in model A, the weights are included as the inverse of the variances, with the variance equal to $\Delta v = (v_{\rm lo} + v_{\rm hi})/2$, and $v_{\rm lo}$, and $v_{\rm hi}$ are the differences between centroid and the lower and upper velocity limits of the measured lines given in Table 3 of Kaspi et al. (2002). The best-fit slope is 0.72 ± 0.20 (solid line in the figure), and the residual standard error (rms) is 17.6 for 25 degrees of freedom (dof). In general, the scatter becomes worse for lines with terminal velocities greater than 1100 km s^{-1}.

5.1. *Modeling global properties - ξ vs velocity*

One of the prime goals of this study is to examine the relationship between the kinematics and the ionization structure of the flow. This is complementary to earlier work (Krongold et al. 2003; Netzer et al. 2003; Krongold et al. 2005) which follows the algorithm of constructing a grid of static photoionization models, with varying ionization parameter and column density, with the selection of this quantities which best reproduce the EW observed in the spectra, in addition to paying attention to the relationship between these physical parameters and the position in wavelength space of the absorption troughs.

Krongold et al. (2003) fitted photoionization models to the 900 ks spectrum of NGC 3783 using

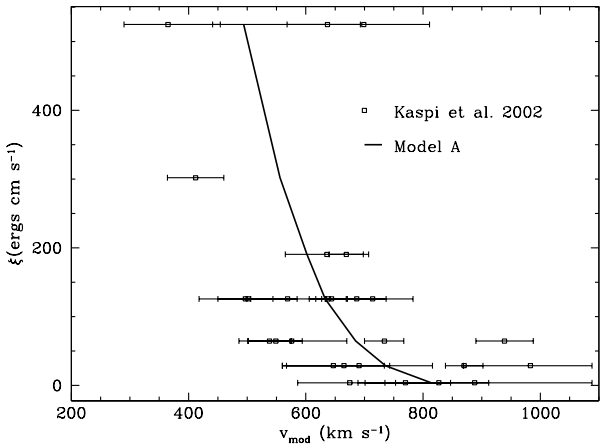

Fig. 8. Relationship between the ionization parameter and velocity. The solid line is the theoretical prediction for model A. The open squares with error bars are points with velocities taken from Kaspi et al. (2002), for the group of lines compared in Figure 5.

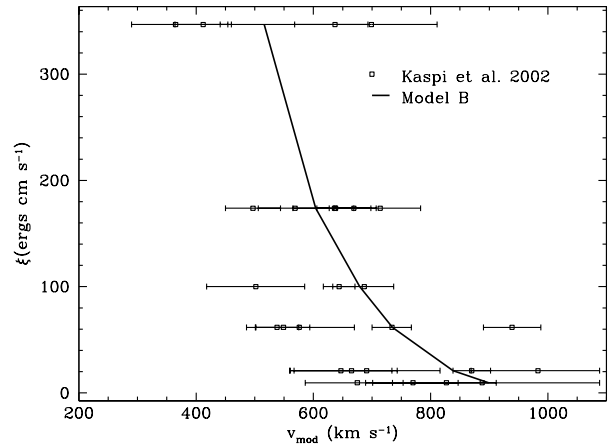

Fig. 9. Relationship between the ionization parameter and velocity. The solid line is the theoretical prediction for model B. The open squares with error bars are points with velocities taken from Kaspi et al. (2002), for the group of lines compared in Figure 7.

two phases; one at high ionization and high temperature log $T \sim 5.98$ (HIP) and one at low ionization and temperature log $T \sim 4.41$ (LIP), finding good agreement between the modeled equivalent width (EW) and the measured one for a set of absorption lines (see Figure 9 of Krongold et al. 2003). They set each of these phases at a single outflow velocity of $\sim$750 km s^{-1}, assuming spatial coexistence of the two absorbers. The approach was similar to that from Netzer et al. (2003), but in the latter they used three components in pressure equilibrium, with two kinematic components each.

One property of our model is the capability of allowing the possibility of establishing[2] a relationship between the ionization and the kinematics of the gas based on a radiatively accelerated wind. Figures 8 and 9 show this relation for models A and B, respectively. These plots show the predicted relationship between the observed velocities and the ionization parameter. While absorption from highly ionized ions originates from low-to-intermediate (200–600 km s^{-1}) velocities, lines from lower ionization stages are formed at intermediate-to-high velocities (600–1000 km s^{-1}).

5.2. *Far-UV and UV absorbers*

The relationship between the X-ray absorption spectrum and the UV absorption spectrum is at present a subject of controversy. Kraemer, Crenshaw, & Gabel (2001) and Gabel et al. (2003, 2005) have analyzed de UV spectrum of NGC 3783. HST/STIS and FUSE spectra show absorption troughs from the low order Lyman series (i.e. Lyα, Lyβ, Lyγ), C IV $\lambda\lambda$1548.2, 1550.8, N V $\lambda\lambda$1238.8, 1242.8, O VI $\lambda\lambda$1032, 1038. All these lines are seen in three kinematic components at -1365, -548, and -724 km s^{-1} (components 1, 2 and 3 respectively). A weak fourth component is reported by Gabel et al. (2003, 2005) at -1027 km s^{-1}. Figure 10 shows the spectrum predicted by model B in the range 700–1700 Å. It is clear from this figure that lines due to the low order Lyman series, He II, C IV, N V, O VI, and Ne VIII would be

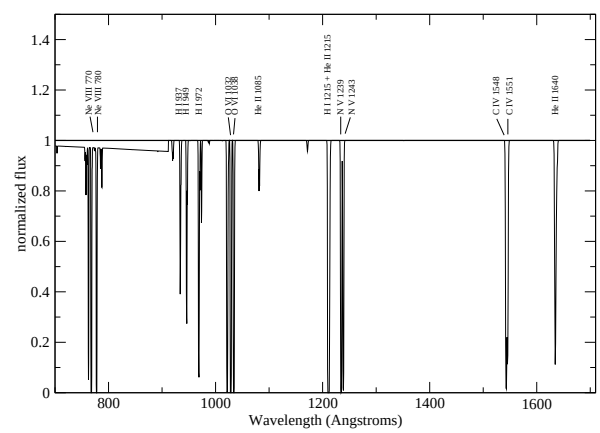

Fig. 10. Predicted UV spectrum by model B (in the range 700–1700 Å). These absorption lines are formed by the faster (or at lower ionization parameters) clouds of model B, i.e., $\log \xi = 0.12, -0.65$. Most of these lines are found in real UV spectra of AGN.

[2]We explicitly state *allow the possibility*, since the limited resolution of the telescope does not allow us to go beyond this possibility.

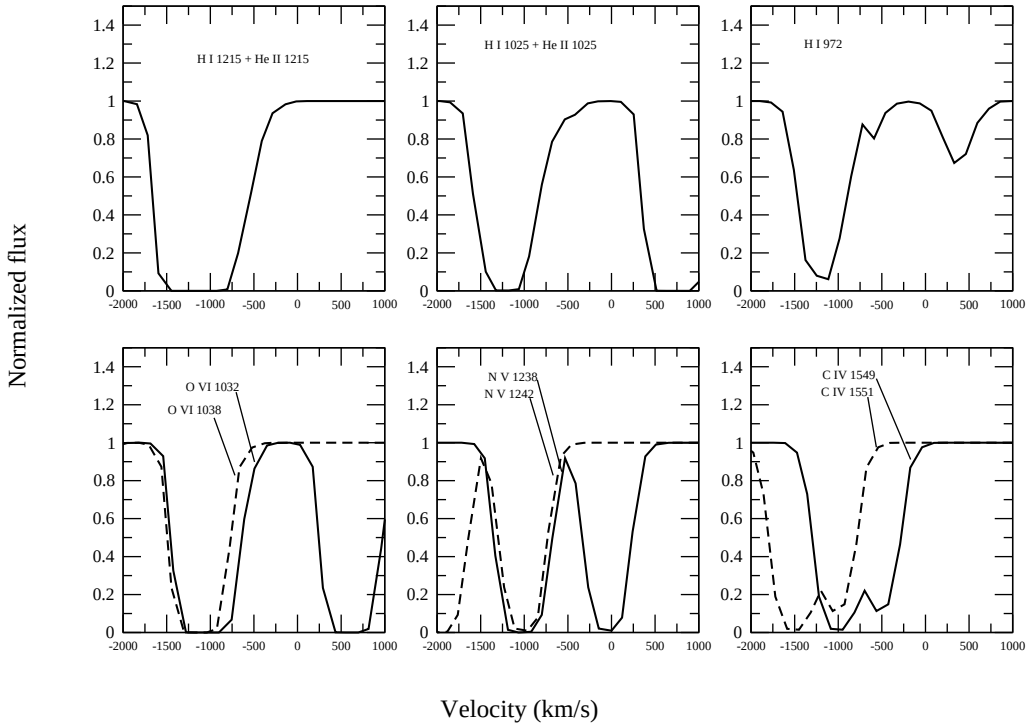

Fig. 11. Predicted UV spectrum by model B (in velocity space). These absorption lines are formed by the faster clouds (or by those at lower ionization parameters) of model B, i.e., $\log \xi = 0.12, -0.65$. Some of the velocities displayed by these lines are shared by lines coming from the X-ray band. For transforming to velocity space, we have taken the shorter rest-wavelength of the doublet (solid line), and also the longer rest-wavelength of the doublet (dashed line).

detectable in the UV band of the spectrum. Figure 11 shows the spectra of several UV lines as a function of radial velocity with respect to the systemic one. At the top of the figure we present the Lyα blended with the He II λ1215 line (upper left) which yields a feature centered at $\sim$−1300 km s^{-1}. Also, an absorption feature is formed with the Lyβ and He II λ1025 lines (upper center) with center at $\sim$−1200 km s^{-1}, and the line Lyγ (upper right) with a velocity $\sim$−1100 km s^{-1}. At the bottom of the figure we plot the spectrum of three important doublets (C IV $\lambda\lambda$1548.2, 1550.8, N V $\lambda\lambda$1238.8, 1242.8, and O VI $\lambda\lambda$1032, 1038). The solid line depicts the velocity spectra constructed taking the shorter wavelength of the doublet. The spectra shown as dashed lines were obtained taking the longer wavelength. One can see the similarity between the velocities predicted by our model and the high-velocity components (1, 4 and likely 3) seen in the UV spectrum of NGC 3783 and other Seyfert 1 galaxies (for example NGC 5548). This is similar to the conclusion reached by Gabel et al. (2005), based on Kaspi et al. (2002) and Gabel et al. (2003), where all X-ray lines having sufficiently high resolution and S/N were found to span the radial velocities of the three UV kinematic components (see also next section). These are predictions which arise naturally from our model because we are modeling the wind self-consistently with a complete treatment of radiative processes in all wavelengths. In our models these UV features as well as the long wavelength absorption lines in the X-ray band, are produced by the low ionization parameter part of the flow (e.g., $\log \xi = 0.12, -1.13$ from Figure 6 lower right panel). This demonstrates that the same absorber can produce X-ray and UV lines with similar velocities. Figure 12 shows the kinematic relationship between the X-ray and the UV absorbers. The model has been shifted (up) for clarity. Here we show the O VIII λ18.969 and the doublet O VI $\lambda\lambda$1032, 1038 (with respect to the shorter wavelength). For comparison we plot the histogram data of the 900 ks of NGC 3783. We see that our model is capable of simultaneously producing X-ray and UV absorption lines with similar velocities around $\sim$1000 km s^{-1}, as it has been suggested from UV data (Gabel et al. 2003).

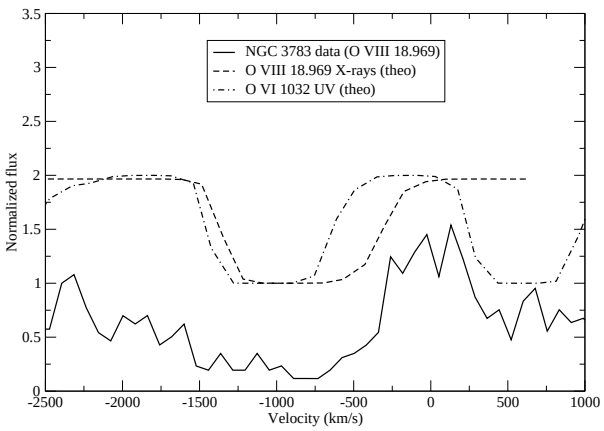

Fig. 12. Possible kinematical relationship between the UV and the X-ray absorbers. In the figure are plotted the theoretical X-ray and UV lines O VIII λ18.969 and O VI λ1032, dashed and short-dotted lines respectively. Also plotted is the profile of the line O VIII λ18.969 taken from the 900 ks spectrum of NGC 3783. All these lines are sharing velocities $\sim$1000 km s^{-1}.

5.3. *Present single wind vs multiphase wind scenario*

However, we want to highlight the most important differences between our model, consisting of a single wind governed by the laws of radiative acceleration, and the multiphase wind subjected to pressure equilibrium.

The first difference is that in our model there is a clear correlation between ionization state of the ions and velocity ($\xi - v$), and ξ and number of particle n_H ($\xi - n_H$). At the same time, because of the dependence of v and n_H on the spatial distance r, there is a dependence of ξ on r. This is different from the multicomponent in pressure equilibrium model, suggested by Netzer et al. (2003). In that model three components (in ionization) may coexist in the same volume of space and lie on the stable regions of the nearly vertical part of the thermal stability curve (log T *vs* log $[U/T]$, see Figure 12 in that paper). Our absorbers are not embedded in an external medium, and they cannot coexist at exactly the same location, but rather follow the physical laws of radiative acceleration. In this context, Gabel et al. (2005) also find that the UV absorbers of NGC 3783 may share some properties of the multiphase thermal wind. The UV kinematic components 1b, 2 and 3 could occupy the low-temperature base of the region of the thermal stability curve where a range of temperatures can coexist in pressure equilibrium. There is one weak point in the picture of inhomogeneities coexisting in pressure equilibrium. The low-ionization high-velocity UV absorber does not fit there, due to a pressure of a factor of 10 larger than that of the other component. If embedded into a more ionized-hotter material, it will eventually evaporate, unless there exists an additional confining mechanism. This extra confinement could be provided by magnetic pressure, requiring moderate magnetic fields ($B \approx 10^{-3}$ G), as predicted by some dynamical models (Emmering, Blandford, & Shlosman 1992; de Kool & Begelman 1995). In our model, there is no need for a confining mechanism, and if anything, the more ionized material is closer to the source, shielding the intense continuum radiation and preventing its evaporation. We conclude by stating that our model represents an additional competitor. It cannot be ruled out by comparison with the pressure equilibrium model. A more detailed comparison between models is beyond the scope of the present work, but could take place in the future.

6. TWO OUTFLOWS

So far we have been concerned with the line velocity shifts as measured with respect to the points of maximum absorption of the lines, but little has been said about the asymmetry of the troughs. To quantify the line asymmetries predicted by the theoretical models we have tabulated the fraction of the terminal velocity at which the absorption is maximum, to be compared with the ratio ($\bar{v}/v_1$), where v_1 is the position of the blue edge of each line, used to quantify the asymmetry in the spectrum of NGC 3783 (see Table 3 Ramírez et al. 2005). We characterize a theoretical line as "red" if $v(\tau_{\max})/v_\infty > 0.5$ and as "blue" if $v(\tau_{\max})/v_\infty < 0.5$, while for observed lines they are grouped according to $\bar{v}/v_1 > 0.5$ and $\bar{v}/v_1 < 0.5$ (see Ramírez et al. 2005). In Table 3 we present the observed troughs. In the first and second columns are given the identifications and the wavelengths of the lines, in the third, the fraction $v(\tau_{\max})/v_\infty$ for model A, and in the fourth the classification from observed lines, as in Ramírez et al. (2005), i.e., $\bar{v}/v_1$. We classify every trough as either (R) if it is red or (B) if it is blue. There are clear discrepancies between model A and the observations. In order to improve the agreement with observations we found it necessary to create a model composed of two outflows, which differ by their log ξ_0, the initial exposition to the source. In Table 4 we can see separately the parameters of the two outflows which compose model C. The first flow, with $\log \xi_0 = 3$, which we call HIF (high ionization flow), is able to create the majority of the high ionization lines (S XVI λ4.729, S XV λ5.039, Fe XXIII λ8.303), with

TABLE 3

ASYMMETRY COMPARISON BETWEEN MODEL A AND OBSERVATIONS

Ion	Line (Å)	$v(\tau_{\max})/900$ km s^{-1}	Ramírez et al. (2005)[a]
S XVI	4.729	0.55 (R)	0.33±0.1 (B)
S XV	5.039	0.67 (R)	0.23±0.1 (B)
Si XIII	5.681	0.70 (R)	0.35±0.1 (B)
Si XIV	6.182	0.67 (R)	0.23±0.08 (B)
Si XIII	6.648	0.70 (R)	0.43±0.074 (B)
Mg XII	7.106	0.70 (R)	0.32±0.070 (B)
Mg XI	7.473	0.76 (R)	0.74±0.067 (R)
Fe XXIII	8.303	0.55 (R)	0.037±0.060 (B)
Mg XII	8.421	0.70 (R)	0.32±0.059 (B)
Mg XI	9.169	0.76 (R)	0.31±0.054 (B)
Ne X	9.708	0.76 (R)	0.45±0.052 (B)
Ne X	10.240	0.76 (R)	0.17±0.048 (B)
Ne IX	11.547	0.82 (R)	0.69±0.043 (R)
Fe XXII	11.770	0.55 (R)	0.22±0.042 (B)
Ne X	12.134	0.76 (R)	0.29±0.041 (B)
Fe XXI	12.284	0.62 (R)	0.42±0.040 (B)
Fe XVIII	14.373	0.70 (R)	0.27±0.035 (B)
Fe XVIII	14.534	0.70 (R)	0.51±0.034 (R)
O VIII	14.832	0.82 (R)	0.21±0.033 (B)
Fe XVII	15.015	0.70 (R)	0.76±0.033 (R)
O VIII	15.188	0.82 (R)	0.38±0.033 (B)
O VIII	16.006	0.82 (R)	0.26±0.030 (B)
O VII	17.200	0.90 (R)	0.29±0.029 (B)
O VII	17.396	0.90 (R)	0.30±0.029 (B)
O VII	17.768	0.90 (R)	0.32±0.028 (B)
O VII	18.627	0.90 (R)	0.32±0.027 (B)
O VIII	18.969	0.82 (R)	0.26±0.026 (B)

[a] $\bar{v}/v_1$, see definition in the text.

extended blue wings, as the flow moves outwards and acquires more velocity, in agreement with the observations. The second, which we call LIF (low ionization flow), characterized by $\log \xi_0 = 2$, is able to create the extended blue wing of the oxygen lines. This model has the fundamental ingredients that explain the asymmetry observed in the lines of NGC 3783 and, at the same time, gives us the bulk velocity of the flow.

In the third column of Table 5 we present the characterization of the lines coming from the two-outflow model. The HIF component is the major contributor to the formation of the high ionization lines, i.e. S XVI, Fe XXI, Fe XXII, Fe XXIII, because their optical depths peak close to $\log \xi_0$ (HIF), and as the velocity of the flow increases their ionization fraction decreases, forming their blue wings. Under this picture, only a few lines are characterized as blue, while the rest are red. Some intermediate-to-low-ionization ions have appreciable fractions in the LIF component, which broadens the lines and yields

TABLE 4

PARAMETERS OF THE TWO OUTFLOW MODEL (MODEL C)

Outflow HIF	Outflow LIF
$\log \xi_0 = 3.0$	$\log \xi_0 = 2.0$
$v_\infty = 1100$ km s^{-1}	$v_\infty = 2200$ km s^{-1}
$N_H = 10^{22}$ cm^{-2}	$N_H = 10^{21}$ cm^{-2}
$w_0 = 0.4$	$w_0 = 0.2$
Solar composition	Solar composition

TABLE 5

ASYMMETRY COMPARISON BETWEEN MODEL C AND OBSERVATIONS

Ion	Line (Å)	$v(\tau_{\max}[\mathrm{HIF}])/1100$ km s^{-1}	$v(\tau_{\max}[\mathrm{HIF+LIF}])/2200$ km s^{-1}
S XVI	4.729	0.47 (B)	0.47 (B)
S XV	5.039	0.55 (R)	0.55 (R)
Si XIII	5.681	0.62 (R)	0.62 (R)
Si XIV	6.182	0.55 (R)	0.55 (R)
Si XIII	6.648	0.62 (R)	0.62 (R)
Mg XII	7.106	0.55 (R)	0.55 (R)
Mg XI	7.473	0.74 (R)	0.74 (R)
Fe XXIII	8.303	0.47 (B)	0.47 (B)
Mg XII	8.421	0.55 (R)	0.55 (R)
Mg XI	9.169	0.74 (R)	0.37 (B)[a]
Ne X	9.708	0.74 (R)	0.74 (R)
Ne X	10.240	0.74 (R)	0.37 (B)[a]
Ne IX	11.547	0.74 (R)	0.37 (B)[a]
Fe XXII	11.770	0.47 (B)	0.47 (B)
Ne X	12.134	0.74 (R)	0.37 (B)[a]
Fe XXI	12.284	0.47 (B)	0.47 (B)
Fe XVIII	14.373	0.55 (R)	0.55 (R)
Fe XVIII	14.534	0.55 (R)	0.55 (R)
O VIII	14.832	0.74 (R)	0.37 (B)[a]
Fe XVII	15.015	0.62 (R)	0.62 (R)
O VIII	15.188	0.74 (R)	0.37 (B)[a]
O VIII	16.006	0.74 (R)	0.37 (B)[a]
O VII	17.200	0.82 (R)	0.41 (B)[a]
O VII	17.396	0.82 (R)	0.41 (B)[a]
O VII	17.768	0.82 (R)	0.41 (B)[a]
O VII	18.627	0.82 (R)	0.41 (B)[a]
O VIII	18.969	0.74 (R)	0.37 (B)[a]

[a]With the addition of the LIF, we mark those line whose symmetry change.

a red appearance to the composed profile. This effect is illustrated by the fourth column of Table 5.

The composite model reproduces the asymmetry of the lines. The present uncertainties in the computation of $v(\tau_{\max})$ are of the order of 60 km s^{-1} (or $\Delta v(\tau_{\max})/v_\infty = 0.055$ with $v_\infty = 1100$ km s^{-1}). So the lines classified as pure red with $v(\tau_{\max})/v_\infty \gtrsim 0.55$ and pure blue with $v(\tau_{\max})/v_\infty \lesssim 0.45$ are more reliable than those with $0.45 \lesssim v(\tau_{\max})/v_\infty \lesssim 0.55$.

It is interesting to analyze why the O VII and O VIII lines are blue, while the lines Mg XI λ7.473 and Fe XVII λ15.015 remain red. The optical depths of Mg XI λ7.473, and Fe XVII λ15.015 are below 10^{-4} at velocities greater than 1100 km s^{-1}, so the LIF component does not contribute to their broadening. Another interesting example is the difference in classification between the lines Mg XI λ7.473 and Mg XI λ9.169. The reason is that while for Mg XI λ7.473 the oscillator strength is $\sim 5 \times 10^{-2}$, the f-value for the line Mg XI λ9.169 is almost one order of magnitude larger ($\sim 7 \times 10^{-1}$), which causes the optical depth of the latter to be significant up to velocities beyond $\sim$1600 km s^{-1}.

Figure 13 compares the modeled velocities of the lines from the two-outflow model with observations. Robust regression using the M estimator gives a slope of 0.63 ± 0.22 (solid line in the figure), and the residual standard error (rms) is 16.6 for 25 degrees of freedom (dof).

A comparison between the predicted trough profiles and those observed in NGC 3783 is shown in Figure 14. Here we plot the theoretical spectrum given by the outflows HIF and LIF in the 18.5–19.3 Å. We have used a power law as continuum, with a spectral

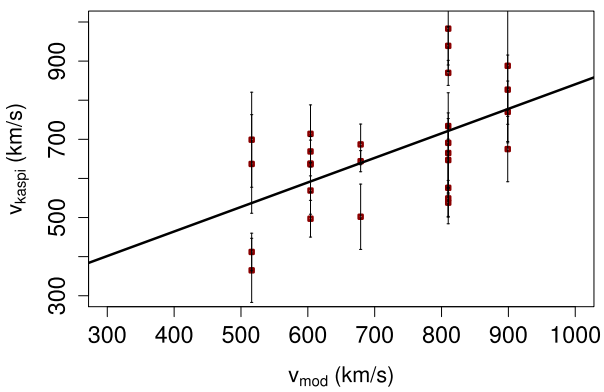

Fig. 13. Measured vs model-predicted velocities for the group of unblended lines given in Table 2 of Ramírez et al. (2005). The measurements are taken from Kaspi et al. (2002). The solid line is the best line after a linear regression for model C.

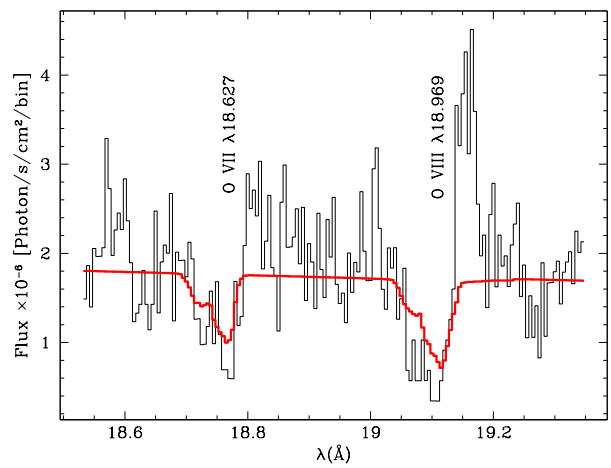

Fig. 14. A graphical representation of the flows HIF and LIF with the line profiles seen in NGC 3783 (histogram). Solid line is the composite model (model C) with two flows. It can be seen that it was necessary to include the second low-ionization flow in order to reproduce the asymmetry of these lines. Otherwise the high-ionization flow would form a more extended red wing.

index of $\Gamma = 1.77$, suitable for this AGN, and have set an extra absorber `the wabs`[3] model in XSPEC, and the composite fluxes generated by the HIF and the LIF components. To compose the O VIII λ18.969 line profile we have summed the fluxes from both flows using equation (12) (where $m = 22$). With this approximation the profile predicted by the two-outflow model is in excellent agreement with observations (Ramírez et al. 2005). The red wing of the troughs in the range 0–1000 km s^{-1} is formed by the HIF, while the blue wing in the range ∼1000–2500 km s^{-1} is formed by the LIF. These values are in agreement with the values measured for this lines in the observed spectrum.

This is the first time that such theoretical work has been carried out to explain the asymmetry seen in absorption in the X-ray spectrum of AGNs. Other work has been able to explain the blue wings of UV lines, like the well-studied C IV λ 1549, for example from radiation-driven disk-wind models (Proga 2003). So we cannot conclude that the model presented here is unique for the description of the asymmetry seen in X-ray lines of AGNs, until detailed comparisons are made with such models, including the X-ray line profile produced by a wind from a Keplerian accretion disk (Knigge, Woods, & Drew 1995; Shlosman, Vitello, & Mauche 1996; Proga et al. 2000; Drew & Proga 2000). Further work is necessary for such a comparison, and we plan to do that in a near future.

7. SUMMARY

We have computed photoionized wind-flow models for the X-ray spectrum of NGC 3783. We studied single continously absorbing models, as well as multiple optically thin components linked through an analytic wind velocity law. We found that the single continuously absorbing model yields gas column densities and optical depths that are too large, unless one adopts very low (∼10^{3-4} cm^{-3}) densities and metal abundances (∼0.01 solar). On the other hand, the multicomponent model is able to reproduce observations very well. For this model we compute ionization properties of the material using a velocity law compatible with a radiative wind. Our model is consistent with $\log n_0 \sim 11.35$ [cm^{-3}], a launching radii of $\log r_0 \sim 15$ [cm], and a terminal velocities of $v_\infty \sim 1500$ km s^{-1}, which yield a mass loss rate of the order of $\dot{M}_{\rm out} \sim 1\ M_\odot$/yr (assuming a volumetric factor $f_{\rm vol} = 0.1$). If we assume an ionizing luminosity $L \sim 2 \times 10^{44}$ erg s^{-1} (Peterson et al. 2004), and an accretion efficiency of $\eta = 0.1$, the Eddington mass accretion rate is $\dot{M}_{\rm edd} \sim 0.01\ M_\odot$/yr. This is consistent with the result of Crenshaw & Kraemer (2007) for NGC 4151, and Ramírez (2008) for APM 08279+5255, of $\dot{M}_{\rm out}/\dot{M}_{\rm edd} > 10$. However, it is different from the supposition made by Gonçalves et al. (2006), of $\dot{M}_{\rm out}/\dot{M}_{\rm edd} \leq 1$, using their photoionization code TITAN, for computing the single medium in pressure equilibrium.

Finally, the asymmetry seen in the lines of the X-ray spectrum of NGC 3783 required a model with two outflows. One flow, with a launching ionization parameter of $\log \xi_0 \sim 3$ and a column density of

[3] $N_{\rm wabs} = 0.1 \times 10^{22}$ cm^{-2}.

$N_H = 10^{22}$ cm^{-2}, recreates the red wings of the low ionization lines from Ne IX to O VII, and the blue wings of the high ionization lines from Fe XXIII to Si XIV. A second flow is necessary to create the blue wing of the oxygen lines, which exhibit a blue character. The theoretical fitting required $\log \xi_0 \sim 2$, terminal velocities of around $\sim$2200 km s^{-1}, and a column density of $N_H = 10^{21}$ cm^{-2}.

Our calculations also predict a relationship between the UV and X-ray bands, as models adjusted to fit the X-ray spectrum naturally predict UV lines like the Lyman serie, and the O VI, N V and C IV doublets, in apparent concordance with Costantini (2010).

REFERENCES

Arav, N., Li, Z., & Begelman, M. C. 1994, ApJ, 432, 62
Bautista, M. A., & Kallman, T. R. 2001, ApJS, 134, 139
Castor, J. I., Abbott, D. C., & Klein, R. I. 1975, ApJ, 195, 157
Chartas, G., Saez, C., Brandt, W. N., Giustini, M., & Garmire, G. P. 2009, ApJ, 706, 644
Costantini, E. 2010, Space Science Reviews, 157, 265
Crenshaw, D. M., & Kraemer, S. B. 2007, ApJ, 659, 250
de Kool, M., & Begelman, M. C. 1995, ApJ, 455, 448
Drew, J. E. 1989, ApJS, 71, 267
Drew, J., & Giddings, J. 1982, MNRAS, 201, 27
Drew, J. E., & Proga, D. 2000, NewA Rev., 44, 21
Drew, J., & Verbunt, F. 1985, MNRAS, 213, 191
Elvis, M. 2000, ApJ, 545, 63
Emmering, R. T., Blandford, R. D., & Shlosman, I. 1992, ApJ, 385, 460
Gabel, J. R., et al. 2003, ApJ, 583, 178
Gabel, J. R., et al. 2005, ApJ, 631, 741
George, I. M., Turner, T. J., Netzer, H., Nandra, K., Mushotzky, R. F., & Yaqoob, T. 1998, ApJS, 114, 73
Gonçalves, A. C., Collin, S., Dumont, A., Mouchet, M., Różańska, A., Chevallier, L., & Goosmann, R. W. 2006, A&A, 451, L23
Grevesse, N., Noels, A., & Sauval, A. J. 1996, in ASP Conf. Ser. 99, Cosmic Abundances, ed. S. Holt & G. Sonneborn (San Francisco: ASP), 117
Huber, P. J. 1964, Ann. Math. Statist., 35, 73
Kaastra, J. S., Mewe, R., Liedahl, D. A., Komossa, S., & Brinkman, A. C. 2000, A&A, 354, L83
Kallman, T., & Bautista, M. 2001, ApJS, 133, 221
Kallman, T. R., & McCray, R. 1982, ApJS, 50, 263
Kaspi, S., Brandt, W. N., Netzer, H., Sambruna, R., Chartas, G., Garmire, G. P., & Nousek, J. A. 2000, ApJ, 535, L17
Kaspi, S., et al. 2002, ApJ, 574, 643
Kaspi, S., et al. 2001, ApJ, 554, 216
Knigge, C., Woods, J. A., & Drew, J. E. 1995, MNRAS, 273, 225
Komossa, S. 1999, in ASCA/ROSAT Workshop on AGN and the X-Ray Background, ed. T. Takahashi & H. Inoue (ISAS Rep. 149) (Tokyo: ISAS), 149
Kraemer, S. B., Crenshaw, D. M., & Gabel, J. R. 2001, ApJ, 557, 30
Krolik, J. H., & Kriss, G. A. 2001, ApJ, 561, 684
Krongold, Y., Nicastro, F., Brickhouse, N. S., Elvis, M., Liedahl, D. A., & Mathur, S. 2003, ApJ, 597, 832
Krongold, Y., Nicastro, F., Elvis, M., Brickhouse, N. S., Mathur, S., & Zezas, A. 2005, ApJ, 620, 165
Lamers, H. J. G. L. M., Cerruti-Sola, M., & Perinotto, M. 1987, ApJ, 314, 726
Murray, N., Chiang, J., Grossman, S. A., & Voit, G. M. 1995, ApJ, 451, 498
Netzer, H., et al. 2003, ApJ, 599, 933
Ogle, P. M., Marshall, H. L., Lee, J. C., & Canizares, C. R. 2000, ApJ, 545, L81
Peterson, B. M., et al. 2004, ApJ, 613, 682
Proga, D. 2003, ApJ, 592, L9
Proga, D., Stone, J. M., & Kallman, T. R. 2000, ApJ, 543, 686
Ramírez, J. M. 2008, A&A, 489, 57
Ramírez, J. M., Bautista, M., & Kallman, T. 2005, ApJ, 627, 166
Reeves, J. N., Nandra, K., George, I. M., Pounds, K. A., Turner, T. J., & Yaqoob, T. 2004, ApJ, 602, 648
Różańska, A., Goosmann, R., Dumont, A., & Czerny, B. 2006, A&A, 452, 1
Saez, C., Chartas, G., & Brandt, W. N. 2009, ApJ, 697, 194
Shields, J. C., & Hamann, F. 1997, ApJ, 481, 752
Shlosman, I., Vitello, P., & Mauche, C. W. 1996, ApJ, 461, 377
Steenbrugge, K. C., Kaastra, J. S., de Vries, C. P., & Edelson, R. 2003, A&A, 402, 477
Tarter, C. B., Tucker, W. H., & Salpeter, E. E. 1969, ApJ, 156, 943
Yaqoob, T., McKernan, B., Kraemer, S. B., Crenshaw, D. M., Gabel, J. R., George, I. M., & Turner, T. J. 2003, ApJ, 582, 105

J. M. Ramírez: Leibniz-Institut für Astrophysik Potsdam, An der Sternwarte 16, 14482 Potsdam, Germany (jramirez@aip.de).

Revista Mexicana de Astronomía y Astrofísica, **47**, 401–407 (2011)

KINEMATIC AGES OF THE CENTRAL STARS OF PLANETARY NEBULAE

W. J. Maciel, T. S. Rodrigues, and R. D. D. Costa

Instituto de Astronomia, Geofísica e Ciências Atmosféricas
Universidade de São Paulo, Brazil

Received 2011 July 01; accepted 2011 August 11

RESUMEN

Se determina la distribución de edades de las estrellas centrales de nebulosas planetarias (CSPN) utilizando dos métodos basados en sus propiedades cinemáticas. En primer lugar, se comparan las velocidades de rotación de las nebulosas esperadas a partir de sus distancias galactocéntricas con los valores predichos por la curva de rotación, y las diferencias encontradas se atribuyen a las distintas edades de las estrellas evolucionadas. Se usa la relación entre las edades y la dispersión de velocidades del relevamiento Geneva-Copenhagen para obtener la distribución de edades. En segundo lugar, se determinan las componentes U, V, W de las velocidades de las estrellas, y se usan las relaciones edad-dispersión de velocidades para inferir la distribución de edades. Hemos aplicado estos métodos a dos muestras de nebulosas planetarias en nuestra galaxia. Los resultados son similares para ambas, y muestran que la distribución de edades de las CSPN está concentrada en edades menores que 5 giga-años, y que tiene un pico entre 1 y 3 giga-años.

ABSTRACT

The age distribution of the central stars of planetary nebulae (CSPN) is estimated using two methods based on their kinematic properties. First, the expected rotation velocities of the nebulae at their Galactocentric distances are compared with the predicted values from the rotation curve, and the differences are attributed to the different ages of the evolved stars. Adopting the relation between the ages and the velocity dispersions determined by the Geneva-Copenhagen survey, the age distribution can be derived. Second, the U, V, W, velocity components of the stars are determined, and the corresponding age-velocity dispersion relations are used to infer the age distribution. These methods have been applied to two samples of PN in the Galaxy. The results are similar for both samples, and show that the age distribution of the PN central stars concentrates at ages lower than 5 Gyr, peaking at about 1 to 3 Gyr.

Key Words: planetary nebulae: general — stars: AGB and Post-AGB — stars: fundamental parameters — stars: general

1. INTRODUCTION

Planetary nebulae (PN) are evolved objects ejected by stars with main sequence masses in the range of 0.8 and 8 $M_\odot$, so that the expected ages of their central stars are of the order of, or greater than, about 1 Gyr. However, the relatively large mass bracket of their progenitor stars implies that an age distribution is to be expected, which has some consequences for the interpretation of the PN data in the Galaxy and other stellar systems. The determination of ages of the central stars is a difficult problem, and most usual methods have large uncertainties when applied to intermediate and old age objects. We have recently developed three different methods to estimate the age distribution of the CSPN (Maciel, Costa, & Idiart 2010, see also Maciel, Costa, & Uchida 2003; Maciel, Lago, & Costa 2005, 2006), and have applied these methods to a sample of PN in the disk of the Galaxy, most of which are located in the solar neighborhood, within

3 kpc of the Sun. These methods include the determination of the age distribution of CSPN using (i) an age-metallicity relation that also depends on the Galactocentric distance, (ii) an age-metallicity relation obtained for the disk, and (iii) the central star masses obtained from the observed nitrogen abundances. We concluded that most CSPN in our sample have ages under 6 Gyr, and that the age distribution is peaked around 2–4 Gyr. The average uncertainties were estimated as 1–2 Gyr, and the results were compared with the expected distribution based both on the observed mass distribution of white dwarfs and on the age distribution derived from available masses of CSPN.

In the present work we develop two additional and more accurate methods to estimate the age distribution of the CSPN based on their kinematical properties, namely: (i) a method based on the expected rotation velocities of the nebulae at their Galactocentric distances, which are then compared with the predicted values for a given rotation curve, the differences being attributed to the different ages of the evolved stars; (ii) a method based on the derived U, V, W, velocity components of the stars and their corresponding dispersions. In both cases, the age-velocity dispersion relations from the Geneva-Copenhagen survey are used to infer the age distribution. These methods are applied to two PN samples, (i) the previous sample of disk PN used by Maciel et al. (2010), for which a detailed data set is available, and (ii) a sample containing all PN for which accurate radial velocities are known. The methods are developed in § 2, and the samples used are described in § 3. The main results and discussion are given in § 4.

2. DETERMINATION OF THE AGE DISTRIBUTION OF CSPN

2.1. *Method 1: The PN rotation velocity*

As objects of intermediate age, PN in the disk of the Galaxy describe a rotation curve similar to the one defined by younger objects, such as HII regions, although with a higher dispersion, as discussed in detail by Maciel & Lago (2005). Therefore, the discrepancies between the rotation velocities inferred from the PN radial velocities and distances and the velocities expected from the known rotation curve may be at least partially ascribed to their evolved status. In other words, a given nebula located at a distance d, with galactic coordinates ℓ and b and observed heliocentric radial velocity V_r(hel) can be associated with a rotation velocity $\theta(R)$, after obtaining its Galactocentric distance R and its radial velocity relative to the Local Standard of Rest (LSR), V_r(LSR). Assuming circular orbits, the rotation velocity $\theta(R)$ at the Galactocentric distance R can be written as

$$\theta(R) = \frac{R}{R_o}\left[\frac{V_r(\mathrm{LSR})}{\sin\ell\,\cos b} + \theta_0\right], \qquad (1)$$

where R_0 and θ_0 are the Galactocentric distance and rotation velocity at the solar position (see for example Maciel & Lago 2005; Maciel & Dutra 1992). On the other hand, the expected rotation velocity at the given Galactocentric distance, $\theta_c(R)$, can be obtained from an adopted rotation curve. The difference $\Delta\theta = |\theta(R) - \theta_c(R)|$ can then be considered as proportional to the age difference between the PN and the objects defining the rotation curve. We have adopted the radial velocities from the catalogue by Durand, Acker, & Zijlstra (1998), and two distance scales, those by Maciel (1984) and Stanghellini, Shaw, & Villaver (2008). The first one was based on a relationship between the ionized mass and the radius of the nebulae, while the second is an update of the distance scale by Cahn, Kaler, & Stanghellini (1992), using a modified Shklovksy method following Daub (1982). Since the distances of planetary nebulae in the Galaxy may contain large individual uncertainties, the use of two different scales which are considered as "short" (Maciel 1984) and "long" (Stanghellini et al. 2008) ensures that these uncertainties will not affect the derived age distributions. We have adopted $R_0 = 8.0$ kpc for the distance of the Sun to the centre and $\theta_0 = 220$ km s^{-1} for the rotation velocity at R_0. Slightly different values can be found in the literature (see for example Perryman 2009, and Reid 2010), but the values above are frequently adopted, so that a comparison with other work is made easier. For the "theoretical" rotation curve we have also adopted two possibilities, namely, the PN curve derived by Maciel & Lago (2005), and the HII region curve derived by Clemens (1985). In the first case, the rotation velocity can be written as

$$\theta_c(R) = a_0 + a_1\,R + a_2\,R^2\,, \qquad (2)$$

where the constants are $a_0 = 269.2549$, $a_1 = -14.7321$, and $a_2 = 0.7847$, the Galactocentric distance R is given in kpc and $\theta_c(R)$ in km s^{-1}. For the CO/HII region based Clemens (1985) curve, we have made an adjustment for $R_0 = 8.0$ kpc and $\theta_0(R) = 220$ km s^{-1}, in which case we have

$$\theta_c(R) = \sum a_i\,R^i\,, \qquad (3)$$

where the constants are given in Table 1, with the same units as in equation (2).

TABLE 1

COEFFICIENTS OF THE POLYNOMIAL GIVEN BY EQUATION (3)

R (kpc)	$0-0.765$	$0.765-2.9$	$2.9-3.825$	$3.825-13$	>13
a_0	0.0	325.0912	329.8	−2346.0	230.6
a_1	3069.81	−248.1467	−250.1	2507.60391	...
a_2	−15809.8	231.87099	231.87099	−1024.068760	...
a_3	43980.1	−110.73531	−110.73531	224.562732	...
a_4	−68287.3	25.073006	25.073006	−28.4080026	...
a_5	54904.0	−2.110625	−2.110625	2.0697271	...
a_6	−17731.0	...	...	−0.080508084	...
a_7	...	...	...	0.00129348	...

TABLE 2

COEFFICIENTS OF EQUATION (4)

	a	b
U	0.39	1.31
V	0.40	1.10
W	0.53	0.94
Total	0.40	1.40

TABLE 3

PARAMETERS FOR METHOD 1

Distance	Rotation Curve	Dispersion	Age
Maciel	PN	σ_V	t_1
Maciel	PN	σ_T	t_2
Maciel	Clemens	σ_V	t_3
Maciel	Clemens	σ_T	t_4
Stanghellini	PN	σ_V	t_5
Stanghellini	PN	σ_T	t_6
Stanghellini	Clemens	σ_V	t_7
Stanghellini	Clemens	σ_T	t_8

The recent Geneva-Copenhagen Survey of the Solar Neighborhood (cf. Nordström et al. 2004; Holmberg, Nordström, & Andersen 2007, 2009) has considerably improved the relations involving the ages, kinematics, and chemical composition of a large sample containing about 14000 F and G nearby stars. Using basically the original *Hipparcos* parallaxes, $uvby-\beta$ photometry and the Padova stellar evolution models, several basic relations were investigated. In particular, high correlations have been obtained between the velocity dispersions σ_U, σ_V, σ_W, and σ_T and the ages of the stars, which clearly show a smooth increase of the velocity dispersions (of the U, V, W components and the total velocity T) with time. From the calibration by Holmberg et al. (2009) these correlations can be approximately written as

$$\log\sigma = a\,\log t + b\,, \tag{4}$$

where the age t is expressed in Gyr and the constants a, b are given in Table 2. This approximation is valid in the age interval $0 < t(\mathrm{Gyr}) < 14$ with an estimated average uncertainty of about 25%. Method 1 consists of assuming that the discrepancy in the rotation velocity $\Delta\theta$ is due to the evolved status of the CSPN, so that we should expect a correlation between $\Delta\theta$ and the velocity dispersion, as given by equation (4). Since in this method we are using the rotation velocity, we have considered two possibilities, according to which the velocity discrepancy $\Delta\theta$ can be associated with (i) the V component of the total velocity (σ_V), or (ii) the total velocity (σ_T). Moreover, since we are adopting two distance scales and two theoretical rotation curves, we have 8 different age distributions for Method 1, characterized by the timescales t_1 to t_8, as explained in Table 3.

2.2. *Method 2: The U, V, W velocity components*

Method 2 is also a kinematic method, and in principle more accurate than Method 1, as discussed in more detail in § 4. From the PN radial velocities and distances, we have estimated their proper motions both in right ascension and declination, μ_α and μ_δ. We have assumed that, on average, the tangential velocities are similar to the radial velocities, namely $V_t \simeq V_r$. In view of the large distances of the nebulae, this hypothesis in practice does not introduce any major uncertainties in the

TABLE 4

PARAMETERS FOR METHOD 2

Distance	Dispersion	Age
Maciel	σ_U	t_9
Maciel	σ_V	t_{10}
Maciel	σ_W	t_{11}
Maciel	σ_T	t_{12}
Stanghellini	σ_U	t_{13}
Stanghellini	σ_V	t_{14}
Stanghellini	σ_W	t_{15}
Stanghellini	σ_T	t_{16}

results. Considering further the equatorial coordinates (α, δ) of the PN, we have used the equations by Boesgaard & Tripicco (1986) to derive the U, V, W velocity components of the nebulae, as well as the total velocity T and the velocity dispersions σ_U, σ_V, σ_W, and σ_T. According to these equations we derive the following parameters: $C = f(d)$, $X = f(C, \mu_\alpha, \mu_\delta, \alpha, \delta, V_r)$, $Y = f(C, \mu_\alpha, \mu_\delta, \alpha, \delta, V_r)$, and $Z = f(C, \mu_\delta, \delta, V_r)$, from which the velocities can be written as $U = f(X, Y, Z)$, $V = f(X, Y, Z)$, $W = f(X, Y, Z)$, and $T = f(X, Y, Z)$, so that the dispersions are given by

$$\sigma_i = \sqrt{(V_i - \bar{V}_i)^2}\,, \tag{5}$$

where V_i stands for the velocities U, V, W, T. Then, we have again used the detailed correlations between the velocity dispersions and the ages as given by the Geneva-Copenhagen survey (Holmberg et al. 2009), adopting the same coefficients given in Table 2. We have used the same distance scales (Maciel 1984; Stanghellini et al. 2008), so that we have again 8 different age distributions, corresponding to the timescales t_9 to t_{16}, as described in Table 4.

In practice, we have considered several additional cases, in order to better investigate the hypothesis of $V_t \simeq V_r$. Assuming that these velocities are of the same magnitude, but allowing for the possibility of different signs, we have as a result several possibilities for the proper motions μ_α and μ_δ, all of which are consistent with either $V_t \simeq V_r$ or $|V_t| \simeq |V_r|$. It turns out that these possibilities produce very similar age distributions, which will be discussed in § 4. Therefore, we will present only the distributions of the ages t_9 to t_{16}, as defined in Table 4, for the cases where $\mu_\alpha \simeq \mu_\delta \simeq 0$.

An interesting alternative to overcome the lack of proper motion and tangential velocity measurements would be to apply the singular value decomposition (SVD) technique, as used by Branham (2010) to solve the inverse problem, that is, obtaining the space velocities from available proper motions. However, in view of the similarity of the results for different assumptions regarding the tangential velocities, it is unlikely that this technique would produce very different results than presented here.

3. THE SAMPLES

As mentioned in the Introduction, we have considered two samples of Milky Way PN. In order to make comparisons with our previous work, we have first considered the same sample used by Maciel et al. (2003, 2005, 2006), which we will call Sample 1. This sample contains 234 well-observed nebulae located in the solar neighborhood and in the disk, for which all data were obtained with the highest accuracy. Their Galactocentric distances are in the range $4 < R(\mathrm{kpc}) < 14$, and most (69%) are located in the solar neighborhood, with distances $d < 3$ kpc.

The second sample considered in this work, called Sample 2, includes all the nebulae for which accurate radial velocities are available in the catalogue by Durand et al. (1998), comprising 867 objects. This is a more complete sample, so that it is expected that the derived results can be extended to the observed population of PN in the Galaxy. In both samples, the number of nebulae used depends on the availability of the statistical distances. The actual numbers of objects from the Maciel (1984) and Stanghellini et al. (2008) distance scales are 195 and 170 for Sample 1 and 493 and 403 for Sample 2, respectively. We have then applied the approximation given by equation (4) for both samples, with the coefficients shown in Table 2, considering only the objects for which ages in the interval $0 < t(\mathrm{Gyr}) < 14$ could be obtained.

4. RESULTS AND DISCUSSION

The main results for the age distribution of the CSPN are shown in Figures 1–4, where we have used the age parameter definitions given in Tables 3 and 4 for Methods 1 and 2, respectively. Figures 1 and 2 refer to Sample 1, while Figures 3 and 4 refer to Sample 2. It can be seen that the age distributions obtained by both methods are similar, in the sense that most objects have ages under 5 Gyr, with a strong peak at ages typically between 1 and 3 Gyr. The histograms of Figures 3–4 are summarized in Table 5, where the fraction of stars obtained by Method 1 (ages t_1 to t_8) and Method 2 (ages t_9 to t_{16}) are shown for three age bins, namely 0-3 Gyr, 3-6 Gyr, and $t > 6$ Gyr.

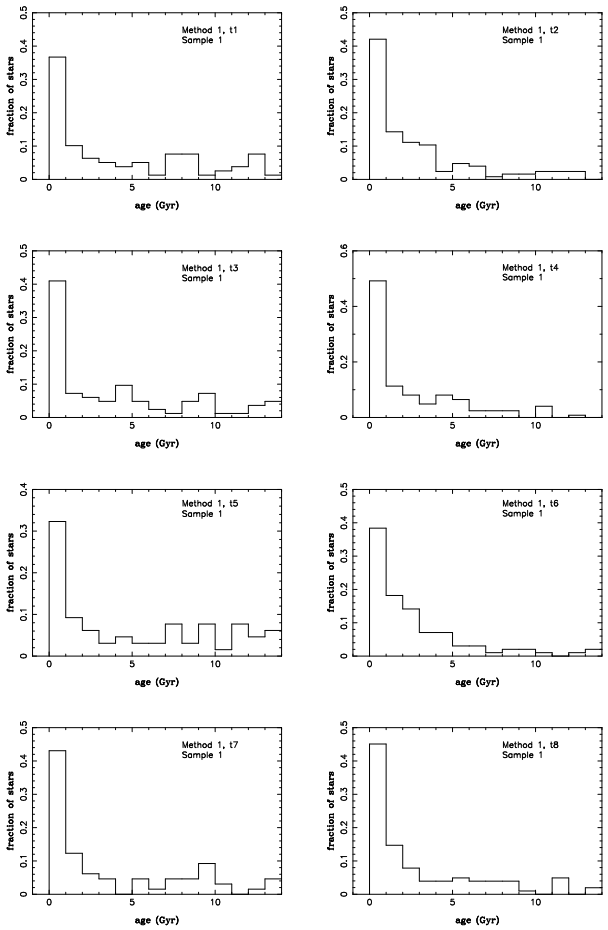

Fig. 1. Age distribution of CSPN, Method 1, Sample 1.

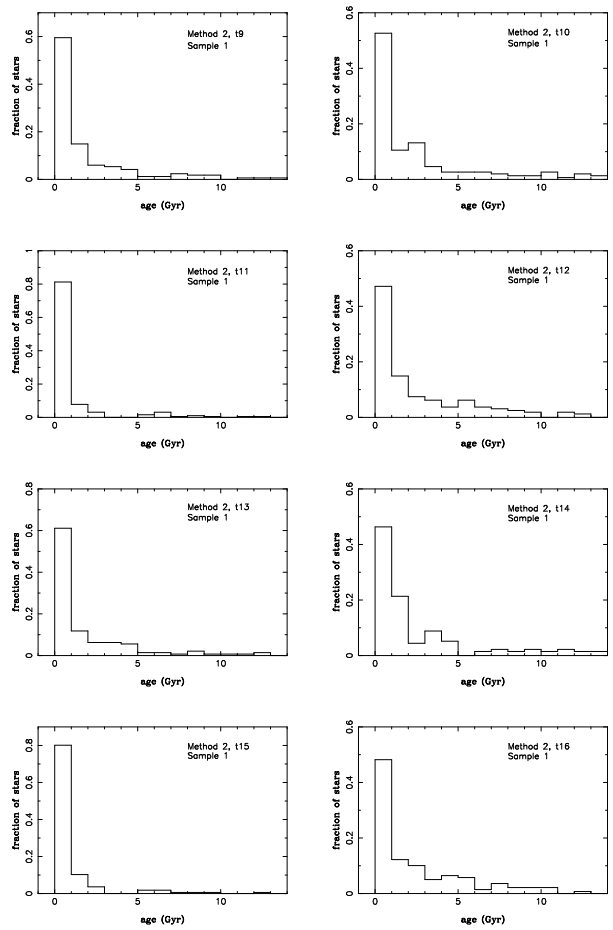

Fig. 2. Age distribution of CSPN, Method 2, Sample 1.

The similarity of the results of both methods is remarkable, especially considering that Method 2 is probably more accurate than Method 1. Method 2 consists of straightforward calculations of the velocities and velocity dispersions followed by an application of relatively accurate correlations involving the kinematics and ages of the objects considered. On the other hand, Method 1 is based on the assumption that the differences between the observed and predicted rotation velocities are essentially due to age effects. However, other processes may be important, such as deviations from the circular rotation, which is particularly important for nearby objects. According to Table 5, in all cases the vast majority of CSPN have ages under 3 Gyr. For Method 1 the total fraction of objects with $t \leq 3$ Gyr is 50–70%, while for Method 2 this fraction is somewhat higher, 70–90%. It is unlikely that this is a result from bias in the samples, as the results for the larger Sample 2 are essentially the same as in the smaller Sample 1. It should be pointed out that the latter, albeit smaller, includes only well studied nebulae, for which all individual parameters (distances, velocities, abundances) are better determined.

Also, there are no significant differences in the results using the different velocity components U, V, W, and T. For Method 1, the distributions using the V velocity component are essentially the same as those using the total velocity, for both distance scales and samples. For Method 2, the distributions are slightly more concentrated in the first few age bins for the W component, compared with the distributions for the U and V components and the total velocity, again for both distance scales and samples. Since the W component is more clearly associated with the disk heating, essentially caused by age effects, the corresponding distributions are probably more accurate.

Similar remarks can be made regarding the adopted values for the proper motions. As mentioned at the end of § 2, the results shown here assume that $\mu_\alpha \simeq \mu_\delta \simeq 0$. Adopting nonzero values

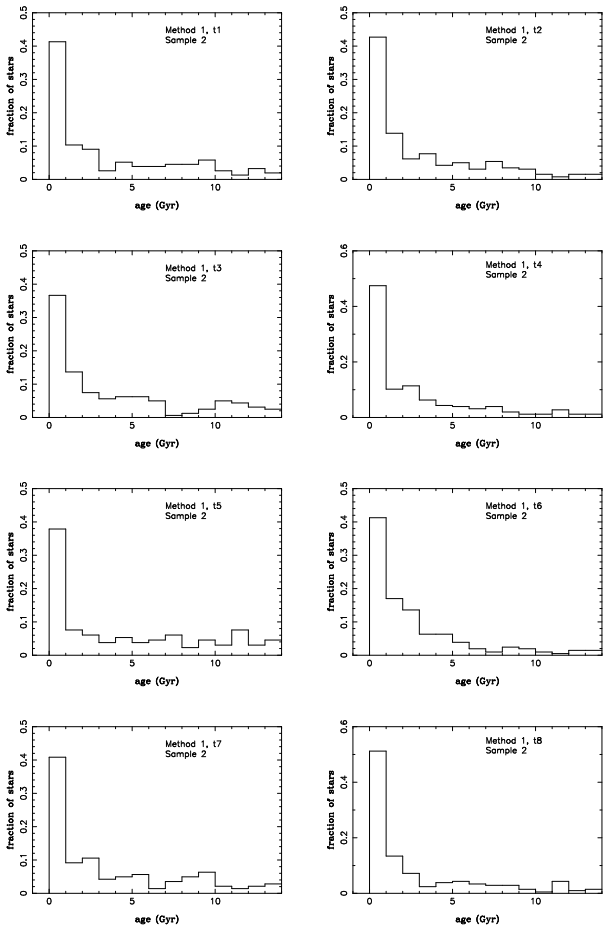

Fig. 3. Age distribution of CSPN, Method 1, Sample 2.

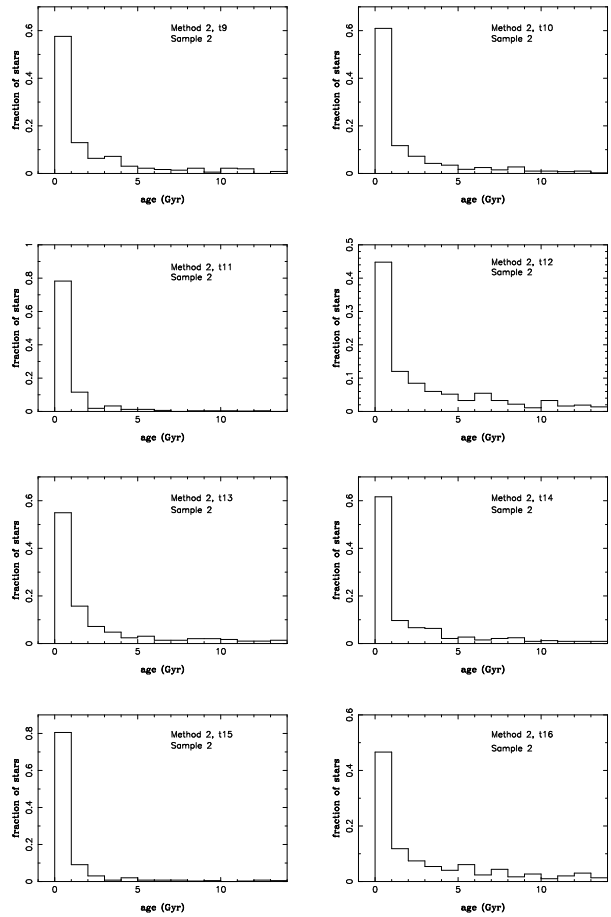

Fig. 4. Age distribution of CSPN, Method 2, Sample 2.

for these quantities ($\mu_\alpha \simeq \mu_\delta \neq 0$), either the V or W component distributions become slightly less concentrated at the first few age bins, but most objects still have ages under about 4 Gyr. Again, the application of the SVD technique could be useful to confirm these results.

The uncertainties in the distances of the Milky Way PN are difficult to estimate, but the procedure adopted here ensures that the obtained age distributions are not particularly affected by the individual distances of the objects in the samples. As mentioned in § 2, we have adopted two very different statistical scales, and the derived age distrbutions are essentially the same in both cases. The individual distances may depend on the particular scale, but the results shown in Figures 1–4 and in Table 5 do not depend on the choice of the distance scale. This can be seen by comparing the results for the timescales $t_1 - t_4$ with those for $t_5 - t_8$, or the results for $t_9 - t_{12}$ with those for $t_{13} - t_{16}$.

The uncertainties in the radial velocities also do not seem to have an important effect on the age distributions. In the catalogue by Durand et al. (1998), most objects (∼90%) have uncertainties smaller than 20 km s^{-1}, and many objects have much lower uncertainties. Concerning Method 1, from Maciel & Lago (2005), the average rms deviation in the rotation velocity is about 50 km s^{-1} for PN, which can be compared with the values of about 20 km s^{-1} for HII regions (see also Clemens 1985, and Maciel & Dutra 1992).

Probably the main uncertainty of the age distributions is due to the calibration between the stellar ages and the velocity dispersions, given by equation (4), which affects both Method 1 and 2. From the Geneva-Copenhagen Survey, this relation has a dispersion of about 20 km s^{-1} in average, which corresponds roughly to an age uncertainty of about 25%, amounting to less than 1.2 Gyr for the objects of Figures 1–4. Therefore, the uncertainties

TABLE 5

FRACTION OF STARS IN THREE AGE INTERVALS

	Δt (Gyr)	0–3	3–6	> 6
Method 1	t_1	0.57	0.13	0.30
	t_2	0.62	0.18	0.20
	t_3	0.57	0.19	0.24
	t_4	0.67	0.18	0.16
	t_5	0.51	0.13	0.36
	t_6	0.71	0.17	0.12
	t_7	0.61	0.15	0.24
	t_8	0.71	0.11	0.18
Method 2	t_9	0.76	0.12	0.12
	t_{10}	0.79	0.10	0.11
	t_{11}	0.92	0.04	0.04
	t_{12}	0.77	0.18	0.05
	t_{13}	0.78	0.10	0.12
	t_{14}	0.78	0.11	0.11
	t_{15}	0.93	0.03	0.04
	t_{16}	0.76	0.18	0.06

of the present method are comparable and probably smaller than in the case of the methods based on age-metallicity relations considered by Maciel et al. (2010).

The results for Sample 2 are not essentially different from those of Sample 1, so that a direct comparison can be made with the results by Maciel et al. (2010). The results of both investigations are similar, even though the present methods are completely independent of the metallicity-based methods used by Maciel et al. (2010). The main difference is that the kinematic methods used in the present investigation suggest somewhat lower ages for the CSPN in our samples. In this respect, these results fit nicely with the probability distribution for the progenitors of the CSPN according to Maciel et al. (2010, cf. Figure 7, dashed line). In this case the well known relation between the main sequence mass and the stellar ages by Bahcall & Piran (1983) was adopted, taking $t = 10$ Gyr for 1 $M_\odot$ stars on the main sequence. Taking into account the uncertainties of the methods, which are typically in the range 1–2 Gyr, this case was considered as the most realistic, so that it is reassuring that the kinematic methods produce similar results.

We thank Dr. R. Branham, Jr., for some interesting comments on an earlier version of this paper. This work was partly supported by FAPESP and CNPq.

REFERENCES

Bahcall, J. N., & Piran, T. 1983, ApJ, 267, L77
Boesgaard, A. M., & Tripicco, M. J. 1986, ApJ, 303, 724
Branham, R. L., Jr. 2010, MNRAS, 409, 1269
Cahn, J. H., Kaler, J. B., & Stanghellini, L. 1992, A&AS, 94, 399
Clemens, D. C. 1985, ApJ, 295, 422
Daub, C. T. 1982, ApJ, 260, 612
Durand, S., Acker, A., & Zijlstra, A. 1998, A&S, 132, 13
Holmberg, J., Nordström, B., & Andersen, J. 2007, A&A, 475, 519
_____. 2009, A&A, 501, 941
Maciel, W. J. 1984, A&AS, 55, 253
Maciel, W. J., Costa, R. D. D., & Idiart, T. E. P. 2010, A&A, 512, A19
Maciel, W. J., Costa, R. D. D., & Uchida, M. M. M. 2003, A&A, 397, 667
Maciel, W. J., & Dutra, C. M. 1992, A&A, 262, 271
Maciel, W. J., & Lago, L. G. 2005, RevMexAA, 41, 383
Maciel, W. J., Lago, L. G., & Costa, R. D. D. 2005, A&A, 433, 127
_____. 2006, A&A, 453, 587
Nordström, B., et al. 2004, A&A, 418, 989
Perryman, M. 2009, Astronomical Applications of Astrometry: Ten Years of Exploitation of the Hipparcos Satellite Data (Cambridge: Cambridge Univ. Press)
Reid, M. 2010, `http://www.cfa.harvard.edu/events/2010/dyn`
Stanghellini, L., Shaw, R. A., & Villaver, E. 2008, ApJ, 689, 194

W. J. Maciel, T. S. Rodrigues and R. D. D. Costa: Instituto de Astronomia, Geofísica e Ciências Atmosféricas, Universidade de São Paulo, Rua do Matão 1226, CEP 05508-090, São Paulo SP, Brazil (maciel, tsrodrigues, roberto@astro.iag.usp.br).

Revista Mexicana de Astronomía y Astrofísica, **47**, 409–424 (2011)

ATMOSPHERIC AEROSOL VARIABILITY OVER THE REGION OF SAN PEDRO MÁRTIR FROM MODIS DATA

Mario R. Araiza Quijano and Irene Cruz-González

Instituto de Astronomía, Universidad Nacional Autónoma de México, Mexico

Received 2010 June 23; accepted 2011 August 15

RESUMEN

Se presenta un estudio del espesor óptico del aerosol atmosférico (AOT por sus siglas en inglés) en el sitio astronómico de San Pedro Mártir, B. C., México durante el periodo 2000–2008. Las mediciones del AOT se realizaron con el instrumento *Moderate Resolution Imaging Spectroradiometer* (MODIS), a bordo de los satélites *Aqua* y *Terra* de la NASA. Se han identificado valores característicos estacionales que muestran un comportamiento de mayor transparencia atmosférica durante el otoño. Las mejores condiciones de transparencia atmosférica ocurren durante octubre y noviembre. El comportamiento anual durante 2000–2008 del AOT de MODIS da valores promedio de 0.147 ± 0.103, 0.128 ± 0.090, 0.115 ± 0.081, 0.087 ± 0.066 en 4700, 5500, 6600 and 21300 Å, respectivamente. Utilizando estos valores promedio se analizó la dependencia del AOT con la longitud de onda, y se encontró que $\alpha_{\rm OIR} \sim 0.31 \pm 0.06$ y la relación $\tau_\lambda \sim 0.0061\lambda^{-0.31}$ para dispersión por aerosoles en el sitio de San Pedro Mártir.

ABSTRACT

A study is presented of the atmospheric aerosol optical thickness (AOT) in the astronomical site of San Pedro Mártir, B. C., Mexico, during the 2000–2008 period. The AOT measurements were made by the *Moderate Resolution Imaging Spectroradiometer* (MODIS) instrumentation, on board of the NASA *Aqua* and *Terra* satellites. Characteristic seasonal values were identified, showing a higher atmospheric transparency in autumn. The best conditions for atmospheric transparency occur in October and November. The annual behavior of MODIS AOT yields average values for SPM during the years 2000–2008 of 0.147 ± 0.103, 0.128 ± 0.090, 0.115 ± 0.081, 0.087 ± 0.066 at 4700, 5500, 6600 and 21300 Å, respectively. We used these mean values to analyze the wavelength dependence and found aerosol scattering slopes $\alpha_{\rm OIR} \sim 0.31 \pm 0.06$, and a relation $\tau_\lambda \sim 0.0061\lambda^{-0.31}$, for aerosol scattering over the San Pedro Mártir location.

Key Words: atmospheric effects — site testing

1. INTRODUCTION

Until recently, the measurements of the atmospheric opacity of aerosol were obtained on ground-based observing stations as AERONET from NASA, that has more than 100 stations distributed around the world. It is not until 2000 and 2002 that the operation of the NASA satellites *Terra* and *Aqua* started, and systematic measurements at different geographic locations of the atmospheric aerosol optical thickness (AOT), among many other parameters, were made available. The ambient AOT of different locations around the world have been obtained using these satellites and compared to AERONET data in several publications (e.g., Ichoku et al. 2002, 2004; de Meij et al. 2006; Pires, Correia, & Paixao 2007; Green, Kondragunta, & Ciren 2008; Xia et al. 2008), to study AOT variations.

The characterization of astronomical sites (e.g., Muñoz-Tuñón, Sarazin, & Vernin 2007; Schöck et al. 2007; Tapia et al. 2007) require a detailed and long term testing, in terms both of precision and variability, of a variety of characteristics includ-

ing fractional cloud cover, precipitable water vapor, long-term weather patterns, prevailing winds, atmospheric seeing and turbulence profiles, geologic activity, local climate variability, light pollution, among others. Mexico's National Astronomical Observatory (OAN) site is at San Pedro Mártir (SPM), located 31°02′40″ N and 115°28′00″ W, some 100 km east of the West Coast of Baja California, Mexico. Astronomical characterization studies of SPM since the 1980's have been reported in a dedicated volume edited by Cruz-González, Ávila, & Tapia (2003), and in a collection of progress reports: Cruz-González et al. (2004), Tapia, Cruz-González, & Ávila (2007), Tapia et al. (2007).

Among the concepts related to geophysical properties that have been recently introduced in astronomical site testing is the role played by aerosols (e.g., Varela et al. 2007; Varela et al. 2008). These authors argue that ambient aerosol content characterization in a site is important because aerosols may produce more stable condensation nuclei, delay precipitation and affect extraterrestrial radiation by extinction, absorption, diffusion and reflection.

We present a study of the optical depth of the atmospheric aerosol in the SPM astronomical site. The observation period considered corresponds to the years 2000 to 2008. The data were obtained from the *Moderate Resolution Imaging Spectroradiometer* (MODIS) instrumentation on board the NASA satellites *Aqua* and *Terra*. We studied the seasonal, monthly and annual behavior of the atmosphere aerosol optical thickness, AOT, at the wavelengths 470, 550, 660 and 2130 nm. This paper's content is as follows: In § 2 we present basic observational atmospheric solar radiation techniques; followed by a description of the satellites and instrumentation presented in § 3. The characteristics of the data are given in § 4 and the methodology is described in § 5, followed by results and analysis description in § 6. Finally, our conclusions are presented in § 7.

2. OBSERVATIONAL ATMOSPHERIC SOLAR RADIATION TECHNIQUES

Atmospheric solar radiation techniques consider both terrestrial and spatial observations. Terrestrial observations of direct radiation have been used to evaluate the optical depth τ_λ of atmospheric aerosols at different wavelengths λ of the electromagnetic spectrum, through the relation given by Iqbal (1983):

$$I(\lambda) = I_0(\lambda)e^{-\tau_\lambda m}\,, \tag{1}$$

where I_λ is the measured irradiance (W m^{-2}), $I_0(\lambda)$ is the atmospheric top irradiance (W m^{-2}), τ_λ is the optical depth (adimensional), m the air mass (adimensional) and λ is the wavelength (nm).

On the other hand, spatial observations of reflected solar radiation have been used to evaluate the optical depth τ_λ of atmospheric aerosols using sophisticated modeling (e.g., Toon & Pollack 1976). The details of the algorithm and the theoretical basis of aerosol data retrieval from the MODIS Collection 5 data base are presented in Remer et al. (2005) and Remer, Tanré, & Kaufman (2006). These authors point out that the ambient aerosol optical depth (AOD) is proportional to the aerosol total loading in the vertical column. They show that the upward reflectance (normalized solar radiance), at the top of the atmosphere (TOA), is a function of successive orders of radiation interactions, within the coupled surface-atmosphere system. The TOA angular (for θ_0, θ, and ϕ = the solar zenith, view zenith and relative azimuth angles) spectral reflectance given by $\rho_\lambda(\theta_0,\theta,\phi)$ at a wavelength λ results from the contribution of scattering of radiation within the atmosphere without interaction with the surface, known as the "atmospheric path reflectance", the reflection of radiation off the surface that is directly transmitted to the TOA ("surface function"), and the reflection of radiation from outside the sensor's field of view ("environment function"). They argue that if the environment function is neglected, the TOA angular spectral reflectance, $\rho^*_\lambda(\theta_0,\theta,\phi)$ can be approximated by (c.f. equation 8 in Remer et al. 2006):

$$\rho^*_\lambda(\theta_0,\theta,\phi) \;=\; \rho^a_\lambda(\theta_0,\theta,\phi) + \frac{F_\lambda(\theta_0)T_\lambda(\theta)\rho^s_\lambda(\theta_0,\theta,\phi)}{1 - s_\lambda\rho^s_\lambda(\theta_0,\theta,\phi)}\,, \tag{2}$$

where ρ^a_λ is the atmospheric path reflectance, F_λ is the normalized downward flux for zero surface reflectance, T_λ represents the upward total transmission into the satellite field of view, s_λ is the atmospheric back-scattering ratios, and ρ^s_λ is the angular spectral surface reflectance. They show that except for the surface reflectance, each term on the right hand side of this equation is a function of the aerosol type and loading, including aerosol optical depth (AOD) and the fine weighting (FW) of the ambient undisturbed aerosol. Assuming that a small set of aerosol types and loadings can describe the range of global aerosol, they have obtained a look-up table that contains their simulations of these aerosol conditions. The goal of their algorithm is to use this look-up table (c.f. their § 4.3) to determine the conditions that best mimic the MODIS-observed spectral reflectance ρ^m_λ, to retrieve the associated aerosol

properties (including AOD and FW). They argue that the difficulty lies in making the most appropriate assumptions about both the surface and atmospheric contributions. Remer et al. (2006) detailed in § 4.3 of their work the strategy, formulation and calibration with the AERONET data, and describe in detail the algorithm to obtain the land aerosol optical depth (AOD). They presented the surface reflectance assumptions in their § 4.4, followed by the retrieval algorithm in § 4.5. From the comparison to AERONET data they demonstrate that their algorithm is quite reliable for AOD and FW data from MODIS Collection 5.

3. SATELLITES AND INSTRUMENTATION

Detailed information on the *Terra* and *Aqua* multinational projects can be obtained at the NASA Web pages[1].

3.1. *Terra spacecraft*

The NASA satellite *Terra*, formerly known as *EOS AM-1*, carries a payload of five sensors that study interactions among Earth's atmosphere, land, oceans, life and radiant energy (heat and light). Each sensor is designed to meet a wide range of science objectives. Two of the instruments were supplied by Canada and Japan. *Terra* is in a 100-minute polar orbit 437 miles above Earth, flying in close formation with the photography satellite *Landsat 7*, which was launched in April 1999. In 2002 *Terra* was joined by a complementary satellite, *Aqua*, formerly known as *EOS PM-1*, that crosses over the equator each orbit at a later time. *Terra* circles Earth from pole to pole in an orbit that descends across the equator at 10:30 AM when cloud cover is minimal and its view of the surface is least obstructed. The orbit is perpendicular to the direction of Earth's spin.

3.2. *Terra sensors*

The sensors on *Terra* do not actively scan the surface like laser beams or microwave pulses do, rather, they work like a camera. Sunlight reflected by Earth, and heat emitted by Earth, pass through the apertures of *Terra*'s sensors. That radiant energy is focused on detectors that are sensitive to selected regions of the electromagnetic spectrum, ranging from visible to infrared light. The information produced by the detectors is transmitted down to Earth and processed by computers into images that people can interpret. *Terra* sends down as much as one terabyte of data per day.

[1] `http://terra.nasa.gov/` and `http://aqua.nasa.gov/`, respectively.

TABLE 1

AQUA AND THE A-TRAIN

Satellite	Launch
Aura	2004 July 15
Aqua	2002 May 4
Terra	1999 December 18

The formation of orbiting satellites is referred to as the *A-Train*, and the launch dates are resented in Table 1. Together, their overlapping radars are providing a more comprehensive picture of weather and climate on global Earth. The *A Train* satellites fly in low polar orbits 438 miles above Earth. They circle Earth 14 times a day. *Aqua* crosses the equator at approximately 1:30 AM and 1:30 PM, local time, about 3 hours behind *Terra*. Due to the narrow field of view of its instruments, it takes about 16 days for *Aqua* to map the entire surface of the planet.

3.3. *Aqua Science Instruments*

Each of the school-bus-sized satellite's six science instruments is designed to monitor a different part of our global plumbing system. The six instruments are:

- Atmospheric Infrared Sounder (AIRS)
- Advanced Microwave Sounding Unit (AMSU-A)
- Humidity Sounder for Brazil (HSB)
- Advanced Microwave Scanning Radiometer for EOS (AMSR-E)
- Moderate-Resolution Imaging Spectroradiometer (MODIS)
- Clouds and the Earth's Radiant Energy System (CERES)

The data obtained by all these instruments is available in a public database supported by NASA.

4. MODIS DATA

The MODIS data was obtained from the NASA public database[2]. The MODIS Aerosol Product monitors the ambient aerosol optical thickness (AOT $\equiv \tau$ in equation 1 above) over the oceans globally and over a portion of the continents.

We extracted MODIS data for the San Pedro Mártir, Baja California, Mexico geographic location,

[2] `http://modis.gsfc.nasa.gov/`.

TABLE 2

SAN PEDRO MÁRTIR AEROSOL OPTICAL THICKNESS (AOT) DATA

Source of solar radiation data:	MODIS Aerosol, NASA
Satellites:	*Aqua* and *Terra*
Instrument:	Moderate Resolution Imaging Spectroradiometer
Site:	San Pedro Mártir, Baja California, Mexico
Location:	
Latitude	31°02′40″ North
Longitude	115°28′00″ West
Elevation:	2830 m
Aerosol optical depth observations (2000–2008):	1078
Data Files:	4008
Format:	HDF
Product Files:	MOD04_ L2
Collection:	5
Parameter:	Corrected_ Optical_ Depth_ Land
Wavelengths, λ (nm):	470, 550, 660
Bandwidth $\Delta\lambda$ (nm):	20, 20, 50
Parameter:	Corrected_ Optical_ Depth_ Land_ wav2p1
Wavelength:	2130 nm
Bandwidth $\Delta\lambda$ (nm):	50
Re projection:	Geographic
Re-projected Files:	8016
Extraction Data Files:	8016

to obtain the ambient land aerosol optical thickness (AOT). Data were obtained for the period from January 2000 to December 2008 at the four spectrometer wavelengths: 470, 550, 660 and 2130 Å, since we are also interested in the wavelength dependence τ_λ. The data characteristics are presented in Table 2. The MODIS photometers channels are presented in Table 1 of Remer et al. (2006), we note that the central wavelength and bandwidth (in parenthesis) presented in their table are 466 (20), 553 (20), 646 (50) and 2119 (50) nm, which are slightly different from the ones in the MODIS Web site.

5. METHODOLOGY

In order to obtain the atmospheric optical thickness (AOT) data of the SPM site at the selected wavelengths (4700, 5500, 6600 y 21300 Å) a set of necessary data processing steps were required. The data were processed as follows.

5.1. *Data files acquisition MOD04*

The data files for the 2000–2008 period were obtained from the LAADS (Level 1 and Atmosphere Archive and Distribution System) Web site, where the location of the site and the required period is provided as input. The daily AOT data are available for retrieval but the supplied images are given in geodetic coordinates.

5.2. *Geographic re-projection*

The necessary transformation from geodetic to geographic coordinates was done using a re-projection script and was applied to each image file using the program HDFLook. The re-projected images were constructed with a resolution of 10 km × 10 km per pixel, which is the maximum possible resolution of the system. In this way, the site location can be obtained at the pixel position of the selected site.

5.3. *Data extraction of AOT (470, 550, 660 y 2130 nm)*

Using the re-projected images the final data extraction of the aerosol optical thickness, AOT, was done with another script, using the HDFLook program.

5.4. *Temporal AOT for SPM*

The data were extracted year by year to avoid errors. For the period 2000–2008 the total number

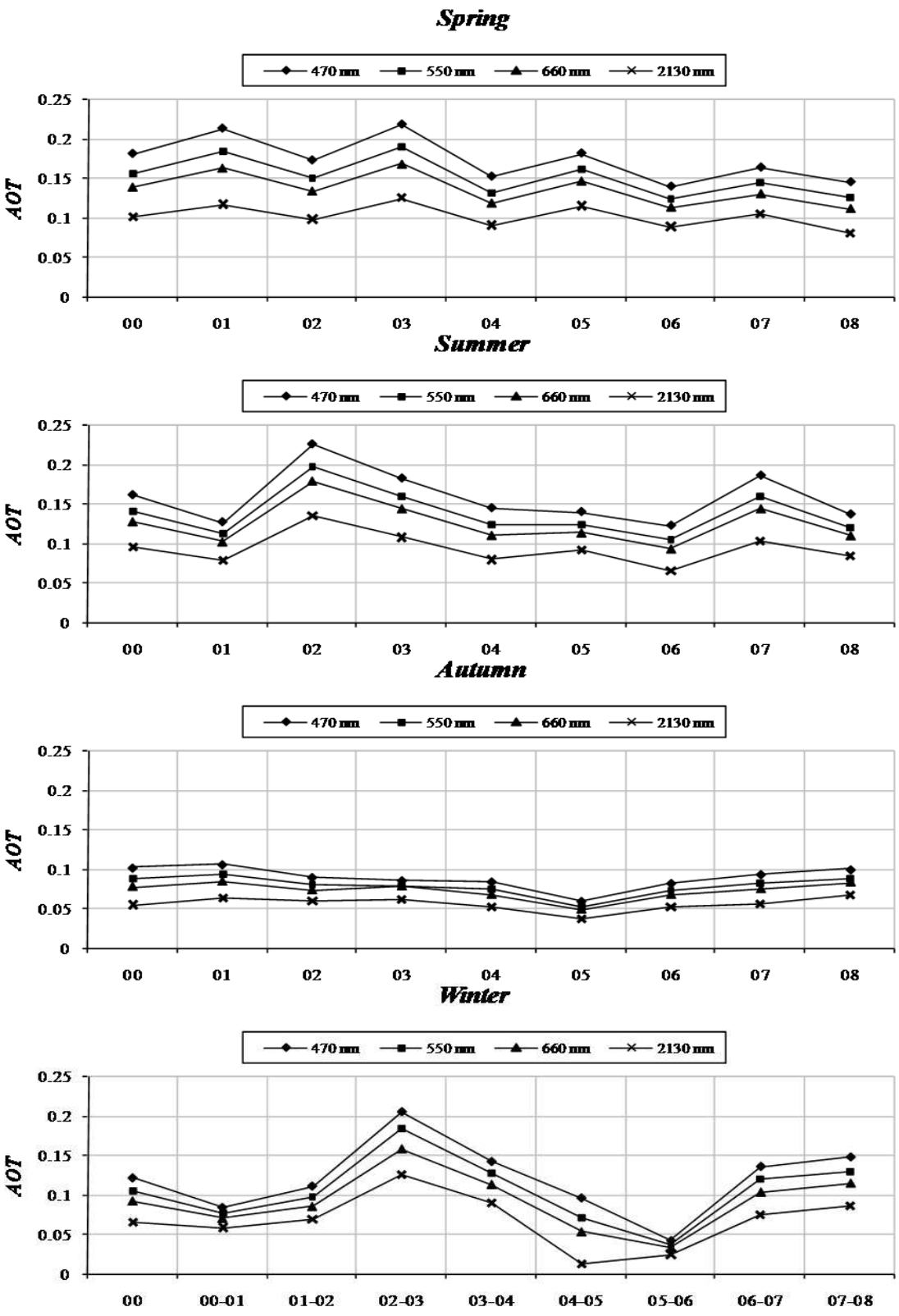

Fig. 1. The average seasonal (March to May for spring, June to August for summer, September to November for autumn, and December to February for winter) AOT above SPM over the years 2000–2008. The color figure can be viewed online.

TABLE 3

MEAN SEASONAL VARIATION OF AOT YEARLY MEASUREMENTS FOR 2000–2008

	Number of AOT Measurements				Seasonal AOT Measurement			
Year	470 nm	550 nm	660 nm	2130 nm	470 nm	550 nm	660 nm	2130 nm
					SPRING			
00	61	61	61	60	0.180 ± 0.089	0.156 ± 0.076	0.138 ± 0.068	0.101 ± 0.058
01	43	43	43	43	0.212 ± 0.084	0.183 ± 0.072	0.162 ± 0.065	0.116 ± 0.061
02	52	52	52	52	0.172 ± 0.097	0.149 ± 0.084	0.133 ± 0.075	0.097 ± 0.063
03	52	52	52	51	0.217 ± 0.134	0.188 ± 0.116	0.168 ± 0.105	0.124 ± 0.089
04	53	53	53	51	0.151 ± 0.094	0.132 ± 0.080	0.118 ± 0.071	0.090 ± 0.056
05	44	44	44	44	0.181 ± 0.121	0.161 ± 0.108	0.146 ± 0.099	0.115 ± 0.081
06	33	33	33	33	0.138 ± 0.083	0.123 ± 0.074	0.113 ± 0.068	0.089 ± 0.054
07	43	43	43	41	0.163 ± 0.089	0.144 ± 0.077	0.130 ± 0.070	0.104 ± 0.054
08	42	42	43	43	0.144 ± 0.083	0.125 ± 0.070	0.111 ± 0.060	0.081 ± 0.045
2000–2008	423	423	424	418	0.173 ±0.026	0.151 ± 0.022	0.135 ± 0.019	0.102 ± 0.014
					SUMMER			
00	29	29	29	29	0.160 ± 0.090	0.141 ± 0.080	0.127 ± 0.073	0.096 ± 0.061
01	33	33	33	33	0.126 ± 0.093	0.112 ± 0.083	0.101 ± 0.075	0.078 ± 0.061
02	49	49	50	50	0.224 ± 0.170	0.197 ± 0.154	0.178 ± 0.142	0.134 ± 0.122
03	30	30	30	30	0.181 ± 0.086	0.159 ± 0.078	0.143 ± 0.074	0.107 ± 0.066
04	44	44	44	43	0.144 ± 0.100	0.124 ± 0.083	0.109 ± 0.072	0.079 ± 0.056
05	31	31	31	30	0.139 ± 0.094	0.124 ± 0.083	0.113 ± 0.075	0.091 ± 0.059
06	29	29	29	29	0.122 ± 0.077	0.105 ± 0.064	0.092 ± 0.055	0.065 ± 0.043
07	34	34	36	36	0.185 ± 0.092	0.160 ± 0.080	0.143 ± 0.071	0.102 ± 0.064
08	34	34	34	34	0.136 ± 0.096	0.120 ± 0.084	0.109 ± 0.076	0.084 ± 0.060
2000–2008	313	313	316	314	0.157 ± 0.032	0.138 ± 0.028	0.124 ± 0.025	0.093 ± 0.019
					AUTUMN			
00	22	22	22	22	0.101 ± 0.066	0.087 ± 0.053	0.077 ± 0.046	0.055 ± 0.034
01	27	27	27	27	0.105 ± 0.062	0.093 ± 0.056	0.084 ± 0.052	0.064 ± 0.043
02	30	30	31	30	0.089 ± 0.058	0.080 ± 0.051	0.073 ± 0.046	0.060 ± 0.034
03	29	28	31	30	0.085 ± 0.079	0.078 ± 0.067	0.078 ± 0.063	0.062 ± 0.048
04	23	23	23	23	0.084 ± 0.052	0.074 ± 0.046	0.067 ± 0.042	0.052 ± 0.034
05	38	38	39	38	0.059 ± 0.062	0.052 ± 0.054	0.048 ± 0.048	0.037 ± 0.037
06	25	25	27	27	0.082 ± 0.056	0.072 ± 0.050	0.067 ± 0.045	0.052 ± 0.036
07	25	25	27	26	0.093 ± 0.068	0.081 ± 0.058	0.074 ± 0.049	0.056 ± 0.037
08	30	30	33	32	0.099 ± 0.071	0.088 ± 0.063	0.083 ± 0.055	0.067 ± 0.043
2000–2008	249	248	260	255	0.089 ± 0.013	0.078 ± 0.011	0.072 ± 0.010	0.056 ± 0.008
					WINTER			
00-01	2	2	2	2	0.084 ± 0.141	0.076 ± 0.124	0.070 ± 0.112	0.058 ± 0.085
01-02	10	10	12	11	0.111 ± 0.074	0.096 ± 0.063	0.085 ± 0.050	0.068 ± 0.037
02-03	8	8	9	9	0.205 ± 0.164	0.183 ± 0.149	0.158 ± 0.132	0.124 ± 0.110
03-04	12	12	13	13	0.142 ± 0.099	0.126 ± 0.089	0.113 ± 0.078	0.089 ± 0.063
04-05	2	2	2	2	0.096 ± 0.018	0.070 ± 0.013	0.053 ± 0.010	0.013 ± 0.002
05-06	11	11	11	11	0.041 ± 0.040	0.036 ± 0.036	0.033 ± 0.033	0.024 ± 0.027
06-07	13	13	14	14	0.135 ± 0.095	0.118 ± 0.082	0.103 ± 0.072	0.074 ± 0.061
07-08	5	5	6	6	0.147 ± 0.047	0.129 ± 0.046	0.114 ± 0.041	0.086 ± 0.040
2000–2008	63	63	69	68	0.120 ± 0.046	0.104 ± 0.042	0.091 ± 0.037	0.067 ± 0.033

of registers found was 1078, with a different number of measurements found at each wavelength.

6. RESULTS

The aerosol optical thickness for the SPM site was obtained and analyzed at the four wavelengths 4700, 5500, 6600 y 21300 Å. We explore the seasonal, monthly and annual behavior of the AOT in the 2000 to 2008 period.

6.1. *Seasonal AOT at SPM*

To study the seasonal variations of the AOT, we use the common season definition for a Northern Hemisphere location, i.e. March to May for spring, June to August for summer, September to November for autumn, and December to February for winter.

In the four panels of Figure 1 we show the seasonal behavior of the AOT at the central wavelengths

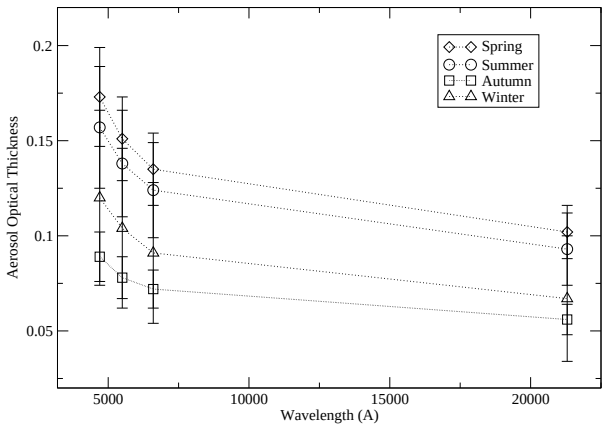

Fig. 2. The average seasonal aerosol optical depth spectral. Error bars show the estimated errors of the mean. The lowest aerosol optical thickness values occur during the autumn months.

4700, 5500, 6600 and 21300 Å. All the plots show that AOT values decrease with wavelength, as expected, and that the same variations are observed at each wavelength. In all the curves we note that the AOT is quite small, less than 0.25 for all wavelengths. In some years AOT values even less than 0.10 were obtained, specially during autumn.

In Table 3 we present the characteristics of the AOT seasonal measurements for each year during the period covered, 2000–2008, together with the resulting AOT mean values for each season and the standard deviation obtained at the four wavelengths.

By comparing the AOT values presented in Table 3 for the four seasons, we note that the lowest values are obtained in the autumn and winter months, being highest during the spring months. This is clearly seen in Figure 2 which shows the average seasonal AOT behavior with wavelength (cf. Table 3). The lowest aerosol optical thickness values occur during the autumn months with average values of 0.089 ± 0.013 at 4700 Å, 0.078 ± 0.011 at 5500 Å, 0.072 ± 0.010 at 6600 Å, and 0.056 ± 0.008 at 21300 Å. This allows us to conclude that in autumn the atmospheric transparency due to aerosols is best at SPM.

6.2. *Monthly AOT at SPM*

In Figure 3 we show the monthly behavior of the AOT at four wavelengths 470, 550, 660 and 2130 nm for the 2000 to 2008 period. For best comparison the AOT scale in all the graphs is the same. We note that in some years the months of January, February and December show scarce or no available data, while in March 2006 we found no data. The months of April to November were well covered throughout the 2000–2008 period and so the average values are more robust.

By comparing the AOT values in the twelve months we note that the lowest values are obtained in October and November, with mean values of less than 0.12 for all wavelengths. At 550 nm, which is close to the Johnson V-band, the average values in October and November are 0.074 ± 0.013 and 0.068 ± 0.021, respectively. We conclude that at all wavelengths October and November are the months with higher atmospheric transparency.

In Table 4 we present the characteristics of the AOT monthly measurements during the period 2000–2008, together with the resulting AOT average values and standard deviation.

Atmospheric extinction measurements at San Pedro Mártir have been reported by Schuster, Parrao, & Guichard (2002), and Schuster & Parrao (2001) for the years 1973–1999, and are summarized in Parrao & Schuster (2003). Individual nightly determinations of the atmospheric extinction above SPM are presented for 82 nights of 13-color photometric observations over the years 1980–1983 and from 287 nights of *ubvy* observations over the years 1984–1999. Monthly and yearly averages are given and compared for the years 1973–1999 in Schuster et al. (2002). Monthly data of atmospheric extinction above SPM covering the full period 2000–2008 are not available and so we can only compare our monthly AOT with the 1973–1999 of Schuster and collaborators. Their Tables 4, 5, and 6 show monthly averages that can be compared with our AOT mean values for the years 2000–2008.

Schuster et al. (2002) conclude that the best months for photometric observations at SPM are October and November when the atmospheric extinction is quite low, $<\kappa_y> \sim 0.1223 \pm 0.0022$ for October and 0.1195 ± 0.0022 for November, and that also during these months the observing runs are mostly stable. From their 13-color photometry they conclude that during the September, October and November months the mean observed atmospheric extinction at 5827 Å reaches the lowest values 0.1042 ± 0.0021, 0.1155 ± 0.0022 and 0.1128 ± 0.0028, respectively. These results for atmospheric extinction agree with our results for the aerosol optical depth over SPM: indeed October and November are the months with higher atmospheric transparency.

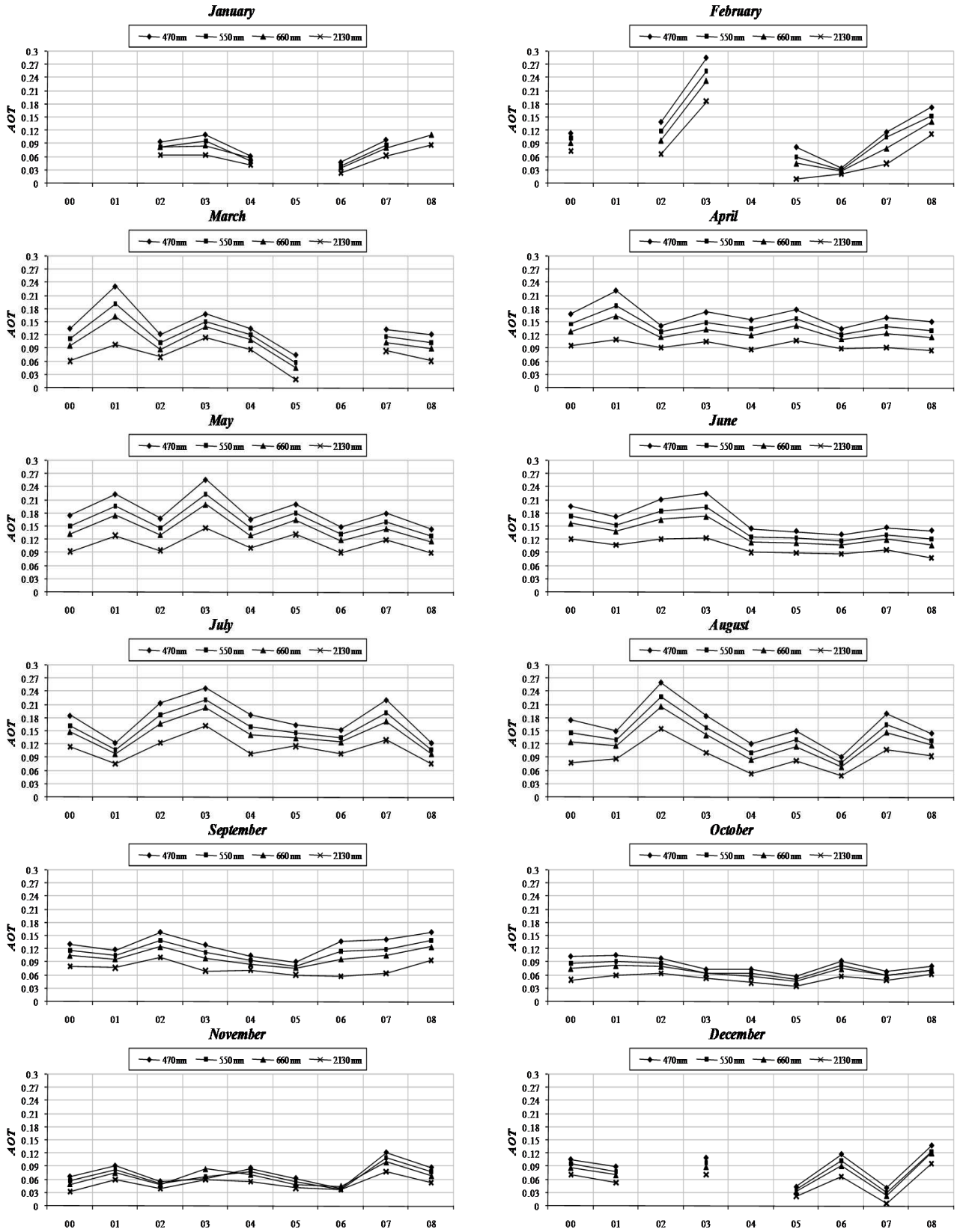

Fig. 3. Monthly Average (January to December) 2000–2008. The color figure can be viewed online.

TABLE 4

AVERAGE MONTHLY AOT ABOVE SPM OVER THE YEARS 2000–2008

	Number of AOT Measurements				Monthly AOT Measurement			
Year	470 nm	550 nm	660 nm	2130 nm	470 nm	550 nm	660 nm	2130 nm
					JANUARY			
02	3	3	4	4	0.095 ± 0.032	0.084 ± 0.029	0.083 ± 0.024	0.066 ± 0.019
03	4	4	5	5	0.111 ± 0.059	0.097 ± 0.055	0.087 ± 0.046	0.065 ± 0.041
04	3	3	4	4	0.062 ± 0.083	0.053 ± 0.073	0.058 ± 0.058	0.043 ± 0.047
06	6	6	6	6	0.048 ± 0.039	0.041 ± 0.036	0.036 ± 0.034	0.024 ± 0.030
07	1	1	1	1	0.099 ± ···	0.089 ± ···	0.081 ± ···	0.064 ± ···
08	0	0	1	1	··· ± ···	··· ± ···	0.111 ± ···	0.088 ± ···
					FEBRUARY			
00	2	2	2	2	0.115 ± 0.063	0.103 ± 0.056	0.093 ± 0.051	0.074 ± 0.040
02	5	5	6	6	0.140 ± 0.085	0.119 ± 0.072	0.098 ± 0.059	0.068 ± 0.050
03	2	2	2	2	0.286 ± 0.051	0.256 ± 0.046	0.234 ± 0.042	0.186 ± 0.035
05	1	1	1	1	0.083 ± ···	0.061 ± ···	0.046 ± ···	0.011 ± ···
06	3	3	3	3	0.035 ± 0.028	0.031 ± 0.025	0.028 ± 0.023	0.022 ± 0.018
07	1	1	2	2	0.117 ± ···	0.105 ± ···	0.080 ± 0.021	0.046 ± 0.043
08	2	2	2	2	0.173 ± 0.045	0.155 ± 0.040	0.141 ± 0.037	0.112 ± 0.029
					MARCH			
00	9	9	9	9	0.135 ± 0.072	0.113 ± 0.057	0.097 ± 0.049	0.062 ± 0.044
01	3	3	3	3	0.232 ± 0.092	0.192 ± 0.070	0.163 ± 0.060	0.099 ± 0.071
02	5	5	5	4	0.123 ± 0.083	0.103 ± 0.064	0.089 ± 0.052	0.071 ± 0.028
03	8	8	8	8	0.169 ± 0.185	0.152 ± 0.166	0.140 ± 0.152	0.114 ± 0.123
04	14	14	14	14	0.135 ± 0.089	0.121 ± 0.080	0.110 ± 0.073	0.087 ± 0.058
05	2	2	2	2	0.075 ± 0.047	0.058 ± 0.030	0.047 ± 0.019	0.020 ± 0.008
07	13	13	13	12	0.133 ± 0.103	0.116 ± 0.090	0.104 ± 0.081	0.084 ± 0.065
08	8	8	8	8	0.122 ± 0.047	0.104 ± 0.043	0.091 ± 0.041	0.062 ± 0.041
					APRIL			
00	19	19	19	18	0.169 ± 0.086	0.146 ± 0.073	0.129 ± 0.065	0.096 ± 0.054
01	14	14	14	14	0.222 ± 0.068	0.188 ± 0.059	0.164 ± 0.056	0.110 ± 0.063
02	15	15	15	15	0.142 ± 0.090	0.127 ± 0.081	0.116 ± 0.073	0.092 ± 0.058
03	11	11	11	10	0.173 ± 0.131	0.150 ± 0.111	0.133 ± 0.098	0.106 ± 0.075
04	11	11	11	11	0.155 ± 0.073	0.135 ± 0.066	0.120 ± 0.062	0.086 ± 0.058
05	19	19	19	19	0.179 ± 0.137	0.157 ± 0.121	0.142 ± 0.111	0.109 ± 0.092
06	12	12	12	12	0.135 ± 0.079	0.121 ± 0.070	0.111 ± 0.063	0.089 ± 0.048
07	14	14	14	14	0.160 ± 0.092	0.140 ± 0.076	0.125 ± 0.067	0.092 ± 0.054
08	11	11	12	12	0.151 ± 0.049	0.131 ± 0.046	0.116 ± 0.042	0.085 ± 0.043
					MAY			
00	22	22	22	22	0.176 ± 0.081	0.151 ± 0.066	0.133 ± 0.058	0.093 ± 0.053
01	16	16	16	16	0.225 ± 0.101	0.196 ± 0.087	0.175 ± 0.078	0.130 ± 0.069
02	18	18	18	18	0.169 ± 0.108	0.147 ± 0.092	0.131 ± 0.081	0.095 ± 0.065
03	20	20	20	20	0.258 ± 0.138	0.224 ± 0.123	0.200 ± 0.113	0.147 ± 0.102
04	23	23	23	22	0.167 ± 0.099	0.145 ± 0.084	0.130 ± 0.074	0.100 ± 0.057
05	18	18	18	18	0.201 ± 0.115	0.180 ± 0.103	0.165 ± 0.095	0.132 ± 0.077
06	10	10	10	10	0.150 ± 0.085	0.132 ± 0.078	0.119 ± 0.073	0.091 ± 0.064
07	14	14	14	13	0.181 ± 0.093	0.160 ± 0.083	0.144 ± 0.077	0.120 ± 0.059
08	13	13	13	13	0.145 ± 0.081	0.128 ± 0.071	0.116 ± 0.064	0.090 ± 0.049
					JUNE			
00	18	18	18	18	0.196 ± 0.102	0.174 ± 0.090	0.157 ± 0.082	0.122 ± 0.066
01	10	10	10	10	0.173 ± 0.071	0.153 ± 0.063	0.139 ± 0.057	0.109 ± 0.044
02	23	23	23	23	0.212 ± 0.119	0.185 ± 0.106	0.166 ± 0.099	0.123 ± 0.087
03	21	21	21	21	0.225 ± 0.108	0.195 ± 0.092	0.173 ± 0.083	0.124 ± 0.073
04	20	20	20	19	0.145 ± 0.100	0.127 ± 0.085	0.115 ± 0.075	0.091 ± 0.056
05	10	10	10	10	0.139 ± 0.089	0.124 ± 0.080	0.113 ± 0.073	0.090 ± 0.058
06	11	11	11	11	0.132 ± 0.093	0.118 ± 0.082	0.108 ± 0.073	0.087 ± 0.056
07	15	15	15	15	0.148 ± 0.082	0.132 ± 0.073	0.120 ± 0.067	0.096 ± 0.054
08	19	19	19	19	0.141 ± 0.104	0.122 ± 0.084	0.108 ± 0.070	0.078 ± 0.045

TABLE 4 (CONTINUED)

	Number of AOT Measurements				Monthly AOT Measurement			
Year	470 nm	550 nm	660 nm	2130 nm	470 nm	550 nm	660 nm	2130 nm
					JULY			
00	12	12	12	12	0.186 ± 0.122	0.164 ± 0.107	0.149 ± 0.097	0.114 ± 0.079
01	12	12	12	12	0.124 ± 0.066	0.109 ± 0.056	0.099 ± 0.049	0.076 ± 0.038
02	16	16	16	16	0.215 ± 0.105	0.187 ± 0.094	0.167 ± 0.087	0.124 ± 0.078
03	6	6	6	6	0.248 ± 0.118	0.222 ± 0.106	0.203 ± 0.097	0.162 ± 0.078
04	16	16	16	16	0.188 ± 0.099	0.161 ± 0.083	0.142 ± 0.074	0.099 ± 0.065
05	13	13	13	12	0.164 ± 0.101	0.147 ± 0.090	0.134 ± 0.083	0.116 ± 0.060
06	8	8	8	8	0.153 ± 0.060	0.137 ± 0.054	0.125 ± 0.049	0.099 ± 0.039
07	13	13	14	14	0.221 ± 0.100	0.194 ± 0.085	0.172 ± 0.073	0.129 ± 0.064
08	11	11	11	11	0.123 ± 0.110	0.109 ± 0.096	0.099 ± 0.086	0.076 ± 0.065
					AUGUST			
00	3	3	3	3	0.175 ± 0.067	0.147 ± 0.058	0.126 ± 0.055	0.079 ± 0.062
01	9	9	9	9	0.150 ± 0.145	0.131 ± 0.131	0.118 ± 0.121	0.088 ± 0.102
02	15	15	16	16	0.261 ± 0.248	0.229 ± 0.227	0.206 ± 0.205	0.156 ± 0.179
03	8	8	8	8	0.184 ± 0.057	0.159 ± 0.056	0.141 ± 0.056	0.101 ± 0.061
04	13	13	13	13	0.121 ± 0.114	0.101 ± 0.090	0.086 ± 0.074	0.053 ± 0.051
05	6	6	6	6	0.150 ± 0.097	0.130 ± 0.084	0.116 ± 0.075	0.084 ± 0.062
06	14	14	14	14	0.091 ± 0.075	0.079 ± 0.062	0.070 ± 0.053	0.049 ± 0.039
07	9	9	9	9	0.190 ± 0.103	0.165 ± 0.091	0.148 ± 0.083	0.109 ± 0.072
08	10	10	10	10	0.145 ± 0.100	0.130 ± 0.089	0.118 ± 0.081	0.094 ± 0.065
					SEPTEMBER			
00	18	18	18	18	0.131 ± 0.054	0.116 ± 0.049	0.105 ± 0.046	0.081 ± 0.039
01	16	16	16	16	0.118 ± 0.067	0.106 ± 0.058	0.097 ± 0.052	0.078 ± 0.040
02	17	17	17	16	0.158 ± 0.109	0.139 ± 0.095	0.125 ± 0.086	0.100 ± 0.068
03	14	14	14	14	0.129 ± 0.052	0.112 ± 0.045	0.099 ± 0.041	0.071 ± 0.038
04	14	14	14	13	0.105 ± 0.068	0.093 ± 0.061	0.085 ± 0.055	0.073 ± 0.041
05	11	11	12	12	0.090 ± 0.060	0.081 ± 0.052	0.077 ± 0.046	0.062 ± 0.036
06	9	9	9	9	0.137 ± 0.075	0.114 ± 0.058	0.097 ± 0.048	0.059 ± 0.037
07	15	15	16	16	0.141 ± 0.060	0.119 ± 0.048	0.106 ± 0.042	0.065 ± 0.037
08	11	11	11	11	0.158 ± 0.091	0.139 ± 0.080	0.125 ± 0.072	0.094 ± 0.060
					OCTOBER			
00	10	10	10	10	0.104 ± 0.067	0.087 ± 0.051	0.076 ± 0.041	0.050 ± 0.027
01	12	12	12	12	0.107 ± 0.060	0.093 ± 0.056	0.082 ± 0.053	0.060 ± 0.047
02	16	16	16	16	0.099 ± 0.052	0.089 ± 0.046	0.081 ± 0.042	0.064 ± 0.034
03	15	15	17	16	0.074 ± 0.090	0.066 ± 0.077	0.065 ± 0.065	0.054 ± 0.048
04	13	13	13	13	0.075 ± 0.047	0.065 ± 0.040	0.059 ± 0.036	0.044 ± 0.029
05	20	20	20	20	0.058 ± 0.071	0.052 ± 0.060	0.047 ± 0.053	0.036 ± 0.039
06	13	13	13	13	0.093 ± 0.046	0.083 ± 0.042	0.075 ± 0.039	0.058 ± 0.033
07	12	12	14	13	0.069 ± 0.065	0.061 ± 0.057	0.061 ± 0.050	0.049 ± 0.039
08	14	14	13	12	0.082 ± 0.068	0.073 ± 0.061	0.072 ± 0.054	0.062 ± 0.041
					NOVEMBER			
00	5	5	5	5	0.067 ± 0.088	0.057 ± 0.071	0.049 ± 0.060	0.033 ± 0.040
01	9	9	9	9	0.092 ± 0.067	0.082 ± 0.060	0.075 ± 0.054	0.060 ± 0.043
02	8	8	9	9	0.056 ± 0.055	0.051 ± 0.047	0.048 ± 0.039	0.040 ± 0.027
03	6	5	6	6	0.064 ± 0.076	0.065 ± 0.067	0.084 ± 0.086	0.061 ± 0.071
04	5	5	5	5	0.087 ± 0.033	0.078 ± 0.030	0.071 ± 0.027	0.056 ± 0.021
05	10	10	10	9	0.063 ± 0.065	0.055 ± 0.058	0.050 ± 0.053	0.041 ± 0.043
06	7	7	9	9	0.040 ± 0.040	0.036 ± 0.035	0.045 ± 0.037	0.036 ± 0.028
07	6	6	6	6	0.123 ± 0.051	0.110 ± 0.045	0.100 ± 0.042	0.079 ± 0.033
08	10	10	13	13	0.088 ± 0.047	0.078 ± 0.043	0.068 ± 0.035	0.053 ± 0.030
					DECEMBER			
00	3	3	3	3	0.106 ± 0.107	0.095 ± 0.094	0.088 ± 0.085	0.071 ± 0.064
01	2	2	2	2	0.090 ± 0.093	0.079 ± 0.081	0.071 ± 0.073	0.053 ± 0.054
03	4	4	4	4	0.110 ± 0.026	0.098 ± 0.023	0.090 ± 0.021	0.071 ± 0.016
05	7	7	7	7	0.043 ± 0.046	0.037 ± 0.039	0.032 ± 0.034	0.022 ± 0.025
06	4	4	4	4	0.118 ± 0.081	0.102 ± 0.074	0.092 ± 0.069	0.067 ± 0.059
07	1	1	1	1	0.041 ± ···	0.030 ± ···	0.023 ± ···	0.005 ± ···
08	2	2	3	3	0.138 ± 0.121	0.123 ± 0.109	0.121 ± 0.072	0.096 ± 0.056

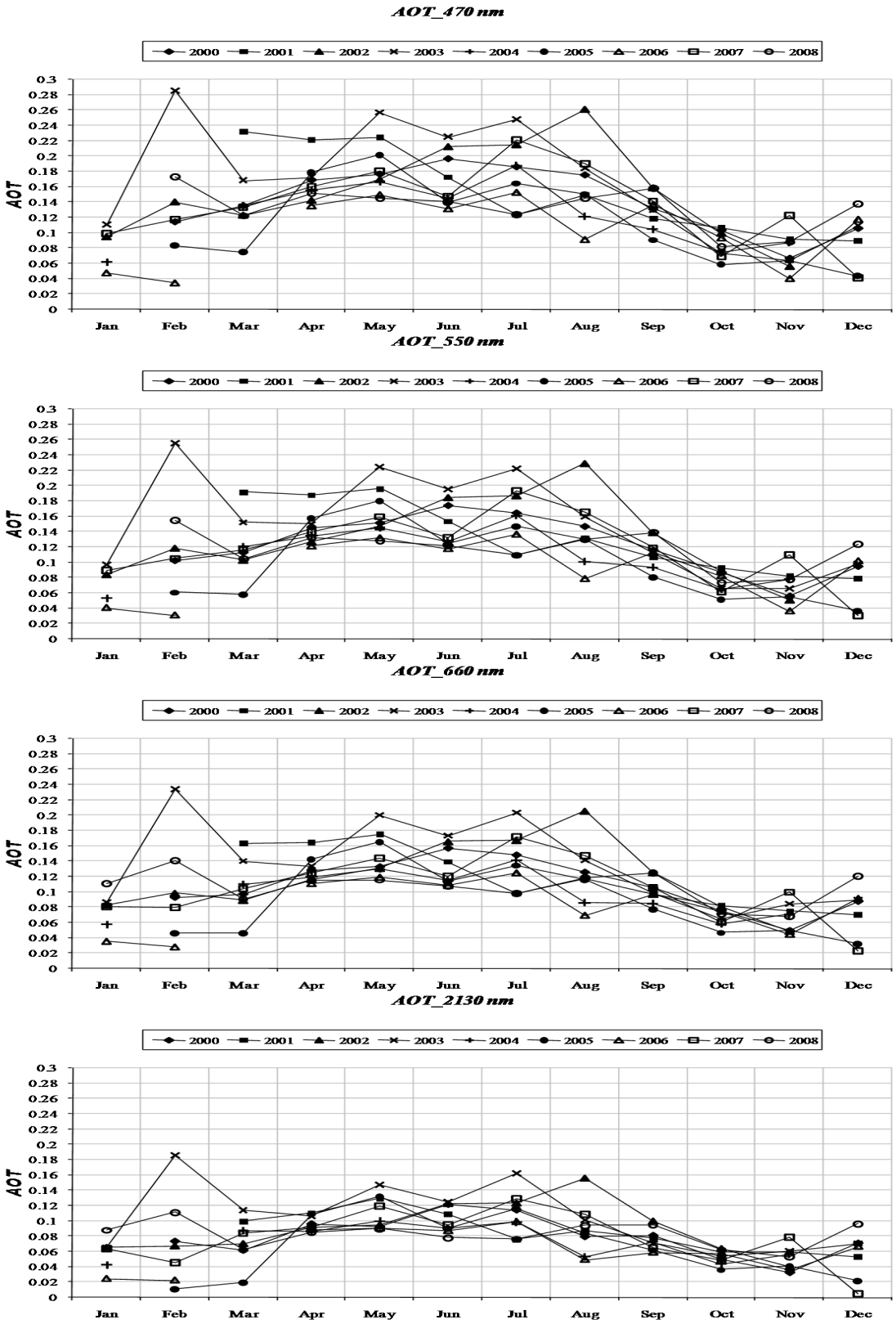

Fig. 4. Annual AOT behavior at the SPM location by monthly average at 470 nm (top), 550 nm (second from top to bottom), 660 nm (third from top to bottom), and 2130 nm (bottom). The color figure can be viewed online.

TABLE 5

AVERAGE ANNUAL AOT ABOVE SPM OVER THE YEARS 2000–2008

		Number of AOT Measurements				Annual AOT Measurement			
Year	Registers	470 nm	550 nm	660 nm	2130 nm	470 nm	550 nm	660 nm	2130 nm
2000	121	121	121	121	120	0.156 ± 0.089	0.135 ± 0.077	0.121 ± 0.069	0.088 ± 0.057
2001	103	103	103	103	103	0.157 ± 0.094	0.137 ± 0.082	0.122 ± 0.074	0.090 ± 0.061
2002	145	141	141	145	143	0.168 ± 0.131	0.147 ± 0.116	0.132 ± 0.106	0.100 ± 0.088
2003	123	119	118	122	120	0.175 ± 0.124	0.154 ± 0.108	0.138 ± 0.097	0.104 ± 0.080
2004	133	132	132	133	130	0.136 ± 0.093	0.119 ± 0.079	0.106 ± 0.070	0.079 ± 0.055
2005	118	117	117	118	116	0.126 ± 0.109	0.112 ± 0.096	0.101 ± 0.088	0.080 ± 0.071
2006	99	97	97	99	99	0.110 ± 0.076	0.097 ± 0.067	0.087 ± 0.060	0.066 ± 0.048
2007	119	114	114	119	116	0.151 ± 0.092	0.132 ± 0.080	0.118 ± 0.071	0.090 ± 0.058
2008	117	111	111	116	115	0.130 ± 0.084	0.114 ± 0.073	0.102 ± 0.063	0.078 ± 0.049
Average 2000–2008	1078	1055	1054	1076	1062	0.147 ± 0.103	0.128 ± 0.090	0.115 ± 0.081	0.087 ± 0.066

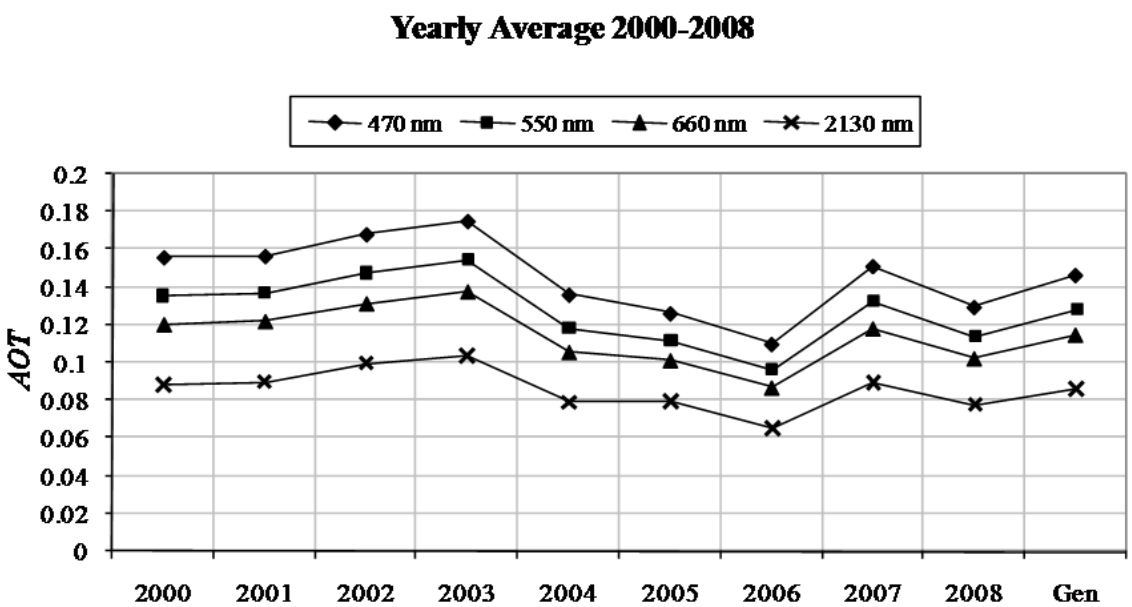

Fig. 5. Annual aerosol optical depth average at SPM at 470, 550, 660 and 2130 nm during the years 2000–2008. The color figure can be viewed online.

6.3. *Annual behavior of AOT in four wavelengths by monthly average*

In Figure 4 we show the annual behavior of the AOT by monthly average at the four wavelengths 470, 550, 660 and 2130 nm. For best comparison the AOT scale in all graphs is kept the same. By comparing the monthly AOT values we note that lowest values for the aerosol optical depth in all wavelength bands are obtained also during October and November in a consistent way through the years 2000–2008. As mentioned above, for the months of January and February there are not enough data in the studied period and mean values are less reliable.

In Table 5 we present the characteristics of the atmospheric optical depth annual measurements during the years 2000–2008 for the SPM location, together with the resulting AOT average values and standard deviation.

6.4. *Annual and general behavior of AOT*

The annual average and the general behavior of the aerosol optical depth for the SPM location for the period 2000–2008 at the four studied wavelengths 470, 550, 660 and 2130 nm is shown in Figure 5.

6.5. *AOT Climatology (2000 – 2008)*

We conclude that MODIS data obtained during the 2000–2008 of the San Pedro Mártir astronomical site in Baja California, Mexico yield an AOT climatology with the values presented in Table 6.

The final results could be compared with other sites in the globe. Gupta et al. (2006) presented

TABLE 6

SAN PEDRO MÁRTIR, BAJA CALIFORNIA (MEXICO) AEROSOL OPTICAL DEPTH CLIMATOLOGY FROM MODIS FOR 2000–2008

Wavelength (nm)	Number of AOT Measurements	AOT 2000-2008
470	1055	0.147 ± 0.103
550	1054	0.128 ± 0.090
660	1076	0.115 ± 0.081
2130	1062	0.087 ± 0.066

TABLE 7

WAVELENGTH DEPENDENCE OF SEASONAL AEROSOL OPACITY OVER SPM FROM MODIS FOR 2000–2008

Season	$\alpha_{\rm OIR}$	$\alpha_{\rm OP}$
spring	0.31 ± 0.06	0.73 ± 0.07
summer	0.31 ± 0.06	0.69 ± 0.07
autumn	0.27 ± 0.05	0.62 ± 0.11
winter	0.35 ± 0.07	0.81 ± 0.05
Average 2000–2008	0.31 ± 0.06	0.72 ± 0.08

AOT results for a collection of 26 locations in Sidney, Delhi, Hong Kong, New York City and Switzerland that cover urban populated to rural areas. The results of the rural areas in Australia and Switzerland compare quite well with the SPM results; at 550 nm they show mean annual values of 0.10 ± 0.08 and 0.16 ± 0.10, respectively, compared to our results that range from 0.10 to 0.15 in the period studied. On the other hand, Varela et al. (2008) show that in the Canarian Observatories site the AOT values found have a much wider range than the SPM values, with some dusty periods that produce a collection of MODIS AOT values at 550 nm above 0.40. But they show that, at this observatory site, most of the time the AOT have values between 0.02 and 0.20 (see Figures 12 and 13 in Varela et al. 2008). From their data in Figures 12 and 13 their average value is probably ∼0.15, reaching values as large as ∼0.7, but no average values are estimated in their work.

6.6. *AOT Spectral Slopes*

In Table 7 we present linear regression fits to the seasonal AOT values assuming that aerosols have a

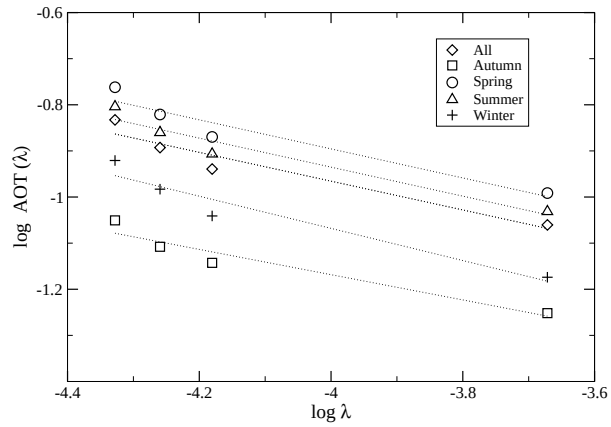

Fig. 6. Spectral dependence of aerosol optical depth obtained from MODIS data for San Pedro Mártir. Seasonal data are shown as follows: spring (circle), summer (triangle), autumn (square) and winter (plus), together with mean values for the 2000–2008 period (diamond). The dotted lines represent the linear regression fits to the data (c.f. slope values in Table 7). The color figure can be viewed online.

power-law behavior with wavelength of the form

$$AOT \equiv \tau_A(\lambda) \propto \lambda^{-\alpha}\,. \tag{3}$$

As is shown by Junge (1963) if the aerosol refractive indices are constant, aerosol particles with power-law size distributions given by $dN(r) \propto r{-}(\beta+1)$ produce wavelength-dependent optical depths of the form

$$\tau \;\propto\; \lambda^{-(\beta-2)}\,. \tag{4}$$

So the slope α above corresponds to the slope $\beta - 2$ of these models.

We have calculated α values, assuming $\tau_\lambda \propto \lambda^\alpha$, for the wavelengths 4700, 5500, 6600 and 21300 Å which are labeled OIR (optical to near-infrared) and for the visible region 4700, 5500 and 6600 Å labeled OP, with linear fits to the average seasonal AOT values presented in Tables 3 and 6. The results are presented in Table 7 and graphically in Figure 6. Note that $\alpha_{\rm OIR}$ has values between 0.27 (autumn) and 0.35 (winter) while $\alpha_{\rm OP}$ has values from 0.62 (autumn) to 0.82 (winter). We conclude that for periods with higher atmospheric transparency the spectral slope α is smaller and steepens for periods with higher opacity.

We have also used the average values for the years 2000–2008 (c.f. Table 6) which yield $\alpha_{\rm OIR} \sim 0.31 \pm 0.06$ ($\tau_\lambda \sim 0.0061\lambda^{-0.31}$) and $\alpha_{\rm OP} \sim 0.72 \pm 0.08$ ($\tau_\lambda \sim 0.0001\lambda^{-0.72}$) for the San Pedro Mártir location.

We can compare these α values with the radiative transfer models of global atmospheric aerosols of Toon & Pollack (1976). In particular, with their Figure 8b where the contribution of different layers of the atmosphere is shown to produce a steepening in their calculated optical depth $\tau(\lambda)$ curves in the 0.1 to 10 μm interval, with values of $\alpha \sim 0.25$ for atmosphere heights between sea-level and 3 km, while $\alpha \sim 0.67$ for the 3–6 km layer. Toon & Pollack (1976) argue that most visible spectral measurements indicate an average $\beta \approx 3 \pm 0.5$. The average values of the aerosol optical depth found for the SPM site show that $\beta_{\rm OP} \sim 2.7$ and $\beta_{\rm OIR} \sim 2.3$, which are thus consistent with expected values from these models. For the visible we derive an aerosol optical depth $\tau_\lambda = 0.0001\lambda^{-0.72}$ and for the OIR $\tau_\lambda = 0.0061\lambda^{-0.31}$ for the average values for the 2000–2008 period of AOT over San Pedro Mártir. As is shown by Toon & Pollack (1976) their global calculated aerosol optical depth spans a larger wavelength interval and it is expected that the OIR one that spans from 4300 to 21300 Å would be a better representation of the mean AOT in a site. Considering all the AOT data from MODIS we derived for the SPM site an average slope $\alpha_{\rm OIR}$ of 0.31 ± 0.06 for the mean aerosol optical depth spectral data.

6.7. *AOT and Stellar Atmospheric Extinction*

In Figure 7 spectral values of our mean and seasonal AOT from MODIS data for the years 2000–2008, are compared with the SPM average atmospheric extinction curve (κ_λ) obtained by Schuster & Parrao (2001) and Schuster et al. (2002) from stellar photometric observations for the years 1973–1999. Although τ_λ due to aerosol scattering and the atmospheric extinction κ_λ cannot be directly related, since the extinction over $3200 \lesssim \lambda \lesssim 6500$ Å has the contributions from aerosol scattering, Rayleigh-Cabannes scattering and ozone absorption (see equation 1 in Schuster & Parrao 2001, and references within), we can only check trends in the wavelength dependence.

On the other hand, Schuster & Parrao (2001) obtained for SPM a slope $\alpha_{\rm OP}$ of 0.87 ± 0.04 from their stellar photometric measurements during the years 1973–1999 for wavelengths from 0.3 to 1.1 μm. Their slope is somewhat larger than our average value of 0.72 ± 0.05 for 2000–2008, but note that our seasonal values vary from 0.62 to 0.81 (c.f. Table 7). Stellar photometry measurements have been used to derive the aerosol scattering slope at several astronomical observatories. For the European Southern Observatory at La Silla (Chile) Burki et al. (1995) obtained a value of $\alpha_{\rm OP}$ of 1.39, while for Cerro Tololo Inter-American Observatory, Chile, Gutiérrez-Moreno, Cortés, & Moreno (1982) found values of $\alpha_{\rm OP}$ varying from 0.2 to 2.6 during the years 1964–1980. Hayes & Latham (1975) summarize in their Table 1 average values from stellar observations for several observatories: Le Houga 0.89, Boyden 0.78, Lick 0.49, Cerro Tololo 0.81, and Mount Hopkins 0.84, and derived a mean value of 0.81 for night-time stellar photometry.

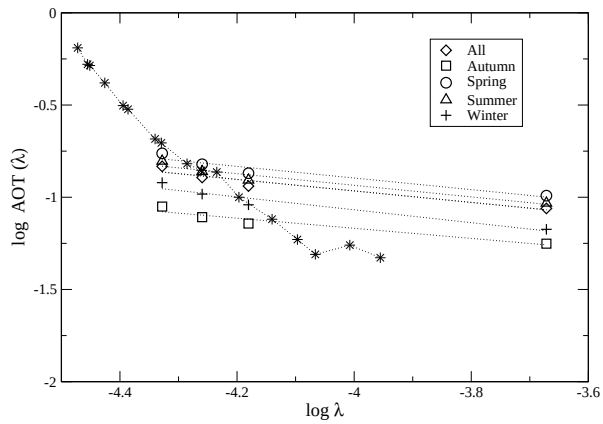

Fig. 7. Wavelength dependence of average atmospheric extinction (κ_λ) from Schuster & Parrao (2001) represented with × symbols, compared to the aerosol optical depth spectral values obtained from MODIS data for the San Pedro Mártir observatory site. The color figure can be viewed online.

If we consider the values of $\alpha_{\rm OIR}$ which probably describe somewhat better the wavelength dependence of aerosol opacity because of the larger wavelength coverage, the mean value found for SPM $\alpha_{\rm aerosol}$ of 0.31 ± 0.10 and the seasonal values 0.27 (autumn) and 0.35 (winter) compare well with the Toon & Pollack (1976) model for the atmosphere layer from 0 to 3 km, which probably indicates that at SPM this layer is dominant in the aerosol opacity.

7. CONCLUSIONS

The aerosol optical depth or thickness (AOT) values, obtained from MODIS database for the San Pedro Mártir (SPM) astronomical site in the period January 2000 to December 2008, show that the highest atmospheric transparency occurs during the autumn months, with average values AOT of 0.089 ± 0.013 at 4700 Å, 0.078 ± 0.011 at 5500 Å, 0.072 ± 0.010 at 6600 Å, and 0.056 ± 0.008 at 21300 Å. This seasonal trend is consistent with the monthly behavior that shows the best transparency conditions in October and November in all the years stud-

ied. This result agrees with Schuster et al. (2002) finding that the best months for photometric observations at SPM are October and November, when the atmospheric extinction is quite low ($<\kappa_y> \sim 0.12$) and the observing runs are mostly photometrically stable. So October and November are the months with higher atmospheric transparency and lowest atmospheric extinction.

The annual behavior of MODIS AOT during the years 2000–2008 yields mean values of 0.147 ± 0.103, 0.128 ± 0.090, 0.115 ± 0.081, 0.087 ± 0.066 at 4700, 5500, 6600 and 21300 Å, respectively.

Wavelength dependence of the aerosol optical thickness in the interval from 0.47 to 2.1 μm is analyzed for all the MODIS data assuming a power-law behavior for the aerosol scattering ($\tau_\lambda \propto \lambda^\alpha$) and indicates a slope $\alpha_{\rm OIR}$ with values between 0.27 (autumn), where the best atmospheric transparency conditions occur, and 0.35 (winter) where conditions are worse; while the 4700 to 6600 Å slope $\alpha_{\rm OP}$ has values from 0.62 (autumn) to 0.82 (winter). We conclude that for periods with higher atmospheric transparency the slope α for aerosol scattering is smaller and steepens for periods with more opacity.

We have also used the mean values for the AOT during the 2000–2008 studied period, which yields $\alpha_{\rm OIR} \sim 0.31 \pm 0.06$ ($\tau_\lambda \sim 0.0061\lambda^{-0.31}$) and $\alpha_{\rm OP} \sim 0.72 \pm 0.08$ ($\tau_\lambda \sim 0.0001\lambda^{-0.72}$) for the San Pedro Mártir location. The latter turns out to be somewhat smaller than the slope value obtained from stellar photometry by Schuster & Parrao (2001) of 0.87 for wavelengths from 0.3 to 1.1 μm. Our results confirm that the atmospheric transparency at SPM is excellent and that the best observing conditions may occur in the months of October and November.

Although we only obtained a partial climatology, since climatology requires a 20 year period, the results in the nine year period of MODIS data show that conditions over SPM are quite stable, possibly indicating that no dramatic changes in the AOT are expected. Nevertheless, further work with MODIS data is needed to obtain better estimates of the AOT, specially in the winter months of January and December, where the data are more scarce. The ambient aerosol optical thickness and the values of the aerosol spectral index of the San Pedro Mártir in Baja California astronomical site found in this paper, corroborate its high atmospheric transparency and strengthen its quality among the prime astronomical sites in the world. Finally, it is important that a long term ground-based campaign of aerosol optical depth measurements be carried out at SPM, for comparison with the MODIS AOT values obtained so far, and to establish the degree of confidence in the satellite measurements for this site.

We thank the staff at Observatorio Astronómico Nacional (Instituto de Astronomía, Universidad Nacional Autónoma de México), the Solar Radiation Observatory (Instituto de Geofísica, Universidad Nacional Autónoma de México), and the MODIS Aerosol NASA for providing valuable information and data. We thank W. Schuster and L. Parrao for kindly providing their extinction data and for helpful discussions. We also thank A. Leyva Contreras for helpful and valuable advice. We are indebted to A. Muhlia Velázquez for his assistance and personnel at the Coordination of Remote Perception in Conabio (Mexico), specially, to A. Cervera Taboada and to G. López Saldaña, for providing assistance with data processing. M. Araiza Quijano acknowledges Conacyt (Mexico) postdoctoral fellowship, and the Instituto de Astronomía, UNAM for providing the facilities and the academic environment for this work. We also thank the referee for his/her helpful comments.

REFERENCES

Burki, G., Rufener, F., Burnet, M., Richard, C., Blecha, A., & Bratschi, P. 1995, A&AS, 112, 383

Cruz-González, I., Ávila, R., & Tapia, M. 2003, RevMexAA (SC), 19, 1

Cruz-González, I., et al. 2004, Proc. SPIE, 5382, 634

de Meij, A., Krol, M., Dentener, F., Vignati, E., Cuvelier, C., & Thunis, P. 2006, Atmos. Chem. Phys., 6, 4287

Green, M. C., Kondragunta, S., & Ciren, P. 2008, Amer. Geophys. Union, Fall Meeting 2007, abst. #A24A-03

Gupta, P., Christopher, S. A., Wang, J., Gehrig, R., Lee, Y. C., & Kumar, N. 2006, Atmospheric Environment, 40, 5880

Gutiérrez-Moreno, A., Cortés, G., & Moreno, H. 1982, PASP, 94, 722

Hayes, D. S., & Latham, D. W. 1975, ApJ, 197, 593

Ichoku, C., et al. 2002, Geophys. Res. Lett., 29, MOD1-1, CiteID 8006

Ichoku, C., Kaufman, Y. J., Remer, L. A., & Levy, R. 2004, Adv. Space Res., 34, 820

Iqbal, M. 1983, An introduction to solar radiation (New York-London: Academic Press Inc.)

Junge, C. E. 1963, Air Chemistry and Radioactivity (New York: Academic Press)

Muñoz-Tuñón, C., Sarazin, M., & Vernin, J. 2007, RevMexAA (SC), 31, 1

Parrao, L., & Schuster, W. J. 2003, RevMexAA (SC), 19, 81

Pires, C., Correia, A. L., & Paixao, M. 2007, Amer. Geophys. Union, Fall Meeting 2007, abst. #A11A-0030

Remer, L. A., Tanré, D., & Kaufman, Y. J. 2006, Algorithm for Remote Sensing of Tropospheric

Aerosol from MODIS: Collection 5, NASA, Product ID: MOD04/MYD04 (http://modis.gsfc.nasa.gov/data/atbd/atbd_mod02.pdf)
Remer, L. A., et al. 2005, J. Atmospheric Sciences 62, 947
Schöck, M., Els, S., Riddle, R., Skidmore, W., & Travouillon, T. 2007, RevMexAA (SC), 31, 10
Schuster, W. J., & Parrao, L. 2001, RevMexAA, 37, 187
Schuster, W. J., Parrao, L., & Guichard, J. 2002, J. Astron. Data, 8, 2
Tapia, M., Cruz-González, I., & Avila, R. 2007, RevMexAA (SC), 28, 9
Tapia, M., Cruz-González, I., Hiriart, D., & Richer, M. 2007, RevMexAA (SC), 31, 47
Toon, O. B., & Pollack, J. B. 1976, J. Appl. Meteorology, 15, 225
Varela, A. M., Bertolin, C., Muñoz-Tuñón, C., Fuensalida, J. J., & Ortolani, S. 2007, RevMexAA (SC), 31, 106
Varela, A. M., Bertolin, C., Muñoz-Tuñón, C., Ortolani, S., & Fuensalida, J. J. 2008, MNRAS, 391, 507
Xia, X., Eck, T. F., Holben, B. N., Phillippe, G., & Chen, H. 2008, J. Geo. Res., 113, 14217

Mario R. Araiza Quijano and Irene Cruz-González: Instituto de Astronomía, Universidad Nacional Autónoma de México, Apdo. Postal 70–264, 04510 México, D. F., Mexico (maraizaq@astroscu.unam.mx, irene@astro.unam.mx).

Revista Mexicana de Astronomía y Astrofísica, **47**, 425–437 (2011)

Review

AN OVERVIEW OF THE OBSERVATIONAL AND THEORETICAL STUDIES OF HH 1 AND 2

A. C. Raga,[1] B. Reipurth,[2] J. Cantó,[3] M. M. Sierra-Flores,[1] and M. V. Guzmán[4]

Received 2011 May 23; accepted 2011 July 21

RESUMEN

Presentamos una descripción de la bibliografía sobre los objetos HH 1 y 2, desde el descubrimiento de los objetos HH (por Herbig y Haro en 1951/2) hasta el año 2010. El trabajo sobre HH 1 y 2 traza la historia del campo de los objetos Herbig-Haro, e incluye la mayor parte de los eventos importantes en el desarrollo de nuestro entendimiento de los flujos de estrellas jóvenes.

ABSTRACT

We present a description of the bibliography of HH 1 and 2, from the discovery of HH objects (by Herbig and Haro in 1951/2) up to the year 2010. The work on HH 1 and 2 traces the history of the field of Herbig-Haro objects, and includes most of the important developments of our understanding of outflows from young stars.

Key Words: ISM: jets and outflows — ISM: kinematics and dynamics — stars: mass-loss — stars: pre-main sequence

1. INTRODUCTION

HH 1 and 2 have played a fundamental role in the development of the field of Herbig-Haro (HH) objects. They were the first HH objects that were discovered, and were the exclusive objective of all of the early studies of HH spectra. Also, many of the main properties of HH objects (for example, the proper motions, and UV, radio continuum and X-ray emission) were first seen in the HH 1/2 system. Finally, many of the theoretical ideas about HH objects were first formulated so as to explain the characteristics of HH 1 and 2.

Given this fundamental role of HH 1 and 2 in the field of HH objects, we have collected a comprehensive bibliography of the (mostly refereed) papers on the HH 1/2 system. These papers include the HH 1/2 observations at all wavelengths and the theoretical papers with models that are specifically applied to HH 1 and 2. We have proceeded to make a commented bibliography[5] describing the contributions of all of these papers.

We first give a description of the region around HH 1 and 2, discussing the general observational results (§ 2). We then describe the criteria that were used to select the papers on HH 1 and 2, and give a short description of the time distribution of the publications (§ 3). We then summarize the work that has been done regarding optical observations (§§ 4 and 5), observations in other wavelength ranges (§ 6), and theoretical models (§ 7). We then choose a set of 8 specific topics for which the HH 1/2 system has played a particularly important role, describe their development, and comment on the still unfinished work on each topic (§ 8). A short bibliographic study describing the collaborations that have dominated the research on HH 1/2 is presented in § 9. The conclusions are presented in § 10.

2. THE HH 1/2 PAPER DATABASE

We have searched on the SAO/NASA Astrophysics Data System (ADS) for papers on the objects "HH 1" or "HH 2". From the 500 papers given (until the end of 2010) by the ADS, we have chosen the

[1]Instituto de Ciencias Nucleares, Universidad Nacional Autónoma de México, Mexico.

[2]Institute for Astronomy, University of Hawaii at Manoa, USA.

[3]Instituto de Astronomía, Universidad Nacional Autónoma de México, Mexico.

[4]Instituto Finlay, La Habana, Cuba.

[5]Available on-line at `http://www.nucleares.unam.mx/astroplasmas/`.

ones that do present either data or theoretical models directly relevant to the HH 1/2 outflow (which of course involves somewhat subjective decisions). We have kept all refereed papers, and included papers in conference proceedings and observatory reports only if they provided information not present in the refereed literature. Finally, we have supplemented the resulting bibliography with papers on HH 1/2 found in the reference lists of the initial selection (but which do not directly appear in the ADS search described above).

In this way, we arrive at a list of 143 papers. A "commented bibliography", in which short comments describing the contributions of each of these papers are included, is available on-line[6]. A histogram showing the yearly publication rate of papers on HH 1 and 2 is shown in Figure 1. In this figure, we see that in the 1950s and 60s one paper on HH 1/2 was published every ∼2–3 years. In the 1970s, the number of papers rose dramatically, to a rate of ∼1.5 papers per year. The 1980s and 1990s had rates of ∼5 papers per year. Finally in the past decade, the rate has gone down to 2 papers per year. It is noteworthy that for the 2005–2009 period, the average publication rate has been of only 1.2 papers per year.

Therefore, unless there is renewed interest in the HH 1/2 system in the future, the papers included in our bibliography will represent the main component of our knowledge of these objects for many years to come.

3. THE HH 1/2 SYSTEM

3.1. *Overall morphology*

In the photographic plate of the original paper of Herbig (1951), one can see 3 HH objects: HH 1, 2 and 3. Figure 2 shows a photographic plate, kindly provided by George Herbig, taken on January 20, 1947 (for details, see Reipurth & Heathcote 1997). In the image from the catalogue of Herbig (1974), HH 1, 2 and the C-S star (lying on the axis joining HH 1 and 2, about 1/4 of the way from HH 1 to 2) are seen. We note that the nature of HH 3 is unclear; Reipurth (1989) identifies HH 3 as being part of a separate outflow system to the W of HH 1/2 with an outflow axis almost parallel to the HH 1/2 axis, but more detailed proper motion studies are required to clarify whether HH 3 is a separate flow.

The first (pre-COSTAR) HST images of HH 2 were obtained by Schwartz et al. (1993). Subsequently HST has imaged both HH 1 and 2 a number of times. Figure 3 shows a pair of deep HST images

[6] http://www.nucleares.unam.mx/astroplasmas/.

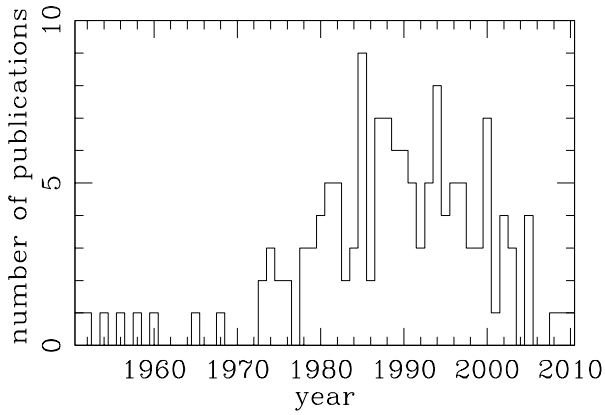

Fig. 1. Yearly number of publications on the HH 1/2 system.

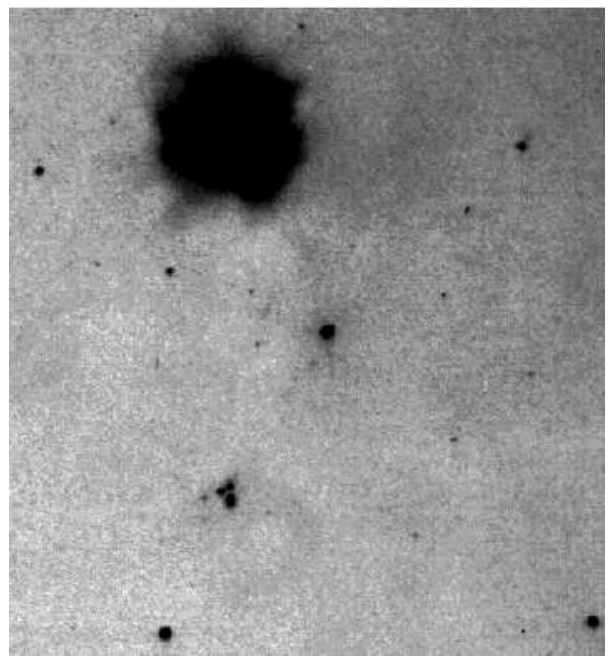

Fig. 2. HH 1, 2, and 3 as seen in an enlargement of an unpublished plate obtained by George Herbig on Jan 20, 1947. For further details, see Reipurth & Heathcote (1997).

of HH 1-2 in Hα and [SII] filters, from Bally et al. (2002). The entire bipolar outflow is almost 3 arcminutes long, corresponding to an overall projected extent of 0.35 pc at the assumed distance of ≈400 pc, which is the currently best distance estimate for the general region (see Muench et al. 2008 for a detailed discussion of the distance to the Orion Nebula Cluster region). HH 1 shows a fine bow shock structure, with an extent of ∼10 arcsec, with wings swept back-

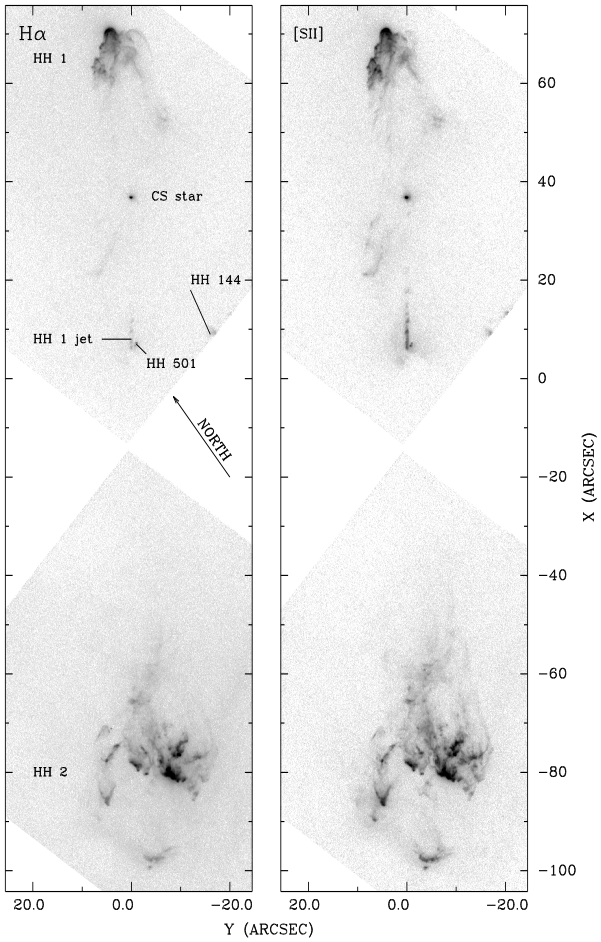

Fig. 3. Hα (left) and [S II] 6716+30 (right) HST images of HH 1 and 2. This figure is Figure 2 in the paper of Bally et al. (2002).

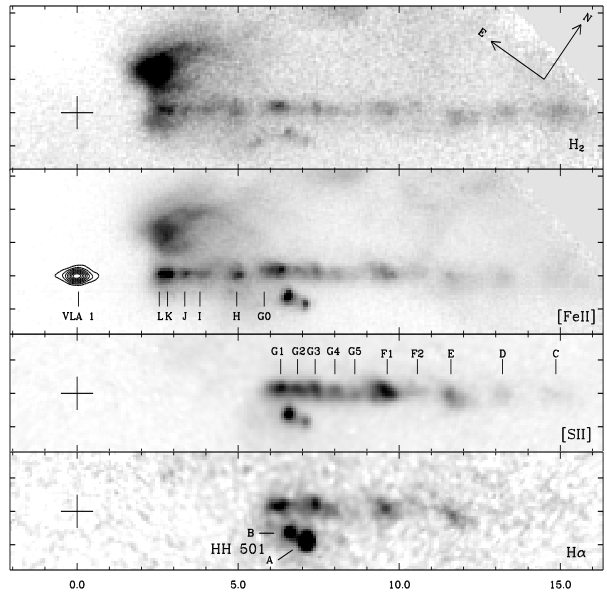

Fig. 4. The HH 1 jet in H_2 2.12 μm (top), [Fe II] 1.64 μm (second from top), [S II] 6716+30 (third) and Hα (bottom). This is Figure 1 of Reipurth et al. (2000).

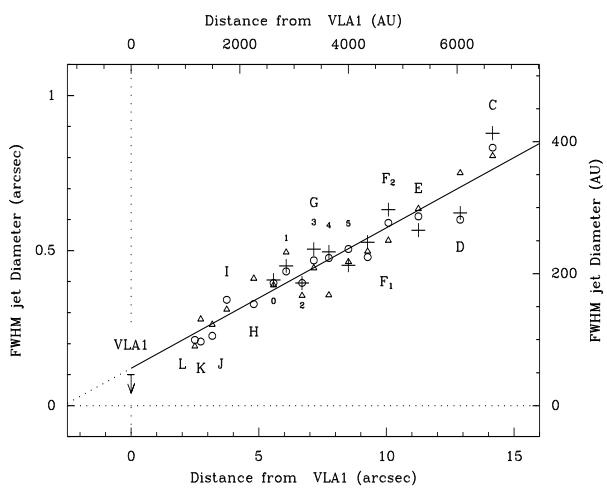

Fig. 5. Lateral expansion of the HH 1 jet. This is Figure 3 of Reipurth et al. (2000).

wards and intense emission at the apex. HH 2, on the other hand, is much larger (≈25×40 arcsec) and is fragmented into a multitude of separate bow-shaped knots and wisps of nebulosity.

Prominently visible in the center of the [SII] image is the HH 1 jet. In the plates of Herbig & Jones (1981), the jet emission can be seen. Attention was drawn to this feature when the first "electronic detector" images of HH 1 and 2 were obtained (Bohigas et al. 1985; Strom et al. 1985), and the HH 1 jet has been studied in great detail since then. Optical HST images are discussed by Hester, Stapelfeldt, & Scowen (1998) and Bally et al. (2002), and IR HST images of the jet are analyzed by Reipurth et al. (2000). Figure 4 shows the HH 1 jet at optical and infrared wavelengths. Measurements of deconvolved FWHM widths of individual knots reveal that the jet is expanding (Figure 5), and also show evidence that near the source the jet must form a wideangle wind. Nisini et al. (2005) obtained long-slit optical and infrared spectra of the HH 1 jet, and discussed the physical conditions along the jet.

Ogura (1995) presented wide field images of two large clusters of HH knots (named HH 401 and 402 for the north and south objects, respectively), with their centers at ∼25′ from the HH 1 jet and centered on the HH 1/2 outflow. These objects most likely correspond to previously ejected bow shocks; they

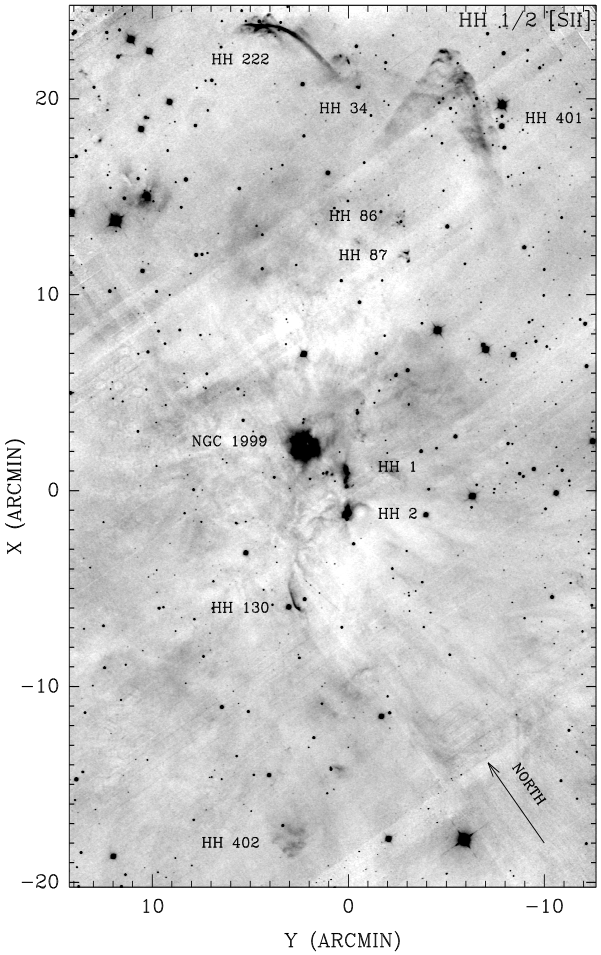

Fig 1

Fig. 6. Wide field [S II] 6716+30 image of the region around HH 1 and 2. This is Figure 1 of Bally et al. (2002).

are seen very clearly in Figure 6, a wide field image from Bally et al. (2002). At smaller angular scales, Reipurth et al. (1993b) reported the discovery of HH 144/145, which emanate from the source region.

As the HH 1 and 2 shocks plough through the ambient medium, they entrain and accelerate the ambient medium, and result in a bipolar molecular outflow. Despite many attempts (e.g., Chernin & Masson 1995; Correia, Griffin, & Saraceno 1997), no certain detection of this molecular counterpart to the optical HH 1/2 flow was achieved until Moro-Martín et al. (1999) obtained high angular resolution and high sensitivity ^{12}CO observations with the IRAM 30 m telescope. The difficulty in detecting this molecular outflow is likely due to the fact that HH 1 and 2 move close to the plane of the sky, as indicated by the high tangential motions and low radial velocities (Herbig & Jones 1981); an approximate angle to the plane of the sky of $\sim 10^\circ$ was suggested by Noriega-Crespo, Böhm, & Calvet (1991).

Several HH flows in the HH 1/2 region share approximately the same outflow direction, which is perpendicular to filaments outlining the presence of tenuous molecular cloud material (Reipurth 1989). It has been speculated that global magnetic fields might be responsible for aligning the outflow activity in the region, but this has not been borne out by more detailed studies (e.g. Kwon et al. 2010).

3.2. *The source of HH 1 and 2*

In the first papers on HH 1 and 2, it was speculated that the stellar sources exciting the emission could lie within the HH objects themselves. Cohen & Schwartz (1979) later suggested that the source of HH 1 could be the C-S star, $\sim 30''$ to the SE of HH 1. The proper motions measured by Herbig & Jones (1981) suggested that both HH 1 and 2 could be the result of a bipolar ejection (the fact that HH 2 is considerably more spatially extended appeared to be consistent with the fact that it is farther away from the C-S star). Mundt & Hartmann (1983) noted that the C-S star does not seem to have a strong enough wind to be able to power HH 1 and 2 (speculating that an eruptive event might have occurred in the past). More recently, Bally et al. (2002) found the C-S star to be a close binary.

Pravdo et al. (1985) reported the radio continuum detection of HH 1 and 2, together with a source lying at mid-distance between the two HH objects. This "VLA 1" source was suggested as producing the HH 1/2 outflow. This is now accepted as being the outflow source, given the fact that a wealth of observational data supports this. Examples of this are the flattened molecular structures (perpendicular to the outflow) surrounding the VLA 1 source (see Torrelles et al. 1994, and references therein) and the resolution of VLA 1 into a radio continuum jet with travelling knots (Rodríguez et al. 2000). The radio continuum study of Rodríguez et al. (2000) also revealed a second, fainter source, VLA 2 about 3 arcsec south of VLA 1. Following the identification of a second small outflow (HH 501, Hester et al. 1998, Reipurth et al. 2000, Bally et al. 2002) emanating from the source region next to the HH 1 jet, Reipurth (2000) argued that VLA 1 must be an unresolved binary, forming a hierarchical triple system with VLA 2.

VLA 1 is a deeply embedded Class 0 source, and the cold infalling envelope around this source was detected at 1300 μm by Reipurth et al. (1993a), who estimated a mass of circumstellar material of $\sim 4\ M_\odot$.

More recently Fischer et al. (2010) used the Herschel Space Telescope to image the HH 1/2 region at far-infrared wavelengths, and in addition to the (unresolved) VLA 1/2 stellar system (their source HOPS 203), they detected another protostar, HOPS 165, only 13 arcseconds away. It thus appears that the HH 1/2 source region contains a small quadruple system of protostellar objects in very early evolutionary stages. Substantial progress in the observations of the region around VLA 1 is to be expected when this region is observed with ALMA.

4. THE DISCOVERY PAPERS

Herbig (1951) obtained spectra of HH 1 and 2, and also showed a photographic image of the region around the two objects. Herbig noted the unusual characteristics of the spectrum, which include the strength of the red [S II] lines, and the wide range of ionization+excitation energies (given by the presence of strong [O I], [O II] and [O III] lines). Herbig (1951) noted that there are no blue stars (which might photoionize the gas) visible in the region, and suggested that the excitation might be powered by accretion onto a late-type dwarf. Haro (1952) and Haro & Minkowski (1960) obtained deeper plates, and lowered the brightness for possible stars within HH 1 and 2. The name "Herbig-Haro objects" was proposed by Ambartsumian (1954).

Böhm (1956) obtained spectra of HH 1, and used diagnostic lines to determine n_e and T (the electron density and temperature) of the object. Böhm noted that the (at least partially) ionized gas cannot be in coronal ionization equilibrium at the measured temperature of ≈7500 K. Böhm (1956) commented that HH 1 is too large (with a size of ∼1000 AU) compared to the accretion radius around a low mass star (∼10 AU) for the object to be powered directly by accretion.

Osterbrock (1958) presented further spectrophotometry of HH 1, confirming the results of Böhm (1956). Osterbrock suggested that high energy particles in a stellar wind might be producing the observed ionization (without mentioning shocks). This idea was followed in more detail by Magnan & Schatzmann (1965). It is notable that these initial papers were very well directed, pointing in the general direction of later developments in the field of HH objects.

5. OPTICAL OBSERVATIONS

5.1. *Imaging*

Including the paper with the first published image of HH 1/2 (Herbig 1951), there are 19 papers with images of this outflow. Photographic plates were published by Haro (1952), Haro & Minkowski (1960), Herbig (1974), Herbig & Jones (1981, the first determination of proper motions in HH flows). Ground-based images with electronic detectors were presented by Bohigas et al. (1985), Strom et al. (1985), Raga et al. (1988), Reipurth (1989), Raga, Barnes, & Mateo (1990), Reipurth et al. (1993b), Eislöffel, Mundt, & Böhm (1994), Ogura (1995) and Warren-Smith & Scarrot (1999, presenting imaging polarimetry). Images obtained with the HST were presented by Schwartz et al. (1993), Ray et al. (1996), Hester et al. (1998), Reipurth et al. (2000) and Bally et al. (2002, who obtained proper motions from HST images).

5.2. *Spectrophotometry*

Starting with the original paper of Herbig (1951), 15 papers have been published with observations of emission line fluxes and/or the optical continuum of HH 1 and 2. The main components of this work are the calculations of n_e and T_e diagnostics and the calculations of the gas-phase abundances.

The first of these studies was published by Böhm (1956), who presented diagnostic line ratios and discussed the possible reddening corrections. This work was later extended with detections of progressively more lines by Böhm, Perry, & Schwartz (1973: 60 lines), Böhm, Siegmund, & Schwartz (1976: reddening from the IR and blue [S II] lines), Schwartz (1976), Dopita (1978), Böhm & Brugel (1979), Brugel, Böhm, & Mannery (1981a), Strom et al. (1985) and Solf, Böhm, & Raga (1988: 175 lines in HH 1). Cohen & Schwartz (1979) and Mundt & Hartmann (1983) presented the spectrum of the "Cohen-Schwartz" (C-S) star, which was suggested as a possible source of the HH 1/2 system (later demoted, see § 3.2). The optical continuum emission of HH 1 and 2 was studied by Böhm, Schwartz, & Siegmund (1974), Brugel, Böhm, & Mannery (1981b) and Solf et al. (1988).

5.3. *High resolution spectroscopy*

There are 12 papers discussing line profiles of the emission of the HH 1/2 region. The first mention of the line profiles of HH 1/2 was that of Böhm et al. (1973), who stated that the line widths are ∼1 Å. Radial velocities and line widths were studied by Schwartz (1978, 1981) and Dopita (1978). Hartmann & Raymond (1984) and Böhm & Solf (1985) and Hartigan, Raymond, & Hartmann (1987) presented the details of short- and long-slit line profiles of HH 1 and 2. The two-dimensional spatial distributions of the line profiles of HH 1 (Solf et al. 1991) and

HH 2 (Böhm & Solf 1992) have also been described. Solf & Böhm (1991) discussed the line profiles of the diffuse emission around HH 1 and 2 (possibly due to scattering on surrounding environmental dust). This effect was also studied by Riera et al. (2005), who presented Fabry-Perot observations of HH 1 and 2.

6. OTHER WAVELENGTH RANGES

6.1. *UV observations*

The far-UV emission of HH 1 was discovered with IUE by Ortolani & D'Odorico (1980). A series of papers described IUE observations of the emission line and continuous UV spectrum of HH 1 (Böhm, Böhm-Vitense, & Brugel 1981), HH 2 (Brugel, Seab, & Shull 1982) and the C-S star (Böhm & Böhm-Vitense 1982). The spatial extent of the UV emission was studied by Böhm-Vitense et al. (1982), Böhm et al. (1987), Lee et al. (1988) and Böhm, Noriega-Crespo, & Solf (1993). The UV variability of HH 1 was discussed by Brugel et al. (1985) and Böhm et al. (1993). The UV extinction was studied by Böhm-Vitense et al. (1982) and Böhm, Raga, & Binette (1991).

The most recent UV observations of HH 2 were obtained by Raymond, Blair, & Long (1997) with the Hopkins Ultraviolet Telescope. In this spectrum, lines of several ions (e.g., O III and IV) as well as H_2 lines were identified.

6.2. *IR observations*

Including the discovery paper of IR H_2 emission in HH 1 and 2 (Elias 1980), 25 papers on the IR spectra of these objects have been published. These papers include searches of potential sources for the HH 1/2 system (Cohen & Schwartz 1980; Cohen et al. 1984) and of the later accepted VLA 1 source (Strom et al. 1985; Rodríguez, Roth, & Tapia 1985; Harvey et al. 1986; Pravdo & Chester 1987; Tapia et al. 1987; Roth et al. 1989). Cernicharo et al. (2000) presented ISO observations of the VLA 1 region. Low and high resolution spectra of the H_2 emission of HH 1 and 2 were presented by Zinnecker et al. (1989), Kelly, Rieke, & Campbell (1994), Schwartz et al. (1995), Gredel (1996), Davis, Smith, & Eislöffel (2000), Eislöffel, Smith, & Davis (2000), Nisini et al. (2005) and García López et al. (2008), the last three papers presenting long-slit spectra. Molinari & Noriega-Crespo (2002), Lefloch et al. (2003) and Lefloch et al. (2005) obtained ISO spectra of HH 1 and 2.

H_2 2.12 μm images of HH 1 and 2 have been presented by Zealey et al. (1992), Noriega-Crespo & Garnavich (1994), Davis, Eislöffel, & Ray (1994), Noriega-Crespo et al. (1997, discovery of H_2 proper motions in HH objects), Davis et al. (2000) and Stanke, McCaughrean, & Zinnecker (2000).

6.3. *Radio observations*

The first paper (out of a total of 19 papers) on radio observations of HH 1/2 (Snell & Edwards 1982) reported the non-detection of a CO outfow. HH 1 and 2 as well as the central VLA 1 source (the source that powers the HH 1/2 system) were first detected in radio continuum by Pravdo et al. (1985) at 20, 6 and 2 cm (HH 1 was actually not detected at the shorter wavelength). Morgan, Snell, & Strom (1990) reported a detection at 6 cm and a non-detection at 20 cm of the radio continuum of HH 1/2 and VLA 1. Rodríguez et al. (1990) detected the radio continuum proper motions of HH 1 and 2, and Rodríguez et al. (2000) obtained proper motions of knots within the elongated VLA 1 source.

Different molecules were detected in dense structures centered on VLA 1 and elongated perpendicularly to the outflow axis (Torrelles et al. 1985; Martín-Pintado & Cernicharo 1987; Marcaide et al. 1988; Davis et al. 1990; Torrelles et al. 1993, 1994; Choi & Lee 1998). Molecular emission associated with clumps which are perturbed (possibly only radiatively) by HH 1 or HH 2 have been studied by Davis et al. (1990), Torrelles et al. (1992, 1993), Choi & Zhou (1997), Girart et al. (2002, 2005) and Dent, Furuya, & Davis (2003).

6.4. *X-ray observations*

Pravdo & Angelini (1993) report ROSAT observations of a region containing HH 1/2, and specifically mention the non-detection of HH 1 (giving an upper limit for its flux). A paper on the X-ray emission of HH 2 (Pravdo et al. 2001) reports the discovery of the X-ray emission of HH objects. The spectrum observed with Chandra implies the presence of gas at $\sim 10^6$ K.

7. MODELS OF HH 1/2

The idea of HH objects being the result of shock waves was first suggested by Schwartz (1975), who noticed similarities between the spectra of supernovae remnants and the spectra of HH 1 and Burnham's nebula. Böhm (1978) proposed that HH 1 might be the result of a spherically expanding shock wave, and Schwartz (1978) proposed that HH 1 and 2 might be bow shocks formed by a fast wind interacting with almost stationary, dense clumps. Cantó & Rodríguez (1980) proposed that the HH 1 shock waves were associated with the convergence region

of a nozzle flow. These three scenarios turned out to be not applicable to HH 1 and 2.

Two other scenarios were proposed for producing HH bow shocks: the "interstellar bullet" model of Norman & Silk (1979, who do not explicitly mention HH 1 and 2) and the "jet" model of Dopita, Schwartz, & Evans (1982b, suggested for HH 46/47). Interestingly, these two scenarios were favored (over the "shocked cloudlet" and "nozzle" models) by the high HH 1/2 proper motions discovered by Herbig & Jones (1981).

Predictions of emission line ratios from stationary, plane-parallel shocks were compared with observations of HH 1/2 by Dopita (1978) and Raymond (1979). The production of the optical continuum in plane-parallel shock waves was discussed by Dopita, Binette, & Schwartz (1982a) and predictions of the radio continuum were made by Curiel, Cantó, & Rodríguez 1987). The H_2 emission of HH 1 was modeled by Wolfire & Königl (1991).

The first "3/2-D" bow shock models (constructed with 1D shocks distributed over a given bow shock shape) were applied to HH 1 and 2 by Hartmann & Raymond (1984). Predictions of line profiles, PV diagrams, line ratios and the spatially resolved line emission from such models were applied to HH 1 and 2 by Choe & Böhm (1985), Raga & Böhm (1985), Hartigan et al. (1987), Raymond, Hartmann, & Hartigan (1988), Noriega-Crespo, Böhm, & Raga (1989, 1990), Indebetouw & Noriega-Crespo (1995), Moro-Martín et al. (1996), Henney (1996, non-axisymmetric bow shocks) and Raga et al. (1997, proper motions in 3/2-D bow shocks).

Axisymmetric, time-dependent bow shock simulations were presented by Raga & Böhm (1987) and Raga et al. (1988), who modeled the proper motions and line profiles of HH 1. A two-plane shock model for the working surface of a jet was described by Hartigan (1989), and axisymmetric simulations of the head of a jet (with predictions of intensity maps for comparisons with HH 1) were presented by Raga (1988), and Blondin, Königl, & Fryxell (1989), Blondin, Fryxell, & Königl (1990). 3D jet head simulations were presented by de Gouveia Dal Pino & Benz (1993) and Stone & Norman (1994, for HH 2). Predictions of the H_2 emission of HH 1 from a jet head simulation were made by Raga et al. (1995), and of the X-ray emission of HH 2 by Raga, Noriega-Crespo, & Velázquez (2002). A precessing jet model was suggested for HH 1 and 2 by Lightfoot & Glencross (1986, most likely incorrect, but being the first suggestion of the importance of precession in HH jets).

Models for scattering of the HH 1 emission in the surrounding, dusty environment were described by Noriega-Crespo et al. (1991) and Henney, Raga, & Axon (1994) and for HH 2 by Riera et al. (2005). The photochemistry of environmental clumps irradiated by HH 1/2 was modeled by Raga & Williams (2000) and Viti et al. (2003).

8. SPECIAL TOPICS

8.1. *Proper motions*

One of the main discoveries made in observations of HH 1 and 2 was the large proper motions of HH objects. Herbig & Jones (1981) measured large proper motions (mostly in the 100–300 km s^{-1} range) for the HH 1 and 2 condensations. These proper motions appear to indicate that the two objects were ejected from a common source, and eliminated stationary flow models for HH 1 and 2 (Cantó & Rodríguez 1980), as well as the "shocked cloudlet" model (Schwartz 1978). Gyul'budagyan (1984) noted that these proper motions indicated a divergence beyond what could be expected from ballistic trajectories from the outflow source (at that time assumed to be the C-S star, though the same argument applies for the VLA 1 source).

This divergence phenomenon was successfully explained in terms of bow shock models. Raga & Böhm (1987) and later Raga et al. (1997) showed numerically and analytically that knots at the head of a bow shock have purely forward motions, and knots associated with the far bow shock wings have mostly lateral motions, therefore producing an "expansion pattern" similar to the one observed in HH 1 and 2.

The proper motions of the HH 1/2 system were later measured in radio continuum maps (Rodríguez et al. 1990, 2000) and in IR H_2 images (Noriega-Crespo et al. 1997). Also, the proper motions of the optical knots were progressively improved and extended (to more knots) by Eislöffel et al. (1994) and by Bally et al. (2002, using HST images).

One should note that HST images allow measurements of proper motions with epochs spaced at intervals of only a few years. Therefore, further HST images of the HH 1/2 system (only two epochs were used by Bally et al. 2002) would provide the possibility of seeing the time-evolution of the proper motions of the line emitting knots. If such a time-evolution were detected, it would again be the first time that HH 1 and 2 show interesting properties possibly shared by HH objects in general.

8.2. *Dispersion of HH emission on dust*

Strom, Strom, & Kinman (1974) measured basically zero polarization in HH 1 and 2. Interestingly,

they interpreted this as evidence of the presence of multiple scattering (on dust), which could lower the polarization associated with the scattering process. This interpretation was introduced to save the idea (being forwarded at the time) of HH objects as dense clouds which reflected the light of (directly unobservable) young stars. Schmidt & Vrba (1975) lowered the limit of the (undetected) polarization of HH 1 and 2 to a fraction of 1%, and (correctly) concluded that the emission from HH 1 and 2 had to be intrinsic. The paper of Mundt & Witt (1983) explored the possibility that the UV continuum of HH 1 and 2 might be contaminated by a reflected, blue star continuum (a suggestion that was later put aside).

Interestingly, the problem of scattering on dust gained new life with the paper of Solf & Böhm (1991), who detected the presence of faint but very broad line profiles off the bright knots of HH 1. They interpreted this as evidence of scattering on environmental dust of the emission spectrum of the HH 1 knots. This idea was explored theoretically by Noriega-Crespo et al. (1991), Henney et al. (1994) and Riera et al. (2005).

Warren-Smith & Scarrot (1999) carried out continuum and Hα imaging polarimetry of the HH 1/2 system, finding polarizations of a few percent in the Hα emission at some positions around HH 1. No comparison has been made with the polarization predictions of Henney et al. (1994). There is clearly room for more work on this topic.

8.3. *The emission line spectrum*

The emission line spectrum (UV, optical, IR and radio) of HH 1 and 2 provides most of the information known about these objects. The best data currently available on the optical emission line ratios of HH 1 were obtained by Solf et al. (1988, who identified 175 lines). The best IR spectrophotometry was carried out by Gredel (1996) and by Molinari & Noriega-Crespo (2002, ISO spectra), and the best UV data were obtained by Böhm et al. (1993, IUE data) and by Raymond et al. (1997, HUT data).

The emission line ratios observed in HH 1 and 2 have motivated the shock interpretation of HH objects (Schwartz 1975). The spectra of HH 1/2 were first compared with predictions of plane-parallel shock models (Dopita 1978; Raymond 1979). The spectrophotometric observations of Brugel et al. (1981a) later showed that the emission of HH 1/2 (and a set of other HH objects) has low filling factors of $\sim 10^{-3} \rightarrow 10^{-2}$ (depending on the emission line), which is one of the main qualitative observational features expected for shock emission.

Later, comparisons with "3/2-D" bow shock models (built as an appropriate superposition of 1D shocks) were done by Hartmann & Raymond (1984) and Hartigan et al. (1987). The last two papers showed that the combination of (normal) shock velocities produced by a continuous bow shock resulted in line ratios that better reproduced the HH 1 and 2 spectra. Predictions of the spatially resolved line emission were later carried out by Noriega-Crespo et al. (1989, 1990).

The main success of the 3/2-D shock models was to reproduce some of the characteristics of the emission line profiles and/or PV diagrams of HH 1 and 2. Raga & Böhm (1985) presented 3/2-D bow shock models that reproduced the general characteristics of the PV diagrams of HH 1 obtained by Böhm & Solf (1985). In an earlier paper, Choe & Böhm (1985) had obtained predicted PV diagrams that actually agreed better with the HH 1 observations, but these models did not have a proper calculation of the line profiles from the bow shock.

Hartigan et al. (1987) modeled the line profiles of HH 1 and 2 (not PV diagrams), assuming that each condensation is a separate bow shock. This was an important difference from the models of Raga & Böhm (1985), in which all of HH 1 was modeled as a single bow shock. Later, higher angular resolution observations of HH 1 and 2 (e.g., Hester et al. 1998) showed that the condensations of HH 1 (some of them shaped as small, bow shaped shocks) do indeed seem to form a single, broken up bow shock, while the condensations of HH 2 do not form a discernible, organized larger scale structure.

While some effort has been done in modelling HH 1 (Raga 1988; Blondin et al. 1989; Völker et al. 1999) and HH 2 (Stone & Norman 1994) with full (axisymmetric or 3D) jet simulations, more work in this direction should clearly be made. For example, it would be important to carry out high resolution 3D simulations of both HH 1 and 2 to see whether or not predictions from the models are successful at reproducing the 2D distributions of emission line ratios and profiles (Solf et al. 1991; Böhm & Solf 1992) and proper motions (Bally et al. 2002). At the same time, these models should reproduce the spatially resolved line emission and line profiles of the HH 1 jet (Nisini et al. 2005; García López et al. 2008).

Such simulations should settle the doubts that still remain as to whether or not the line ratios, line profiles and proper motions observed in HH 1 and 2 can indeed be reproduced by a single model. Furthermore, this model should also be able to reproduce the observed X-ray emission of HH 2 (Pravdo

et al. 2001), and the H_2 (Noriega-Crespo et al. 1997) and CO (Moro-Martín et al. 1999) emission of the HH 1/2 system. Clearly, a lot of effort will have to be done for such modelling to be successful, and non-trivial problems might be encountered.

Finally, it is notable that most of the best available observations of HH 1 and 2 have been obtained more than a decade ago. Clearly, new spectrophotometric and high dispersion spectroscopic observations would be worthwhile, as they would provide data of considerably improved quality.

8.4. *The continuum emission*

The optical and UV continua of HH 1 and 2 apparently have strong contributions from collisionally enhanced 2-photon H emission (Brugel et al. 1982; Dopita et al. 1982a). At UV wavelengths, there might also be a contribution from the H_2 dissociation continuum (Böhm et al. 1987; Lee et al. 1988).

Very little theoretical work has been done regarding the continuum emission of HH 1 and 2, and basically no effort has been done to model the spatial distribution of the continuum emission (e.g., the radio continuum predictions of Curiel et al. 1987 and Ghavamian & Hartigan 1998 were restricted to p-p shocks). Clearly, more observational and theoretical efforts will be necessary in order to contribute to the understanding of the continuum emission of HH 1/2 (and of HH objects in general).

8.5. *Abundances*

An interesting line of research has been the determination of the gas phase abundances of the HH 1/2 system. Böhm et al. (1976) found that HH 1 and 2 had abundances consistent with Population I abundances, indicating that no depletion due to dust grains was present. This result was strengthened with further data by Böhm & Brugel (1979) and Brugel et al. (1981a). Beck-Winchatz, Böhm, & Noriega-Crespo (1994) presented a re-analysis of older data, confirming the absence of dust in HH 1 (but found evidence of dust depletion in Burnham's nebula).

The paper of Nisini et al. (2005, who present 0.6–2.5 μm long-slit spectra) somewhat surprisingly find that the spectrum of the HH 1 jet (to the NW of the VLA 1 source) does show evidence for Fe, C, Ca and Ni depletions. This result implies that the gas along the jet flow does have dust.

This is a problem that merits further study. More spatially-resolved abundance determinations would be useful, as well as theoretical models of dust destruction in the shocks associated with the jet knots and jet head.

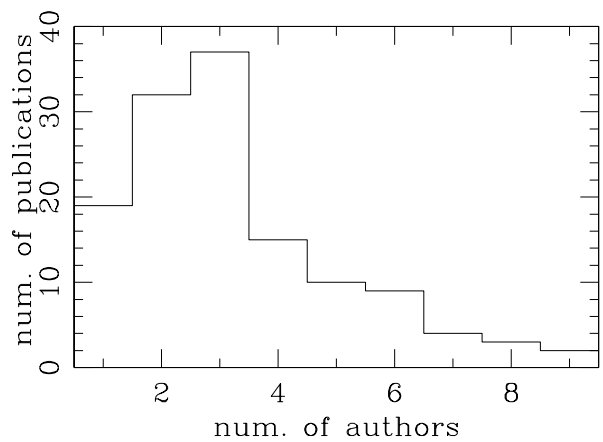

Fig. 7. Frequency distribution of the number of co-authors in the papers of the HH 1/2 database.

8.6. *Time-variability*

Herbig (1968, 1973) showed that the optical emission of both HH 1 and 2 is variable. This time-dependence was followed at later times by Herbig & Jones (1981) and Raga et al. (1990). Böhm et al. (1976) found that n_e and T_e determined from diagnostic lines also appeared to change over periods of ∼15 yr (in HH 1/2). Brugel et al. (1985) and Böhm et al. (1993) found that the UV spectrum of HH 1/2 showed substantial changes over periods of a few years.

Apparently, there are no more recent discussions of the variability of HH 1 and 2. What has happened during the last ∼10 years? Have the brightening trends (Herbig & Jones 1981) of some of the HH 2 condensations continued? Clearly, it would be worthwhile to have more up-to-date studies of this time-evolution.

9. CONTRIBUTIONS OF INDIVIDUAL AUTHORS AND COLLABORATIONS

The papers on HH 1/2 have had relatively small numbers of co-authors. Figure 7 shows the frequency distribution of the number of co-authors, with a clear peak at three co-authors, and an extended wing, ending with two papers with nine co-authors. The mean is of 3.27 authors per paper.

In order to evaluate the contribution of individual authors, we have calculated their "normalized contribution" as $c_a = \sum_i (n_{a,i})^{-1}$, where $n_{a,i}$ are the number of coauthors of the papers which include author a. We first make a list of authors in order of decreasing c_a contributions, and we then compute a cumulative distribution function.

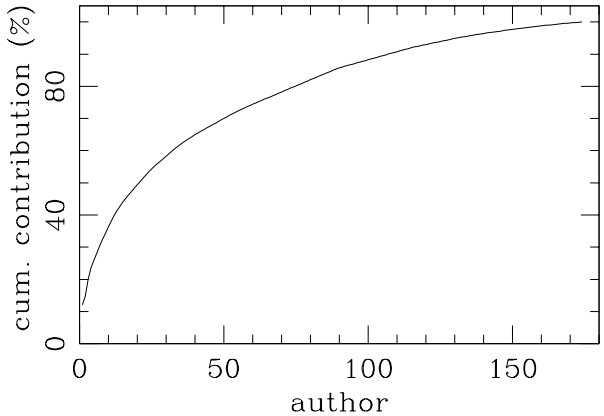

Fig. 8. Cumulative distribution of the contributions of authors to the publications of HH 1/2.

This cumulative distribution is shown in Figure 8. We find that the first author (author 1, who has the largest c_a value, see above) has a contribution of ≈12% of the total (normalized) publications on HH 1/2. From Figure 8 we see that 21 authors have contributed ≈50% of the total publications, and 107 authors have contributed ≈90%. These numbers represent the characteristic size of the group of authors who have worked on HH 1 and 2.

We have selected a "high production" set, composed of the 20 authors that have collaborated in at least 5 of the papers in our HH 1/2 database (see § 2). We have ordered this set of authors in such a way that close collaborators occupy neighbouring positions along the list. Figure 9 shows this list of authors, together with a "collaboration matrix". The diagonal elements ($C_{i,i}$) of this matrix correspond to the number of papers co-authored by each of the authors in the list. The non-diagonal elements ($C_{i,j}$; $i \neq j$) give the number of papers in which both the authors i and j appear in the list of co-authors.

In Figure 9, we note the presence of 4 groups of collaborators:

Group 1: there is a remarkably unified group of 5 collaborators (Rodríguez, Cantó, Torrelles, Ho and Curiel) in the upper right hand corner of the matrix. As can be seen from the references, this group has concentrated on line and continuum radio observations as well as models of the HH 1/2 system. It is clear that each of these authors has collaborated with all of the other four members of the group,

Groups 2 and 3: two small groups of three authors (Group 2 being composed by Raymond, Hartigan and Hartmann, and Group 3 by Eislöffel, Ray and Davis) are also evident. The papers of these two groups cover optical and IR observations. The papers of Group 2 also cover models of HH 1/2,

Group 4: the first 8 authors in our list (on the bottom, left-hand corner of Figure 9) also form a collaboration group. This group has a "core" of three authors (Böhm, Raga and Noriega-Crespo), who appear together in many papers. There is also a "secondary group" of 5 authors (Schwartz, Brugel, Solf, Reipurth and Mundt) who have collaborated with one or more of the members of the "core group" (see above), but not with all of the other members of the "secondary group". If one peruses the list of references, one sees that this group encompasses collaborations that have occurred over 5 decades, most of which are characterized by the unifying participation of K. H. Böhm. The papers of this group cover optical/IR/UV observations and models of HH 1/2.

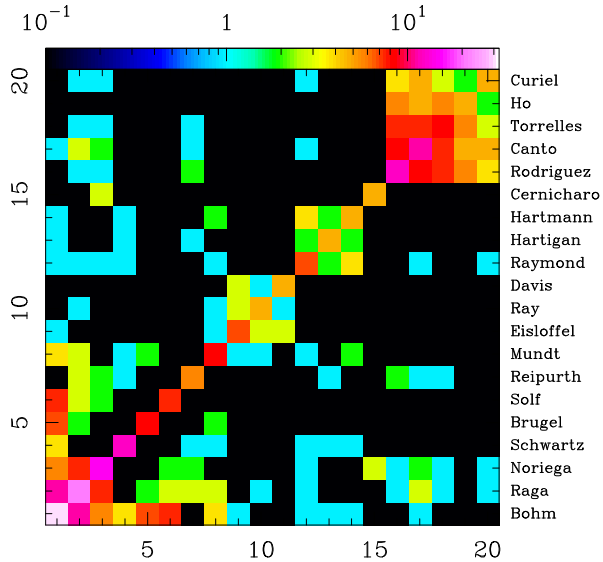

Fig. 9. Collaboration matrix. The diagonal elements give the papers including each of the authors, and the non-diagonal elements give the papers in which pairs of authors have collaborated. The order numbers correspond to the authors listed on the right of the plot. The color figure can be viewed online.

It is also clear from Figure 9 that occasional collaborations have also occurred between the members of the four groups, evidenced by the presence of non-zero elements far away from the main diagonal of the collaboration matrix.

We end this discussion of the groups of collaborators by noting again that our analysis is restricted to the researchers who are co-authors in at least 5 of the HH 1/2 papers. Individual authors (collaborating with the more active researchers) or even independent research groups with lower levels of activity in this field do not appear in our analysis.

10. SUMMARY

We have collected all the papers through 2010 that have made a substantial contribution to the study of the Herbig-Haro objects HH 1 and 2, and made a commented bibliography[7] with short comments on all papers. This excercise is meant to serve as a guide to researchers who plan future work on these objects.

The choice of the papers in this bibliography is of course somewhat subjective, because some important papers might have been missed, and also because many papers (treating, e.g., many objects or theoretical models) have only passing references to HH 1 and 2 and have therefore not been included. Nevertherless, the vast majority of papers with substantial contributions to the understanding of HH 1 and 2 are probably included in our bibliography. Furthermore, given the fact that the yearly number of publications has fallen over the past decade (see § 2), the papers in our bibliography are likely to represent the larger part of the work that will be done on these objects (unless there is renewed future interest in HH 1 and 2).

However, it is clear that research on HH 1 and 2 is still alive. Evidence of this is the paper by Hartigan et al. (2011), which presents new HST images of HH 1 and 2, leading to new results on the proper motions and variability of these objects.

In the present paper we carry out a description of the HH 1/2 system (§ 3), a discussion of the early papers (§ 4), of the observations (§§ 5 and 6), and models (§ 7) of this system. We then discuss a few special topics regarding HH objects in general, which have shown considerable progress or have been resolved through studies of HH 1 and 2 (§ 8). This discussion has references to most of the papers in our HH 1/2 bibliography.

Finally, we make a short study of the contributions of individual authors and research groups to the HH 1/2 bibliography (§ 9). From this study, it is evident that Karl-Heinz Böhm has been the driving force for a substantial part of the work done on HH 1/2 (on optical/UV observations and theoretical models), as well as Luis Felipe Rodríguez (radio observations). Most of the work that has been done on HH 1/2 involves collaborations which include one of these two authors.

[7]Available on-line at `http://www.nucleares.unam.mx/astroplasmas/`.

AR and JC acknowledge support from the Conacyt grants 61547, 101356 and 101975. We thank an anonymous referee for pointing out several papers on HH 1/2 which we had initially missed. We thank George Herbig for providing the photograph shown in Figure 2.

REFERENCES

Ambartsumian, V. A. 1954, Comm. Byurakan Obs., 13, 3
Bally, J., Heathcote, S., Reipurth, B., Morse, J., Hartigan, P., & Schwartz, R. D. 2002, AJ, 123, 2627
Beck-Winchatz, B., Böhm, K. H., & Noriega-Crespo, A. 1994, PASP, 106, 1271
Blondin, J. M., Königl, A., & Fryxell, B. A. 1989, ApJ, 337, L37
Blondin, J. M., Fryxell, B. A., & Königl, A. 1990, ApJ, 360, 370
Bohigas, J., et al. 1985, RevMexAA, 11, 149
Böhm, K. H. 1956, ApJ, 123, 379
_____. 1978, A&A, 64, 115
Böhm, K. H., & Böhm-Vitense, E. 1982, ApJ, 263, L35
Böhm, K. H., Böhm-Vitense, E., & Brugel, E. W. 1981, ApJ, 245, L113
Böhm, K. H., & Brugel, E. W. 1979, A&A, 74, 297
Böhm, K. H., Bührke, Th., Raga, A. C., Brugel, E. W., Witt, A. N., & Mundt, R. 1987, ApJ, 316, 349
Böhm, K. H., Noriega-Crespo, A., & Solf, J. 1993, ApJ, 416, 647
Böhm, K. H., Perry, J. F., & Schwartz, R. D. 1973, ApJ, 179, 149
Böhm, K. H., Raga, A. C., & Binette, L. 1991, PASP, 103, 85
Böhm, K. H., Schwartz, R. D., & Siegmund, W. A. 1974, ApJ, 193, 353
Böhm, K. H., Siegmund, W. A., & Schwartz, R. D. 1976, ApJ, 203, 399
Böhm, K. H., & Solf, J. 1985, ApJ, 294, 533
_____. 1992, AJ, 104, 1193
Böhm-Vitense, E., Cardelli, J. A., Nemec, J. M., & Böhm, K. H. 1982, ApJ, 262, 224
Brugel, E. W., Böhm, K. H., Böhm-Vitense, E., & Shull, J. M. 1985, ApJ, 292, L75
Brugel, E. W., Böhm, K. H., & Mannery, E. 1981a, ApJS, 47, 117
_____. 1981b, ApJ, 243, 874
Brugel, E. W., Seab, C. G., & Shull, J. M. 1982, ApJ, 262, L35
Cantó, J., & Rodríguez, L. F. 1980, ApJ, 239, 982
Cernicharo, J., et al. 2000, Science, 288, 649

Chernin, L. M., & Masson, C. R. 1995, ApJ, 443, 181
Choe, S. U., Böhm, K. H., & Solf, J. 1985, ApJ, 288, 338
Choi, M., & Lee, Y. 1998, ApJ, 498, L71
Choi, M., & Zhou, S. 1997, ApJ, 477, 754
Cohen, M., Harvey, P. M., Wilking, B. A., & Schwartz, R. D. 1984, ApJ, 278, 671
Cohen, M., & Schwartz, R. D. 1979, ApJ, 233, L77
_____. 1980, MNRAS, 191, 165
Correia, J. C., Griffin, M., & Saraceno, P. 1997, A&A, 322, L25
Curiel, S., Cantó, J., & Rodríguez, L. F. 1987, RevMexAA, 14, 595
Davis, C. J., Dent, W. R. F., Burnell, S. J., & Bell, S. J. 1990, MNRAS, 244, 173
Davis, C. J., Eislöffel, J., & Ray, T. P. 1994, ApJ, 426, L93
Davis, C. J., Smith, M. D., & Eislöffel, J. 2000, MNRAS, 318, 747
de Gouveia Dal Pino, E. M., & Benz, W. 1993, ApJ, 410, 686
Dent, W. R. F., Furuya, R. S., & Davis, C. J. 2003, MNRAS, 339, 633
Dopita, M. A. 1978, ApJS, 37, 117
Dopita, M. A., Binette, L., & Schwartz, R. D. 1982a, ApJ, 261, 183
Dopita, M. A., Schwartz, R. D., & Evans, I. 1982b, ApJ, 263, L73
Eislöffel, J., Mundt, R., & Böhm, K. H. 1994, AJ, 108, 1042
Eislöffel, J., Smith, M. D.,& Davis, C. J. 2000, A&A, 359, 1147
Elias, J. H. 1980, ApJ, 241, 728
Fischer, W. J., et al. 2010, A&A, 518, L122
García López, R., Nisini, B., Giannini, T., Eislöffel, J., Bacciotti, F., & Podio, L. 2008, A&A, 487, 1019
Ghavamian, P., & Hartigan, P. 1998, ApJ, 501, 687
Girart, J. M., Viti, S., Estalella, R., & Williams, D. A. 2005, A&A, 439, 601
Girart, J. M., Viti, S., Williams, D. A., Estalella, R., & Ho, P. T. P. 2002, A&A, 388, 1004
Gredel, R. 1996, A&A, 305, 582
Gyul'budagyan, A. L. 1984, Astrofizika, 20, 75
Haro, G. 1952, ApJ, 115, 572
Haro, G., & Minkowski, R. 1960, AJ, 65, 490
Hartigan, P. 1989, ApJ, 339, 987
Hartigan, P., Raymond, J. C., & Hartmann, L. W. 1987, ApJ, 316, 323
Hartigan, P., et al. 2011, ApJ, 736, 29
Hartmann, L. W., & Raymond, J. C. 1984, ApJ, 276, 560
Harvey, P. M., Joy, M., Lester, D. F., & Wilking, B. A. 1986, ApJ, 301, 346
Henney, W. J. 1996, RevMexAA, 32, 3
Henney, W. J., Raga, A. C., & Axon, D. 1994, ApJ, 427, 305
Herbig, G. H. 1951, ApJ, 113, 697
_____. 1968, in Non-Periodic Phenomena in Variable Stars, ed. L. Detre (Dordrecht: Reidel), 75
_____. 1973, Inf. Bull. Variable Stars, 832, 1
_____. 1974, Lick Obs. Bull., 658, 1
Herbig, G. H., & Jones, B. F. 1981, AJ, 86, 1232
Hester, J. J., Stapelfeldt, K. R., & Scowen, P. A. 1998, AJ, 116, 372
Indebetouw, R., & Noriega-Crespo, A. 1995, AJ, 109, 752
Kelly, D. M., Rieke, G. H., & Campbell, B. 1994, ApJ, 425, 231
Kwon, J., Choi, M., Pak, S., Kandori, R., Tamura, M., Nagata, T., & Sato, S. 2010, ApJ, 708, 758
Lee, M. G., Böhm, K. H., Temple, S. D., Raga, A. C., Mateo, M. L., Brugel, E. W., & Mundt, R. 1988, AJ, 96, 1690
Lefloch, B., Cernicharo, J., Cabrit, S., & Cesarsky, D. 2005, A&A, 433, 217
Lefloch, B., Cernicharo, J., Cabrit, S., Noriega-Crespo, A., Moro-Martín, A., & Cesarsky, D. 2003, ApJ, 590, L41
Lightfoot, J. F., & Glencross, W. M. 1986, MNRAS, 221, 47
Magnan, C., & Schatzman, E. 1965, C. R. Acad. Sci. Paris, 260, 6289
Marcaide, J. M., Torrelles, J. M., Gusten, R., Menten, K. M., Ho, P. T. P., Moran, J. M., & Rodríguez, L. F. 1988, A&A, 197, 235
Martín-Pintado, J., & Cernicharo, J. 1987, A&A, 176, L27
Molinari, S., & Noriega-Crespo, A. 2002, AJ, 123, 2010
Morgan, J. A., Snell, R. L., & Strom, K. M. 1990, ApJ, 362, 274
Moro-Martín, A., Cernicharo, J., Noriega-Crespo, A.,& Martín-Pintado, J. 1999, ApJ, 520, L111
Moro-Martín, A., Noriega-Crespo, A., Böhm, K. H., & Raga, A. C. 1996, RevMexAA, 32, 75
Muench, A. A., Getman, K., Hillenbrand, L., & Preibisch, Th. 2008, in Handbook of Star Forming Regions, ed. B. Reipurth, (Vol. I.; San Francisco: ASP), 483
Mundt, R., & Hartmann, L. W. 1983, ApJ, 268, 766
Mundt, R., & Witt, A. N. 1983, ApJ, 270, L59
Nisini, B., Bacciotti, F., Giannini, T., Massi, F., Eislöffel, J. Podio, L., & Ray, T. P. 2005, A&A, 441, 159
Noriega-Crespo, A., Böhm, K. H., & Calvet, N. 1991, ApJ, 379, 676
Noriega-Crespo, A., Böhm, K. H., & Raga, A. C. 1989, AJ, 98, 1388
_____. 1990, AJ, 99, 1918
Noriega-Crespo, A., & Garnavich, P. M. 1994, AJ, 108, 1432
Noriega-Crespo, A., Garnavich, P. M., Curiel, S., Raga, A. C., & Ayala, S. 1997, ApJ, 486, L55
Norman, C., & Silk, J. 1979, ApJ, 228, 197
Ogura, K. 1995, ApJ, 450, L23
Ortolani, S., & D'Odorico, S. 1980, A&A, 83, L8
Osterbrock, D. E. 1958, PASP, 70, 3990
Pravdo, S. H., & Angelini, L. 1993, ApJ, 407, 232
Pravdo, S. H., & Chester, T. J. 1987, ApJ, 314, 308
Pravdo, S. H., Feigelson, E. D., Garmire, G., Maeda, Y., Tsuboi, Y., & Bally, J. 2001, Nature, 413, 708

Pravdo, S. H., Rodríguez, L. F., Curiel, S., Cantó, J., Torrelles, J. M., Becker, R. H., & Sellgren, K. 1985, ApJ, 293, L35
Raga, A. C. 1988, ApJ, 335, 820
Raga, A. C., Barnes, P. J., & Mateo, M. 1990, AJ, 99, 1912
Raga, A. C., & Böhm, K. H. 1985, ApJS, 58, 201
_____. 1987, ApJ, 323, 193
Raga, A. C., Cantó, J., Curiel, S., Noriega-Crespo, A., & Raymond, J. C. 1997, RevMexAA, 33, 157
Raga, A. C., Mateo, M., Böhm, K. H., & Solf, J. 1988, AJ, 95, 1783
Raga, A. C., Noriega-Crespo, A., & Velázquez, P. F. 2002, ApJ, 576, L149
Raga, A. C., Taylor, S. D., Cabrit, S., & Biro, S. 1995, A&A, 296, 833
Raga, A. C., & Williams, D. A. 2000, A&A, 358, 701
Ray, T. P., Mundt, R., Dyson, J. E., Falle, S. A. E. G., & Raga, A. C. 1996, ApJ, 468, L103
Raymond, J. C. 1979, ApJS, 39, 1
Raymond, J. C., Blair, W. P., & Long, K. S. 1997, ApJ, 489, 314
Raymond, J. C., Hartmann, L. W., & Hartigan, P. 1988, ApJ, 326, 323
Reipurth, B. 1989, A&A, 220, 249
_____. 2000, AJ, 120, 3177
Reipurth, B., Chini, R., Krügel, E., Kreysa, E., & Sievers, A. 1993b, A&A, 273, 221
Reipurth, B., & Heathcote, S. 1997, in IAU Symp. 182, Herbig-Haro Flows and the Birth of Low Mass Stars, ed. B. Reipurth & C. Bertout (Dordrecht: Kluwer), 3
Reipurth, B., Heathcote, S., Roth, M., Noriega-Crespo, A., & Raga, A. C. 1993a, ApJ, 408, L49
Reipurth, B., Heathcote, S., Yu, K. C., Bally, J., & Rodríguez, L. F. 2000, ApJ, 534, 317
Riera, A., Raga, A. C., Reipurth, B., Amram, P., Boulesteix, J., & Toledano, O. 2005, ReMexAA, 41, 371
Rodríguez, L. F., Ho, P. T. P., Torrelles, J. M., Curiel, S., & Cantó, J. 1990, ApJ, 352, 645
Rodríguez, L. F., Roth, M., & Tapia, M. 1985, MNRAS, 214, 9
Rodríguez, L. F., et al. 2000, AJ, 119, 882
Roth, M., Tapia, M., Rubio, M., & Rodríguez, L. F. 1989, A&A, 222, 211
Schmidt, G. D., & Vrba, F. J. 1975, ApJ, 201, L33
Schwartz, R. D. 1975, ApJ, 195, 631
_____. 1976, PASP, 88, 159
_____. 1978, ApJ, 223, 884
_____. 1981, ApJ, 243, 197
Schwartz, R. D., Schultz, A. S. B., Cohen, M., & Williams, P. M. 1995, ApJ, 446, 318
Schwartz, R. D., et al. 1993, AJ, 106, 740
Snell, R. L., & Edwards, S. 1982, ApJ, 259, 668
Solf, J., & Böhm, K. H. 1991, ApJ, 375, 618
Solf, J., Böhm, K. H., & Raga, A. C. 1988, ApJ, 334, 229
Solf, J., Raga, A. C., Böhm, K. H., & Noriega-Crespo, A. 1991, AJ, 102, 1147
Stanke, T., McCaughrean, M. J., & Zinnecker, H. 2000, A&A, 355, 639
Stone, J. M., & Norman, M. L. 1994, ApJ, 420, 237
Strom, K. M., Strom, S. E., & Kinman, T. D. 1974, ApJ, 191, L93
Strom, S. E., et al. 1985, AJ, 90, 2281
Tapia, M., Roth, M., Carrasco, L., & Ruiz, M. T. 1987, MNRAS, 224, 587
Torrelles, J. M., Cantó, J., Rodríguez, L. F., Ho, P. T. P., & Moran, J. M. 1985, ApJ, 294, L117
Torrelles, J. M., Gómez, J. F., Ho, P. T. P., Anglada, G., Rodríguez, L. F., & Cantó, J. 1993, ApJ, 417, 655
Torrelles, J. M., Gómez, J. F., Ho, P. T. P., Rodríguez, L. F., Anglada, G., & Cantó, J. 1994, ApJ, 435, 290
Torrelles, J. M., Rodríguez, L. F., Cantó, J., Anglada, G., Gómez, J. F., Curiel, S., & Ho, P. T. P. 1992, ApJ, 396, L95
Viti, S., Girart, J. M., Garrod, R., Williams, D. A., & Estalella, R. 2003, A&A, 399, 187
Völker, R., Smith, M. D., Suttner, G., & Yorke, H. W. 1999, A&A, 343, 953
Warren-Smith, R. F., & Scarrot, S. M. 1999, MNRAS, 305, 875
Wolfire, M. G., & Königl, A. 1991, ApJ, 383, 205
Zealey, W. J., Williams, P. M., Sandell, G., Taylor, K. N. R., & Ray, T. P. 1992, A&A, 262, 570
Zinnecker, H., Mundt, R., Geballe, T. R., & Zealey, W. J. 1989, ApJ, 342, 337

J. Cantó: Instituto de Astronomía, Universidad Nacional Autónoma de México, Apdo. Postal 70-264, 04510 México, D. F., Mexico.
M. V. Guzmán: Instituto Finlay, P. O. Box 16017, Cod. 11600, La Habana, Cuba (mvguzman@finlay.edu.cu).
A. C. Raga and M. M. Sierra-Flores: Instituto de Ciencias Nucleares, Universidad Nacional Autónoma de México, Apdo. Postal 70-543, 04510, México, D. F., Mexico (raga, sierra@nucleares.unam.mx).
B. Reipurth: Institute for Astronony, University of Hawaii at Manoa, 640 N. Aohoku Place, Hilo, HI 96720, USA (reipurth@ifA.Hawaii.Edu).

Revista Mexicana de Astronomía y Astrofísica, **47**, 439–440 (2011)

OBITUARY

JOHN PETER PHILLIPS
1949–2011

If we wanted to describe Peter using only two words we might choose "Indefatigable Scientist", his incredible productivity would certainly bear it out. But we would be forced to add: good friend, admired teacher, loving husband, a human being of many qualities, an enthusiast of classical music and archaeological sites, and many other interests besides.

He started his research career in his native England, obtaining his PhD in Astrophysics in Imperial College (University of London) in 1978. Afterwards he worked in various postdoctoral positions, holding Research Fellowships in Imperial, Queen Mary College (University of London) and the European Space Agency, ESTEC, Netherlands. He was a Visiting Professor in the Instituto de Astrofísica de Canarias, Spain before relocating to Mexico to work in the Instituto Nacional de Astrofísica, Óptica y Electrónica, Puebla, where he met Maru, his wife for 14 years, with whom he lived a happy and full life.

In 1997 he moved to Guadalajara, Mexico, where he created a research group in Astrophysics based in the Instituto de Astronomía y Meteorología at the Universidad de Guadalajara. He continued to work there for the rest of his life as a *Profesor Investigador Titular B* and the head of the group.

In Guadalajara he enjoyed one of the most successful periods of his academic life, publishing approximately 70 papers in international refereed journals between 2000–2010, and 4 more by April 2011. In total he published more than 150 papers in international refereed journals (more than 200 papers in total) with more than 1600 citations. He was named 'International Scientist of the Year 2004' by the International Biographical Centre of Cambridge, England.

His principal research interest was in planetary nebulae. According to a poster by Jiménez Fragoso in the 2009 National Astronomy Conference (Mexico) he was the world's 4th most productive researcher in this field. He made many important contributions, such as determinations of PNe distances, and radial density profiles. His other areas of interest included star formation, HII regions, supernova remnants and galaxies such as M82. He also analyzed large samples of such objects using new data from *Spitzer* and *Akari*.

Peter was from the county of Yorkshire in the north of England and displayed all the traditional grit and determination of Yorkshire people in his efforts to create, support and expand the new group of astronomers in Guadalajara, which now has 6 researchers included in the Mexican National System of Researchers. He was very proud to be awarded level III in this System in 2010, although sadly had little time to enjoy this distinction.

He supervised two successful PhD students in Spain and one in Mexico; one more student is now well advanced in his thesis. His students learnt an enormous amount from him, and his daily and constant supervision demanded the best work from them and their continuous improvement.

Although he liked to work in a quiet environment, he had a loud voice and a strong and contagious laugh; he was good company on social occasions, although he often preferred to work. There were many times when he told us the rather improbable story that when he was studying for his PhD in Imperial College he knew the musician Brian May, at that time a fellow student of his doing a PhD in infrared astronomy, who invited him to be keyboard player in the group Queen (Peter did not accept).

He died on 29 April 2011, at the age of 61, leaving his wife, Maru, and his mother and sister in the UK.

Simon Kemp, Silvana G. Navarro, & Luis J. Corral

Revista Mexicana de Astronomía y Astrofísica, **47**, 441–442 (2011)

OBITUARY

ALFONSO SERRANO
1950–2011

At the Eastern edge of the high altitude plateau known as Altiplano Mexicano, a majestic white structure stands on the summit of a dormant volcano 4600 meters above sea level, seemingly defying Citlaltépetl, the "mountain of the stars". The Large Millimeter Telescope, perceptible on a clear day from a distance of sixty kilometers, is the most visible homage to the man who first conceived it as a necessary step for Mexico to overcome its underdevelopment, and who tirelessly lobbied for this cause until his final breath. Alfonso Serrano Pérez Grovas, an exceptional force in Mexican science, died on the 12th of July 2011. He was a natural leader who followed the vision set by Guillermo Haro, that Mexico had to develop its own technology to achieve progress. This effective political advocate worked in that direction, shaping his destiny and that of his adherents by moving institutions towards the development of large projects, often in contention with colleagues, but always with the underlying belief of the ultimate benefit for Mexican society. A charming personality with a strong temperament and tough negotiating skills, he became well-known in Mexican society, admired and criticized, but seldom ignored.

Born in Mexico on the first day of February 1950, Alfonso made his undergraduate studies at the Universidad Nacional Autónoma de México (UNAM), and obtained his Master's and PhD in England, at the Universities of Cambridge and Sussex, respectively. He returned to Mexico as an active researcher of the Instituto de Astronomía of UNAM, working on the chemical evolution of galaxies. His production encompasses around seventy papers with 1500 citations, shared with the likes of Manuel Peimbert, James Lequeux, Luis Carrasco,

Steve and Karen Strom. However, the main contribution of Alfonso was beyond scientific research itself. In the mid 1980s, around the time I made his acquaintance, Alfonso started the transformation from an off-hand and rebel academic to professor Serrano, seeking and obtaining the position of Director of the Instituto de Astronomía in 1987, the year before the passing of Guillermo Haro. During his term he started promoting the Large Millimeter Telescope (LMT), a 50 meter diameter antenna for millimeter-wave astronomy, a formidable instrument poised to be the largest of its kind in the world and meant to position Mexico at the forefront of research. The proposal, jointly with the University of Massachusetts Amherst (UMass), was attractive but polemical for a scientific community doubtful of the feasibility of a project of this magnitude within Mexico. The opposition was an important factor for Alfonso to move in 1991 from the Instituto de Astronomía to lead the Programa Universitario de Investigación y Desarrollo Espacial at UNAM for a year, during which he promoted the construction of UNAMSAT, a small scientific satellite entirely made in Mexico. After the failed launch of UNAMSAT-1 in 1995, its twin UNAMSAT-2 was successfully sent to orbit from the Russian cosmodrome of Plesetsk and it operated for a year. The engineering team of PUIDE received recognition in Russia, but by then the man who had initiated this space project had moved to Tonantzintla, Puebla.

Alfonso Serrano directed the Instituto Nacional de Astrofísica, Óptica y Electrónica (INAOE), from 1992 to 2001. He took over an institution in critical conditions to raise it to the forefront of Mexican science, developing in a balanced way the areas of astrophysics, optics and electronics. The LMT project was approved by the Consejo Nacional de Ciencia y Tecnología (CONACyT) on the 20th of June 1994, and the high altitude site of volcán Sierra Negra was selected for its installation in February 1997. The design presented by the German company MAN Technologie was chosen in 1998 and construction started at the end of 1999. The thin air of Sierra Negra, or Tliltépetl, proved to be the least of the difficulties that project was to face. The unprecedented initiative of investing tens of millions of dollars in a single scientific project was certain to meet supporters and opponents from the academic arena and beyond. Alfonso's skillfulness moved ahead the project against financial and political adversity, over costs and overruns. His vision of an independent technological development went beyond the LMT, initiating a collaboration with the University of Arizona for casting a large optical mirror that should become the core of the largest optical telescope in Mexico. In his last years he also became a promoter of the Mexican space agency, hopeful of becoming its first director.

An unanticipated burden for the project laid on his natural leadership and work capacity, led him to make inroads within CONACyT, where he was first appointed director of its network of research centers in 1997, whilst still director of INAOE, and then director of scientific research from 2001 to 2003. The combined commitment of heading LMT, INAOE and his CONACyT office proved too much even for this vigorous leader, who from 2003 on concentrated his efforts towards the completion of the telescope. He kept the sole control of the project, which he ran with a polemical management style, challenged by colleagues and scrutinized stringently by Mexican federal agencies. Once more, he overcame the challenges and took the telescope up to its first millimeter-wave observations. Over twenty years after he first raised the flag, on the 17th of June 2011, INAOE and UMass made the joint announcement of the detection of molecular lines in the galaxy M82 with the Redshift Search Receiver instrument of LMT.

Alfonso was admired for his capacity, despite a stressful life, of keeping healthy with good food and wine. At the end, fate was merciless, and a pancreatic cancer took his life within two months of a late diagnostic. His tragic passing occurred three weeks after the observations of high redshift galaxies with LMT. And though Alfonso did see his masterpiece come to life, he still had much to contribute to Mexico. Leadership and patriotism are two words embodying Alfonso's life. He once told me that leaders created spaces; he certainly did so.

Alberto Carramiñana

AUTHOR INDEX

Andernach, H. The nature and origin of Narrow Line AGN activity in a sample of isolated SDSS galaxies. *R. Coziol, J. P. Torres-Papaqui, I. Plauchu-Frayn, J. M. Islas-Islas, R. A. Ortega-Minakata, D. M. Neri-Larios, & H. Andernach.* 361

Ángeles, F. Speckle Interferometry at the Observatorio Astronómico Nacional. III. *V. G. Orlov, V. V. Voitsekhovich, C. A. Guerrero, F. Ángeles, A. Farah Simon, E. Luna, & R. Vázquez Robledo.* 211

Araiza Quijano, M. R. Atmospheric Aerosol Variability over the Region of San Pedro Mártir from MODIS Data. *M. R. Araiza Quijano & I. Cruz-González.* 409

Avila, R. Recalibrated turbulence profiles at San Pedro Mártir. *R. Avila, L. Sánchez, I. Cruz-González, E. Carrasco, & V. M. Castaño.* 75

Avila-Reese, V. On the stellar and baryonic mass fractions of central blue and red galaxies. *A. Rodríguez-Puebla, V. Avila-Reese, C. Firmani, & P. Colín.* 235

Berdnikov, L. N. Space reddenings for fifteen Galactic Cepheids. *D. G. Turner, R. F. MacLellan, A. A. Henden, & L. N. Berdnikov.* 345

Borka Jovanović, V. Temperature, brightness and spectral index of the Cygnus radio loop. *V. Borka Jovanović & D. Urošević.* 159

Branham, R. L., Jr. The Kinematics and Velocity Ellipsoid of the G III Stars. *R. L. Branham Jr.*. 197

Çakırlı, Ö. V1898 Cygni: An interacting eclipsing binary in the vicinity of North America nebula. *A. Dervişoğlu, Ö. Çakırlı, C. İbanoğlu, & E. Sipahi.* 297

Cantó, J. An overview of the observational and theoretical studies of HH 1 and 2. *A. C. Raga, B. Reipurth, J. Cantó, M. M. Sierra-Flores, & M. V. Guzmán.* 425

Cantó, J. The cometary cavity created by an aligned streaming environment/collimated outflow interaction. *D. López-Cámara, A. Esquivel, J. Cantó, A. C. Raga, P. F. Velázquez, & A. Rodríguez-González.* 323

Cardona, O. Wind structure of the Wolf-Rayet star EZ CMa=HD 50896. *A. Flores, G. Koenigsberger, O. Cardona, & L. de la Cruz.* 261

Carey, S. J. An intepretive ballistic model for quasi-symmetric bipolar jet systems. *A. C. Raga, A. Noriega-Crespo, J. C. Rodríguez-Ramírez, V. Lora, K. R. Stappelfeldt, & S. J. Carey.* 289

Carigi, L. H II Regions and the Protosolar Helium, Carbon, and Oxygen Abundances in the Context of Galactic Chemical Evolution. *L. Carigi & M. Peimbert.* 139

Carramiñana, A. Obituary – Alfonso Serrano. *A. Carramiñana.* 441

Carrasco, E. Recalibrated turbulence profiles at San Pedro Mártir. *R. Avila, L. Sánchez, I. Cruz-González, E. Carrasco, & V. M. Castaño.* 75

Castaño, V. M. Recalibrated turbulence profiles at San Pedro Mártir. *R. Avila, L. Sánchez, I. Cruz-González, E. Carrasco, & V. M. Castaño.* 75

Cavichia, O. Planetary nebulae in the inner Milky Way II: the Bulge-Disk transition. *O. Cavichia, R. D. D. Costa, & W. J. Maciel.* 49

Colín, P. Mass and metal ejection efficiency in disk galaxies driven by young stellar clusters of nuclear starburst. *A. Rodríguez-González, A. Esquivel, A. C. Raga, & P. Colín.* 113

Colín, P. On the stellar and baryonic mass fractions of central blue and red galaxies. *A. Rodríguez-Puebla, V. Avila-Reese, C. Firmani, & P. Colín.* 235

Corral, L. J. Obituary – John Peter Phillips. *S. Kemp, S. G. Navarro, & L. J. Corral.* 439

Costa, R. D. D. Kinematic ages of the central stars of planetary nebulae. *W. J. Maciel, T. S. Rodrigues, & R. D. D. Costa.* 401

Costa, R. D. D. Planetary nebulae in the inner Milky Way II: the Bulge-Disk transition. *O. Cavichia, R. D. D. Costa, & W. J. Maciel.* 49

Coziol, R. The nature and origin of Narrow Line AGN activity in a sample of isolated SDSS galaxies. *R. Coziol, J. P. Torres-Papaqui, I. Plauchu-Frayn, J. M. Islas-Islas, R. A. Ortega-Minakata, D. M. Neri-Larios, & H. Andernach.* 361

Cruz-González, I. Atmospheric Aerosol Variability over the Region of San Pedro Mártir from MODIS Data. *M. R. Araiza Quijano & I. Cruz-González.* 409

Cruz-González, I. Recalibrated turbulence profiles at San Pedro Mártir. *R. Avila, L. Sánchez, I. Cruz-González, E. Carrasco, & V. M. Castaño.* 75

De Colle, F. Variable jets with non-top hat ejection cross sections: a model for the knots of the HH 34 jet. *A. C. Raga, A. Noriega-Crespo, P. Kajdic, F. De Colle, D. López-Cámara, & A. Esquivel.* 277

de la Cruz, L. Wind structure of the Wolf-Rayet star EZ CMa=HD 50896. *A. Flores, G. Koenigsberger, O. Cardona, & L. de la Cruz.* 261

Dervişoğlu, A. V1898 Cygni: An interacting eclipsing binary in the vicinity of North America nebula. *A. Dervişoğlu, Ö. Çakırlı, C. İbanoğlu, & E. Sipahi.* 297

Espinosa, A. $uvby-\beta$ photoelectric photometry of the open clusters NGC 6811 and NGC 6830. *J. H. Peña, L. Fox Machado, H. García, A. Rentería, S. Skinner, A. Espinosa, & E. Romero.* 309

Esquivel, A. Mass and metal ejection efficiency in disk galaxies driven by young stellar clusters of nuclear starburst. *A. Rodríguez-González, A. Esquivel, A. C. Raga, & P. Colín.* 113

Esquivel, A. The cometary cavity created by an aligned streaming environment/collimated outflow interaction. *D. López-Cámara, A. Esquivel, J. Cantó, A. C. Raga, P. F. Velázquez, & A. Rodríguez-González.* 323

Esquivel, A. Variable jets with non-top hat ejection cross sections: a model for the knots of the HH 34 jet. *A. C. Raga, A. Noriega-Crespo, P. Kajdic, F. De Colle, D. López-Cámara, & A. Esquivel.* 277

Farah Simon, A. Speckle Interferometry at the Observatorio Astronómico Nacional. III. *V. G. Orlov, V. V. Voitsekhovich, C. A. Guerrero, F. Ángeles, A. Farah Simon, E. Luna, & R. Vázquez Robledo.* 211

Firmani, C. On the stellar and baryonic mass fractions of central blue and red galaxies. *A. Rodríguez-Puebla, V. Avila-Reese, C. Firmani, & P. Colín.* 235

Flores, A. Wind structure of the Wolf-Rayet star EZ CMa=HD 50896. *A. Flores, G. Koenigsberger, O. Cardona, & L. de la Cruz.* 261

Flores-Gutiérrez, J. D. A variant of the Titius-Bode Law. *J. D. Flores-Gutiérrez & C. García-Guerra.* 173

Fox Machado, L. $uvby-\beta$ photoelectric photometry of the open clusters NGC 6811 and NGC 6830. *J. H. Peña, L. Fox Machado, H. García, A. Rentería, S. Skinner, A. Espinosa, & E. Romero.* 309

García, H. $uvby-\beta$ photoelectric photometry of the open clusters NGC 6811 and NGC 6830. *J. H. Peña, L. Fox Machado, H. García, A. Rentería, S. Skinner, A. Espinosa, & E. Romero.* 309

García-Guerra, C. A variant of the Titius-Bode Law. *J. D. Flores-Gutiérrez & C. García-Guerra.* 173

Gómez, Y. ERRATUM. *C. Neria, Y. Gómez, & L. F. Rodríguez.* 193

Grosso, M. Spectral morphology and rotation in the open cluster NGC 6025. *M. Grosso & H. Levato.* 255

Guerrero, C. A. Speckle Interferometry at the Observatorio Astronómico Nacional. III. *V. G. Orlov, V. V. Voitsekhovich, C. A. Guerrero, F. Ángeles, A. Farah Simon, E. Luna, & R. Vázquez Robledo.* 211

Guerrero, C. A. $uvby-\beta$ Photoelectric Photometry of the Open Clusters NGC 1647 and NGC 1778. *C. A. Guerrero, J. H. Peña, & J. P. Sareyan.* 185

Guzmán, M. V. An overview of the observational and theoretical studies of HH 1 and 2. *A. C. Raga, B. Reipurth, J. Cantó, M. M. Sierra-Flores, & M. V. Guzmán.* 425

Henden, A. A. Space reddenings for fifteen Galactic Cepheids. *D. G. Turner, R. F. MacLellan, A. A. Henden, & L. N. Berdnikov.* 345

Hiriart, D. *UBVR* polarimetry of high-galactic latitude carbon stars. *J. M. López & D. Hiriart.* 63

Islas-Islas, J. M. The nature and origin of Narrow Line AGN activity in a sample of isolated SDSS galaxies. *R. Coziol, J. P. Torres-Papaqui, I. Plauchu-Frayn, J. M. Islas-Islas, R. A. Ortega-Minakata, D. M. Neri-Larios, & H. Andernach.* 361

İbanoğlu, C. V1898 Cygni: An interacting eclipsing binary in the vicinity of North America nebula. *A. Dervişoğlu, Ö. Çakırlı, C. İbanoğlu, & E. Sipahi.* 297

Kajdic, P. Variable jets with non-top hat ejection cross sections: a model for the knots of the HH 34 jet. *A. C. Raga, A. Noriega-Crespo, P. Kajdic, F. De Colle, D. López-Cámara, & A. Esquivel.* 277

Kemp, S. Obituary – John Peter Phillips. *S. Kemp, S. G. Navarro, & L. J. Corral.* 439

Koenigsberger, G. Wind structure of the Wolf-Rayet star EZ CMa=HD 50896. *A. Flores, G. Koenigsberger, O. Cardona, & L. de la Cruz.* 261

Levato, H. Spectral morphology and rotation in the open cluster NGC 6025. *M. Grosso & H. Levato.* 255

Levato, H. Upper Main Sequence Stars with Anomalous Abundances. The HgMn stars HR 3273, HR 8118, HR 8567 and HR 8937. *C. Saffe, N. Núñez, & H. Levato.* 219

López, J. M. *UBVR* polarimetry of high-galactic latitude carbon stars. *J. M. López & D. Hiriart.* 63

López-Cámara, D. The cometary cavity created by an aligned streaming environment/collimated outflow interaction. *D. López-Cámara, A. Esquivel, J. Cantó, A. C. Raga, P. F. Velázquez, & A. Rodríguez-González.* 323

López-Cámara, D. Variable jets with non-top hat ejection cross sections: a model for the knots of the HH 34 jet. *A. C. Raga, A. Noriega-Crespo, P. Kajdic, F. De Colle, D. López-Cámara, & A. Esquivel.* 277

Lora, V. An intepretive ballistic model for quasi-symmetric bipolar jet systems. *A. C. Raga, A. Noriega-Crespo, J. C. Rodríguez-Ramírez, V. Lora, K. R. Stappelfeldt, & S. J. Carey.* 289

Luna, E. Speckle Interferometry at the Observatorio Astronómico Nacional. III. *V. G. Orlov, V. V. Voitsekhovich, C. A. Guerrero, F. Ángeles, A. Farah Simon, E. Luna, & R. Vázquez Robledo.* 211

Maciel, W. J. Kinematic ages of the central stars of planetary nebulae. *W. J. Maciel, T. S. Rodrigues, & R. D. D. Costa.* 401

Maciel, W. J. Planetary nebulae in the inner Milky Way II: the Bulge-Disk transition. *O. Cavichia, R. D. D. Costa, & W. J. Maciel.* 49

MacLellan, R. F. Space reddenings for fifteen Galactic Cepheids. *D. G. Turner, R. F. MacLellan, A. A. Henden, & L. N. Berdnikov.* 345

Márquez-Lugo, R. A. Mid- and Far-Infrared Photometry of Galactic Planetary Nebulae with the AKARI All-Sky Survey. *J. P. Phillips & R. A. Márquez-Lugo.* 83

Navarro, S. G. Obituary – John Peter Phillips. *S. Kemp, S. G. Navarro, & L. J. Corral.* 439

Neri-Larios, D. M. The nature and origin of Narrow Line AGN activity in a sample of isolated SDSS galaxies. *R. Coziol, J. P. Torres-Papaqui, I. Plauchu-Frayn, J. M. Islas-Islas, R. A. Ortega-Minakata, D. M. Neri-Larios, & H. Andernach.* 361

Neria, C. ERRATUM. *C. Neria, Y. Gómez, & L. F. Rodríguez.* 193

Noriega-Crespo, A. An intepretive ballistic model for quasi-symmetric bipolar jet systems. *A. C. Raga, A. Noriega-Crespo, J. C. Rodríguez-Ramírez, V. Lora, K. R. Stappelfeldt, & S. J. Carey.* 289

Noriega-Crespo, A. Variable jets with non-top hat ejection cross sections: a model for the knots of the HH 34 jet. *A. C. Raga, A. Noriega-Crespo, P. Kajdic, F. De Colle, D. López-Cámara, & A. Esquivel.* 277

Núñez, N. Upper Main Sequence Stars with Anomalous Abundances. The HgMn stars HR 3273, HR 8118, HR 8567 and HR 8937. *C. Saffe, N. Núñez, & H. Levato.* 219

Orlov, V. G. Speckle Interferometry at the Observatorio Astronómico Nacional. III. *V. G. Orlov, V. V. Voitsekhovich, C. A. Guerrero, F. Ángeles, A. Farah Simon, E. Luna, & R. Vázquez Robledo.* 211

Ortega-Minakata, R. A. The nature and origin of Narrow Line AGN activity in a sample of isolated SDSS galaxies. *R. Coziol, J. P. Torres-Papaqui, I. Plauchu-Frayn, J. M. Islas-Islas, R. A. Ortega-Minakata, D. M. Neri-Larios, & H. Andernach.* 361

Pedreros, M. H. The Proper Motion of the Large Magellanic Cloud Revisited. *M. H. Pedreros.* 333

Peimbert, M. H II Regions and the Protosolar Helium, Carbon, and Oxygen Abundances in the Context of Galactic Chemical Evolution. *L. Carigi & M. Peimbert.* 139

Peña, J. H. $uvby - \beta$ Photoelectric Photometry of the Open Clusters NGC 1647 and NGC 1778. *C. A. Guerrero, J. H. Peña, & J. P. Sareyan.* 185

Peña, J. H. $uvby - \beta$ Photoelectric Photometry of the Open Clusters NGC 6811 and NGC 6830. *J. H. Peña, L. Fox Machado, H. García, A. Rentería, S. Skinner, A. Espinosa, & E. Romero.* 309

Phillips, J. P. Mid- and Far-Infrared Photometry of Galactic Planetary Nebulae with the AKARI All-Sky Survey. *J. P. Phillips & R. A. Márquez-Lugo.* 83

Phillips, J. P. Mid-Infrared Observations of Planetary Nebulae detected in the GLIMPSE 3D Survey. *J. A. Quino-Mendoza, J. P. Phillips, & G. Ramos-Larios.* 31

Plauchu-Frayn, I. The nature and origin of Narrow Line AGN activity in a sample of isolated SDSS galaxies. *R. Coziol, J. P. Torres-Papaqui, I. Plauchu-Frayn, J. M. Islas-Islas, R. A. Ortega-Minakata, D. M. Neri-Larios, & H. Andernach.* 361

Quino-Mendoza, J. A. Mid-Infrared Observations of Planetary Nebulae detected in the GLIMPSE 3D Survey. *J. A. Quino-Mendoza, J. P. Phillips, & G. Ramos-Larios.* 31

Raga, A. C. An intepretive ballistic model for quasi-symmetric bipolar jet systems. *A. C. Raga, A. Noriega-Crespo, J. C. Rodríguez-Ramírez, V. Lora, K. R. Stappelfeldt, & S. J. Carey.* 289

Raga, A. C. An overview of the observational and theoretical studies of HH 1 and 2. *A. C. Raga, B. Reipurth, J. Cantó, M. M. Sierra-Flores, & M. V. Guzmán.* 425

Raga, A. C. Mass and metal ejection efficiency in disk galaxies driven by young stellar clusters of nuclear starburst. *A. Rodríguez-González, A. Esquivel, A. C. Raga, & P. Colín.* 113

Raga, A. C. The cometary cavity created by an aligned streaming environment/collimated outflow interaction. *D. López-Cámara, A. Esquivel, J. Cantó, A. C. Raga, P. F. Velázquez, & A. Rodríguez-González.* 323

Raga, A. C. Variable jets with non-top hat ejection cross sections: a model for the knots of the HH 34 jet. *A. C. Raga, A. Noriega-Crespo, P. Kajdic, F. De Colle, D. López-Cámara, & A. Esquivel.* 277

Ramírez, J. M. Kinematics from spectral lines for AGN outflows based on time-independent radiation-driven wind theory. *J. M. Ramírez.* 385

Ramos-Larios, G. Mid-Infrared Observations of Planetary Nebulae detected in the GLIMPSE 3D Survey. *J. A. Quino-Mendoza, J. P. Phillips, & G. Ramos-Larios.* 31

Reipurth, B. An overview of the observational and theoretical studies of HH 1 and 2. *A. C. Raga, B. Reipurth, J. Cantó, M. M. Sierra-Flores, & M. V. Guzmán.* 425

Rentería, A. $uvby-\beta$ photoelectric photometry of the open clusters NGC 6811 and NGC 6830. *J. H. Peña, L. Fox Machado, H. García, A. Rentería, S. Skinner, A. Espinosa, & E. Romero.* 309

Rodrigues, T. S. Kinematic ages of the central stars of planetary nebulae. *W. J. Maciel, T. S. Rodrigues, & R. D. D. Costa.* 401

Rodríguez, L. F. ERRATUM. *C. Neria, Y. Gómez, & L. F. Rodríguez.* 193

Rodríguez-González, A. Mass and metal ejection efficiency in disk galaxies driven by young stellar clusters of nuclear starburst. *A. Rodríguez-González, A. Esquivel, A. C. Raga, & P. Colín.* 113

Rodríguez-González, A. The cometary cavity created by an aligned streaming environment/collimated outflow interaction. *D. López-Cámara, A. Esquivel, J. Cantó, A. C. Raga, P. F. Velázquez, & A. Rodríguez-González.* 323

Rodríguez-Puebla, A. On the stellar and baryonic mass fractions of central blue and red galaxies. *A. Rodríguez-Puebla, V. Avila-Reese, C. Firmani, & P. Colín.* 235

Rodríguez-Ramírez, J. C. An intepretive ballistic model for quasi-symmetric bipolar jet systems. *A. C. Raga, A. Noriega-Crespo, J. C. Rodríguez-Ramírez, V. Lora, K. R. Stappelfeldt, & S. J. Carey.* 289

Romero, E. $uvby-\beta$ photoelectric photometry of the open clusters NGC 6811 and NGC 6830. *J. H. Peña, L. Fox Machado, H. García, A. Rentería, S. Skinner, A. Espinosa, & E. Romero.* 309

Saffe, C. FUNDPAR: A program for Deriving Fundamental Parameters from Equivalent Widths. *C. Saffe.* 3

Saffe, C. Upper Main Sequence Stars with Anomalous Abundances. The HgMn stars HR 3273, HR 8118, HR 8567 and HR 8937. *C. Saffe, N. Núñez, & H. Levato.* 219

Sánchez, L. Recalibrated turbulence profiles at San Pedro Mártir. *R. Avila, L. Sánchez, I. Cruz-González, E. Carrasco, & V. M. Castaño.* 75

Sánchez-Salcedo, F. J. The Parker instability in axisymmetric filaments: final equilibria with longitudinal magnetic field. *F. J. Sánchez-Salcedo & A. Santillán.* 15

Santillán, A. The Parker instability in axisymmetric filaments: final equilibria with longitudinal magnetic field. *F. J. Sánchez-Salcedo & A. Santillán.* 15

Sareyan, J. P. $uvby-\beta$ Photoelectric Photometry of the Open Clusters NGC 1647 and NGC 1778. *C. A. Guerrero, J. H. Peña, & J. P. Sareyan.* 185

Sierra-Flores, M. M. An overview of the observational and theoretical studies of HH 1 and 2. *A. C. Raga, B. Reipurth, J. Cantó, M. M. Sierra-Flores, & M. V. Guzmán.* 425

Sipahi, E. V1898 Cygni: An interacting eclipsing binary in the vicinity of North America nebula. *A. Dervişoğlu, Ö. Çakırlı, C. İbanoğlu, & E. Sipahi.* 297

Skinner, S. $uvby-\beta$ photoelectric photometry of the open clusters NGC 6811 and NGC 6830. *J. H. Peña, L. Fox Machado, H. García, A. Rentería, S. Skinner, A. Espinosa, & E. Romero.* 309

Stappelfeldt, K. R. An intepretive ballistic model for quasi-symmetric bipolar jet systems. *A. C. Raga, A. Noriega-Crespo, J. C. Rodríguez-Ramírez, V. Lora, K. R. Stappelfeldt, & S. J. Carey.* 289

Torres-Papaqui, J. P. The nature and origin of Narrow Line AGN activity in a sample of isolated SDSS galaxies. *R. Coziol, J. P. Torres-Papaqui, I. Plauchu-Frayn, J. M. Islas-Islas, R. A. Ortega-Minakata, D. M. Neri-Larios, & H. Andernach.* 361

Tovmassian, H. M. Missing Seyfert Galaxies. *H. M. Tovmassian & O. Yam.* 357

Turner, D. G. Space reddenings for fifteen Galactic Cepheids. *D. G. Turner, R. F. MacLellan, A. A. Henden, & L. N. Berdnikov.* 345

Turner, D. G. The usefulness of 2MASS JHK_s photometry for open cluster studies. *D. G. Turner.* 127

Urošević, D. Temperature, brightness and spectral index of the Cygnus radio loop. *V. Borka Jovanović & D. Urošević.* 159

Vázquez Robledo, R. Speckle Interferometry at the Observatorio Astronómico Nacional. III. *V. G. Orlov, V. V. Voitsekhovich, C. A. Guerrero, F. Ángeles, A. Farah Simon, E. Luna, & R. Vázquez Robledo.* 211

Velázquez, P. F. The cometary cavity created by an aligned streaming environment/collimated outflow interaction. *D. López-Cámara, A. Esquivel, J. Cantó, A. C. Raga, P. F. Velázquez, & A. Rodríguez-González.* 323

Voitsekhovich, V. V. Speckle Interferometry at the Observatorio Astronómico Nacional. III. *V. G. Orlov, V. V. Voitsekhovich, C. A. Guerrero, F. Ángeles, A. Farah Simon, E. Luna, & R. Vázquez Robledo.* 211

Yam, O. Missing Seyfert Galaxies. *H. M. Tovmassian & O. Yam.* 357